

NAVAL POSTGRADUATE SCHOOL MONTEREY, CALIFORNIA



THESIS

DTIC QUALITY INSPECTED 4

**APPLICATION OF CYCLOSTATIONARY
SIGNAL SELECTIVITY TO THE CARRY-
ON MULTI-PLATFORM GPS ASSISTED
TIME DIFFERENCE OF ARRIVAL
SYSTEM**

by

David Alan Streight

March 1997

Thesis Co-Advisors:

Herschel. H. Loomis, Jr.
Gus K. Lott

Approved for public release; distribution is unlimited.

19970828 052

REPORT DOCUMENTATION PAGE			Form Approved OMB No. 0704-0188	
Public reporting burden for this collection of information is estimated to average 1 hour per response, including the time for reviewing instruction, searching existing data sources, gathering and maintaining the data needed, and completing and reviewing the collection of information. Send comments regarding this burden estimate or any other aspect of this collection of information, including suggestions for reducing this burden, to Washington Headquarters Services, Directorate for Information Operations and Reports, 1215 Jefferson Davis Highway, Suite 1204, Arlington, VA 22202-4302, and to the Office of Management and Budget, Paperwork Reduction Project (0704-0188) Washington DC 20503.				
1. AGENCY USE ONLY (Leave blank)	2. REPORT DATE March 1997	3. REPORT TYPE AND DATES COVERED Engineer's Thesis		
4. TITLE AND SUBTITLE: Application of Cyclostationary Signal Selectivity to the Carry-on Multi-Platform GPS Assisted Time Difference of Arrival System		5. FUNDING NUMBERS		
6. AUTHOR(S) David Alan Streight				
7. PERFORMING ORGANIZATION NAME(S) AND ADDRESS(ES) Naval Postgraduate School Monterey CA 93943-5000		8. PERFORMING ORGANIZATION REPORT NUMBER		
9. SPONSORING/MONITORING AGENCY NAME(S) AND ADDRESS(ES)		10. SPONSORING/MONITORING AGENCY REPORT NUMBER		
11. SUPPLEMENTARY NOTES The views expressed in this thesis are those of the author and do not reflect the official policy or position of the Department of Defense or the U.S. Government.				
12a. DISTRIBUTION/AVAILABILITY STATEMENT Approved for public release; distribution is unlimited.		12b. DISTRIBUTION CODE		
13. ABSTRACT (maximum 200 words) Traditional methods of time difference of arrival (TDOA) determination suffer significantly in environments fraught with co-channel interference and low signal to noise ratios. Cyclostationary signal processing techniques offer solutions to the shortcomings of the traditional TDOA methods. Specifically, the Spectral Coherence Alignment (SPECCOA) method of TDOA determination, developed by the Mission Research Corp. and Statistical Signal Processing Inc., performs exceptionally in very poor signal to noise ratio environments. The Applied Research Lab at the University of Texas at Austin (ARL:UT) has developed a prototype TDOA system, the Carry-on Multi-platform GPS Assisted Time Difference of Arrival System for the Naval Information Warfare Activity. It currently utilizes a traditional complex ambiguity function (CAF) to determine the TDOA(s) between multiple observers and an ARL:UT developed closed form solution for the geolocation of the emitter. The work presented here takes the first step in applying SPECCOA to the ARL:UT system. Coding both SPECCOA and the ARL:UT closed form solution in MATLAB® makes possible a quantitative comparison between the CAF and SPECCOA using ARL:UT real world test signals.				
14. SUBJECT TERMS cyclostationarity, geolocation, time difference of arrival			15. NUMBER OF PAGES 277	
			16. PRICE CODE	
17. SECURITY CLASSIFICATION OF REPORT Unclassified	18. SECURITY CLASSIFICATION OF THIS PAGE Unclassified	19. SECURITY CLASSIFICATION OF ABSTRACT Unclassified	20. LIMITATION OF ABSTRACT UL	

Approved for public release; distribution is unlimited.

**APPLICATION OF CYCLOSTATIONARY SIGNAL SELECTIVITY
TO THE CARRY-ON MULTI-PLATFORM GPS ASSISTED TIME
DIFFERENCE OF ARRIVAL SYSTEM**

David Alan Streight
Lieutenant, United States Navy
B.S., United States Naval Academy, 1990
M.B.A., National University, 1994

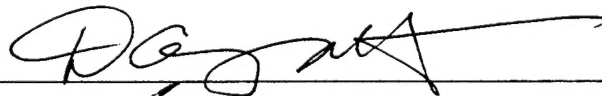
Submitted in partial fulfillment
of the requirements for the degrees of

**MASTER OF SCIENCE IN ELECTRICAL ENGINEERING
and
ELECTRICAL ENGINEER**

from the

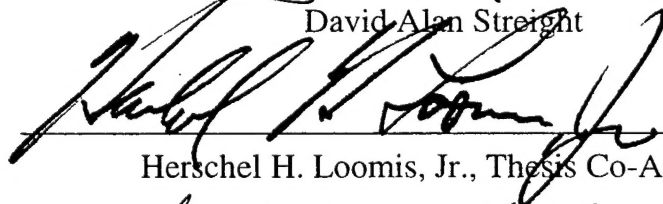
**NAVAL POSTGRADUATE SCHOOL
March 1997**

Author:

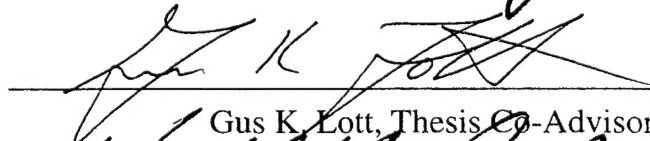


David Alan Streight

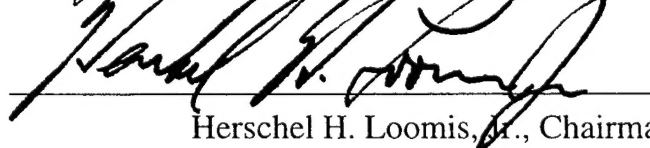
Approved by:



Herschel H. Loomis, Jr., Thesis Co-Advisor



Gus K. Lott, Thesis Co-Advisor



Herschel H. Loomis, Jr., Chairman

Department of Electrical and Computer Engineering

ABSTRACT

Traditional methods of time difference of arrival (TDOA) determination suffer significantly in environments fraught with co-channel interference and low signal to noise ratios. Cyclostationary signal processing techniques offer solutions to the shortcomings of the traditional TDOA methods. Specifically, the Spectral Coherence Alignment (SPECCOA) method of TDOA determination, developed by the Mission Research Corp. and Statistical Signal Processing Inc., performs exceptionally in very poor signal to noise ratio environments. The Applied Research Lab at the University of Texas at Austin (ARL:UT) has developed a prototype TDOA system, the Carry-on Multi-platform GPS Assisted Time Difference of Arrival System for the Naval Information Warfare Activity. It currently utilizes a traditional complex ambiguity function (CAF) to determine the TDOA(s) between multiple observers and an ARL:UT developed closed form solution for the geolocation of the emitter. The work presented here takes the first step in applying SPECCOA to the ARL:UT system. Coding both SPECCOA and the ARL:UT closed form solution in MATLAB® makes possible a quantitative comparison between the CAF and SPECCOA using ARL:UT real world test signals.

24

TABLE OF CONTENTS

I. INTRODUCTION.....	1
A. BACKGROUND	1
B. ORGANIZATION.....	7
II. TRADITIONAL TDOA DETERMINATION.....	9
A. GENERALIZED MODEL.....	9
B. GENERALIZED CROSS CORRELATION	11
C. COMPLEX AMBIGUITY FUNCTION	13
D. PERFORMANCE.....	16
III. CYCLOSTATIONARY TDOA DETERMINATION	19
A. DEFINITIONS.....	19
B. CYCLIC AUTOCORRELATION FUNCTION	22
C. SPECTRAL-CORRELATION FUNCTION	25
D. CYCLOSTATIONARY TDOA SIGNAL MODEL.....	28
E. SPECTRAL COHERENCE ALIGNMENT	30
IV. TDOA GEOLOCATION CLOSED FORM SOLUTION.....	33
A. BACKGROUND	33
B. MATHEMATICAL MODEL	34
C. DETERMINATION OF THE TRANSMITTER STATE VECTOR.....	36
D. ERROR PROPAGATION	39
V. THE CARRY-ON MULTI-PLATFORM GPS-ASSISTED TIME DIFFERENCE OF ARRIVAL SYSTEM	43
A. PROJECT BASIS	43
B. PROJECT OVERVIEW	44
C. HARDWARE DESCRIPTION.....	45
D. ERROR ANALYSIS	48
E. PRELIMINARY TEST RESULTS	49
VI. ALGORITHMS.....	51
A. BACKGROUND	51
B. STRIP SPECTRAL CORRELATION ANALYZER IN MATLAB®.....	52
C. SPECTRAL COHERENCE ALIGNMENT IN MATLAB®	58
D. THE TDOA CLOSED FORM SOLUTION IN MATLAB®	59
VII. TEST PLAN.....	61
A. GENERATED SIGNALS.....	61
B. ARL:UT COLLECTED DATA	71
VIII. GEOLOCATION SOFTWARE WORKBENCH BLOCKS.....	77
A. SIMULINK® BLOCK CONSTRUCTION.....	77
B. SPECCOA BLOCK	77

C. GEOLOCATION BLOCK.....	79
D. SIMULATION SCENARIO.....	79
IX. RESULTS	83
A. BACKGROUND	83
B. TDOA COMPARISON	83
C. GEOLOCATION COMPARISON	87
D. COMMENTS.....	91
X. CONCLUSIONS	93
A. OBSERVATIONS	93
B. AREAS OF FURTHER STUDY	94
LIST OF REFERENCES	97
BIBLIOGRAPHY	99
APPENDIX A	101
APPENDIX B.....	113
INITIAL DISTRIBUTION LIST.....	265

ACKNOWLEDGEMENTS

I would like to extend my gratitude to the members of the ARL:UT project team for their time and effort. Specifically, thanks to Dr. Lisa Giulianelli for acting as my point of contact and providing me with help and motivation along the way. Also thanks to Dr. Petre Rusu for his time and aid with respect to his closed form geolocation solution. Finally, a special thanks to Camille Tucker whose ready answers and endless supply of data made this work possible.

In addition, I must thank Dr. Mike Shields for his loan of powerful computing time and signal processing advice. His generosity reduced the plotting time from weeks to days and facilitated the algorithm testing.

I am also greatly indebted to my advisors, Dr. Herschel H. Loomis Jr. and Dr. Gus K. Lott. Their guidance in all aspects of my education and Naval career has been invaluable. Perhaps their greatest gift was the room they gave me to experiment, fail and try again. I look forward to working with them in the years to come.

I am additionally grateful to the U. S. Navy TENCAP Office for their continued support of signal processing and communications research. This work was funded under the geolocation workbench project, a U. S. Navy TENCAP Office sponsored program.

Finally, I am deeply grateful to my family. To my parents, Jim, Lynda and Carolyn, I have always appreciated your encouragement of my educational pursuits. Your emotional and financial support as well as your babysitting efforts have not gone unnoticed. Lastly and most importantly, to my wife Shannon - this is yours as much mine. Without your infinite patience and unwavering support this would not have been possible, TTDT.

I. INTRODUCTION

A. BACKGROUND

The passive geolocation of electromagnetic (EM) emitters plays an increasingly important role in all three aspects of Information Warfare (IW). In order to protect friendly communications from hostile jamming and interference, information warriors must first locate the source of that jamming and interference. The geolocation of an enemy radar exploits the enemy by gathering information ascertained from his own information gathering system. Finally, in order to attack an enemy communications node, its coordinates must be passed to the strike aircraft or the cruise missile. In addition to its importance in the military arena of IW, passive geolocation of EM emitters finds use in law enforcement surveillance, search and rescue operations, navigation and the enforcement of communications regulations.

Three aspects of EM waves lend themselves to exploitation for geolocation purposes. The path of an EM wave can be closely approximated from transmitter to receiver given the frequency of the transmission and some basic characteristics about the atmosphere through which it traveled. In addition, when EM waves arrive at two moving, spatially separated receivers, the receivers measure different Doppler shifts in the frequency of the transmission. Finally, the time that an EM wave arrived at two spatially separate receivers yields valuable information. These three characteristics naturally enough, are the basis for the three basic methods of geolocation, Angle of Arrival (AOA), Frequency Difference of Arrival (FDOA) and Time Difference of Arrival (TDOA).

AOA geolocation involves the use of highly directional antenna arrays. By measuring the phase difference in the EM wave at each antenna element the receiver can calculate the direction from which the wave emanated. Drawing a line from the precise position of the receiver in this direction yields a vector containing the position of the transmitter called a line of bearing (LOB). Moving the receiver and taking another measurement or using an additional receiver located elsewhere produces another LOB. At the intersection of these LOB(s) is the transmitter. AOA is the oldest of the three methods and has been known by many names throughout the years of its use. Beginning

just prior to World War II, the name most commonly associated with AOA was triangulation. With small measurement errors, the three vectors had a finite width when drawn and thus intersected to form a small triangle within which the emitter was located. This point is illustrated in Figure 1-1 below.

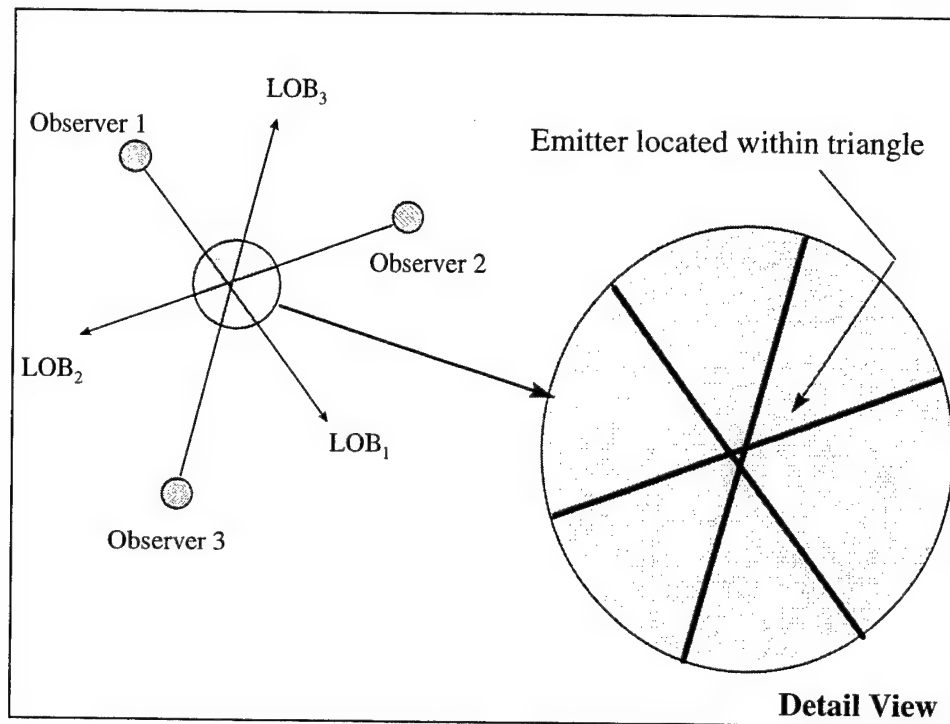


Figure 1-1 - Angle of Arrival geolocation

For moving collectors, the Doppler effect ensures that the receiver will measure a different frequency of arrival than it would as a stationary collector. Given two collectors that measure two different frequencies of arrival (FOA), the difference of these FOAs (FDOA) can be used to determine the position of the emitter. FDOA produces a locus of points called an isodop along which the emitter lies. This isodop represents all the locations from which the EM wave could emanate and produce the difference in Doppler shifts measured between the two receivers. Figure 1-2 shows a two dimensional depiction of a family of FDOA contours in the plane of the paper. Each contour represents a specific FDOA between the observers. The emitter could lie anywhere along the appropriate contour, and thus multiple measurements are required to determine its

location precisely. While these contours can be approximated as two dimensional when the emitter is on the surface of the earth, for an emitter in three dimensions they would be

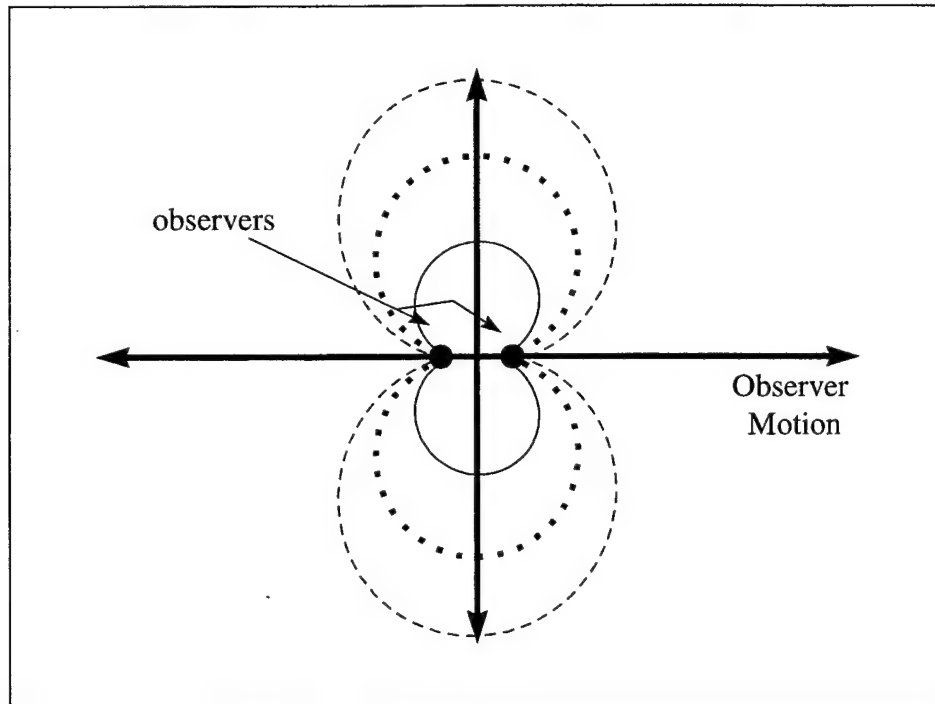


Figure 1-2 - FDOA contours

surfaces. A receiver wishing to use Doppler for geolocation purposes must possess the ability to measure frequency more precisely than the smallest Doppler shift expected. Otherwise, the small Doppler shifts go undetected as they are below the noise in the frequency measurement. This has been the limiting factor in the usage of FDOA for precise geolocation. Measurement of frequency precisely is much more difficult and costly than the measurement of time precisely.

The precise measurement of time has been revolutionized by the high speed digital technology of the Global Positioning System (GPS) and synchronization circuits for atomic time standards. Using the difference in arrival times of an EM wave at two spatially separated receivers, a locus of points called an isochron includes all possible

locations from which the EM wave could emanate and arrive at the two receivers at the two different times measured. In two dimensions, like the situation that approximately

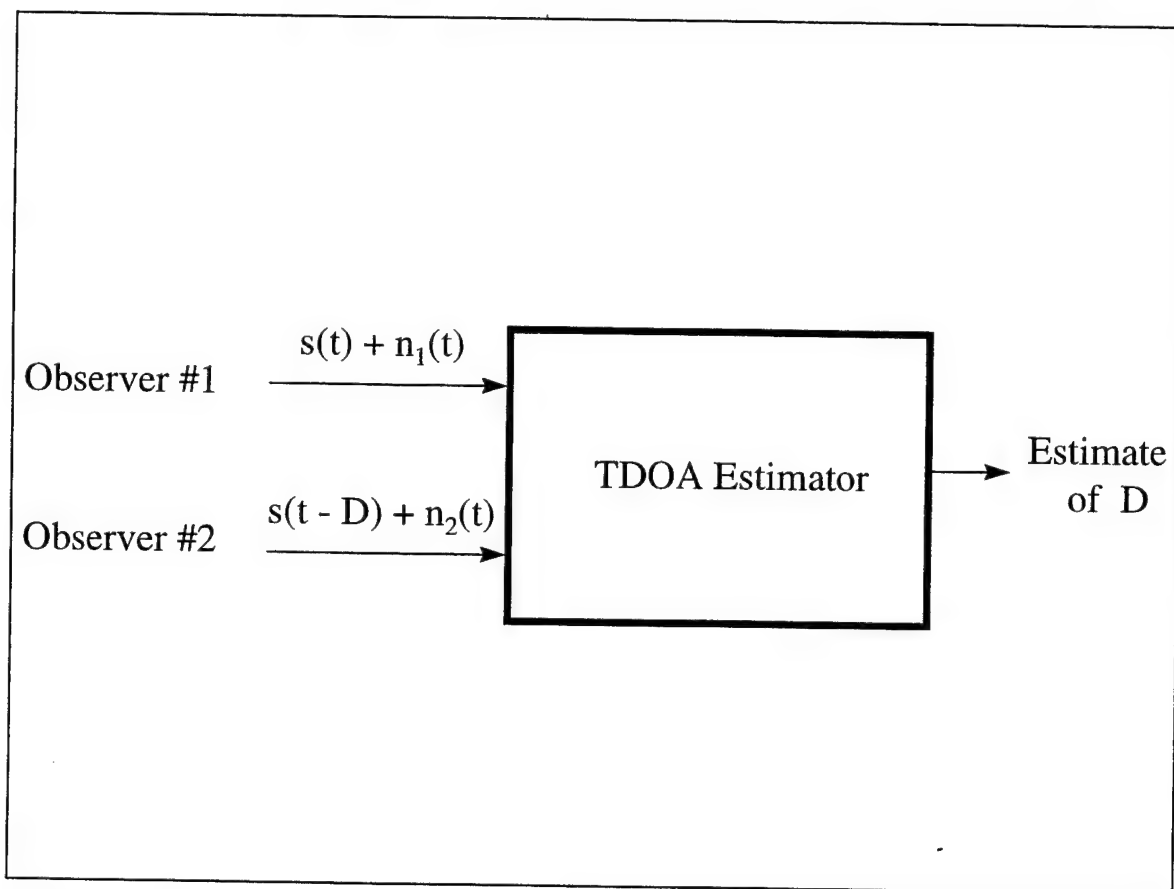


Figure 1-3 - Generic TDOA estimator

exists when an emitter is constrained to the surface of the earth, the isochron can be represented by a hyperbola. In three dimensions, the hyperbola becomes a hyperboloid of revolution. A simple block diagram for a generic TDOA estimator appears in Figure 1-3.

The traditional methods used for TDOA determination include the general cross correlation (GCC) (in the absence of Doppler shift) and the cross ambiguity function (CAF) (both TDOA and FDOA simultaneously). These two methods perform well in benign signal environments. That is, with a signal of interest (SOI) with a high signal to noise ratio (SNR), in the absence of jammers and other signals not of interest (SNOI) in

the frequency band around the signal of interest (SOI), the GCC and CAF methods are superb estimators of TDOA. However, in a peacetime EM spectrum increasingly packed with signals, and a battlespace spectrum potentially flooded with SNOI(s), hostile jamming and weak SOI(s) the GCC and CAF methods suffer from severely decreased signal to noise and interference ratio (SNIR). In light of these weaknesses in hostile environments, a relatively new concept in signal processing called cyclostationarity has been applied to the TDOA problem.

Cyclostationary processes are characterized by time-periodic statistics. A wide-sense cyclostationary signal specifically has a mean and an autocorrelation that vary periodically in time. These periodicities are usually hidden in traditional second order stationary processing techniques such as the autocorrelation function or its frequency domain counterpart, the spectral density function. However, when second order cyclostationary techniques such as the cyclic autocorrelation function and the cyclic spectral density function are used, wide sense cyclostationary signals readily display these hidden periodicities. These periodicities now revealed may be utilized for the detection, classification and parameter estimation of the signal. Among those parameters that may be estimated is the TDOA of a signal impinging upon two spatially separated antennas.

The robustness of the cyclostationary technique for TDOA lies within the fact that every signal has a unique set of periodicities that depend on such parameters as modulation scheme, bit rates and spreading codes. Two signals that may appear as spectrally overlapping in the traditional stationary spectral density function can be separated with great accuracy by the cyclic autocorrelation function. In highly corrupt environments, cyclostationary processing techniques provide the capability to select specific signals for geolocation, nearly independent of the presence of jamming, inference and SNOI(s) that may spectrally overlap the SOI.

The United States Navy has historically relied upon AOA techniques for direction finding. Beginning in the 1950's, the Navy began constructing the High Frequency Direction Finding (HFDF) network of circularly disposed antenna arrays (CDAA). These CDAA(s) consist of a circular array of elements and reflectors that serve to detect the direction of incoming energy. Given the mass of recent base closures, their numbers have

dwindled significantly. In addition, they are not an organic asset for battle group commanders considering the current tactical communications environment that relies less on long-haul HF and more on Very High Frequency (VHF) and Ultra High Frequency(UHF) point-to-point links and Super High Frequency (SHF) satellite communications links.

In addition to the HFDF network, the Navy added the OUTBOARD and OUTBOARD II systems to some of its Spruance-class destroyers. These too are primarily HFDF assets and have been followed by the current construction of COMBAT DF equipped Essex-class amphibious ships and Arleigh Burke-class guided missile destroyers. These three shipboard systems have proven extremely useful during the past years but as they have become the object of intense scrutiny with shrinking ship-building budgets and increasing decommissionings. Consequently, the Naval Security Group Support Activity (NSGSA), in June 1993, contracted with the Applied Research Lab at the University of Texas at Austin (ARL:UT) to develop an affordable, low-risk TDOA/FDOA geolocation system using commercial off the shelf (COTS) and government off the shelf (GOTS) technologies.

The Carry-on Multi-platform Global Positioning System (GPS) Assisted TDOA System was tested for the first time in August 1995 after fifteen months of research and development. In further testing off the coast of San Diego, California, the prototype system geolocated HF, VHF and UHF emitters with a mean square error of approximately 100 meters, using a CAF based TDOA determination algorithm.

As noted above, the CAF has performed exceptionally well in the relatively favorable conditions during prototype testing but in theory, is susceptible to low SNR conditions and co-channel interference. Cyclostationary processing techniques for TDOA determination offer potential improvement to the performance of the ARL:UT system in highly corrupt environments. The evaluation of a cyclostationary TDOA algorithm in conjunction with the closed form geolocation algorithm used in the ARL:UT prototype is the primary objective of the work presented here.

As a secondary objective, the cyclostationary TDOA determination algorithm and the closed form geolocation algorithm will also serve as the first two blocks for testing in

a developing geolocation software workbench at Naval Postgraduate School. The intent is to model the system in the Simulink® environment developed by The Mathworks Inc. and allow different algorithms to be exchanged by merely interchanging the appropriate Simulink® blocks. This will allow for the testing of all aspects of the geolocation problem from data conversion, filtering, AOA, FDOA and TDOA determination and various geolocation solutions.

B. ORGANIZATION

The traditional TDOA determination algorithms, the GCC and the CAF along with their disadvantages in corrupt environments are present in Chapter II. Following the illustration of the vulnerabilities of these two algorithms, the theory of cyclostationarity and TDOA determination by cyclostationary techniques are presented in Chapter III. Chapter IV depicts the closed form solution to the TDOA geolocation problem developed by Dr. Petre Rusu at ARL:UT for the prototype geolocation system which is described in Chapter V.

Chapters VI, VII, VIII and IX constitute the bulk of the investigation, summarizing the new algorithms developed in MATLAB®, the test plan and the results of those tests including the plans for Simulink® block development. Finally, Chapter X draws some conclusions, offers explanations for the anomalies encountered and suggests areas for further research.

II. TRADITIONAL TDOA DETERMINATION

A. GENERALIZED MODEL

For the development of the two traditional methods of TDOA determination, assume a stationary signal from a remote emitter impinges upon two spatially separated antenna elements as illustrated in Figure 2-1. In the presence of additive white Gaussian noise (AWGN) noise, the two signals at receivers 1 and 2 can be modeled as

$$x(t) = s(t) + n_1(t) \quad (2-1)$$

and

$$y(t) = A \cdot s(t - D) + n_2(t) \quad (2-2)$$

where $n_1(t)$ and $n_2(t)$ are assumed to contain only AWGN with no strong SNOI(s) in the frequency band of interest for the SOI, $s(t)$. A represents the complex valued relative magnitude and phase mismatch between the receivers; D is the TDOA of the SOI between the signals.

It follows that the autocorrelation and cross-correlation functions are given by

$$R_x(\tau) = R_s(\tau) + R_{n_1}(\tau) \quad (2-3)$$

$$R_y(\tau) = |A|^2 R_s(\tau) + R_{n_2}(\tau) \quad (2-4)$$

$$R_{yx}(\tau) = A \cdot R_s(\tau - D) + R_{n_1 n_2}(\tau) \quad (2-5)$$

and the respective spectral density functions are

$$S_x(f) = S_s(f) + S_{n_1}(f) \quad (2-6)$$

$$S_y(f) = |A|^2 S_s(f) + S_{n_2}(f) \quad (2-7)$$

$$S_{yx}(f) = A \cdot S_s(f) \cdot e^{-j2\pi f D} + S_{n_1 n_2}(f) \quad (2-8)$$

These relationships contain the parameter of interest, specifically, D , the TDOA. The next two sections show two different methods used to extract D from these equations. The first, the General Cross Correlation (GCC) function, can be used in the absence of relative motion between the two receivers and the emitter. The second, the Complex Ambiguity Function (CAF), can be used to estimate FDOA and TDOA simultaneously as is necessary when relative motion between the receivers and emitter exists.

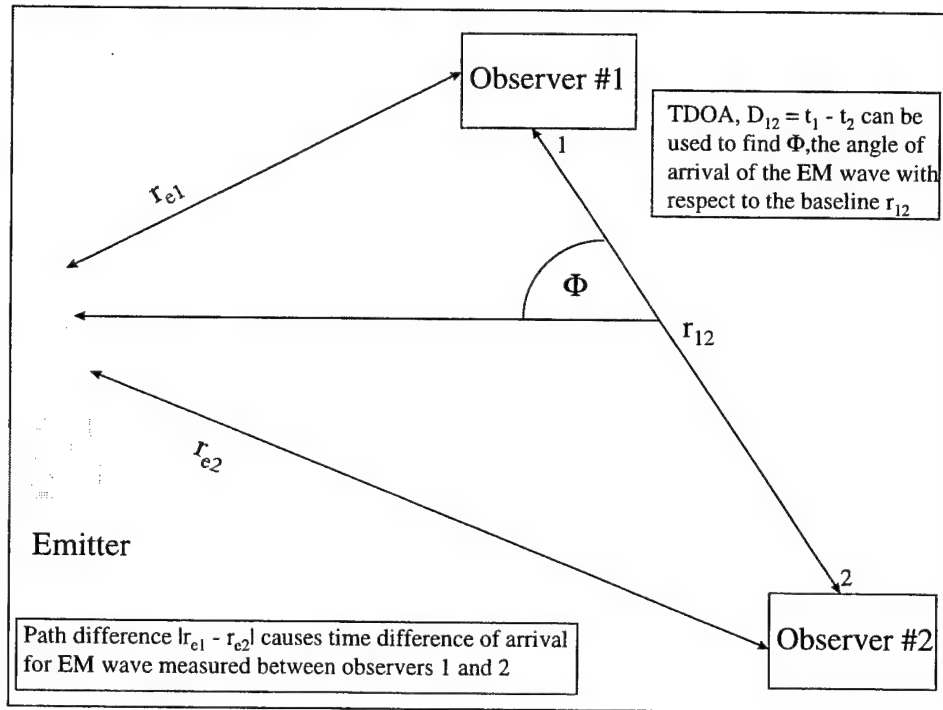


Figure 2-1 - Signal model scenario

Of key importance to the development illustrated here is the statistical independence of $s(t)$, $n_1(t)$ and $n_2(t)$ and the absence of in band interference. While it may be argued that the signals and noise measured at the two receivers can be correlated to some extent, that scenario greatly complicates this case and is beyond the scope of this

demonstration. The derivations that follow are drawn from [1], [2], which treat the GCC more specifically and [3] and [4] which address the CAF more so than the GCC. All assume the three components to be uncorrelated.

B. GENERALIZED CROSS CORRELATION

Applying (2-5) in the absence of SNOI in the SOI band of interest and statistically independent $s(t)$, $n_1(t)$ and $n_2(t)$ yields

$$R_{yx}(\tau) = A \cdot R_s(\tau - D) + R_{n_1 n_2}(\tau) \quad (2-9)$$

This function will peak at $\tau = D$, the TDOA between receivers 1 and 2. Because $n_1(t)$ and $n_2(t)$ contain merely AWGN, their cross-correlation term in (2-9) above reduces the SNR of the measurement but does not add interference in the form of SNOI(s). Further analysis using (2-6) - (2-8) in a similar manner reveals

$$S_x(f) = S_s(f) + S_{n_1}(f) \quad (2-10)$$

$$S_y(f) = |A|^2 S_s(f) + S_{n_2}(f) \quad (2-11)$$

$$S_{yx}(f) = A \cdot S_s(f) \cdot e^{-j2\pi f D} + S_{n_1 n_2}(f) \quad (2-12)$$

To extract D from (2-12), first note

$$S_s(f) = \begin{cases} > 0 & f_o - \frac{B}{2} \leq f \leq f_o + \frac{B}{2} \\ = 0 & \text{otherwise} \end{cases} \quad (2-13)$$

which assumes the SOI effectively occupies a finite bandwidth B around the carrier or intermediate frequency f_o . Taking the ratio of the spectra and using (2-10) with (2-13),

$$\frac{S_{yx}(f)}{S_x(f)} = \begin{cases} A \cdot e^{-j2\pi f D} & f_o - \frac{B}{2} \leq f \leq f_o + \frac{B}{2} \\ 0 & \text{otherwise} \end{cases} \quad (2-14)$$

and taking the inverse Fourier transform of this ratio gives

$$\begin{aligned} h_o(\tau) &= \int_{f_o - B/2}^{f_o + B/2} \frac{S_{yx}(f)}{S_x(f)} e^{+j2\pi f \tau} df \\ &= \frac{A \sin[\pi B(\tau - D)]}{\pi(\tau - D)/2} \cos[2\pi f_o(\tau - D)] \end{aligned} \quad (2-15)$$

which peaks at $\tau = D$. This in turn may be rewritten as

$$h'_o(\tau) = \int_{f_o - B/2}^{f_o + B/2} W(f) S_{yx}(f) e^{+j2\pi f \tau} df \quad (2-16)$$

The weighting function, $W(f)$, is defined in this instance as $1/S_x(f)$ in (2-16) which is the best choice given no a priori information about the SOI [5]. In addition, it distinguishes this case as the generalized cross correlation method. Assigning a weighting function, $W(f) = 1$ reduces the TDOA determination to a simple cross-correlation as in (2-5). Given prior knowledge of the noise and interference characteristics, other choices for $W(f)$ include the Roth impulse, SCOT and PHAT among many others [3] which are designed to reduce specific noise and interference problems.

It is clear that, in the absence of significant noise, co-channel interference and relative motion between receivers and emitter, the GCC produces the desired estimate of the TDOA of a signal from the ratio of the estimates of the spectral density function of the signal at one receiver and the cross spectral density function of the two received signals. Figure 2-2 above illustrates the generalized cross correlation process. The two filters, $H_1(f)$ and $H_2(f)$ are specifically designed to remove out of band interference.

While in practice the GCC is often done in the frequency domain, Figure 2-2 depicts the time domain correlation of the input signals. The processes are theoretically equivalent.

Clearly, the presence of an interference signal in the bandwidth B defining the spectral densities would corrupt the estimate. In addition, as is shown in the next section, Doppler shifts at each receiver also must be accounted for in order to accurately determine TDOA.

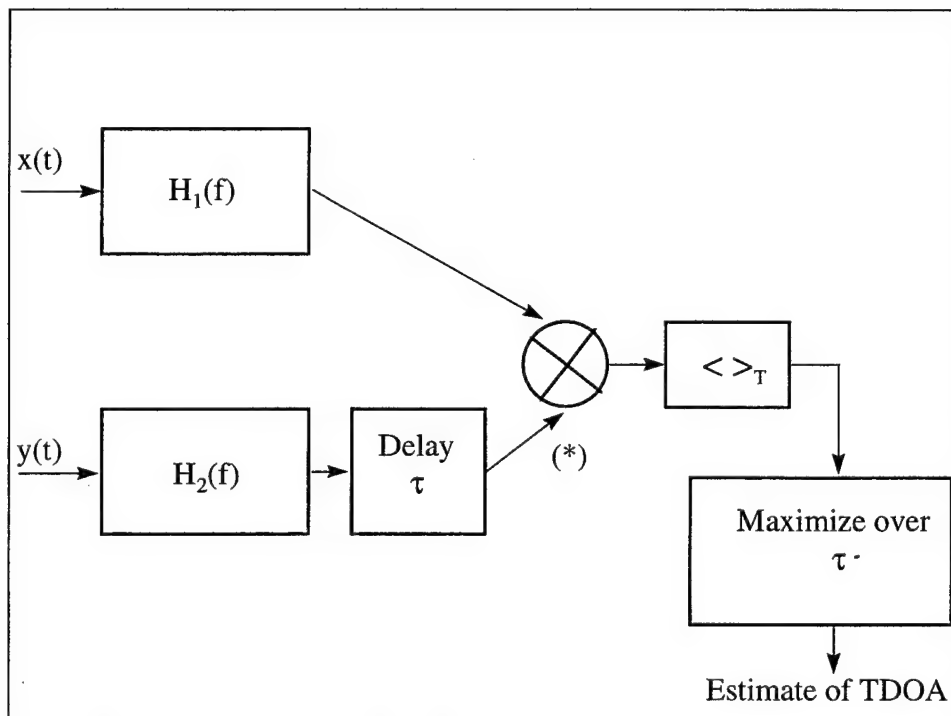


Figure 2-2 - GCC block diagram

C. COMPLEX AMBIGUITY FUNCTION

The complex ambiguity function (CAF) can be interpreted as an extension of the GCC for moving transmitters and/or receivers. Stein in [4], showed that in order to properly determine the TDOA between two receivers in the presence of a Doppler difference at each receiver, the spectrum of one of the signals first must be translated in frequency by an amount f equal to the Doppler difference (FDOA) measured between the

observers. In order to show this, a Doppler shift is introduced into the generalized model from above. Equations (2-1) and (2-2) can now be written as

$$x(t) = s(t) + n_1(t) \quad (2-17)$$

$$y(t) = As(t - D)e^{-j2\pi f_d t} + n_2(t) \quad (2-18)$$

where f_d is the Doppler difference as measured between observer 1 and 2.

Now, in place of calculating TDOA with the two dimensional GCC from (2-16), which in the presence of significant Doppler could peak at a value that does not truly correspond to the TDOA, it is necessary to calculate the three dimensional CAF given by

$$A(D, f_d) = \int_0^T x(t)y^*(t - D)e^{-j2\pi f_d t} dt \quad (2-19)$$

The simultaneous determination of the TDOA D and the Doppler shift f_d causes $|A(D, f_d)|$ to peak. At $f_d = 0$, the CAF reduces to a GCC problem as outlined above. For $f_d \neq 0$, the CAF may be thought of as a GCC performed after frequency shifting the spectrum of $y(t)$ up or down as necessary by an amount equal to f_d . A block diagram of the CAF operation appears in Figure 2-3. Note the similarity between it and the GCC diagram of Figure 2-1.

The three-dimensional width of the correlation lobe is directly proportional to the accuracy of the estimates of TDOA and FDOA. Stein further points out in [4] that the variance of the estimate for each parameter can be related to the noise bandwidth, the signal bandwidth, the integration time and the effective input signal to noise ratio as follows

$$\sigma_{\text{TDOA}} = \frac{1}{\beta} \frac{1}{\sqrt{BT\gamma}} \quad (2-20)$$

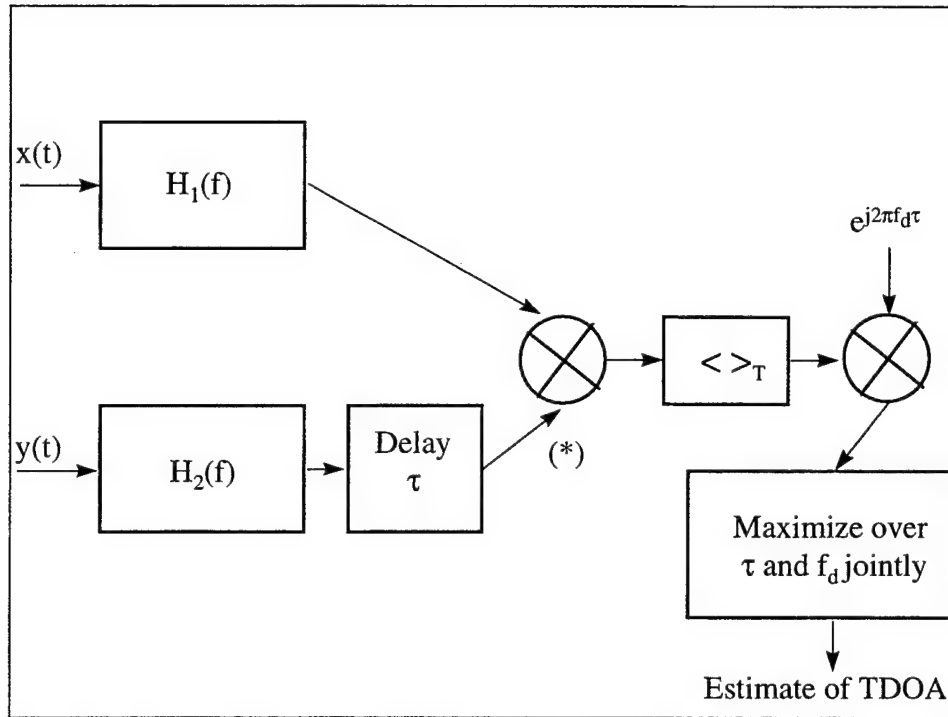


Figure 2-3 - CAF block diagram

$$\sigma_{\text{FDOA}} = \frac{1}{T_e} \frac{1}{\sqrt{BT\gamma}} \quad (2-21)$$

where

B = noise bandwidth at the input of both receivers

$$\beta_{\Delta} = 2\pi \left[\frac{\int_{-\infty}^{+\infty} f^2 W_s(f) df}{\int_{-\infty}^{+\infty} W_s(f) df} \right]^{1/2} \quad (2-22)$$

where $W_s(f)$ is the spectral density of the signal as shaped by the receiver.

T_e = rms integration time

$$\frac{1}{\gamma} = \frac{1}{2} \left[\frac{1}{\gamma_1} + \frac{1}{\gamma_2} + \frac{1}{\gamma_1 \gamma_2} \right] \quad (2-23)$$

where $\frac{1}{\gamma_1}$ and $\frac{1}{\gamma_2}$ are the SNR(s) for each receiver respectively.

D. PERFORMANCE

Given (2-20) and (2-21), it is clear that both the GCC and the CAF can be rendered ineffective by moderate in-band noise. Figure 2-4 below is an illustration of the theoretical standard deviation of a TDOA measurement made at various SNR(s) and integration times. It considers only the errors introduced by AWGN according to the theory presented above and includes no error from any other source such as instrumentation or machine precision for example. Because theory dictates these values as the minimum errors, they may be considered the lower bound for this scenario.

The model for this demonstration assumes a rectangular signal spectrum with rectangular, full bandwidth Gaussian noise with no Doppler between observers. It assumes no magnitude or phase mismatch between receivers and the same SNR at both receivers. It approaches the ideal situation given the perfect match between signal bandwidth, noise bandwidth and receiver measurements. In reality, the signal bandwidth would be more Gaussian or raised cosine pulse shaped and the receivers' measurements would not be matched in phase or magnitude. These differences would corrupt the TDOA estimation further, requiring more SNR and integration time to achieve the lower bounds determined by this idealized model.

Clearly, below approximately 10 dB SNR and 400 ms the idealized model exceeds a TDOA standard deviation of 100 m. Given three TDOA measurements at this level and a simple Euclidean norm combination of these errors, a geolocation derived in the absence of any geometric dilution (see Chapter V) would have a standard deviation on the order of 173 m. This exceeds the 100 m goal of the ARL:UT project without considering the additional errors introduced in an actual system (again see Chapter V).

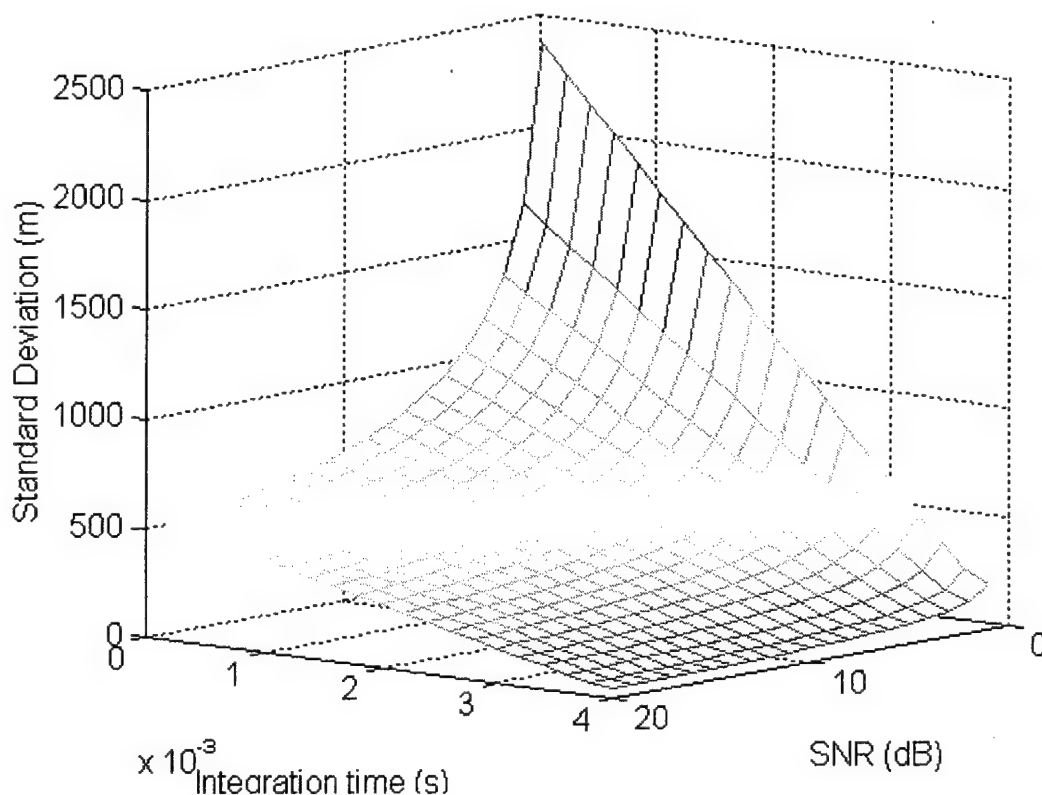


Figure 2-4 - Theoretical standard deviation of TDOA measurement given various SNR(s) and integration times

Poor SNR(s) and SNIR(s) are obviously problematic for the GCC and CAF given the need for geolocation accuracy on the order of 100 m. While increased integration times can solve some low SNR problems, this solution has an upper bound. The integration time must not exceed the coherence of the SOI. That is, the statistics of the SOI must remain relatively stationary during the integration time for the GCC and CAF to operate properly. A significant increase in integration time to combat poor SNR may exceed the coherence time of the SOI and introduce yet more error. Modeling the SOI as cyclostationary vice stationary and employing the appropriate processing techniques can in many cases overcome most of these problems.

Cyclostationary techniques exploit periodicities introduced to man-made signals in a number of ways. These periodicities can be unique to specific signals and thus can be used to distinguish one signal from another in the same bandwidth as well as significantly reduce the level of post-processing noise. Thus, with cyclostationary signal processing, it

is possible to tolerate significantly lower SNR(s) and still obtain excellent TDOA measurements. Chapter III introduces the theory of cyclostationarity in communications signals and develops a method for TDOA determination.

III. CYCLOSTATIONARY TDOA DETERMINATION

A. DEFINITIONS

The concepts of cyclostationarity have been examined in theory for over two decades. Beginning in the late 1960's, Dr. Franks of the University of Massachusetts at Amhurst and Dr. Gardner of the University of California at Davis (UCD) began extensive research in the area of cyclostationary signal processing. Dr. Gardner has since produced multiple publications in the field. His paper on the general theory of cyclostationary signal processing, published in the April 1991 edition of the IEEE Signal Processing Magazine [6], stands as the key reference for most aspects of the theory. As is always the case when one individual has contributed so much to an important engineering development, much of the theory and examples presented here follow Dr. Gardner's work closely. His solo efforts and collaboration with others appear in references [6], [7], [8] and [9] and is redundant in many instances. Where appropriate, the specific source of unique information is referenced below.

As previously noted, most modern signal processing techniques associated with communications applications treat SOI(s) as stationary random processes. However, because most manmade signals are generated through some repetitive, periodic process such as the amplitude, frequency or phase modulation of a sinusoidal carrier, the encoding of data or the encryption of a message, their statistics inevitably vary periodically with time. While in many instances, receivers may successfully ignore the underlying periodicity of a manmade signal, often the detection of the signal and the estimation of its parameters is more successfully accomplished by modeling the signal as cyclostationary vice stationary.

Simply stated, a process with statistics that vary periodically with time is termed cyclostationary. Figure 3-1 depicts a block diagram of the procedure that leads to a cyclostationary signal for most communications processes. A stationary random message such as digital data or analog voice is modulated, clocked or framed by a periodic communications process through some nonlinear system and a cyclostationary signal results.

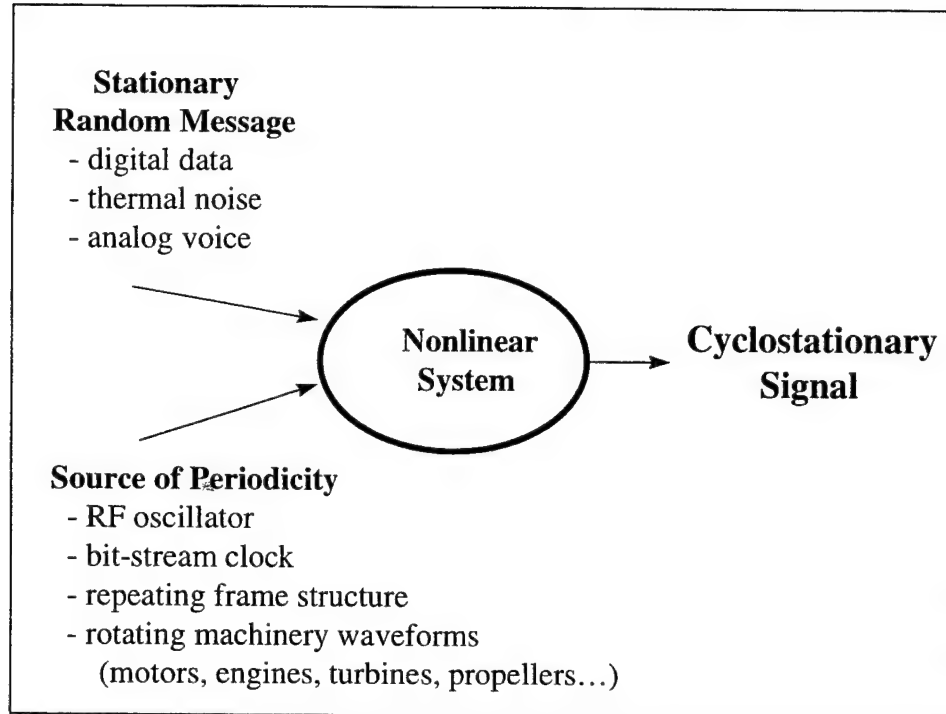


Figure 3-1 - Origins of cyclostationarity, adapted from [10]

From a strictly mathematical point of view, a cyclostationary signal of order n is one that will have additive sine-wave components that result in spectral lines for some n^{th} order nonlinear transformation of the signal. In the case of $n = 2$, a signal is said to be second order cyclostationary if a quadratic transformation produces additive sine-wave components that generate spectral lines. This characteristic may be thought of as akin to a process being considered wide sense stationary or stationary through order 2.

To continue the case of $n = 2$ more specifically, a signal $x(t)$ is cyclostationary with cycle frequency α if and only if some of its delay products $y(t) = x(t)x(t - \tau)$ produce a spectral line at frequency α . If not all cycle frequencies α for which $x(t)$ exhibits cyclostationarity are harmonics of a single fundamental frequency, then $x(t)$ is polycyclostationary. Polycyclostationarity implies the existence of more than one periodicity in the statistics of a signal. This in turn implies more than one source of periodicity such as the case when clocked-digital-data phase modulates a sinusoidal carrier in an M-ary phase shift keying scheme [6].

To further illustrate the concept, consider a signal $x(t)$ that contains an additive sine-wave component at frequency α and is of the form

$$a \cos(2\alpha t + \theta) \quad \text{with } \alpha \neq 0 \quad (3-1)$$

The Fourier coefficient defined as

$$M_x^\alpha = \langle x(t) e^{-j2\pi\alpha t} \rangle \quad (3-2)$$

where $\langle \bullet \rangle$ denotes time-averaging, will be non-zero. Note that this is of the form of the common representation of the Power Spectral Density (PSD) of $x(t)$ with a spectral line at $+\alpha$ and its mirror at $-\alpha$. In simple terms, $x(t)$ contains first-order periodicity at frequency α given by

$$|M_x^\alpha|^2 [\delta(f - \alpha) + \delta(f + \alpha)] \quad (3-3)$$

Now, considering contributions to $x(t)$ from other sources, the total signal may be represented as

$$x(t) = a \cos(2\pi\alpha t + \theta) + n(t) \quad (3-4)$$

where $n(t)$ can be thought of as the random energy outside that of the SOI. If $n(t)$ is strong in comparison to the SOI such that it masks the sine-wave components in $x(t)$ from detection during casual inspection of the waveform, then $x(t)$ can be thought of as possessing hidden periodicity. This hidden periodicity can still be exploited by using signal processing techniques such as the PSD function as noted above. However more powerful cyclostationary signal processing techniques are more sophisticated and can unmask periodicities in signals that are hidden even from common traditional techniques like the PSD function.

B. CYCLIC AUTOCORRELATION FUNCTION

Traditionally, a common second order, time-domain statistic used in signal processing is the autocorrelation function given by the quadratic transformation

$$R_{xx}(\tau) = \langle x(t)x(t-\tau) \rangle \quad (3-5)$$

In the case of a signal that can be modeled as cyclostationary, this transform will produce spectral lines at non-zero frequencies a such that

$$M_y^\alpha = \langle y(t)e^{-j2\pi\alpha t} \rangle \neq 0 \quad (3-6)$$

where

$$y(t) = x(t)x(t-\tau) \quad (3-7)$$

This signal $x(t)$ as noted above contains second order periodicity manifested in the PSD of the delay product given in equation (3-5) above. Transforming (3-5) into a symmetric delay product and accommodating complex signals as well gives

$$y(t) = x\left(t + \frac{\tau}{2}\right)x^*\left(t - \frac{\tau}{2}\right) \quad (3-8)$$

which forms the basis for the fundamental second order cyclic moment known as the cyclic autocorrelation function:

$$R_x^\alpha(\tau) \triangleq \left\langle x\left(t + \frac{\tau}{2}\right)x^*\left(t - \frac{\tau}{2}\right)e^{-j2\pi\alpha t} \right\rangle \quad (3-9)$$

Of note, the cyclic autocorrelation function assumes the form of the Fourier coefficients of the additive sine-wave components produced by the periodicity of the delay product in (3-6).

Another interpretation of (3-9) is as the traditional stationary autocorrelation function multiplied by a kernel $e^{-j2\pi\alpha t}$ that produces spectral lines at frequencies where the stationary autocorrelation function contains additive sine-wave components indicative of its periodicity. Consequently, for either interpretation, at $\alpha = 0$, the cyclic autocorrelation function reduces to the traditional autocorrelation function.

A final interpretation of the cyclic autocorrelation function can be seen by defining first

$$u(t) = x(t)e^{-j\pi\alpha t} \quad (3-10)$$

and

$$v(t) = x(t)e^{+j\pi\alpha t} \quad (3-11)$$

so that $u(t)$ and $v(t)$ are frequency shifted versions of $x(t)$. Now $R_x^\alpha(\tau)$ can be written

$$R_x^\alpha(\tau) = \left\langle u\left(t + \frac{\tau}{2}\right)v^*\left(t + \frac{\tau}{2}\right) \right\rangle = R_{uv}(\tau) \quad (3-12)$$

which is the cross-correlation of the two versions of $x(t)$ shifted up and down by frequency $\alpha/2$. In other words, the cyclic autocorrelation function may be viewed as the correlation in the time domain between two values of $x(t)$ separated in frequency by α .

Consider as an example, a Binary Phase Shift Keyed (BPSK) signal given by

$$s(t) = A_c d(t) \cos(2\pi f_c t + \phi) \quad (3-13)$$

where $d(t)$ is the binary modulating wave form consisting of positive and negative rectangular pulses given by

$$d(t) = \sum_{n=-\infty}^{\infty} d_n q(t - t_o - nT_b) \quad (3-14)$$

Approximated as a random binary wave, it contains no first order periodicity and thus no spectral lines in its PSD. Consequently, the PSD of the BPSK signal $s(t)$ is a scaled sinc squared function and will also contain no spectral lines as is evident its expression

$$S_{\text{BPSK}}(f) = A_c^2 T_b \left(\frac{\sin \pi f_c T_b}{\pi f_c T} \right)^2 \quad (3-15)$$

Thus, the autocorrelation function of the BPSK signal, the inverse Fourier transform of (3-15), will contain no additive sinusoidal components to indicate any periodicity.

Multiplying the conventional autocorrelation function by the cyclic kernel $e^{-j2\pi\alpha\tau}$, the cyclic autocorrelation function follows as

$$\begin{aligned} R_s^\alpha = & \frac{1}{2T_b} r_q^\alpha(\tau) \cos(2\pi f_c \tau) e^{-j2\pi\alpha\tau_o} \\ & + \frac{1}{4T_b} \left[r_q^{\alpha+2f_c}(\tau) e^{-j2\pi[\alpha+2f_c]\tau_o} + r_q^{\alpha-2f_c}(\tau) e^{-j2\pi[\alpha-2f_c]\tau_o} \right] \end{aligned} \quad (3-16)$$

where

$$r_q^\alpha(\tau) = \int_{-\infty}^{\infty} q\left(t + \frac{\tau}{2}\right) q\left(t - \frac{\tau}{2}\right) e^{-j2\pi\alpha t} dt \quad (3-17)$$

This clearly shows additive sine-wave components at $\alpha = \pm 2f_c \pm R_b$ and $\alpha = \pm R_b$ [9].

Thus, the quadratic transform that is the cyclic autocorrelation function unmasks hidden periodicity in this simple BPSK signal and proves it polycyclostationary in the process.

Naturally, the conventional cross-correlation function and the cyclic cross-correlation functions are related in a similar manner.

C. SPECTRAL-CORRELATION FUNCTION

The frequency domain equivalent for the cyclic autocorrelation function is the spectral correlation function (SCF). It follows directly from the Fourier transform of (3-9) and has the form

$$S_{X_T}^{\alpha}(t, f)_{\Delta t} = \frac{1}{T\Delta t} \int_{t-\Delta t/2}^{t+\Delta t/2} X_T(u, f + \alpha/2) X_T^*(u, f - \alpha/2) du \quad (3-18)$$

where

$$X_T(t, f) = \int_{t-T/2}^{t+T/2} x(u) e^{-j2\pi fu} du \quad (3-19)$$

is the finite-time Fourier transform of $x(t)$. More commonly used in cyclostationary signal processing, the SCF reduces to the conventional PSD at $\alpha = 0$ just as the cyclic autocorrelation function reduced to the conventional autocorrelation function at $\alpha = 0$.

Continuing the BPSK example from above, the SCF can be found directly from (3-17) or by taking the Fourier transform of (3-15). It has the form

$$S_x^{\alpha}(f) = \frac{1}{4T_b} \left[Q\left(f + f_o + \frac{\alpha}{2}\right) Q^*\left(f + f_o - \frac{\alpha}{2}\right) + Q\left(f - f_o + \frac{\alpha}{2}\right) Q^*\left(f - f_o - \frac{\alpha}{2}\right) \right] e^{-j2\pi\alpha t_o}$$

for $\alpha = n/T_b$ and $(3-20)$

$$S_x^{\alpha}(f) = \frac{1}{4T_b} \left[Q\left(f + f_o + \frac{\alpha}{2}\right) Q^*\left(f - f_o - \frac{\alpha}{2}\right) e^{-j2\pi[\alpha + 2f_c]t_o} + Q\left(f + f_o + \frac{\alpha}{2}\right) Q^*\left(f - f_o - \frac{\alpha}{2}\right) e^{-j2\pi[\alpha - 2f_c]t_o} \right]$$

for $\alpha = \pm 2f_c \pm n/T_b$ with $Q(f)$ being the Fourier transform of the keying envelope $q(t)$ [8].

The SCF derives its name from the fact that it is in fact a correlation of the SOI in the frequency domain. The SCF at frequency f_0 and cyclic frequency α_0 is merely the correlation of two values of the signal in the frequency domain separated in frequency by α_0 and centered at frequency f_0 . Figure 3-2 shows this process concept graphically.

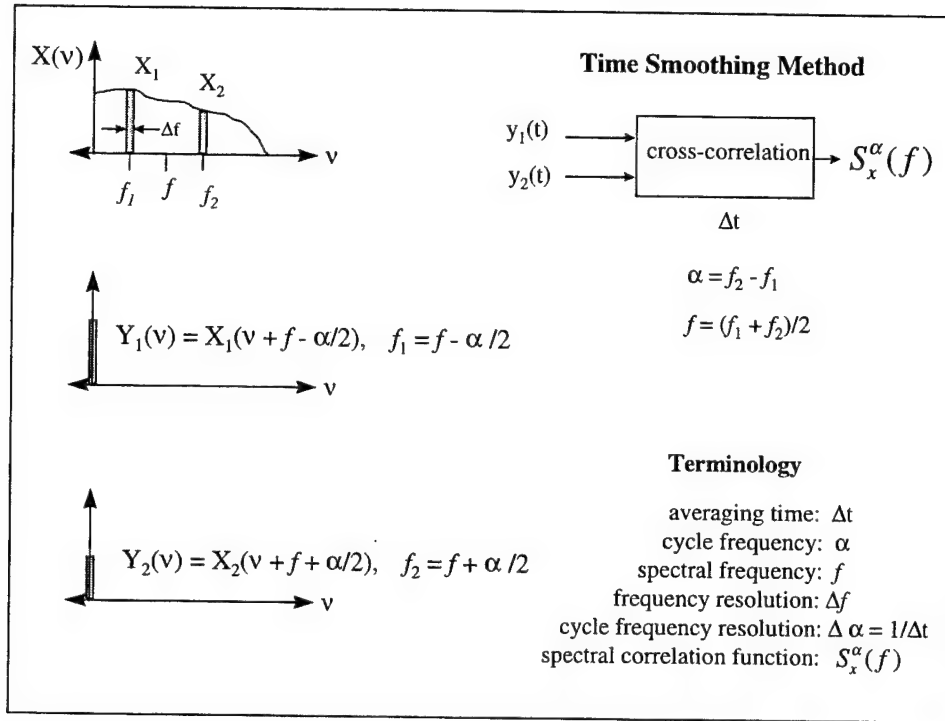


Figure 3-2 - Spectral Correlation Function illustrated, from [10]

The SCF is plotted on what is called the bi-frequency plane. The plane is defined along one axis as spectral frequency f and along the opposing axis as cyclic frequency α . Figure 3-3 illustrates this point. The magnitude of the SCF corresponds to a height above the bi-frequency plane and is often plotted in that fashion. Note that the values for α range from $-f_s$ to f_s while values for spectral frequency f naturally range from $-f_s/2$ to $f_s/2$. Because α corresponds to the separation distance of the correlated values in the frequency domain, its range extends twice that of f .

The SCF computation can be highly complex and demanding on any processor. For that reason, two algorithms were developed in [7] and designed specifically for computation efficiency. The Fast Fourier Transform Accumulation Method (FAM) and

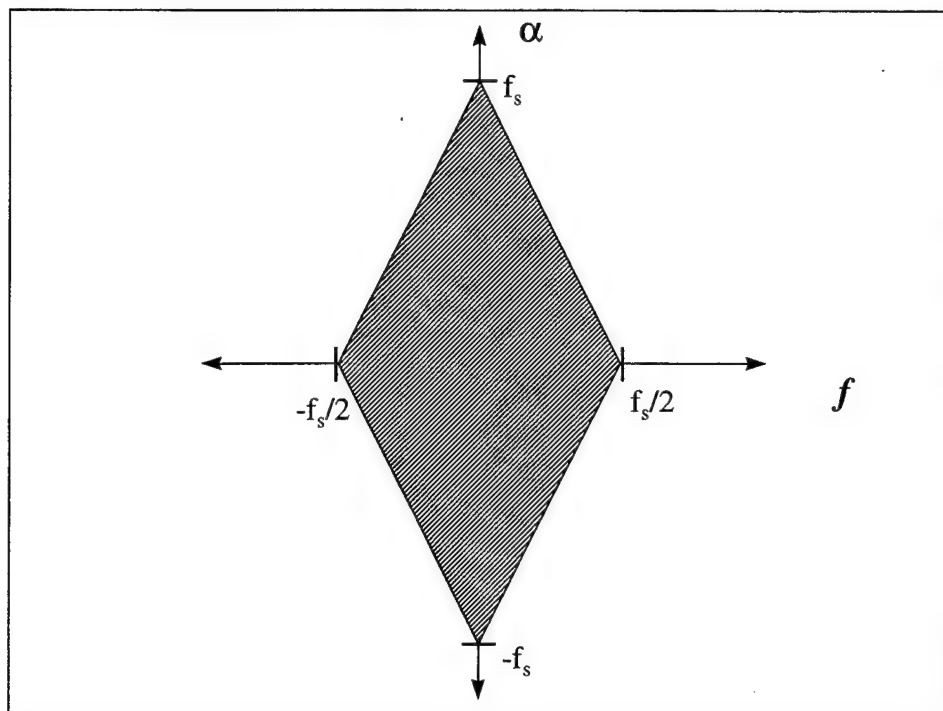


Figure 3-3 - Bi-frequency plane

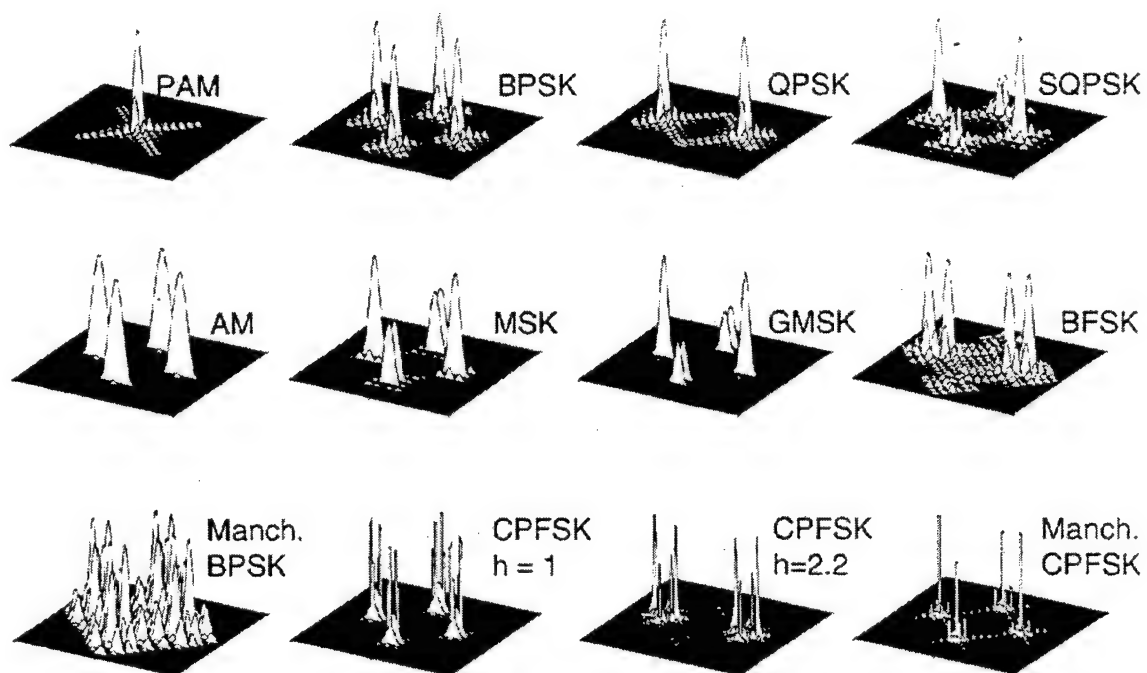


Figure 3-4 - SCF of some common modulated signals, adapted from [10]

the Strip Spectral Correlation Analyzer (SSCA) both simplify and thereby accelerate the computation of the SCF. Because both the SCF and the Cross Spectral Correlation Function (CSCF) are necessary for cyclostationary TDOA algorithms, SSCA plays an important role in this work. It is presented in more detail in Chapter VI.

Finally, in addition to their role in the TDOA computations, the SCF and CSCF can also be used for purposes ranging from signal detection to characterization and estimation of parameters. Specifically, the modulation type of an unknown signal can be found using the SCF of that unknown signal and comparing it to SCF(s) of known modulation type. Figure 3-4 shows a small library of SCF(s) from several more common modulation schemes.

D. CYCLOSTATIONARY TDOA SIGNAL MODEL

The signal model used to develop cyclostationary TDOA algorithms is very similar to that presented in Chapter II. Recall the signals received at two spatially separated observers can be given by (2-1) and (2-2) and are below for clarity

$$x(t) = s(t) + n_1(t) \quad (3-21)$$

and

$$y(t) = A \cdot s(t - D) + n_2(t) \quad (3-22)$$

The difference between the two models lies in the temporal and spectral relationships between $s(t)$, $n_1(t)$ and $n_2(t)$. In Chapter II, $n_1(t)$ and $n_2(t)$ were assumed to have no temporally and spectrally components that overlapped the SOI, $s(t)$. In the cyclostationary TDOA signal model, $n_1(t)$ and $n_2(t)$ represent all SNOI(s) and noise present at the respective observers. They may or may not contain co-channel interferers in reality, however for purposes of this work, they are assumed to contain interference that in fact spectrally overlaps the SOI. Figure 3-5 portrays this situation graphically.

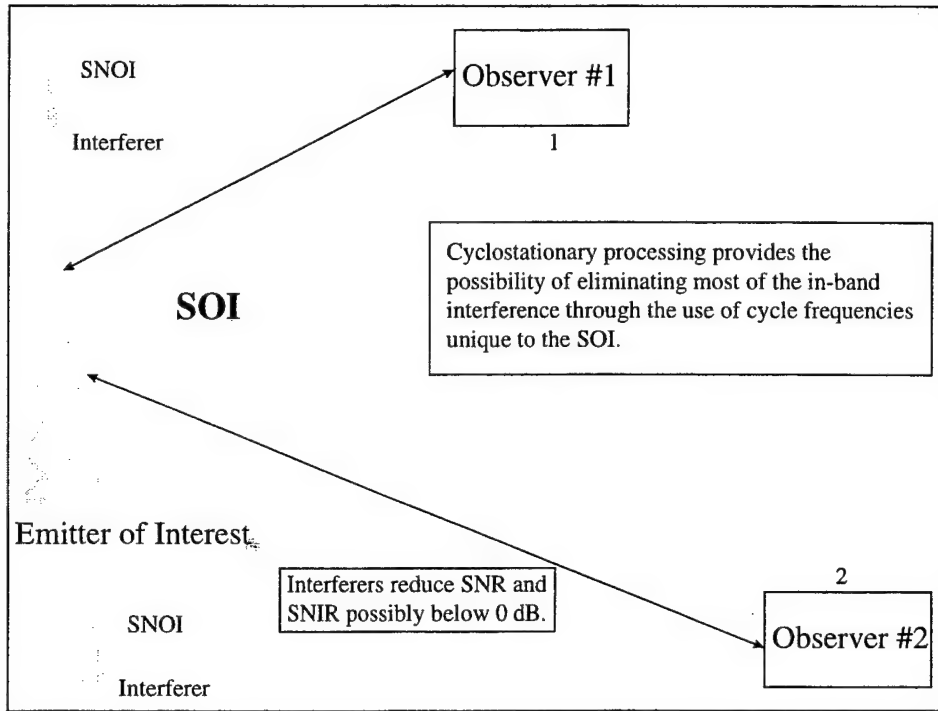


Figure 3-5 - Cyclostationary signal model scenario

Given this model, the cyclic auto and cross-correlation functions in general can be written as

$$R_x^\alpha(\tau) = R_s^\alpha(\tau) + R_{n_1}^\alpha(\tau) \quad (3-23)$$

$$R_y^\alpha(\tau) = |A|^2 R_s^\alpha(\tau) e^{-j2\pi\alpha D} + R_{n_2}^\alpha(\tau) \quad (3-24)$$

$$R_{yx}^\alpha(\tau) = A R_s^\alpha(\tau - D) e^{-j\pi\alpha D} + R_{n_1 n_2}^\alpha(\tau) \quad (3-25)$$

just as (2-3) - (2-5) represented the conventional auto and cross-correlation functions. In addition, as with (2-6) - (2-8), the spectral correlation functions are

$$S_x^\alpha(f) = S_s^\alpha(f) + S_{n_1}^\alpha(f) \quad (3-26)$$

$$S_y^\alpha(f) = |A|^2 S_s^\alpha(f) e^{-j2\pi\alpha D} + S_{n_2}^\alpha(f) \quad (3-27)$$

$$S_{yx}^\alpha(f) = A S_s^\alpha(f) e^{-j2\pi(f+\alpha/2)D} + S_{n_1 n_2}^\alpha(f) \quad (3-28)$$

Though (3-26) - (3-28) contain the TDOA of the signal D , this parameter is now masked by the spectrally overlapping components of $n_1(t)$ and $n_2(t)$. Thus, any attempt to estimate D with traditional methods that compute the above equations at $\alpha = 0$, like those illustrated in Chapter II, would result in a corrupted value. However, if $s(t)$ contains some cycle frequency, α_0 , that it does not share with any component of $n_1(t)$ and $n_2(t)$, then cyclostationary techniques can discriminate those contributions to D made by $s(t)$ from those contributions of $n_1(t)$ and $n_2(t)$ that would otherwise corrupt the estimate. Essentially this eliminates the SNOI(s). Thus a reliable estimate of D is possible even in highly corrupt environments provided a unique α exists for the SOI. Spectral Coherence Alignment is a cyclostationary TDOA algorithm employing measurements of both the SCF and CSCF. It determines the TDOA(s) for the TDOA processor developed here and appears in detail below.

E. SPECTRAL COHERENCE ALIGNMENT

Spectral Coherence Alignment (SPECCOA) was developed and presented in [8] using an ad hoc minimum least squares (MLS) approach. Using equations (3-23) - (3-25), and the assumption that $s(t)$ contains a unique α , it can be seen that

$$R_{yx}^\alpha(u) = C R_x^\alpha(u - D) e^{-j\pi\alpha D} \quad (3-29)$$

The cross-correlation term for $n_1(t)$ and $n_2(t)$ is eliminated by the use of a cycle frequency unique only to the SOI. An estimate of the TDOA, \hat{D} that minimizes the sum of the squares of error magnitudes between the measured value of the left side of (3-29), R_{yx}^α

and the measurement of the right side of (3-29), R_x^α with \hat{D} substituted yields the MLS optimized value for the TDOA.

Mathematically, from [8],

$$\hat{D} = \arg \min_{\hat{c}, \tau} \left\{ \hat{c}_\alpha(\tau) \right\} \quad (3-30)$$

where $\hat{c}_\alpha(\tau)$ is the estimate of the MLS function. It was further be shown in [8], that the solution of the MLS problem is of the form

$$\hat{D} = \arg \max_{\tau} \left\{ \hat{c}_\alpha(\tau) \right\} \quad (3-31)$$

where

$$\hat{c}'_\alpha(\tau) = \left| \int R_{yx}^\alpha(u) R_x^\alpha(u - \tau)^* du \right| \quad (3-32)$$

$$= \left| \int S_{yx}^\alpha(f) S_x^\alpha(f)^* e^{j2\pi f \tau} df \right| \quad (3-33)$$

where (3-33) derives from (3-32) through Parseval's relation. Gardner and Chen go on to further prove that (3-33) does indeed peak at $\tau = D$.

SPECCOA derives its name from the fact that the peak in (3-33) occurs by maximizing the correlation in f of the two *spectral* correlation functions through the *alignment* of the phases of the respective functions.

SPECCOA proves more useful in tactical applications than other cyclic TDOA algorithms (see [5] and [9]) by virtue of its ease of implementation and performance in corrupt environments [9]. Though other cyclostationary algorithms consistently outperform SPECCOA [5], they do so at the expense computational complexity and speed. Because this work is intended to demonstrate the feasibility of implementing a cyclostationary TDOA algorithm in an operational tactical system, SPECCOA was the logical choice for its efficiency and performance. Chapter IV discusses the algorithm

which utilizes TDOA(s) to determine the geolocation of an emitter. Chapter V presents the ARL:UT prototype TDOA geolocation system. Chapter VI contains specific implementation issues for SPECCOA in the MATLAB® environment.

IV. TDOA GEOLOCATION CLOSED FORM SOLUTION

A. BACKGROUND

Given the TDOA(s) from pairs of receivers, the problem now lies in determining the location of the transmitter from the intersection of the isochrons generated. Many distinct methods appear from the geometric interpretation of Schau and Robinson in [11] to the iterative solution proposed by Loomis in [12] and the closed form solution illustrated by Ho and Chen in [13]. While somewhat similar, they all take a specific course in determining the location of the transmitter given the determined case. What becomes more difficult for each of these solutions is the determination of the contribution of errors in the measurement of the TDOA(s) to the final result, the geolocation.

In [14], Rusu develops a closed form solution avoiding the initial guesswork involved in an iterative technique. Unlike [13], his solution is completely general. In addition, he shows that the errors in the measurements may be propagated through the mathematical model in a linear fashion, simplifying the determination of uncertainty in the geolocation. The following development draws exclusively from his derivation.

The problem of determining the location of an emitter in three dimensions given the times of arrival (TOA) at four spatially separated receivers has often been treated as a TDOA problem. That is, time is treated as absolute time. However, as Rusu points out, the mathematical model is invariant to time translation and thus may be treated as a TOA problem by setting the arrival time at any one of the receivers as the origin of the problem, $t = 0$. This simplification without loss of generality facilitates the development of linear error propagation from the initial measurements through the mathematical model to the final result as noted above.

In the presence of moving emitters or receivers, both TDOA and FDOA must be determined by one process as shown in the development of the CAF in Chapter II. The case of FDOA can be similarly simplified by assigning a Doppler shift of zero to one of the receivers reducing the problem to one of frequencies of arrival (FOA). Fortunately, given the independence of the TOA portion of the model from the frequency of transmission and Doppler shifts, the TOA and FOA equations may be treated separately.

Though TDOA is the emphasis of this thesis, for completeness both the TOA and the FOA solutions will be developed here.

B. MATHEMATICAL MODEL

The explicit functional model relating the observable \mathbf{X} to the dependent variable of interest \mathbf{Y} , in the TOA case is the solution of the set of scalar equations of the form $\mathbf{F}(\mathbf{X}, \mathbf{Y}) = 0$. \mathbf{F} may be referred to as the implicit functional model, \mathbf{X} the independent variable and \mathbf{Y} the dependent variable. In the development of the TOA-FOA problem, \mathbf{X} is a 32-dimensional real vector state space of observations while \mathbf{Y} is an 8-dimensional status vector state space. Figure 4-1 illustrates the scenario in general.

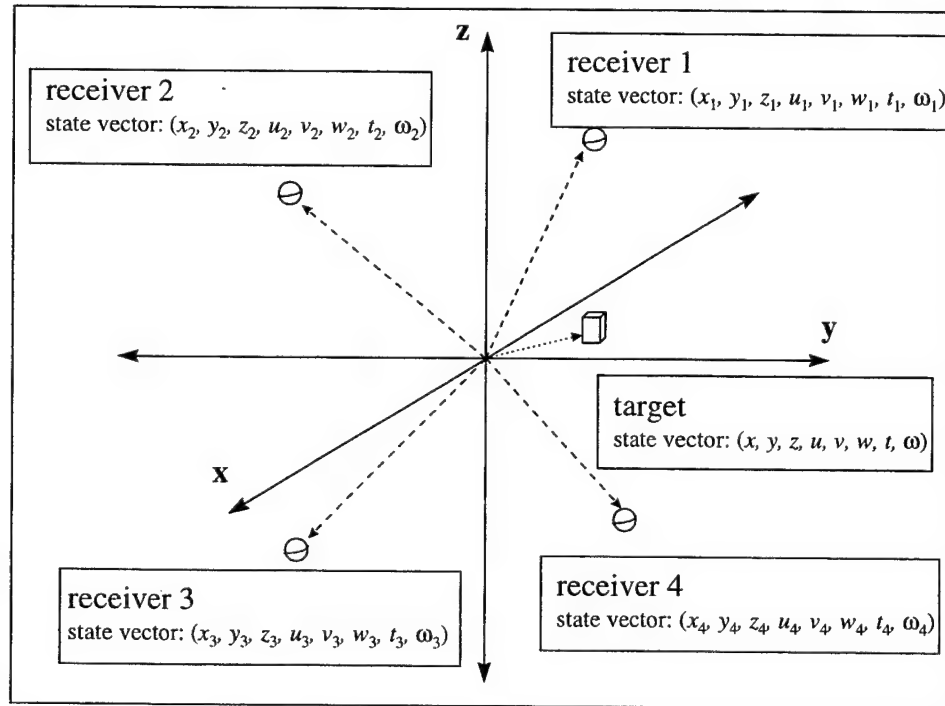


Figure 4-1 - TDOA model

The TOA-FOA case assumes that the i -th receiver located at $\mathbf{r}_i = (x_i, y_i, z_i)$ and moving with velocity $\mathbf{v}_i = (u_i, v_i, w_i)$ detects a signal at time t_i with frequency ω_i . Four observers for the determined 3-dimensional case, constitute the observation state space

vector of 32-dimensions. The parameters of the transmitter, its location and velocity given by $\mathbf{r} = (x, y, z)$ and $\mathbf{v} = (u, v, w)$ respectively, its transmit time t and frequency ω compose the 8-dimesional status vector state space.

The fundamental equation relating the signal travel time to the separation distance between observer i and an emitter assuming the signal travels at the speed of light is

$$\sqrt{(x_i - x)^2 + (y_i - y)^2 + (z_i - z)^2} = c(t_i - t) \quad (4-1)$$

where $\sqrt{(x_i - x)^2 + (y_i - y)^2 + (z_i - z)^2}$ is the Euclidean distance between \mathbf{r}_n and \mathbf{r} denoted hereafter by $\|\mathbf{r}_n - \mathbf{r}\|$ and c is the speed of light. Forming appropriate vectors using a single equation to include all four observers produces the implicit functional TOA model

$$F_i(\mathbf{X}, \mathbf{Y}) = \|\mathbf{r}_i - \mathbf{r}\| - c(t_i - t), \quad i = 1, 2, 3, 4. \quad (4-2)$$

Simple algebraic transformation leads to

$$\left[(x_i - x)^2 + (y_i - y)^2 + (z_i - z)^2 - (t_i - t)^2 \right]^{\frac{1}{2}} = 0, \quad i = 1, 2, 3, 4. \quad (4-3)$$

In vector form the TOA equations are defined as $\mathbf{F}_T = (F_1, F_2, F_3, F_4)$.

The Doppler equations can be similarly treated. The fundamental relationship between the Doppler shift observed by receiver n and the relative velocities of the emitter and observer is

$$\omega_d = \omega \left(\frac{\mathbf{v}_n - \mathbf{v}}{c} \right) \cdot \frac{\mathbf{r}_n - \mathbf{r}}{\|\mathbf{r}_n - \mathbf{r}\|} \quad (4-4)$$

where ω_d is the Doppler shift observed, ω is the transmitted frequency, $(\mathbf{v}_n - \mathbf{v})$ is the relative velocity and $\frac{\mathbf{r}_n - \mathbf{r}}{\|\mathbf{r}_n - \mathbf{r}\|}$ is the unit vector from the observer to the transmitter.

Again forming vectors based upon this relationship yields the implicit FOA functional model

$$F_{i+4}(\mathbf{X}, \mathbf{Y}) = \omega_i - \omega \left[1 - (v_i - v) \cdot \frac{r_i - r}{t_i - t} \right], \quad i = 1, 2, 3, 4. \quad (4-5)$$

defined as $\mathbf{F}_F = (F_5, F_6, F_7, F_8)$.

Combining the TOA and FOA models produces the TOA-FOA implicit functional model defined as $\mathbf{F} = (\mathbf{F}_T, \mathbf{F}_F)$.

C. DETERMINATION OF THE TRANSMITTER STATE VECTOR

The determination of the 8-dimensional transmitter state vector involves finding for \mathbf{X} , the parameter \mathbf{Y} that satisfies the combined TOA-FOA implicit functional model, $F_i(\mathbf{X}, \mathbf{Y}) = 0$, $i = 1, 2, \dots, 8$, where the functions F_i are defined in (4-3) and (4-5). The solution of such a system of equations occurs in two steps. First, the TOA equations can be solved for $\mathbf{Y}_T = (\mathbf{r}, t)$. The resulting solution can then be used in the FOA equations to solve for the unknowns $\mathbf{Y}_F = (v, \omega)$.

The TOA equations are irrational in their form in (4-3) and thus must be squared in order to be solved. This produces a set of quadratics for which two sets of solutions exist corresponding to the two roots of the equations. In most cases, Rusu points out, the two solutions to the rational quadratics are also solutions to the original irrational set of equations. Rarely, most often in the 2-dimensional case, only one of the two solutions also solves the irrational set of equations and leads to a unique solution to the geolocation problem.

Since each solution to the TOA case also produces a unique solution to the FOA equations, more often than not, there are two distinct solutions to the problem. This is the classic case of ambiguity encountered with every TDOA solution proposed thus far. Rusu handles this problem by noting that information outside the algorithm must resolve the ambiguity. Prior knowledge of the general area of the target's position might eliminate one of the solutions. Multiple measurements may also reveal one solution

converging in one location while the other solution diverges and produces seemingly unrelated geolocations.

To solve the TOA equations, (4-3) must be squared to produce

$$(x_i - x)^2 + (y_i - y)^2 + (z_i - z)^2 - (t_i - t)^2 = 0, \quad i = 1, 2, 3, 4. \quad (4-6)$$

The solution to (4-6) is found by subtracting the equations two-by-two to eliminate x^2 , y^2 , z^2 and t^2 . This produces a set of linear equations in \mathbf{r} and t that may be written as

$$\mathbf{A}\mathbf{r} = \mathbf{q}t + \mathbf{s} \quad (4-7)$$

As the equations can be subtracted in any order to produce such an elimination, there exists many possible resulting systems of equations. One more obvious possibility used by Rusu is

$$\mathbf{A} = \begin{pmatrix} x_1 - x_2 & y_1 - y_2 & z_1 - z_2 \\ x_2 - x_3 & y_2 - y_3 & z_2 - z_3 \\ x_3 - x_4 & y_3 - y_4 & z_3 - z_4 \end{pmatrix} \quad (4-8)$$

$$\mathbf{q} = \begin{pmatrix} t_1 - t_2 \\ t_2 - t_3 \\ t_3 - t_4 \end{pmatrix} \quad (4-9)$$

$$\mathbf{s} = \frac{1}{2} \begin{pmatrix} \|r_1\|^2 - \|r_2\|^2 - t_1^2 + t_2^2 \\ \|r_2\|^2 - \|r_3\|^2 - t_2^2 + t_3^2 \\ \|r_3\|^2 - \|r_4\|^2 - t_3^2 + t_4^2 \end{pmatrix} \quad (4-10)$$

This system makes it possible to solve for \mathbf{r} in terms of t producing a t -parametrized solution to the TOA equations

$$\mathbf{r} = \mathbf{g}t + \mathbf{h}, \quad (4-11)$$

where

$$\mathbf{g} = \mathbf{A}^{-1}\mathbf{q} \quad \text{and} \quad \mathbf{h} = \mathbf{A}^{-1}\mathbf{s}. \quad (4-12)$$

The introduction of this result into the k^{th} range equation from (4-6) yields a quadratic in time t . This equation, with some algebraic manipulation can be written as

$$at^2 + 2bt + c = 0 \quad (4-13)$$

where,

$$a = \|\mathbf{g}\|^2 - 1 \quad (4-14)$$

$$b = \mathbf{g} \cdot \mathbf{h} + \mathbf{g} \cdot \mathbf{r}_k + t_k \quad (4-15)$$

$$c = \|\mathbf{h} - \mathbf{r}_k\|^2 - t_k^2 \quad (4-16)$$

The two roots that are the solution to (4-13) produce two values for \mathbf{r} when inserted into (4-11). Rusu notes that the roots are usually real but in the rare cases when they are complex, experience has shown him that the real part of the complex roots suffices as a solution.

Once the TOA equations provide the emitter position and time of transmission, these values produce the transmitter's velocity and transmitting frequency from the FOA equations. If the FOA equations are rewritten as

$$\frac{\mathbf{r}_{i0}}{t_{i0}} \cdot \mathbf{v} - \omega_i \frac{1}{\omega} = -1 + \frac{\mathbf{r}_{i0}}{t_{i0}} \cdot \mathbf{v}_i, \quad i = 1, 2, 3, 4, \quad (4-17)$$

the FOA case becomes a non-homogeneous linear system that may be solved using standards procedures like Gauss-Jordan elimination [14].

D. ERROR PROPAGATION

Perhaps the most valuable portion of Rusu's solution comes with the error propagation. He developed a linear method through which errors in the measurement can be propagated through the model and result in predictable errors in the fix. The following derivation is based solely on his development of this method. Though he develops both the TOA and the FOA propagations, only the TOA case will be presented here.

The key to the linear propagation of errors is based upon the assumptions. First, $\mathbf{Y} = \mathbf{Y}(\mathbf{X})$ is assumed to be differentiable in the neighborhood of the measured value \mathbf{X} containing the exact (error free) value of the observable $\underline{\mathbf{X}}$. Second, if the errors in the observation and the parameter are denoted $\delta\mathbf{X} = \mathbf{X} - \underline{\mathbf{X}}$ and $\delta\mathbf{Y} = \mathbf{Y} - \underline{\mathbf{Y}}$, \mathbf{Y} is assumed to be linear in the region of these errors and thus $\delta\mathbf{Y}$ can be written

$$\delta\mathbf{Y} \approx \left(\frac{\partial \mathbf{Y}}{\partial \mathbf{X}} \right) \delta\mathbf{X} \quad (4-18)$$

The following Jacobian matrix represents the derivative of a vector valued function, $\mathbf{Y} = (Y_1, Y_2, \dots, Y_n)$ with respect to a vector variable $\mathbf{X} = (x_1, x_2, \dots, x_n)$

$$\left(\frac{\partial \mathbf{Y}}{\partial \mathbf{X}} \right) = \begin{pmatrix} \frac{\partial}{\partial x_1} Y_1 & \frac{\partial}{\partial x_2} Y_1 & \dots & \frac{\partial}{\partial x_m} Y_1 \\ \vdots & \vdots & \ddots & \vdots \\ \vdots & \vdots & \ddots & \vdots \\ \frac{\partial}{\partial x_1} Y_n & \frac{\partial}{\partial x_2} Y_n & \dots & \frac{\partial}{\partial x_m} Y_n \end{pmatrix} \quad (4-19)$$

Given the linear approximation in (4-18), the covariance matrix of the parameter can be related to the covariance matrix of the observation through

$$C_y = \left(\frac{\partial \mathbf{Y}}{\partial \mathbf{X}} \right) C_x \left(\frac{\partial \mathbf{Y}}{\partial \mathbf{X}} \right)^T \quad (4-20)$$

The implicit function theorem provides a convenient method for computing the derivatives of \mathbf{Y} with respect to \mathbf{X} from the relation $\mathbf{F}(\mathbf{X}, \mathbf{Y}) = 0$. This provides the general formula

$$\left(\frac{\partial \mathbf{Y}}{\partial \mathbf{X}} \right) = - \left(\frac{\partial \mathbf{F}}{\partial \mathbf{Y}} \right)^{-1} \left(\frac{\partial \mathbf{F}}{\partial \mathbf{X}} \right) \quad (4-21)$$

Just as the relationship of the TOA and FOA solutions allowed the separation of the TOA case from the FOA case, the matrices involved in (4-21) can be written such that the TOA and FOA contributions are separated as

$$\frac{\partial \mathbf{Y}}{\partial \mathbf{X}} = \begin{pmatrix} \frac{\partial \mathbf{Y}_T}{\partial \mathbf{X}_T} & \frac{\partial \mathbf{Y}_T}{\partial \mathbf{X}_F} \\ \frac{\partial \mathbf{Y}_F}{\partial \mathbf{X}_T} & \frac{\partial \mathbf{Y}_F}{\partial \mathbf{X}_F} \end{pmatrix} \quad (4-22)$$

$$\frac{\partial \mathbf{F}}{\partial \mathbf{X}} = \begin{pmatrix} \frac{\partial \mathbf{F}_T}{\partial \mathbf{X}_T} & 0 \\ \frac{\partial \mathbf{F}_F}{\partial \mathbf{X}_T} & \frac{\partial \mathbf{F}_F}{\partial \mathbf{X}_F} \end{pmatrix} \quad (4-23)$$

$$\frac{\partial \mathbf{F}}{\partial \mathbf{Y}} = \begin{pmatrix} \frac{\partial \mathbf{F}_T}{\partial \mathbf{Y}_T} & 0 \\ \frac{\partial \mathbf{F}_F}{\partial \mathbf{Y}_T} & \frac{\partial \mathbf{F}_F}{\partial \mathbf{Y}_F} \end{pmatrix} \quad (4-24)$$

The independence of the TOA solution from the FOA equations is evident in the zeros found above corresponding to $\frac{\partial \mathbf{F}_T}{\partial \mathbf{X}_F}$ and $\frac{\partial \mathbf{F}_T}{\partial \mathbf{Y}_F}$.

The problem of inverting the Jacobian, $\partial \mathbf{F} / \partial \mathbf{Y}$, can be solved numerically however, Rusu managed to express the inverse of $\partial \mathbf{F} / \partial \mathbf{Y}$ in terms of the inverses of the TOA-FOA blocks forming it. He points out that this formally separates the TOA and FOA error propagations and allows computation of just the TOA solution and errors if just the transmitter location is desired. The block inverse of (4-24) is

$$\left(\frac{\partial \mathbf{F}}{\partial \mathbf{Y}} \right)^{-1} = \begin{pmatrix} \left(\frac{\partial \mathbf{F}_T}{\partial \mathbf{Y}_T} \right)^{-1} & 0 \\ \left(\frac{\partial \mathbf{F}_F}{\partial \mathbf{Y}_F} \right)^{-1} \frac{\partial \mathbf{F}_F}{\partial \mathbf{Y}_T} \left(\frac{\partial \mathbf{F}_T}{\partial \mathbf{Y}_T} \right)^{-1} & \left(\frac{\partial \mathbf{F}_F}{\partial \mathbf{Y}_F} \right)^{-1} \end{pmatrix} \quad (4-25)$$

It is now possible to write the components of the right hand side of (4-22) as

$$\frac{\partial \mathbf{Y}_T}{\partial \mathbf{X}_T} = - \left(\frac{\partial \mathbf{F}_T}{\partial \mathbf{Y}_T} \right)^{-1} \left(\frac{\partial \mathbf{F}_T}{\partial \mathbf{X}_T} \right) \quad (4-26)$$

$$\frac{\partial \mathbf{Y}_T}{\partial \mathbf{X}_F} = 0 \quad (4-27)$$

$$\frac{\partial \mathbf{Y}_F}{\partial \mathbf{X}_T} = \left(\frac{\partial \mathbf{F}_F}{\partial \mathbf{Y}_F} \right)^{-1} \left(\frac{\partial \mathbf{F}_F}{\partial \mathbf{Y}_T} \right) \left(\frac{\partial \mathbf{F}_T}{\partial \mathbf{Y}_T} \right)^{-1} \left(\frac{\partial \mathbf{Y}_T}{\partial \mathbf{X}_T} \right) - \left(\frac{\partial \mathbf{F}_F}{\partial \mathbf{Y}_F} \right)^{-1} \left(\frac{\partial \mathbf{F}_F}{\partial \mathbf{X}_T} \right) \quad (4-28)$$

$$\frac{\partial \mathbf{Y}_F}{\partial \mathbf{X}_F} = \left(\frac{\partial \mathbf{F}_F}{\partial \mathbf{Y}_F} \right)^{-1} \left(\frac{\partial \mathbf{F}_F}{\partial \mathbf{X}_F} \right) \quad (4-29)$$

using (4-21), (4-23) and (4-25).

Now the TOA Jacobian matrices related to the TOA error propagation can be explicitly expressed using the functional model given in (4-3). The Jacobians can be expressed as

$$\frac{\partial \mathbf{F}_T}{\partial \mathbf{X}_T} = \begin{pmatrix} x_{01} & y_{01} & z_{01} & -t_{01} \\ x_{02} & y_{02} & z_{02} & -t_{02} \\ x_{03} & y_{03} & z_{03} & -t_{03} \\ x_{04} & y_{04} & z_{04} & -t_{04} \end{pmatrix} \quad (4-30)$$

$$\frac{\partial \mathbf{F}_T}{\partial \mathbf{Y}_T} = \begin{pmatrix} x_{10} & y_{10} & z_{10} & t_{01} & 0 & 0 & 0 & 0 & \cdots & 0 & 0 & 0 & 0 \\ 0 & 0 & 0 & 0 & x_{20} & y_{20} & z_{20} & t_{02} & \cdots & 0 & 0 & 0 & 0 \\ 0 & 0 & 0 & 0 & 0 & 0 & 0 & 0 & \cdots & 0 & 0 & 0 & 0 \\ 0 & 0 & 0 & 0 & 0 & 0 & 0 & 0 & \cdots & x_{40} & y_{40} & z_{40} & t_{04} \end{pmatrix} \quad (4-31)$$

where

$$x_{ij} = x_i - x_j.$$

Implementation of Dr. Rusu's algorithm into MATLAB® followed naturally given its matrix and vector nature. It plays an integral part in the ARL:UT prototype TDOA geolocations system which is discussed in Chapter V. Specifics regarding the encoding of Dr. Rusu's algorithm can be found in Chapter VI.

V. THE CARRY-ON MULTI-PLATFORM GPS-ASSISTED TIME DIFFERENCE OF ARRIVAL SYSTEM

A. PROJECT BASIS

Given the problem of developing a portable, GPS assisted TDOA system with commercially available products, the project team at ARL:UT set out to define the problem and develop solutions based on which portions of the problem could be most influenced. The descriptions and performance reports below are based upon [15] and numerous conversations with team members.

The TDOA problem can be reduced to three sub-problems: geometry, signal timing and measurement. All three are related to the rms error of the geolocation by

$$\sigma_{position} \approx GDOP \cdot \sigma_{measurement} \quad (5-1)$$

The Geometric Dilution of Precision (GDOP) is a scalar multiplicative factor which serves to magnify any timing and measurement error. It is directly related to the relative positions of the observers and the emitter. Poor GDOP(s), generally numbers greater than three in this application, result from geometries where the observers are lined up or clustered in one area with respect to the emitter. Conversely, good GDOP(s), numbers smaller than about three, result from situations where the observers are positioned such that their TDOA(s) intersect at nearly right angles. In three dimensions, the most favorable GDOP occurs by maximizing the volume of the polyhedron formed by pointing four vectors from the four observers to the emitter and enclosing the figure that results.

The geometry of the situation is essentially out of the control of the TDOA system as the location of the emitter is not known a priori but would be needed in order to position the observers in an optimal configuration. Only when many more observers participate than the minimum needed for a determined solution (three are needed for 2D and four for 3D) can the geometry of the situation be better controlled by the TDOA system. In practice, this occurs rarely and thus, the best course of action considering (5-1) above is to minimize the timing and measurement error to the greatest extent possible.

GPS provides the capability to reduce both these error sources significantly. It was with this in mind that the ARL:UT project team, led by Mark Leach, pursued the design and implementation of a new GPS-assisted TDOA system.

NSGSA in its tasking to ARL:UT added some additional requirements in the area of component sources, architectures and interfaces with existing equipment. The following sections outline the system in progressively more detail starting with a general summary and concept of operations, continuing into a hardware description and ending with a more detailed discussion of error sources and system performance in operational tests.

B. PROJECT OVERVIEW

The system would receive only a frequency of interest in the HF, VHF or UHF line of sight communications frequency bands. It must utilize an open system architecture and maximize the use of commercial and government of the shelf hardware (COTS and GOTS respectively). It was permitted just a single voice grade channel for communication between observers and needed to interface with existing Navy hardware for that purpose (i.e. AN/WSC-3 transceiver). Finally, the system needed to be compatible with the Navy's Unified Build (UB) environment and interact seamlessly with the Joint Maritime Command and Information System (JMCIS).

The system in its current configuration consists of a network of observers (minimum of three for a geolocation in 2D and four for 3D) with one observer acting as the master node, the others as slave nodes. It employs the distributed processing technique depicted in Figure 5-1. Once given the frequency of interest by an existing signal acquisition system, the master node tunes its receiver to that frequency and notifies the slaves to do likewise. Each node samples the incoming signal and buffers the data in mass memory storage. The master logically determines the 400 ms portion of its samples that contains the most energy from the SOI and computes the Fast Fourier Transform (FFT) of this 400ms. The Master then broadcasts the FFT to the slaves with a GPS time stamp.

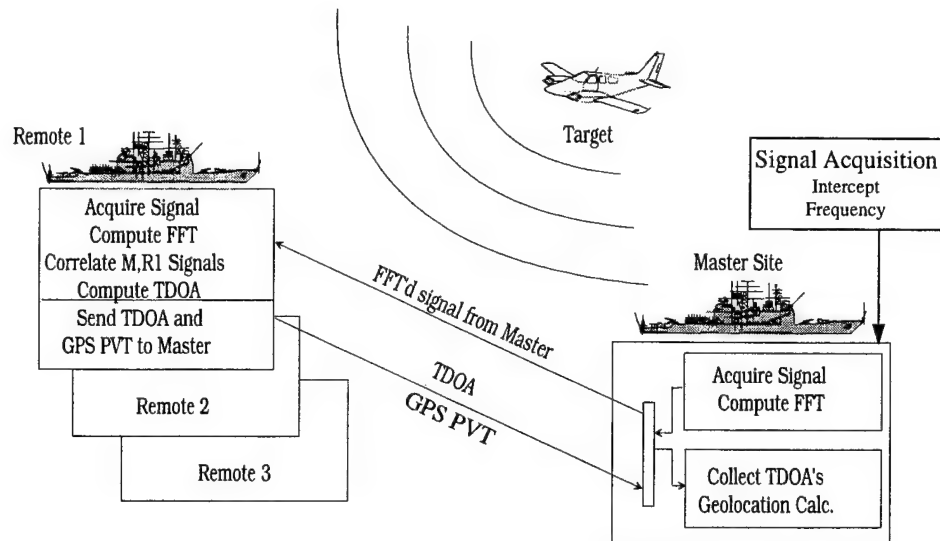


Figure 5-1 - Distributed processing, from [15]

Once the slaves receive the FFT from the master they search their buffers for the 400 ms of samples that correspond to the epoch of the time stamped FFT. They then take the FFT of their data and perform a CAF to extract the TDOA. In addition to this TDOA, the slaves send their GPS derived position, time and velocity (PVT) measurements corresponding to the time of intercept to the master.

The master collects the TDOA(s) and PVT(s) and forwards the package to a standard Navy TAC3/4 workstation which calculates the geolocation.

C. HARDWARE DESCRIPTION

The system is comprised of two major sub-systems: the measurement subsystem and the geolocation subsystem. Each is designed in modular fashion accepting certain formatted inputs and producing certain formatted outputs. This modularity facilitates changes internal to either system including entire components or software modules as the process within each of these subsystems is inconsequential to the other module. Only the inputs and outputs are relevant.

The measurement subsystem includes the hardware and software used to compute the TDOA(s). It is based on a 13 slot, C-size VXI chassis housing an HP Signal Analyzer package. This package includes a Motorola 68040 based VXI controller, a 10 MHz, 23-

bit (18 linear) analog to digital converter (A/D), a digital signal processing (DSP) card, 200 MB of disk storage and software. The DSP module is a Motorola 96002 based floating point DSP chipset on a VXI card. Also on the chassis are a Ball-Efratom model FRK 10 MHz Rubidium (**Rb**) reference oscillator, a Precise Positioning Service (PPS) capable GOTS GPS receiver by Ashtech Inc. and E-systems and an ARL:UT developed clock synchronization module. The phase lock loop (PPL) module allows the **Rb** reference oscillator to be in synch with the GPS 1 pulse per second (pps) timing output. The bulk of this subsystem is shown in Figure 5-2.

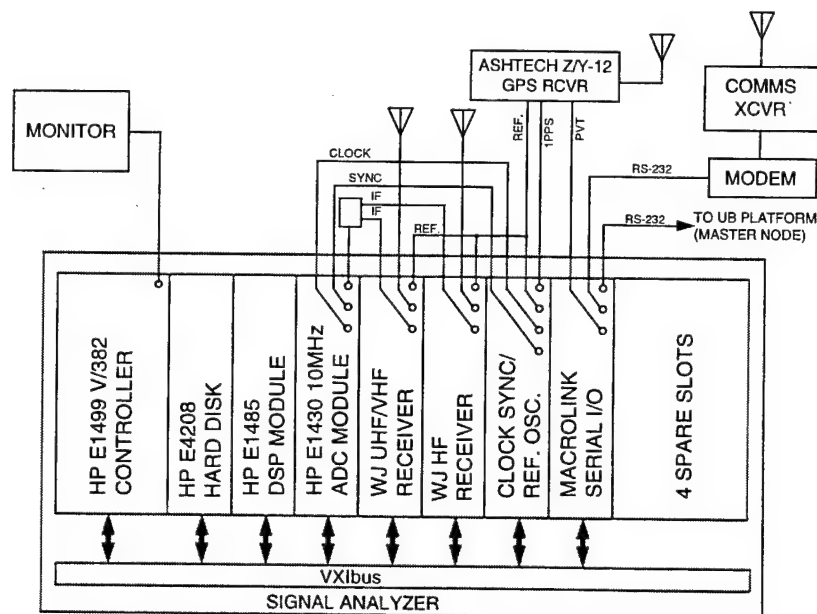


Figure 5-2 - Hardware configuration, from [15]

The geolocation subsystem includes a TAC3/4 computer on which reside the algorithms both to compute the geolocation and communicate that fix to the JMCIS. In addition, it also holds the system's capability for simulation and playback modes. The TDOA algorithms consist of the closed form solution presented in Chapter V and a Kalman filter method. The closed form or determined solution is the primary solution and lends itself quite naturally to situations where the emitter has short transmission durations which preclude the use of the Kalman filter method. In the event of long

duration transmission, the determined solution will feed the Kalman filter a first prediction and allow the Kalman filter to produce fixes as a function of time over the duration of the transmission. The Kalman filter, when given sufficient data and a starting point, has better error prediction capabilities and is thus the preferred method in the correct situations.

The interface with JMCIS provides the system a data display capability. By updating the track database through a standard UB message, the system is able to both communicate with the Navy's latest command and information system and avoid having to produce its own man-machine interface on this output level.

Finally, this system is also capable of simulating scenarios in order to investigate the effects of variations on the many factors involved from the receipt of the signals to the processing of the data to the computation and display of the fix. In addition, a capability to playback sessions recorded and stored on tape is built in to the geolocation subsystem. This feature allows for post processing and analysis of operational tests enabling finer detailed analysis of many of the variables including error source investigation.

Perhaps the one key point that stands above the other accomplishments of the system is the significant reduction of signal timing errors between the collection nodes. With the use of the PPS-capable GPS receivers, the 1 pps output from the GPS satellites in concert with differential GPS techniques enables the time offset between two GPS receivers, separated by up to hundreds of kilometers, to be on the order of 20 ns. In addition, the PPL circuitry allows each node's Rb standard to be synchronized to within 5 ns of this 1 pps output giving a total signal timing error of a mere 25 ns. In terms of light distance, that translates to 7.5 meters. Figure 5-3 shows the entire system's functional relationships in summary.

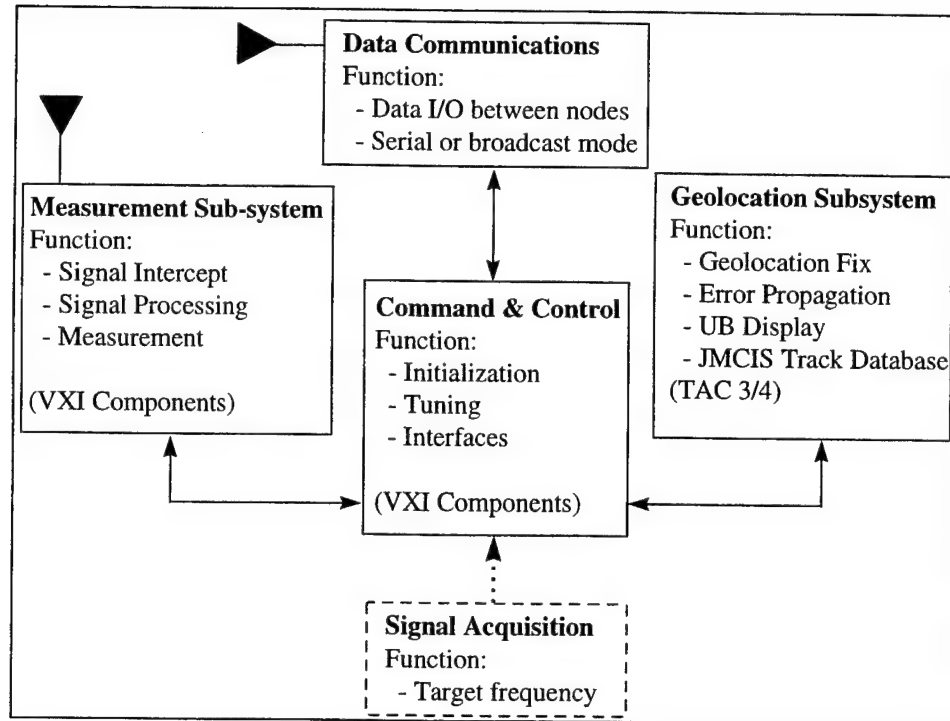


Figure 5-3 - Tactical TDOA Functional Diagram, courtesy ARL:UT

D. ERROR ANALYSIS

Many sources of errors exist in the operational system. Another accomplishment of the project is the detailed identification and prediction of the magnitude of those error sources which have been validated by the operational tests outlined in the next section. In their investigations, the ARL:UT team was able to collect the sources into four major categories: fundamental limits, instrumentation limits, operational environment and network geometry.

The lower bound on timing and measurement accuracy may be related to the variance of the TDOA estimator. This in turn is related to the incoming SNR, signal and noise bandwidth and integration time as first shown by Hertz and Azaria in [2] and later extended more specifically to this system by Rusu and Giulianelli in [16].

Instrumentation limits add significantly to the errors in signal arrival time determination. Specifically, though ideally each GPS receiver will output the GPS 1 pps

at the same time during each one second epoch, there will be some offset in reality. In addition, that 1 pps timing pulse is used to trigger the sampling of the incoming signal. Delays from the time the A/D converter receives the 1 pps and the onset of sampling for that clock cycle will vary from one A/D to another. This compounds the 1 pps offset error and translates directly to error in the cross-correlation computation of the TDOA(s). The cross-correlation methods of TDOA determination measure the time difference by determining a peak in the computed function. Five unknowns exist in this computation: signal frequency, signal bandwidth, noise bandwidth, SNR, and statistical properties of both signal and noise. The width of this peak and the presence of multiple peaks is indicative of the magnitude of the lower bound on the error in the measurement discussed above and is the direct result of a combination of these factors.

The operational environment and network geometry constituted the bulk of the uncontrollable error contributions. While during testing, the environment is somewhat controlled, the operational system would certainly be subject to the conditions of the current tactical situation. This holds true as well for the geometries.

E. PRELIMINARY TEST RESULTS

Published test results include both static and dynamic emitters as targets. In November 1994, the geolocation of a static emitter in 2 dimensions was demonstrated in the Austin, Texas area using three observers with baselines of approximately 33 km. The target was a stationary NOAA FM transmitter at 162.4 MHz. The system at this point tested with a 2-D rms error of 124 m. Details can be seen in [15].

Dynamic tests were conducted in January 1995 using a moving emitter, two stationary observers and one moving observer. Again the tests were conducted in the Austin area and in just two dimensions only given just three observers. The target emitter was an aircraft at approximately 2000 feet, traveling at speeds of approximately 100 knots and transmitting with a 20 W UHF signal at 461.1 MHz. The moving observer was a van mounted node traveling at speeds of up to 35 mph in a 2 square mile area. During this test, the prototype system performed geolocations to within 277 m rms error using the

Kalman filter solution. This accuracy was achieved despite various geometries that ranged from outstanding GDOP(s) of almost 1 to very poor GDOP(s) of 10.

While these tests failed to achieve the goal of 100 m rms error, instrumentation changes promised to increase the accuracy without significant changes to the system. Two additional tests, each more extensive and demanding than the previous, have been conducted with the system. While no performance results have been formally published, shipboard tests off the coast of San Diego California have proven the system capable of 120 m rms error against representative VHF/UHF dynamic emitters with excellent geometry and ~400 m rms error with poorer geometries [17]. Further changes in receivers promise to remove biases in the measurements created by the current radios and improve performance proportionally.

In addition, the use of a cyclostationary TDOA determination algorithm should provide some improvement in the performance of the system low SNR environments. The initial step for the incorporation of cyclostationary signal processing into the ARL:UT system is to code the algorithms in MATLAB® and test them with ARL:UT test data. The coding of the algorithms in MATLAB® appears in Chapter VI.

VI. ALGORITHMS

A. BACKGROUND

Any implementation of a TDOA processor utilizing SPECCOA must provide both an SCF as well as a CSCF at a cycle frequency α_0 , characteristic of the SOI. In [19], Loomis and Bernstein develop a functional TDOA processor using SPECCOA that provides for the efficient computation of both spectral correlation functions as well as the selection α_0 . This system represents the basis for the implementation of SPECCOA and the geolocation algorithm in MATLAB® for this project and appears in Figure 6-1.

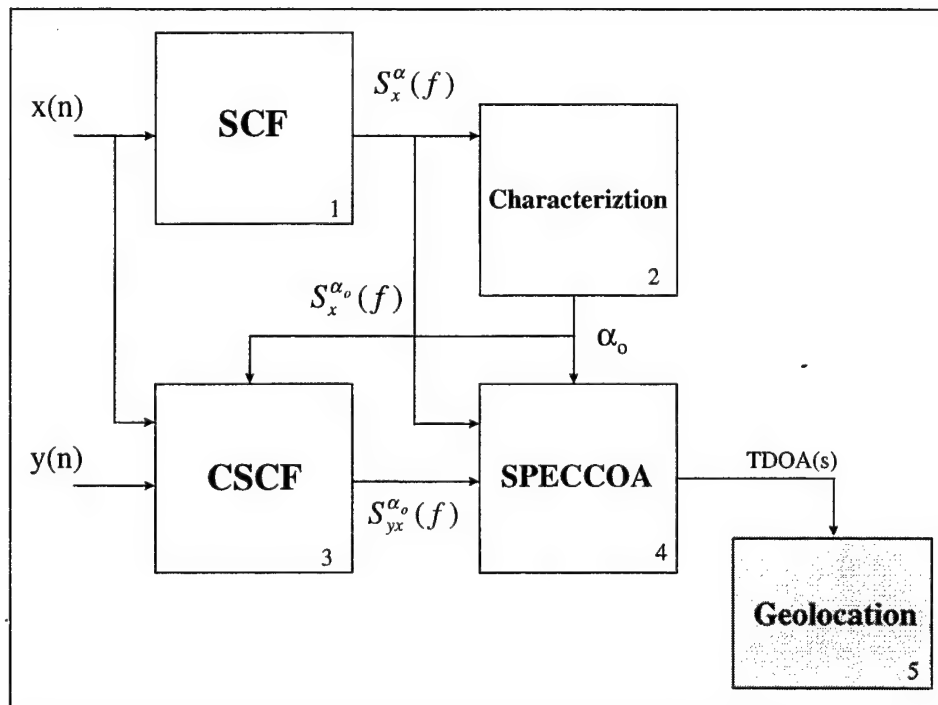


Figure 6-1 - TDOA geolocation processor functional diagram, adapted from [19]

The four blocks of the TDOA processor constitute progressively lesser degrees of computational complexity. The most complex of the operations is the calculation of the SCF(s) in the first operation of the processor. The SCF(s) of the master and the four slaves are necessary for the selection of the appropriate cycle frequency in the next operation of the processor, the characterization. The SSCA algorithm computes the four

SCF(s) and uses a plotting routine to display them. In the next operation, the characterization is performed manually using a plot of the maximum values of the SCF(s) for each value of cycle frequency. This plot facilitates the choice of the optimum cycle frequency for use in SPECCOA. The third operation involves the computation of the SCF and CSCF at the cycle frequency selected during characterization. Computed with a simple frequency smoothing algorithm, the SCF and CSCF at the cycle frequency of interest feed the final TDOA processor operation, SPECCOA. SPECCOA in turn determines the TDOA by plotting the solution to the ad hoc MLS optimization found in (3-32). The maximum value of this function represents the TDOA.

The SCF(s) in the first operation as well as the characterization must be computed for all four observers for each set of data. Cycle frequencies for the same emitter vary with observer due to instrumentation mismatches at each location. Details of cycle frequency selection in these situations appear in Chapters VII and VIII. The cycle frequency specific SCF and CSCF are computed just three times because as noted in Chapter V, the only TDOA(s) used in practice are those between the master node and the three slaves. No cross slave TDOA(s) are computed or used in the prototype system and thus they are not computed here. Finally, three runs of SPECCOA are required to feed the geolocation algorithm.

B. STRIP SPECTRAL CORRELATION ANALYZER IN MATLAB®

The SCF(s) computed in the first operation of the TDOA processor can place a significant burden on the processor if not optimized for computational efficiency. In order to achieve the efficiency necessary for use in a tactical environment, a highly expeditious method for computing and plotting the SCF is used. Directly from its definition, (3-17), the SCF can be computed using a traditional time-smoothing approach as depicted in Figure 6-2. While this approach provides the most accurate estimate of the SCF, it proves prohibitively time consuming and inappropriate for most applications [20]. The SSCA algorithm, a modification of the time-smoothing method, provides the best combination of accurate estimation of cycle frequencies of interest and computational efficiency [21]. By eliminating one of the band-pass filters in Figure 6-2 and using a Fourier transformer at the input and output, SSCA computes the SCF along

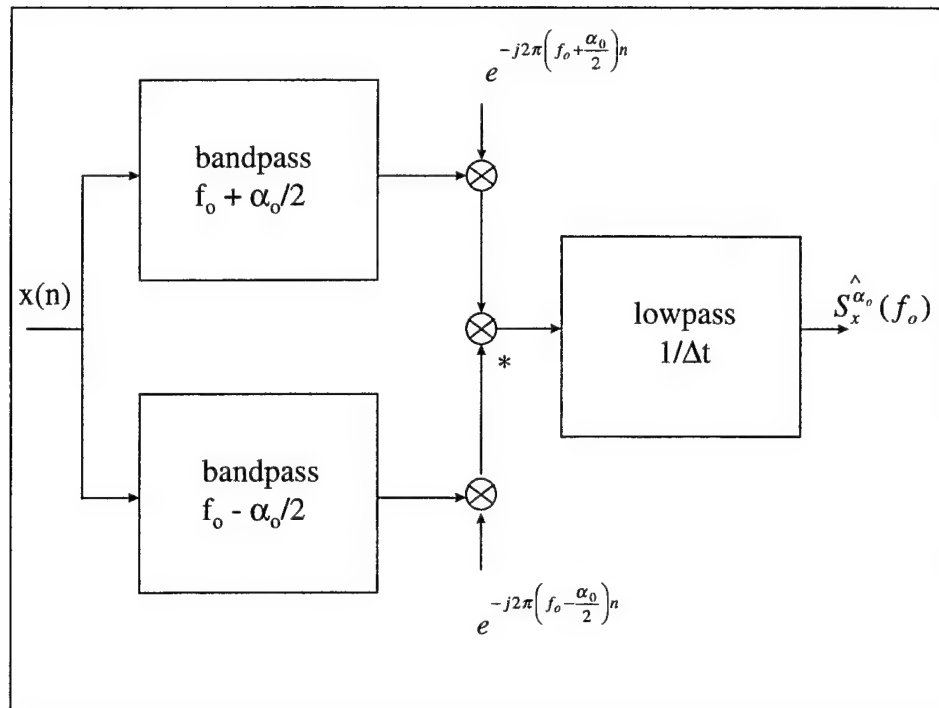


Figure 6-2 - Time-smoothing spectral correlation analyzer [20]

diagonal strips of the bi-frequency plane as depicted in Figure 6-3. While the SSCA does manage to compute the SCF in the most efficient manner developed thus far, it has some compromise. The output signal to noise ratio suffers slightly as a result of the efficiency gained by the elimination of the filter and the use of the Fourier transform. However, the computational savings gained far outweigh the minor degradation in signal power to noise power at the output of the analyzer.

Figure 6-4 illustrates the SSCA architecture. The input filter consists of a sliding, Hamming-windowed coarse FFT of length N' . Each of these N' length segments is essentially the output of a band-pass filter with a bandwidth of $1/N'$. This band-pass output is then downconverted to baseband by a complex exponential multiplication. These products are termed the complex demodulates of the input signal and appear in greater

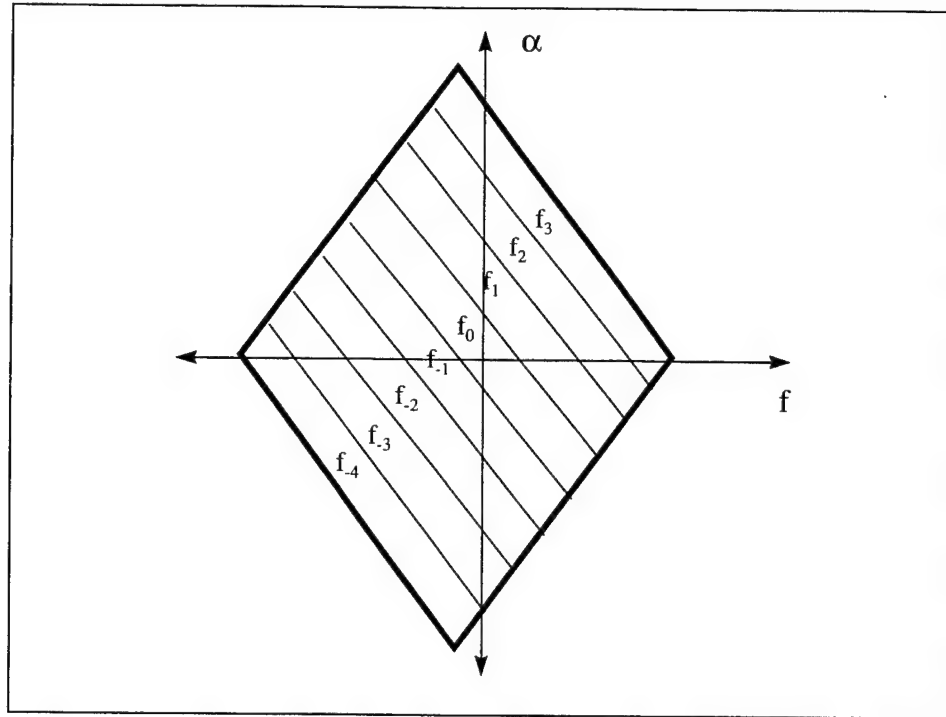


Figure 6-3 - SSCA computation in the bi-frequency plane, $N' = 8$

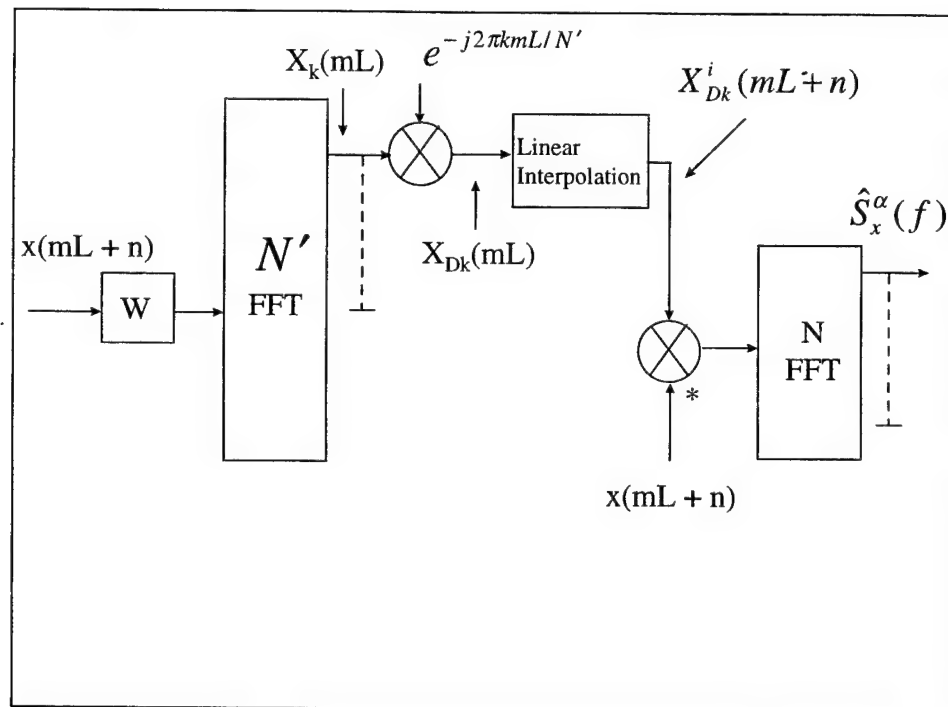


Figure 6-4 - SSCA architecture, from [20]

detail in Figure 6-5. As can be seen, the input sequence is essentially decimated by the process of windowing and sliding at the input filter. Loomis and Brown found that the most appropriate value for the decimation factor or subsampling parameter L was $N'/4$ [20].

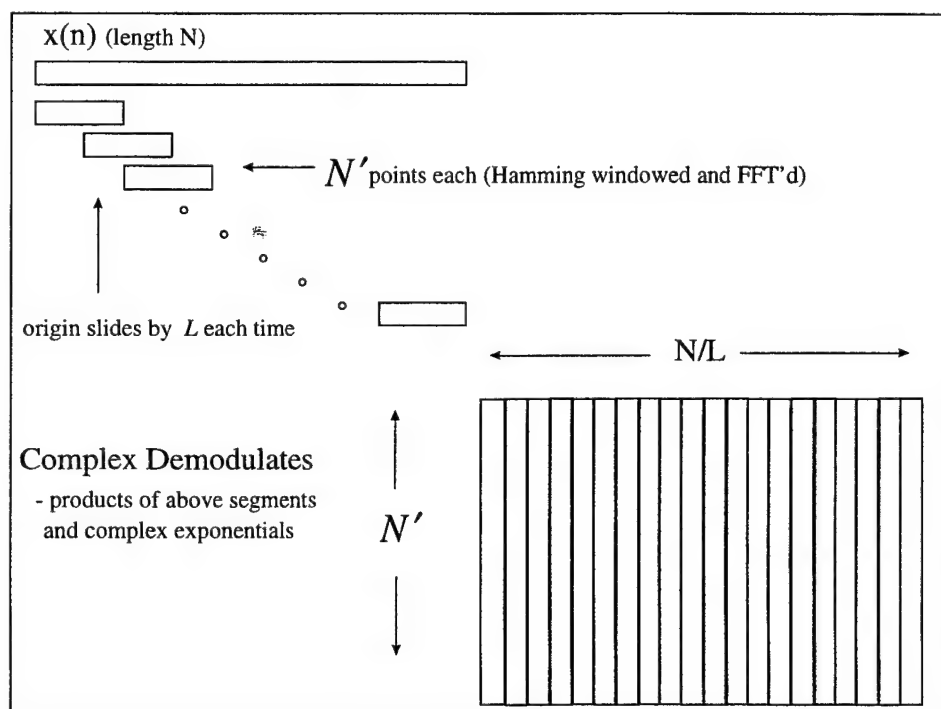


Figure 6-5 - Detail of the computation of complex demodulates

Because these complex demodulates are multiplied by the original sequence before the final FFT, they must be interpolated to the original sampling rate. In [20] and [21] Loomis and Brown use a simple hold operation. Linear interpolation induces less high frequency error and adds little in computational complexity. It is used here in place of the first order sample and hold interpolation. Finally, the interpolated complex demodulates and the original sequence are complex multiplied and the product Fourier transformed by a full length, unwindowed FFT. The relationship of the output to the bi-frequency plane appears in Figure 6-6. Each row of output represents one of the N' diagonal strips in the bi-frequency plane as depicted on the previous page in Figure

6-3. Each column represents the values of the SCF along the diagonal lines. The resolution along lines of f is coarse at $1/N'$ as a byproduct of the computational savings. However, the resolution in α , at $1/N$, is much higher which accommodates the characterization nicely.

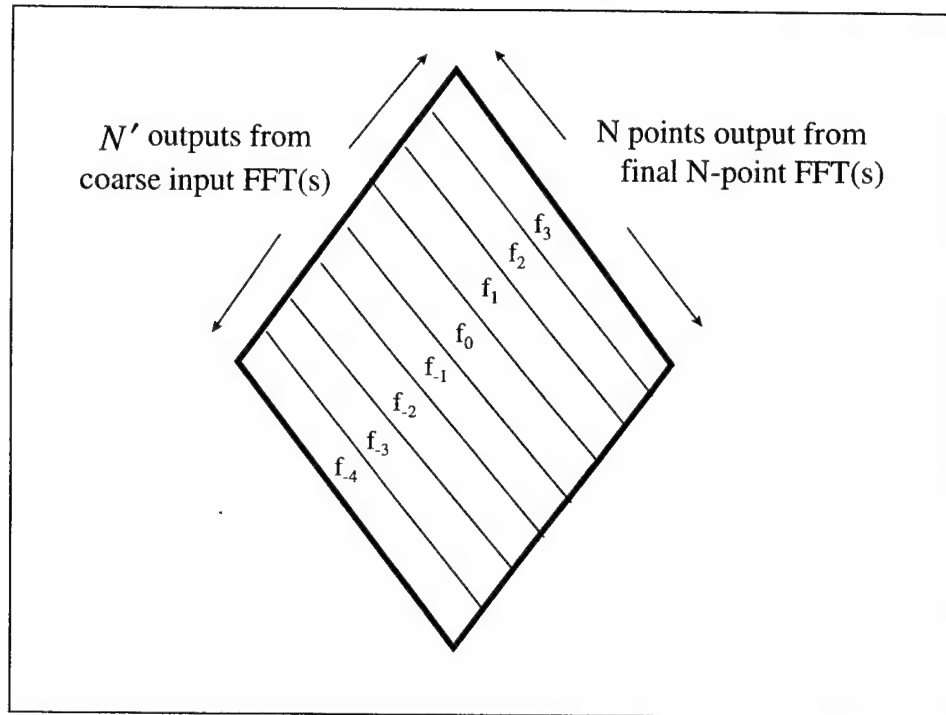


Figure 6-6 - Block form of SSCA output

Given that the majority of operations in the SSCA can be implemented as vector or matrix operations, its implementation in MATLAB® is fairly simple. The pseudocode for the algorithm appears in Figure 6-7. The MATLAB® code for the computation of the SCA over the entire bi-frequency plane, called `ssca`, appears in Appendix A. Of note, several MATLAB® functions forced the use of additional statements that might not otherwise be found given the pseudocode. The `fft` function in MATLAB® computes both positive and negative frequencies but does not place the origin in the center of the output vector. Instead, the output of `fft` takes advantage of the cyclic nature of the DFT. Its output begins at the origin of the frequency, moves through $f_s/2$ and then mirrors the negative frequencies with the positive continuing at $-f_s/2$ and ending with zero again.

This forces any application needing a double sided spectrum to rearrange the vector so that the negative frequencies start the output rather than end it. MATLAB® has an *fftshift* function that performs such an operation and appears in the code in several places for that reason. The output of **ssca** is a matrix with N' rows corresponding to the N' diagonal strips of the computation and columns corresponding to the SCF along the respective strips. Referring again to Figures 6-3 and 6-5, these strips are not computed along lines of f and α and must therefore be transposed along those lines before plotting.

```

/* Compute Complex Demodulates of x */
Do p:= 0 to P-1
  Compute  $x_T(pL, f_k) = \text{FFT}[a(r)x(pL+r)]$ 
  Do k :=  $-N'/2$  to  $N'/2 - 1$ 
    Compute  $X_T(pL, f_k) = x_T(pL, f_k) \exp\{-j2\pi pLk/N\}$ 
  end
end
/* Interpolate  $X_T(pL, f_k)$  */
Compute  $X_T(pL, f_k) \Rightarrow \tilde{X}_T(n, f_k)$ 

/* Compute and Smooth Product Waveforms
Do k :=  $-N'/2$  to  $N'/2 - 1$ 
  Compute  $S_{xy_T}^{f_k}(n, f_k) = y^*(n) \tilde{X}_T(n, f_k)$ 
  Compute  $S_{xy_T}^{\alpha_0}(n, f_k)_{\Delta t} = \text{FFT}\{g(n) S_{xy_T}^{f_k}(n, f_k)\}$ 
end

```

Figure 6-7 - Psuedocode for SSCA computation, from [21]

The program **plotscf** performs that function transposing the matrix output of the **ssca** program and plotting both the 3-D SCF and the 2-D magnitude of SCF versus α for the characterization operation. The transformation involves applying the relationship between the diagonal strip subscript k , the frequency f and the cyclic frequency α . Those relationships from [22] are

$$f_k = k \left(\frac{f_s}{N'} \right), \quad -\frac{N'}{2} \leq k \leq \frac{N'}{2} - 1 \quad (6-1)$$

$$\alpha = 2f_k - 2f \quad (6-2)$$

Given these relations and the MATLAB® *surf* function, the SCF plots easily along lines of f and α . The 2-D plot for additional characterization aid follows directly from the SCF plot.

C. SPECTRAL COHERENCE ALIGNMENT IN MATLAB®

SPECCOA represents yet another algorithm highly suited for MATLAB®. The majority of functions associated with computing (3-32) are vector operations which simplifies the MATLAB code considerably. Figure 6-8 is a basic block diagram of SPECCOA.

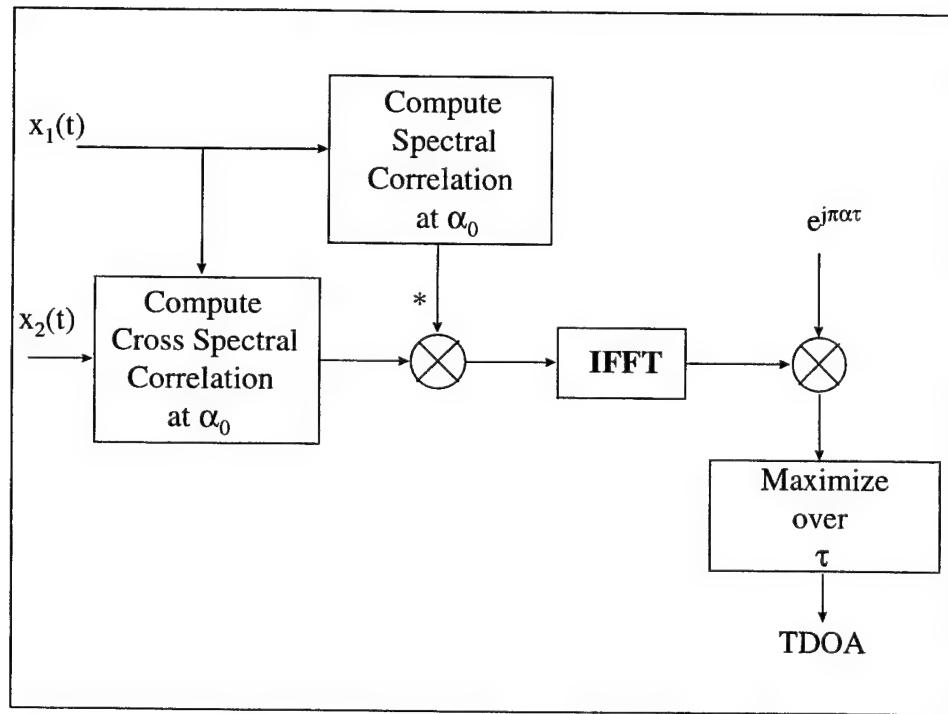


Figure 6-8 - SPECCOA block diagram

Once the characterization has determined the cycle frequency of interest, α_0 , a frequency smoothing algorithm estimates the SCF and CSCF for α_0 . The inverse Fourier transform of the complex product is then multiplied by the kernel $e^{j\pi\alpha_0\tau}$. The maximum value of the real portion of this product represents the TDOA of the SOI between the observers.

SPECCOA is used three times to determine the TDOA between the master node and the three slave nodes. These TDOA(s) along with observer positions are inputs to Dr. Rusu's geolocation algorithm the output of which is the location of the emitter.

D. THE TDOA CLOSED FORM SOLUTION IN MATLAB®

Dr. Rusu's closed form solution lends itself readily to MATLAB implementation. The inputs include four observer position vectors in WGS84 coordinates and three TDOA(s), D_{12} , D_{13} and D_{14} . All the intermediate variables are either vectors of length 3 or matrices no larger than 3×3 . The final solution involves finding the roots of a quadratic that represent the time of emission of the SOI and substituting that time into a range equation to find the WGS84 coordinates of the transmitter.

Of particular note to the MATLAB® code that appears in Appendix A is the use of the backslash function, \backslash , in lieu of the matrix inverse in the algorithm. This function was specifically developed for use in solving equations of the form

$$\mathbf{A}g = q \quad (6-3)$$

for g where \mathbf{A} is a matrix and g and q vectors. Normally, in matrix algebra the solution has the form

$$g = \mathbf{A}^{-1}q \quad (6-4)$$

if \mathbf{A} has an inverse. However in MATLAB®, it is more accurate to use the *matrix division* function or backslash. The accuracy of the backslash in this scenario approaches

machine precision while the use of the matrix inverse can reduce that accuracy several orders of magnitude [23].

One problem persists with the algorithm but is a function of the closed form solution rather than its implementation. The two roots both represent viable solutions to the problem. Information outside the algorithm must be used to eliminate the ambiguity. Multiple solutions from moving observers would more often than not cause one solution to converge while the other diverged. No matter how its resolved outside the algorithm, the ambiguity always poses a problem insurmountable by the mathematics.

The algorithms need to be tested on controlled data prior to evaluation with ARL:UT test data. Several signals were generated using Simulink®. These signals serve to ensure the proper functioning of all the code written for this work. Following the generated data, ARL:UT data provides a vehicle for comparing the current CAF based ARL:UT method with SPECCOA. The test plan is detailed in Chapter VII.

VII. TEST PLAN

A. GENERATED SIGNALS

Three signals are used in initially testing the TDOA processor. Generated with Simulink®, all three are BPSK signals and vary from noiseless to very poor SNR. Each signal was sampled at 100 kHz. They had carrier frequencies of $0.25 f_s$ and data rates of $0.05 f_s$. All were modulated with a random binary signal generator. They are used in various combinations to verify the functions of the three major programs, **ssca**, **plotscf** and **speccoa**.

The first set of tests involves using a noiseless BPSK signal to first verify **ssca** and **plotscf**. Given that these programs function properly, **speccoa** is tested finally. Figure 7-1 shows the simulation used to generate noiseless BPSK. A total of 1 second of signal is actually collected and stored as **testbpsk.mat**.

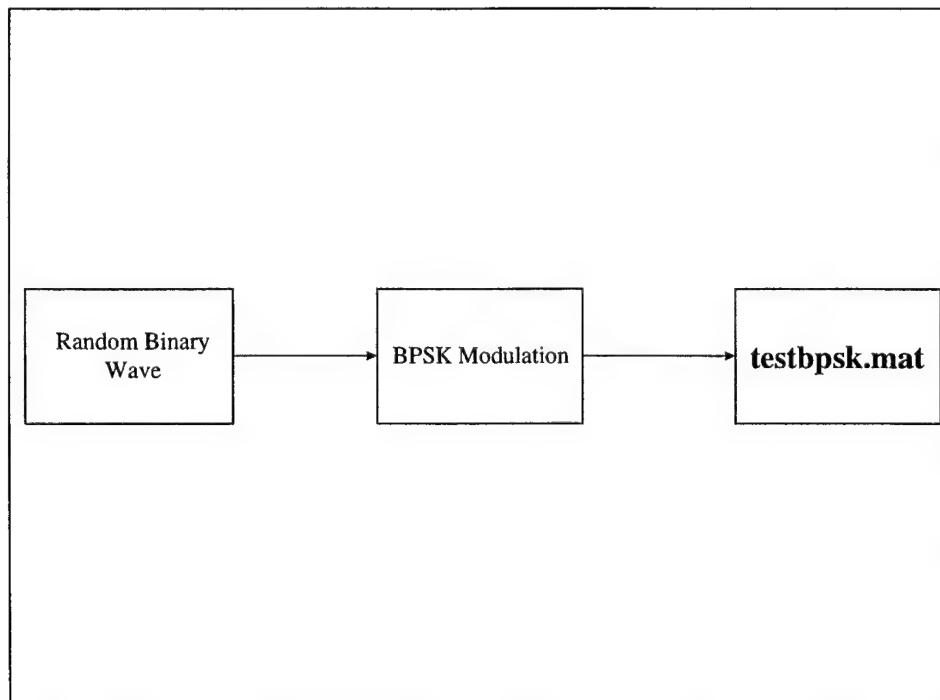


Figure 7-1 - Generation of noiseless BPSK as **testbpsk.mat**

This signal approaches the ideal for the processor for several reasons. First, it is completely binary from its inception. No analog to digital conversion is necessary and thus introduces no error in the process. Second, it is completely noiseless. Finally, it is modulated by a random binary wave which introduces no biases in the modulated waveform. Given this, its SCF should approach that given by theory taking into account the time smoothing effects of the SSCA algorithm. Figures 7-2 and 7-3 are the time domain and frequency domain plots respectively for **testbpsk.mat**.

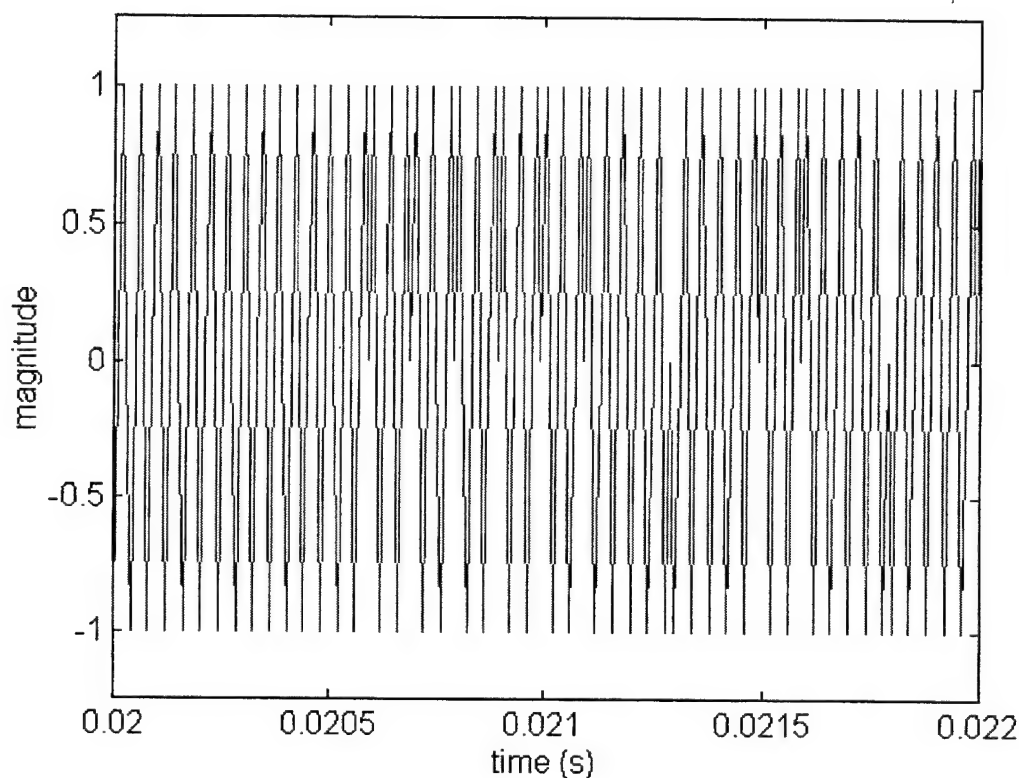


Figure 7-2 - Time domain plot of **testbpsk.mat**

The ideal SCF of a noiseless BPSK signal can be seen in Chapter III, Figure 3-4. The data feature of **testbpsk.mat** should appear at $0.05 f_s$ while the twice carrier feature in conjunction with the data feature appear at $0.45 f_s$, $0.5 f_s$ and $0.55 f_s$. Figure 7-4 displays the results of **ssca** and **plotscf** for $N = 4096$ point sample. Only the positive cycle frequency portion of the bi-frequency plane is plotted. The cycle frequency axis

draws from upper right to lower left and is plotted in terms of nf_s/N , n as axis label, $1/N$ as cycle frequency resolution. The spectral frequency follows from upper left to lower right labeled in the same manner. They are unlabeled in the figure to eliminate the additional clutter. As noted in Chapter VI, the SSCA algorithm trades resolution in the frequency domain for computational efficiency without losing the four key features.

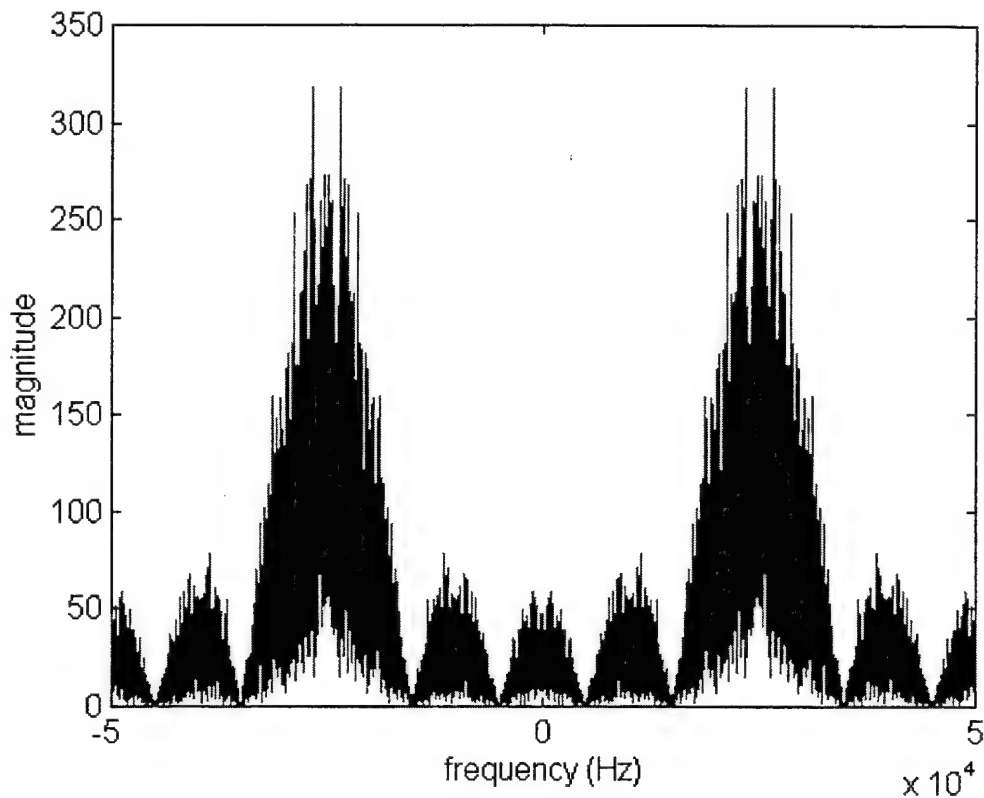


Figure 7-3 - Frequency domain plot for **testbpsk.mat**

Finally for **testbpsk.mat**, **speccoa** is run with observer 1 collecting **testbpsk.mat** samples 1 to 8192 and observer 2 collecting **testbpsk.mat** samples 71 to 8263 for a 70 sample delay. The results of this test appear in Figure 7-5. Because the signals at the two observers are completely correlated, this scenario represents an ideal situation for the algorithm. Its complete success is expected for this case but serves as an initial check of **speccoa**. The remaining two signals introduce both noise and poorly correlated signals to the scenario.

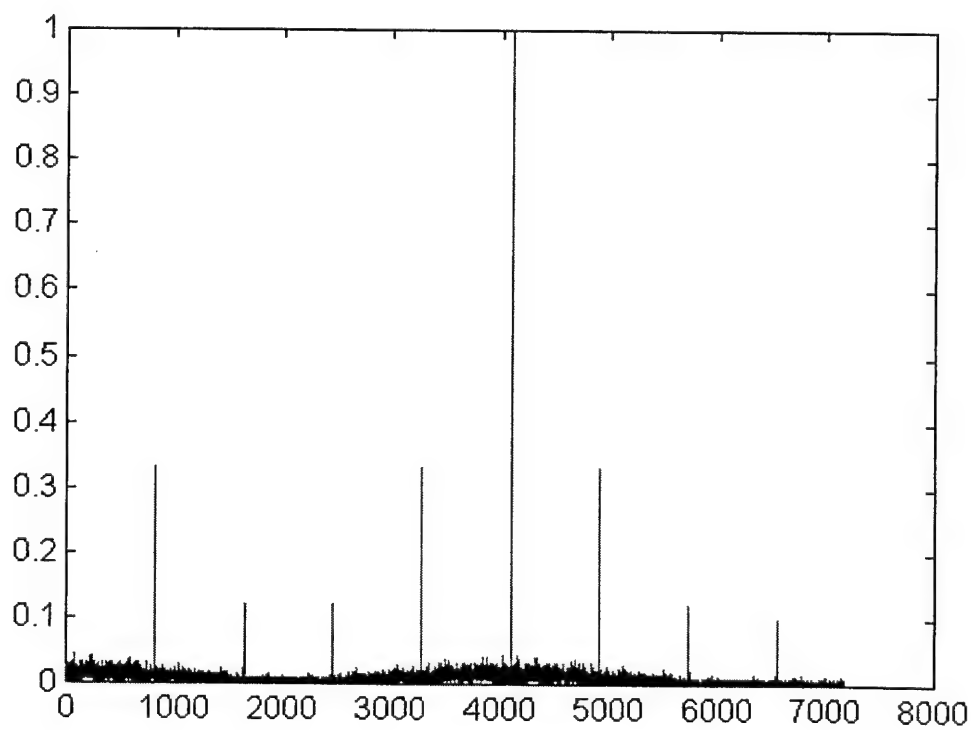
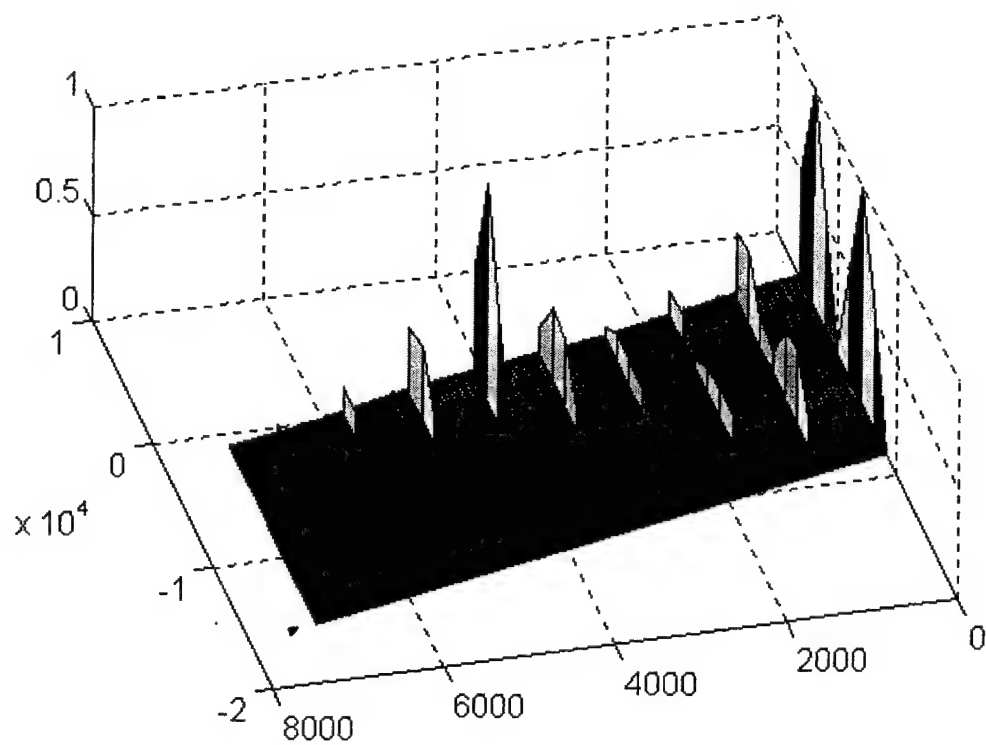


Figure 7-4 - SCF (top) and Mag(SCF) vs alpha (bottom) for **testbpsk.mat**
computed and plotted by **ssca** and **plotscf**

Two very noisy BPSK signals constitute the remaining generated signal testing for the system. They were created by passing the noiseless BPSK signal through separate AWGN channels with E_b/N_0 of 0.88 or -0.534 dB. This corresponds to probability of bit error of 10^{-2} . Figure 7-6 shows the generation of **n1bpsk.mat** and **n2bpsk.mat**. Because the AWGN channel introduces significant noise the BPSK signals, **n1bpsk.mat** and **n2bpsk.mat** are highly corrupted. Figures 7-7 and 7-8 show the time domain and frequency domain plots respectively for the two signals.

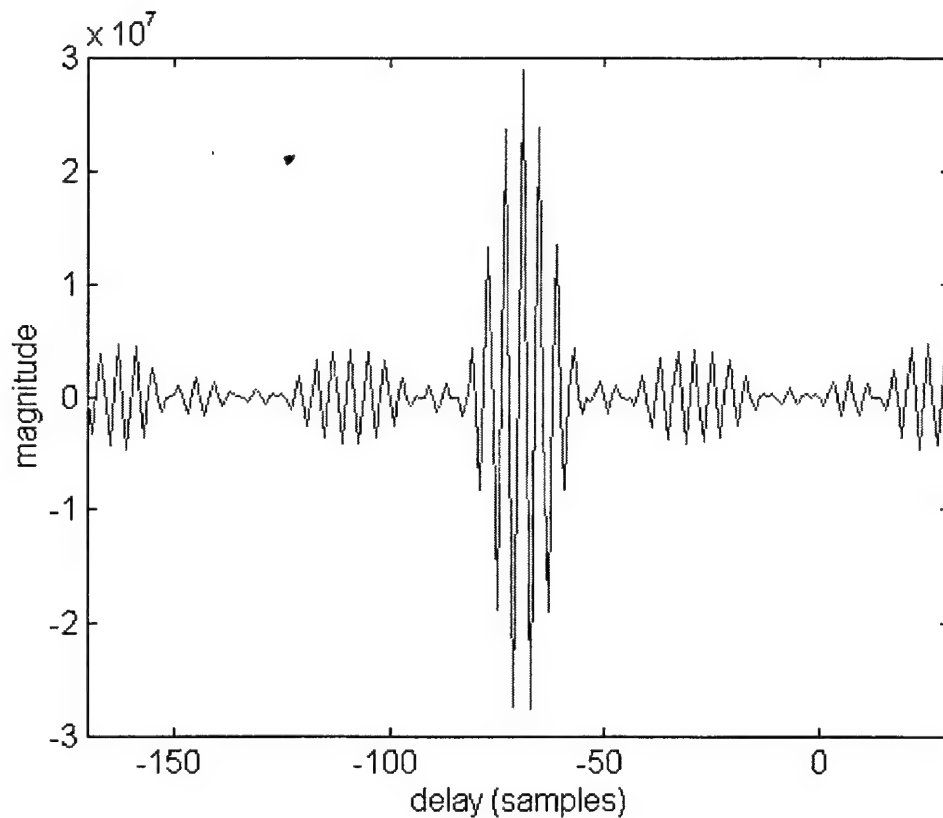


Figure 7-5 - Output of **speccoa** routine for **testbpsk.mat** with 70 sample delay

Naturally, the level of noise in these BPSK signals will be evident in their SCF(s). Figures 7-9 and 7-10 display the output of **ssca** and **plotscf**. Note that the reduction in SNR compared to **testbpsk** has added noise to the plots but has not masked the important features. While in theory as presented in Chapter III, the AWGN should have no features

other than those evident at $\alpha = 0$, it does add noise to the higher values of a in the SCF plots in Figure 7-9. It does so because the AWGN channel used in the simulation is not ideal AWGN and thus is not truly random and Gaussian. Thus, some statistical impurities in the channel as well as the computational trade-offs in the estimation procedure of the SSCA algorithm lead to contributions above $\alpha = 0$.

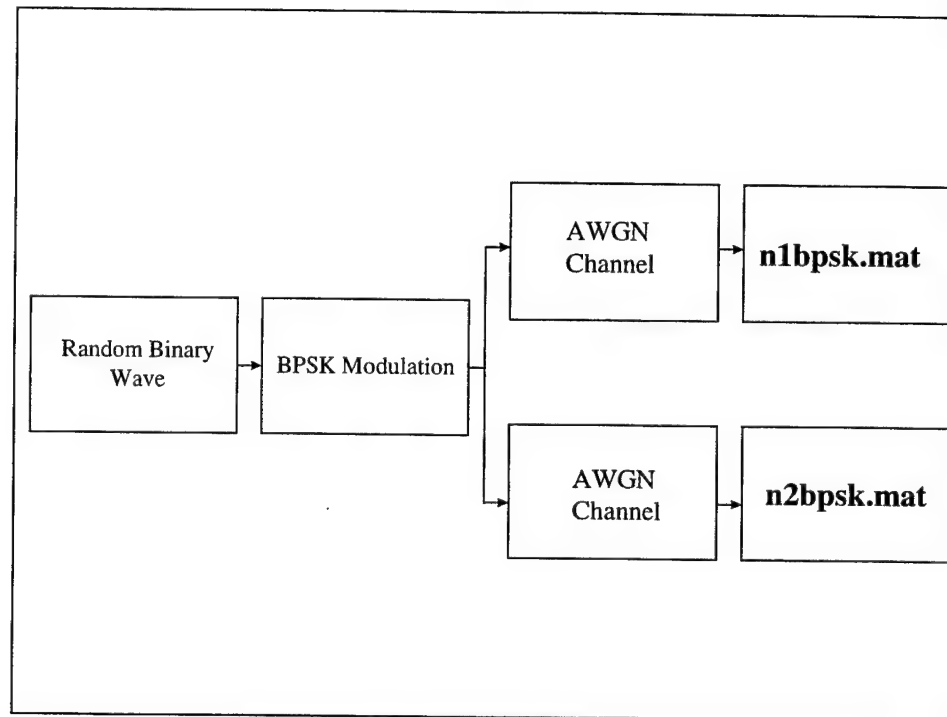


Figure 7-6 - Generation of corrupted BPSK as **n1bpsk.mat** and **n2bpsk.mat**

Finally, **speccoa** uses **n1bpsk.mat** for observer 1 and **n2bpsk.mat** delayed by 70 samples for observer 2 to verify that it indeed works in highly corrupt environments given the proper signal features as inputs. The results appear in Figure 7-11. The successful conclusion of testing with generated signals leads next to testing of the ARL:UT data from a November 1995 test in the Austin, Texas area.

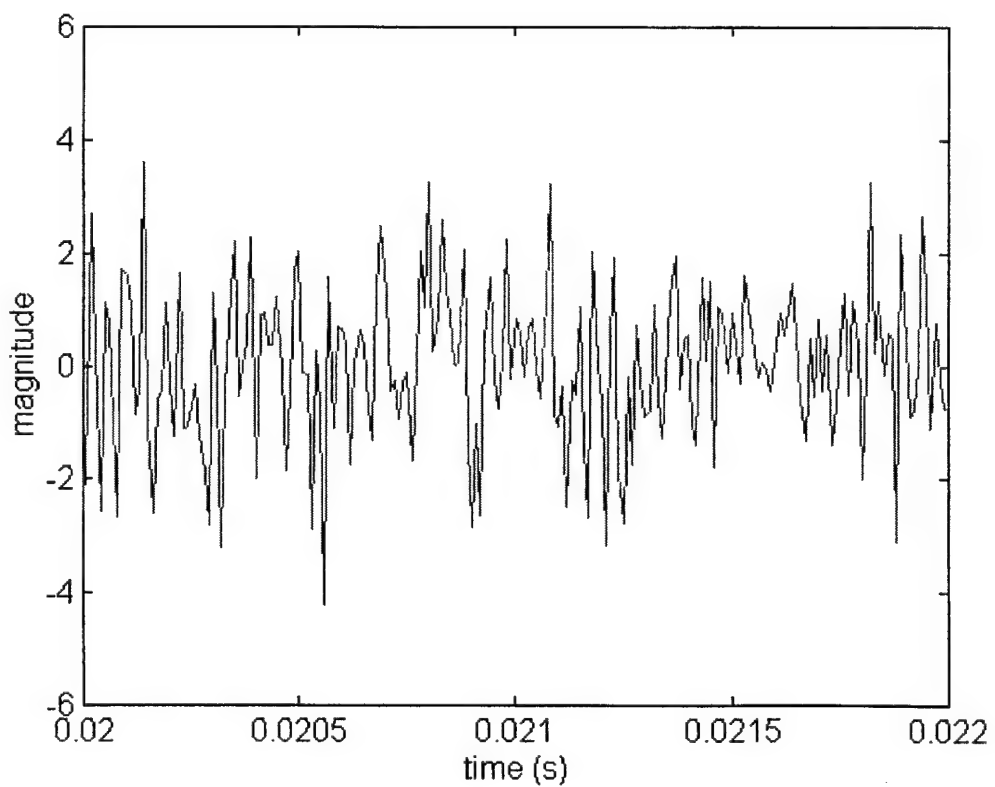
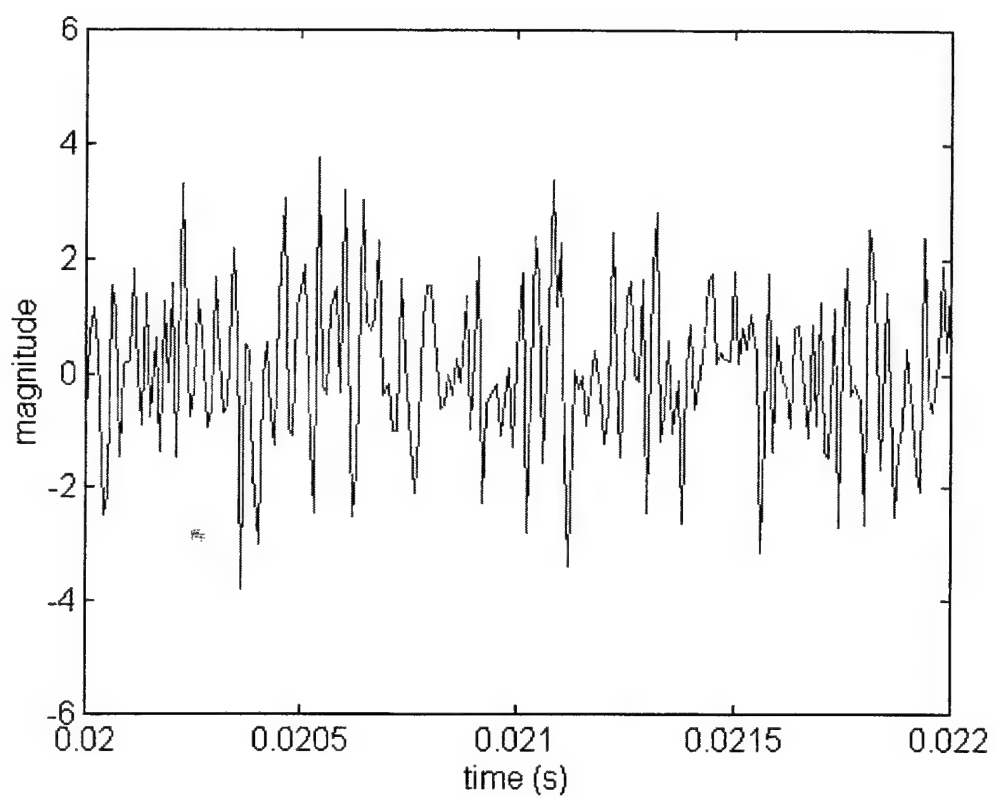


Figure 7-7 - Time domain plots for **n1bpsk.mat** (top) and **n2bpsk.mat** (bottom)

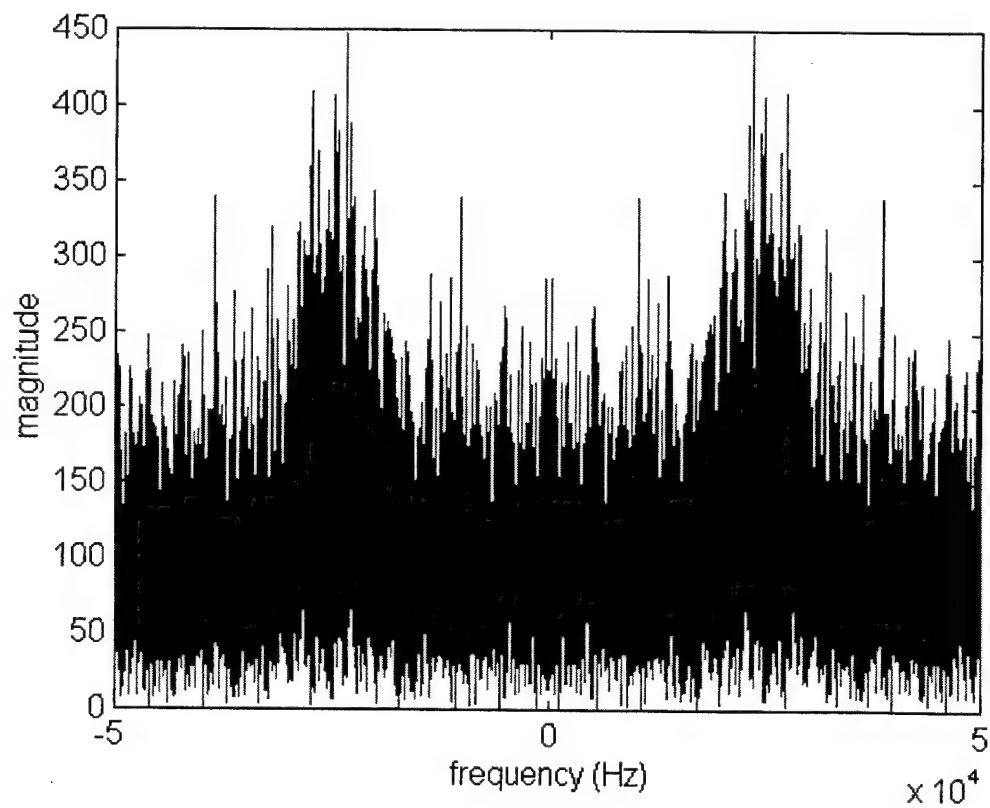
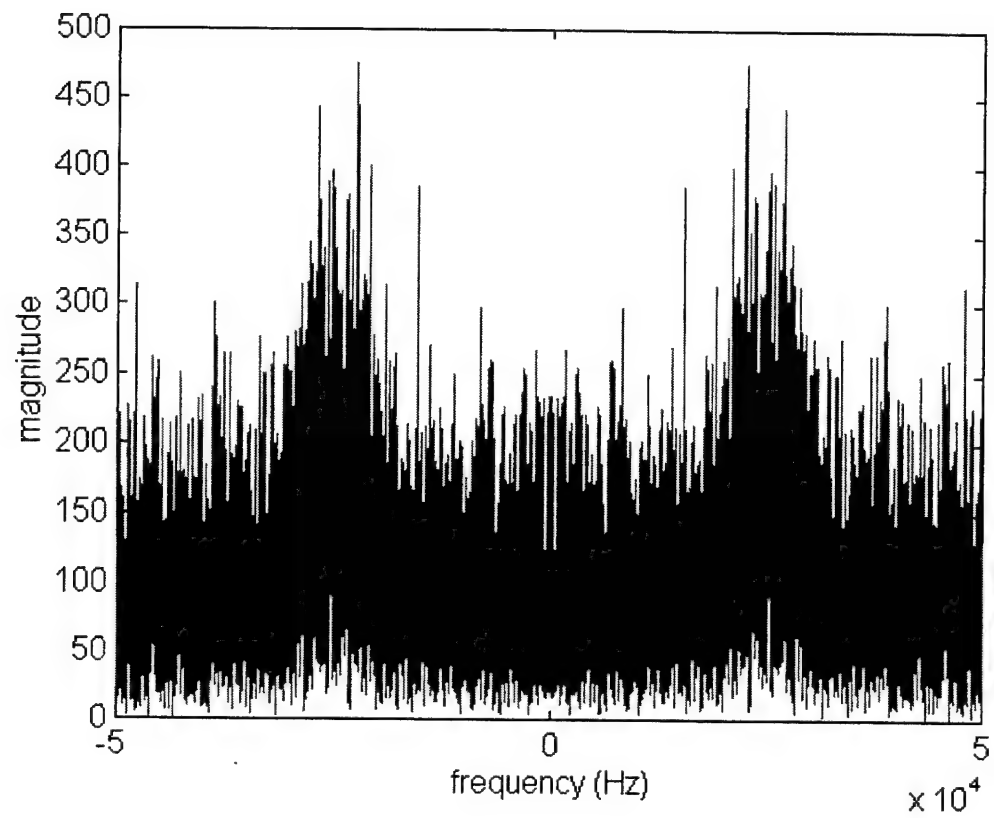


Figure 7-8 - Frequency domain of **n1bpsk.mat** (top) and **n2bpsk.mat** (bottom)

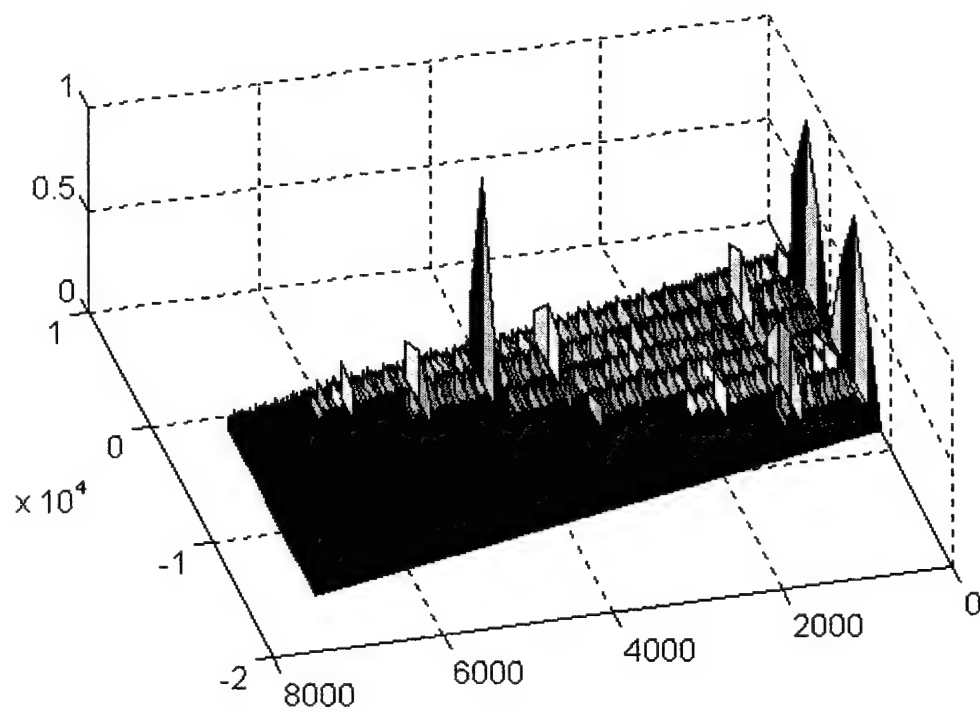
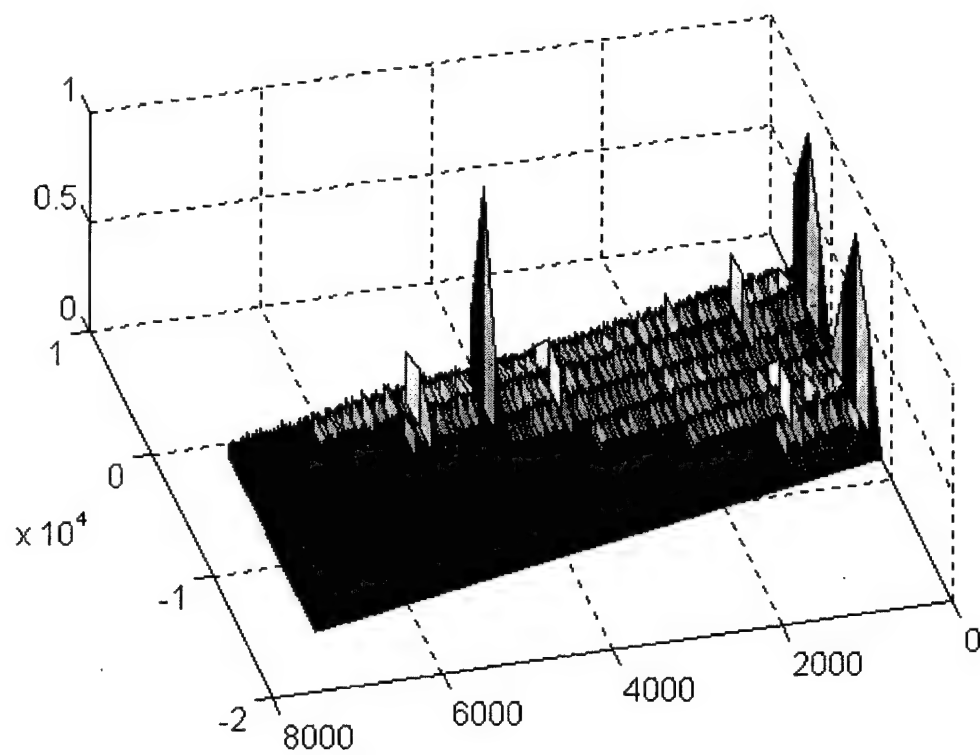


Figure 7-9 - SCF(s) for `n1bpsk.mat` (top) and `n2bpsk.mat` (bottom)

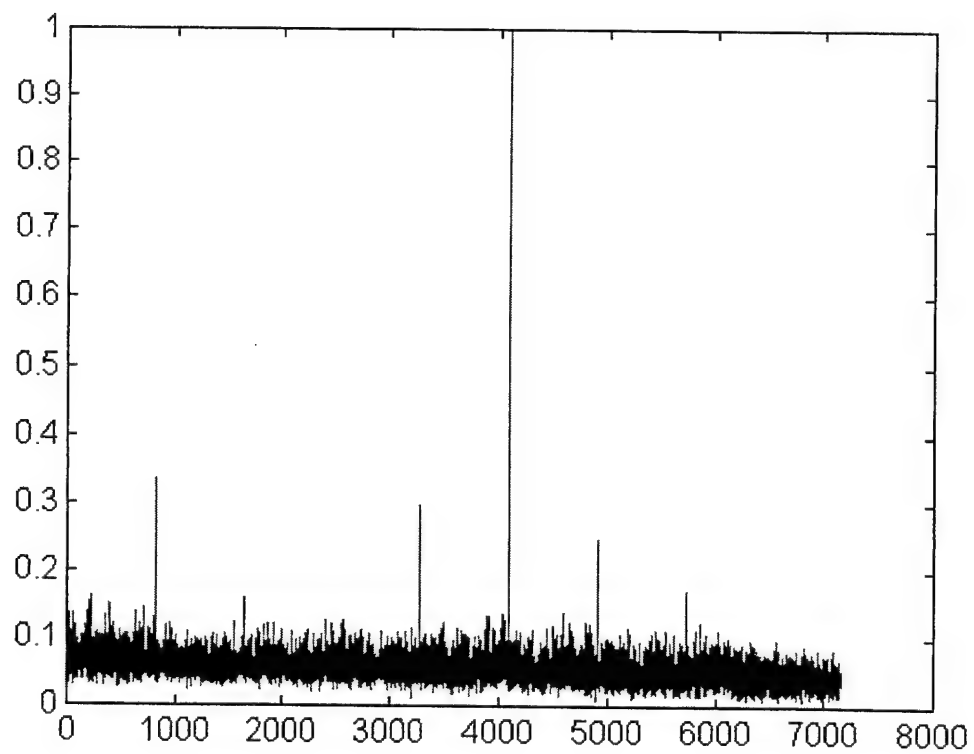
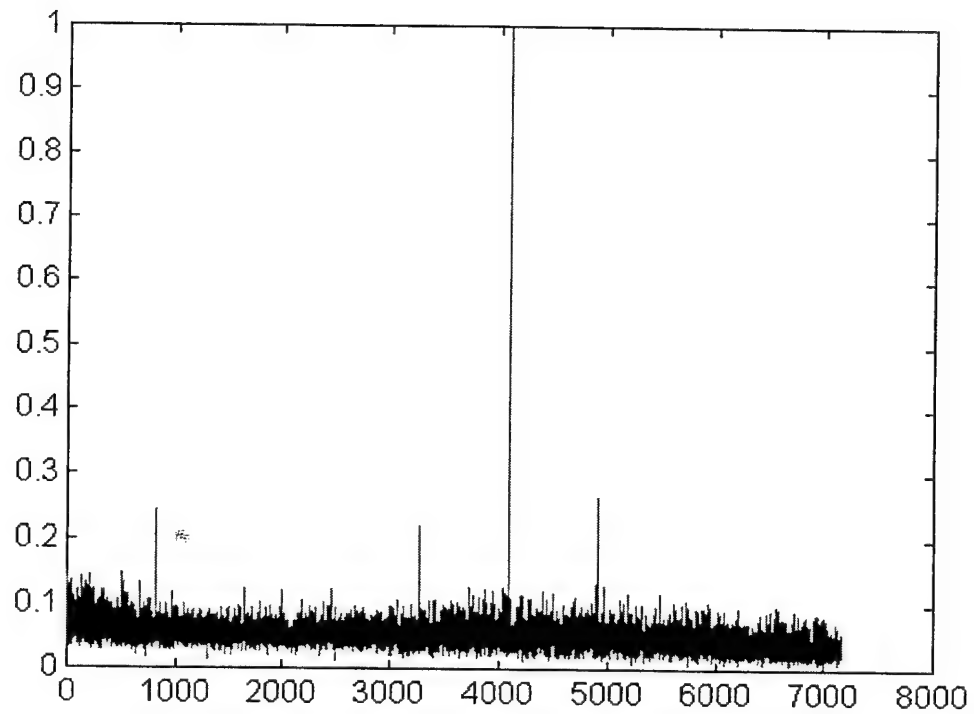


Figure 7-10 - Mag(SCF) vs. α for **n1bpsk.mat** (top) and **n2bpsk.mat** (bottom)

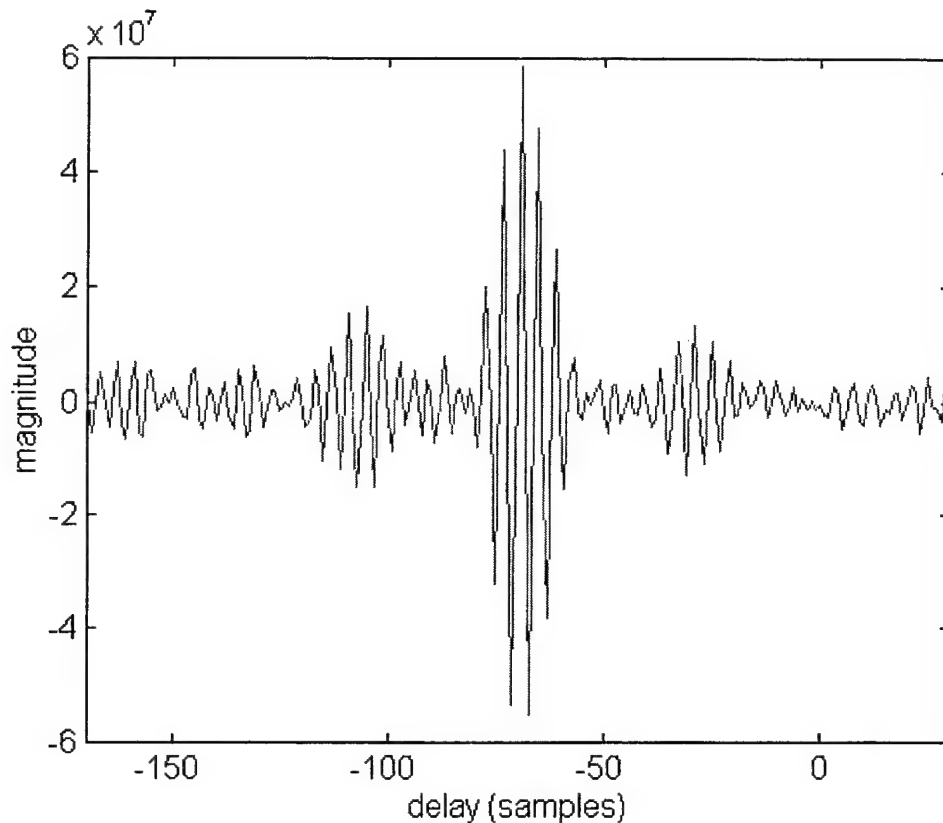


Figure 7-11 - Output of **speccoa** routine for **n1bpsk.mat** and **n2bpsk.mat**

B. ARL:UT COLLECTED DATA

The portion of the November 1995 Austin tests that are used in this work were collected by four stationary observers in the Austin area. The emitter was a push-to-talk narrow-band FM (NBFM), 1 W transmitter located near the center of the four observers. The GDOP of the scenario, given the positions of observation and the stationary target, was excellent at less than two.

During the test, each observer records ~800 ms of data every 5 seconds. This data was stored to magnetic tape for post test analysis and further off-line testing. It is used to compare both TDOA determination and geolocation performance of the ARL:UT algorithms and those developed here. In order to best understand the output of **ssca**, **plotsf** and **speccoa** for the ARL:UT data, it is necessary to follow the signals' processing from antenna to storage media. The processing at each observer is identical with respect

to archiving the data for later use and thus a single explanation serves for all four observers in this case.

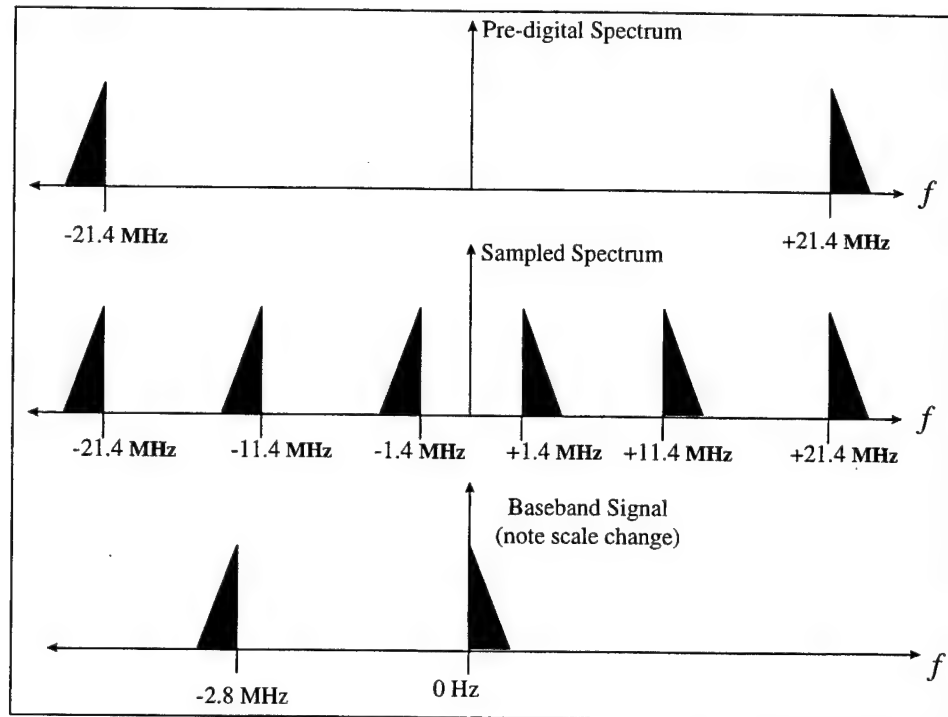


Figure 7-12 - Beginning of ARL:UT signal processing

Following reception, the 10 kHz bandwidth signal is heterodyned to an intermediate frequency (IF) of 21.4 MHz. At the IF, the 10 Msamples/second A/D converter aliases the signal at +1.4 MHz and -1.4 MHz with additional spectra added at intervals of the sampling rate. The spectrum at 1.4 MHz is downconverted to baseband as the product of an appropriate complex exponential multiplication. Its mirror at -1.5 MHz is shifted to -2.8 MHz in the process. This series of steps is summarized in Figure 7-12 with a spectrum relatively representative of that of the test data.

At this point, the data is decimated in time by a factor of 1024. This step again aliases the signal at intervals of the new sampling rate, $f_s = 9765.625$ Hz. The result is a set of four spectra in the interval $-f_s/2$ to $+f_s/2$. Figure 7-13 shows the results of this process in the time domain and frequency domain. Note the relationship between the highest negative frequency spectral line at approximately -440 Hz and the highest positive frequency

spectral line at approximately 4440 is exactly $f_s/2$ as they are related, aliased versions of the spectrum. The lowest negative frequency at approximately -4460 Hz and lowest positive frequency at approximately 420 Hz share that same relationship for the same reason. The frequencies are approximated above as they change slightly throughout the test and vary by observer as well.

The corresponding SCF has features along the cyclic frequency axis that correspond to the various combinations of separation between the four spectral lines in the PSD of the signal. The greatest contribution to the SCF occurs at a separation of $f_s/2$ given the two constant relationships between the spectral lines cited above. At $\alpha = f_s/2$, all four lines contribute to the SCF thus the $\alpha = f_s/2$ feature contains the most energy. This is best illustrated the SCF and the magnitude vs. cycle frequency plots in Figure 7-14. Note the greatest peak in the SCF occurs at $f_s/2$.

Finally, using this greatest feature, **speccoa** finds the TDOA between observers. While other features may also lead to reliable answers, the $f_s/2$ feature is a constant throughout the testing. All observers have this feature and it is always the strongest feature of the SCF. An example of the output from **speccoa** appears in Figure 7-15. It depicts the TDOA between the master node and slave #1. Specific results from the testing including some additional steps taken for more resolution in the TDOA computations appear in Chapter IX.

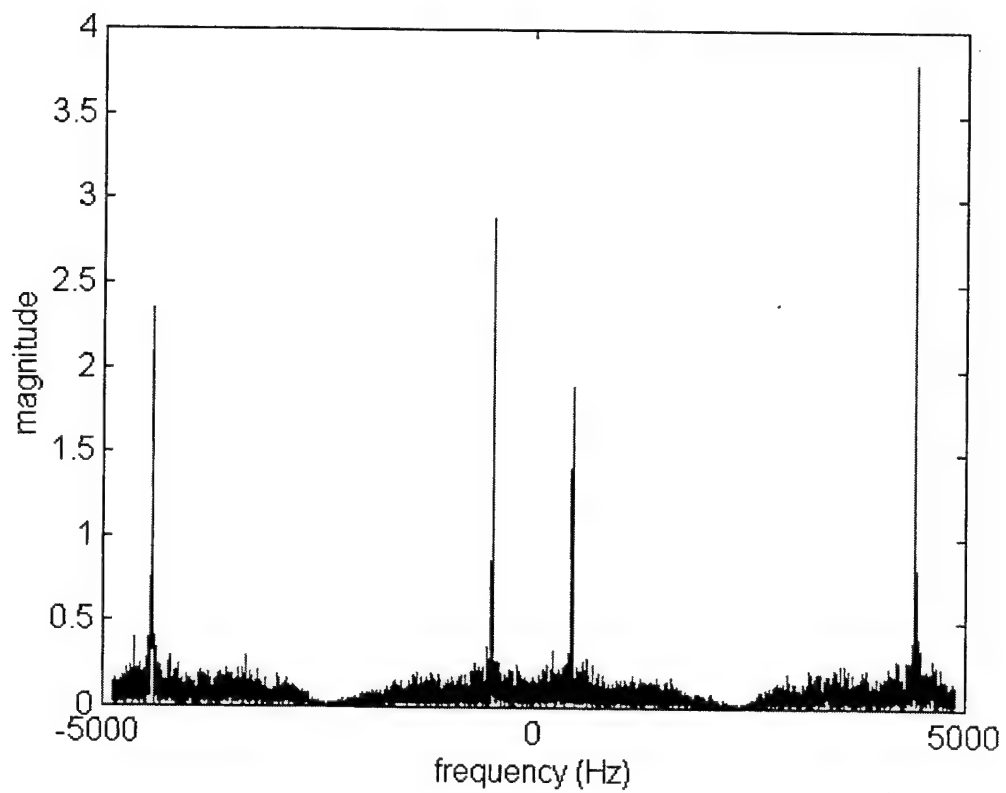
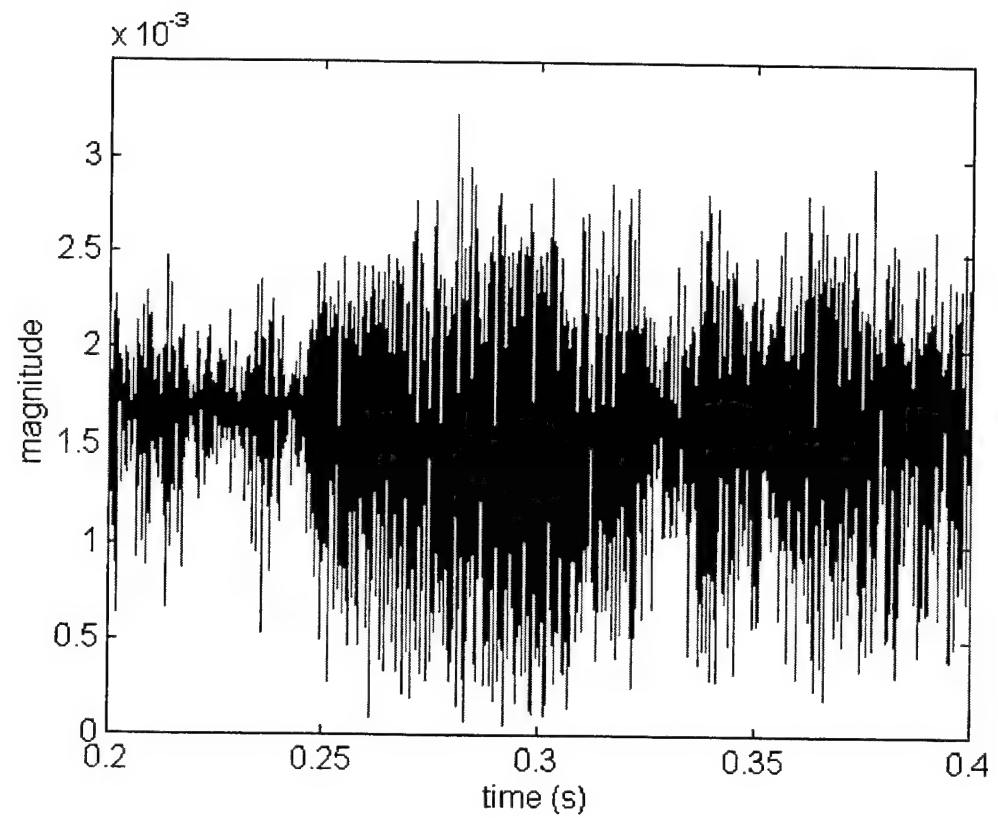


Figure 7-13 - Time (top) and frequency (bottom) plots of master signal, time 409400

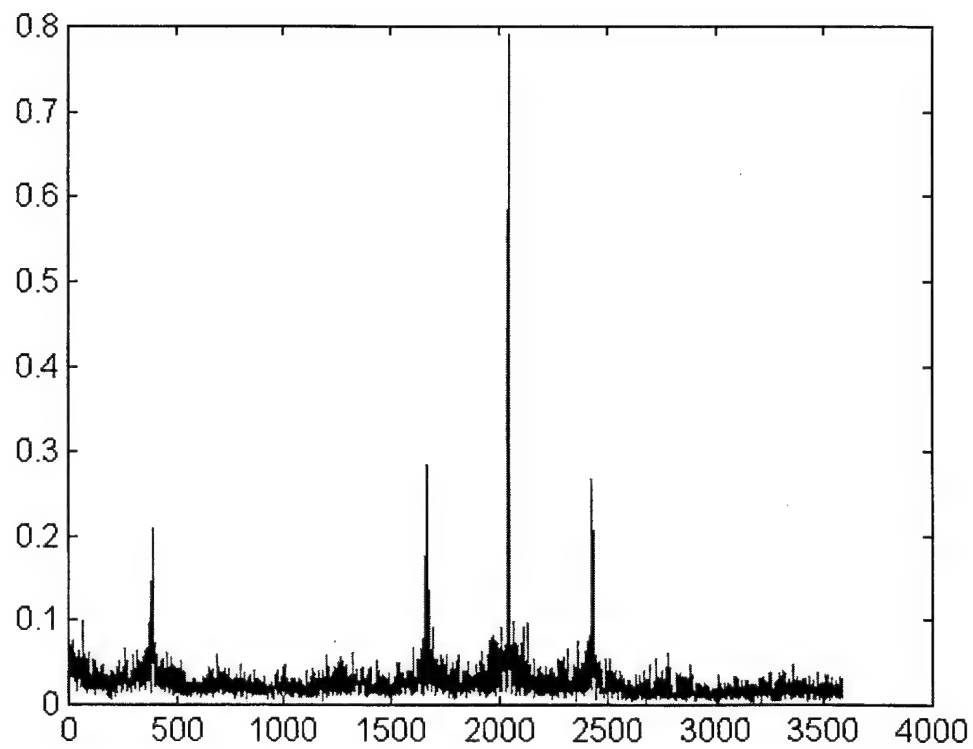
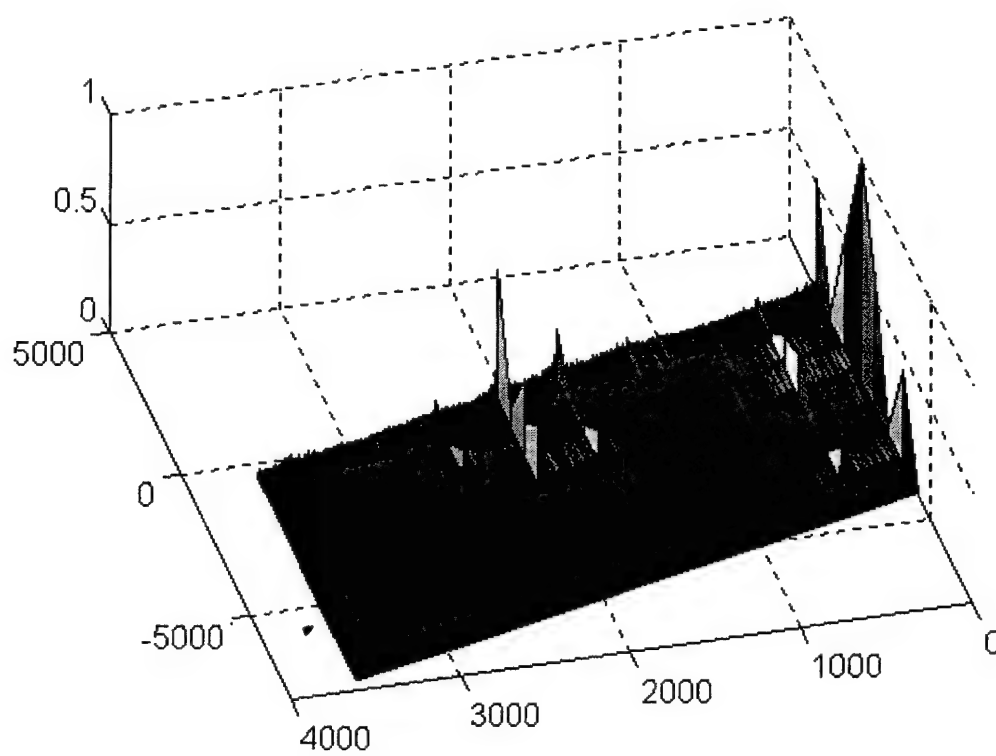


Figure 7-14 - SCF (top) and Mag(SCF) vs. alpha for master signal, time 409400

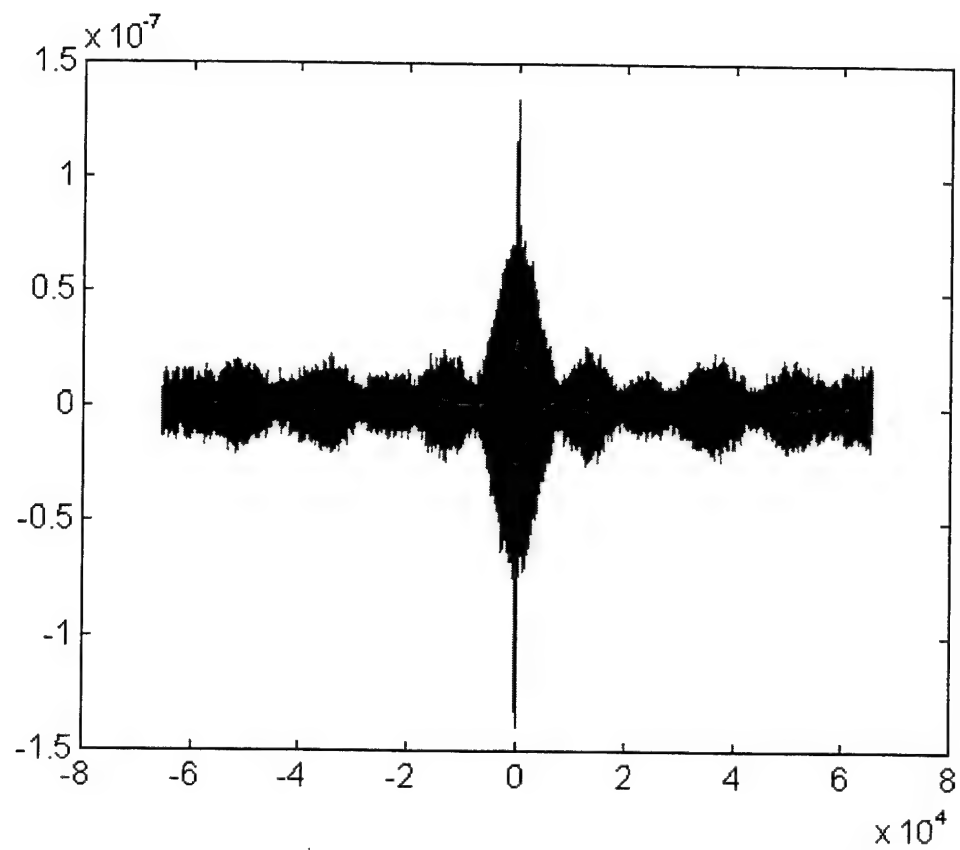


Figure 7-15 - Output of `speccoa` for master and slave #3, time 409510

VIII. GEOLOCATION SOFTWARE WORKBENCH BLOCKS

A. SIMULINK® BLOCK CONSTRUCTION

In addition to the testing of the combination of SPECCOA and Rusu's closed form TDOA geolocation solution, the algorithms serve as the first blocks readied for construction for a developing geolocation software workbench. The details of their construction are outlined below in theory.

Blocks that may be used in simulations run in the Simulink® environment conform to a general, highly flexible standard created by The Mathworks, Inc. programmers. They may be implemented in one of three ways: graphically, through m-files or through another language such as ANSI C which produces a mex-file. No matter the method, the result is an S-function that operates according to the rules and protocols of the Simulink® environment.[24]

Graphical creation of an S-function involves connecting the existing blocks that perform the needed function, collecting them as a single entity and masking that collection as the new block. This procedure forces Simulink® to create an S-function that describes the new system. This is by far the easiest method of creation for a **speccoa** block and a closed form TDOA geolocation block. The other two methods, m-files and mex-files, are appropriate in some instances such as certain state-space systems or other applications where the system can easily be written as a set of differential equations. Though more complex to create, S-functions created as m-files and mex-files simulate considerably faster. However, with the addition of the Simulink Accelerator®, graphically created S-functions enjoy some improvement in execution time as well.[24]

B. SPECCOA BLOCK

All the functions needed to use the **speccoa** code written for the testing described in both Chapters VII and IX, exist in Simulink® or one of the toolboxes. The Signal Processing Toolbox ® and DSP Blockset® contain the necessary buffers and functions needed by the **speccoa** code. A user defined Matlab® function block serves as the

vehicle for the **speccoa** code to be used in the Simulink® environment. Connecting the buffers with the user defined function block constitutes the majority of the **speccoa** block.

In general, a geolocation workbench block of **speccoa** requires two scalar sequences, the time samples of the two signals and one scalar parameter, the cycle frequency of interest as inputs. Time domain samples feed a buffer of length defined by the user in order to achieve the desired resolution. These time domain samples come to the **speccoa** block from an appropriately designed data conversion block. Regardless of its input, the conversion block must provide the **speccoa** block with single real or complex values for each simulation time period. In addition, the characteristic cycle frequency enters the block following the operation of a characterizer (defined elsewhere) to complete the inputs. The output of the **speccoa** block is a 2 x 1 vector, a time-stamp and a TDOA. Figure 8-1 shows a schematic of the **speccoa** block. Its role in a possible simulation scenario appears in Figure 8-3.

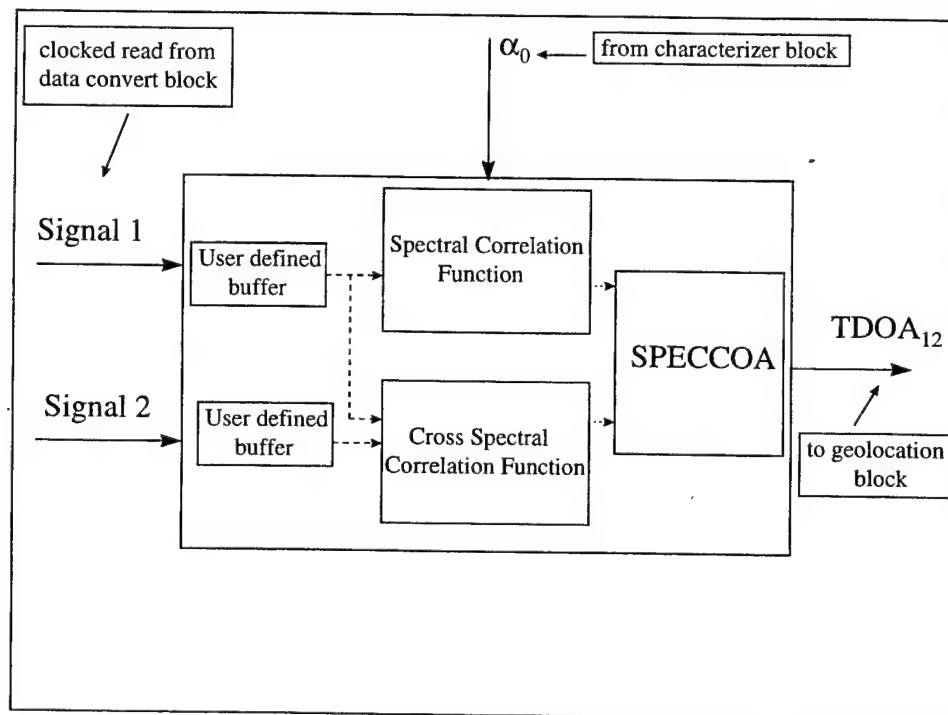


Figure 8-1 - Schematic of **speccoa** geolocation workbench block

C. GEOLOCATION BLOCK

The closed form TDOA geolocation block is the more complex of the two algorithm blocks. Its inputs include four 3 x 1 observer position vectors with x, y and z parameters for each observer. In addition, it must have the output of three **speccoa** blocks. The geolocation block's output is a 4 x 1 vector that includes the target's x, y and z coordinates and a time corresponding to that geolocation. Figure 8-2 illustrates a basic diagram of the block. Its role in a possible simulation scenario appears in Figure 8-3 as well.

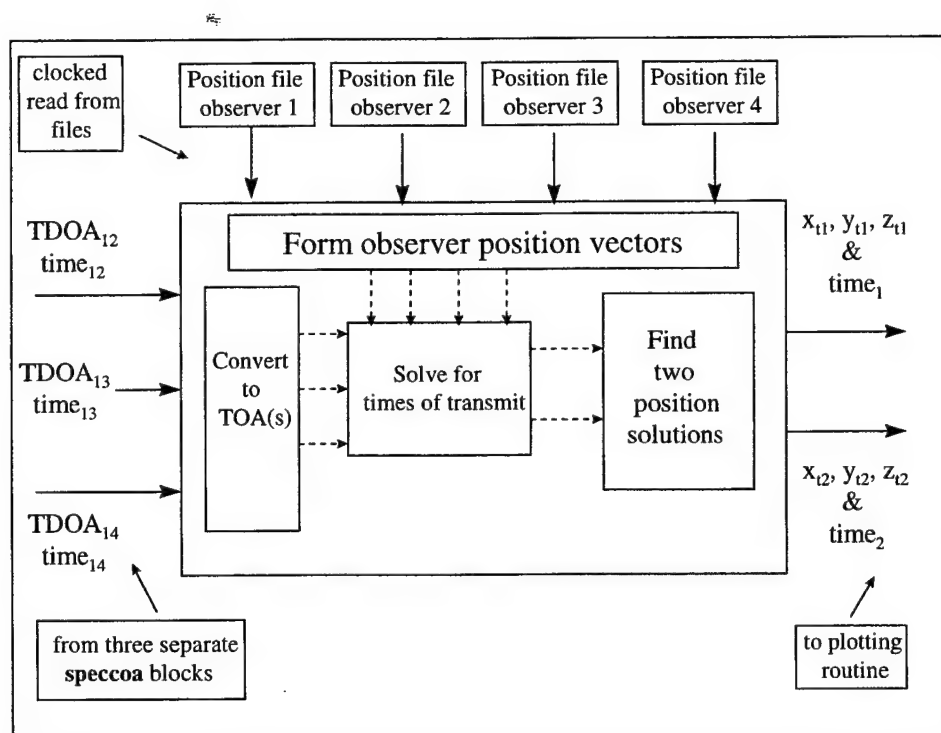


Figure 8-2 - Closed form TDOA geolocation solution block schematics

D. SIMULATION SCENARIO

One possible scenario that might be simulated using the two blocks described above is the November 1995 Austin test of the ARL:UT system. Using the signal data files and position files for each of the four observers, both the **speccoa** block and the

closed TDOA form geolocation block are testable. The addition of a characterizer is necessary to feed the **speccoa** block. This function could be performed by a user defined block that calculates the maximum value of the SCF for each value of cycle frequency as **plotscf** plotted (see Chapter VII). The maximum value of this function could be the characteristic cycle frequency used in the **speccoa** block. In addition, the geolocation block could feed a plotting routine to display each geolocation. A diagram of this implementation appears in Figure 8-3.

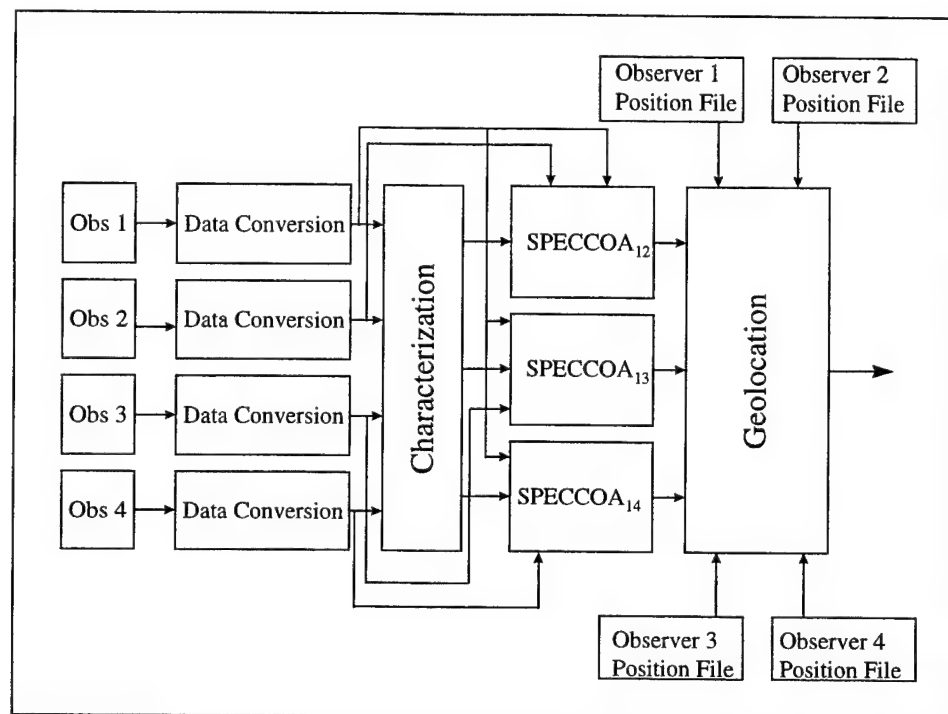


Figure 8-3 - Simulation scenario

Clearly the Simulink® environment is ideal for testing the many aspects of geolocation from data processing to parameter computation to geolocation estimation. The user defined MATLAB® function block provides for easy introduction of m-file routines into the S-function domain. It allows the interchange of various blocks in any scenario. This fact alone lends great flexibility and power to a geolocation software workbench centered around this environment. Other blocks such as pre-filters for the data or logic to evaluate the quality of the TDOA(s) or geolocation can also be

constructed. In addition, data from many different sources is handled simply by modifying the data conversion block to accept a different form of input. Its output remains the same. Using the Simulink® environment eliminates the need to define standards for module construction and provides an established simulation engine with many options. It is surely the most expeditious and intelligible implementation of a geolocation simulation system.

IX. RESULTS

A. BACKGROUND

Two comparisons are made between the cyclostationary TDOA processor measurements and those of the ARL:UT system. Both the TDOA(s) and the resulting geolocations serve as benchmarks of performance. In comparing the two systems' results, theoretical TDOA(s) calculated from the target's position and the positions of the four observers, using a value of 2.998×10^8 for c , the speed of propagation, are the baseline for comparison of the TDOA measurements. The target's actual position throughout the test acts as the baseline for comparison of the geolocations.

The TDOA(s) measured by both systems are biased by the radios used in the test. This constant bias was discovered in post test analysis and removed from the ARL:UT published results. However, the biases remain intact here to simplify the calculations and comparison. The geolocations suffer from the same biases and are also left uncorrected for the comparison.

The comparison consists of 25 time periods of data from the November 1995 Austin test. Because all four observers recorded data during these times, geolocations in three dimensions are possible. The process of arriving at three TDOA(s) and a geolocation involves plotting the SCF(s) for the four observers, choosing a cycle frequency, feeding that data to **speccoa** and finally running the closed form solution for the geolocation. The plots for the four SCF(s), the four magnitude of SCF vs cycle frequency and the three **speccoa** outputs appear in Appendix B for each of the 25 time periods. As noted in Chapter VII, the feature of the SCF at $f_s/2$ provides **speccoa** the needed cycle frequency in every time instance. A summary of the results appears below.

B. TDOA COMPARISON

The comparison of TDOA(s) between the master node and slaves 1, 2 and 3 appear below in Figures 9-1 through 9-6 below. Figures 9-1, 9-2 and 9-3 merely plot the TDOA(s) in the order in which they were determined.

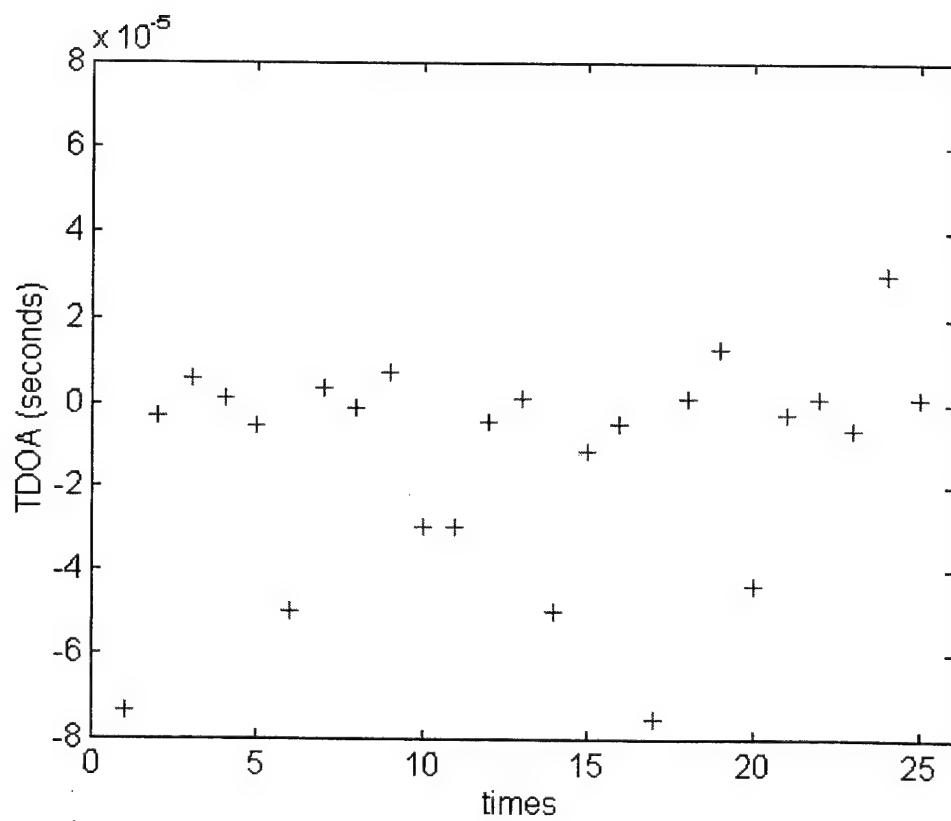
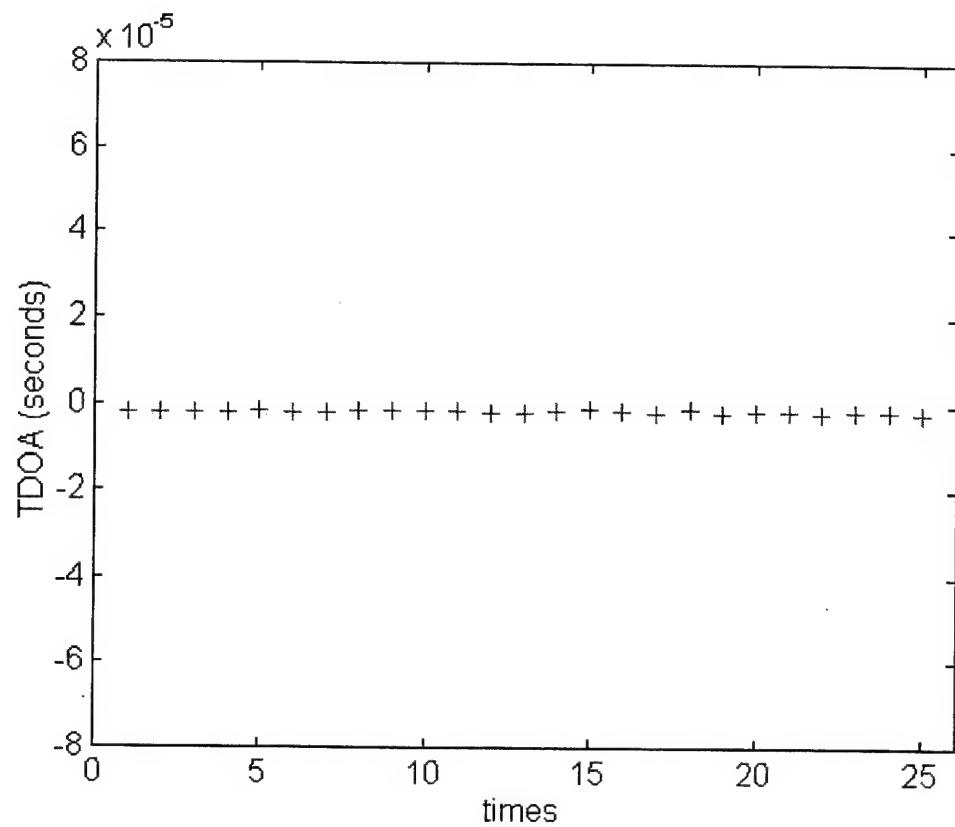


Figure 9-1 - TDOA(s) for master node and slave #1, ARL:UT (top), **speccoa** (bottom)

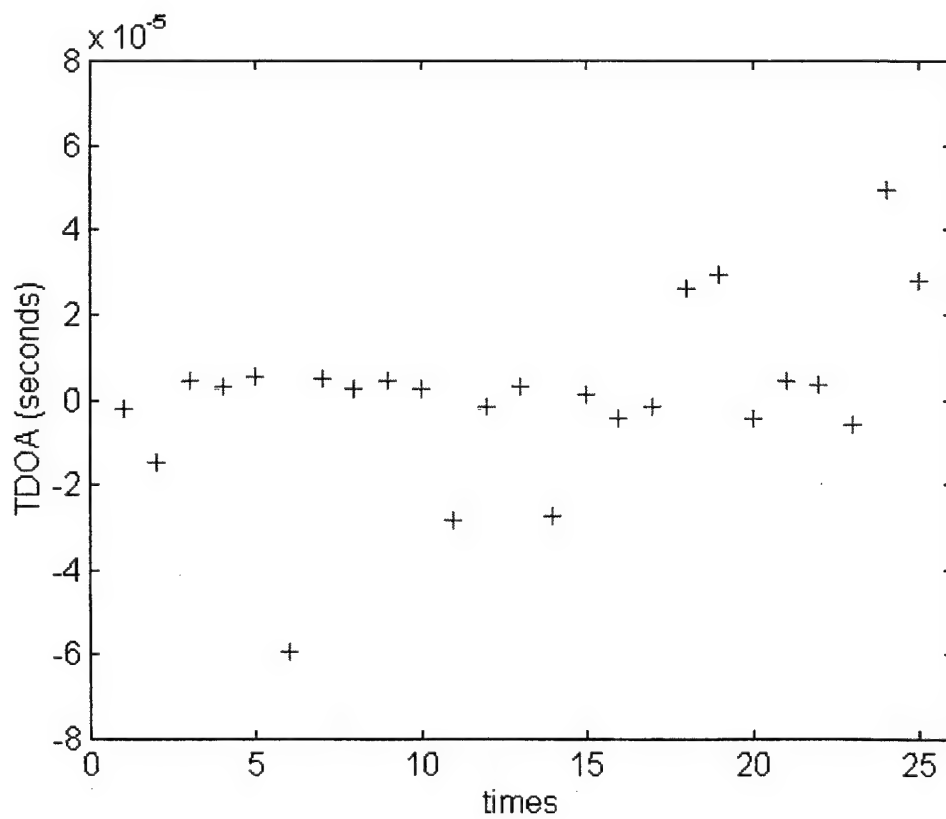
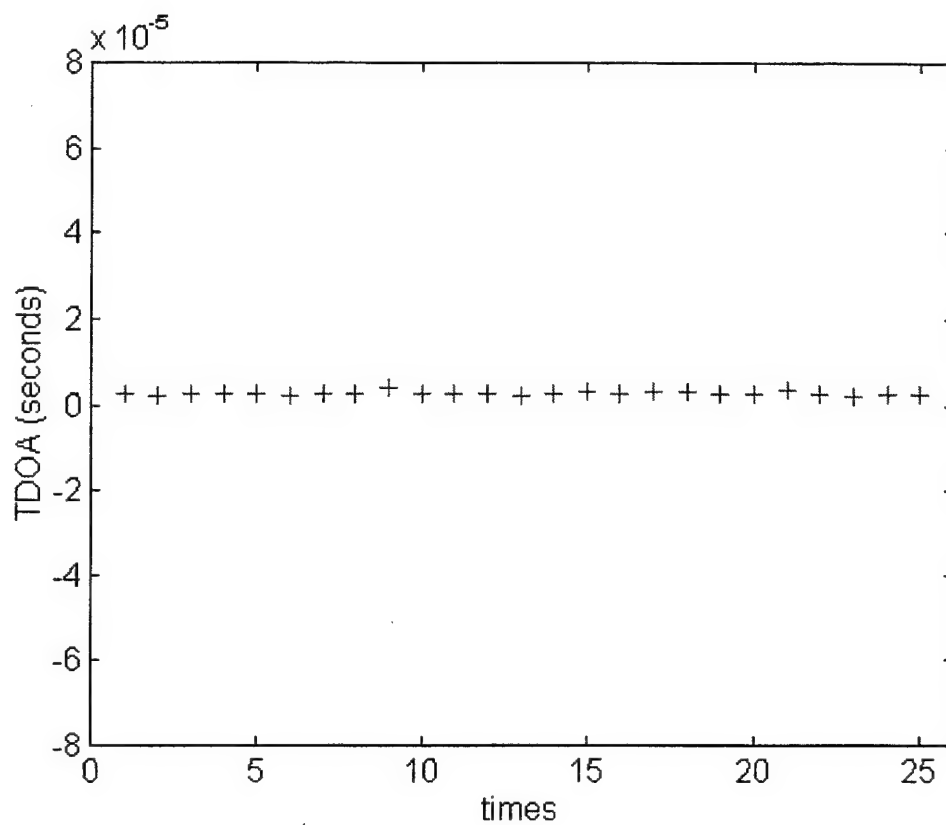


Figure 9-2 - TDOA(s) for master node and slave #2, ARL:UT (top), **speccoa** (bottom)

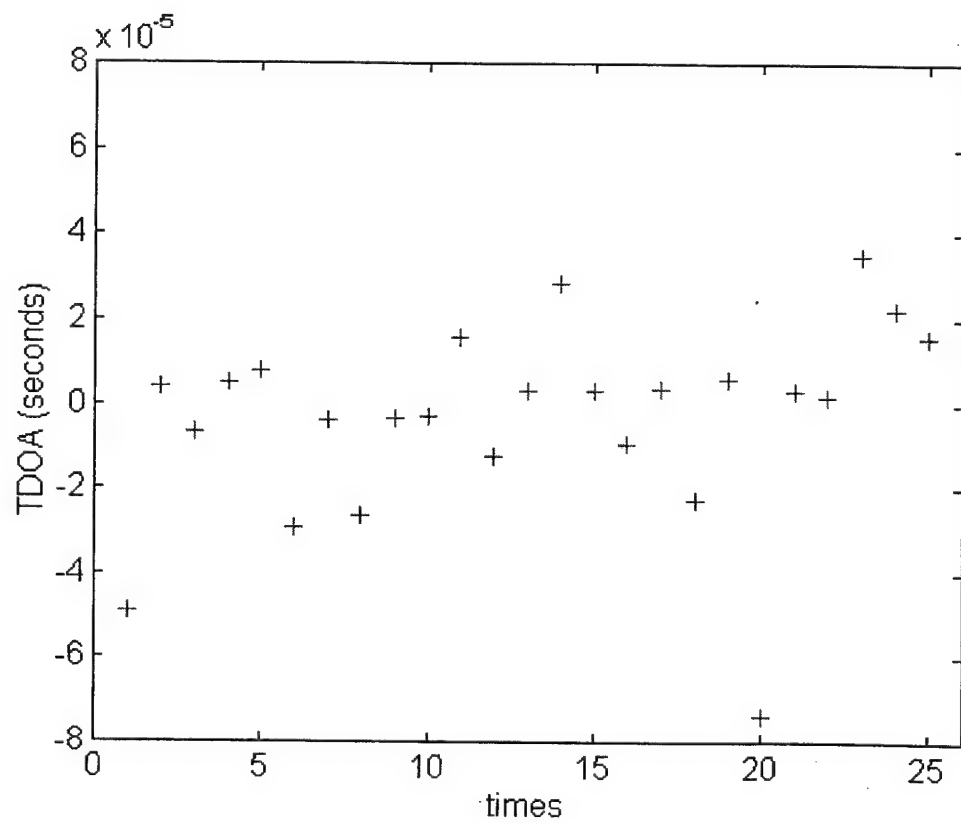
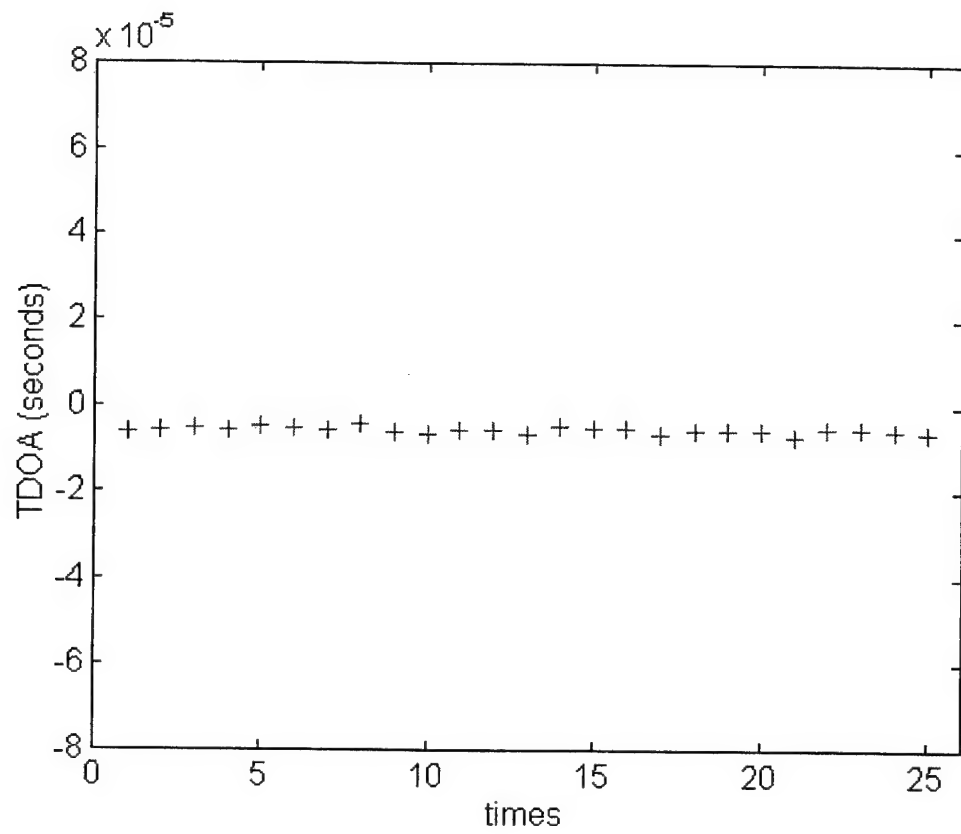


Figure 9-3 - TDOA(s) for master node and slave #3 ARL:UT (top), **speccoa** (bottom)

Figures 9-4, 9-5 and 9-6 show the deviation in seconds, from the calculated, theoretical TDOA, for each of the 25 time periods along the horizontal axis. The top plots in each figure again show results from the ARL:UT test; the lower plots show results of the cyclostationary TDOA processor.

C. GEOLOCATION COMPARISON

While the algorithm in both instances is identical, a comparison of the results serves to further illustrate the performance of the two different TDOA determination algorithms. The method of comparison is merely the geolocation performance. Unfortunately, even given the wide variety of TDOA(s) determined by the cyclostationary TDOA processor, the version of the closed form TDOA geolocation solution coded in MATLAB® produced nearly the same result for all 25 time instances. While this consistency is commendable, the various TDOA(s) should have produced fixes separated by several kilometers. This lack of definite variation in the geolocations reflects poorly on the quality of the algorithm's outputs.

The actual location of the transmitter is given by the coordinates $x_t = -741941.474$ m, $y_t = -5462120.413$ m and $z_t = 3198242.718$ m. The MATLAB® solution produces $x_M = -740591$ m, $y_M = -5443692$ m and $z_M = 3187478$ m. The only change to these rounded integer values over the course of the 25 time periods occurs in the decimal places. Clearly this is a very poor fix in addition to the lack of variation. The ARL:UT system successfully found the coordinates to within 100 m on all three axis for all 25 time periods. More often than not, the errors in the ARL:UT calculated values were on the order of 10 to 20 meters.

Because the MATLAB® algorithm did not perform properly, a valuable comparison is impossible. The TDOA(s) discussed above are the only viable measure of comparison available.

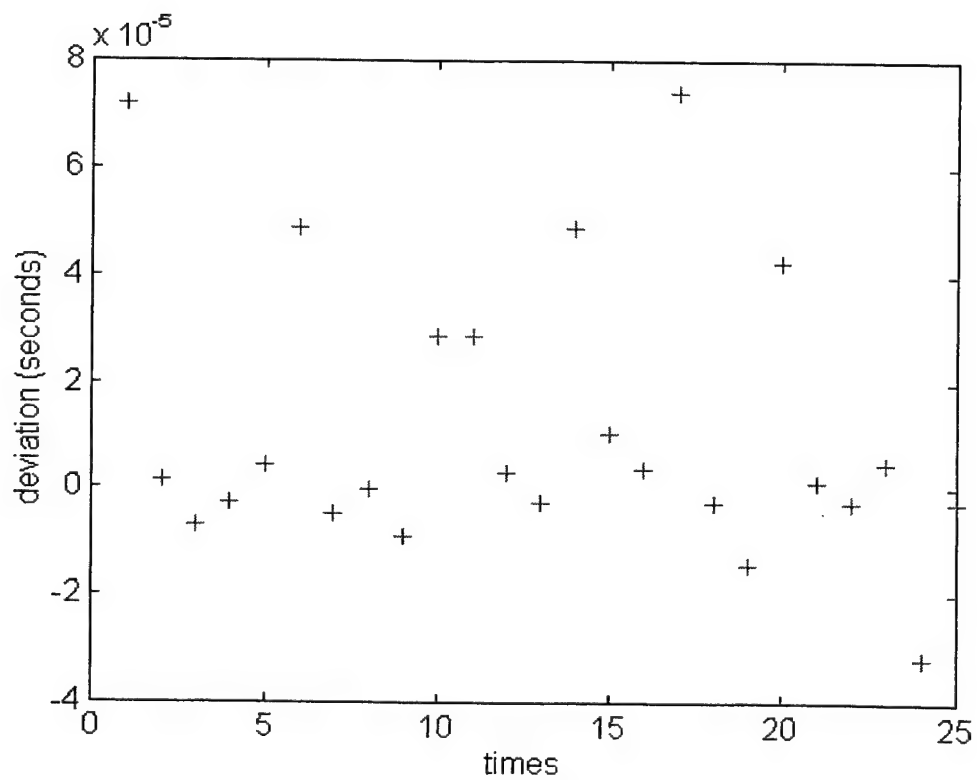
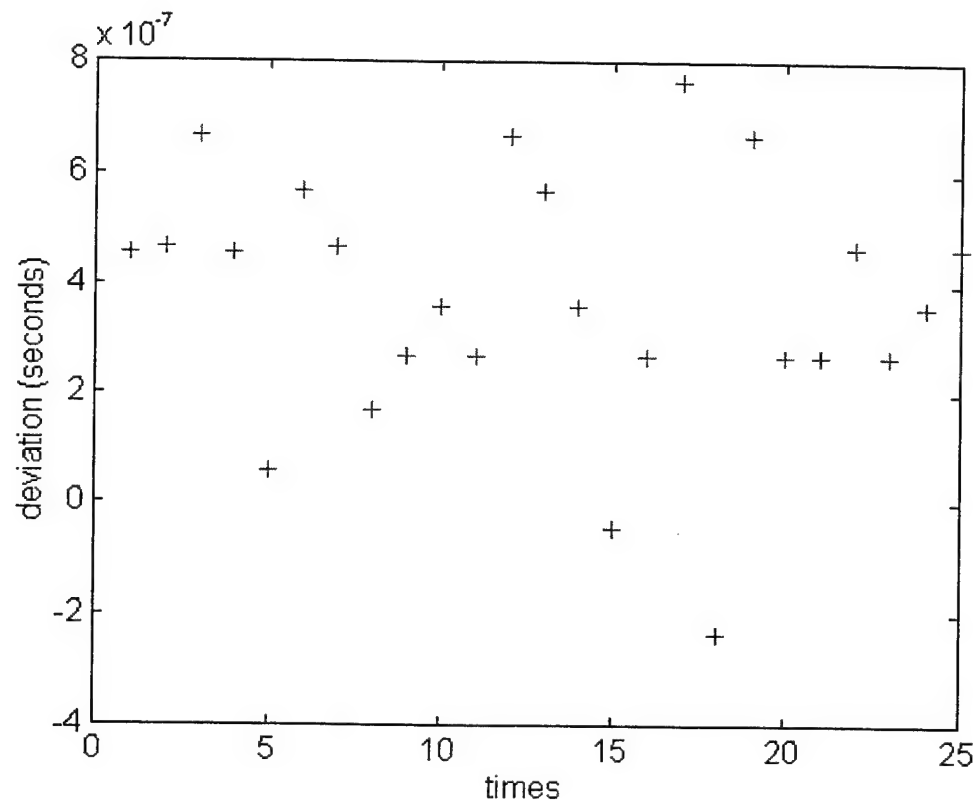


Figure 9-4 - Deviation from theoretical for TDOA between master node and slave #1,
ARL:UT (top), **speccoa** (bottom)

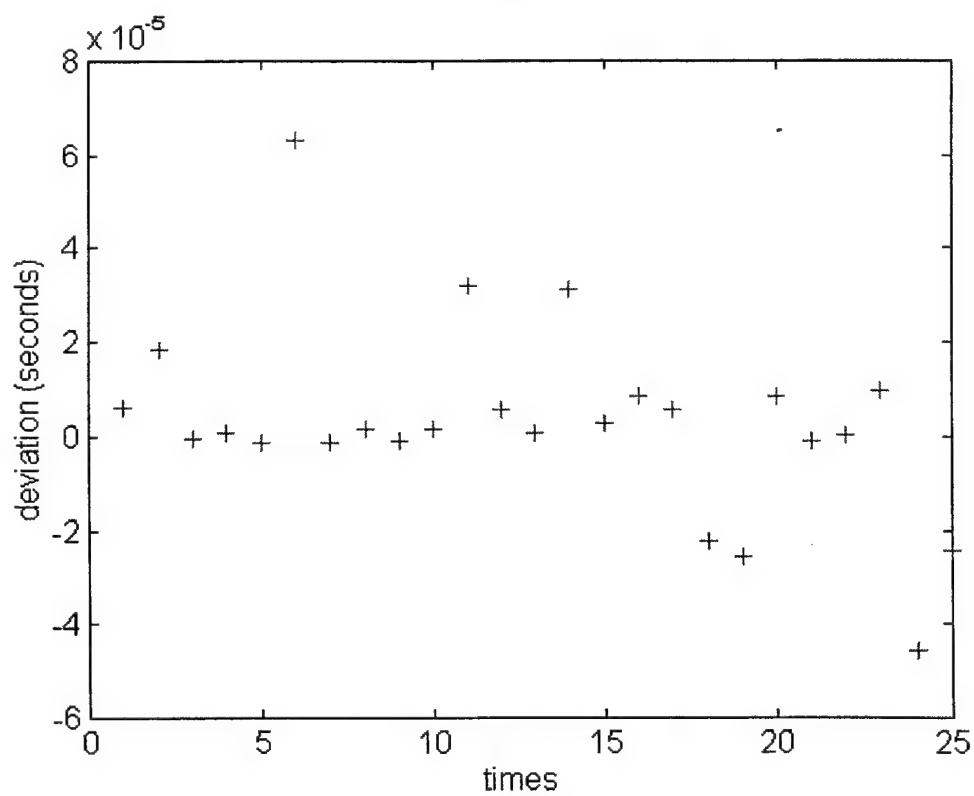
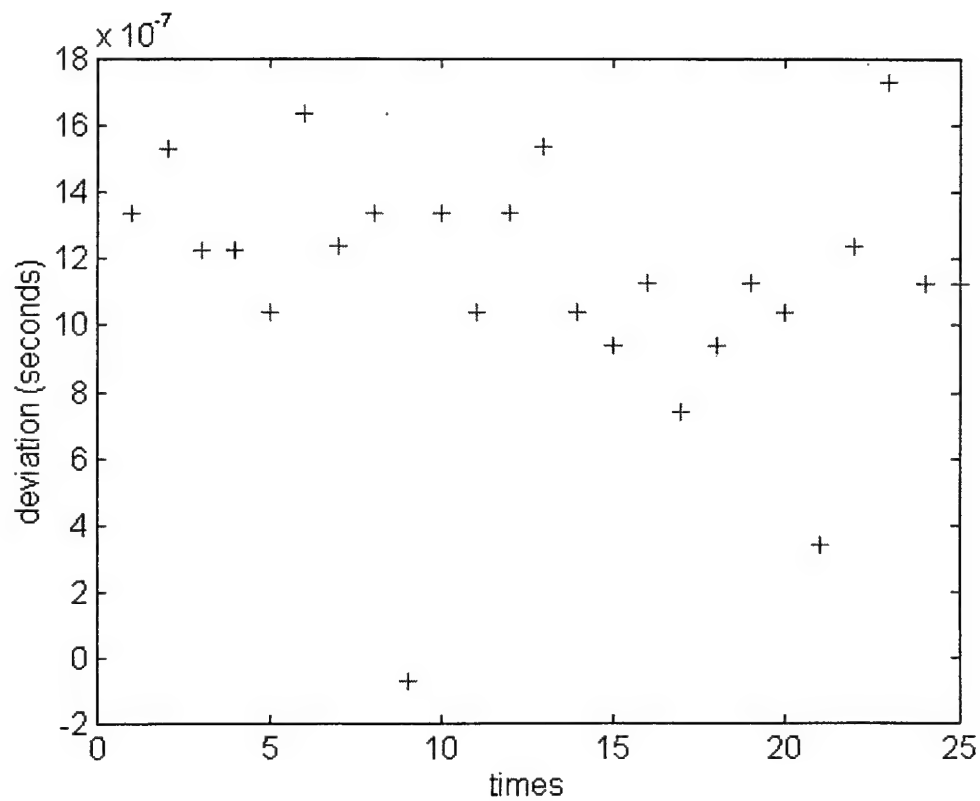


Figure 9-5 - Deviation from theoretical for TDOA between master node and slave #2, ARL:UT (top), speccoa (bottom)

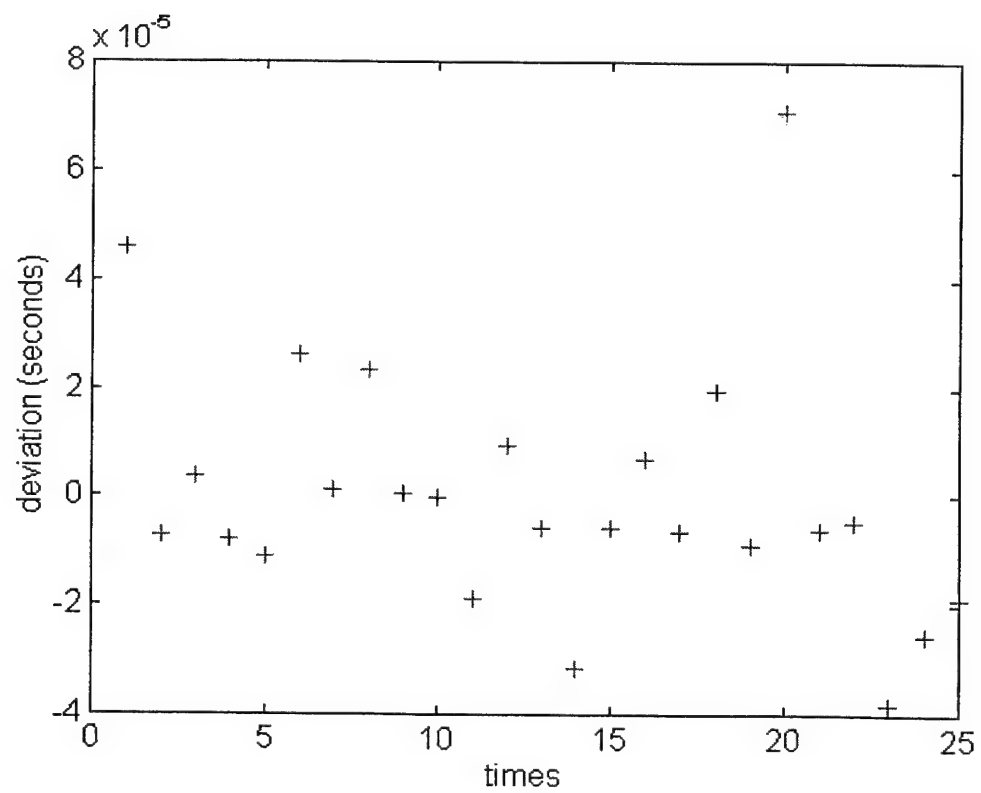
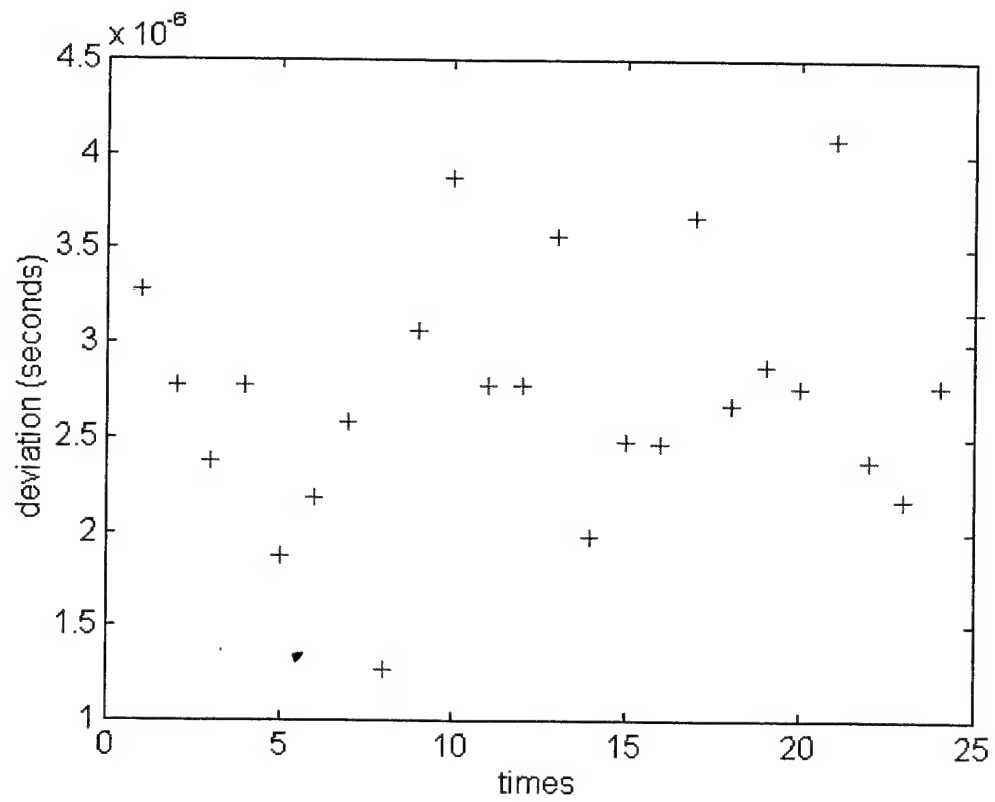


Figure 9-6 - Deviation from theoretical for TDOA between master node and slave #3,
ARL:UT (top), **speccoa** (bottom)

D. COMMENTS

Clearly the cyclostationary TDOA processor does not perform as predicted by theory and as verified by simulation. Due to the decimation of the original time domain signals, several additional processing steps are necessary in order to achieve the needed resolution in the TDOA computation. These steps include resampling the signal at a much higher rate in order to measure a TDOA on the order of 10^{-6} . This step causes problems for the **speccoa** code.

The average values for the two TDOA determination methods appear in Tables 9-1 to 9-3 below. Also in the table are the values for the average deviation of the TDOA(s) from the theoretical values.

The code for the geolocation algorithm obviously has flaws as well. Its inability to distinguish between the widely varying sets of TDOA(s) with widely varying geolocations indicates a fundamental programming flaw.

Algorithm	TDOA _{M1}	Theoretical TDOA _{M1}	Deviation _{M1}
Cyclostationary TDOA	-1.308e-5	1.434e-6	1.165e-5
ARL:UT System	-1.805e-6	1.434e-6	3.66e-7

Table 9-1 - TDOA_{M1} summary

Algorithm	TDOA _{M2}	Theoretical TDOA _{M2}	Deviation _{M2}
Cyclostationary TDOA	8.44e-7	3.828e-6	2.984e-6
ARL:UT System	2.697e-6	3.828e-6	1.131e-6

Table 9-2 - TDOA_{M2} summary

Algorithm	TDOA_{M3}	Theoretical TDOA_{M3}	Deviation_{M3}
Cyclostationary TDOA	-5.869e-6	-3.124e-6	2.745e-6
ARL:UT System	-3.471e-6	3.124e-6	3.47e-7

Table 9-3 - TDOA_{M3} summary

X. CONCLUSIONS

A. OBSERVATIONS

The cyclostationary TDOA processor in combination with the closed form geolocation solution in MATLAB® does not outperform the CAF based system. Because the results deviate significantly from the theory, several additional tests are necessary to isolate the cause of the anomaly. First, **speccoa** must run with fully decimated ARL:UT data. Because the decimation exceeds the resolution needed to determine the TDOA(s), properly the result should be zero in every instance. It is not. The algorithms returns random, obviously unreliable answers for the real world test data.

The next step is the verification of zero delay with generated data. The generated BPSK signals with zero delay produce zero as a result with **speccoa**. Thus, **speccoa** indeed functions properly even at delays below the resolution of the sampling rate. However, it does not function properly with the ARL:UT data.

Finally, since the SPECCOA algorithm reduces to a GCC at $\alpha = 0$ in the absence of Doppler shift, **speccoa** can be tested as a GCC to reproduce the ARL:UT results. This test produces random, unreliable results yet again with ARL:UT data. It does, however, produce the correct results with the generated BPSK signals once again.

To summarize, **plotsf** and the cycle frequencies it produces are verified by the correct plots of the generated signals and the correct determination of the dominant cyclic features of the BPSK signals even in the presence of significant noise. Thus, the cycle frequencies used in **speccoa** for both the generated signals and the ARL:UT data are deemed reliable. **Speccoa** on the other hand, produces perfect results for the generated signals at all significant cycle frequencies and at $\alpha = 0$. However, it does not produce consistent results for the dominant cyclic feature in the ARL:UT data; nor does it produce results at other cycle frequencies that are consistent with the $f_s/2$ feature's results.

These additional details lead to one most likely conclusion. The ARL:UT data does not reach the algorithms in the correct form from storage to processing. Most probably, the format is incorrect. In its reading into the MATLAB® environment, the

data is essentially corrupted producing such seemingly contrary results. The generated signals are generated in the MATLAB® environment, producing no such format problems. The ARL:UT data is originally stored in UNIX format, byte reversed for PC usage and then loaded into the MATLAB® environment for processing. It is this last step that is believed to cause the anomalies in the results.

As a positive outcome, the testing did provide an idea for the computational complexity that a cyclostationary TDOA system would require. The process from loading the signals to finding a geolocation required approximately 2 minutes per geolocation on a Pentium Pro™ based machine with 64 MB EDO RAM. This is not tactically feasible. While coding the system in C would increase the speed significantly, the computations of the system would remain the limiting factor in its implementation.

The cyclostationary TDOA processor holds promise for near future implementation. The problems encountered are tractable. All that remains is the computational power to run the system in a tactical environment.

B. AREAS OF FURTHER STUDY

Determining the proper method with which to load the ARL:UT data into the MATLAB® environment remains the highest priority for solving the major problems of the current algorithms. If this is the cause of the significant inconsistency encountered, its solution will surely improve the results to accuracies predicted in theory.

The polynomial fit used by the *resample* function in MATLAB® needs to be examined closely to determine the extent of phase error it introduces to the resampled signal. This would allow for the development of a more accurate method of interpolating back to a sampling rate that provides sufficient resolution for the TDOA measurement.

The closed form solution error must be found and corrected. It is likely that the error involves the reintroduction of $c = 2.998 \times 10^8$ once the contributions of the TDOA(s) are mapped to the three coordinates. In his solution, Rusu sets $c = 1$ for simplicity. While this works for the derivation, it most likely must be given its proper value before the final solution can be reached.

Once the two algorithms were corrected, using real world signals from a more hostile signal environment for comparison would highlight the benefits of cyclostationary processing best.

Finally, further development of Geolocation Software Workbench blocks would accelerate the introduction of a simplified testing platform for all aspects of geolocation.

LIST OF REFERENCES

1. Torrieri, Don J., "Statistical Theory of Passive Location Systems", *IEEE Transaction on Aerospace and Electronic Systems*, Vol., AES-20, Number 2, March 1984, p.183.
2. Azaria, M., and Hertz, D., "Time Delay Estimation by Generalized Cross Correlation Methods", *IEEE Transactions on Acoustics, Speech and Signal Processing*, Vol. ASSP-32, No. 2, April, 1984.
3. Knapp, C. H., and Carter G. C., "The Generalized Correlation Method for Estimation of Time Delay", *IEEE Transactions on Acoustics, Speech and Signal Processing*, Vol. ASSP-24, No. 4, August, 1976.
4. Stein, Seymour, "Algorithms for Ambiguity Function Processing", *IEEE Transactions on Acoustics, Speech and Signal Processing*, Vol. ASSP-29, No. 3, June 1981.
5. Brown, W. A., and Spooner, C., "Cyclostationary Time Difference of Arrival Techniques for Signals Intelligence: Part I of II", Statistical Signal Processing Inc. and Mission Research Corporation Inc., technical report, June 1996.
6. Gardner, William A., "Exploitation of Spectral Redundancy in Cyclostationary Signals", *IEEE Signal Processing Magazine*, April, 1991.
7. Gardner, William A., ed., *Cyclostationarity in Communications and Signal Processing*, IEEE Press, 1994.
8. Chen, Chih-Kang and Gardner, William A., "Signal-Selective Time-Difference-of-Arrival Estimation for Passive Location of Man-Made Signal Sources in Highly Corruptive Environments, Part I: Theory and Method", *IEEE Transactions on Signal Processing*, Vol. 40, Number 5, May 1992.
9. Chen, Chih-Kang and Gardner, William A., "Signal-Selective Time-Difference-of-Arrival Estimation for Passive Location of Man-Made Signal Sources in Highly Corruptive Environments, Part II: Algorithms and Performance", *IEEE Transactions on Signal Processing*, Vol. 40, Number 5, May 1992.
10. Brown, W. A., *Introduction to Second-Order Cyclostationary Signals*, Mission Research Corp. briefing, April 22, 1996.
11. Schau, H. C., and Robinson, A. Z., "Passive Source Location Employing Spherical Surfaces from Time-of-Arrival Differences", *IEEE Transactions on Acoustics, Speech and Signal Processing*, Vol. ASSP-35, No. 8, August 1987.
12. Loomis, Herschel H. Jr., "Geolocation of Electromagnetic Emitters", Unpublished work, Naval Postgraduate School, Monterey, CA, 1993.

13. Ho, K. C. and Chen, Y. T., "Solution and Performance Analysis of Geolocation by TDOA", *IEEE Transactions on Aerospace and Electronic Systems*, Vol. 29, No. 4, October 1993.
14. Rusu, Petre, "The Equivalence of TOA and TDOA RF Transmitter Location", Unpublished work, Applied Research Laboratory: The University of Texas at Austin, Austin, TX, 1995.
15. Leach, M. and Feuerstein, D., "Preliminary Test Results from a Carry-on Multi-platform GPS-Assisted Time Difference of Arrival System", *Proceedings of the Symposium on Radiolocation and Direction Finding*, San Antonio, Texas, June 1995.
16. Rusu, P. and Giulianelli, L., "A Stochastic Model for Time Difference of Arrival Error Estimation", ARL:UT Inter-office Memorandum, 1995.
17. Applied Research Laboratories: University of Texas at Austin, briefing, September 1996.
18. Rusu, Petre, "On the Dilution of Precision Factors in TDOA Computations", ARL:UT Inter-office Memorandum, 1995.
19. Loomis, H. H. Jr. And Bernstein, R. F. Jr., "Realization of TDOA Estimation Architectures", *IEEE Transactions on Signal Processing*, Vol 50, No. 3, August 1995.
20. Brown, W. A. and Loomis, H. H. Jr., "Digital Implementation of Spectral Correlation Analyzers", *IEEE Transactions on Signal Processing*, Vol. 41, No. 2, February 1993.
21. Brown, W. A. and Loomis, H. H. Jr., "A Review of Digital Spectral Correlation Analysis: Theory and Implementation", *Cyclostationarity in Communications and Signal Processing*, William A. Gardner, ed., IEEE Press, 1994.
22. Roberts, R., Brown, W. A. and Loomis, H. H. Jr., "Computationally Efficient Algorithms for Cyclic Spectral Analysis", *IEEE Signal Processing Magazine*, Vol 39 No. 4 , April 1991.
23. *MATLAB Reference Guide*, Version 4.2c, The Mathworks, Inc., August 1992.
24. *Simulink User's Guide*, The Mathworks, Inc., 1995.

BIBLIOGRAPHY

Janiczek, P. M., ed., Global Positioning System Volume I, The Institute of Navigation, Washington, D.C., 1980.

Leick, Alfred, GPS Satellite Surveying, John-Wiley & Sons, New York, NY, 1990.

Parkinson, Bradford W. and Spilker, James J. Jr., ed., Global Positioning System: Theory and Applications Volume I, American Institute of Aeronautics and Astronautics, Inc., Washington, D.C., 1996.

Parkinson, Bradford W. and Spilker, James J. Jr., ed., Global Positioning System: Theory and Applications Volume II, American Institute of Aeronautics and Astronautics, Inc., Washington, D.C., 1996.

Price, Michael G., "Mathematics of Geolocation", Informal report, Systeka, Inc., Seabrook, MD, 1995.

Rusu, Petre, "The Equivalence of TOA and TDOA RF Transmitter Location", Unpublished work, Applied Research Laboratory: The University of Texas at Austin, Austin, TX, 1995.

Rusu, Petre, "A TOA-FOA Approach to Find the Status of RF Transmitters", Unpublished work, Applied Research Laboratory: The University of Texas at Austin, Austin, TX, 1995.

Spooner, Chad M., "An Overview of Recent Developments in Cyclostationary Signal Processing", Proceedings of the Second Workshop on Cyclostationary Signals, Mission Research Corporation, Monterey, CA, August 1-2, 1994.

APPENDIX A. MATLAB CODE FOR ALGORITHMS

The programs that follow constitute the major sections of code used in this work. They all contain headers and commenting for explanation purposes. They are described briefly in Table A-1 below.

Program Title	Purpose
loaddata.m	Loads headers and signal data, converts 4 bytes real, 4 bytes imaginary to complex vector notation.
ssca.m	Strip-spectral correlation analyzer. Calculates the SCF of the input sequence along diagonal lines according to the SSCA algorithm.
plotscf.m	Transforms the diagonal lines of ssca.m into lines along f and α . Plots both the SCF and the magnitude of SCF vs cycle frequency.
speccoa.m	Resamples time domain data to user specified value (p). Calculates the TDOA of two input sequences in terms of samples using SPECCOA algorithm.
rusugeo.m	Takes positions of observers and three TDOA(s) to produce geolocation in WGS84 ECEF coordinates. Finds both solutions. User must eliminate one.

Table A-1 - Summary of code

```

%*****
%*****
%
% Name: David A Streight
%
% Naval Postgraduate School - Monterey, California
%
% loaddata.m
%
% Operating Environment
% Windows 95
%
% Description
% Loads 32-bit float ARL:UT data into four header and data vectors.
% Master site is obs1, other sites are 2, 3 and 4.
%
% Date of last revision
% 20 December 1996
%
% Inputs
% Four ARL:UT stored files
%
% Outputs
% None
%
%*****
%*****

```

clear all;

```

% open four observer files read only
obs1 = fopen('F:\data\nov_ut~2\mcc\409400.rev','r');
obs2 = fopen('F:\data\nov_ut~2\berg\409400.rev','r');
obs3 = fopen('F:\data\nov_ut~2\beecaves\409400.rev','r');
obs4 = fopen('F:\data\nov_ut~2\expo\409400.rev','r');

% load 3 header variables into header vectors
[header1] = fread(obs1,3,'float');
[header2] = fread(obs2,3,'float');
[header3] = fread(obs3,3,'float');
[header4] = fread(obs4,3,'float');

% load data into 4 data matrices col#1 - real col#2 - imaginary
[x1] = fread(obs1,[8192,2],'float');
[x2] = fread(obs2,[8192,2],'float');
[x3] = fread(obs3,[8192,2],'float');
[x4] = fread(obs4,[8192,2],'float');

```

```
% convert data matrices to complex vectors
```

```
s1 = x1(:,1)+j*x1(:,2);
```

```
s2 = x2(:,1)+j*x2(:,2);
```

```
s3 = x3(:,1)+j*x3(:,2);
```

```
s4 = x4(:,1)+j*x4(:,2);
```

```
% clear xi's
```

```
clear x1;
```

```
clear x2;
```

```
clear x3;
```

```
clear x4;
```

```
% close all files
```

```
fclose('all');
```

```

%*****
%*****
%
% Name: David A Streight
%
% Naval Postgraduate School - Monterey, California
%
% ssca.m
%
% Operating Environment
% Windows 95
%
% Description
% Calculates the auto spectral density function using the strip
% spectral correlation algorithm (ssca)
%
% Date of last revision
% 18 November 1996
%
% Inputs
% x - SOI
%
% Outputs
% SDF - the results of the ssca computation. Must be converted
% and plotted by plotsdf.m
%
%*****
%*****

```

```

x = [s1(1:2^12,1)].';

```

```

% prepare variables
s = size(x);
N = s(1,2);
Np = 8;
xp = [x zeros(1,Np)];
w = (hamming(Np))';
W = (hamming(N))';
L = Np/4;
P = floor(N/L);
p = zeros(1,floor(P/L));
xT = zeros(1,Np);
k = -Np/2:Np/2-1;
dm = zeros(1,Np);
XTi = zeros(N,Np);
SXT = zeros(Np,N);

```

% number of points in vector
 % course FFT number
 % zero pad input variable for Np length slices
 % hamming window for course FFT
 % hamming window for P point FFT at the end
 % decimation factor

```

% find complex demodulates
for p = 0:P-1
    xT = fft((xp(1,p*L+1:p*L+Np) .* w), Np); % take Np point FFT of windowed data
    xT = [xT(1,5:8) xT(1,1:4)]; % fold fft to account for neg freq's
    dm = exp(-j*2*pi*k*p*L/Np); % calculate freq shifts for this set
    XTi(p*L+1,:) = xT .* dm; % freq shift and populate odd col's of interp
matrix
end

% interpolate ***works for Np = 8 only at this point***
for v = 1:P-1
    XTi(L*v,:) = (XTi(L*v-1,:) + XTi(L*v+1,:))./2; % fill in even col's linearly
end
XTi(N,:) = XTi(1,:); % hold next to last col for last col values

%finish up
xm = [x;x;x;x;x;x;x]'; % matrix of original signal
%Wm = [W;W;W;W;W;W;W;W]; % matrix of column-wise hamming
window
SXT = fft(XTi .* xm, N); % take N-point FFT of products
SDF = SXT.'; % transpose after FFT
SDF = [SDF(:,1:P-1) SDF(:,P:N)]; % fold fft to account for negative freq's

```

```

%*****
%*****
%
% Name: David A Streight
%
% Naval Postgraduate School - Monterey, California
%
% PLOTSDF: Convert and plot SSCA output
%
% Operating Environment
% Windows 95
%
% Description
%
%
%
%
% Date of last revision
% 15 November 1996
%
% Inputs
% Matrix of Spectral Density Function values from the SSCA algorithm
% SDF
%
% All variables used in the SSCA computation (no clear executed)
%
% Outputs
% Plot in 3D of the SDF function drawn along lines of cycle frequency
%
%*****
%*****

% determine the span of alpha
alphamax = 2*N - 2*N/Np - 2;
alphamin = -2*N;
alphaspan = alphamax - alphamin;

% setup intermediate matrices
I = zeros(alphaspan+1,Np);
X = zeros(alphaspan+1,Np);
Y = zeros(alphaspan+1,Np);

%
maxalpha = zeros(1,alphamax+1);

% populate matrices from SDF
for q = -N/2:N/2-1

```



```

        for k = -Np/2:Np/2 - 1
            I(2*N*k/Np+2*q+2*N+1,k+Np/2+1) = abs(SDF(k+Np/2+1,q+N/2+1));
        end
    end

% normalize magnitudes
I = I/max(max(I));

% populate f and alpha coordinate matrices
j = 1:8;
y = ones(1,8);
for i = 1:alphaspan+1
    X(i,:) = 2*N*(j-Np/2-1)/Np-(i-2*N-1)/2;
    Y(i,:) = ((i-2*N-1).*y)/2;
end

% plot the positive alpha half of the plane
figure(1);
surf(X(alphaspan-alphamax:alphaspan+1,:),Y(alphaspan-
alphamax:alphaspan+1,:),I(alphaspan-alphamax:alphaspan+1,:));
view(-105,60),grid,axis([-20000 10000 0 8000 0 1])

% now plot alpha vs mag of SDF for those values
for l = 1:alphamax+1
    maxa(l) = max(I(alphaspan-alphamax+1-l,:));
end

maxalphas = nonzeros(maxa);
maxalphas = maxalphas';
sz = size(maxalphas);
alphanum = 0:sz(1,2)-1;
figure(2);
plot(alphanum,maxalphas)

clear i;
clear j;

```

```

%*****
%*****
%
% Name: David A Streight
%
% Naval Postgraduate School - Monterey, California
%
% SPECCOA - Cyclostationary Time Difference of Arrival Algorithm
%
% Operating Environment
% Windows 95
%
% Description
% Produces an estimate of the time difference of arrival of a
% signal of interest between two spatially separated receivers
% in terms of multiples of the sampling frequency
%
% Date of last revision
% 06 January 1997
%
% Inputs
% p - up sample integer
% q - down sample integer
% terms - number of terms used in linear interpolation
% N - number of samples of decimated sequence to use
% a - cycle frequency of interest in terms of decimated fs/N
% SOI1 - signal captured at receiver 1 (N samples)
% SOI2 - signal captured at receiver 2 (N samples)
%      *both SOI(s) sampled at rate fs samples per sec
%
% Outputs
% Plot of SPECCOA function versus samples. Peak is TDOA estimate
%
%*****
%*****

```

```

loaddata;                                % load decimated signals

% resample variables
p = 256;                                % up sample
q = 1;                                  % down sample
terms = 3;                              % terms in the linear interpolation
I = p/q;                                % total interpolation

% cyclostationary variables
a = 2049 * I;                            % cycle frequency at new sample rate

```

```

N = 4096 * I; % length of sequence at new sample rate
fs = 9765.625;

% prepare loop variables
SXT = zeros(1,N); % SCF of SOI1 at alpha0
SYXT = zeros(1,N); % Cross SCF at alpha0

Sig1 = s1(1:(N/I),1).'; % set up vectors
Sig2 = s2(1:(N/I),1).';

SOI1 = resample(Sig1,p,q,terms); % resample and set as SOI1
SOI2 = resample(Sig2,p,q,terms); % resample and set as SOI2

Xf = fft(SOI1,N); % freq spectrum of SOI1
XT = fftshift(Xf); % adjust for MATLAB fft
Yf = fft(SOI2,N); % freq spectrum of SOI2
YT = fftshift(Yf); % adjust as above

XT = [zeros(1,a/2) XT zeros(1,a/2)]; % zero pad at each end for correlation loop
YT = [zeros(1,a/2) YT zeros(1,a/2)]; % ditto

SXT(1,:) = XT(1,1:N) .* conj(XT(1,a+1:N+a));
SYXT(1,:) = YT(1,1:N) .* conj(XT(1,a+1:N+a));

isp = ifft((conj(SXT) .* SYXT), N); % IFFT of complex product from above
s = -N/2:N/2-1; % time in samples
kernel = exp(j*pi*a*s/N); % freq kernel at alpha0
sp = fftshift(isp) .* kernel; % adjust and multiply
plot(s,real(sp)) % plot to find TDOA

```

```

%*****
%*****
%
% Name: David A Streight
%
% Naval Postgraduate School - Monterey, California
%
% Closed Form TDOA Geolocation Solution
%
% Operating Environment
% Windows 95
%
% Description
% Produces two WGS84 based 3-dimensional geolocation solutions for a transmitter
% given the location of each of four observers and the TDOAs for their observations
% Data outside the algorithm must be used to eliminate the ambiguity.
%
% Date of last revision
% 10 October 1996
%
% Inputs
% WGS84 based x, y and z coordinates for each of four observers
% xi, yi zi, i = 1,2,3,4
%
% TDOAs for the observers
% Dij, i = 1,2,3,4 and j = 1,2,3,4 where  $i \neq j$  and  $D_{ij} = -D_{ji}$ 
%
% Outputs
% WGS84 based x, y and z coordinates for the transmitter
% rt1 and rt2 (vectors)
%
%*****
%*****

```

% positions

```

xt = -741941.47; yt = -5462120.41; zt = 3198242.728;
x1 = -741203.52; y1 = -5456323.70; z1 = 3208396.55;
x2 = -735740.31; y2 = -5467456.78; z2 = 3190514.57;
x3 = -754177.92; y3 = -5459066.31; z3 = 3200764.99;
x4 = -731248.92; y4 = -5463237.87; z4 = 3198800.64;

```

% set up inputs and utility vectors

```

t1 = 0; % relative times of arrival using observer 1 as
baseline
t2 = -D12; % D12 is defined as  $t_1 - t_2$  thus  $t_2 = -D12$  if  $t_1 = 0$ 
t3 = -D13; % ditto

```

```

t4 = -D14;                                % ditto

r1 = [x1;y1;z1];                          % observer position vectors
r2 = [x2;y2;z2];
r3 = [x3;y3;z3];
r4 = [x4;y4;z4];

Euclid_sq1 = x1^2 + y1^2 + z1^2;           % squares of Euclidean distances
Euclid_sq2 = x2^2 + y2^2 + z2^2;
Euclid_sq3 = x3^2 + y3^2 + z3^2;
Euclid_sq4 = x4^2 + y4^2 + z4^2;

% set up solution matrices
A = [x1-x2 y1-y2 z1-z2; x2-x3 y2-y3 z2-z3; x3-x4 y3-y4 z3-z4];

q = [t1-t2; t2-t3; t3-t4];

s = zeros(3,1);
s(1,1) = (Euclid_sq1 - Euclid_sq2 - t1^2 + t2^2).*0.5;
s(2,1) = (Euclid_sq2 - Euclid_sq3 - t2^2 + t3^2).*0.5;
s(3,1) = (Euclid_sq3 - Euclid_sq4 - t3^2 + t4^2).*0.5;

g = A\q;                                  % use matrix division (MATLAB)...
                                          % in lieu of the inverse function...
h = A\s;                                  % to solve this part

% find terms for  $at^2 + bt + c$ 
a = ((g(1,1))^2 + (g(2,1))^2 + (g(3,1))^2) - 1; % find quadratic term

b = (g.' * h) + (g.' * r1) + t1;          % find first order term

c = (norm(h - r1).^2) - t1^2;              % find constant

p = [a 2*b c];                            % form polynomial in t

% find the two times as roots of this equation
t = roots(p);                             % find roots of  $at^2 + 2bt + c$ 

% substitute into t-parametrized equation for r and solve for real part of two solutions
rt1 = real(g .* t(1,1) + h);
rt2 = real(g .* t(2,1) + h);

```


APPENDIX B. PLOTS FOR ARL:UT TEST DATA

The following 150 figures are the result of testing 25 the cyclostationary TDOA processor for 25 time periods. For each time period, 6 figures appear: one SCF plot for each of the four observers grouped two to a figure, one magnitude of SCF vs cycle frequency for each of the four observers grouped two to a figure and three SPECCOA plots grouped two and one to a figure.

For the SCF plots, only the positive cycle frequency values are plotted. The spectral frequency axis runs from the upper left to the lower right; the cycle frequency axis runs from the upper right to the lower left. Both the spectral frequency and the cycle frequency are plotted in terms of f_s/N where $f_s = 9765.625$ Hz and $N = 4096$. The magnitude is of course the axis pointing to the top of the page. The magnitude of the plots is normalized by the maximum value of the SCF and thus ranges from 0 to 1.

The magnitude of the SCF versus cycle frequency plots also display only the positive cycle frequencies. The horizontal axis is cycle frequency in terms of f_s/N as above. The vertical axis is again normalized magnitude. These plots merely represent looking at the SCF plots from the cycle frequency axis side. They aided in choosing the best cycle frequency for SPECCOA.

Finally, the SPECCOA plots show the output of the **speccoa** code. The horizontal axis represents the TDOA in terms of the numbers of samples of delay. The horizontal axis is once again magnitude.

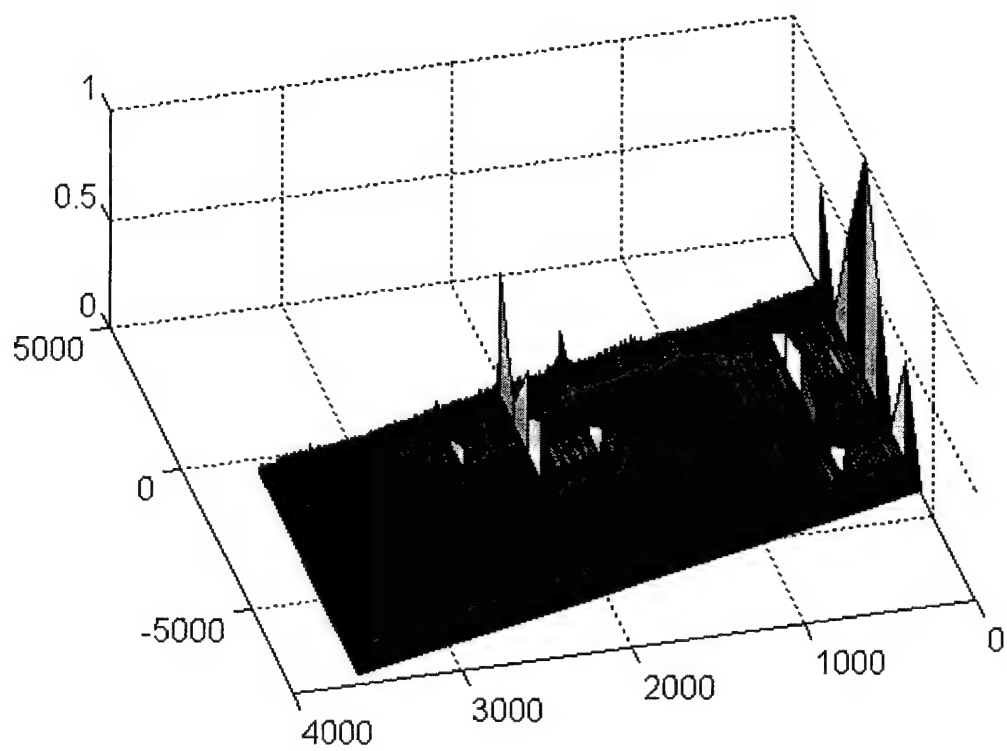
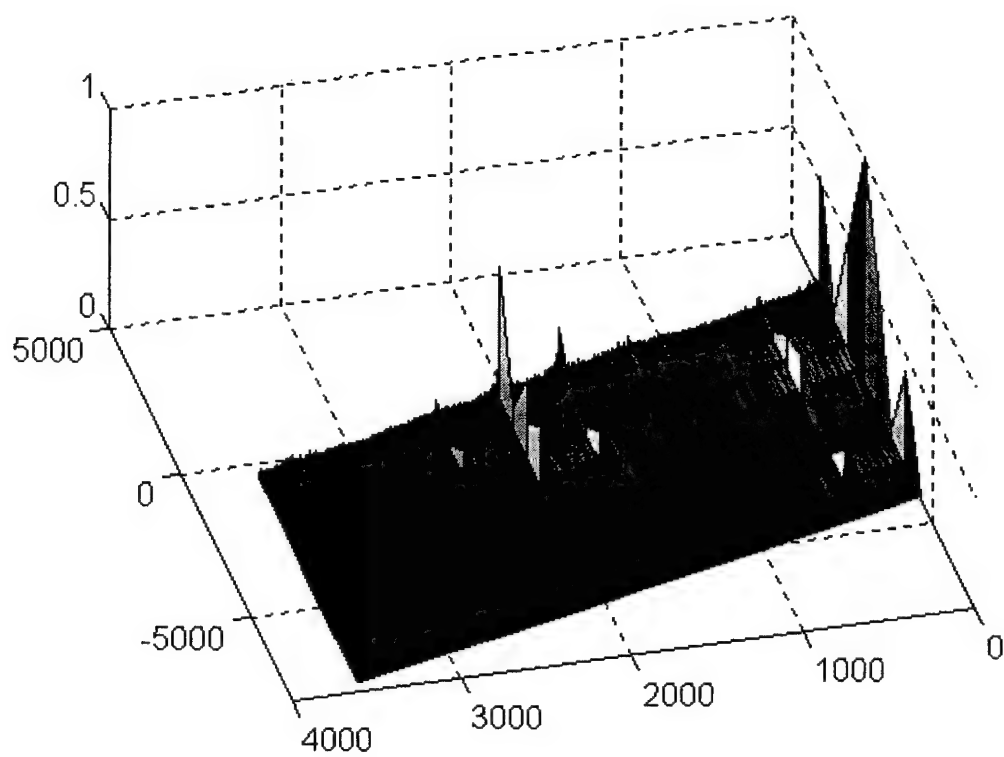


Figure B-1 - SCF for master (top) and slave #1 (bottom), time 409400

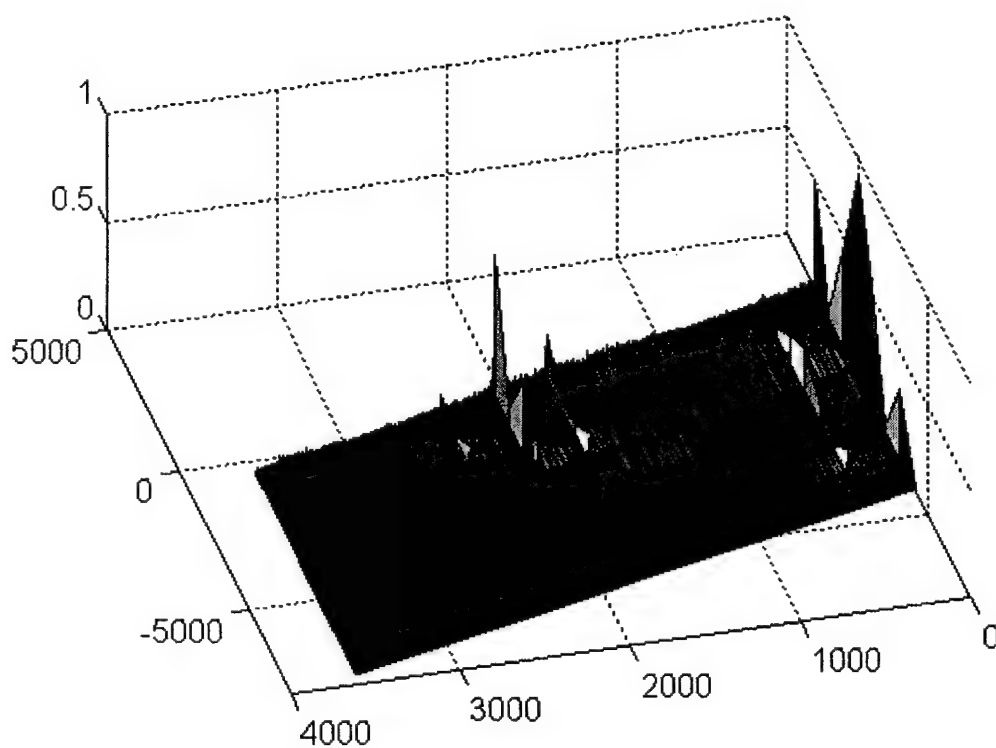
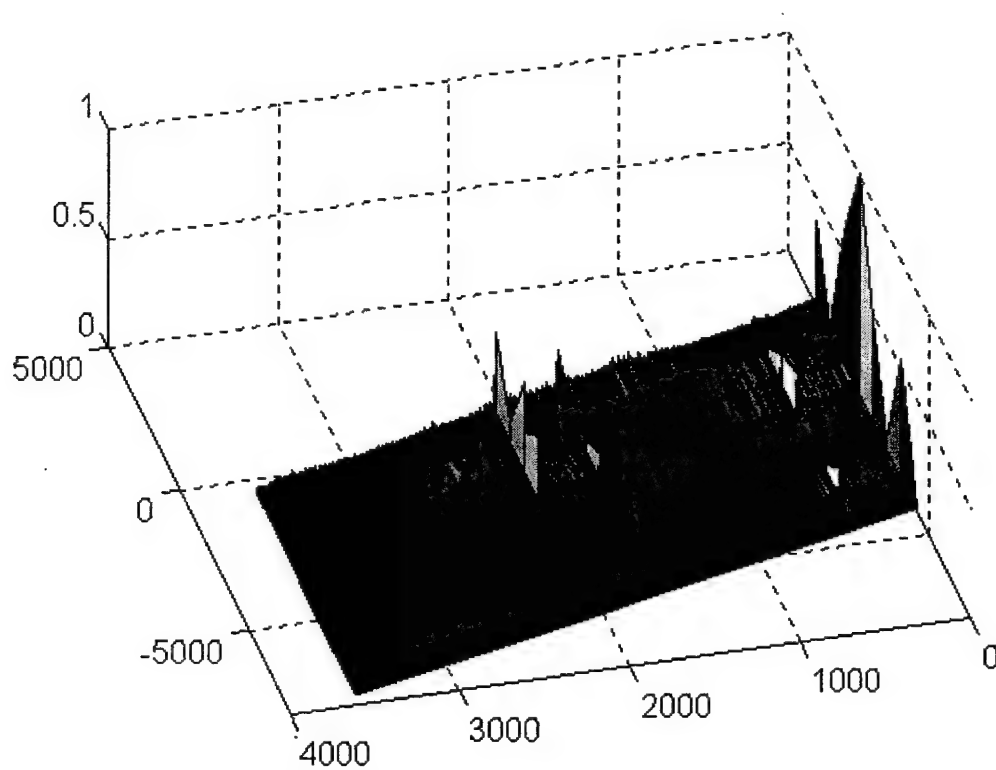


Figure B-2 - SCF for slave #2 (top) and slave #3 (bottom), time 409400

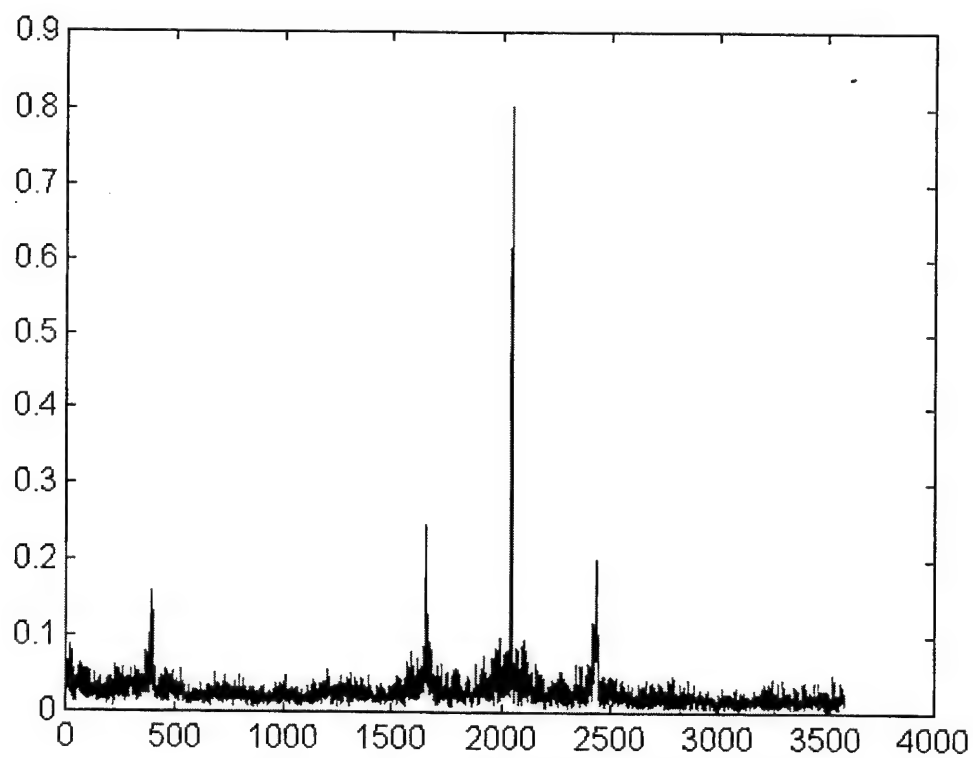
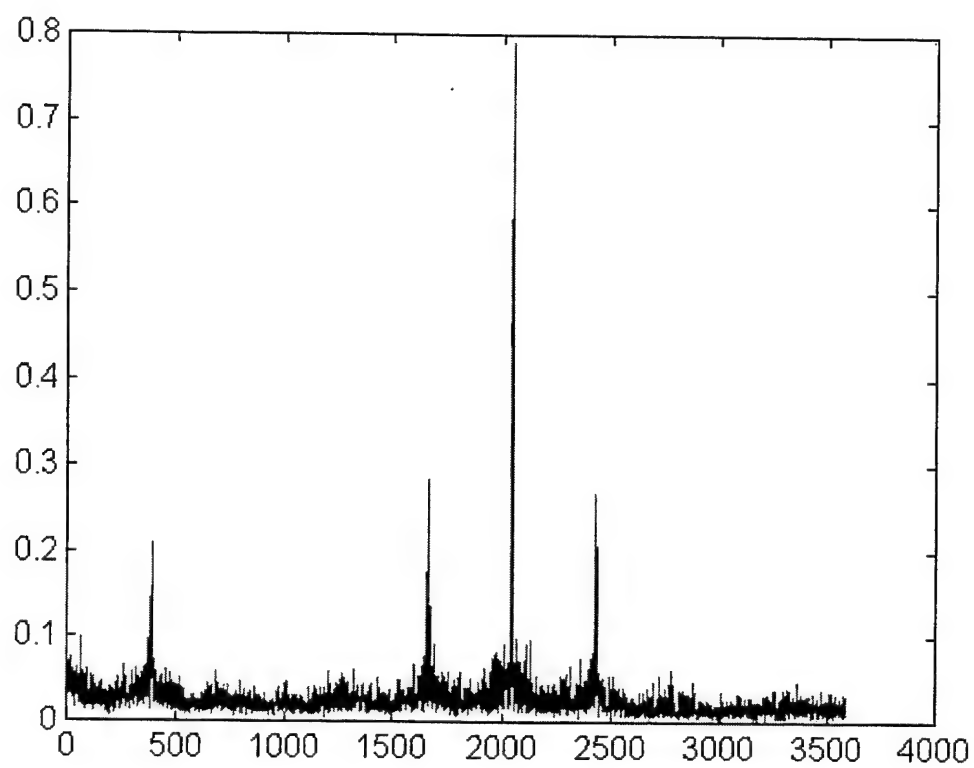


Figure B-3 - Cycle freq vs Max-magnitude of SCF for master (top) and slave #1 (bottom), time 409400

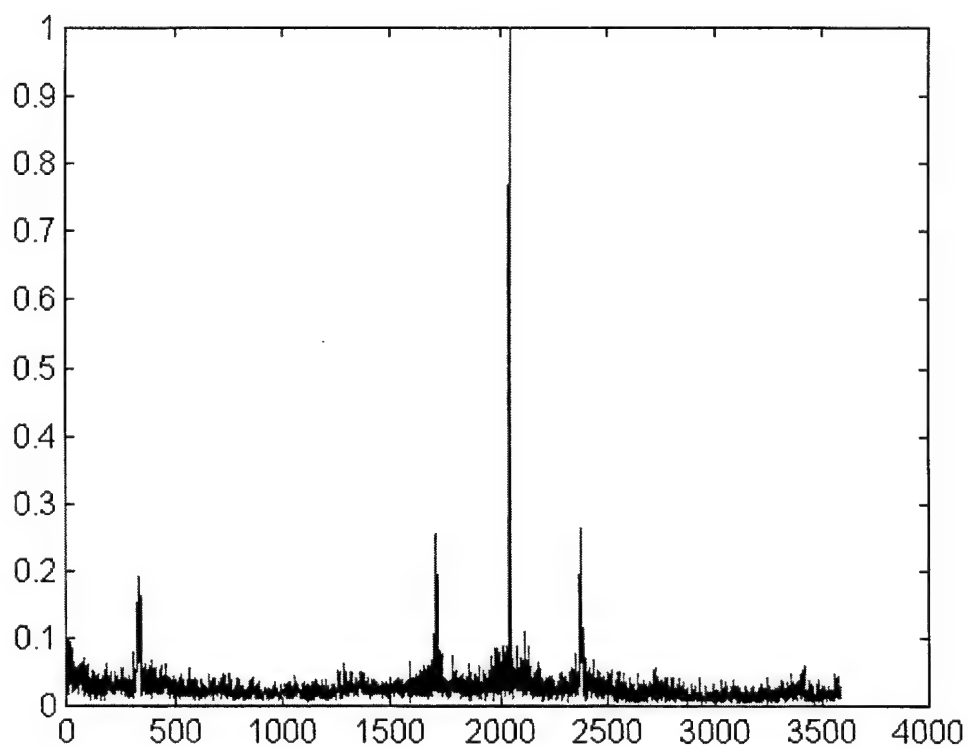
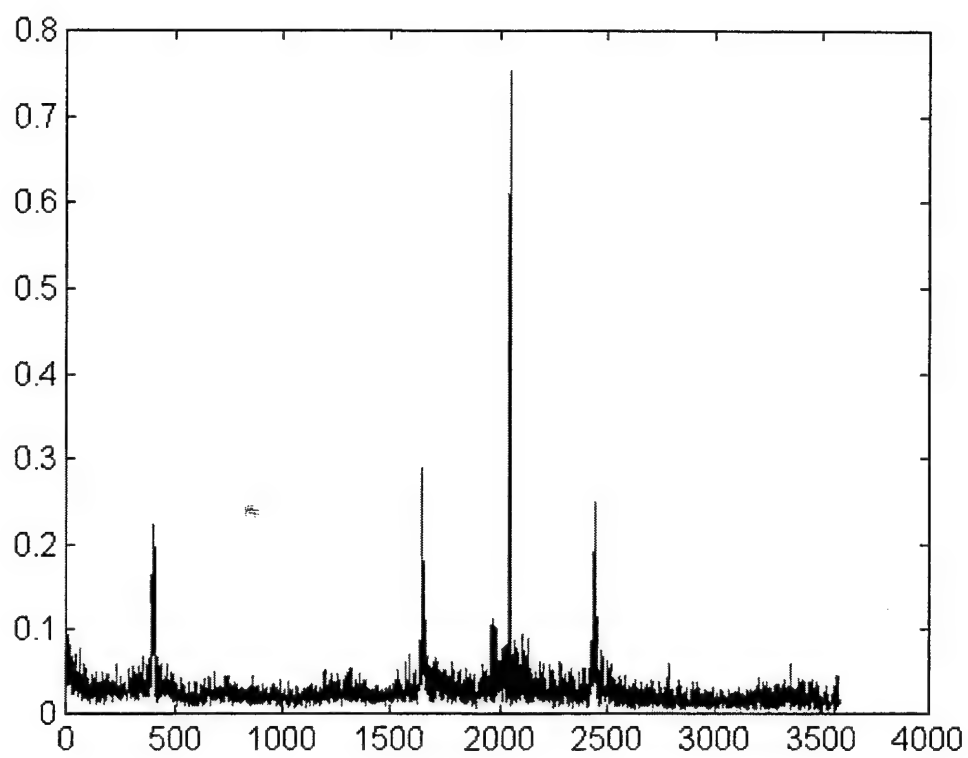


Figure B-4 - Cycle freq vs Max-magnitude of SCF for slave #2 (top) and slave #3 (bottom), time 409400

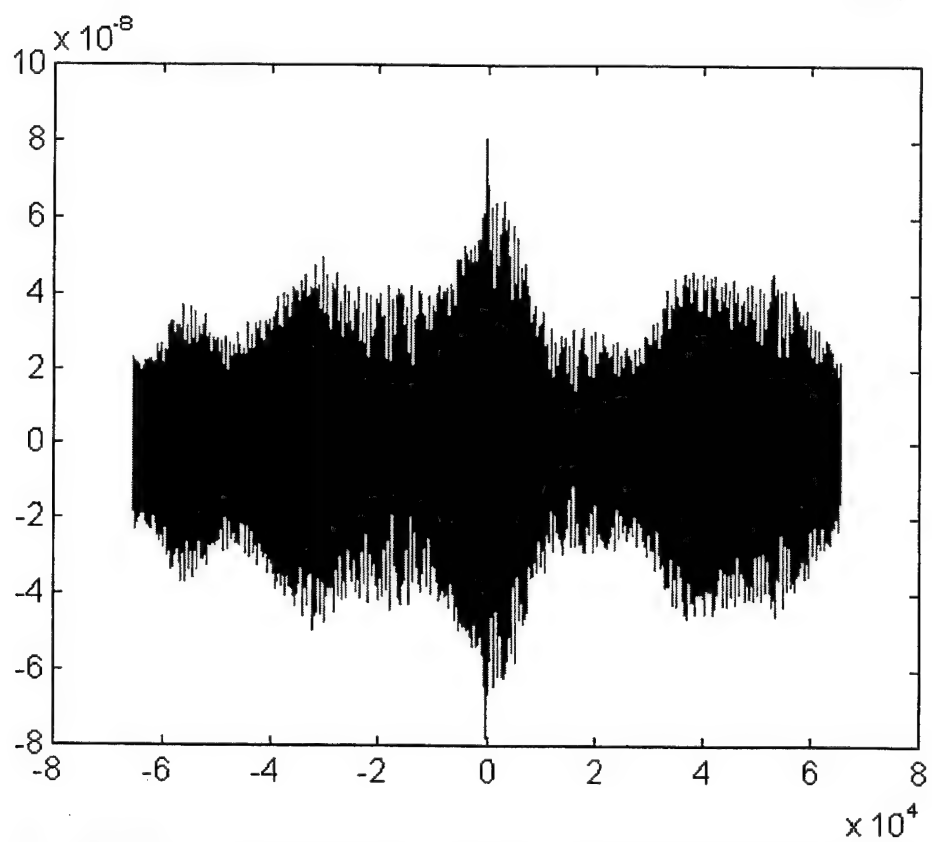
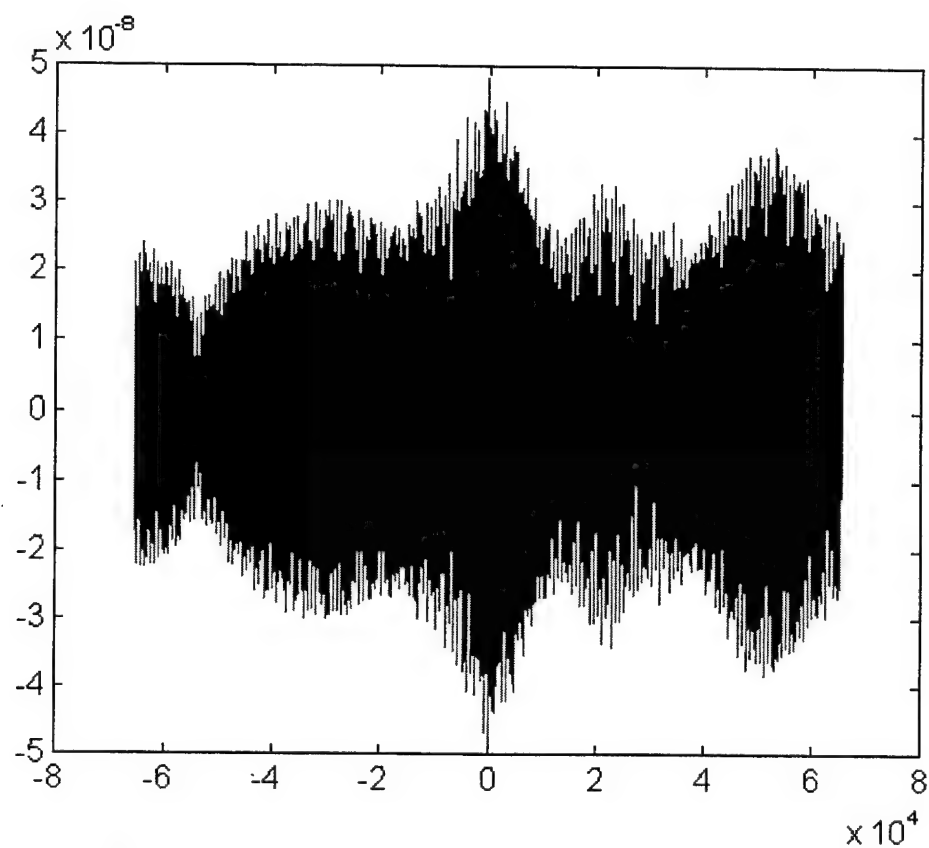


Figure B-5 - SPECCOA for master and slave #1 (top) and master and slave #2 (bottom), time 409400

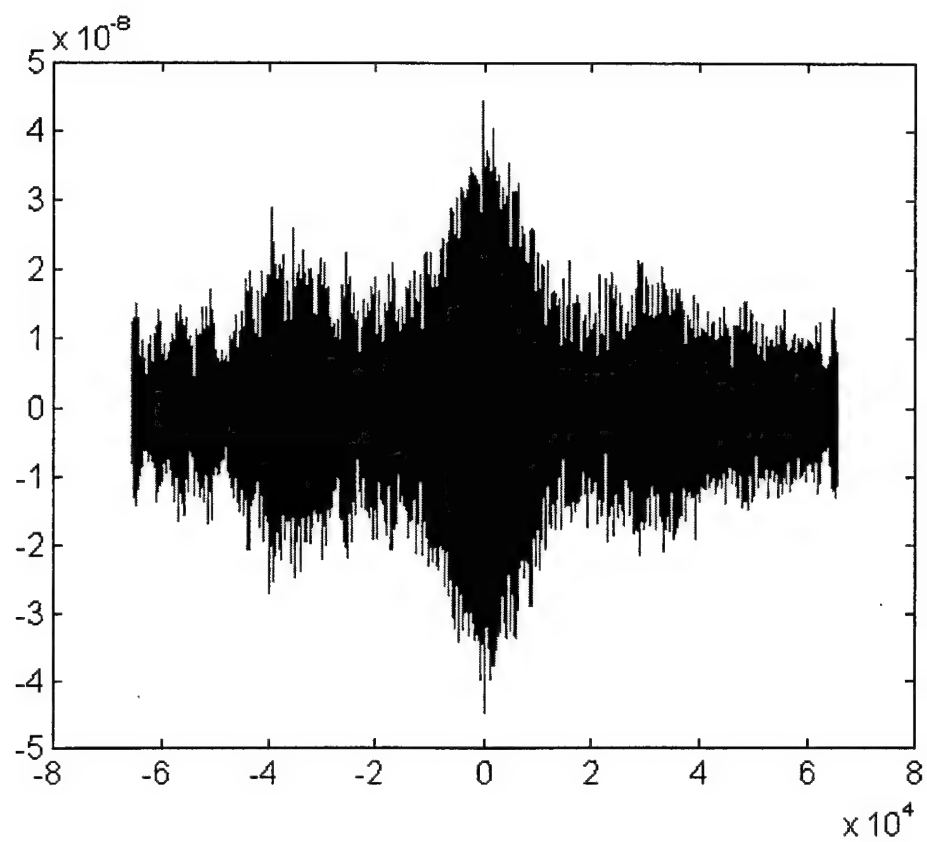


Figure B-6 - SPECCOA for master and slave #3, time 409400

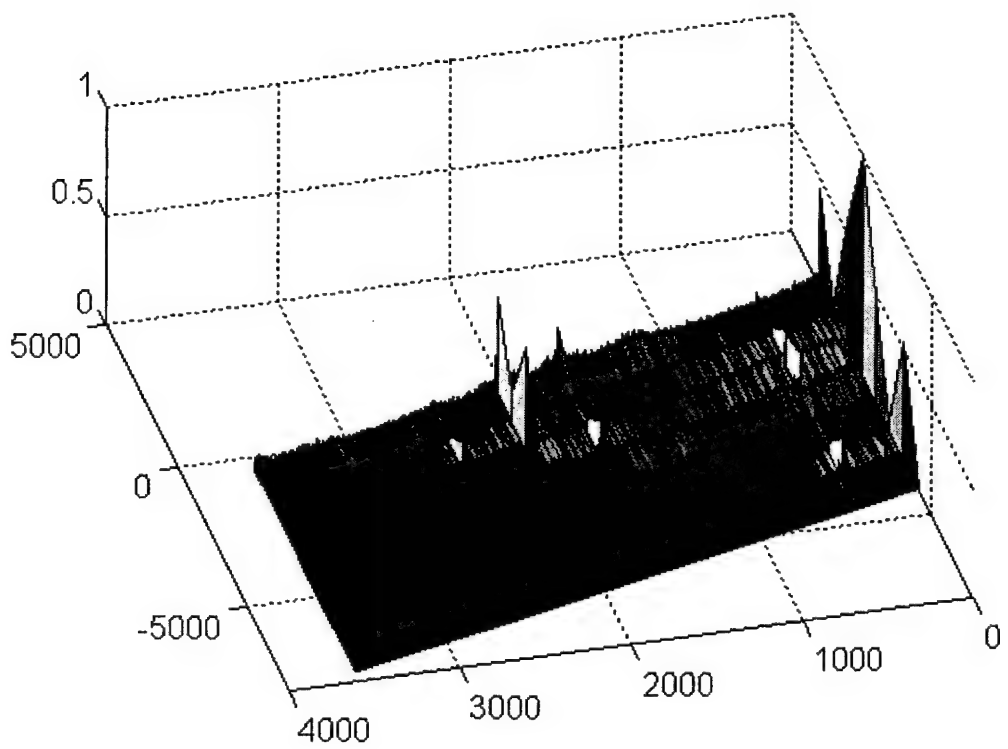
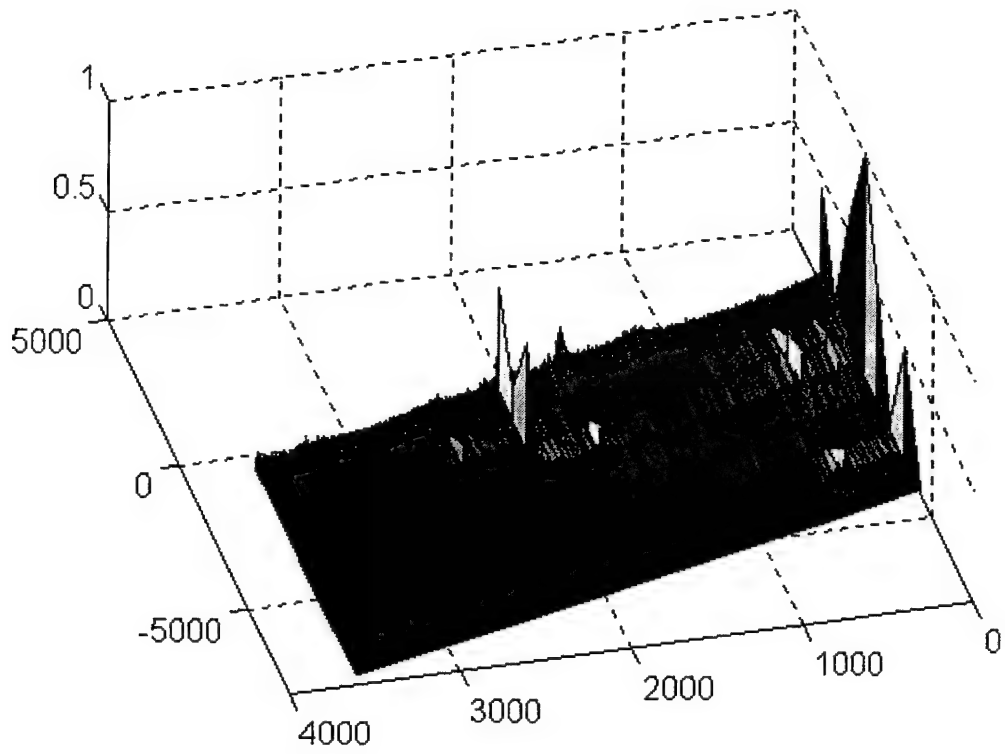


Figure B-7 - SCF for master (top) and slave #1 (bottom), time 409405

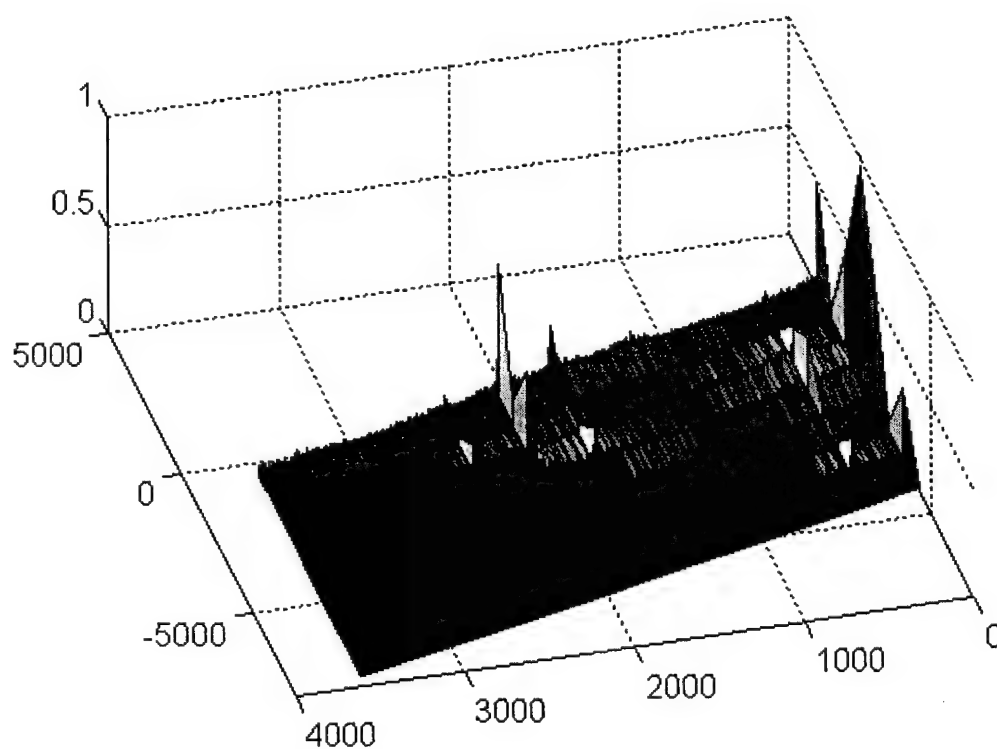
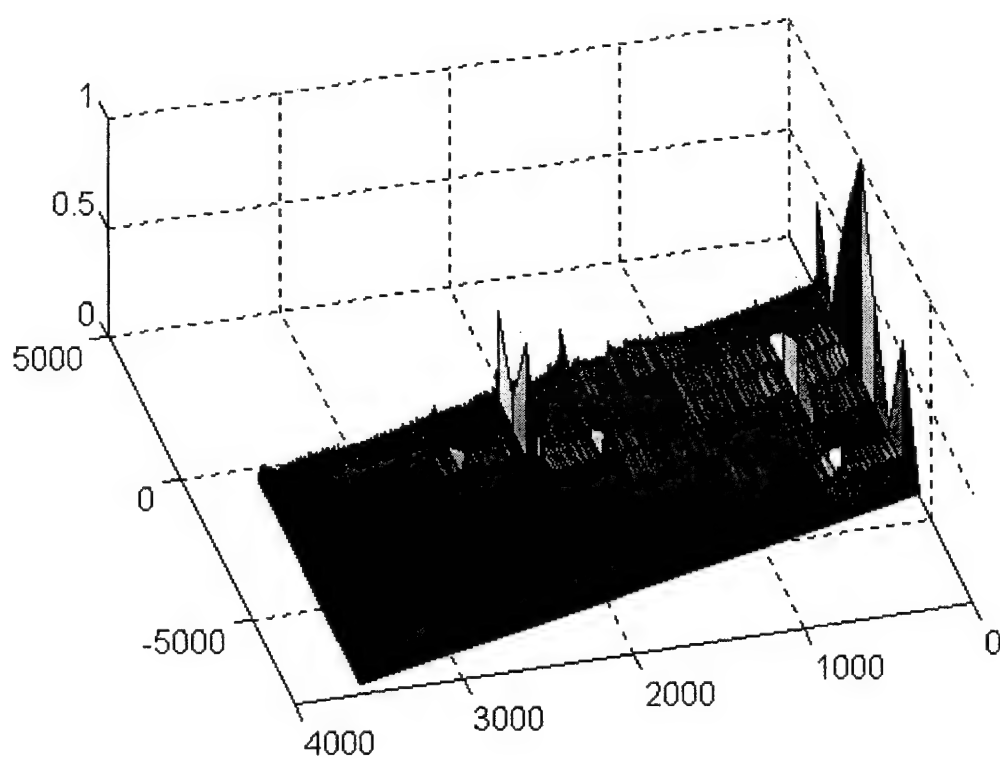


Figure B-8 - SCF for slave #2 (top) and slave #3 (bottom), time 409405

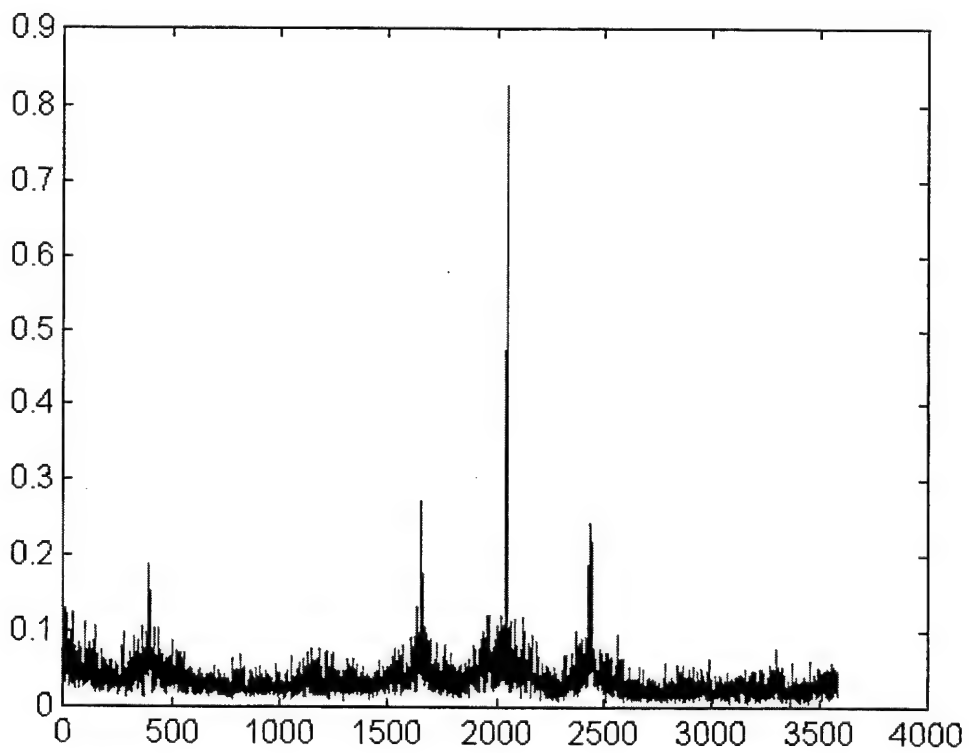
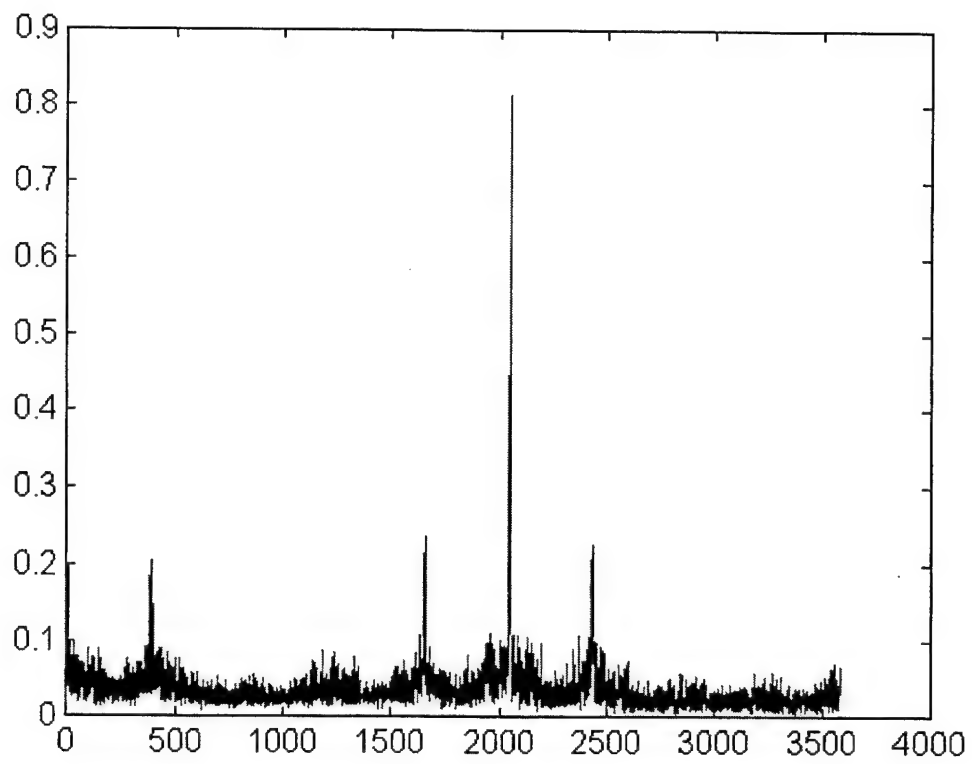


Figure B-9 - Cycle freq vs Max-magnitude of SCF for master (top) and slave #1 (bottom), time 409405

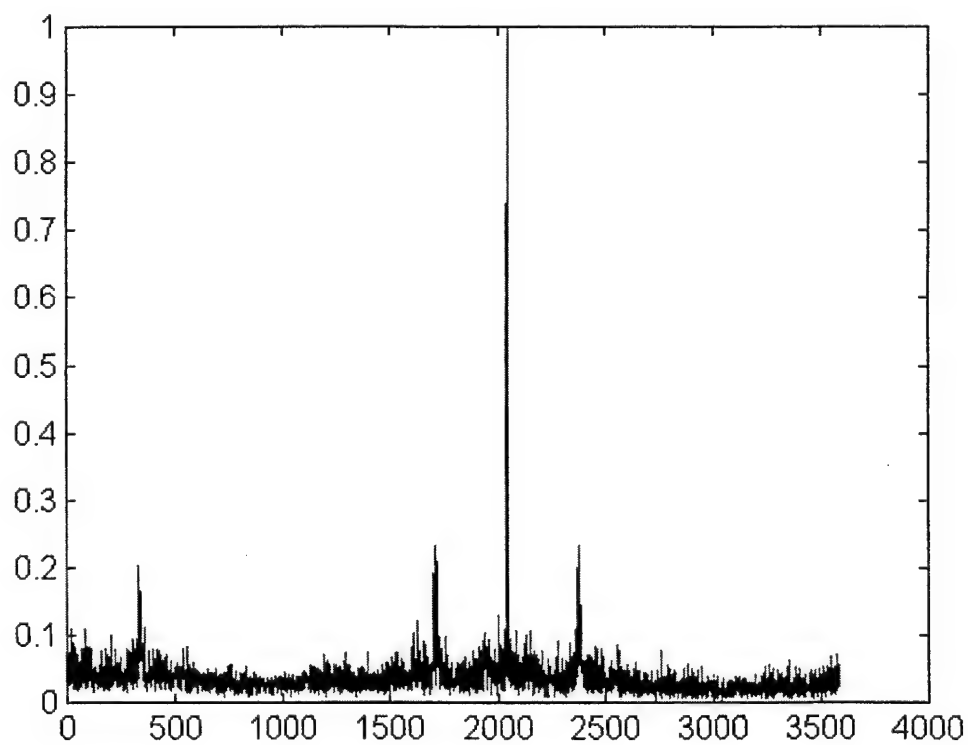
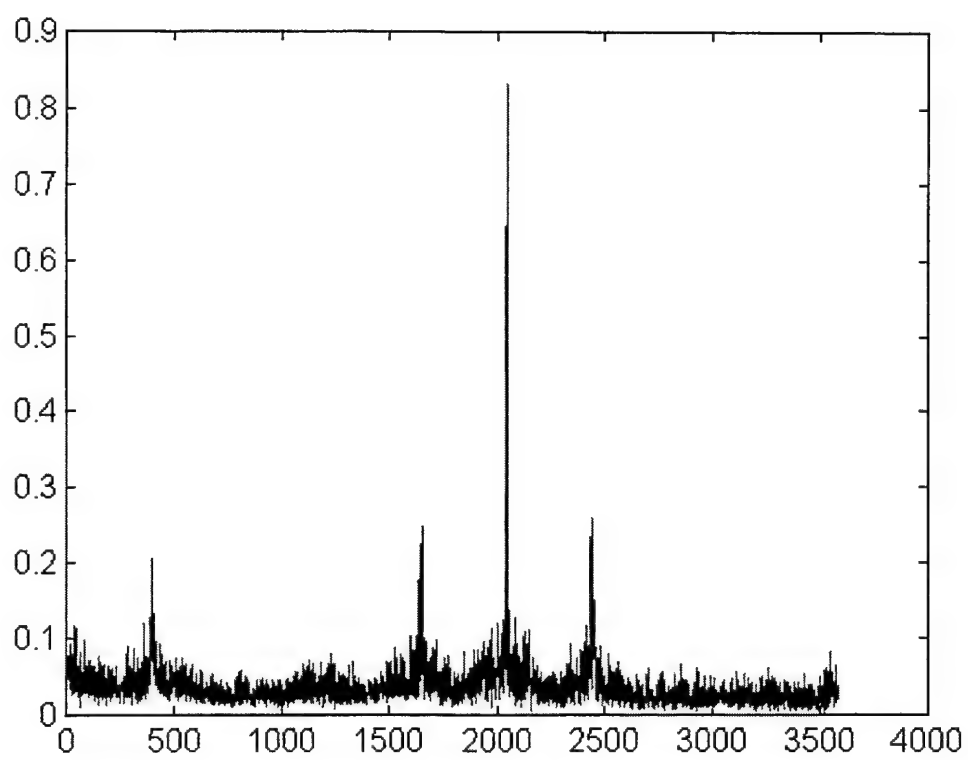


Figure B-10 - Cycle freq vs Max-magnitude of SCF for slave #2 (top) and slave #3 (bottom), time 409405

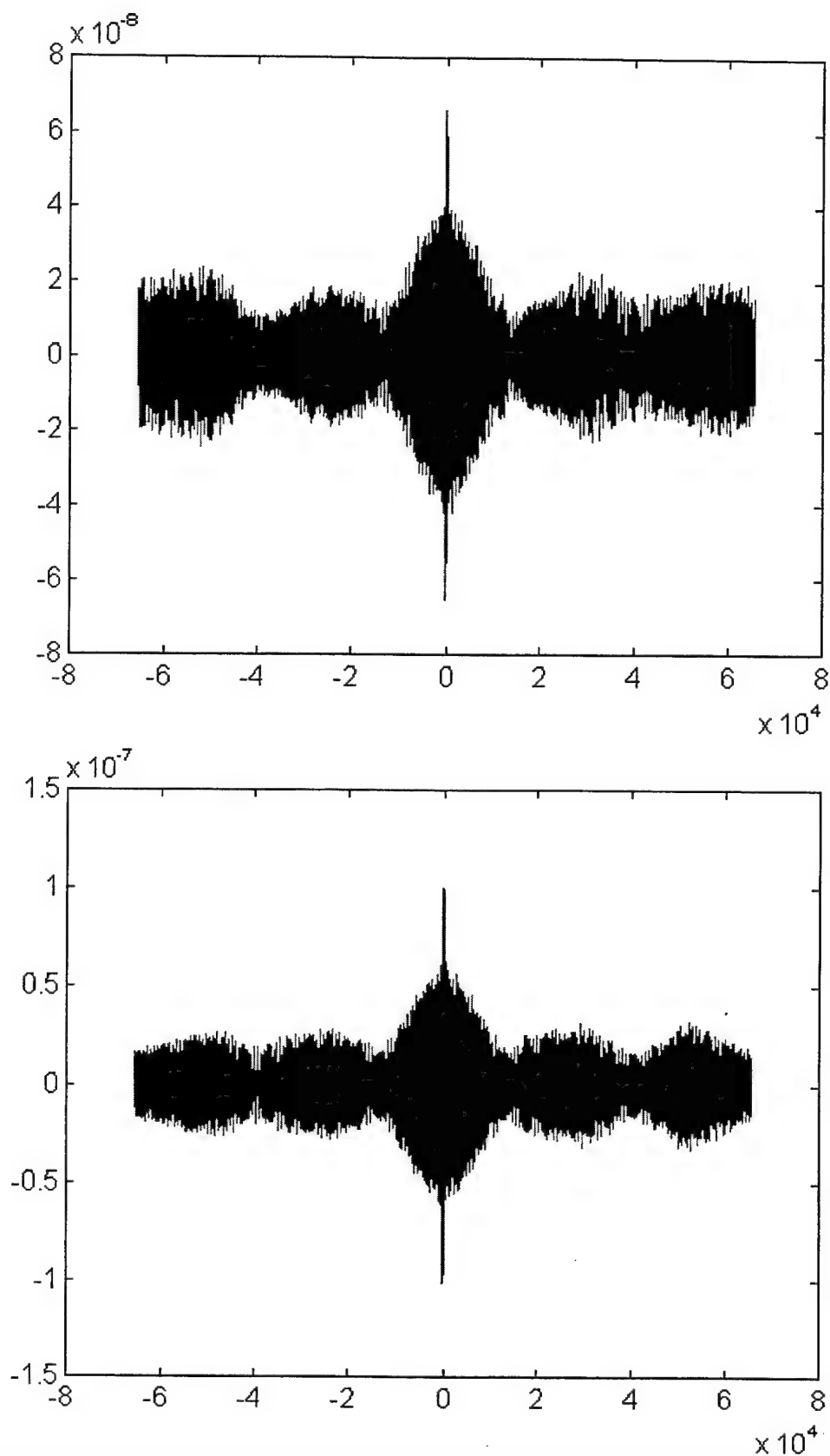


Figure B-11 - SPECCOA for master and slave #1 (top) and master and slave #2 (bottom), time 409405

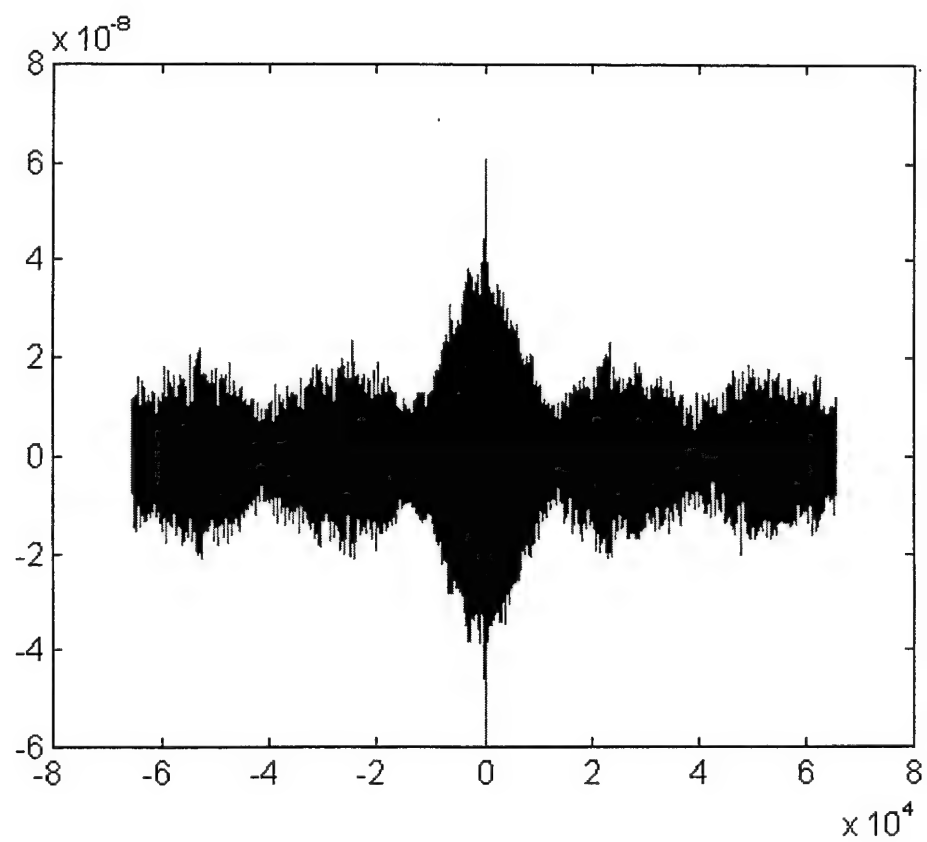


Figure B-12 - SPECCOA for master and slave #3, time 409405

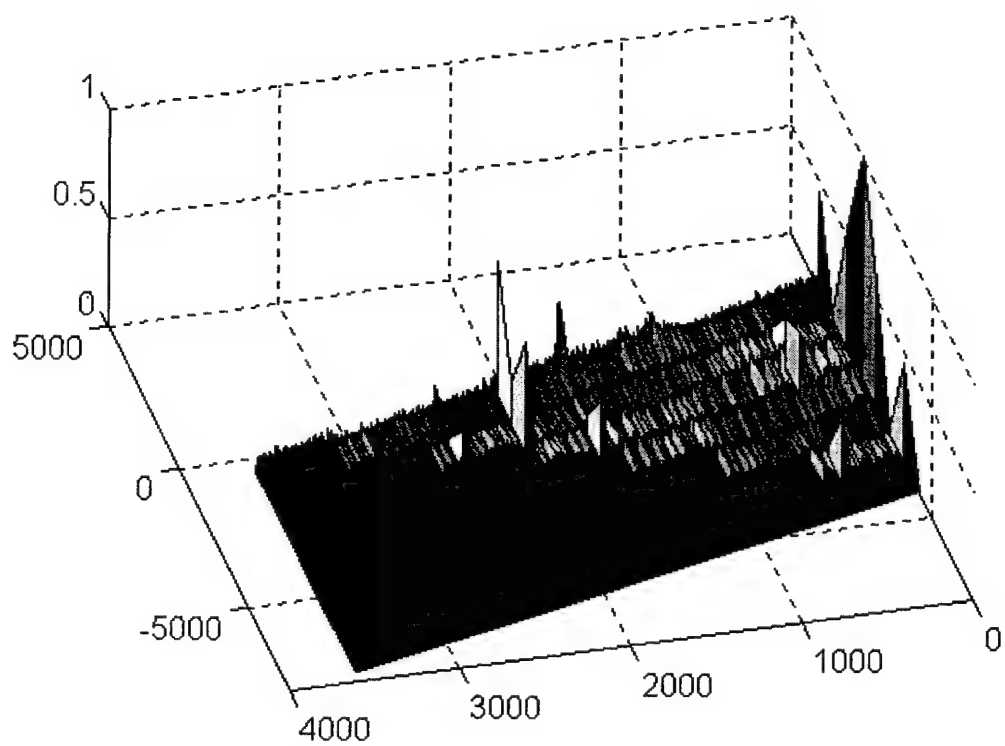
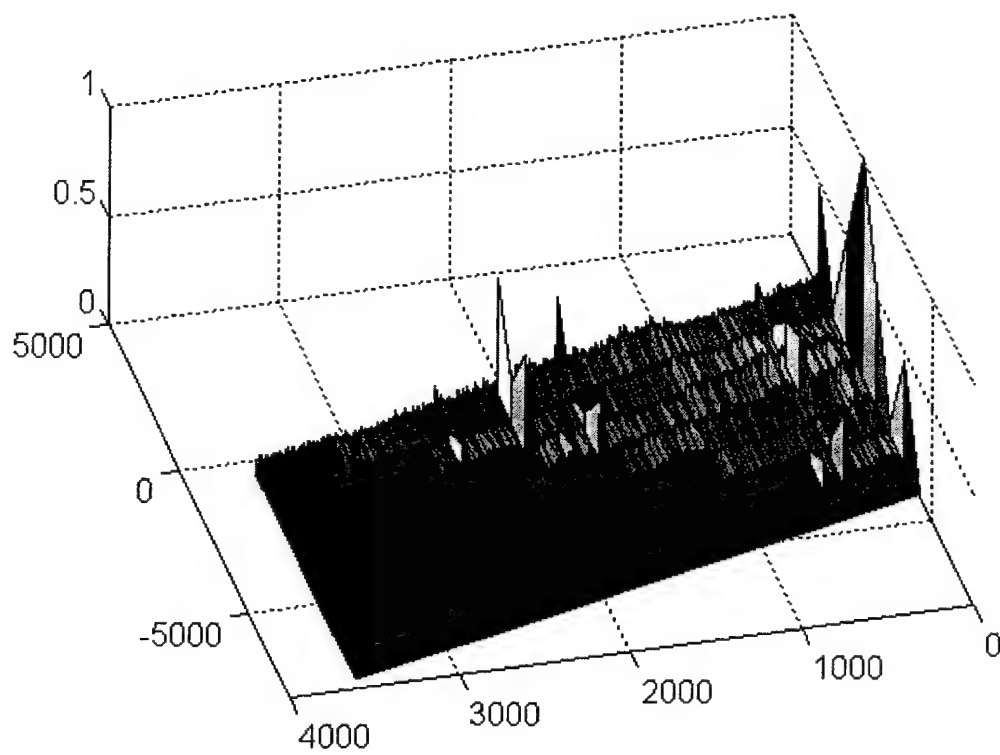


Figure B-13 - SCF for master (top) and slave #1 (bottom), time 409410

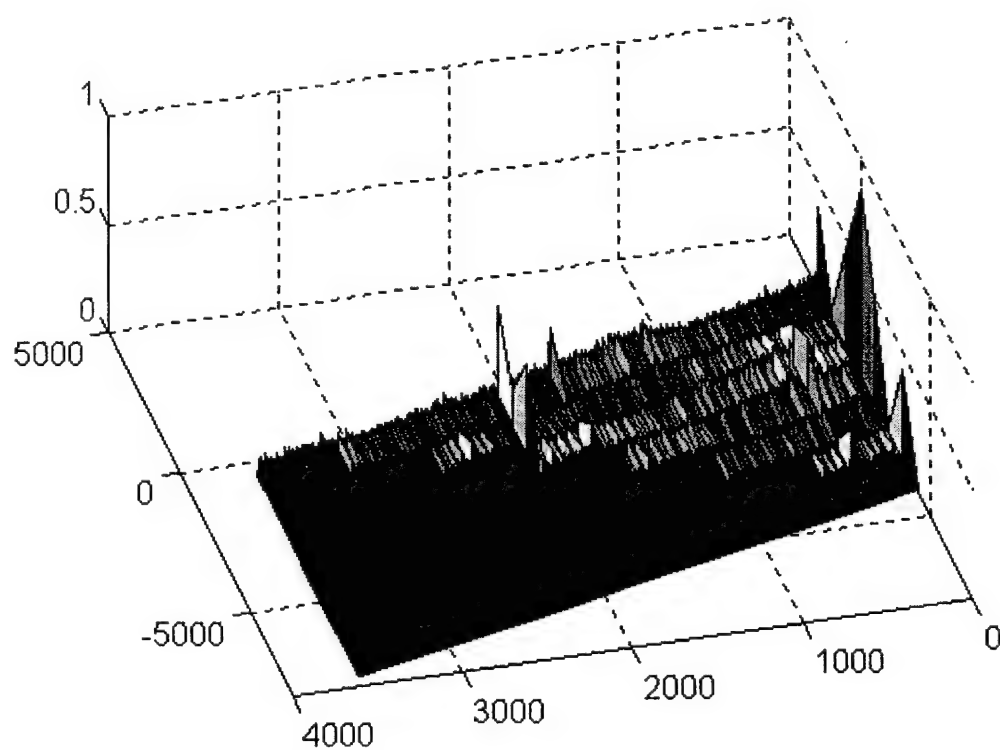
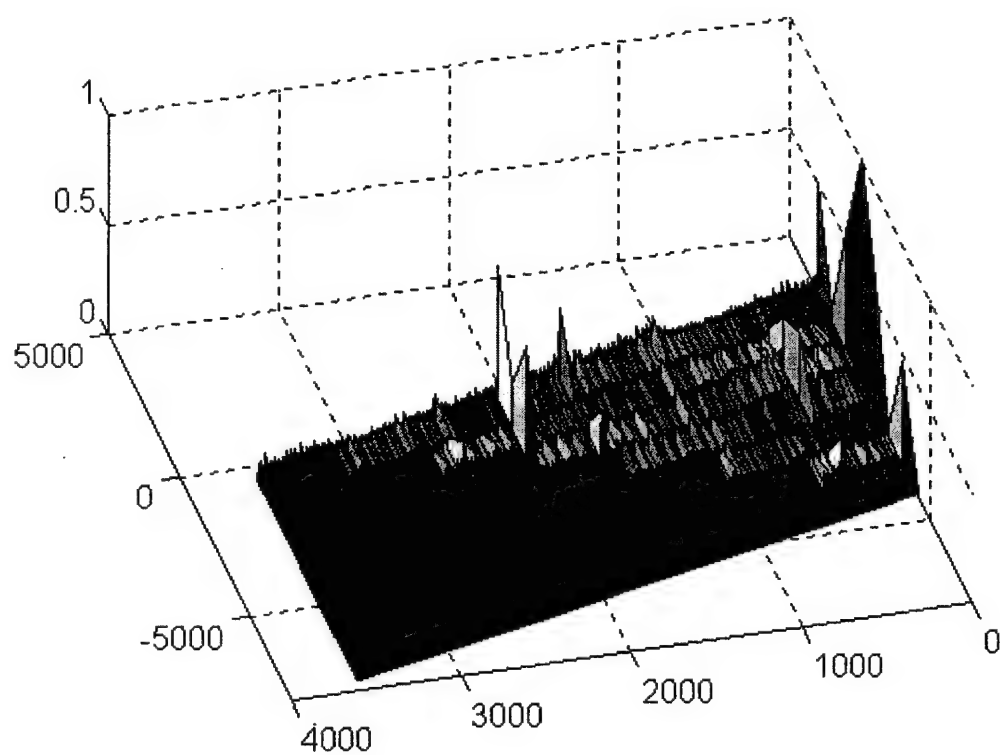


Figure B-14 - SCF for slave #2 (top) and slave #3 (bottom), time 409410

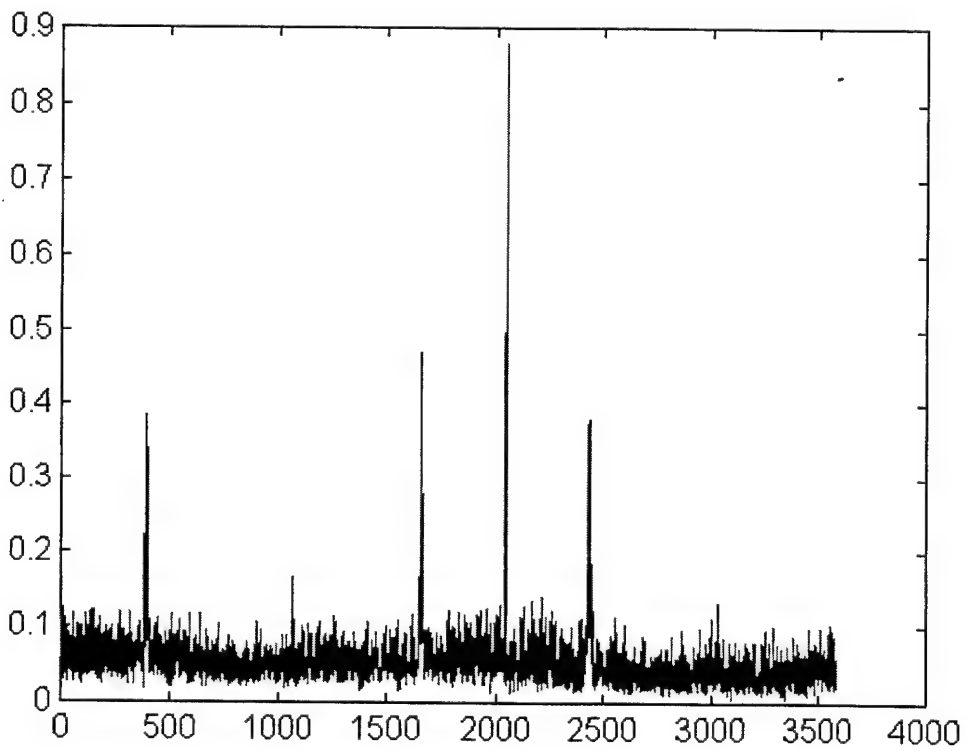
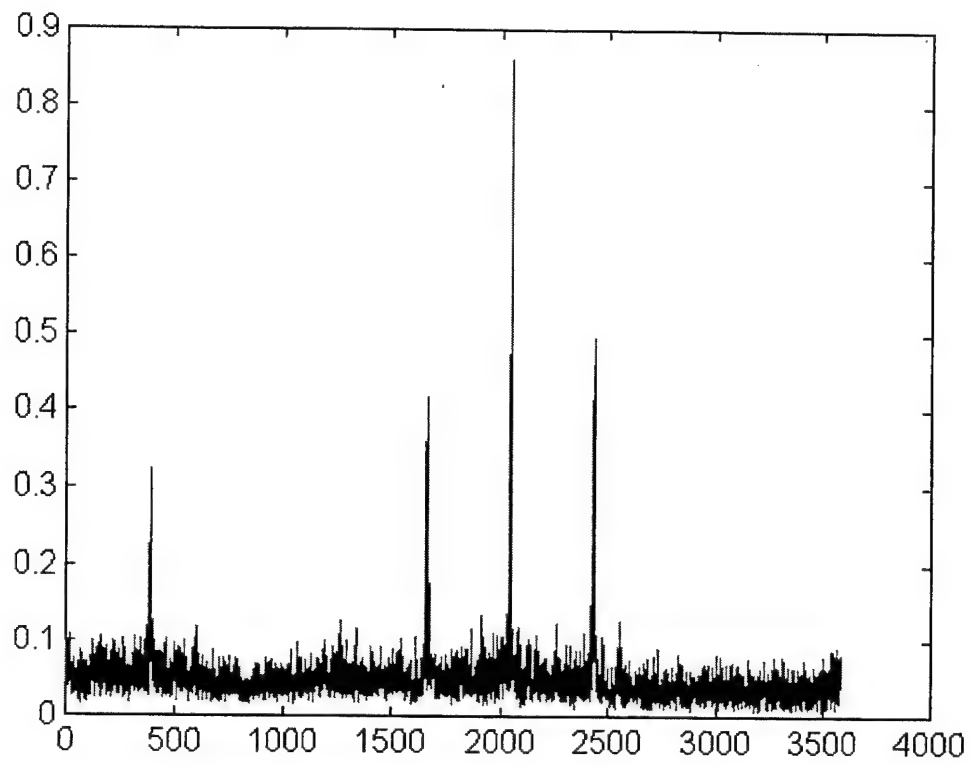


Figure B-15 - Cycle freq vs Max-magnitude of SCF for master (top) and slave #1 (bottom), time 409410

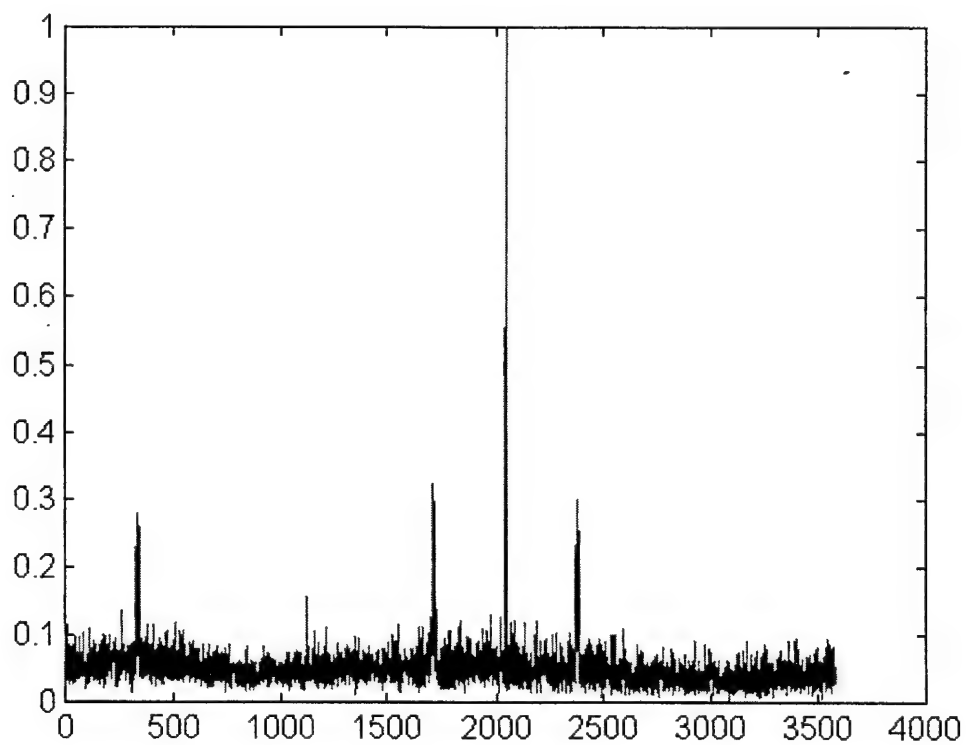
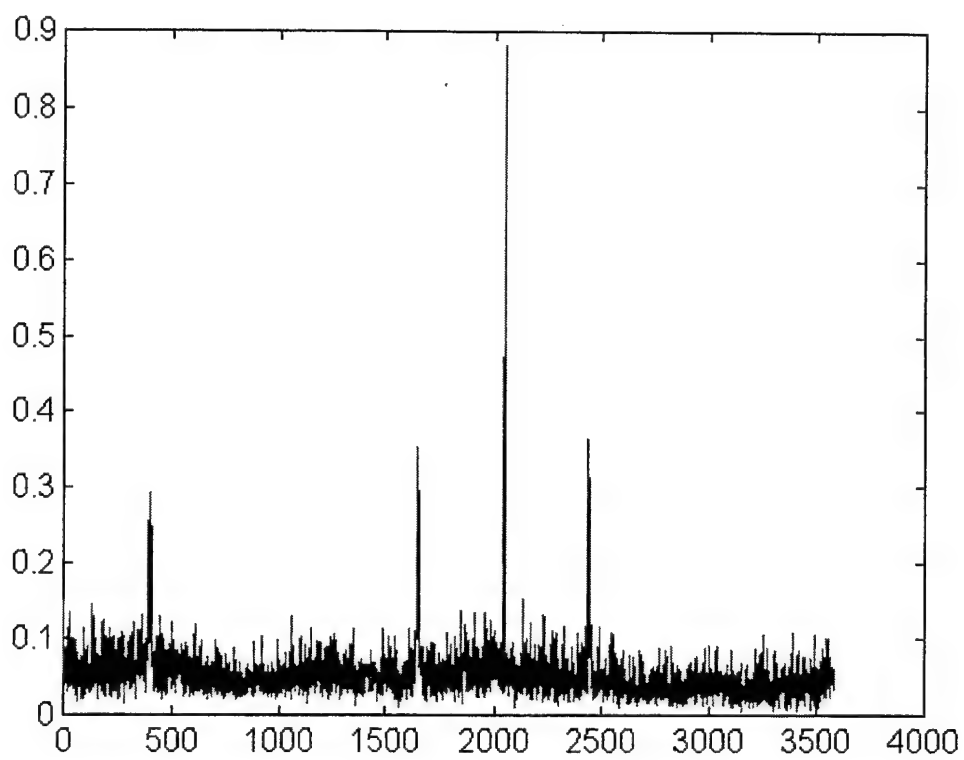


Figure B-16 - Cycle freq vs Max-magnitude of SCF for slave #2 (top) and slave #3 (bottom), time 409410

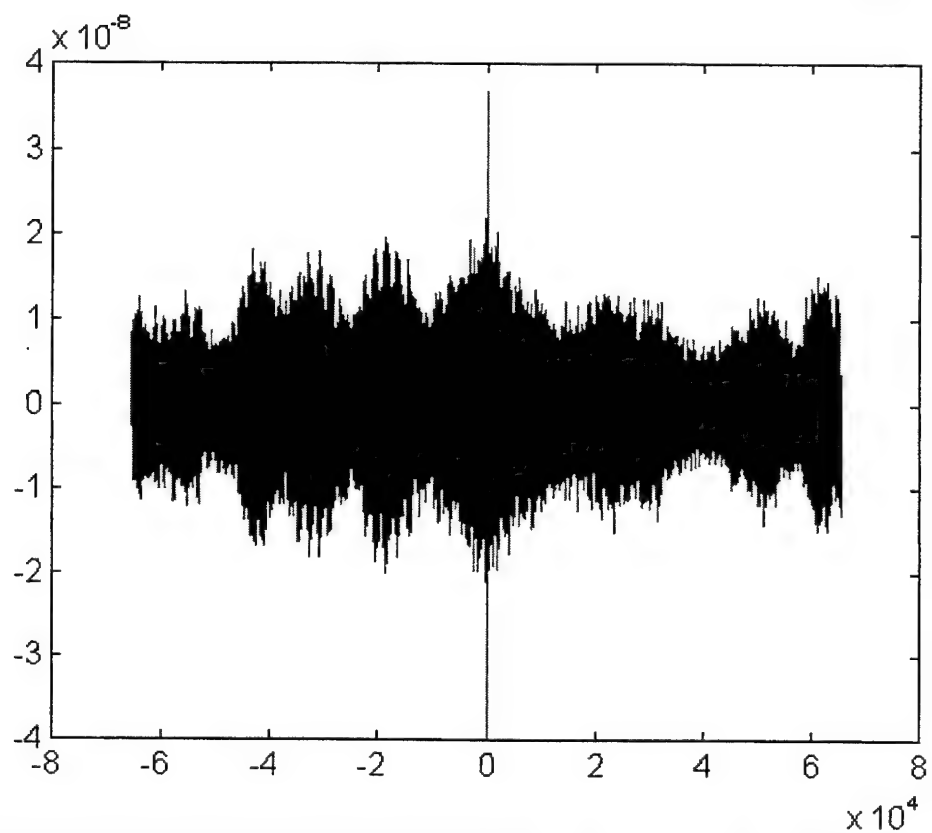
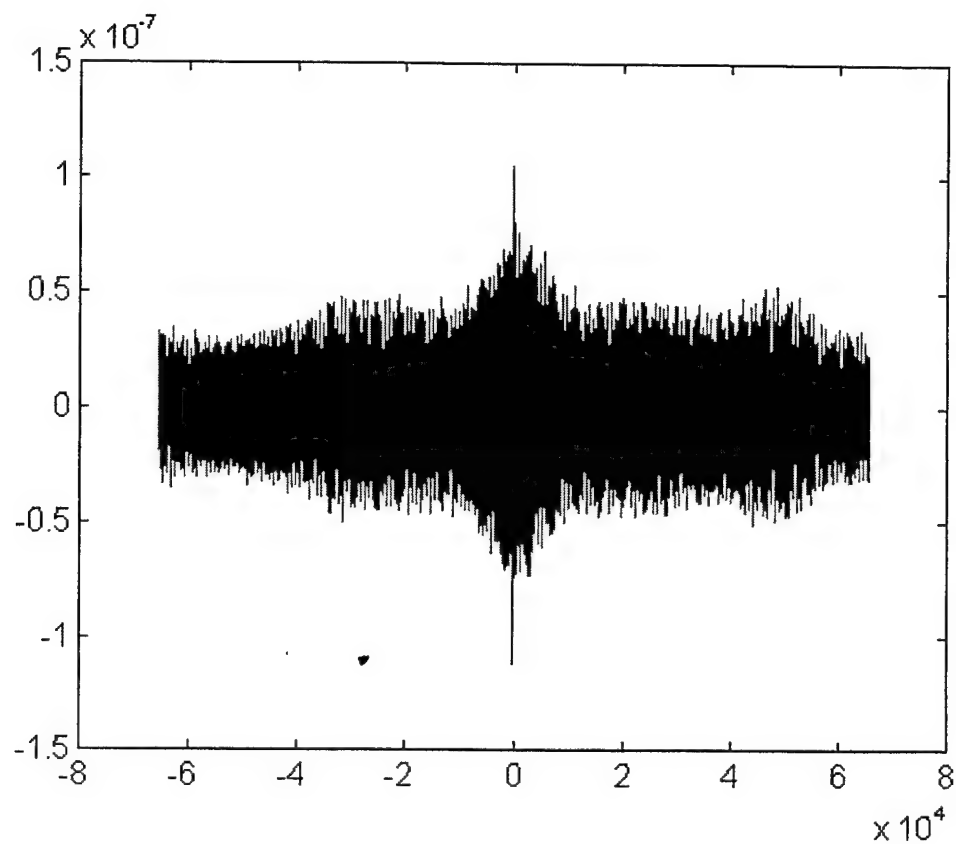


Figure B-17 - SPECCOA for master and slave #1 (top) and master and slave #2 (bottom), time 409410

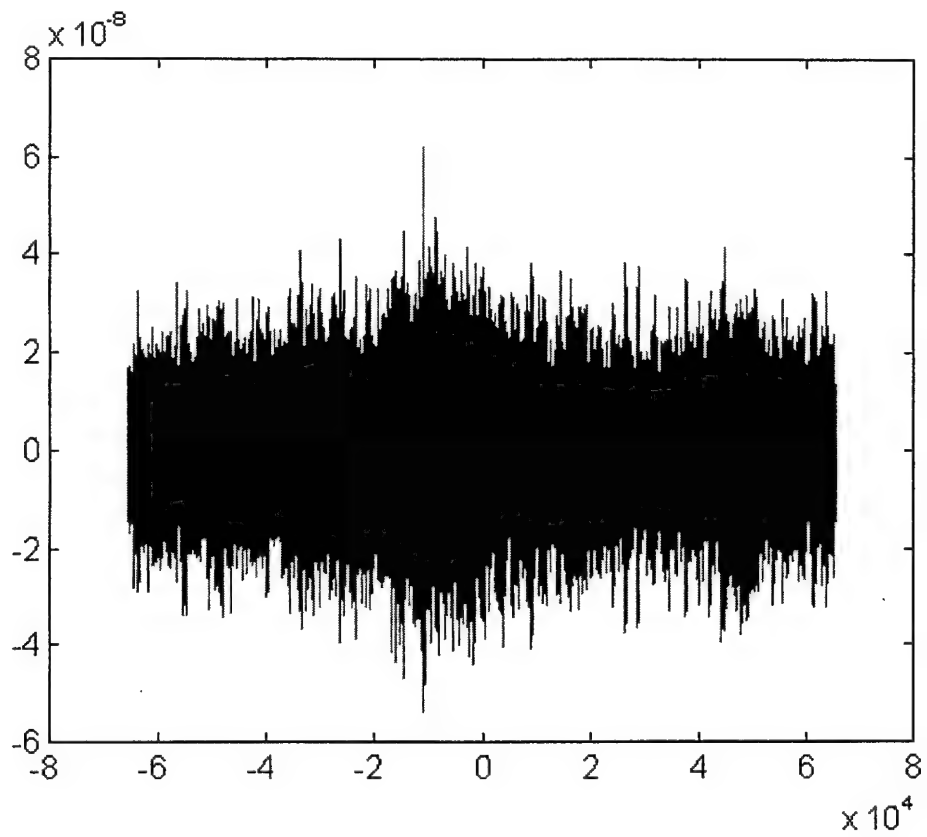


Figure B-18 - SPECCOA for master and slave #3, time 409410

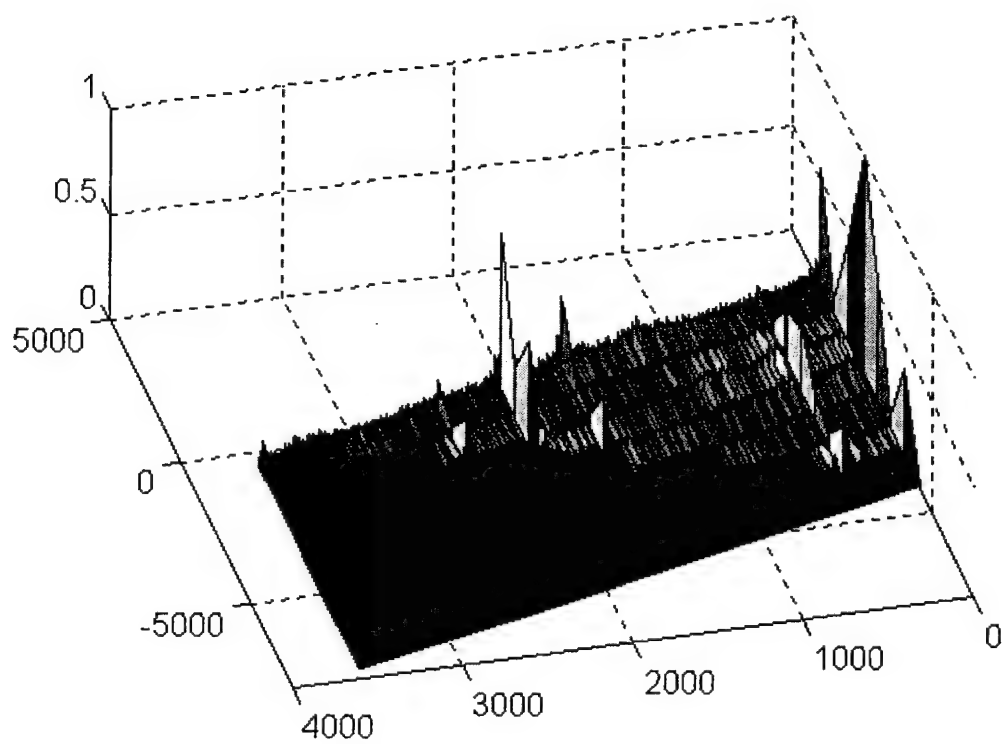
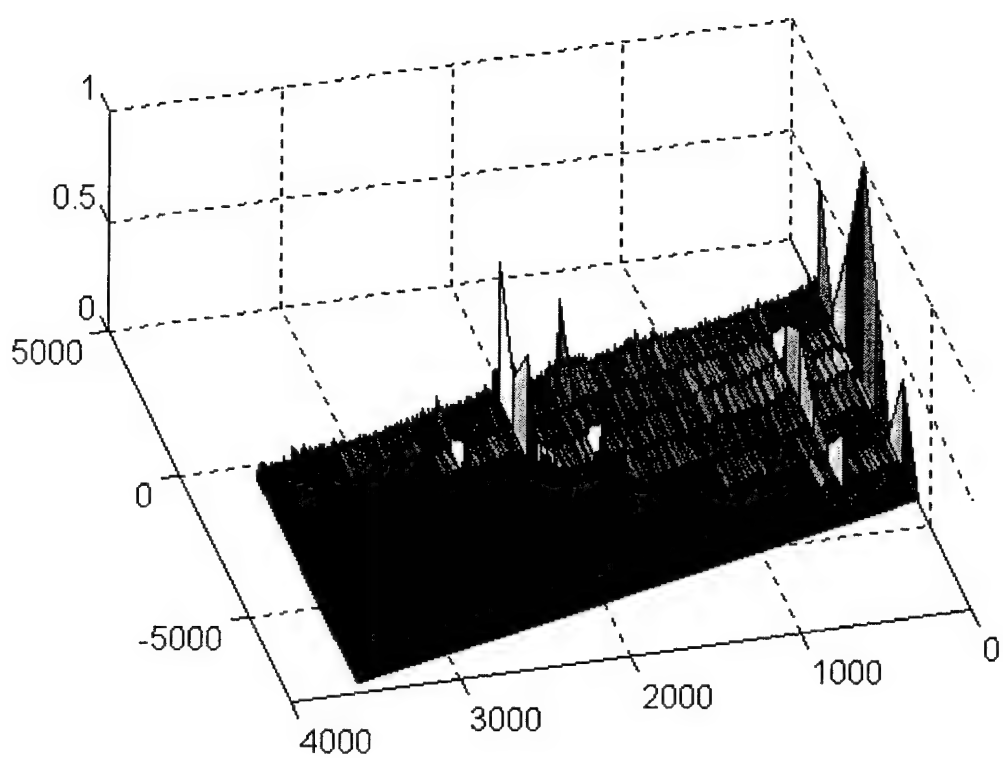


Figure B-19 - SCF for master (top) and slave #1 (bottom), time 409415

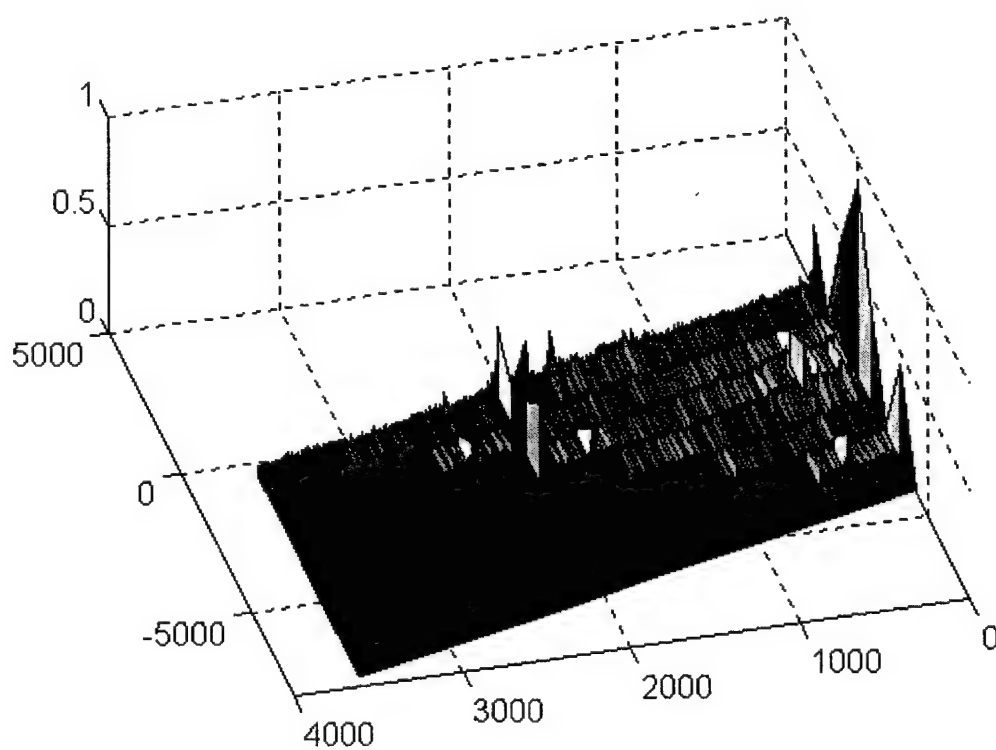
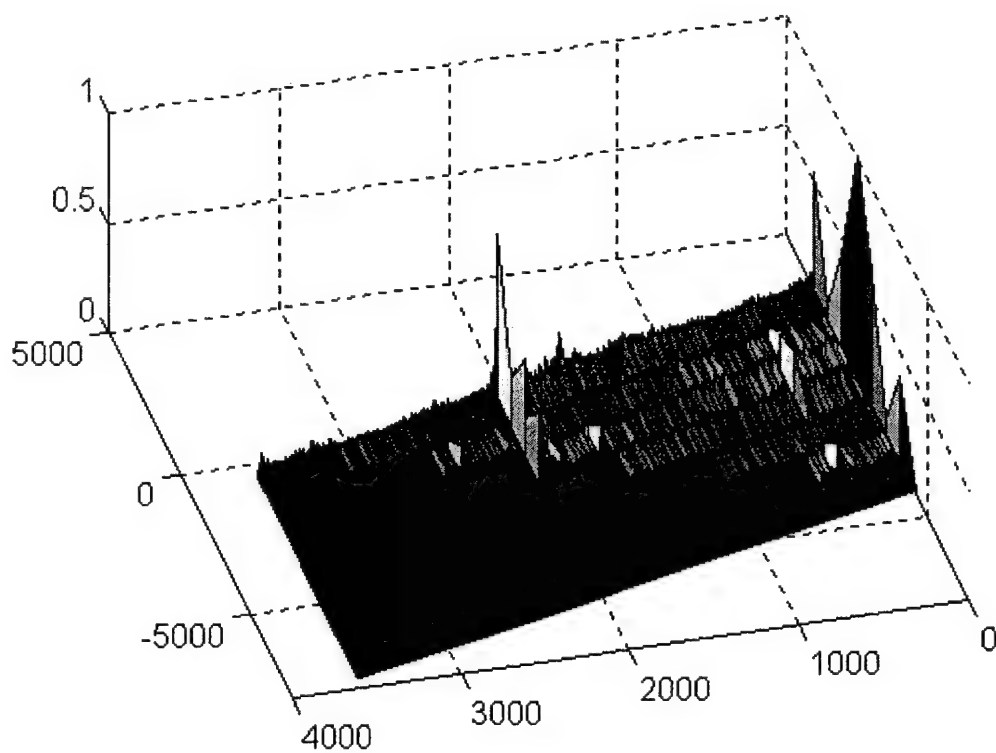


Figure B-20 - SCF for slave #2 (top) and slave #3 (bottom), time 409415

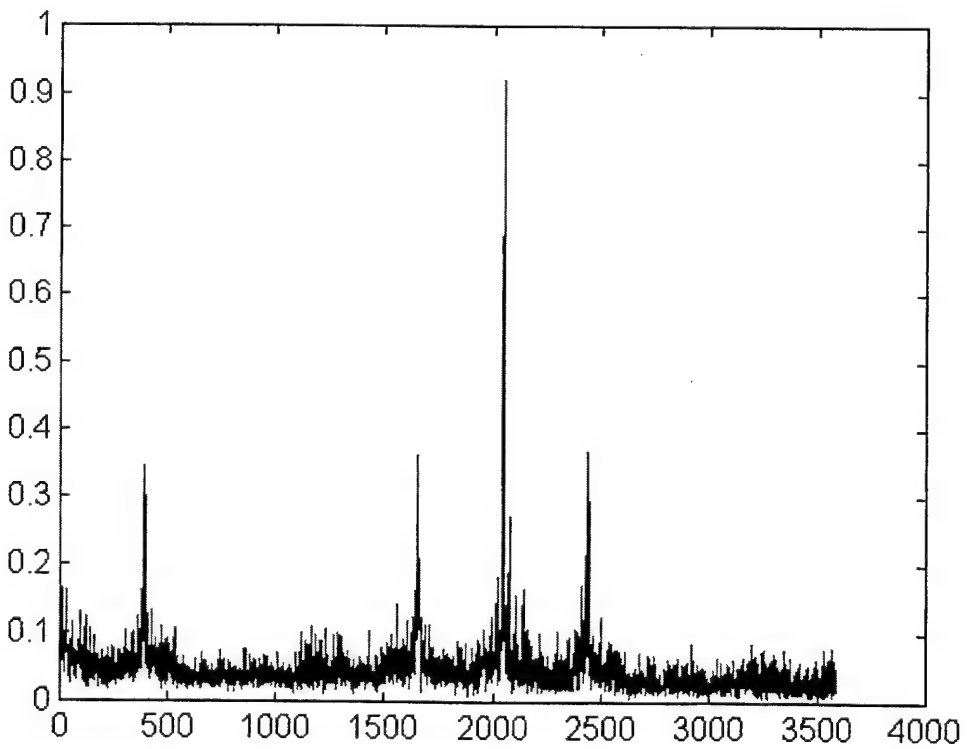
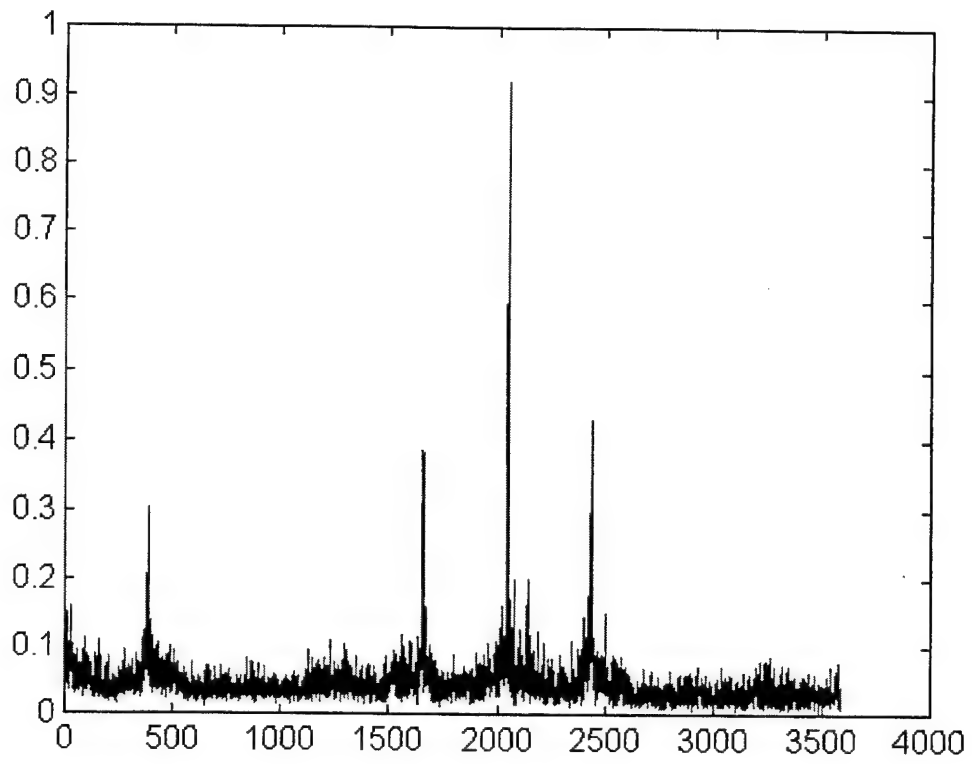


Figure B-21 - Cycle freq vs Max-magnitude of SCF for master (top) and slave #1 (bottom), time 409415

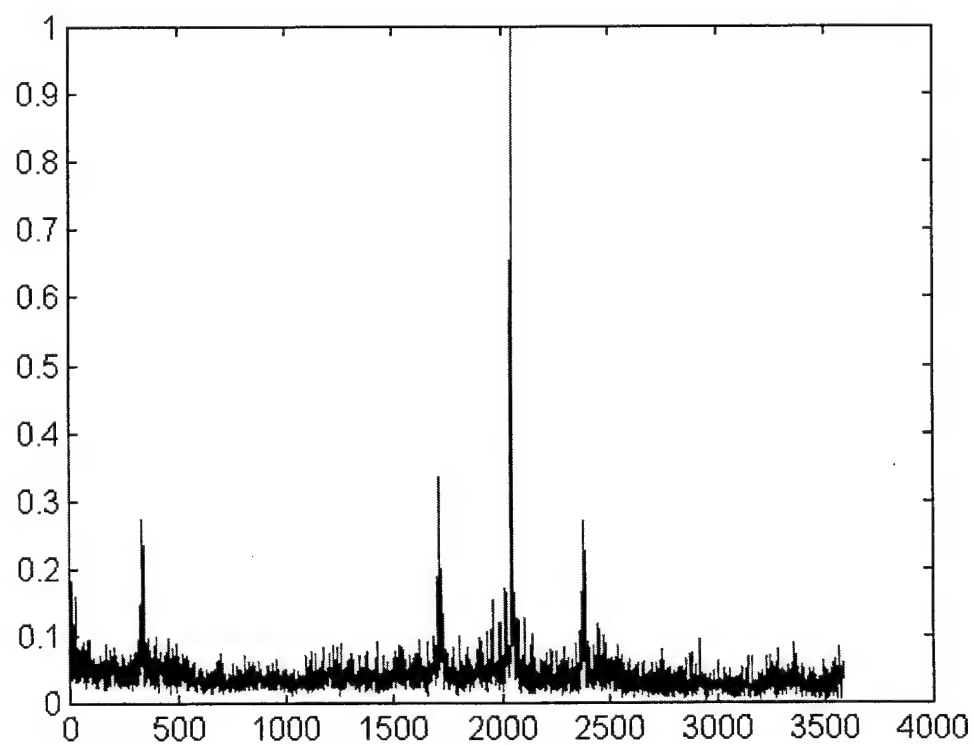
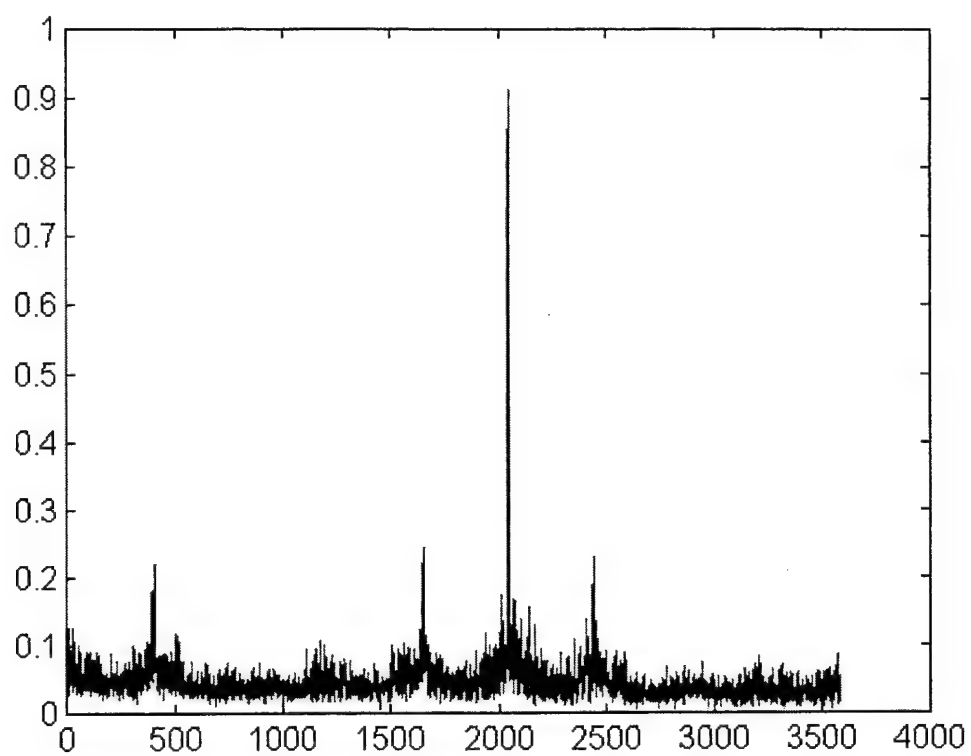


Figure B-22 - Cycle freq vs Max-magnitude of SCF for slave #2 (top) and slave #3 (bottom), time 409415

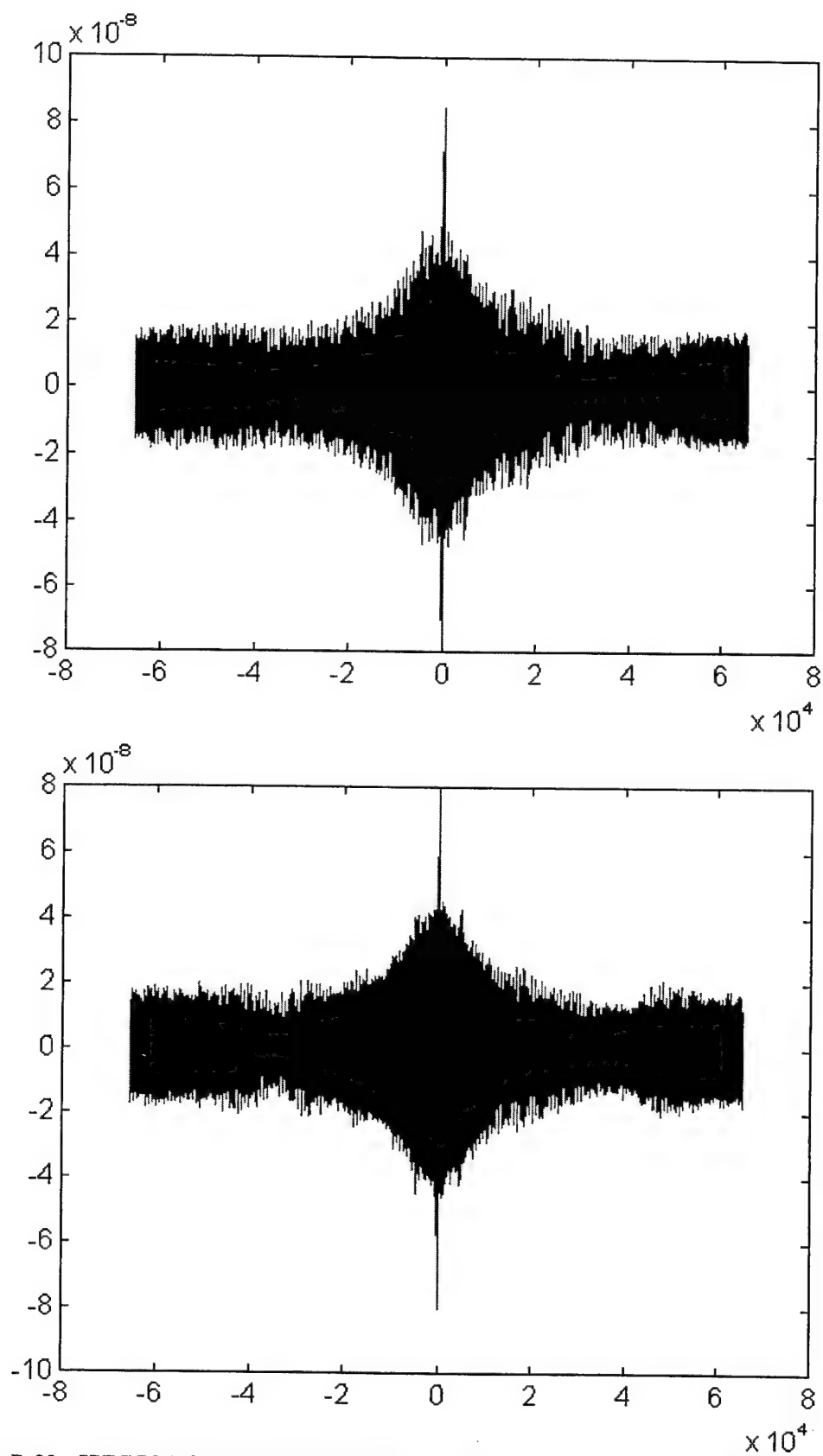


Figure B-23 - SPECCOA for master and slave #1 (top) and master and slave #2 (bottom), time 409415

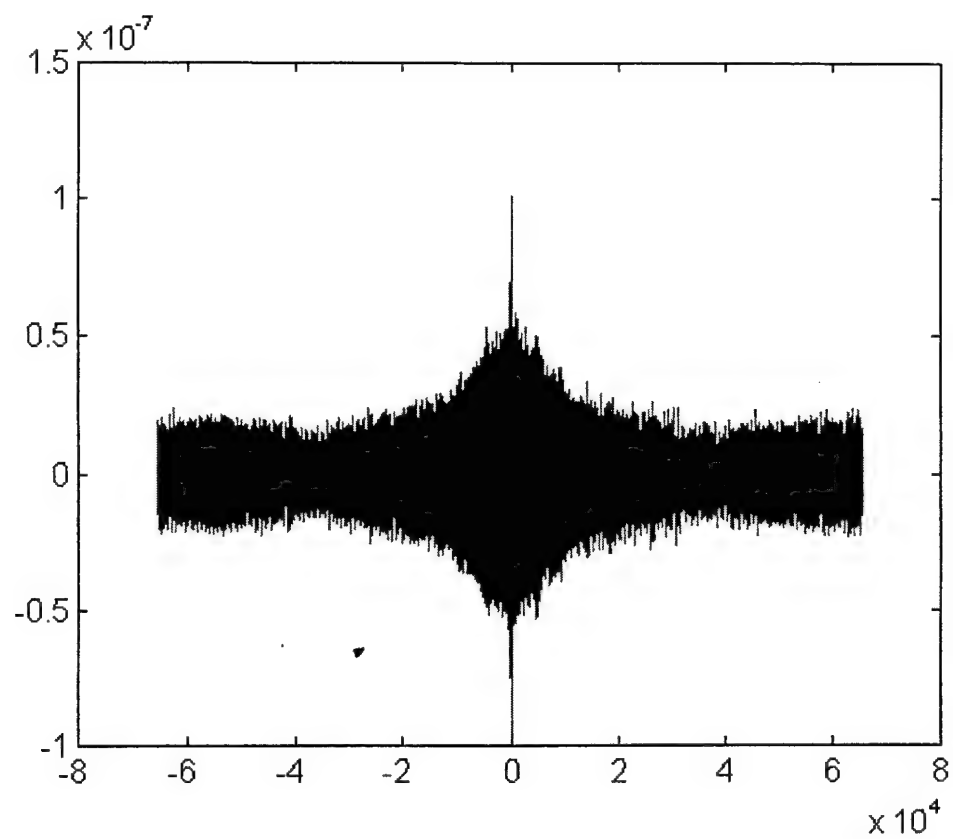


Figure B-24 - SPECCOA for master and slave #3, time 409415

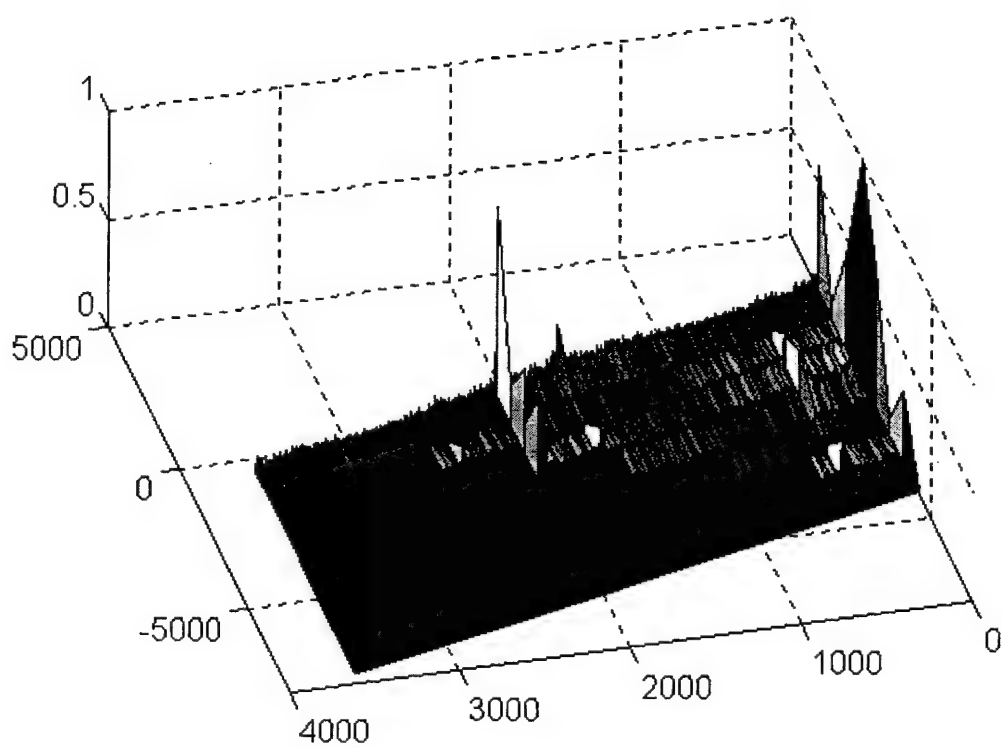
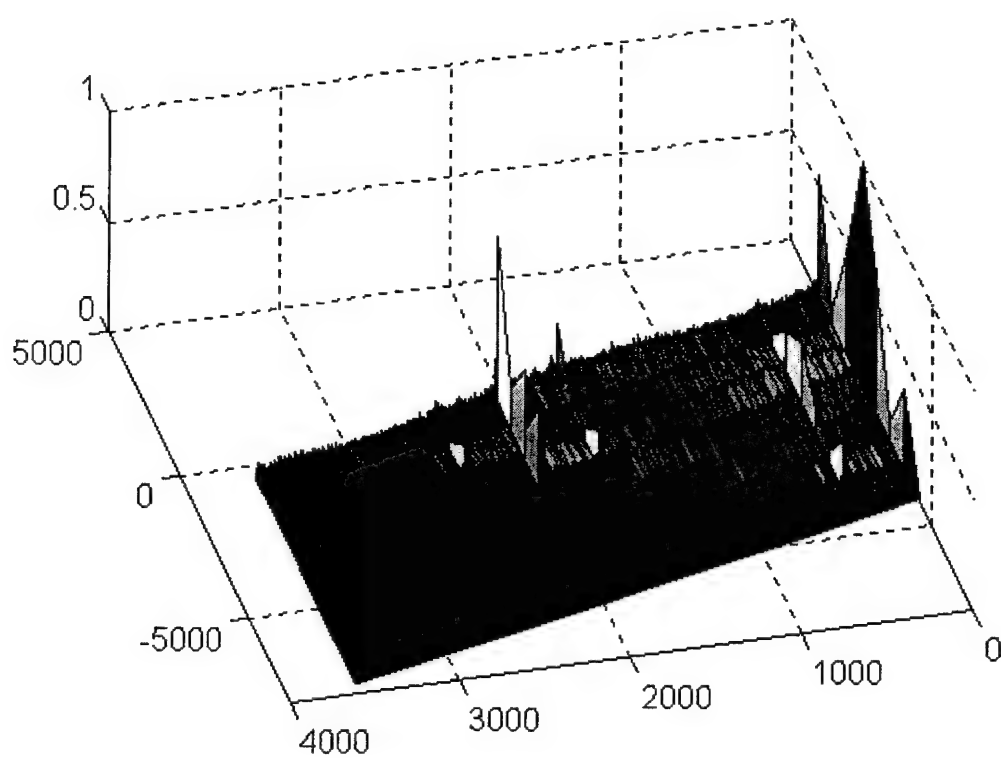


Figure B-25 - SCF for master (top) and slave #1 (bottom), time 409420

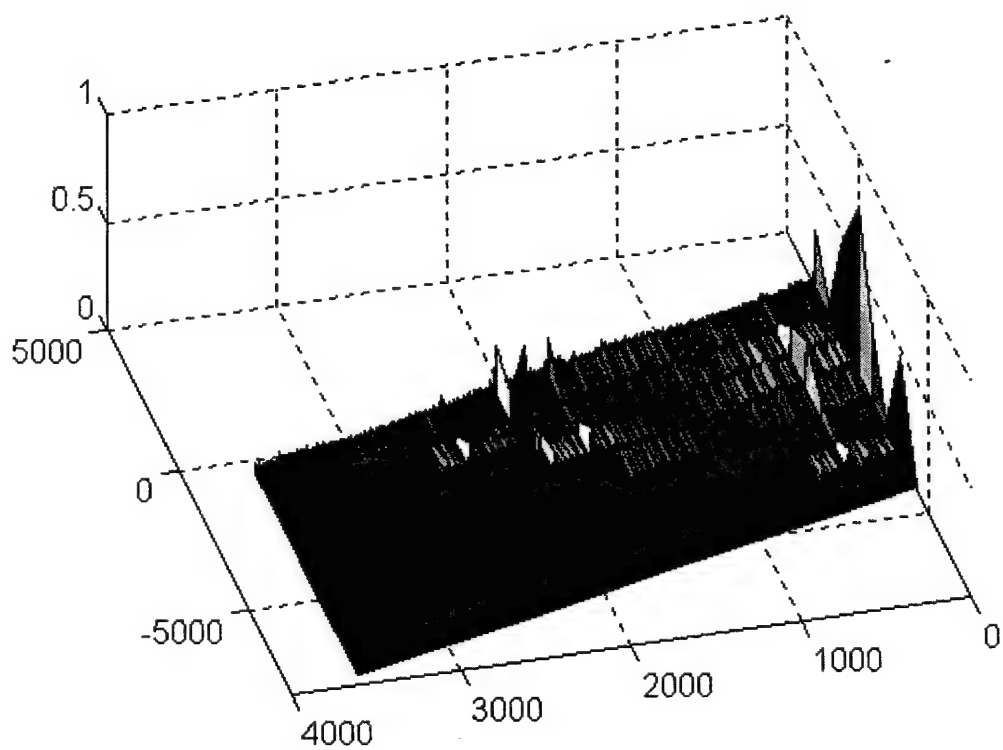
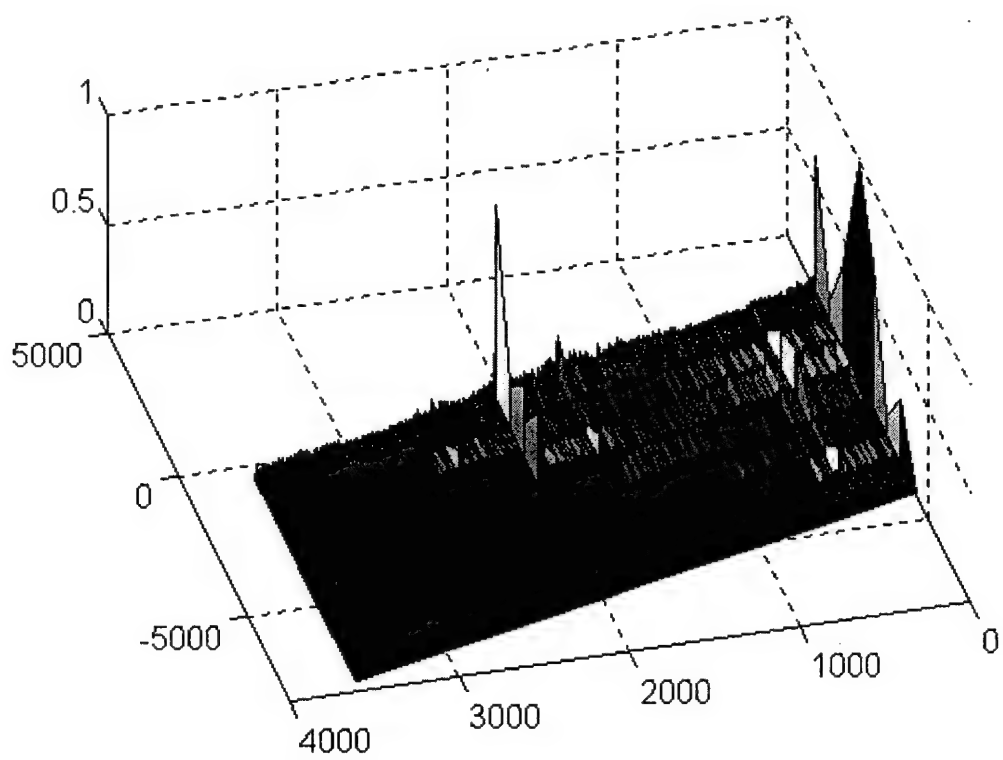


Figure B-26 - SCF for slave #2 (top) and slave #3 (bottom), time 409420

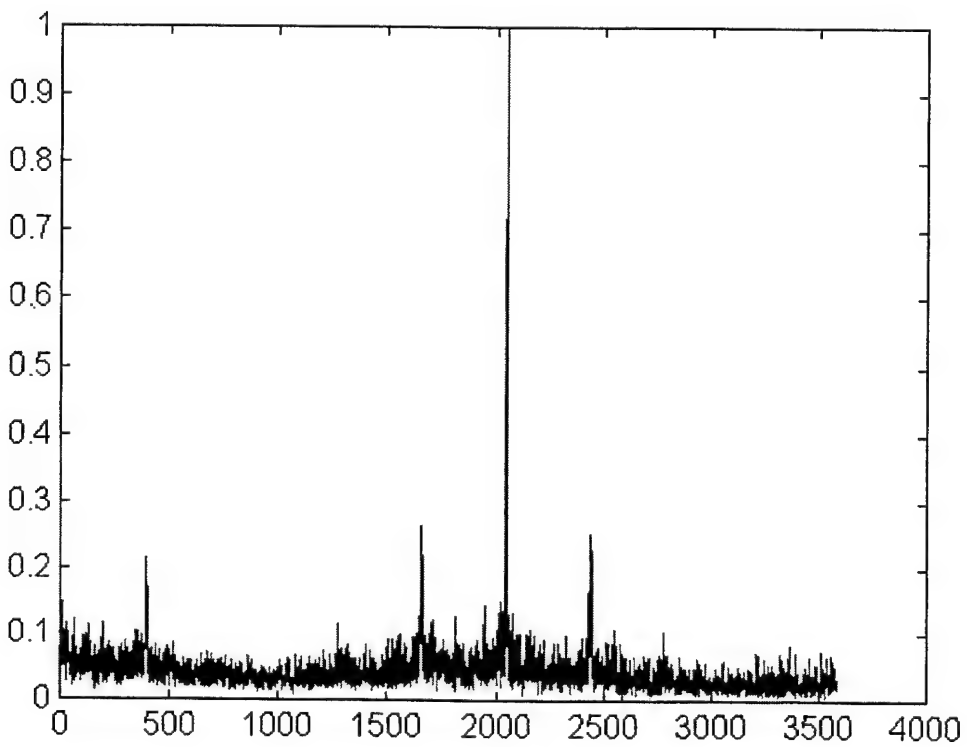
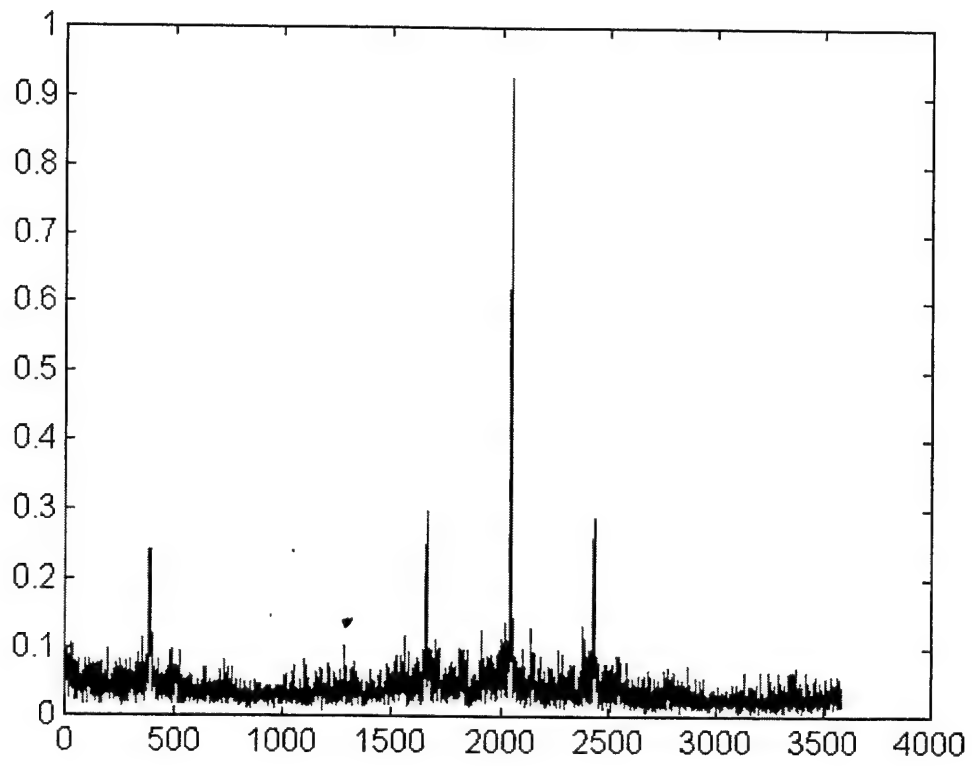


Figure B-27 - Cycle freq vs Max-magnitude of SCF for master (top) and slave #1 (bottom), time 409420

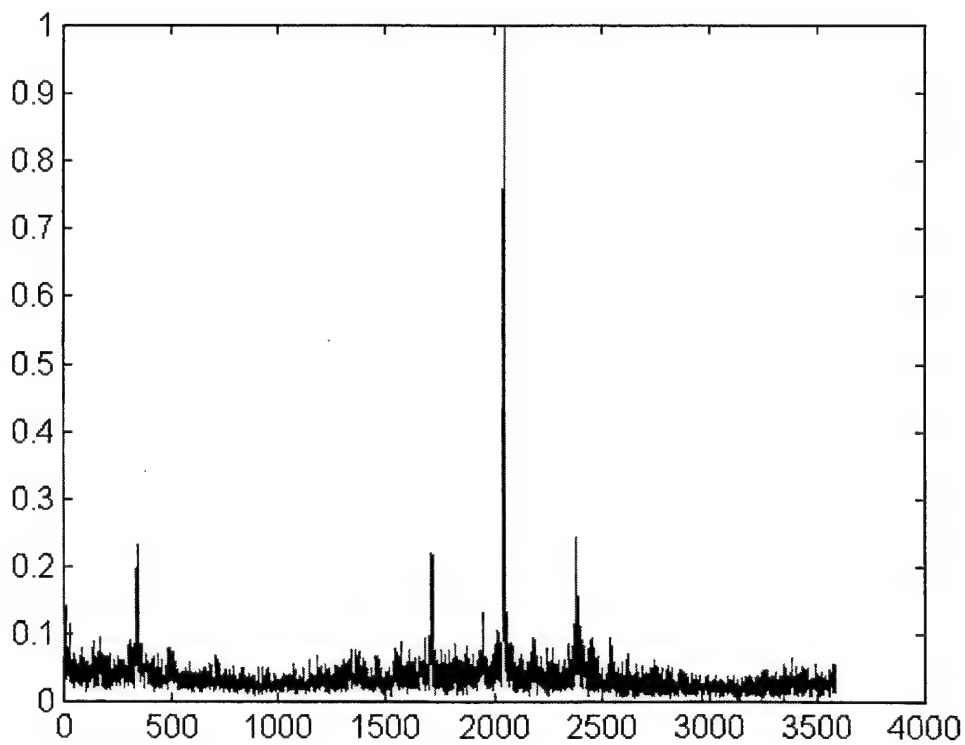
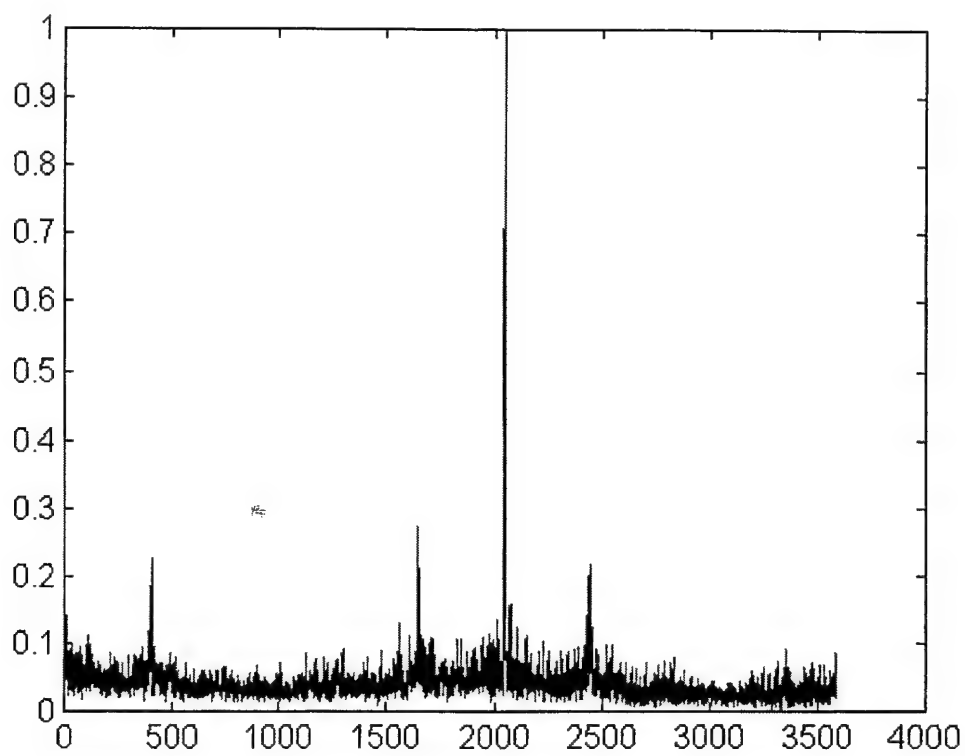


Figure B-28 - Cycle freq vs Max-magnitude of SCF for slave #2 (top) and slave #3 (bottom), time 409420

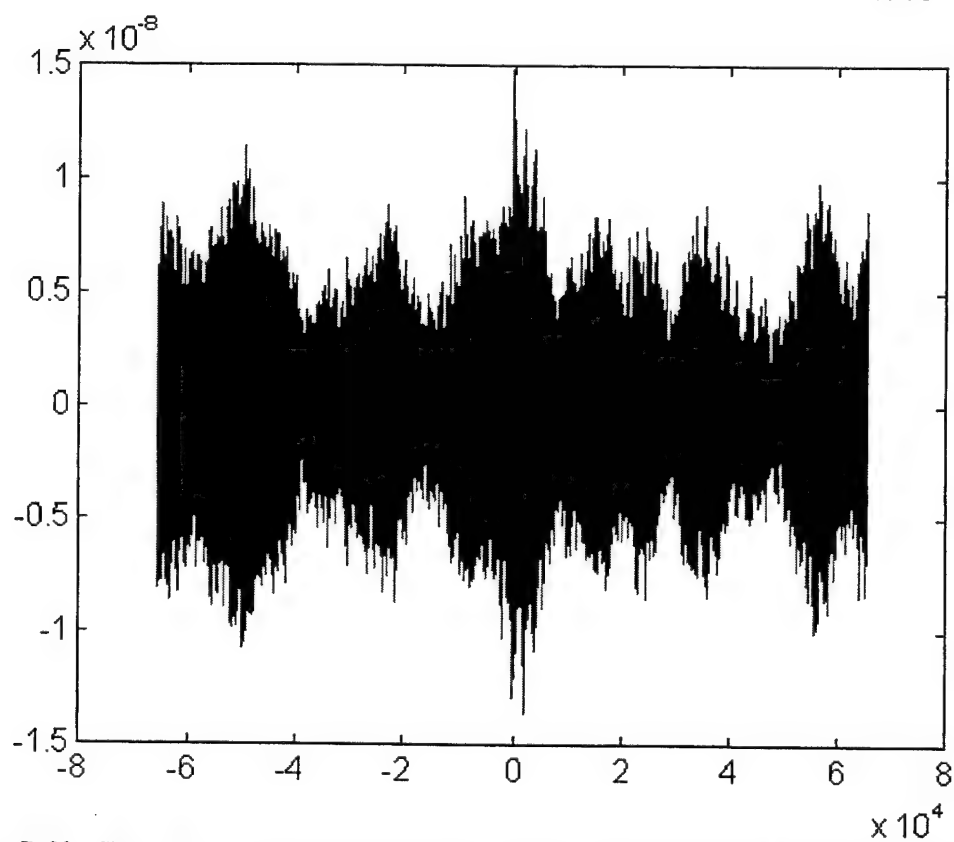
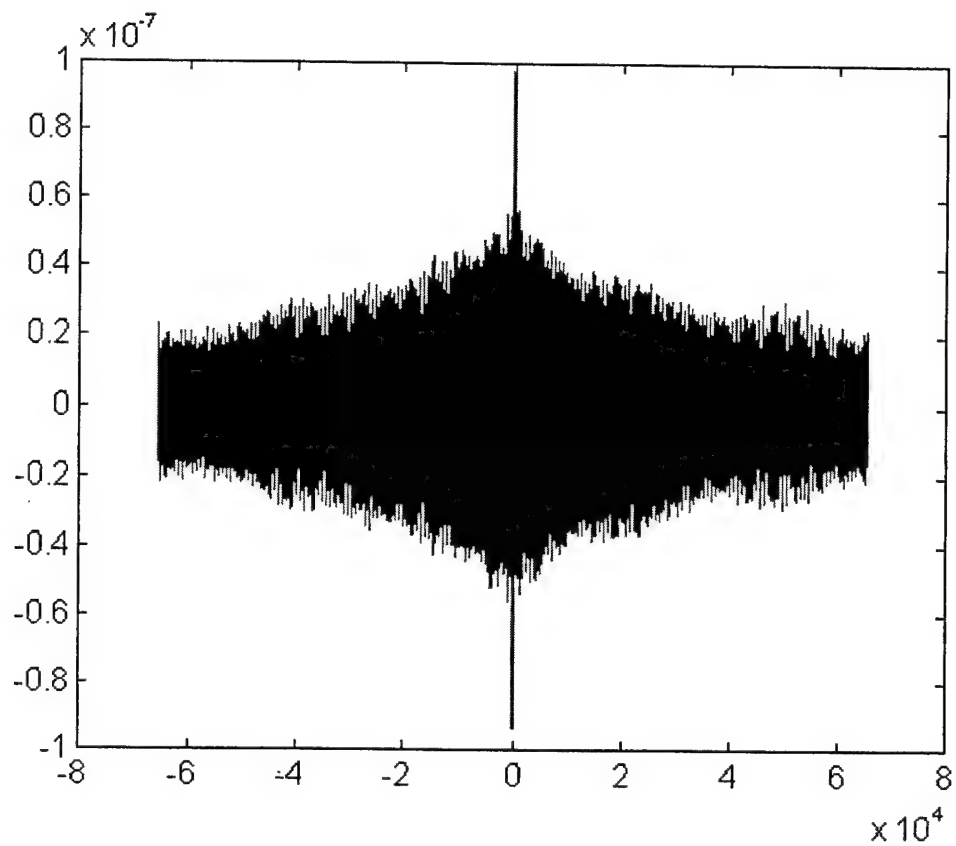


Figure B-29 - SPECCOA for master and slave #1 (top) and master and slave #2 (bottom), time 409420

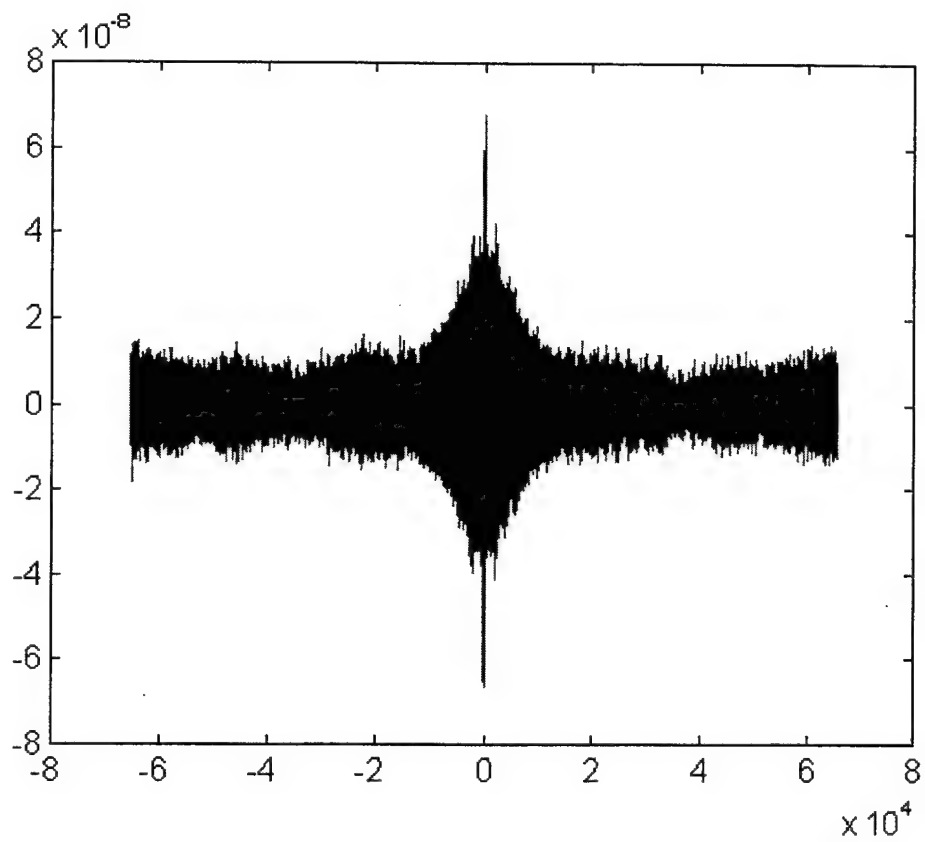


Figure B-30 - SPECCOA for master and slave #3, time 409420

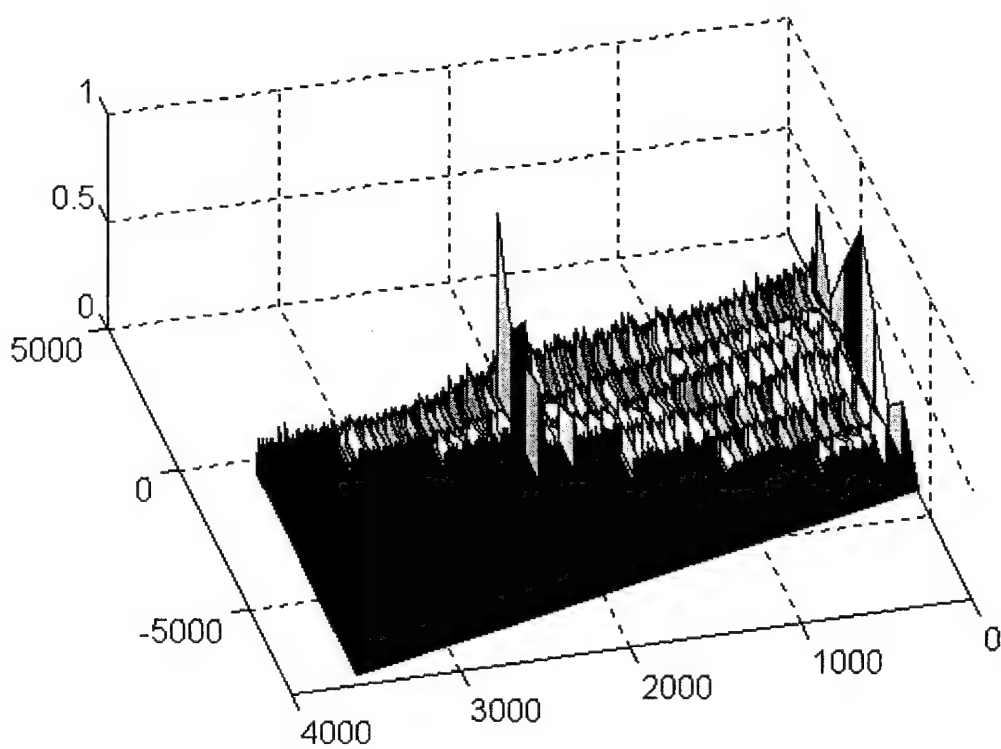
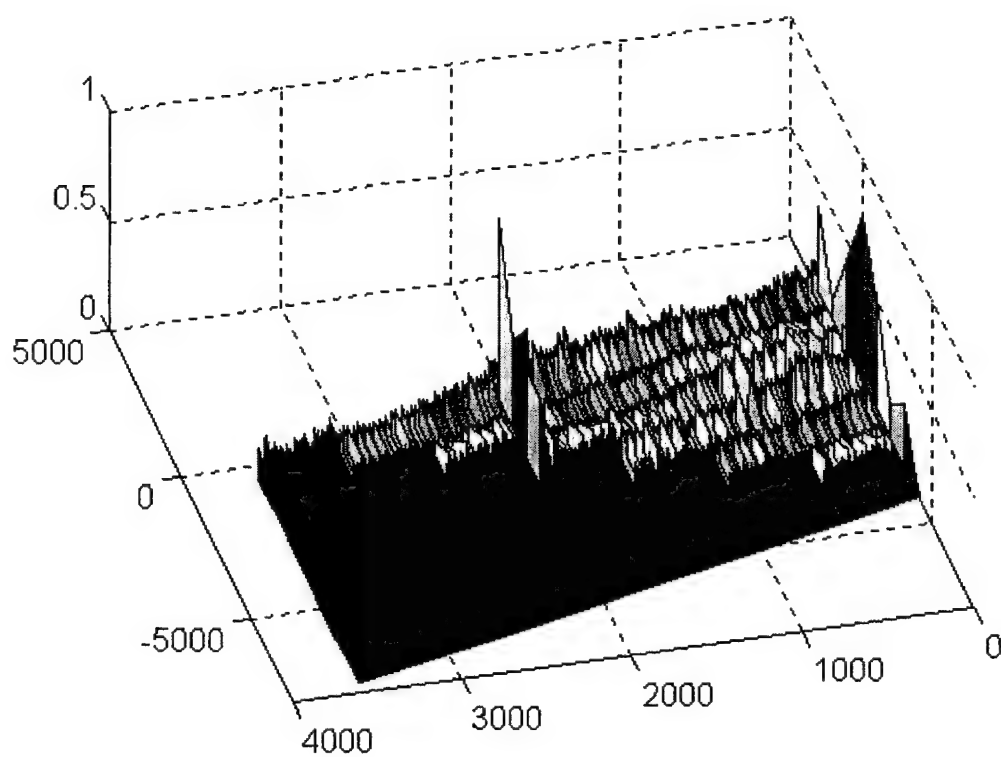


Figure B-31 - SCF for master (top) and slave #1 (bottom), time 409425

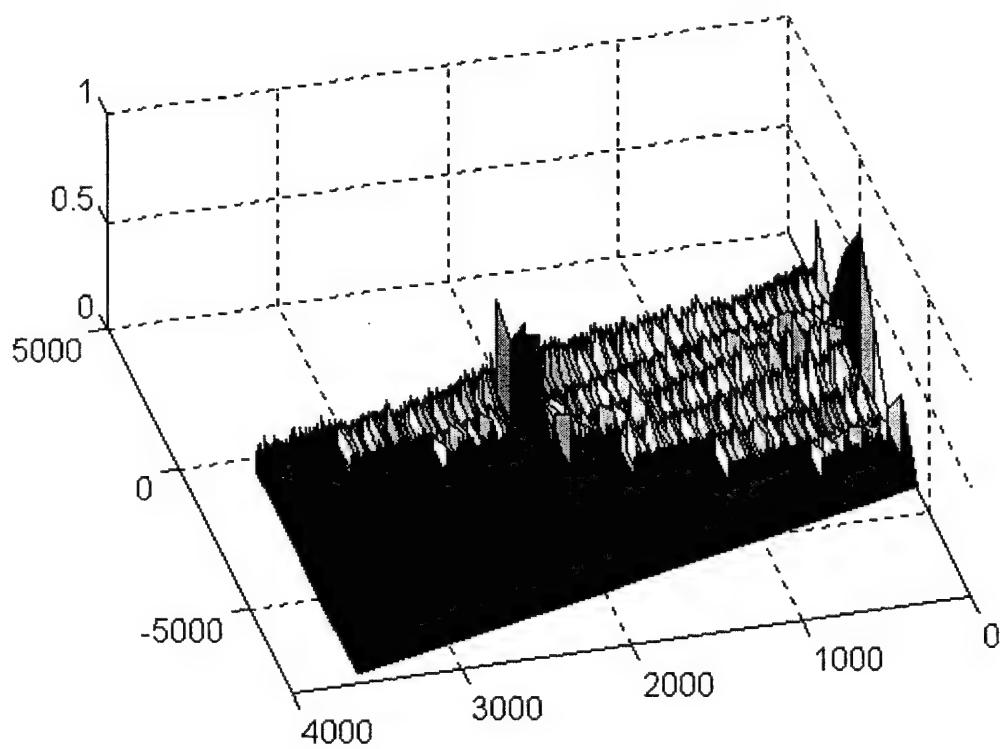
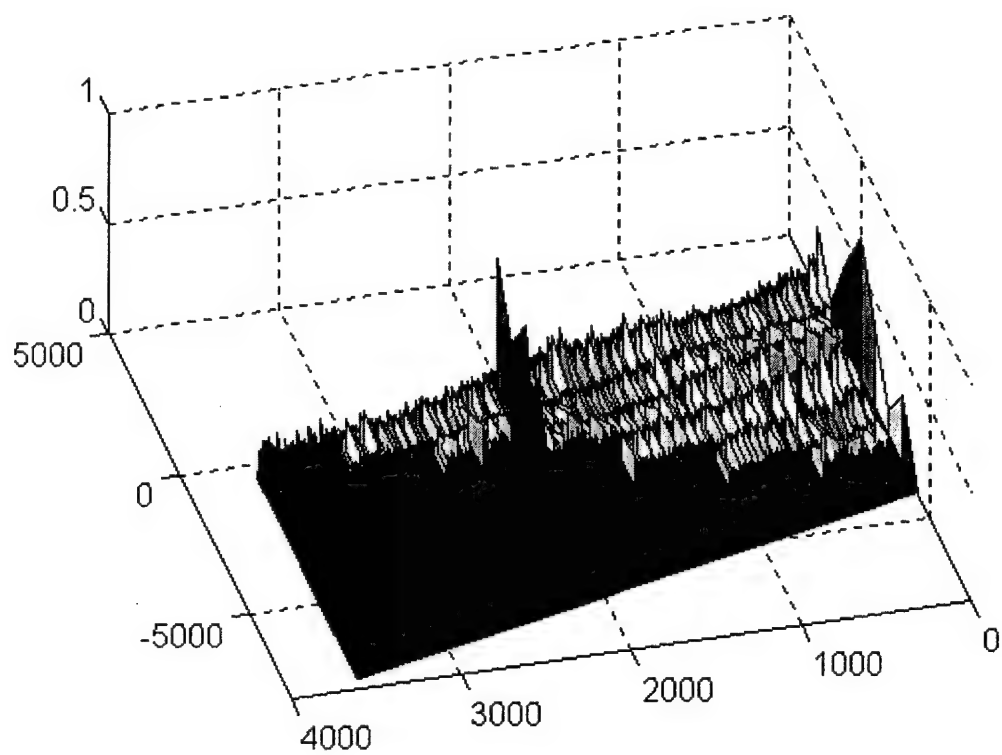


Figure B-32 - SCF for slave #2 (top) and slave #3 (bottom), time 409425

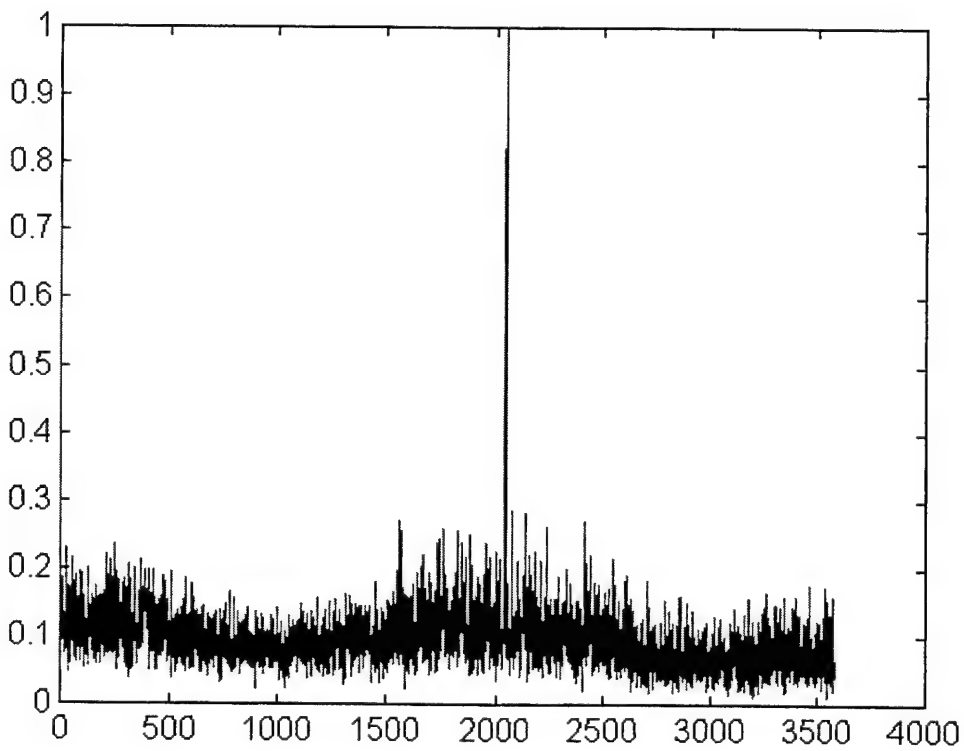
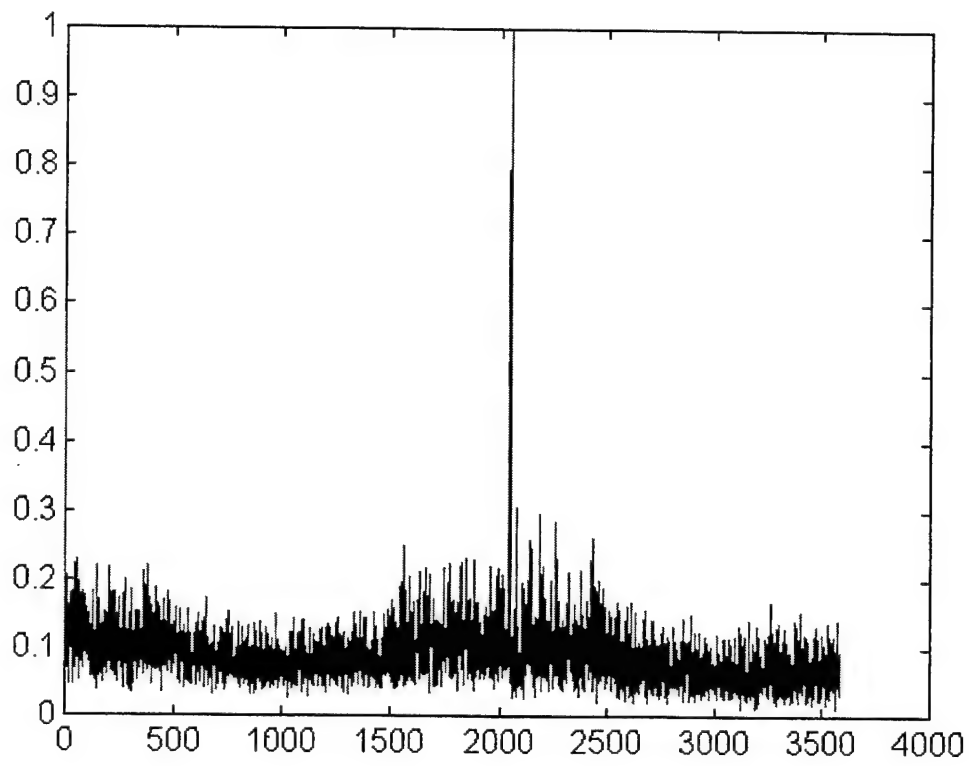


Figure B-33 - Cycle freq vs Max-magnitude of SCF for master (top) and slave #1 (bottom), time 409425

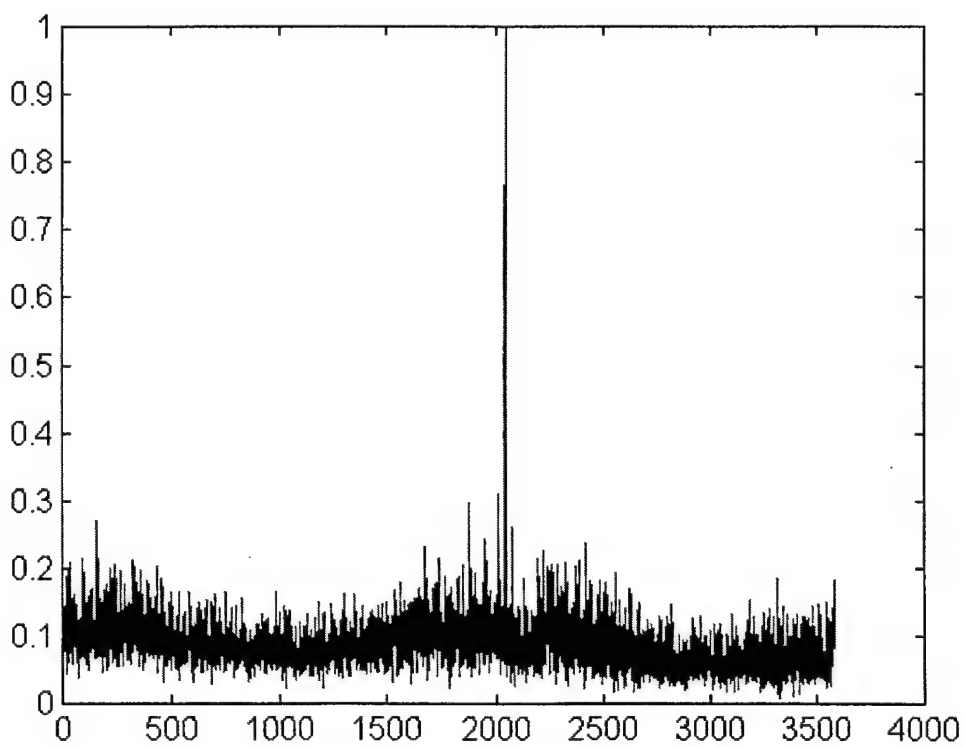
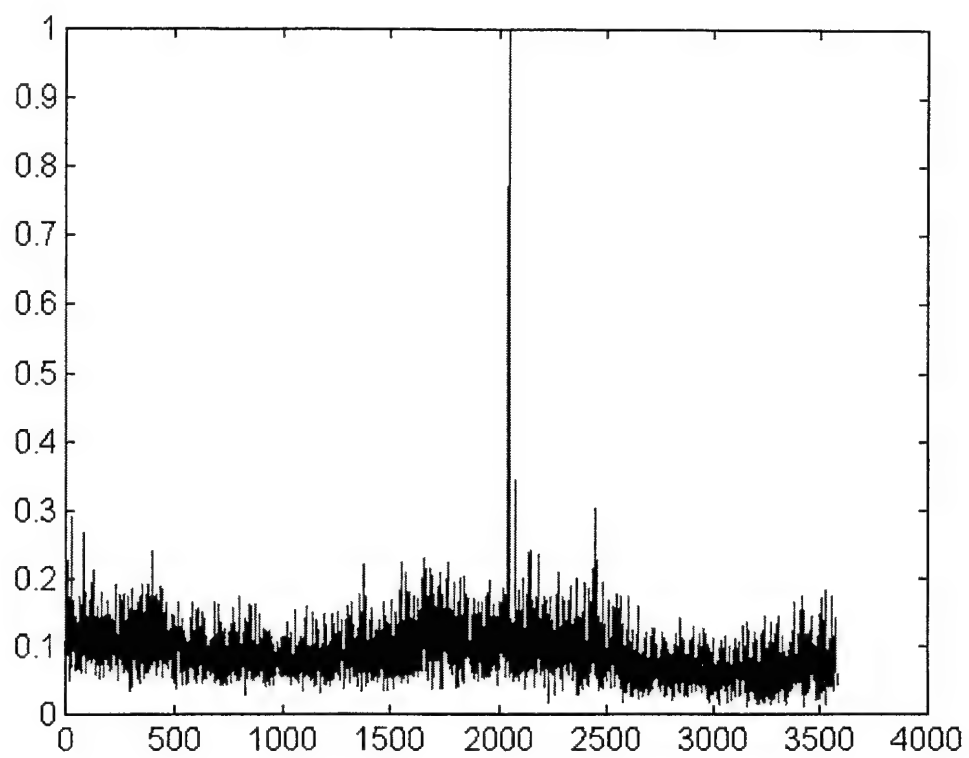


Figure B-34 - Cycle freq vs Max-magnitude of SCF for slave #2 (top) and slave #3 (bottom), time 409425

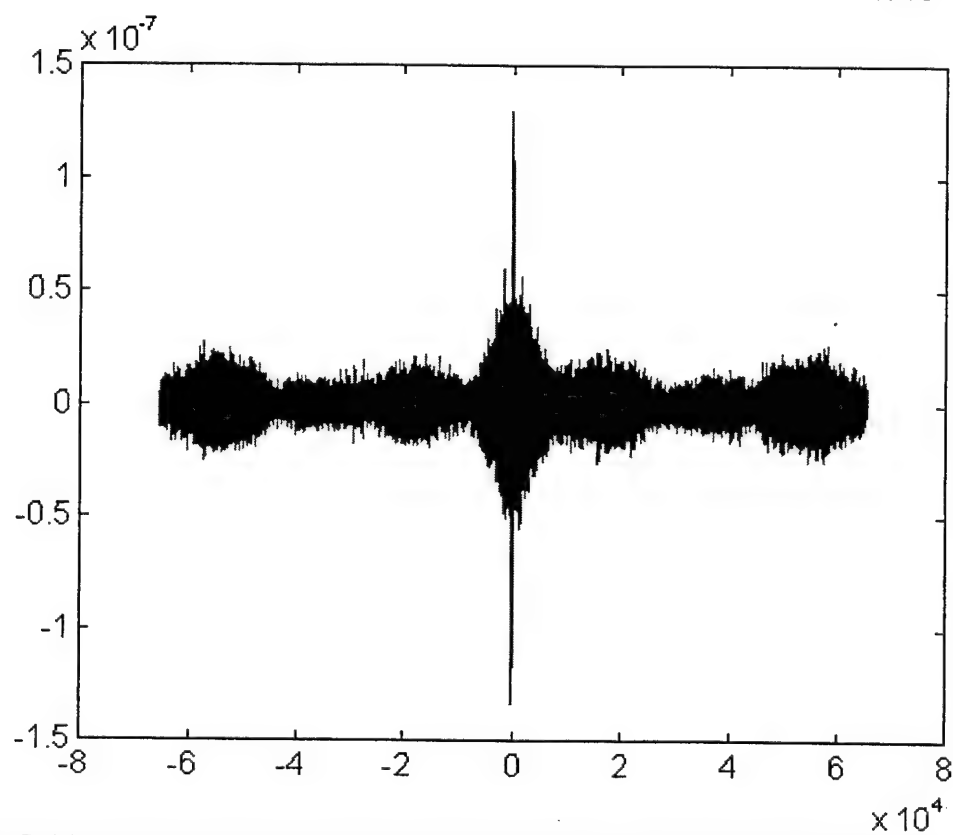
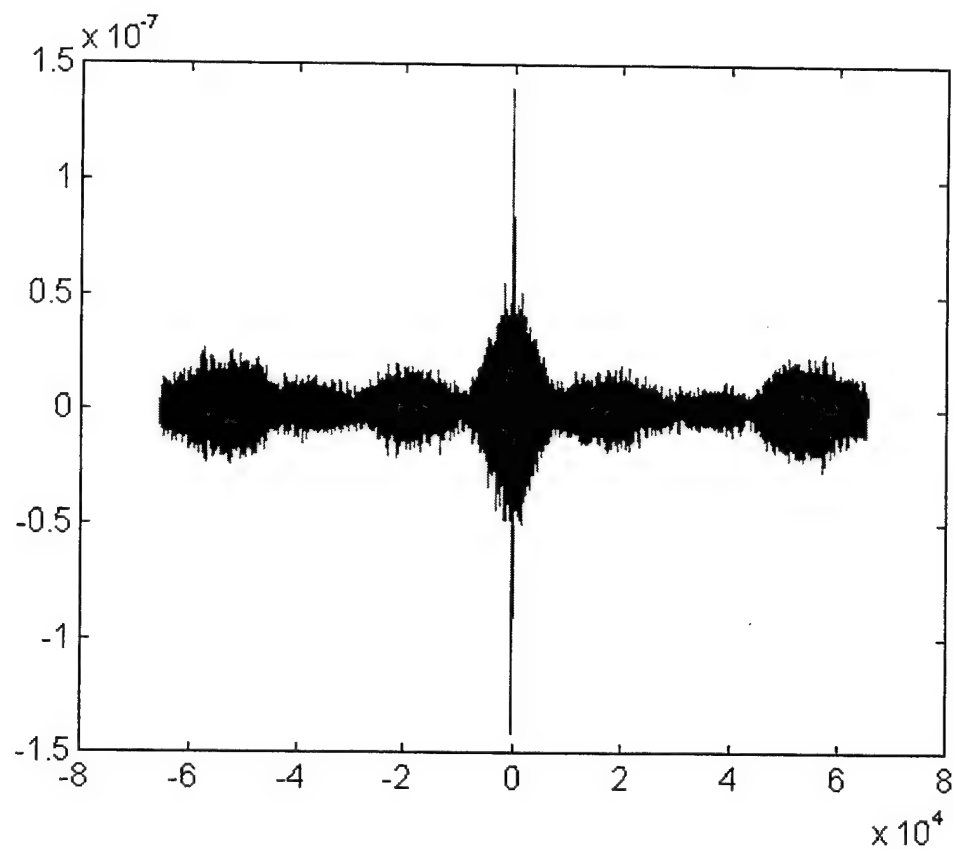


Figure B-35 - SPECCOA for master and slave #1 (top) and master and slave #2 (bottom), time 409425

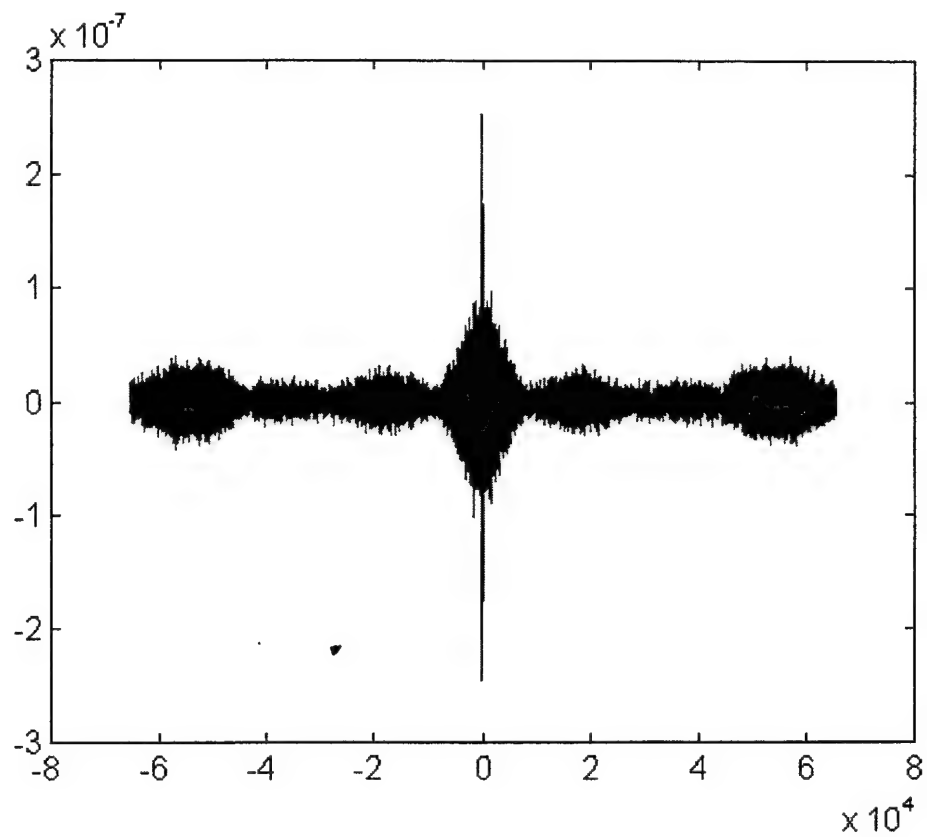


Figure B-36 - SPECCOA for master and slave #3, time 409425

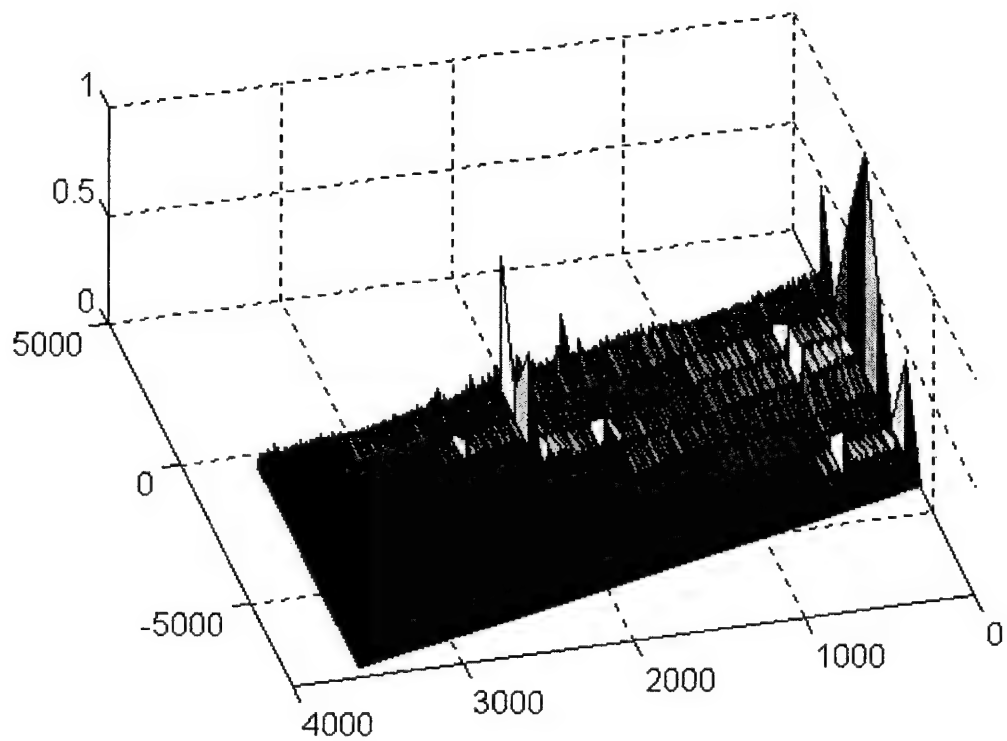
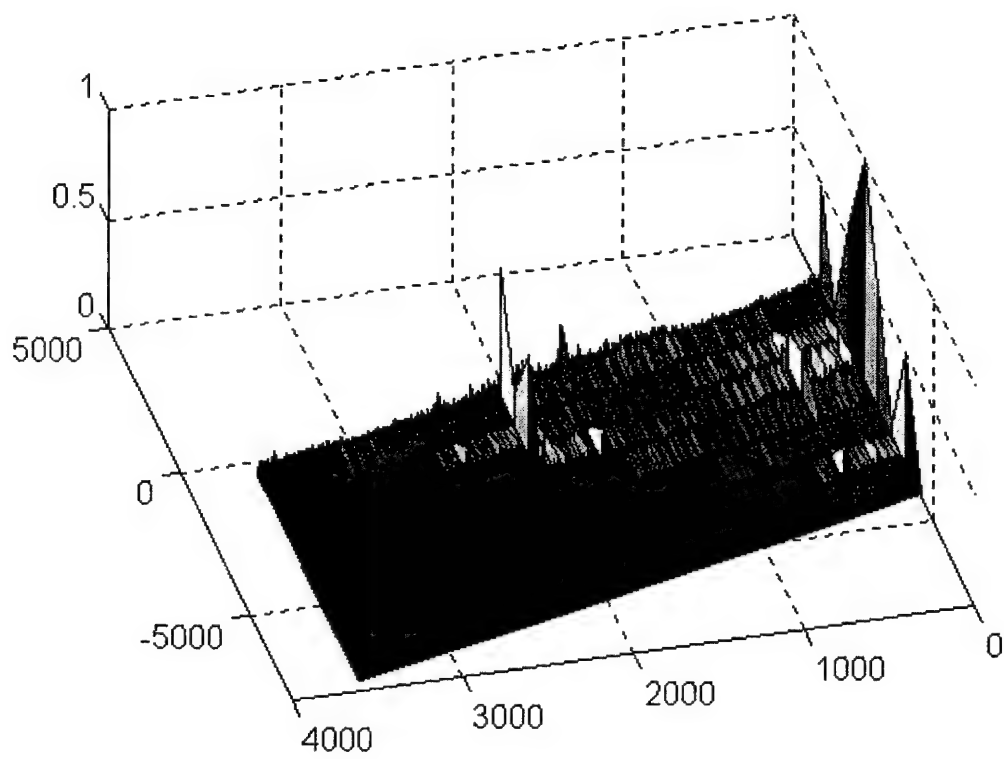


Figure B-37 - SCF for master (top) and slave #1 (bottom), time 409430

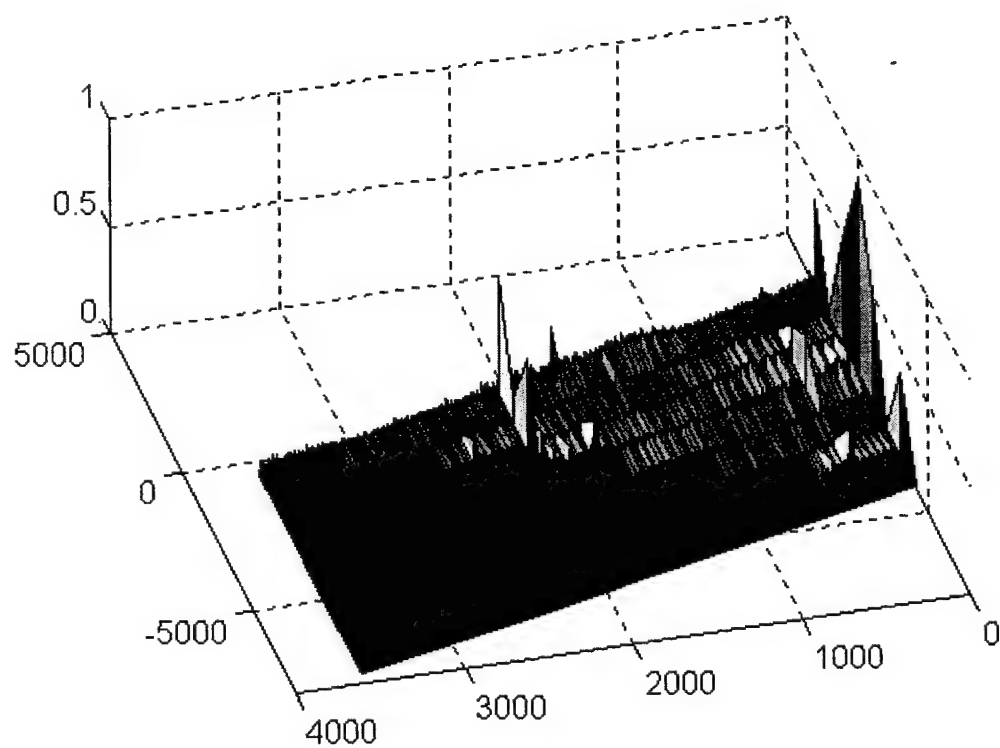
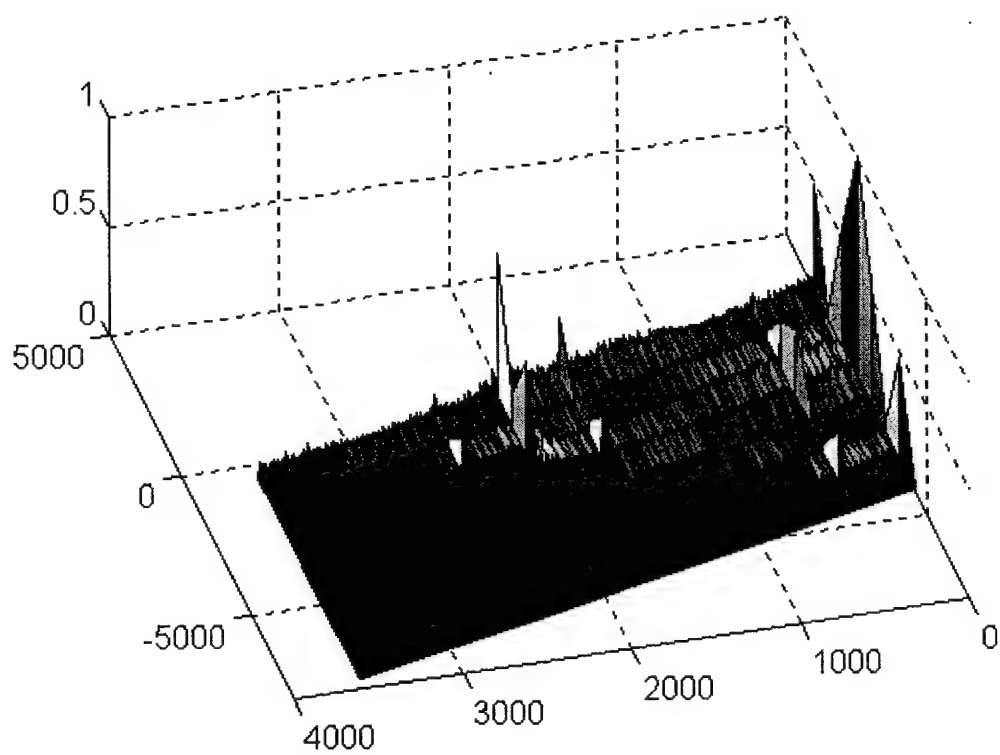


Figure B-38 - SCF for slave #2 (top) and slave #3 (bottom), time 409430

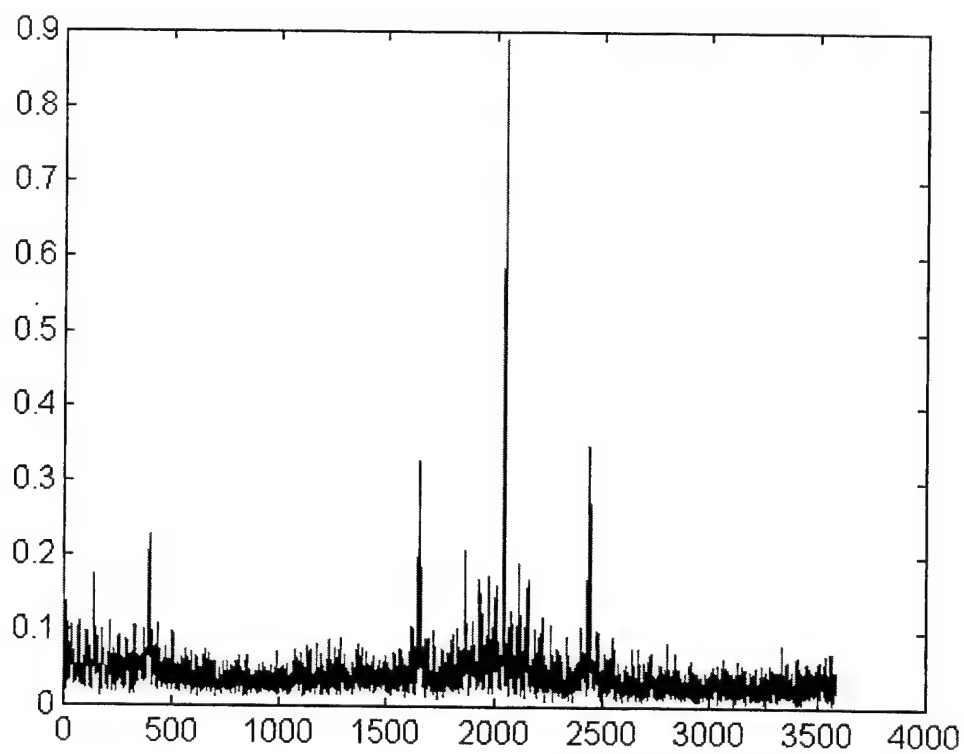
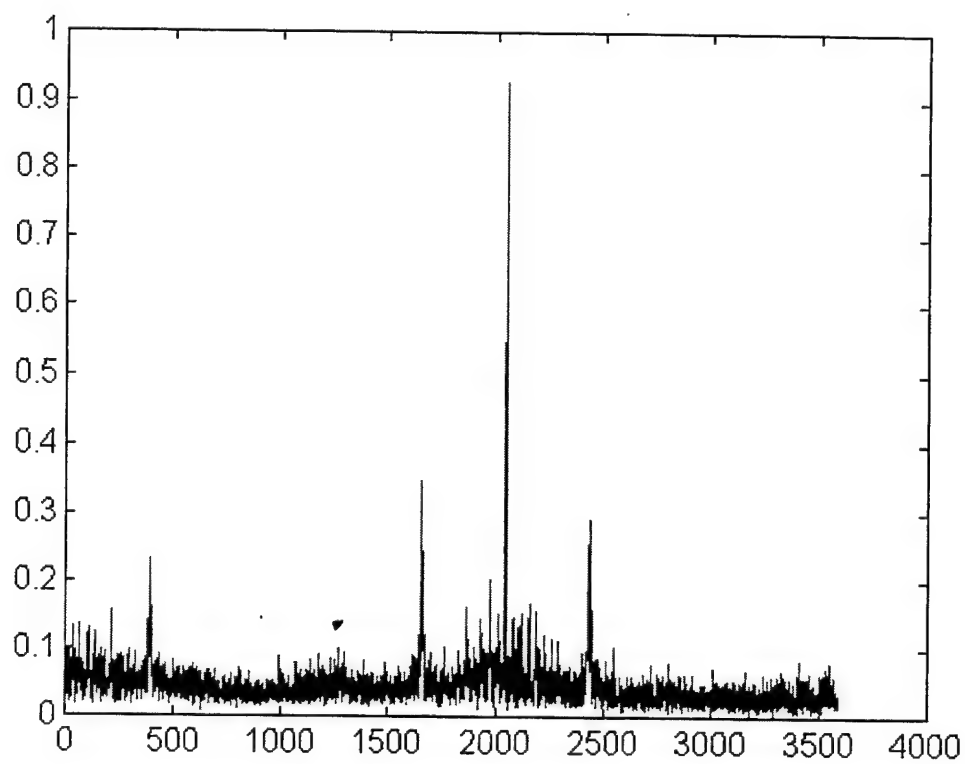


Figure B-39 - Cycle freq vs Max-magnitude of SCF for master (top) and slave #1 (bottom), time 409430

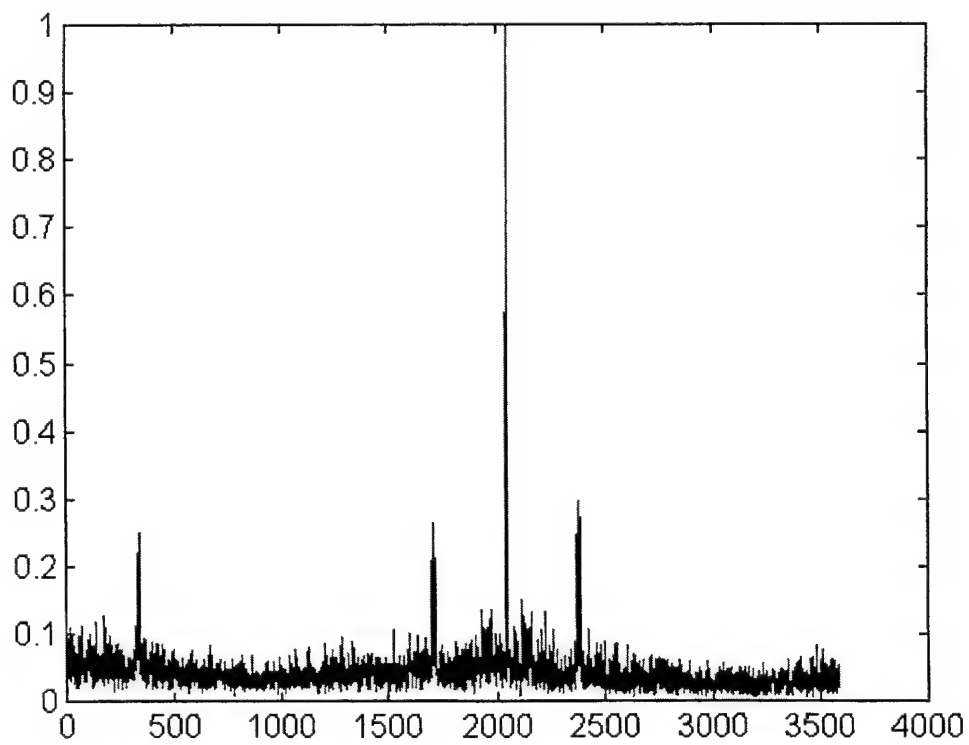
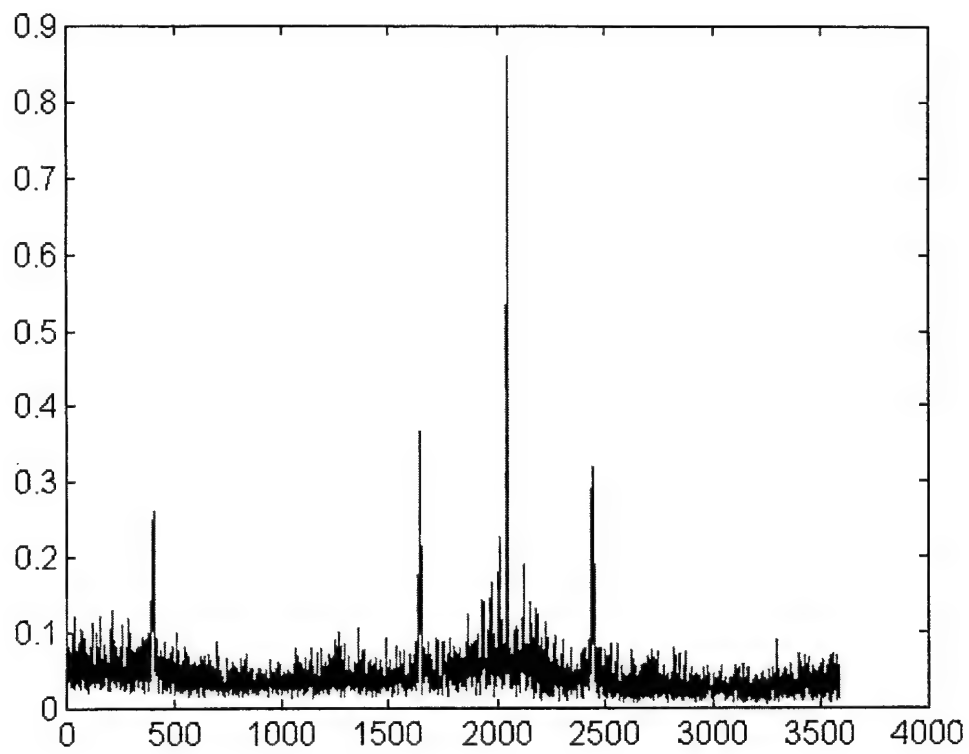


Figure B-40 - Cycle freq vs Max-magnitude of SCF for slave #2 (top) and slave #3 (bottom), time 409430

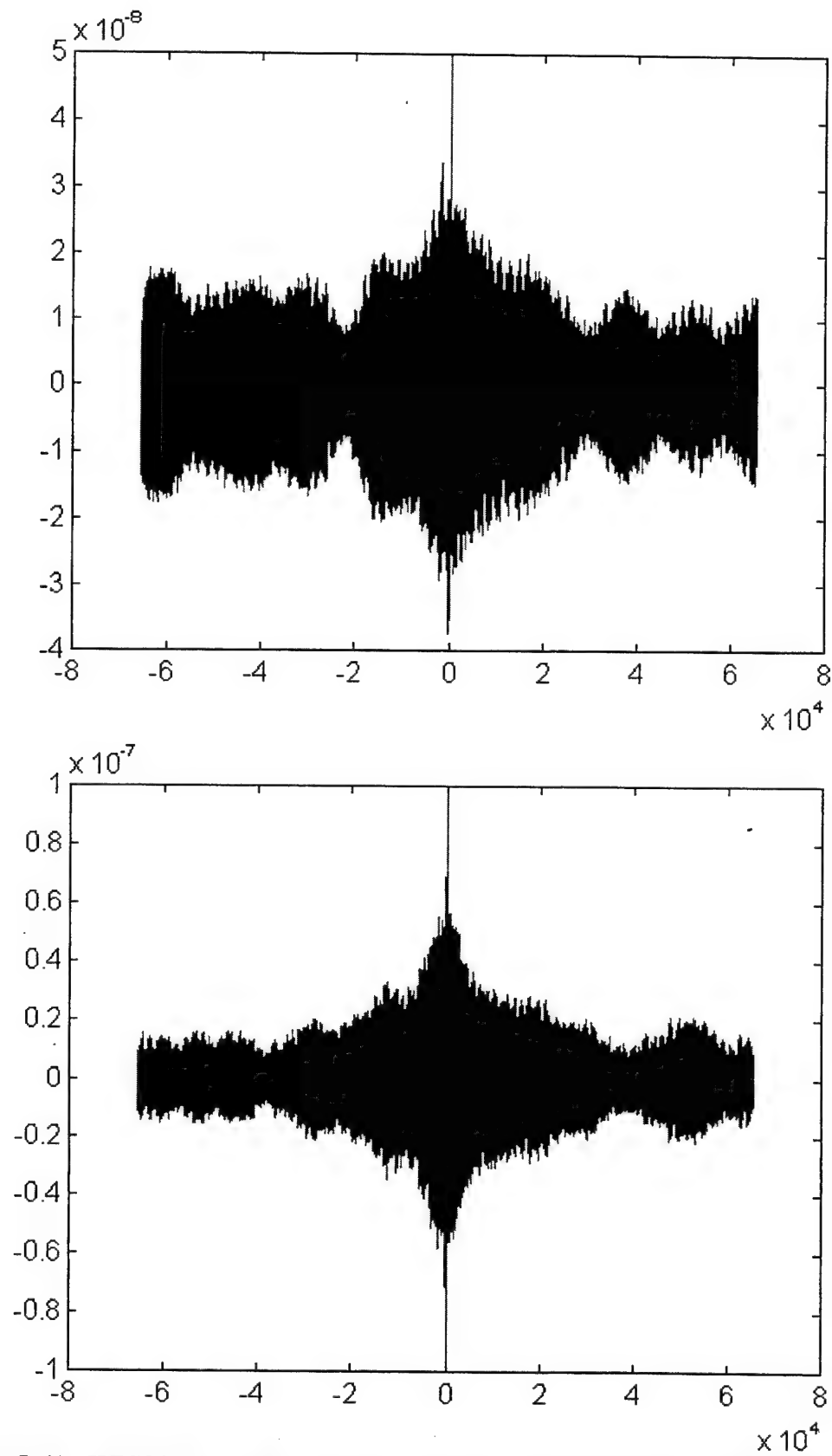


Figure B-41 - SPECCOA for master and slave #1 (top) and master and slave #2 (bottom), time 409430

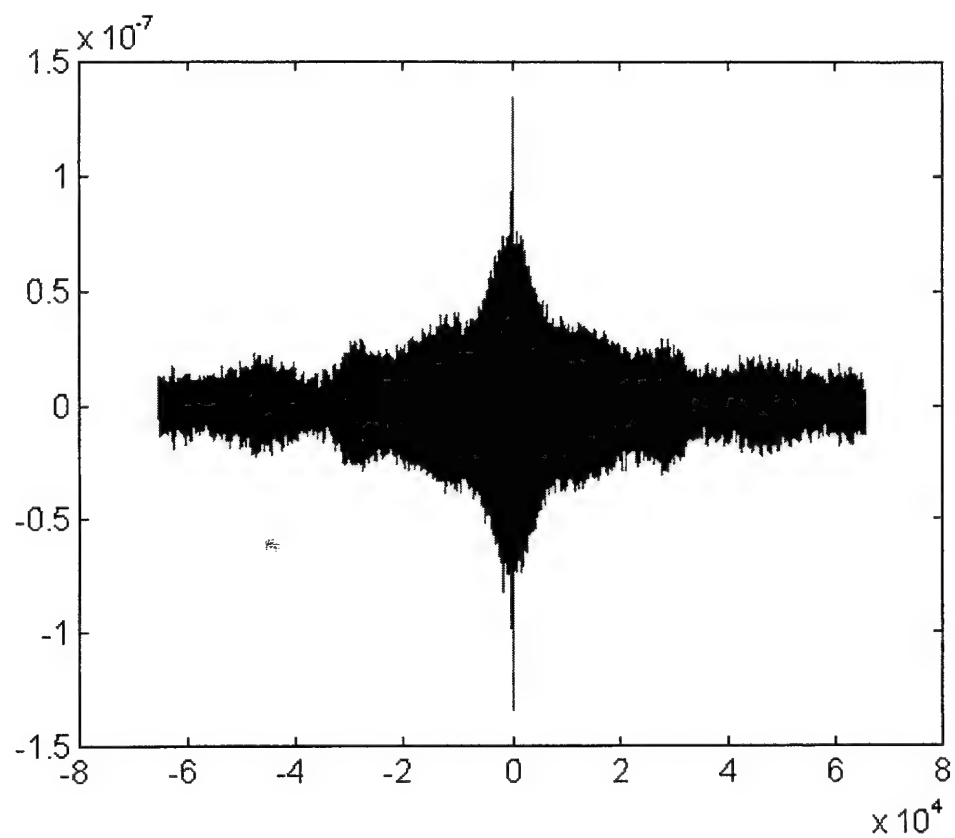


Figure B-42 - SPECCOA for master and slave #3, time 409430

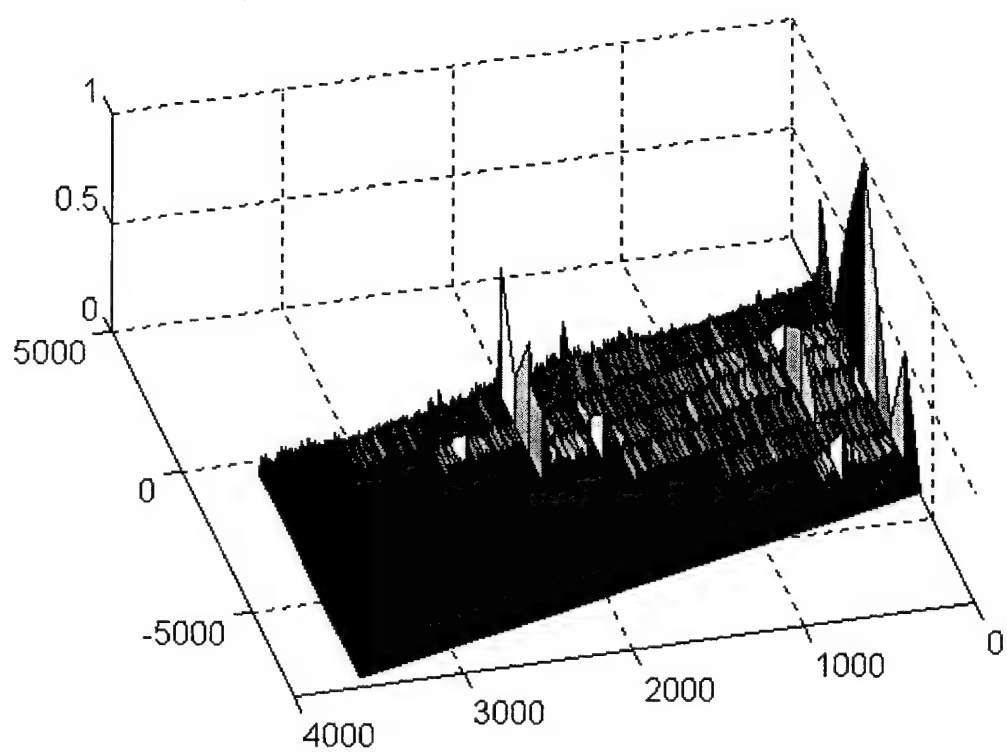
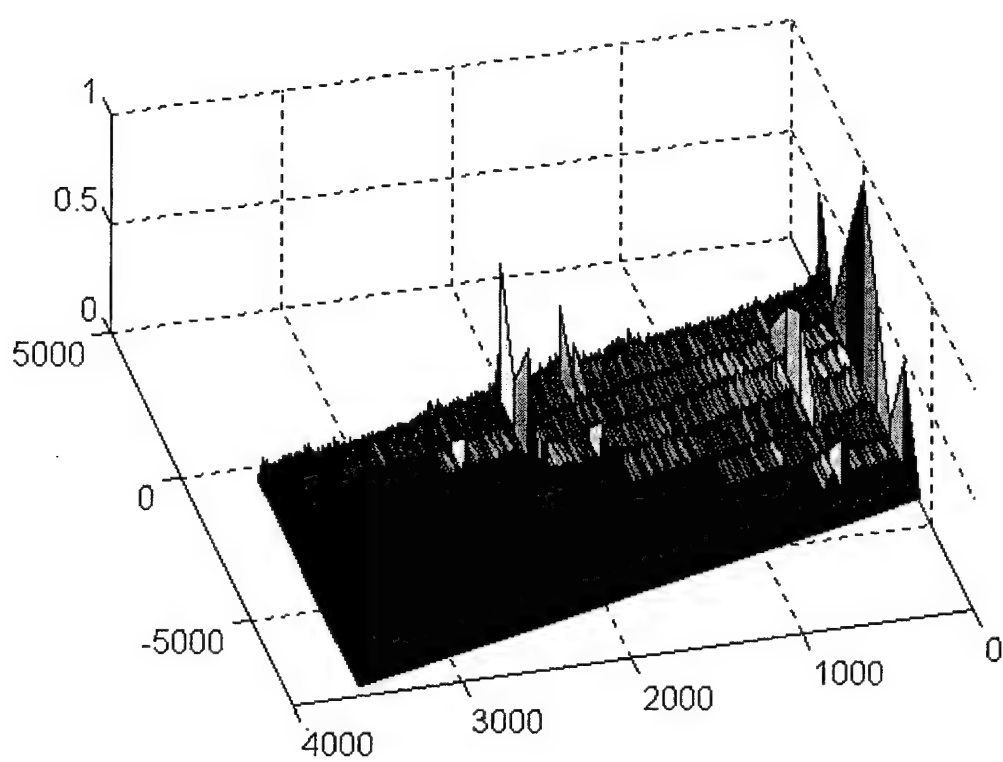


Figure B-43 - SCF for master (top) and slave #1 (bottom), time 409435

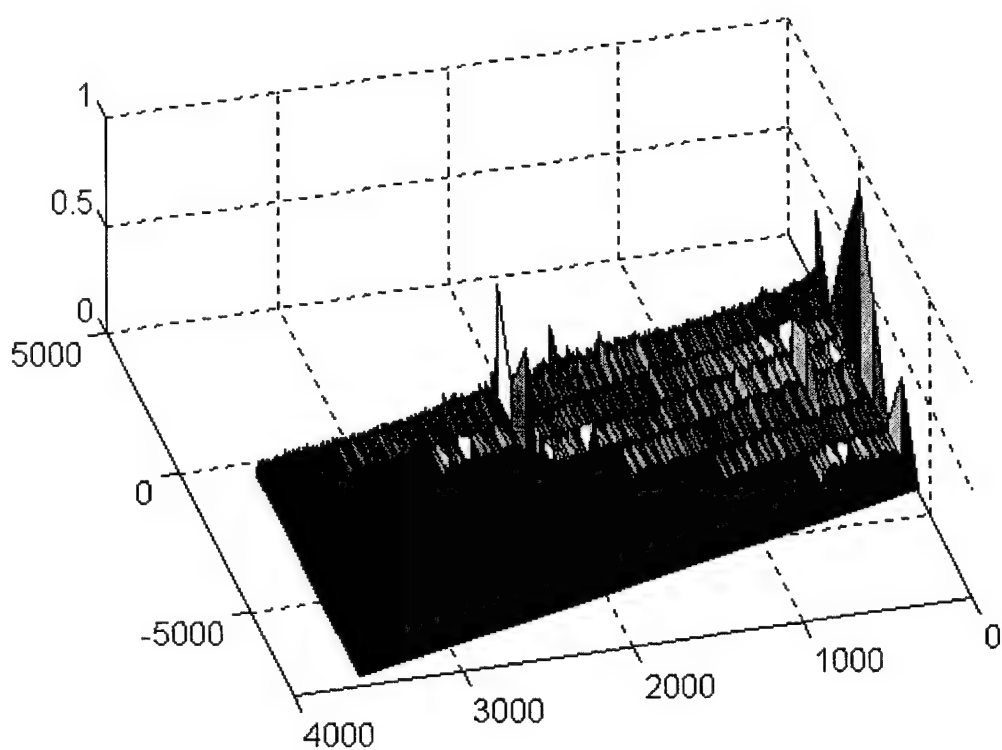
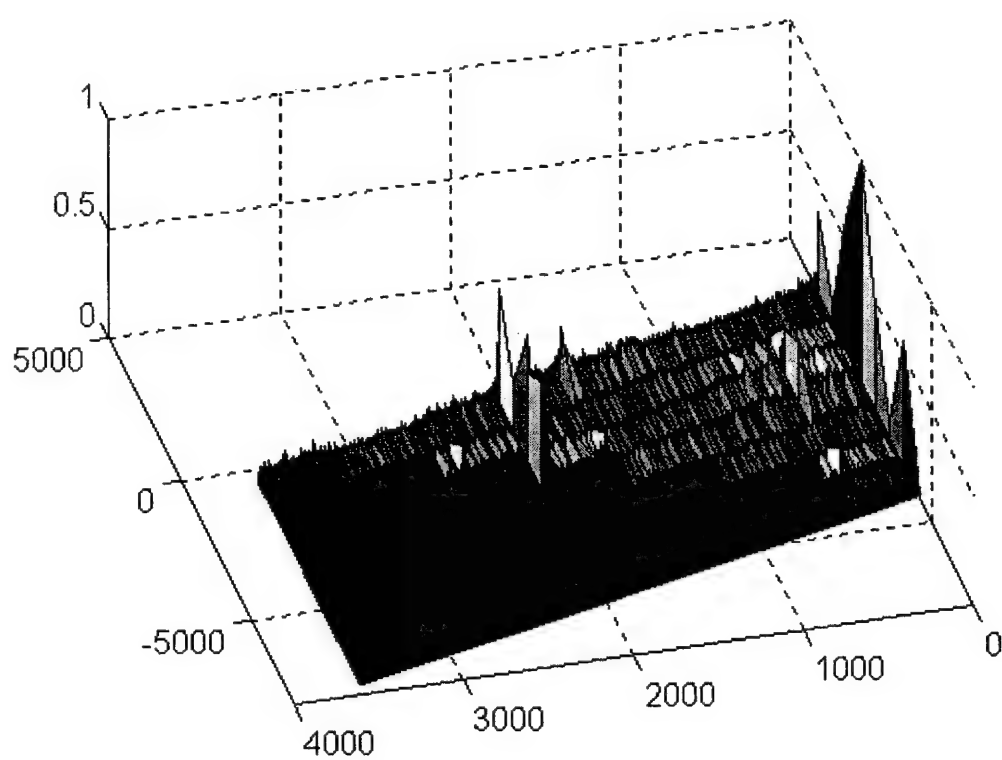


Figure B-44 - SCF for slave #2 (top) and slave #3 (bottom), time 409435

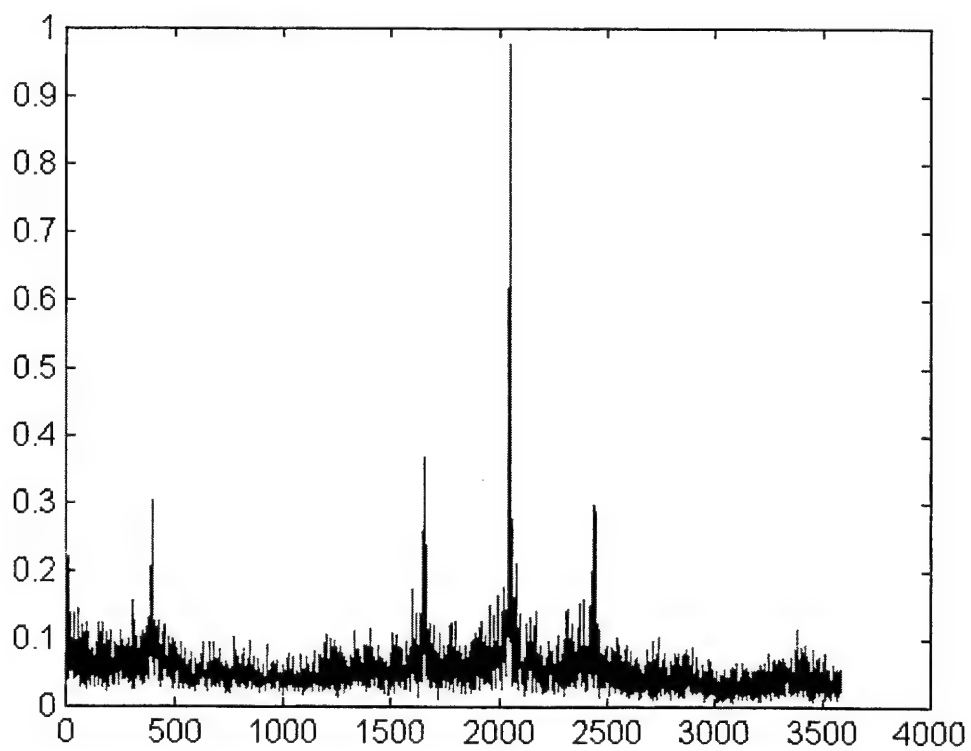
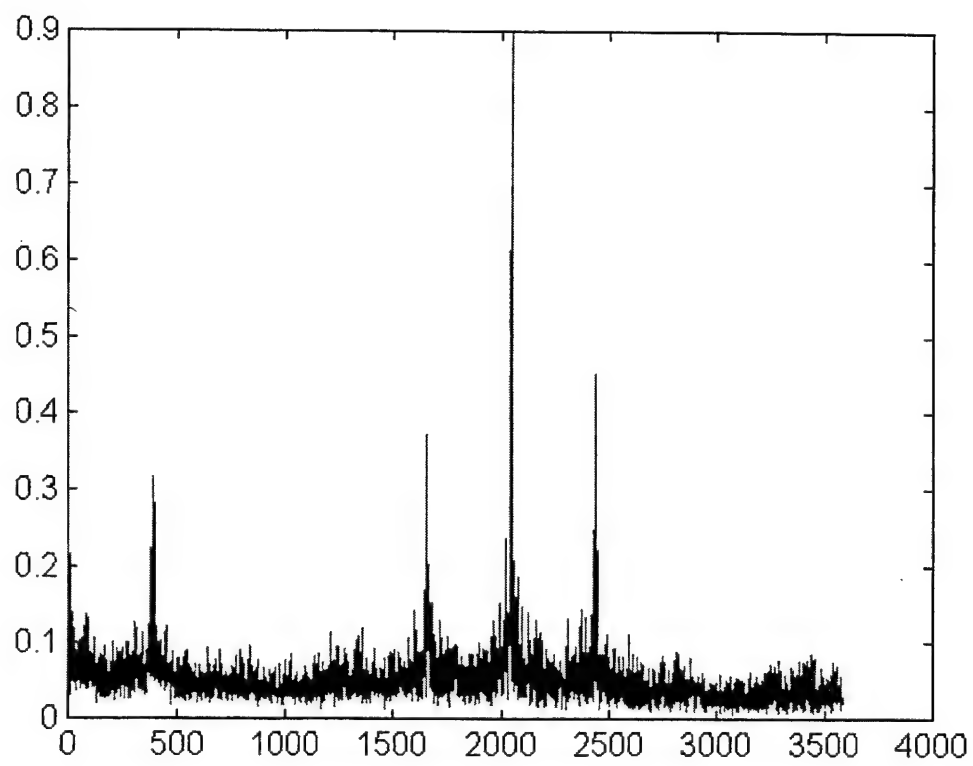


Figure B-45 - Cycle freq vs Max-magnitude of SCF for master (top) and slave #1 (bottom), time 409435

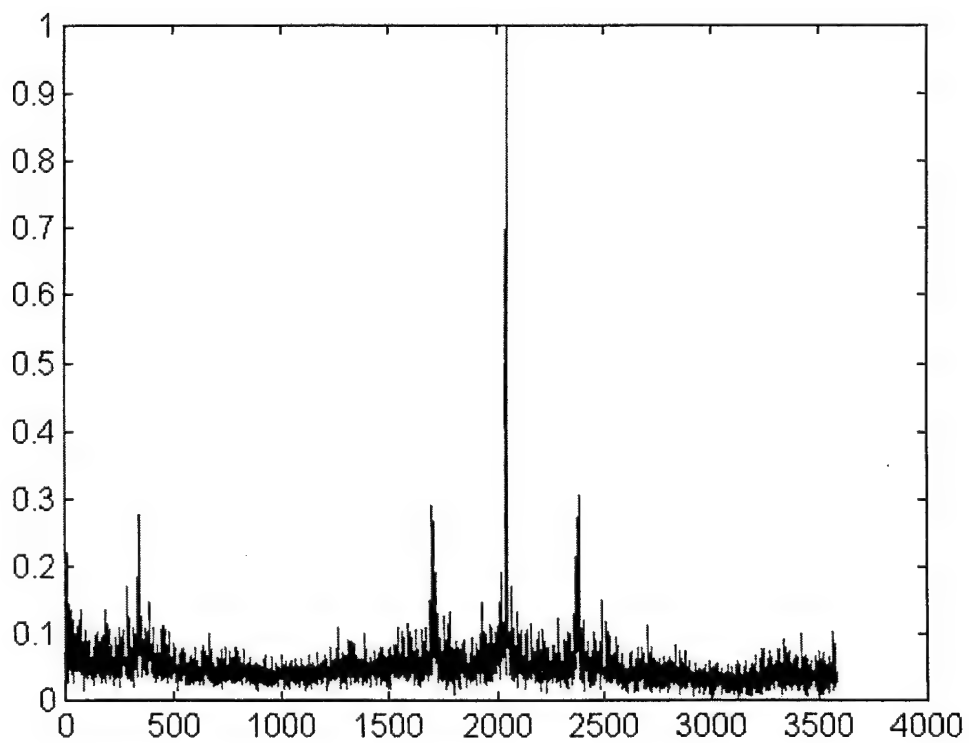
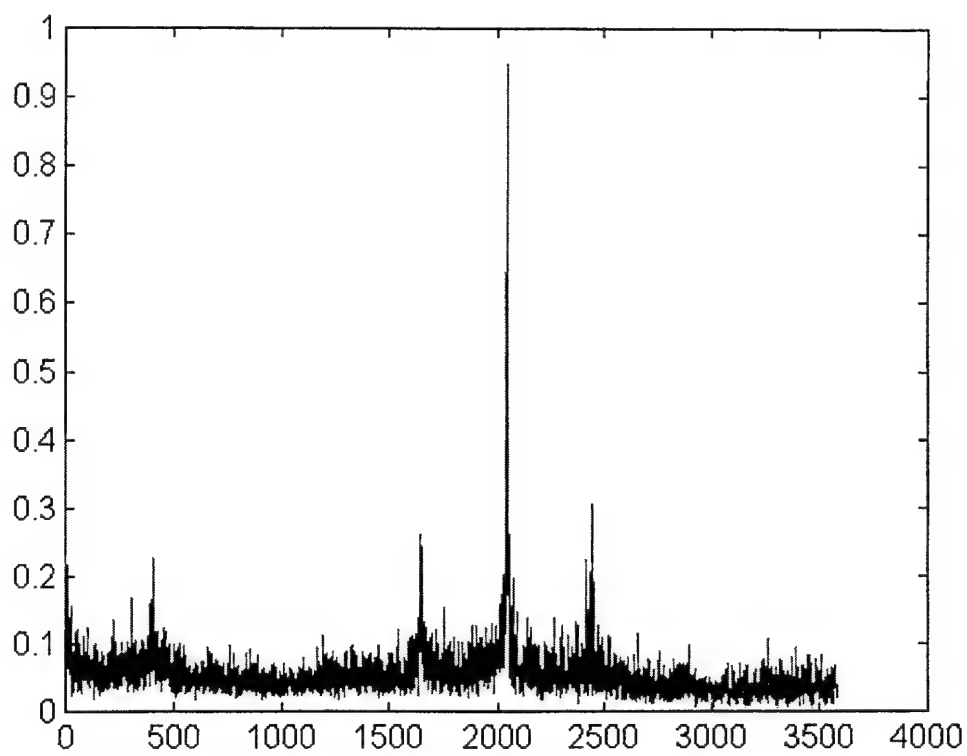


Figure B-46 - Cycle freq vs Max-magnitude of SCF for slave #2 (top) and slave #3 (bottom), time 409435

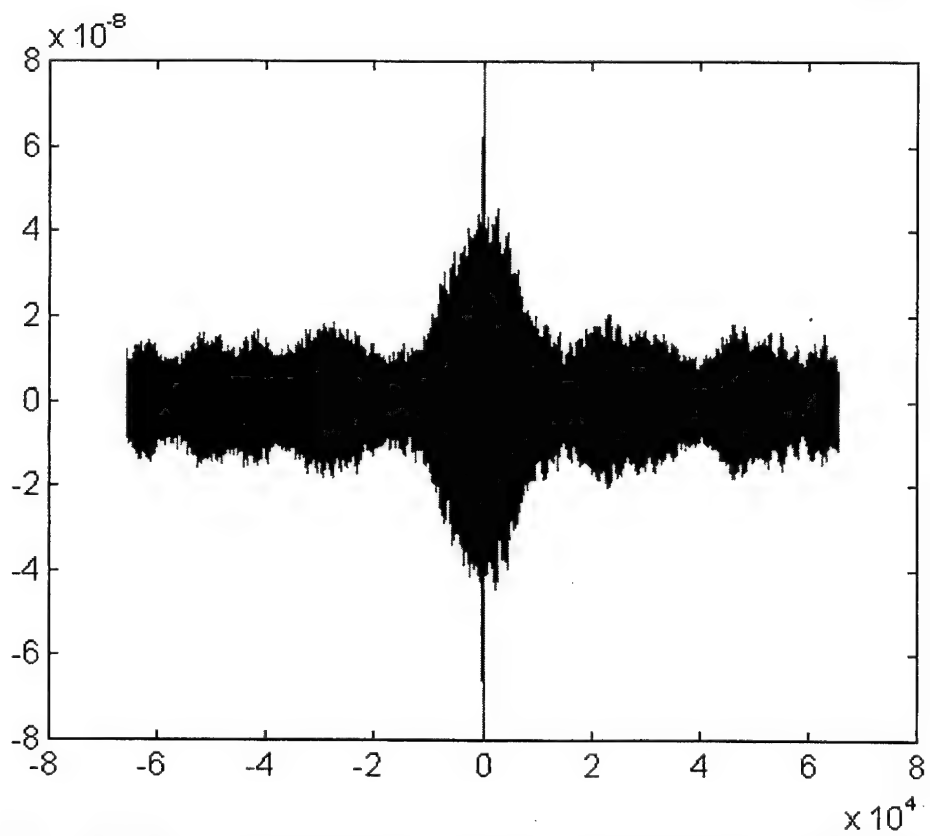
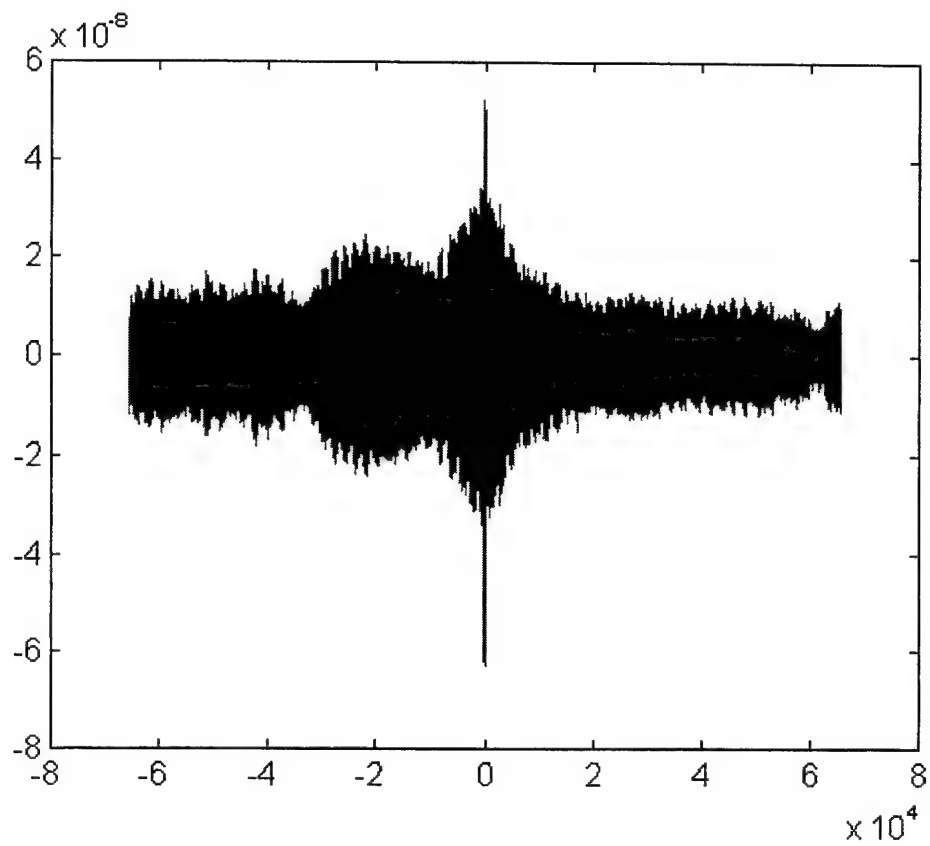


Figure B-47 - SPECCOA for master and slave #1 (top) and master and slave #2 (bottom), time 409435

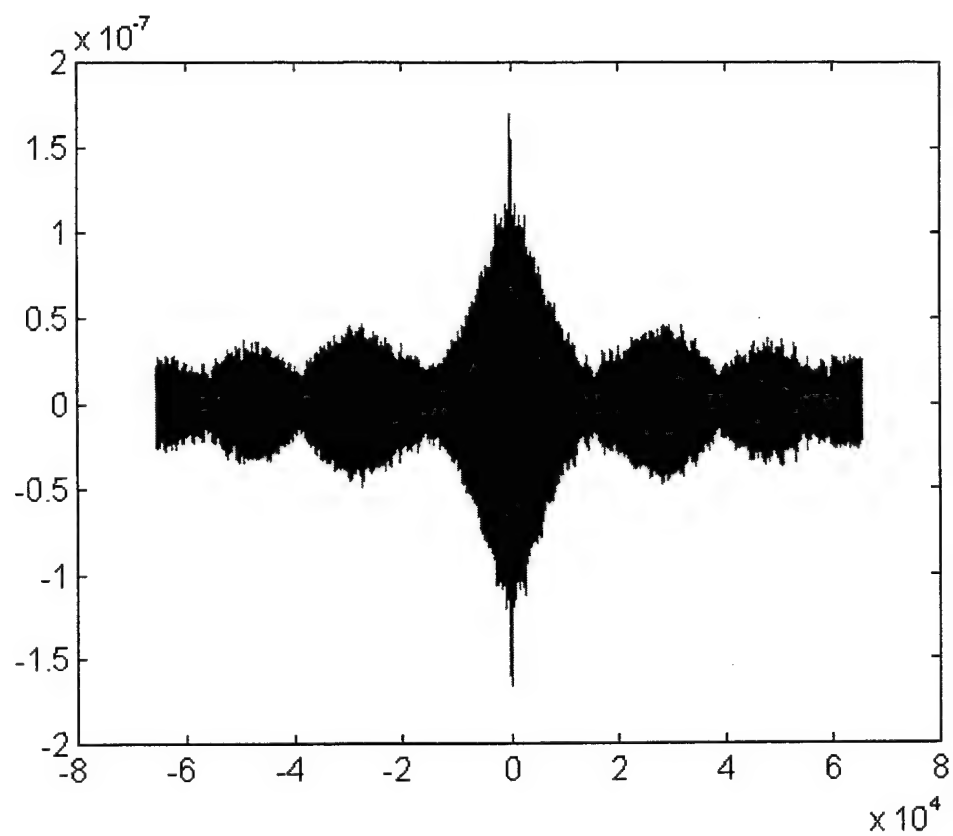


Figure B-48 - SPECCOA for master and slave #3, time 409435

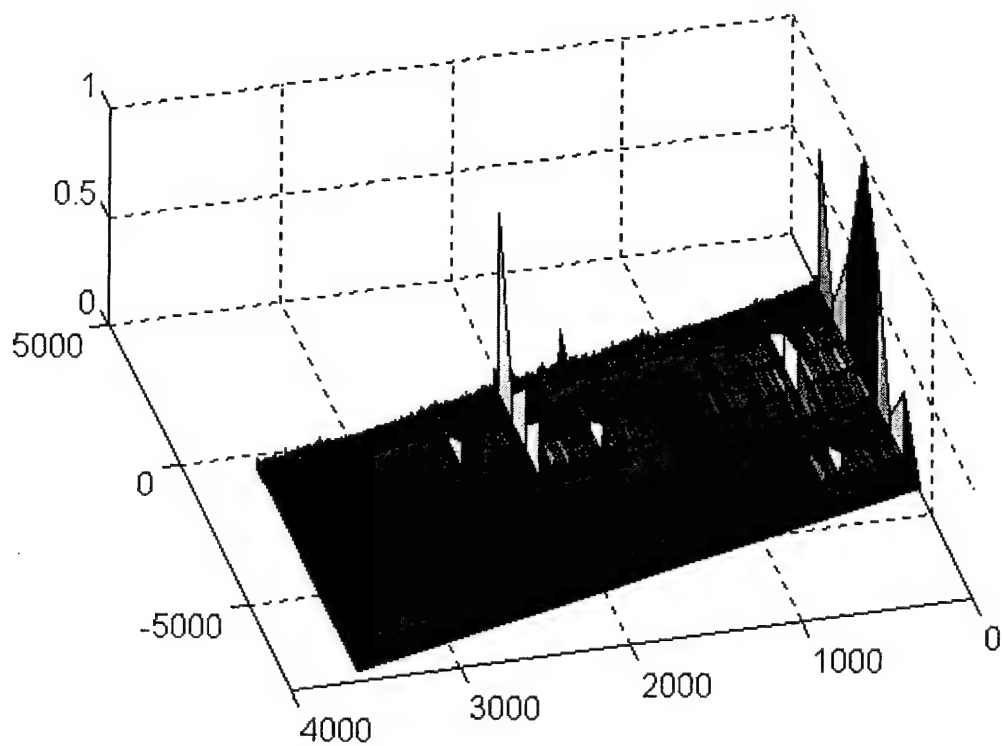
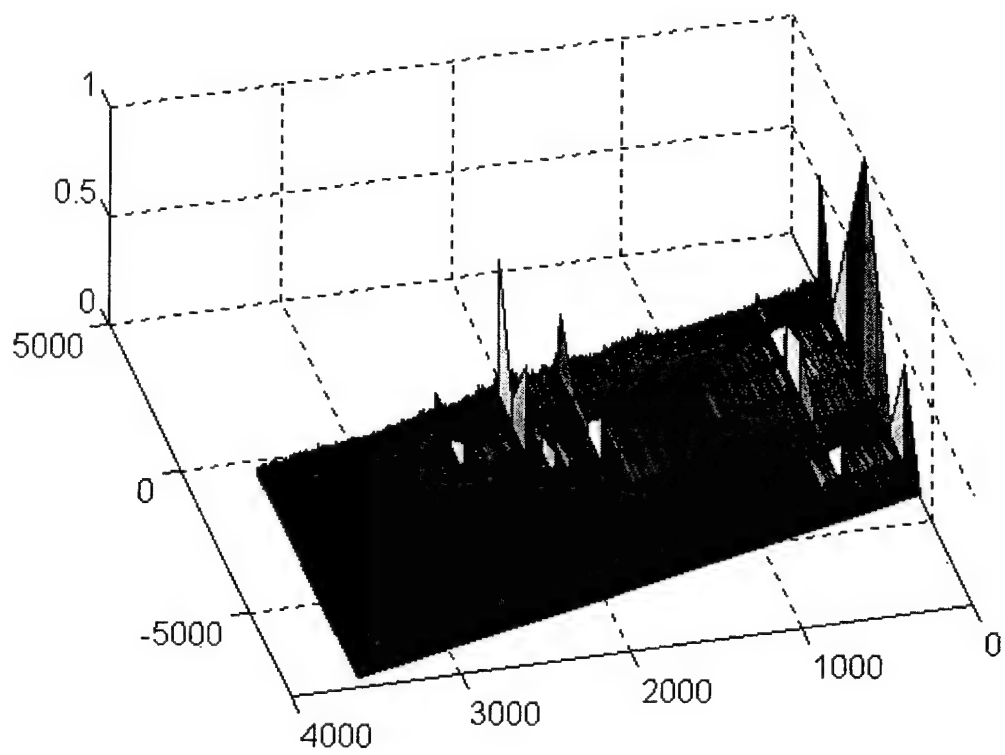


Figure B-49 - SCF for master (top) and slave #1 (bottom), time 409455

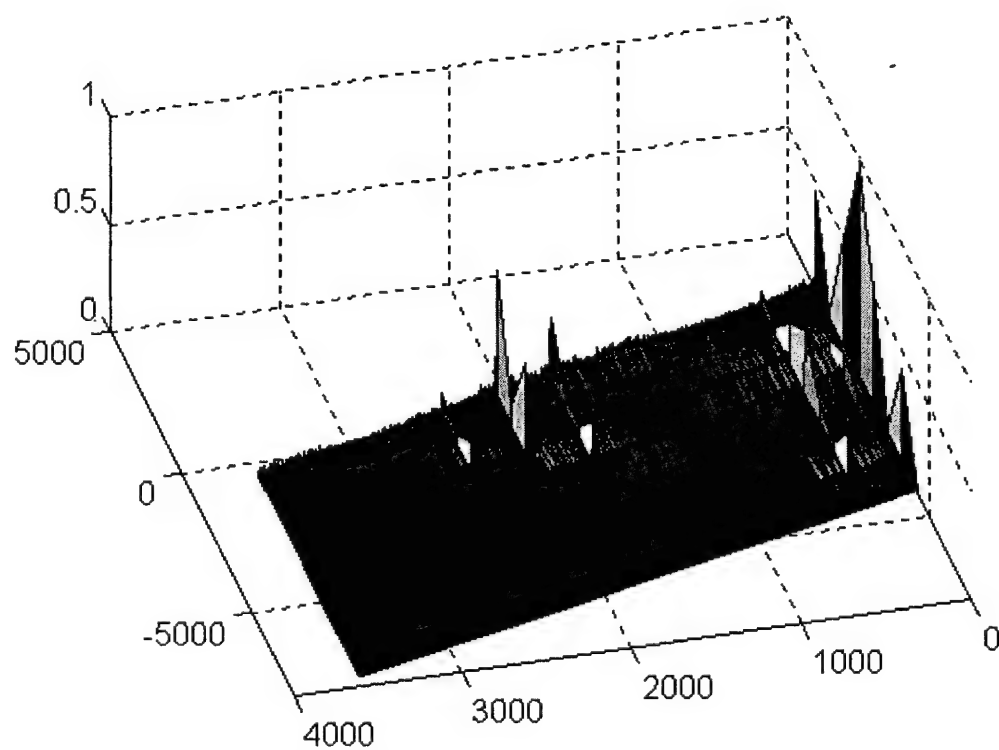
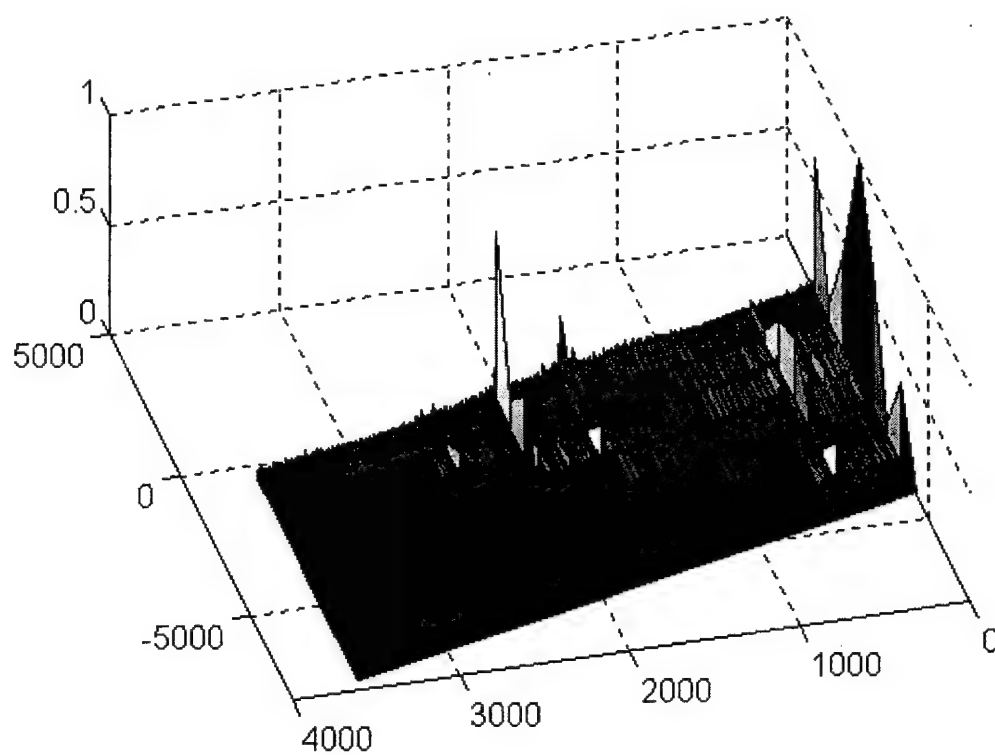


Figure B-50 - SCF for slave #2 (top) and slave #3 (bottom), time 409455

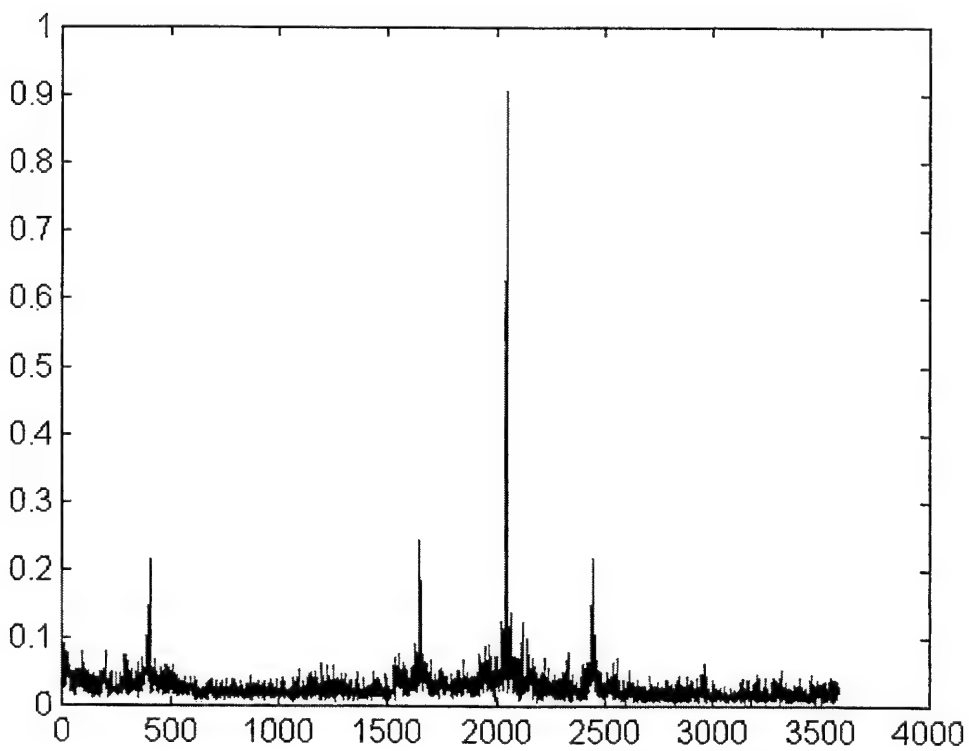
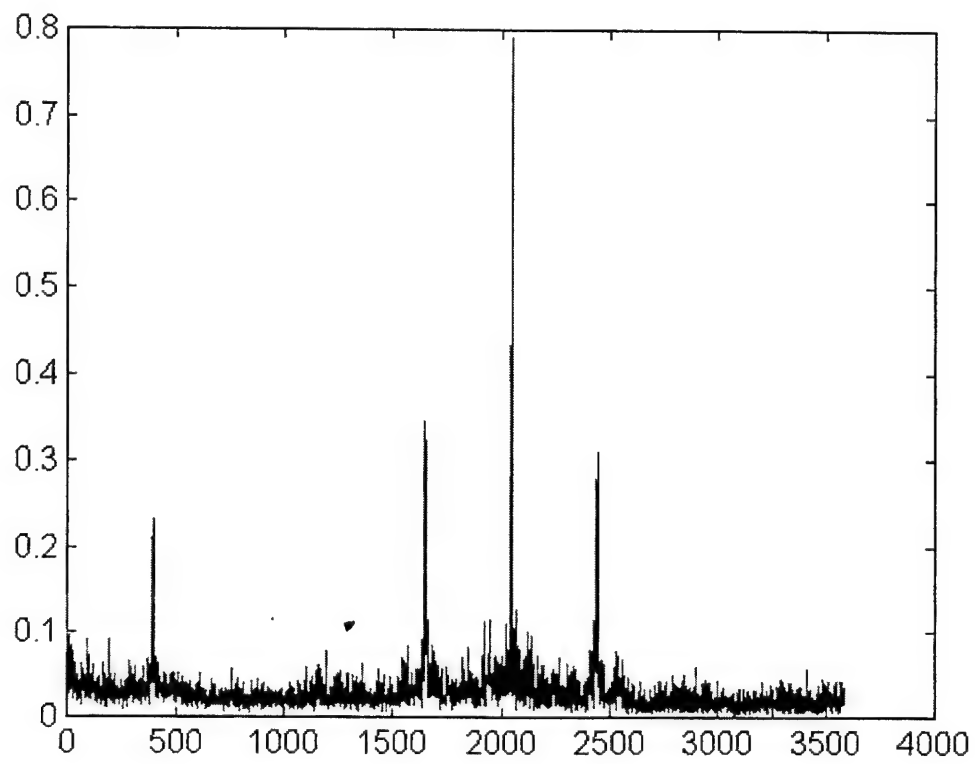


Figure B-51 - Cycle freq vs Max-magnitude of SCF for master (top) and slave #1 (bottom), time 409455

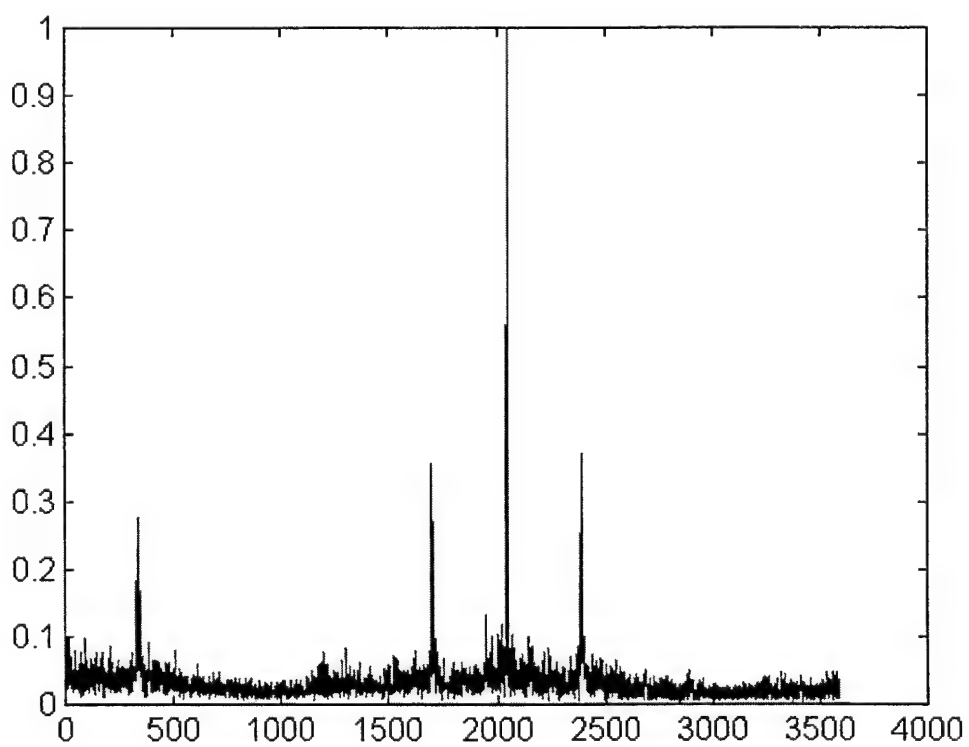
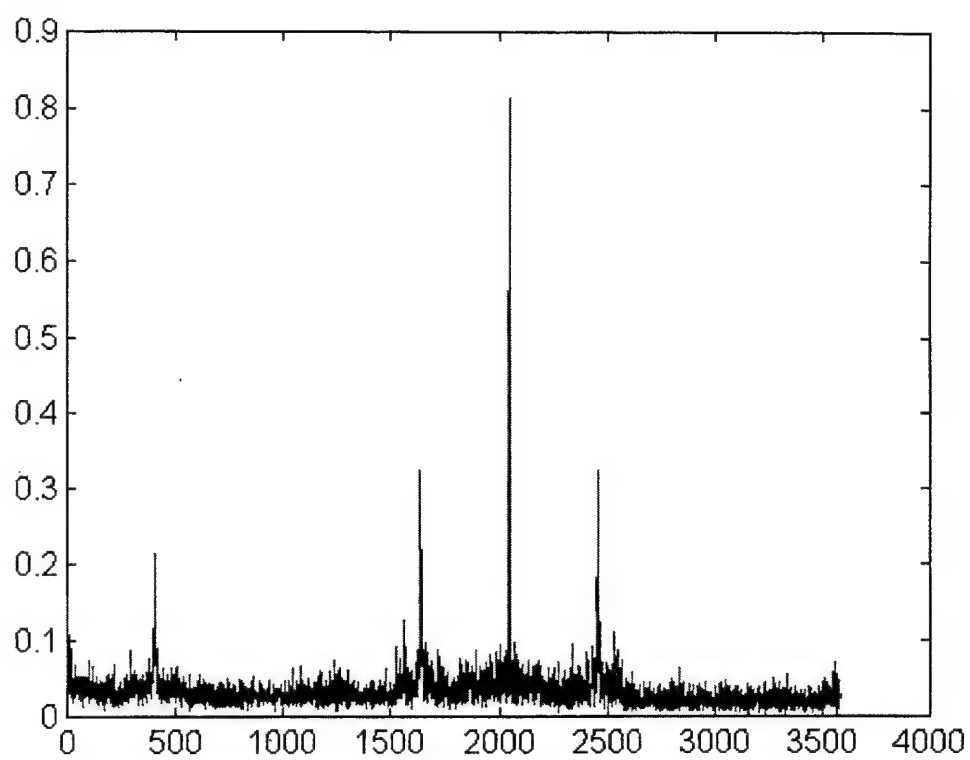


Figure B-52 - Cycle freq vs Max-magnitude of SCF for slave #2 (top) and slave #3 (bottom), time 409455

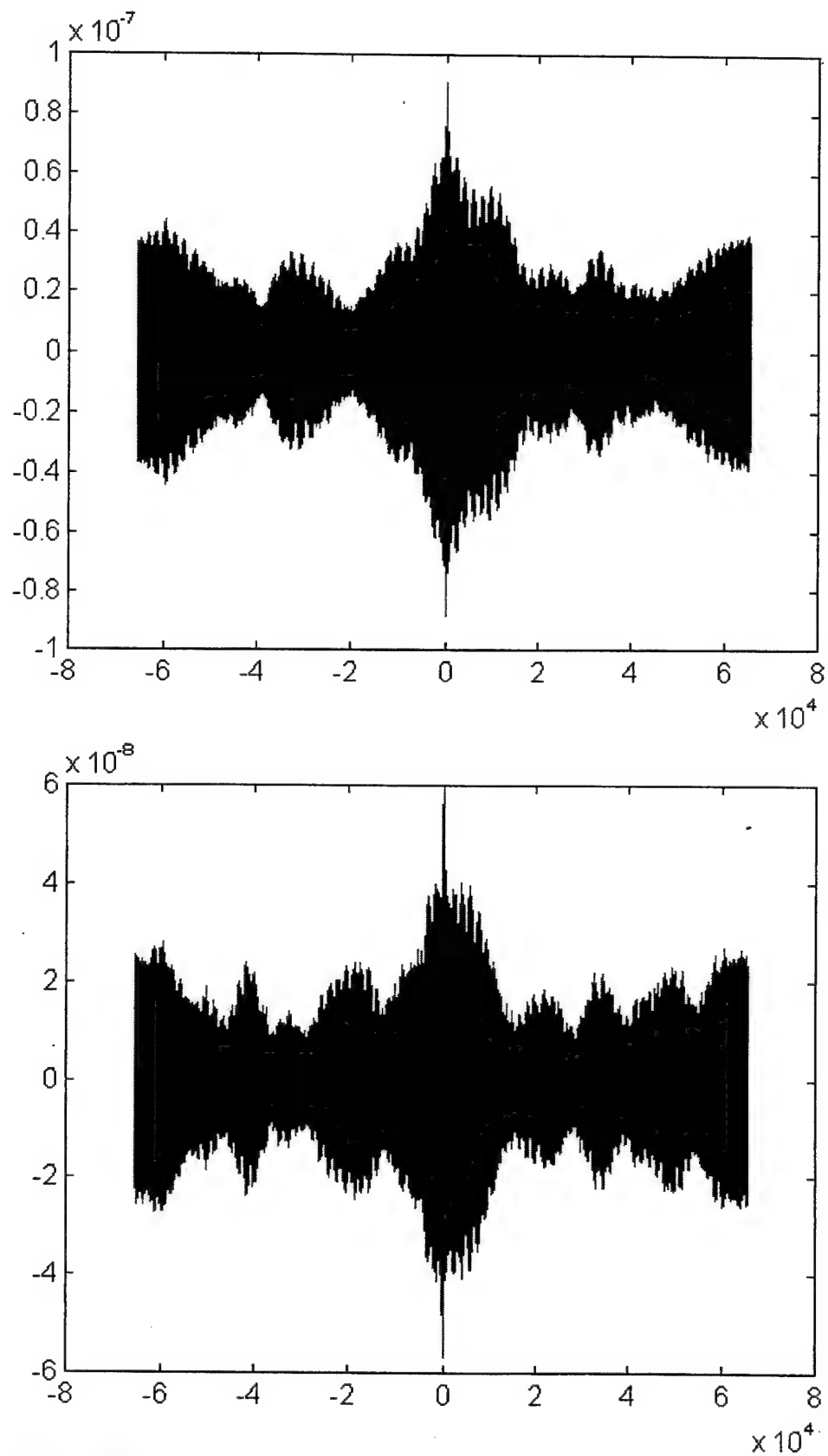


Figure B-53 - SPECCOA for master and slave #1 (top) and master and slave #2 (bottom), time 409455

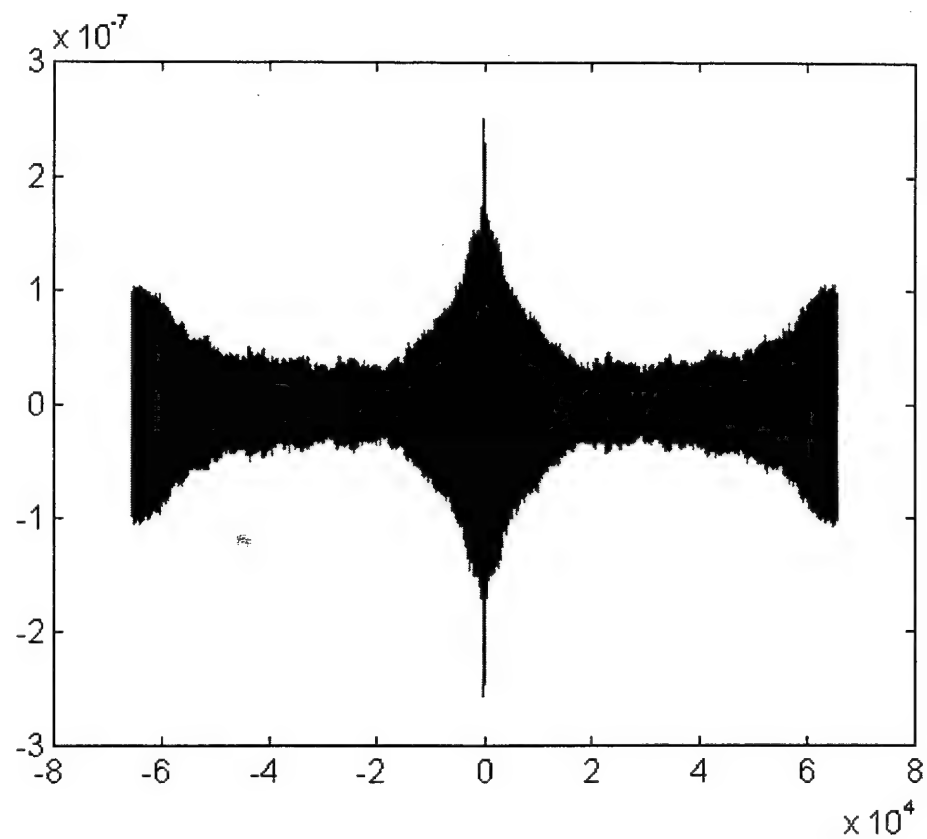


Figure B-54 - SPECCOA for master and slave #3, time 409455

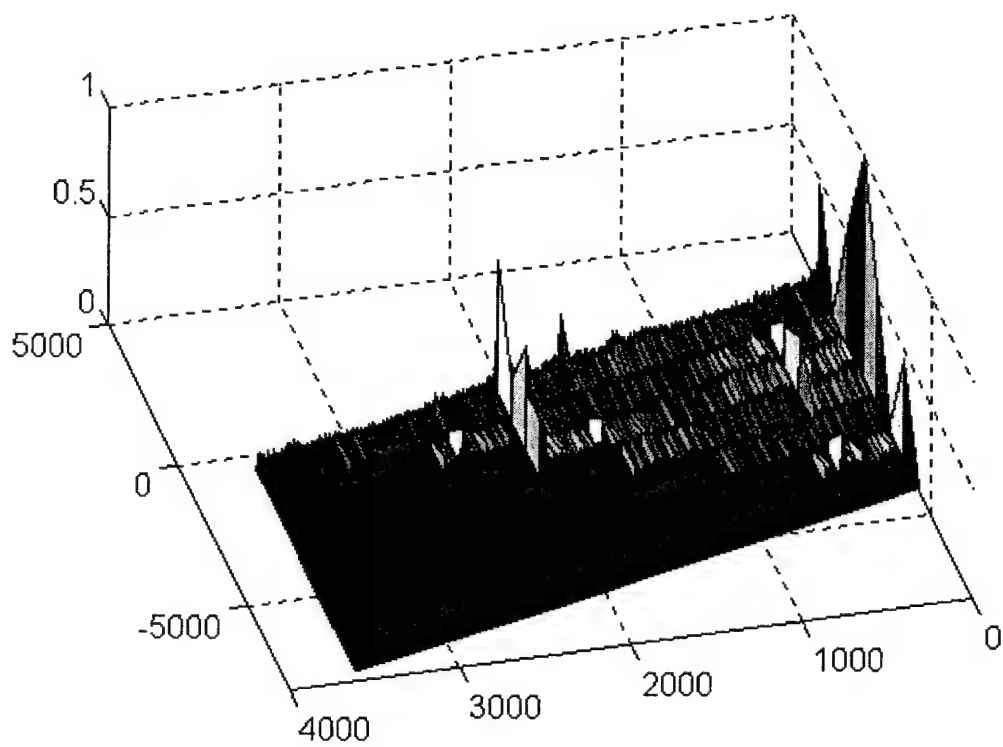
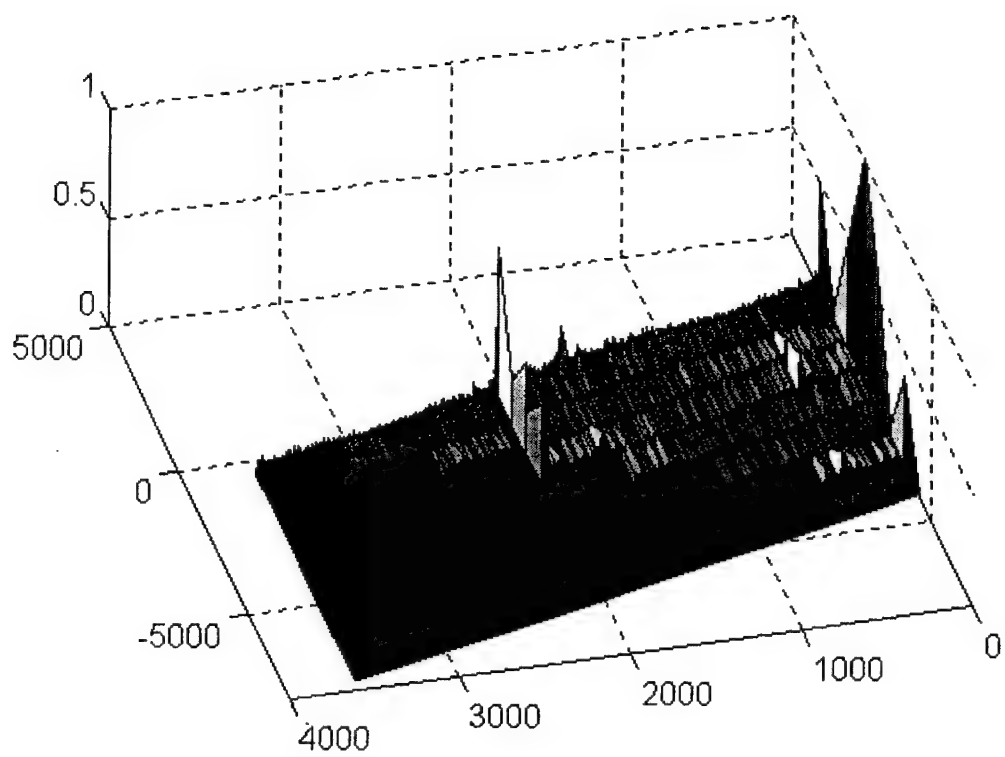


Figure B-55 - SCF for master (top) and slave #1 (bottom), time 409460

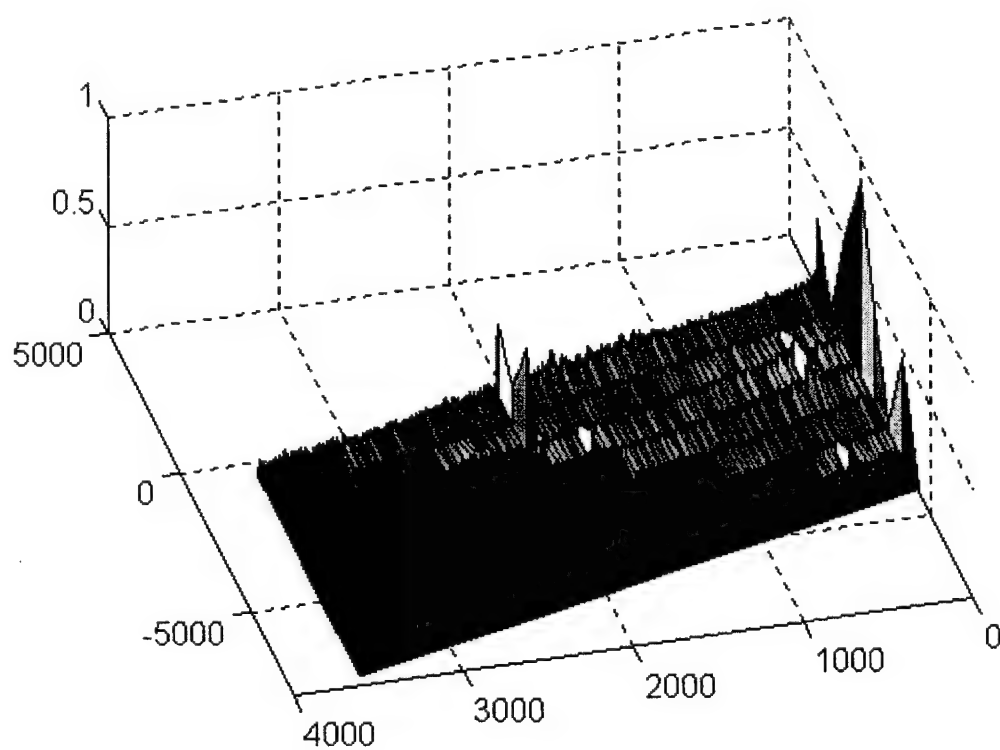
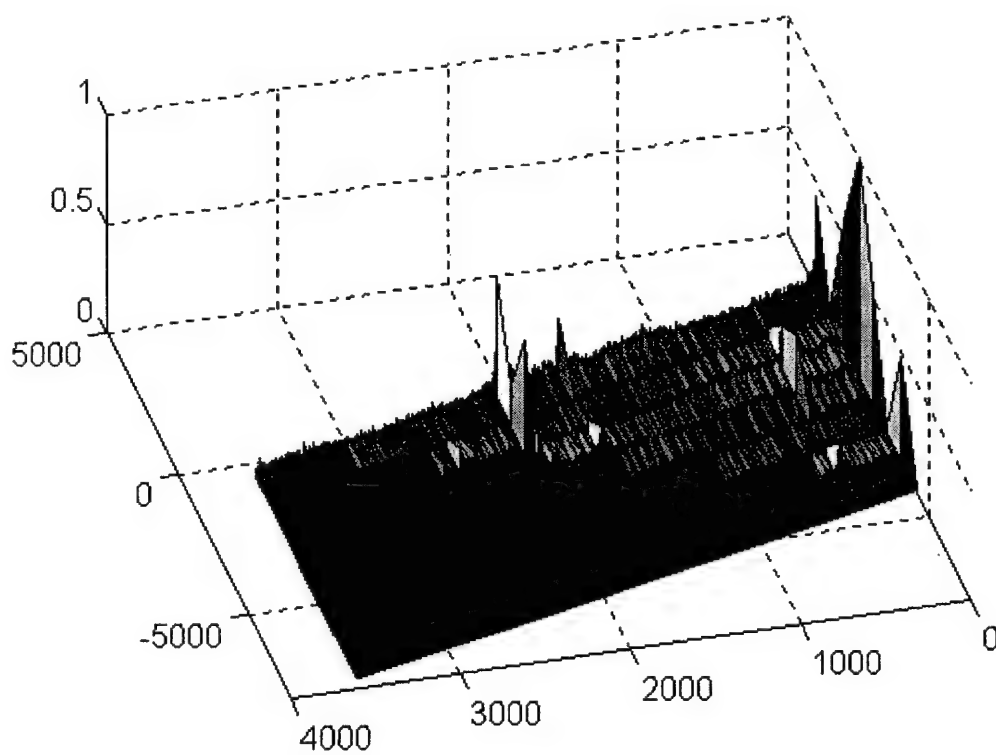


Figure B-56 - SCF for slave #2 (top) and slave #3 (bottom), time 409460

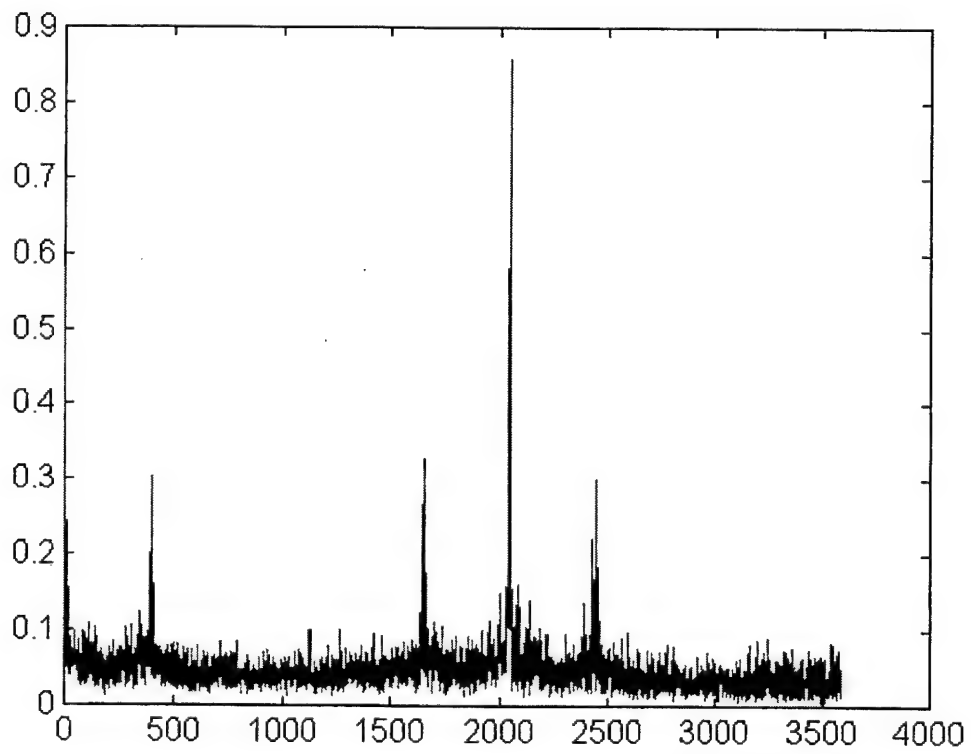
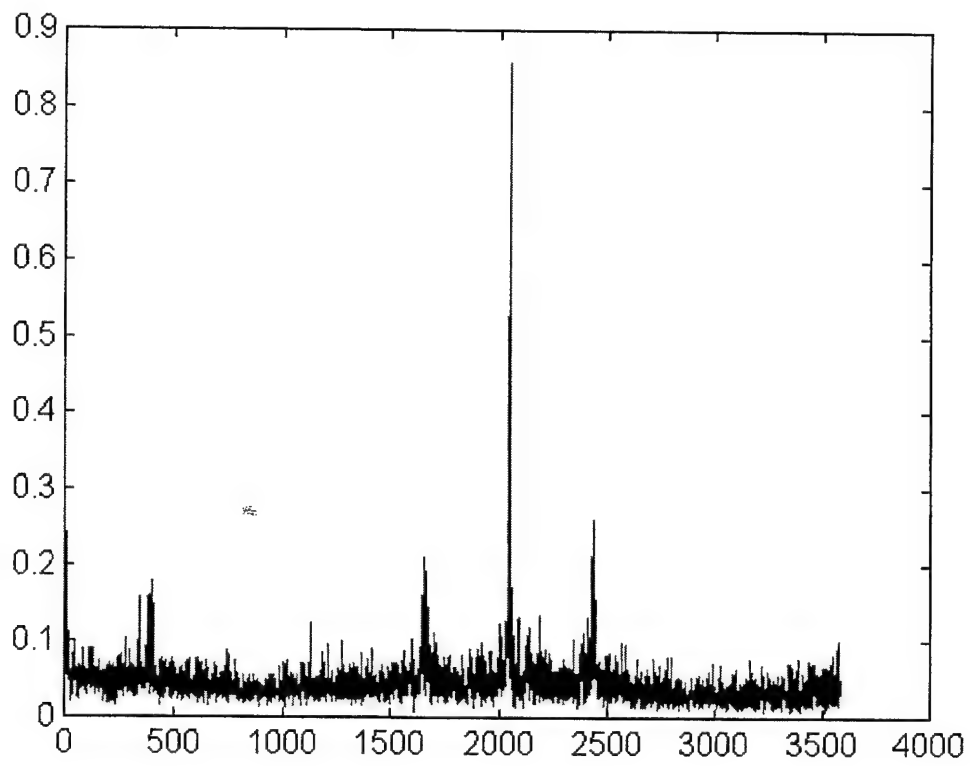


Figure B-57 - Cycle freq vs Max-magnitude of SCF for master (top) and slave #1 (bottom), time 409460

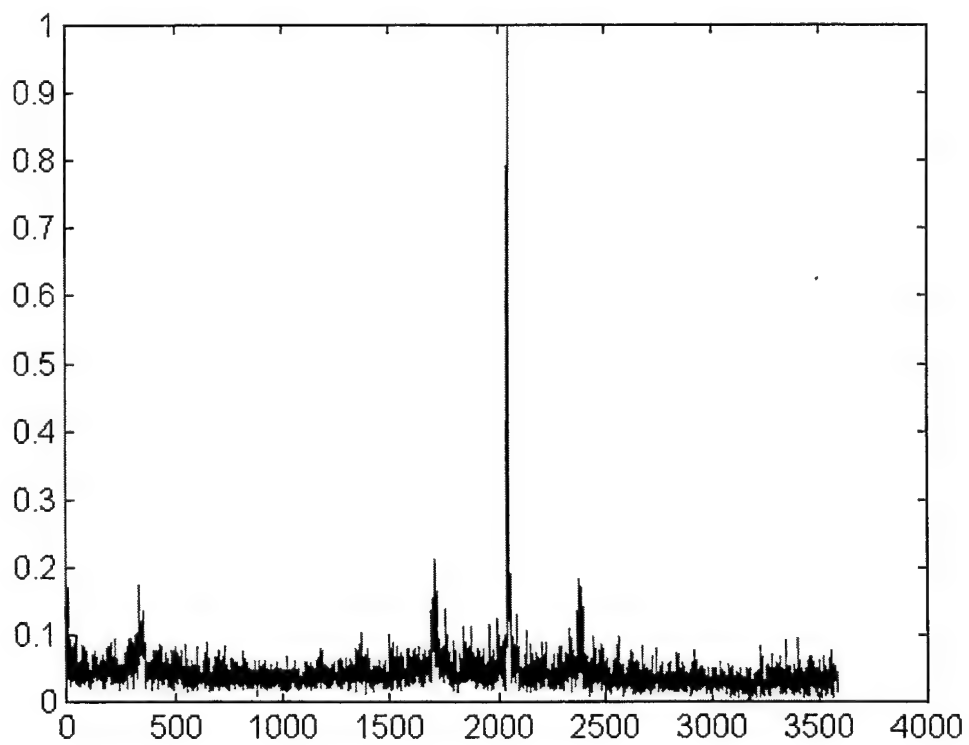
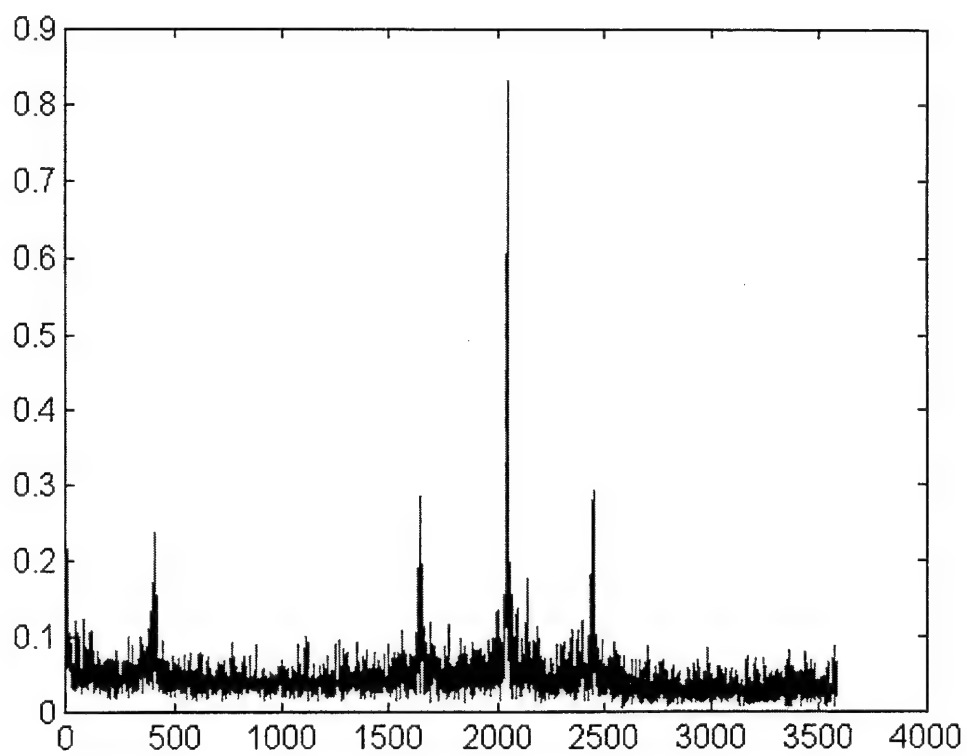


Figure B-58 - Cycle freq vs Max-magnitude of SCF for slave #2 (top) and slave #3 (bottom), time 409460

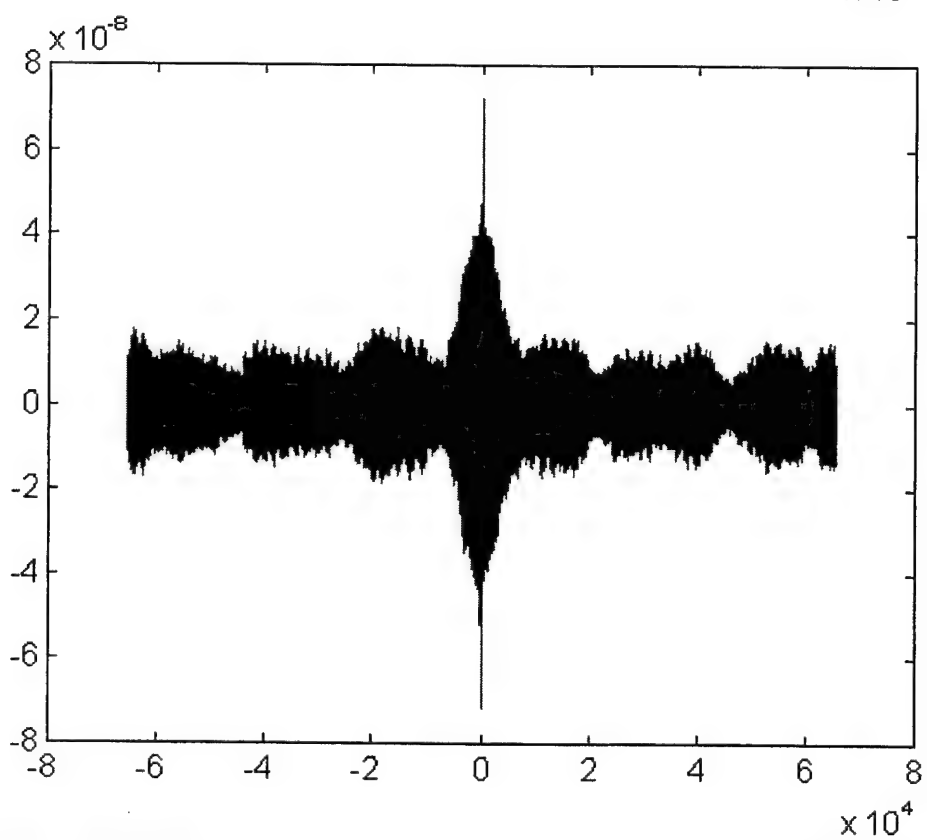
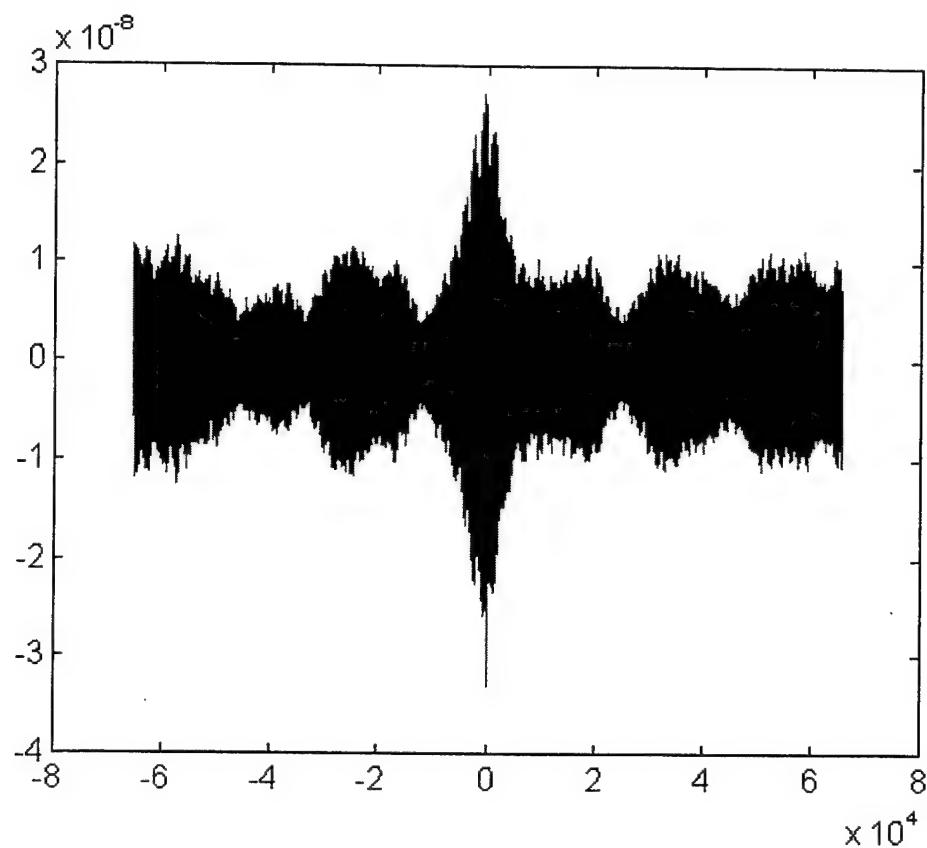


Figure B-59 - SPECCOA for master and slave #1 (top) and master and slave #2 (bottom), time 409460

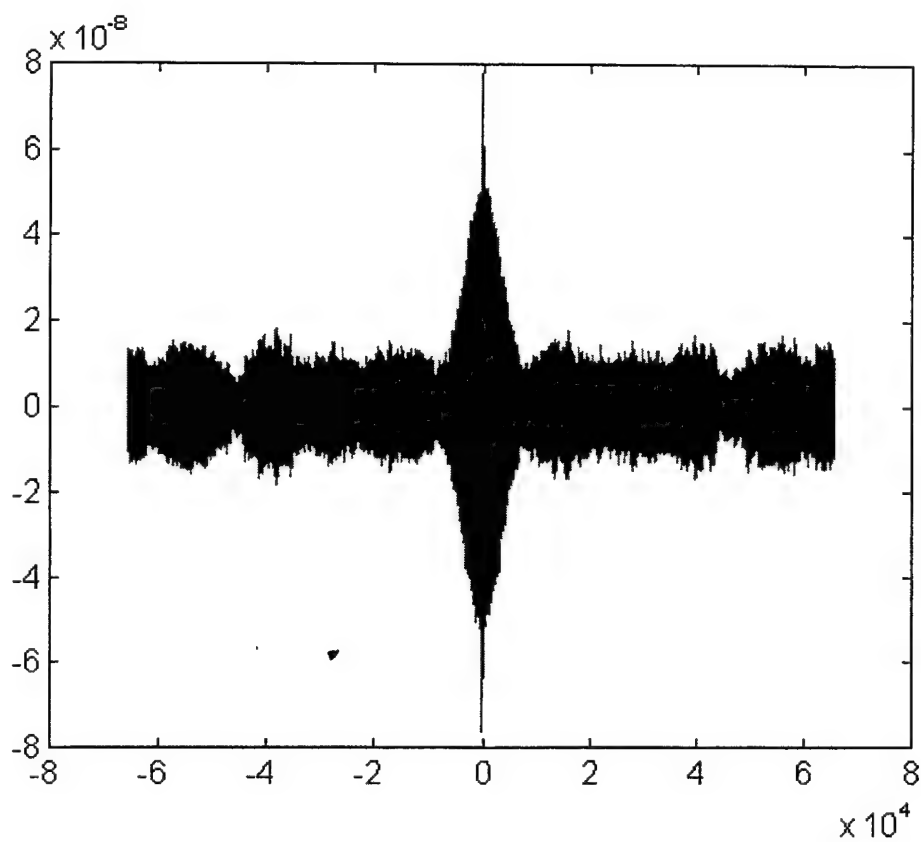


Figure B-60 - SPECCOA for master and slave #3, time 409460

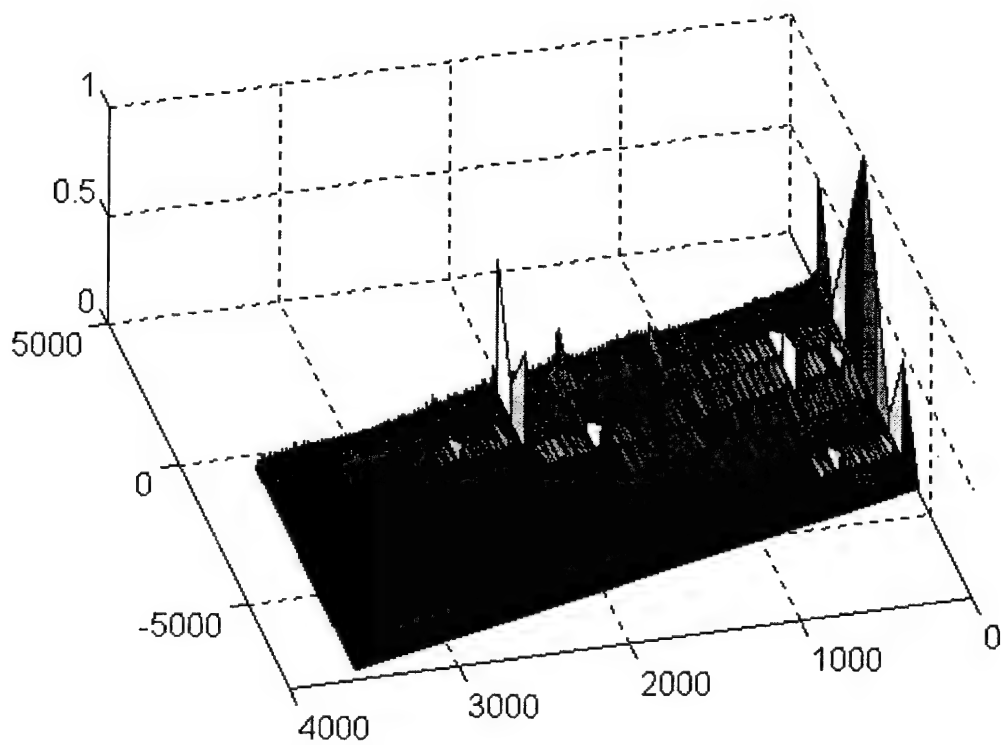
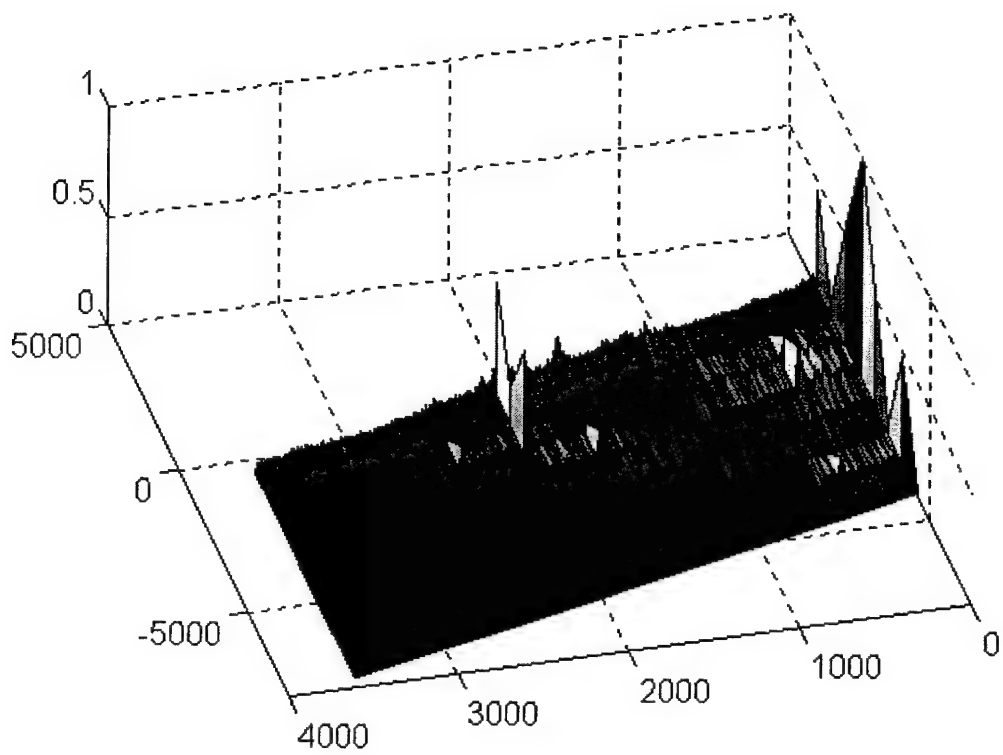


Figure B-61 - SCF for master (top) and slave #1 (bottom), time 409465

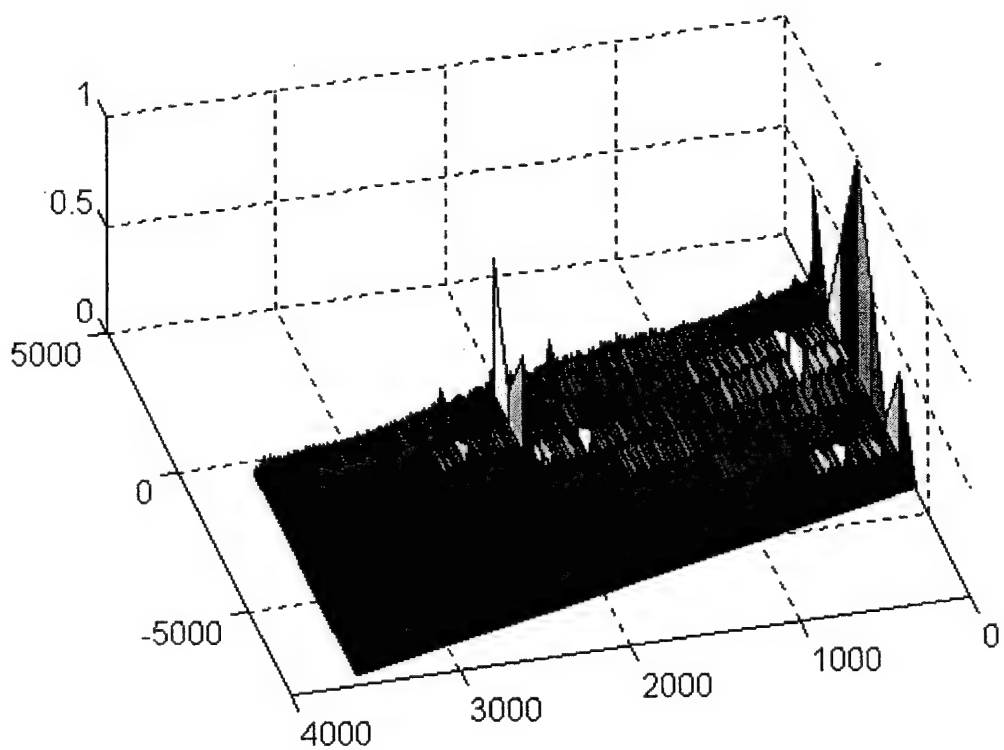
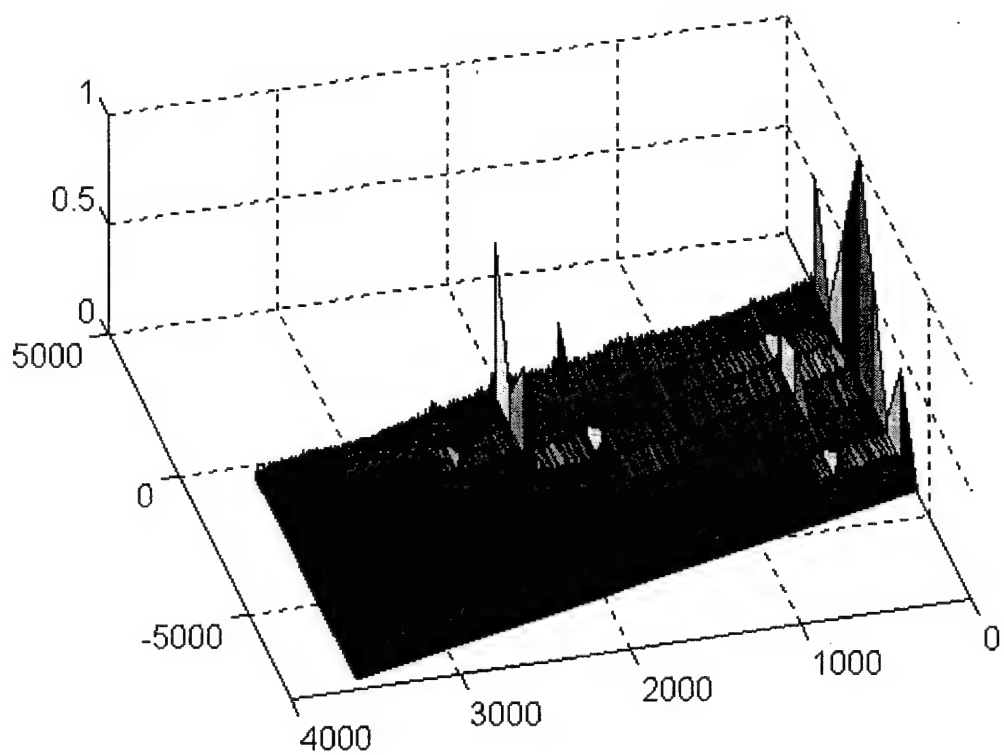


Figure B-62 - SCF for slave #2 (top) and slave #3 (bottom), time 409465

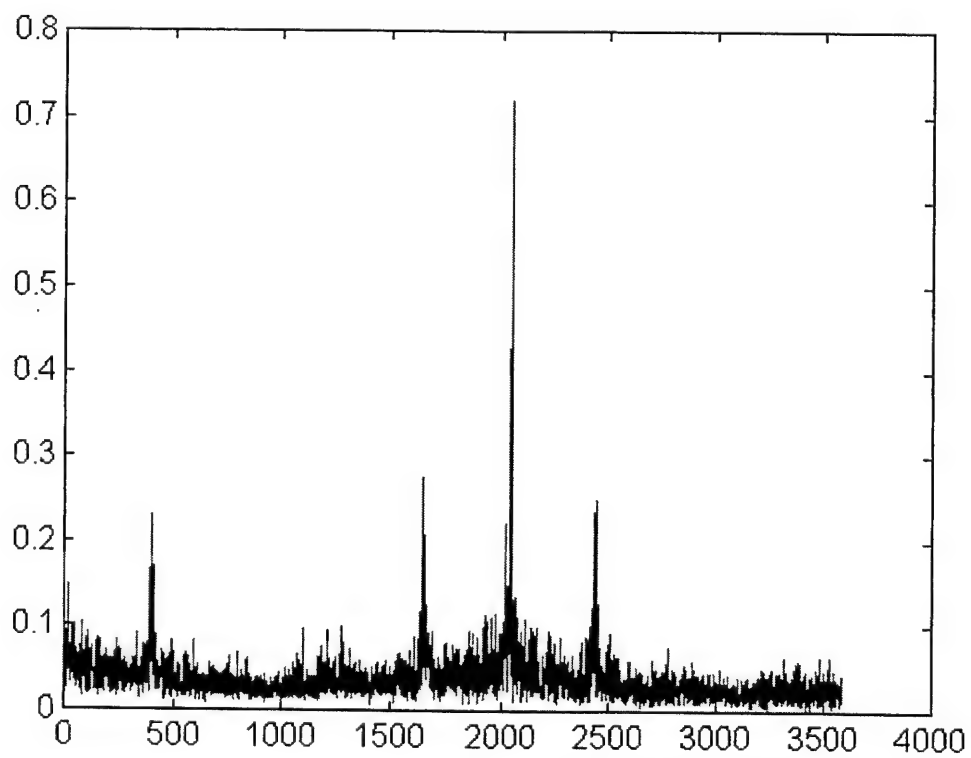
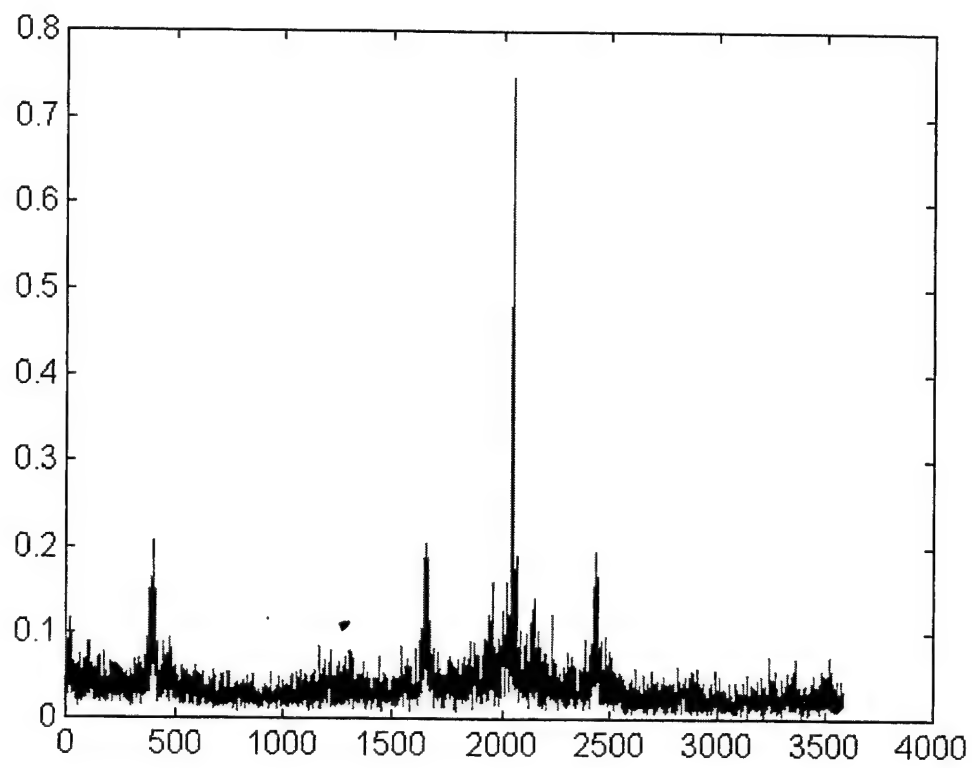


Figure B-63 - Cycle freq vs Max-magnitude of SCF for master (top) and slave #1 (bottom), time 409465

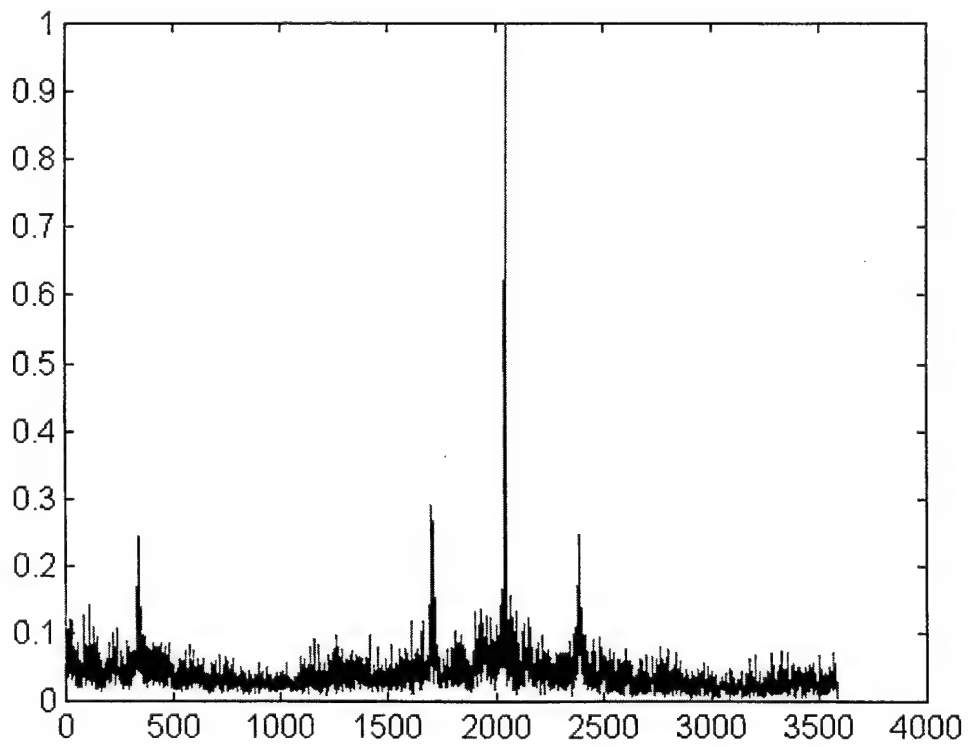
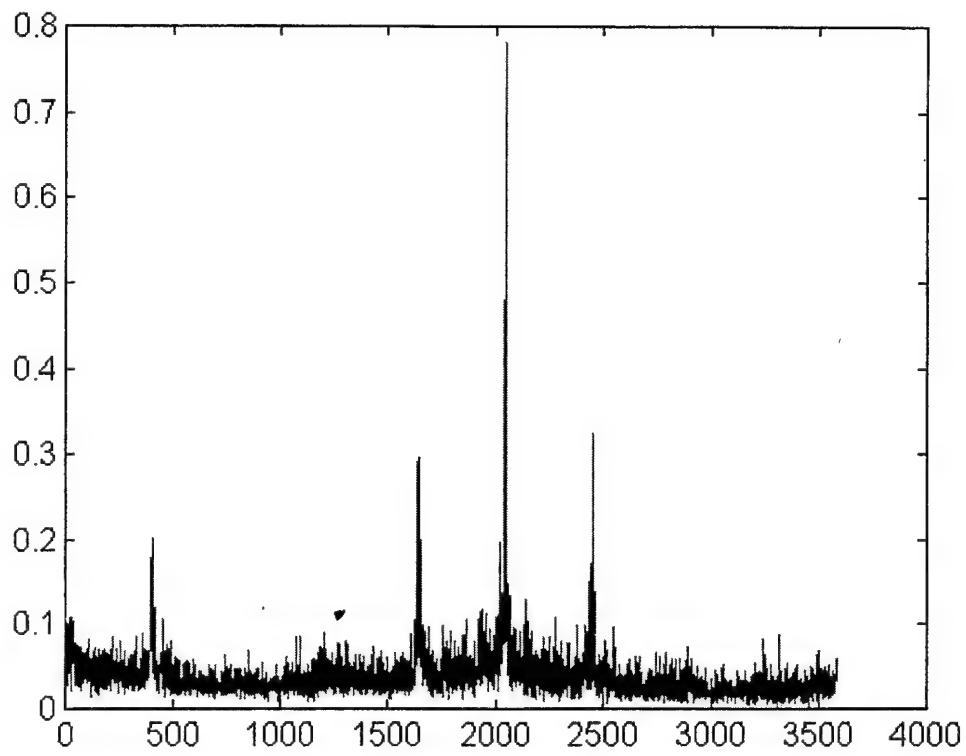


Figure B-64 - Cycle freq vs Max-magnitude of SCF for slave #2 (top) and slave #3 (bottom), time 409465

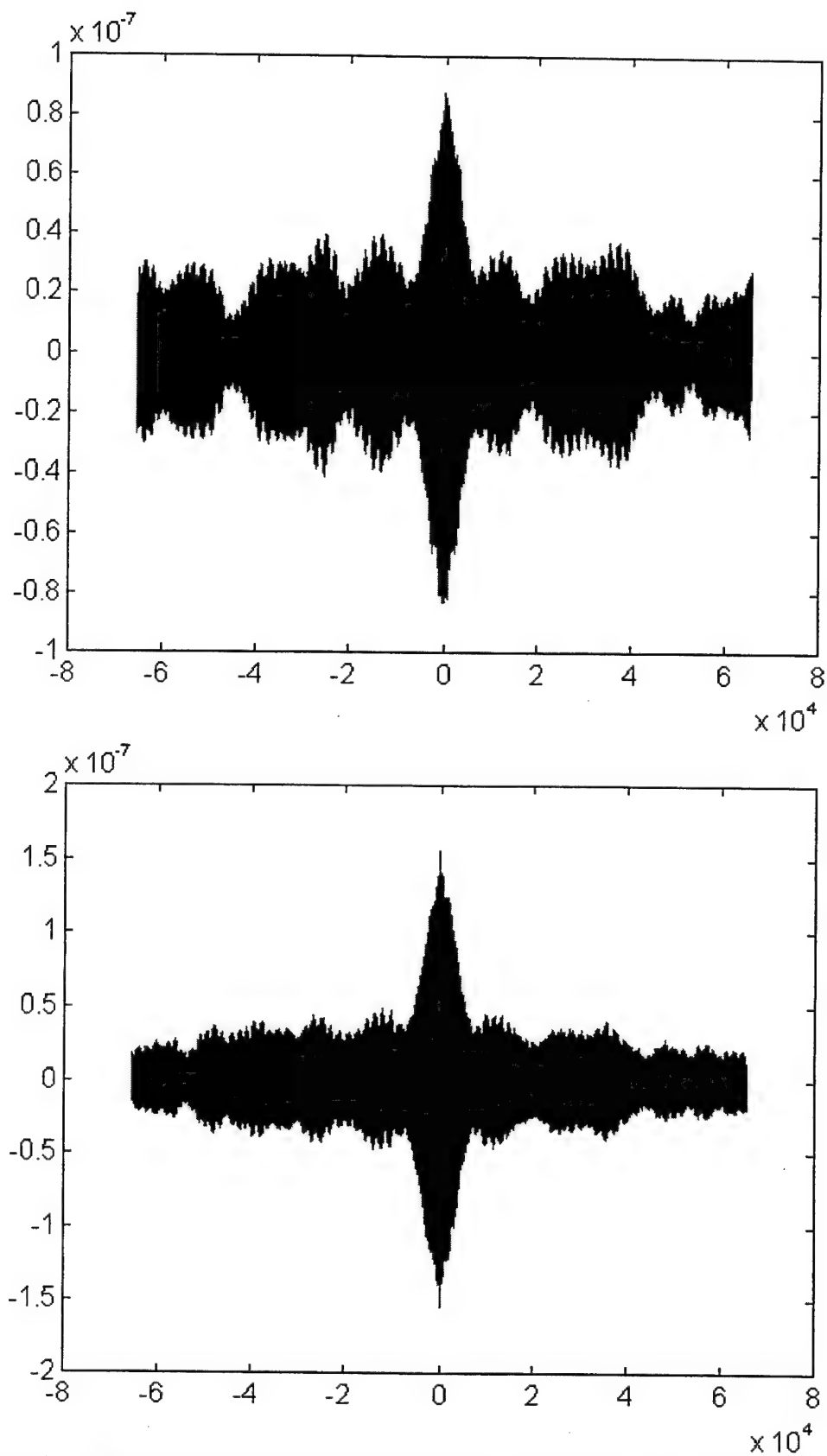


Figure B-65 - SPECCOA for master and slave #1 (top) and master and slave #2 (bottom), time 409465

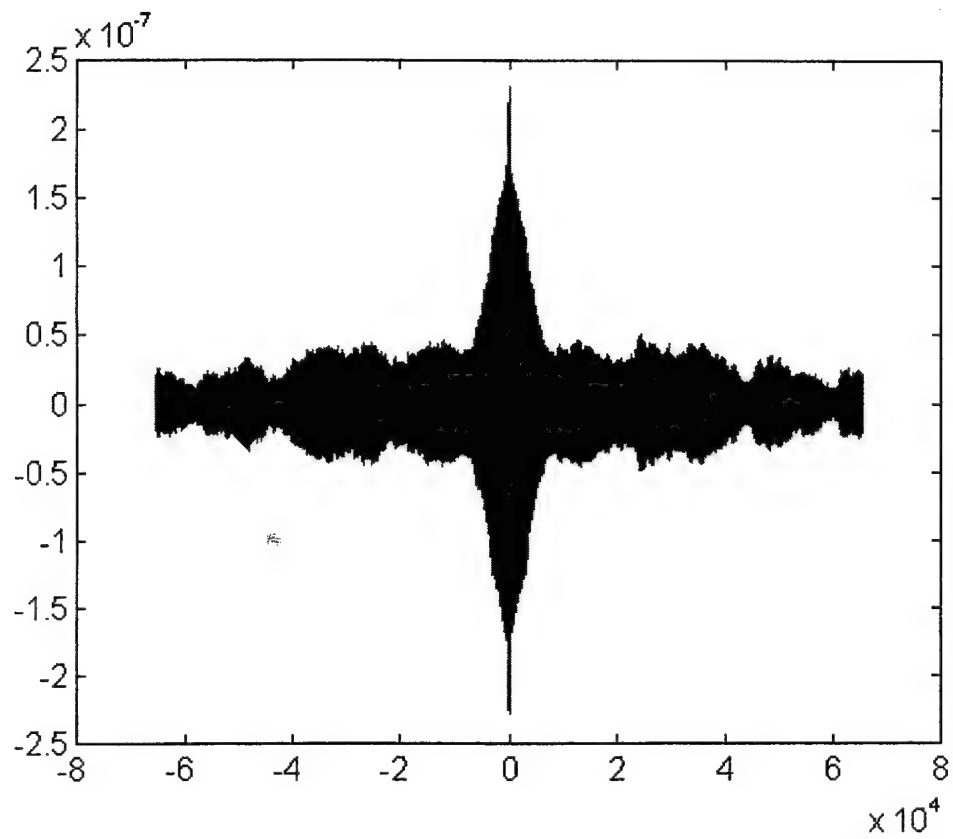


Figure B-66 - SPECCOA for master and slave #3, time 409465

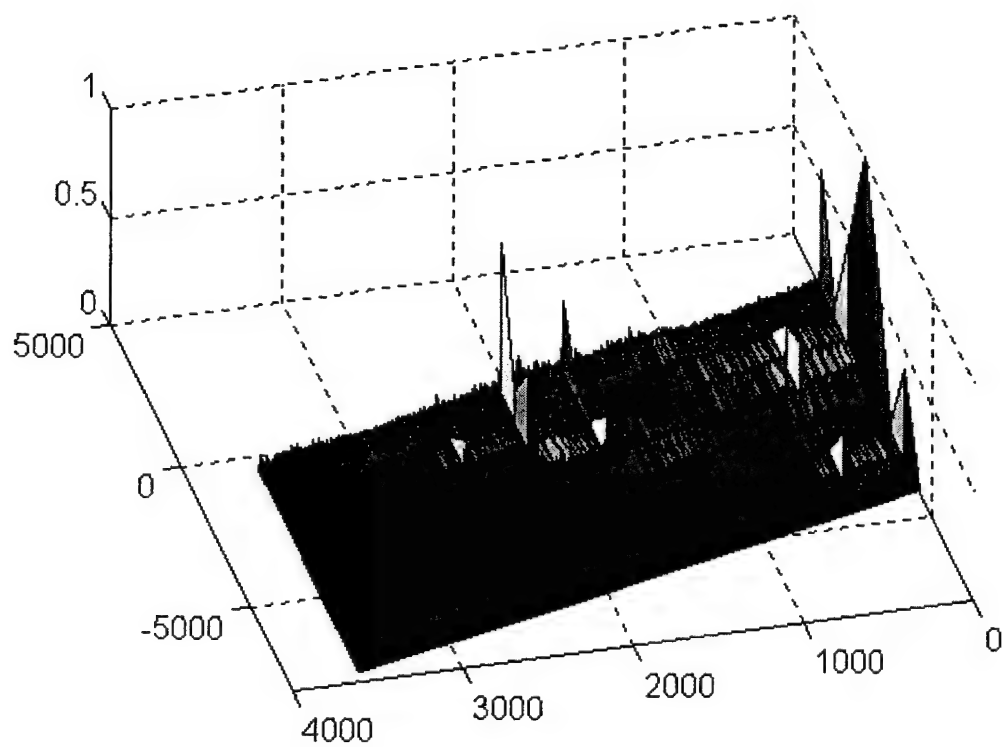
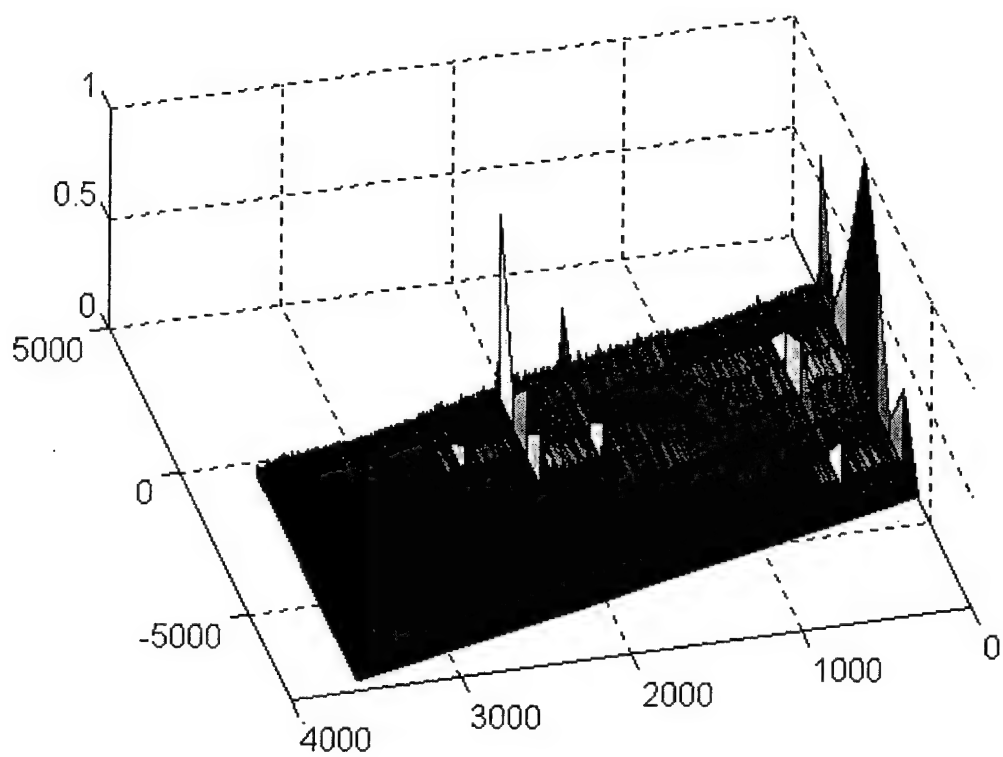


Figure B-67 - SCF for master (top) and slave #1 (bottom), time 409470

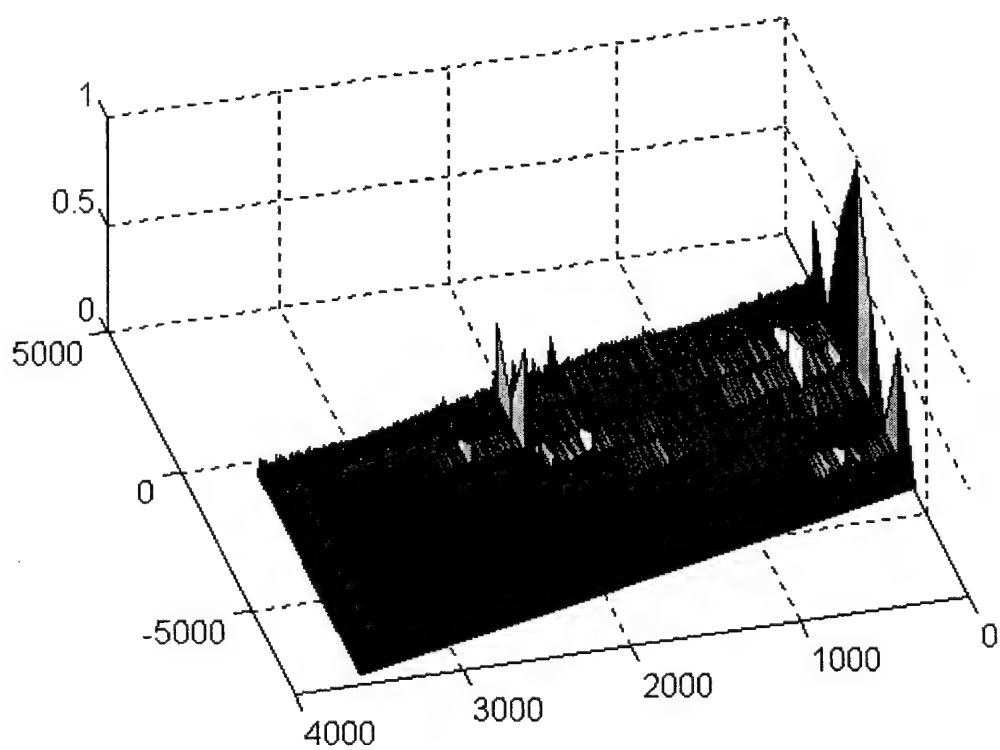
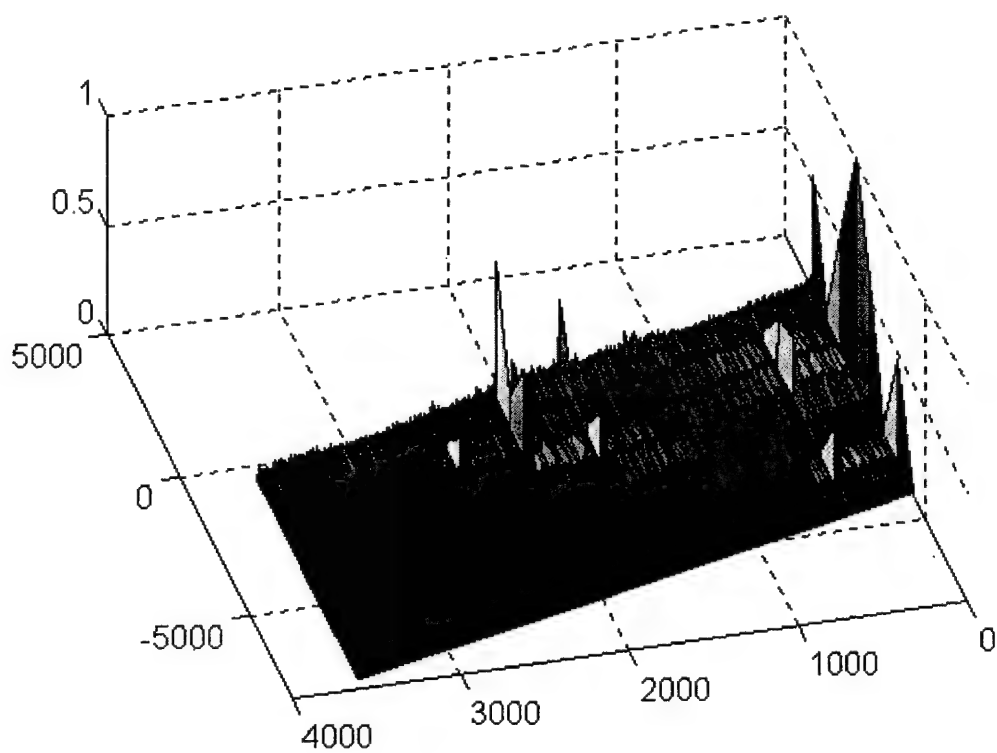


Figure B-68 - SCF for slave #2 (top) and slave #3 (bottom), time 409470

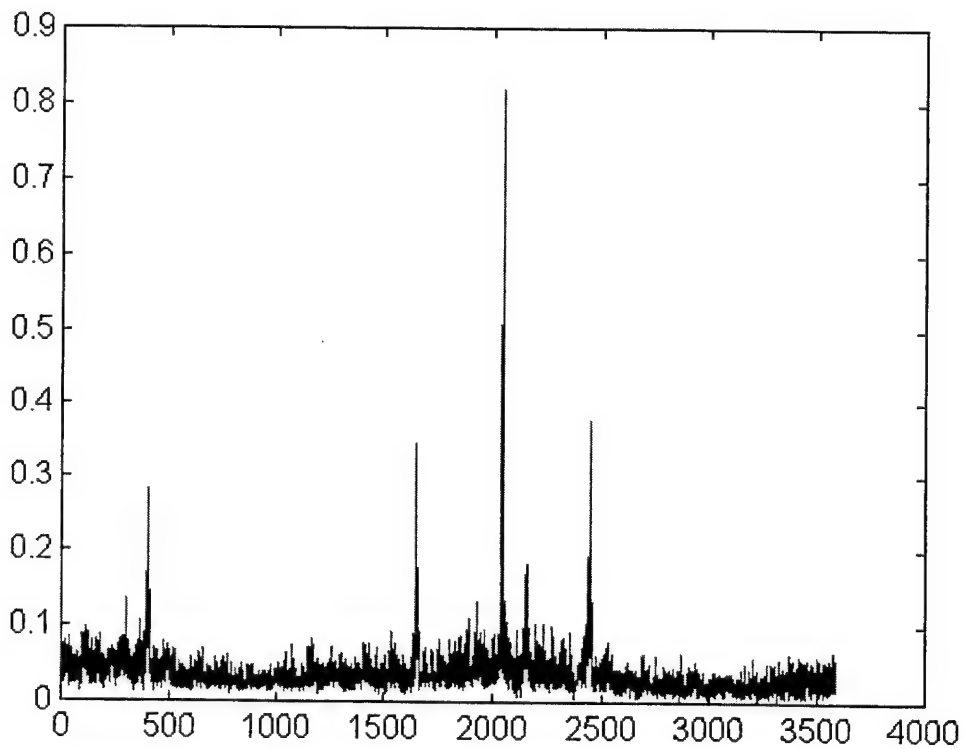
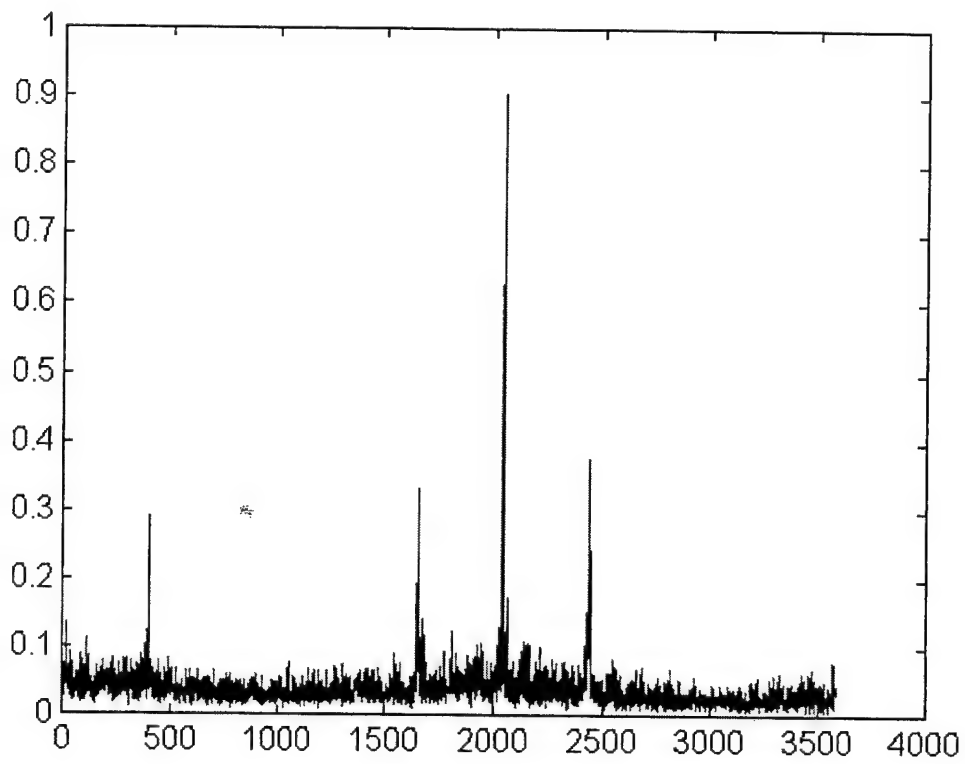


Figure B-69 - Cycle freq vs Max-magnitude of SCF for master (top) and slave #1 (bottom), time 409470

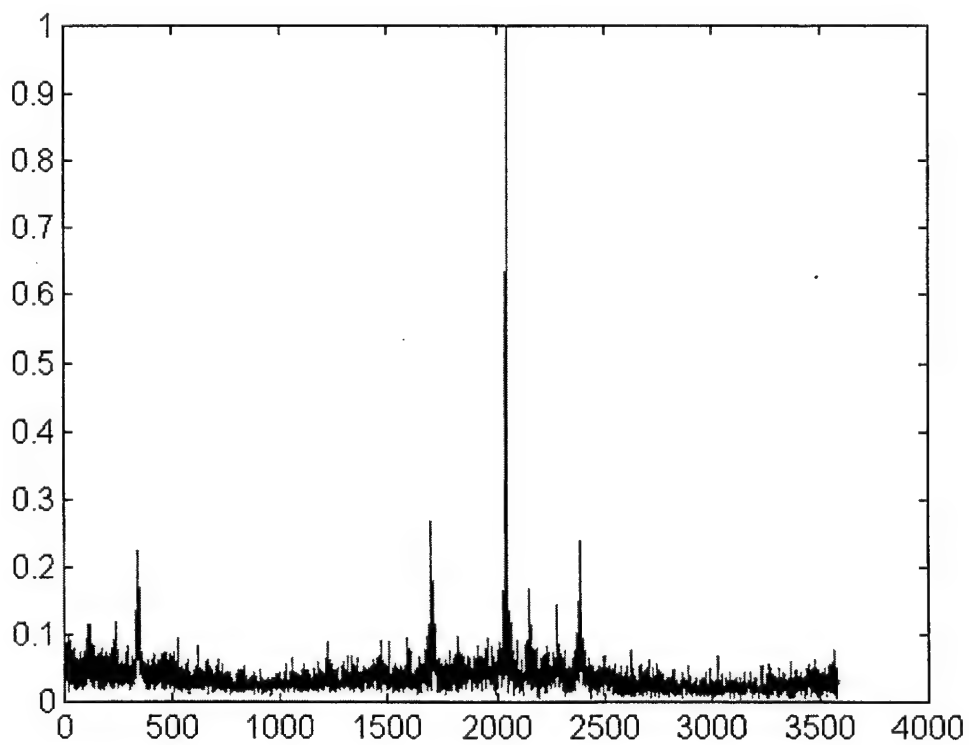
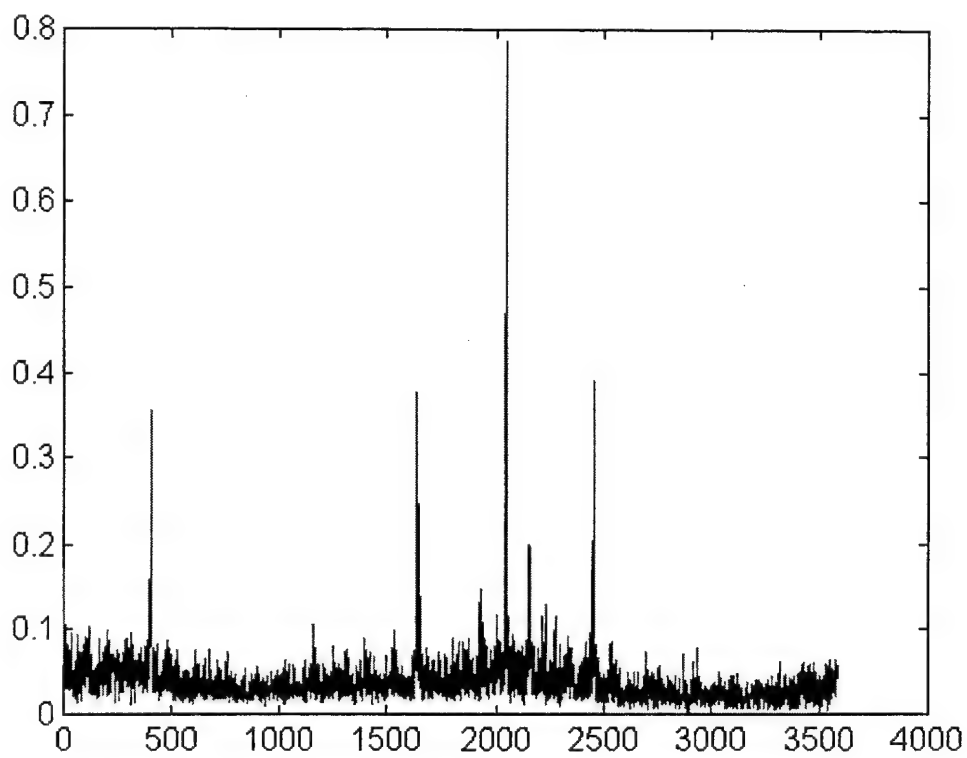


Figure B-70 - Cycle freq vs Max-magnitude of SCF for slave #2 (top) and slave #3 (bottom), time 409470

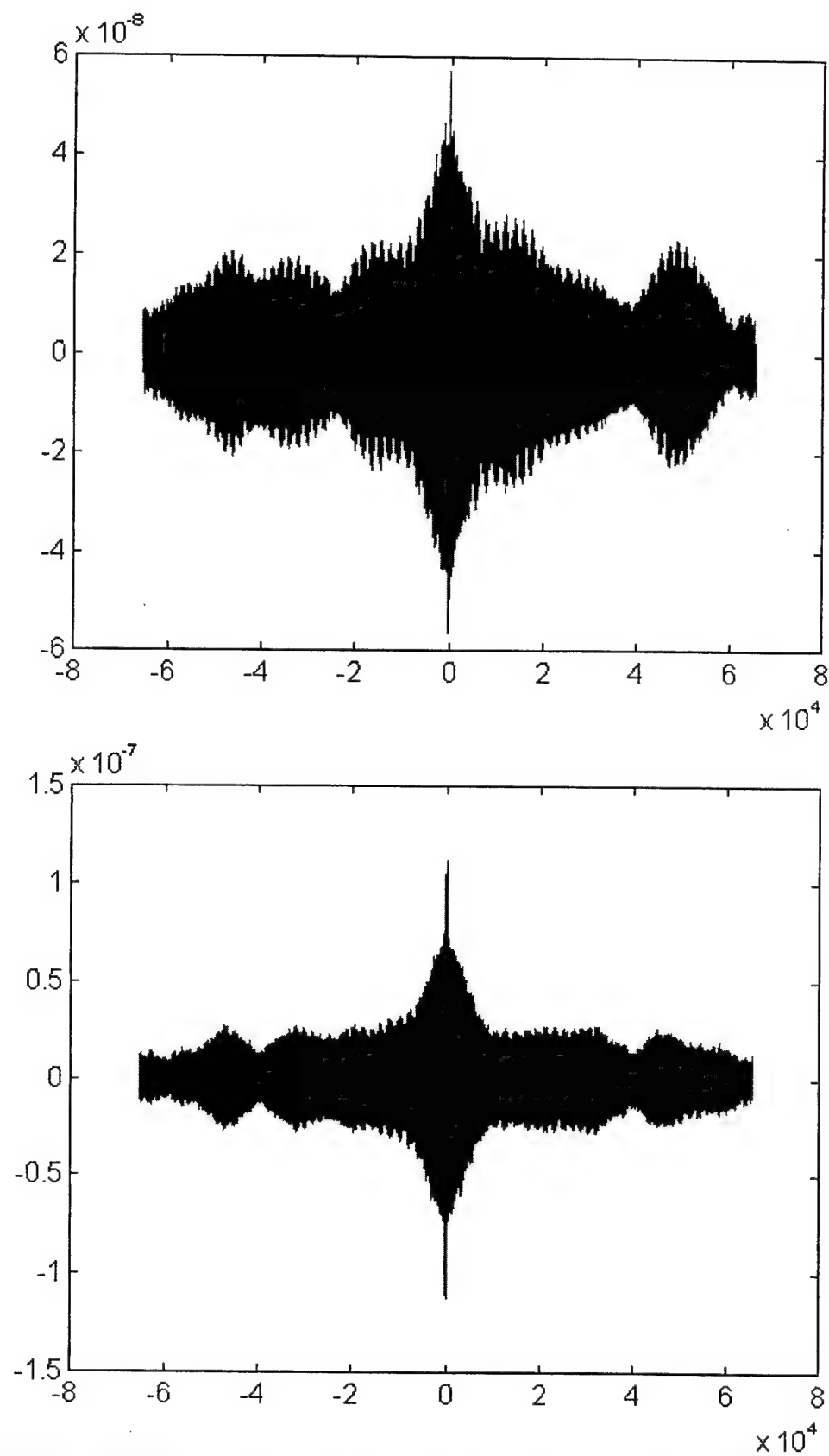


Figure B-71 - SPECCOA for master and slave #1 (top) and master and slave #2 (bottom), time 409470

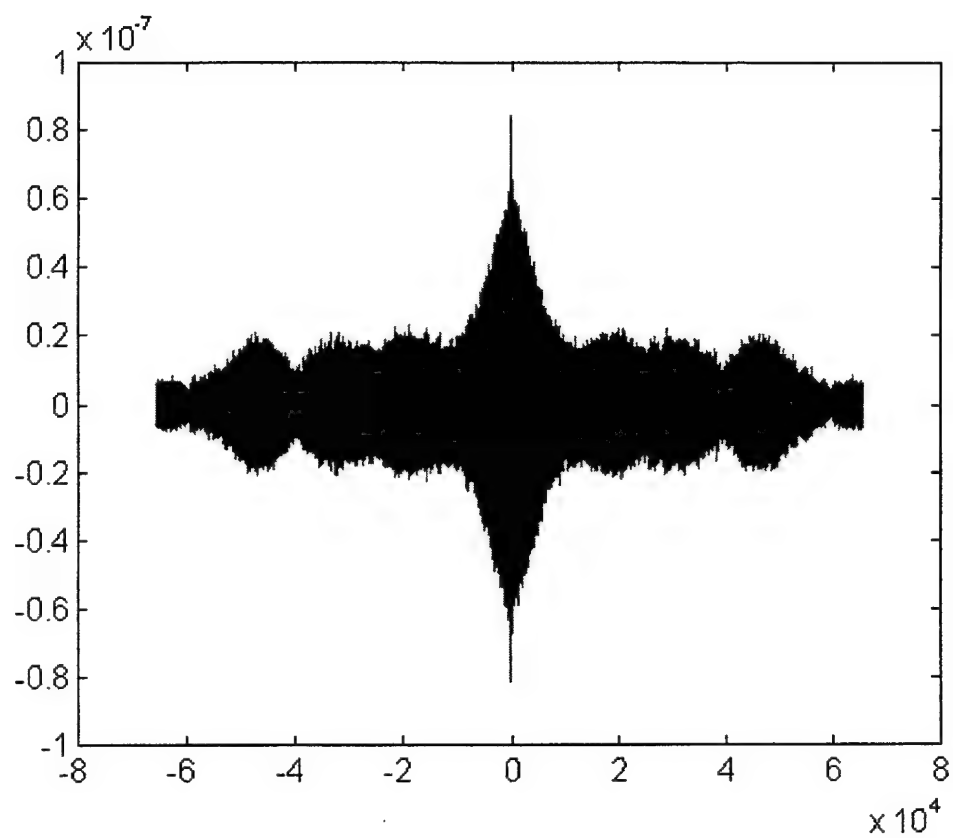


Figure B-72 - SPECCOA for master and slave #3, time 409470

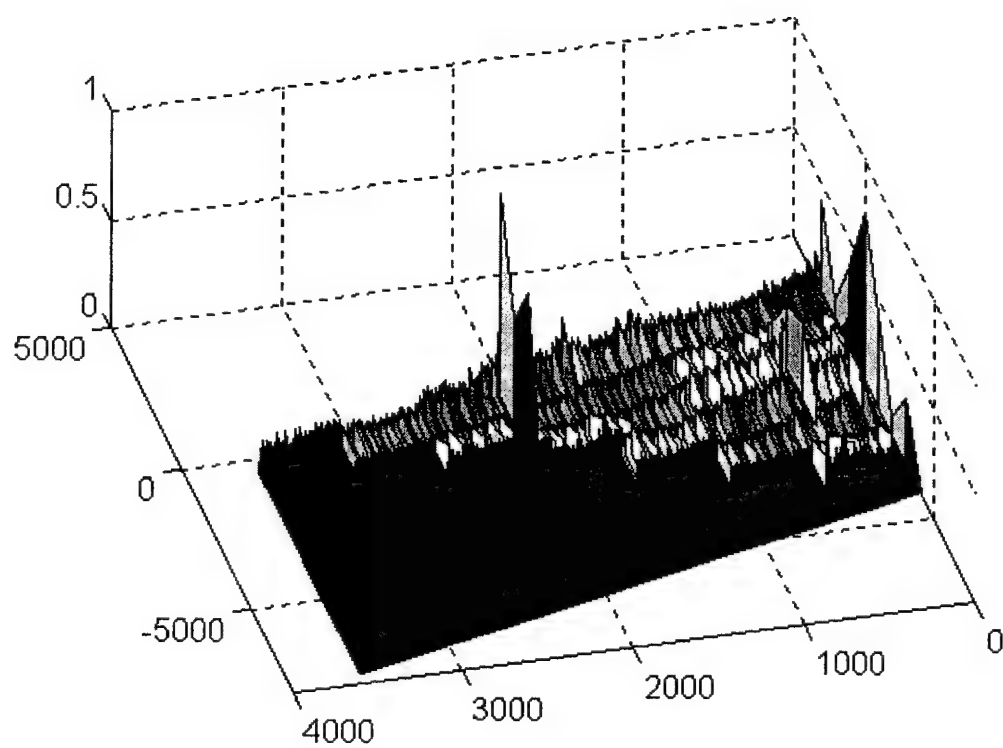
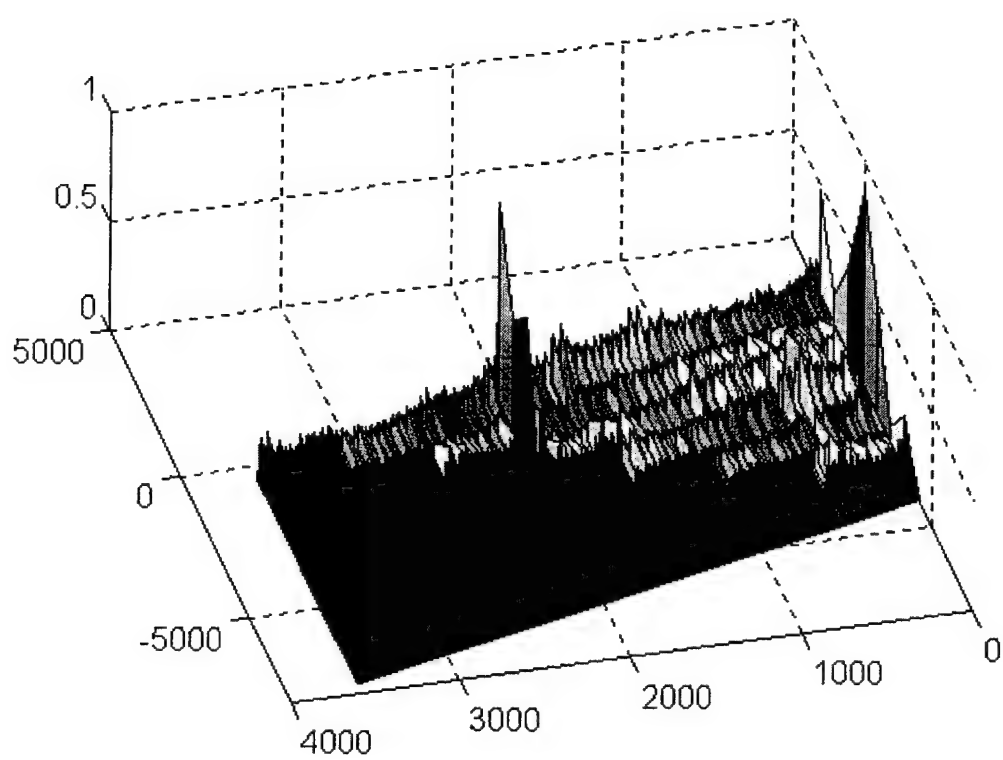


Figure B-73 - SCF for master (top) and slave #1 (bottom), time 409475

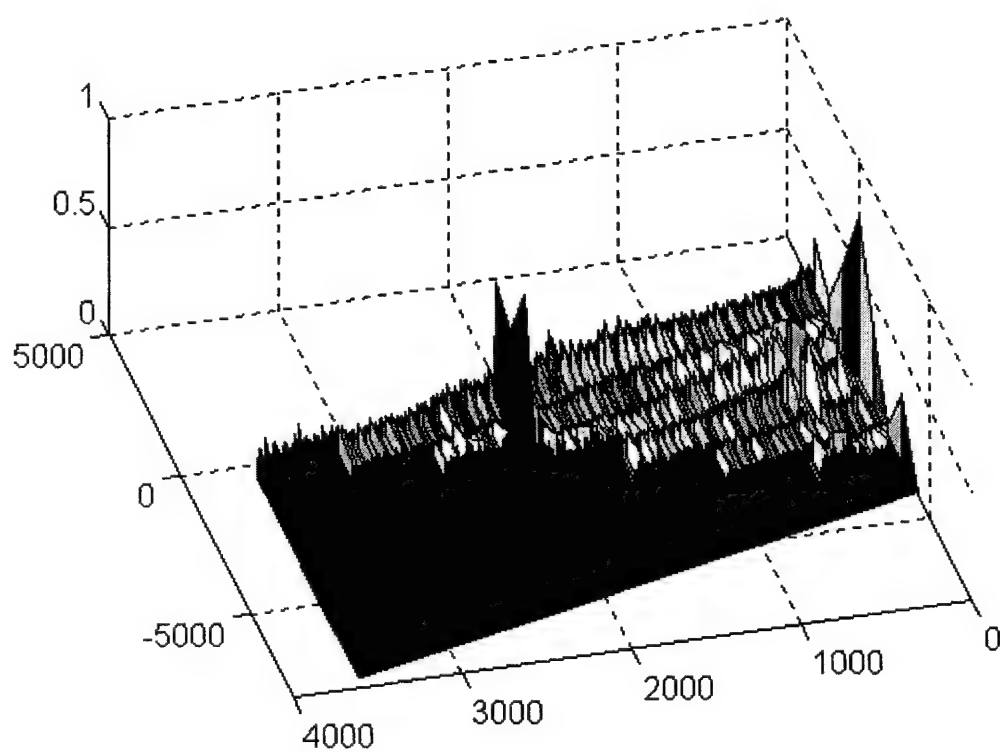
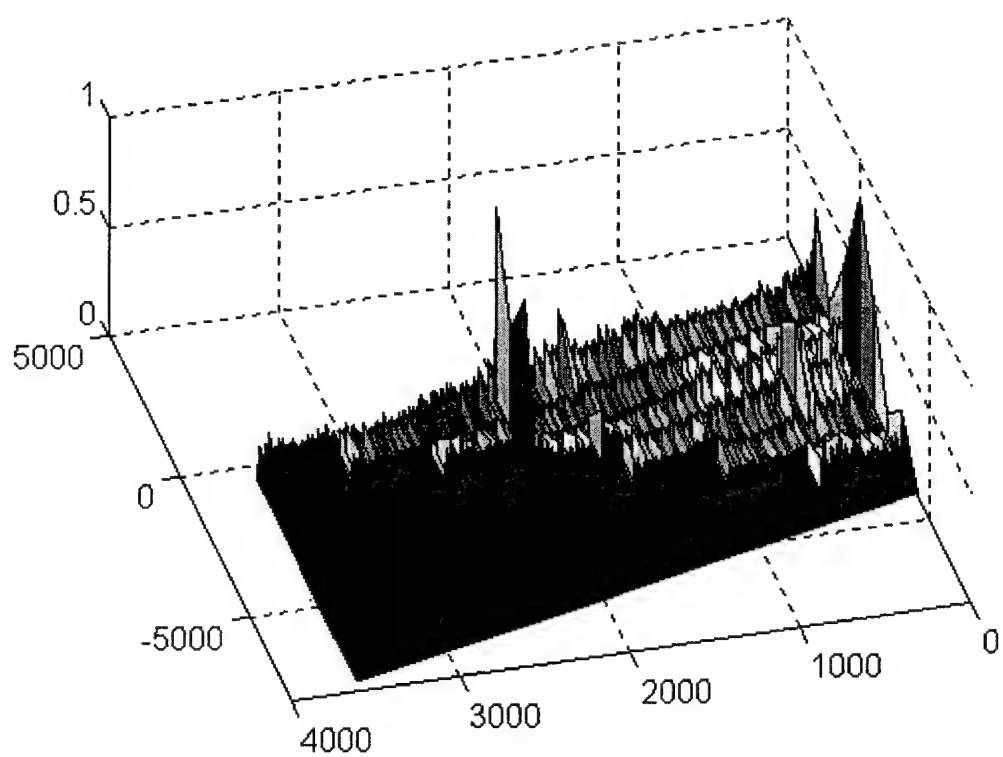


Figure B-74 - SCF for slave #2 (top) and slave #3 (bottom), time 409475

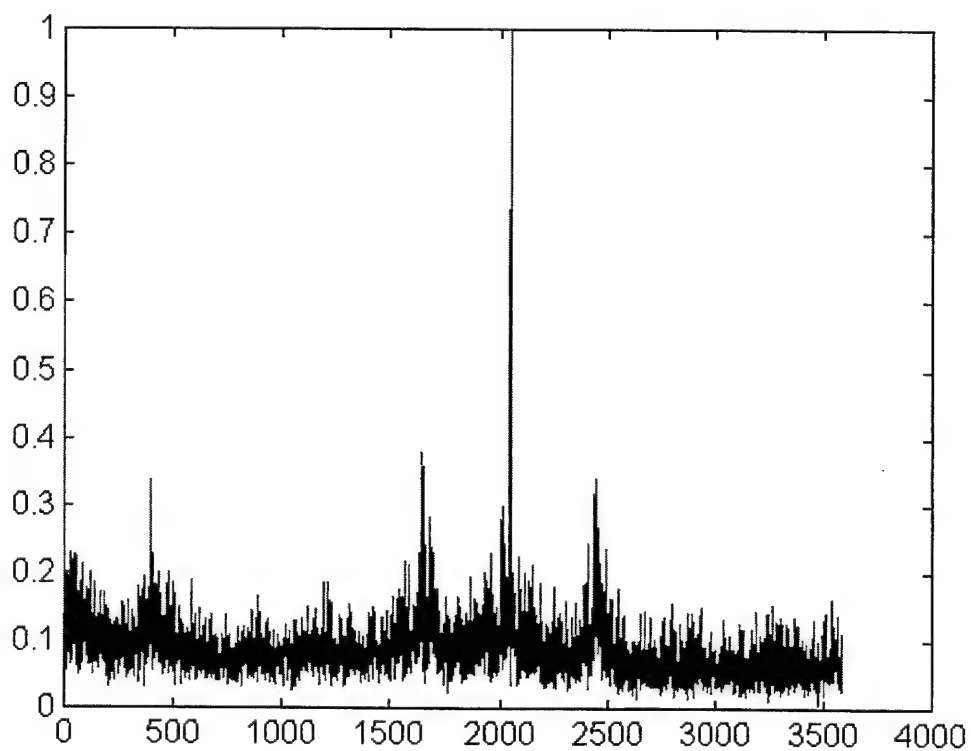
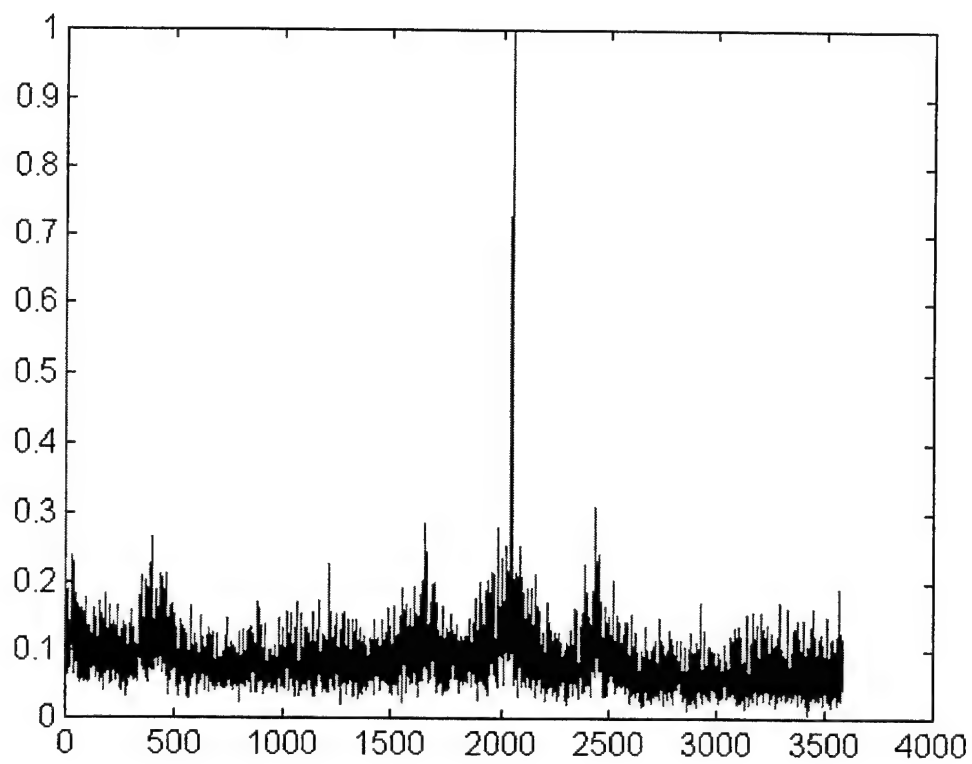


Figure B-75 - Cycle freq vs Max-magnitude of SCF for master (top) and slave #1 (bottom), time 409475

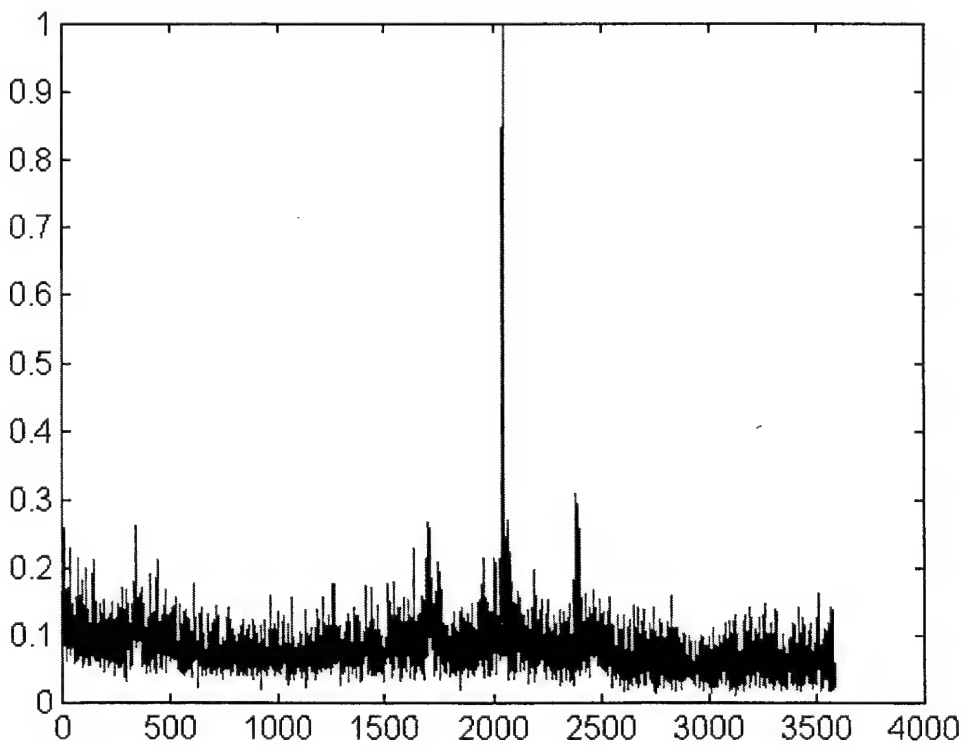
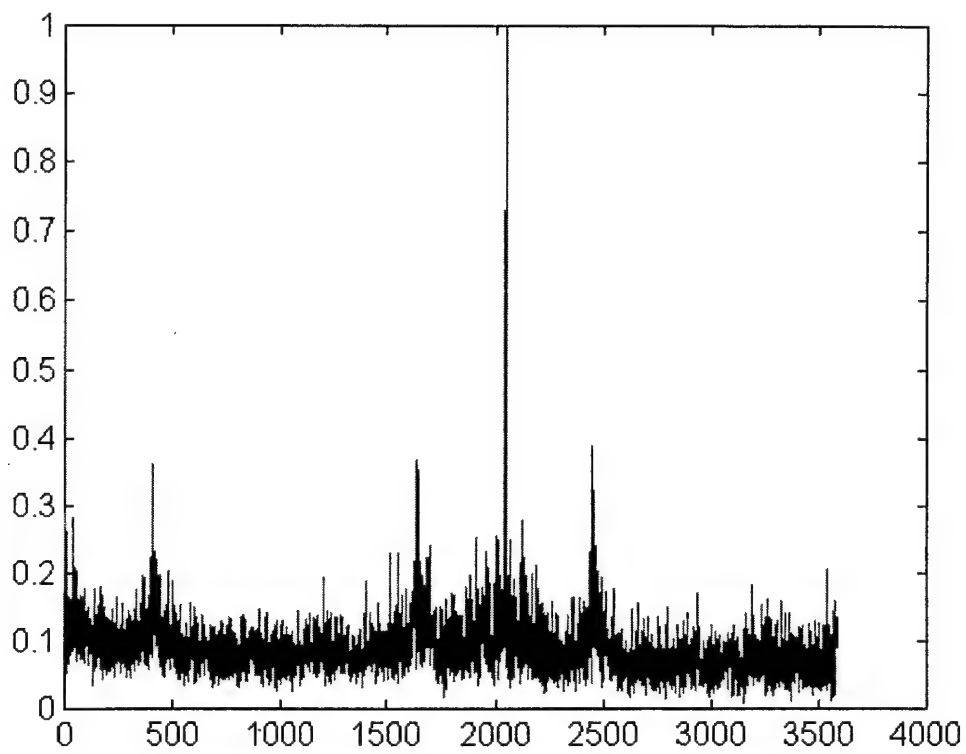


Figure B-76 - Cycle freq vs Max-magnitude of SCF for slave #2 (top) and slave #3 (bottom), time 409475

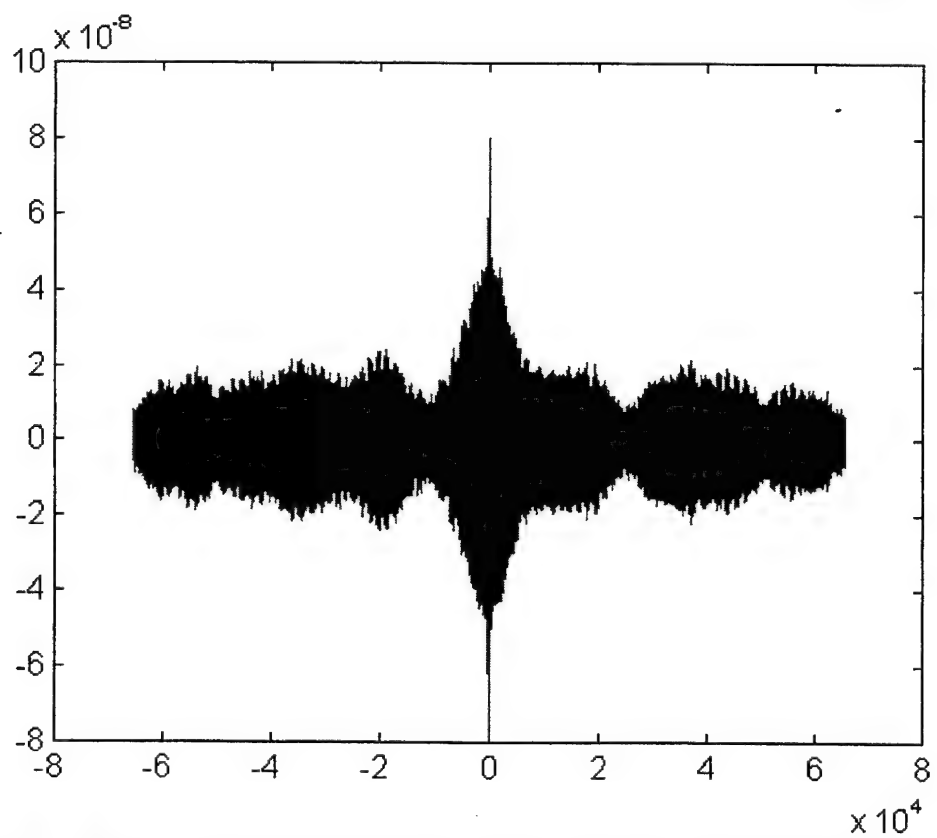
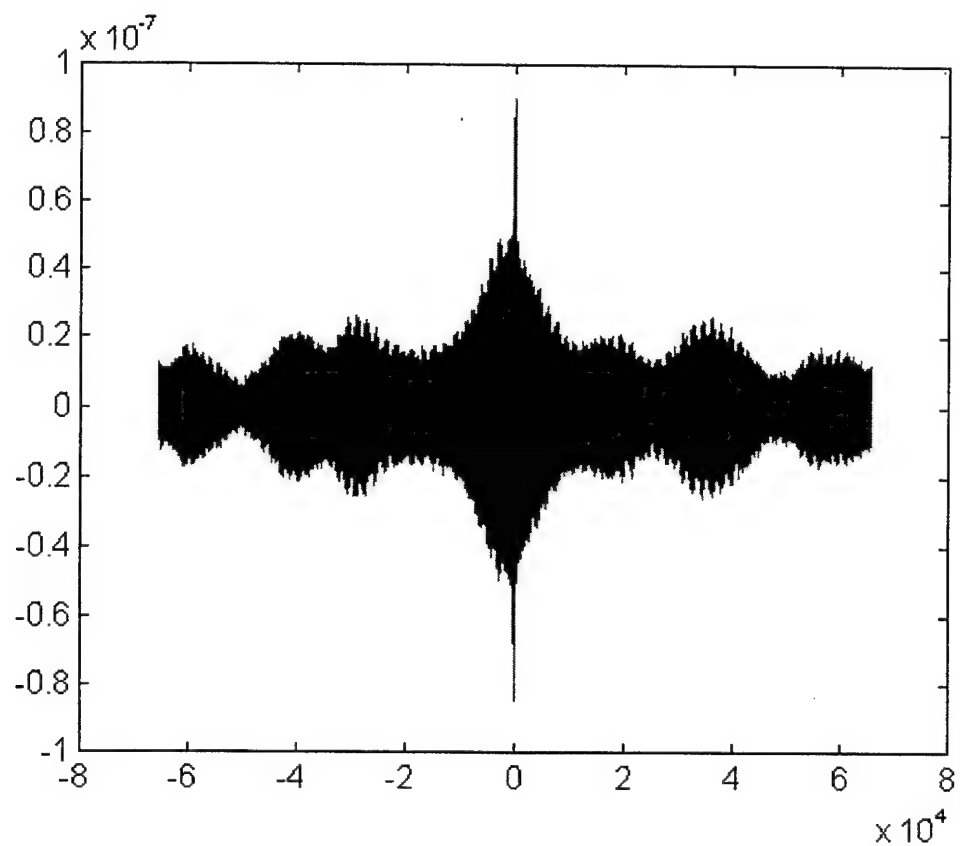


Figure B-77 - SPECCOA for master and slave #1 (top) and master and slave #2 (bottom), time 409475

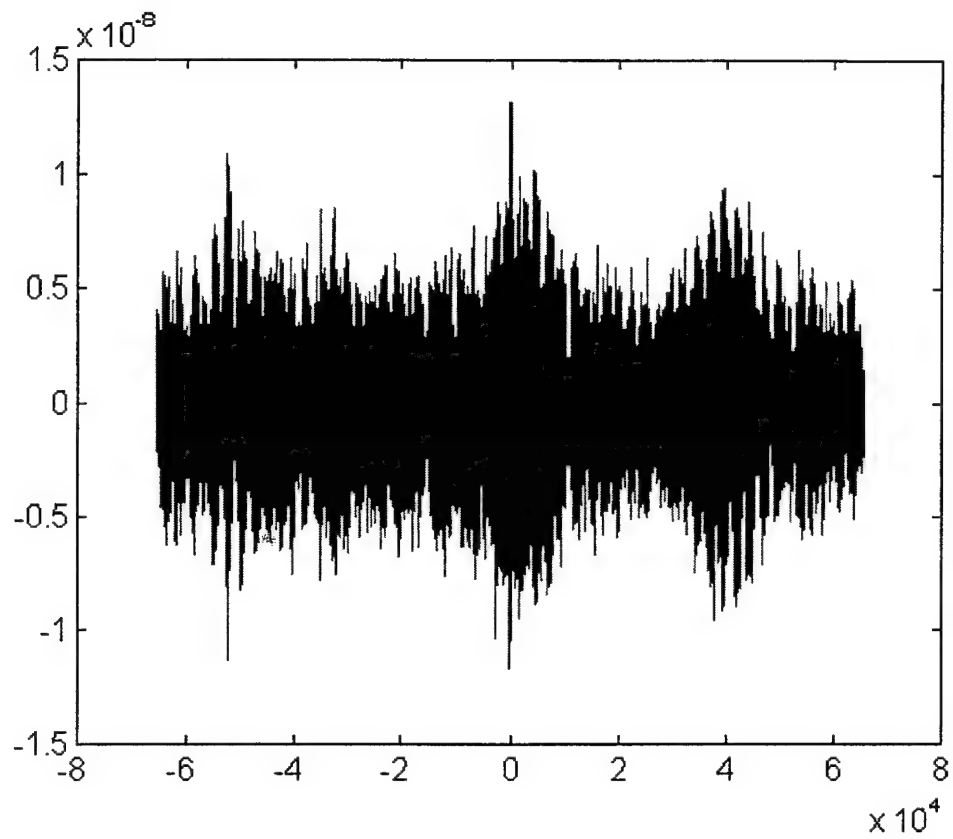


Figure B-78 - SPECCOA for master and slave #3, time 409475

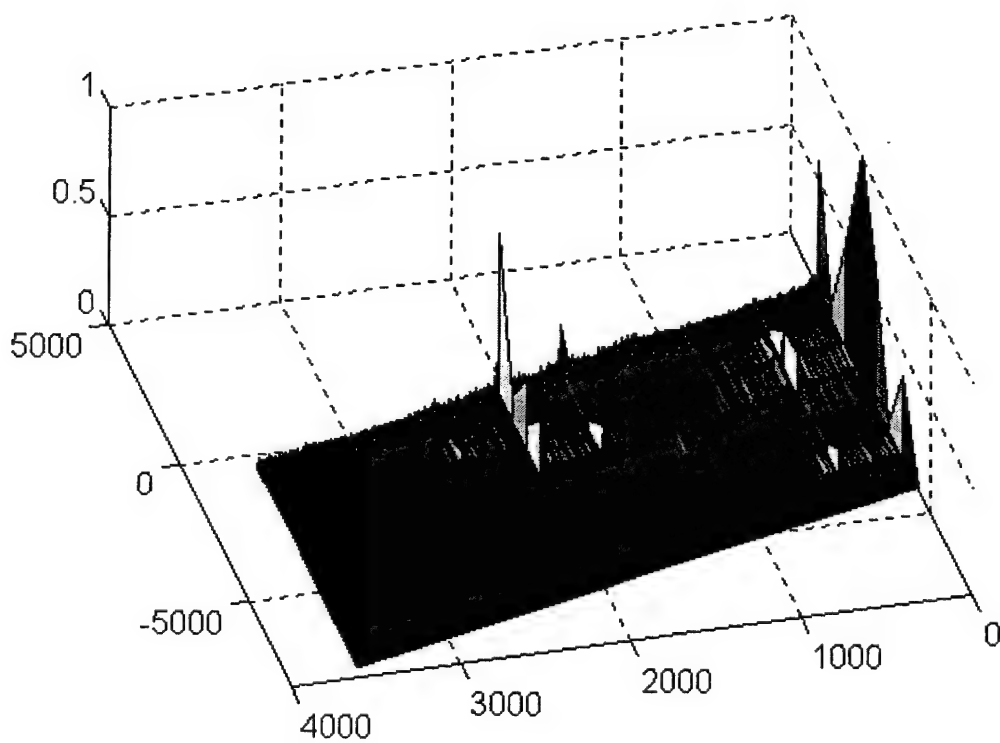
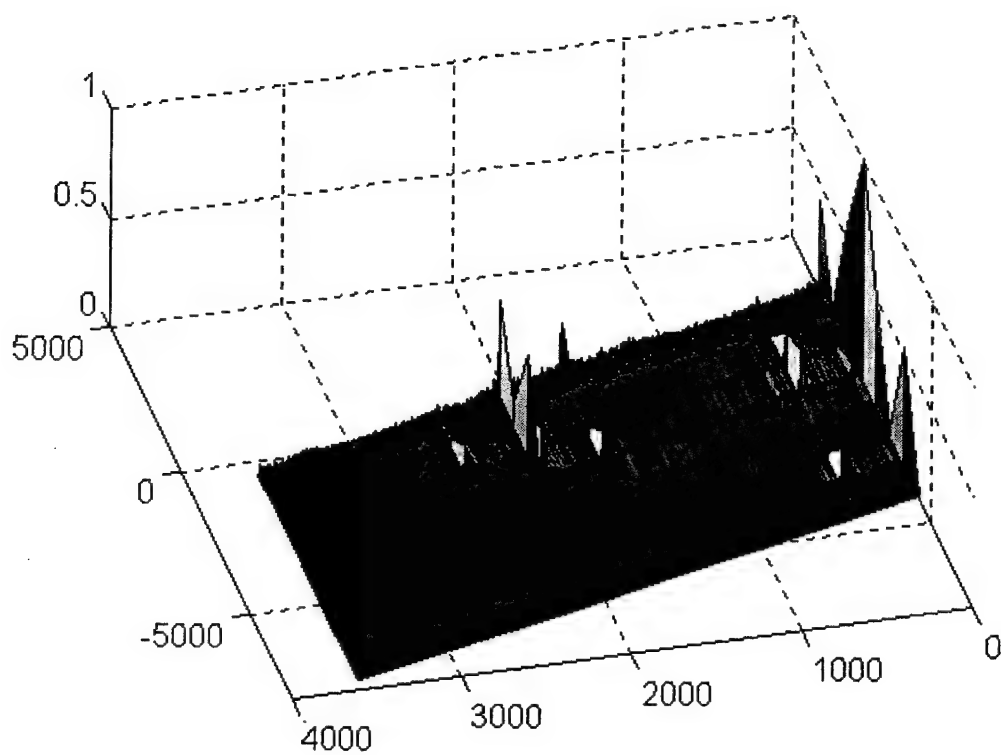


Figure B-79 - SCF for master (top) and slave #1 (bottom), time 409480

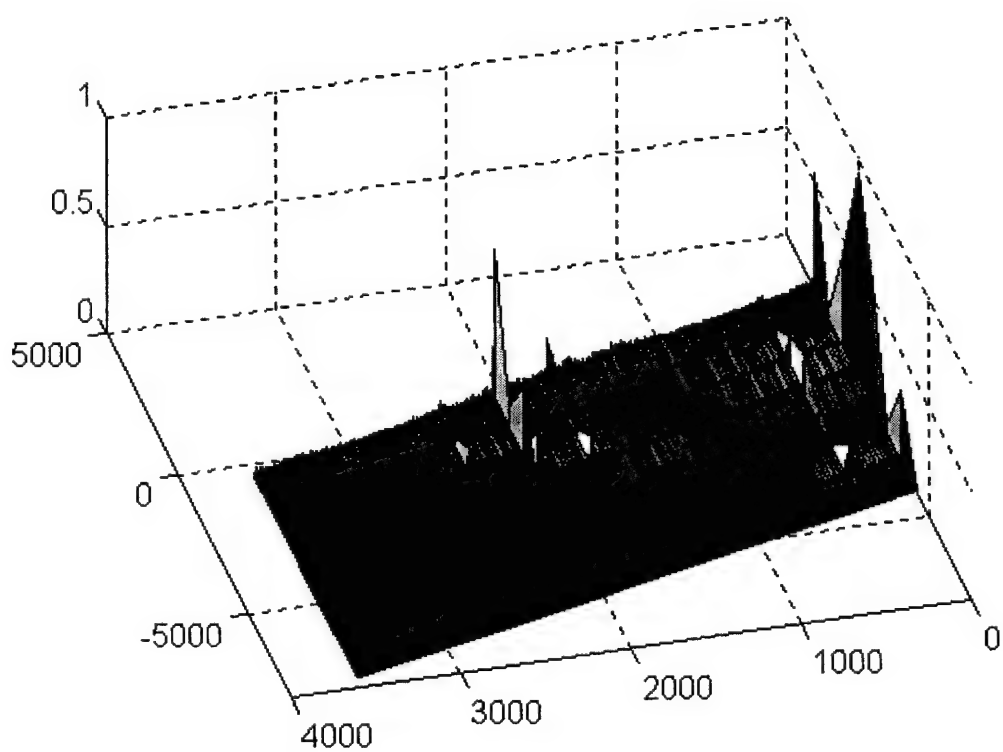
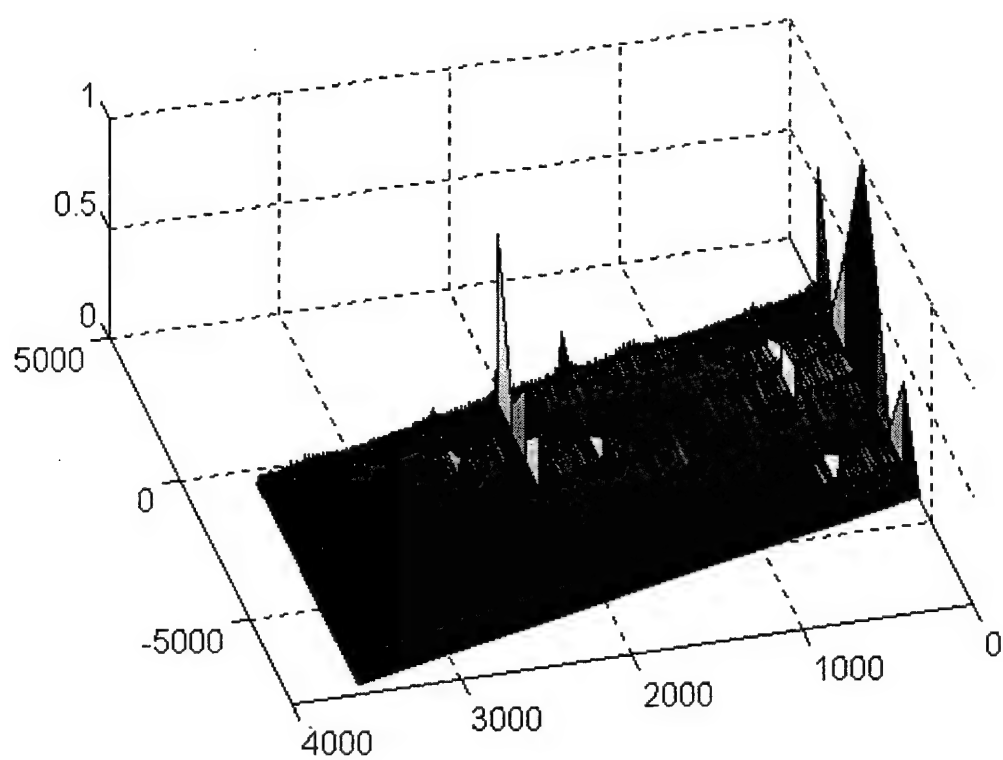


Figure B-80 - SCF for slave #2 (top) and slave #3 (bottom), time 409480

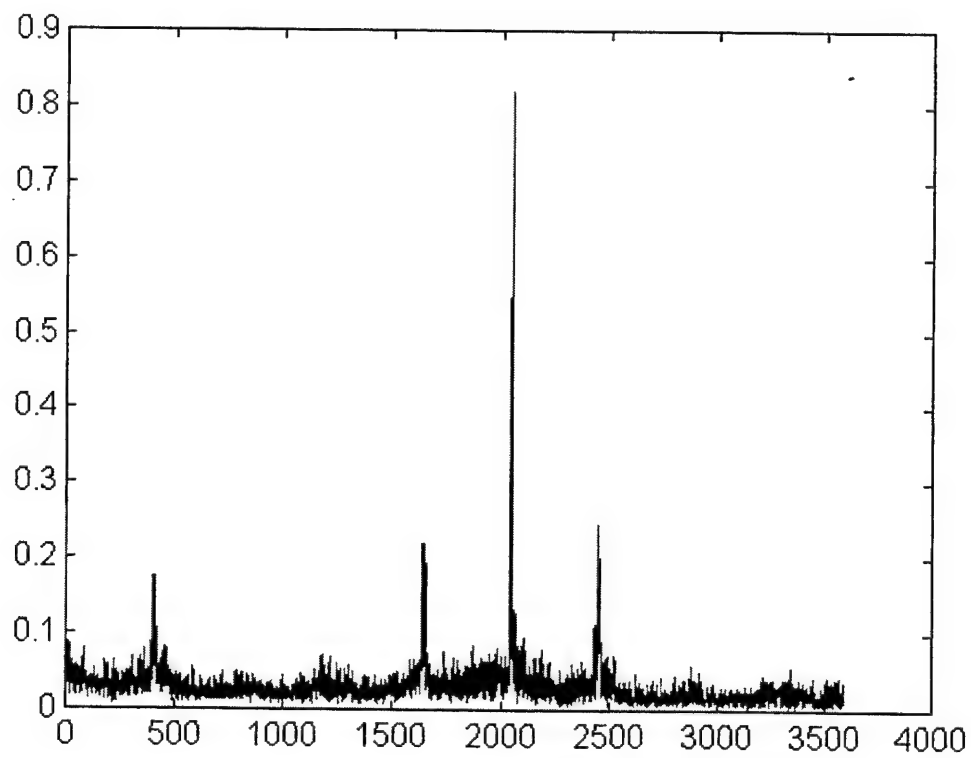
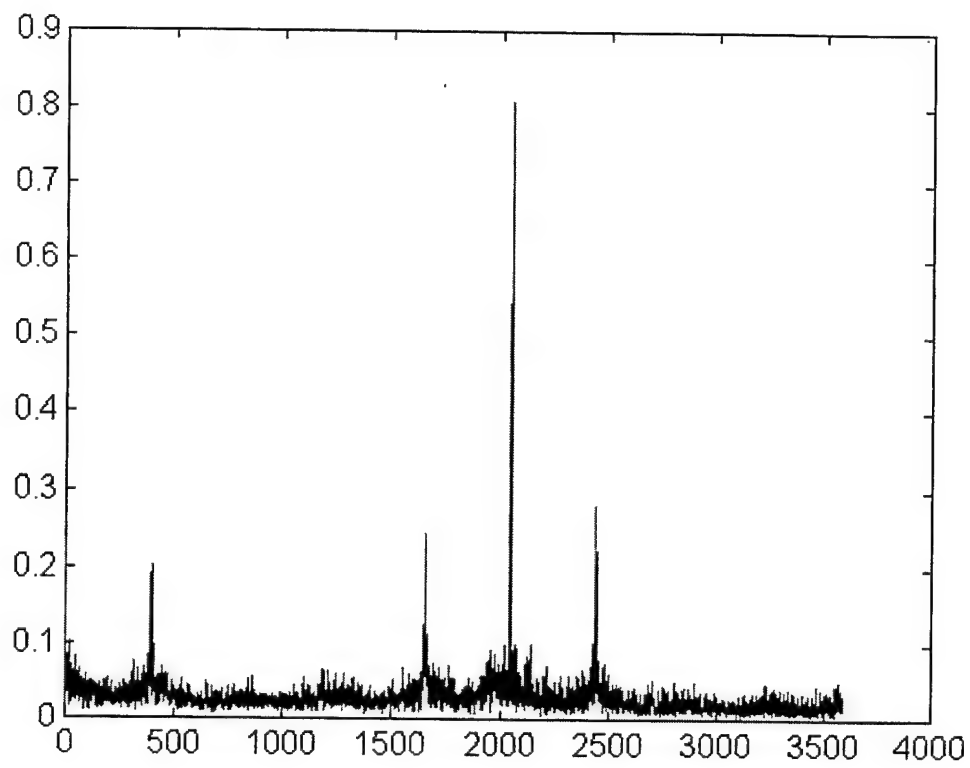


Figure B-81 - Cycle freq vs Max-magnitude of SCF for master (top) and slave #1 (bottom), time 409480

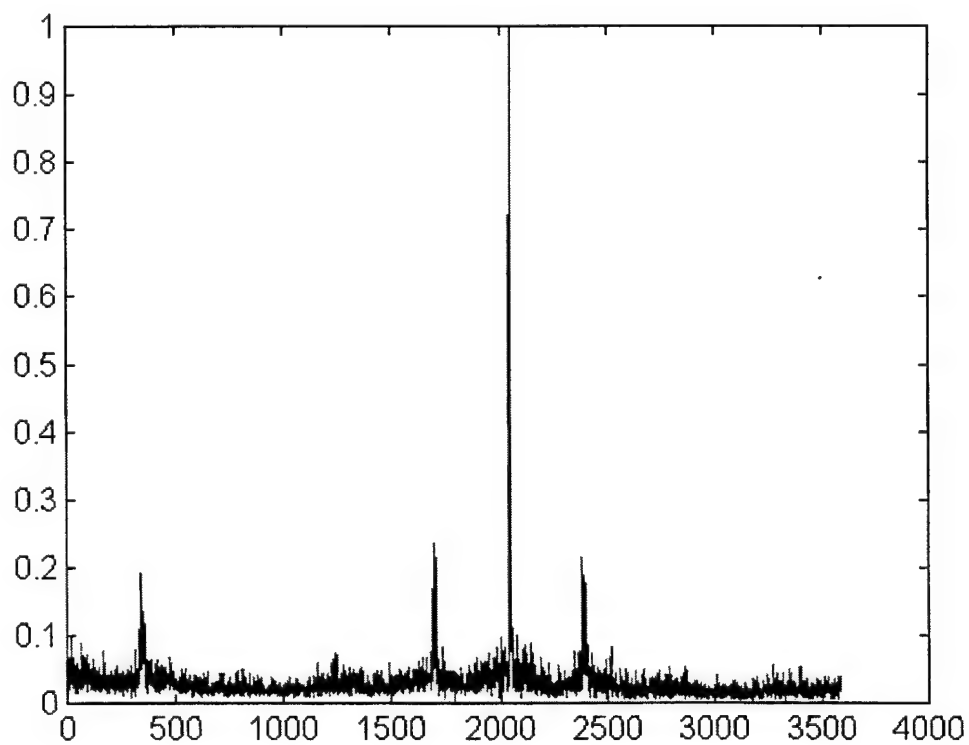
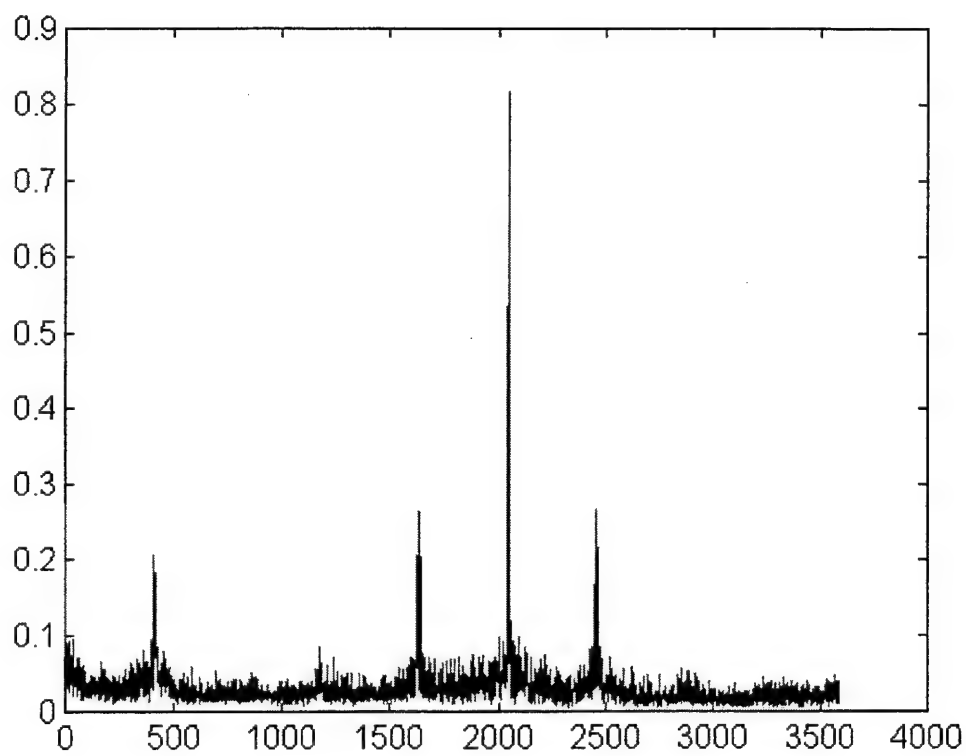


Figure B-82 - Cycle freq vs Max-magnitude of SCF for slave #2 (top) and slave #3 (bottom), time 409480

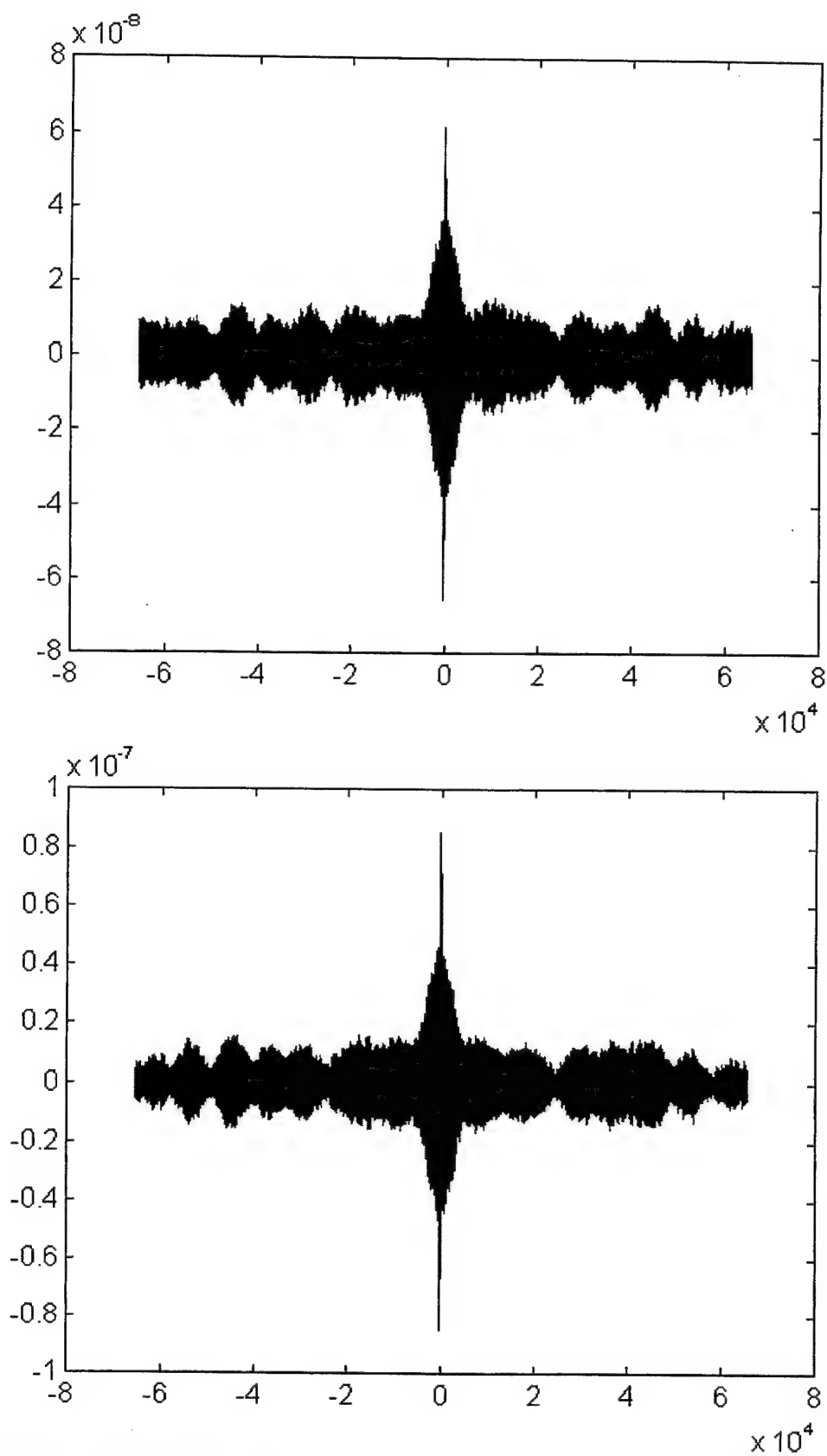


Figure B-83 - SPECCOA for master and slave #1 (top) and master and slave #2 (bottom), time 409480

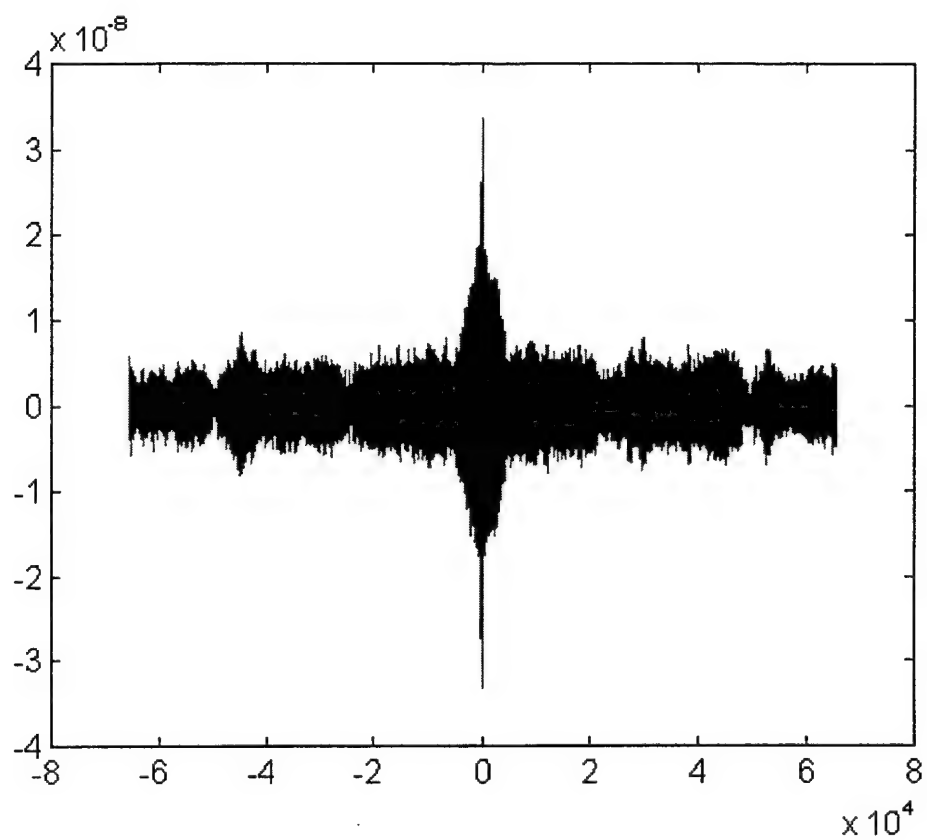


Figure B-84 - SPECCOA for master and slave #3, time 409480

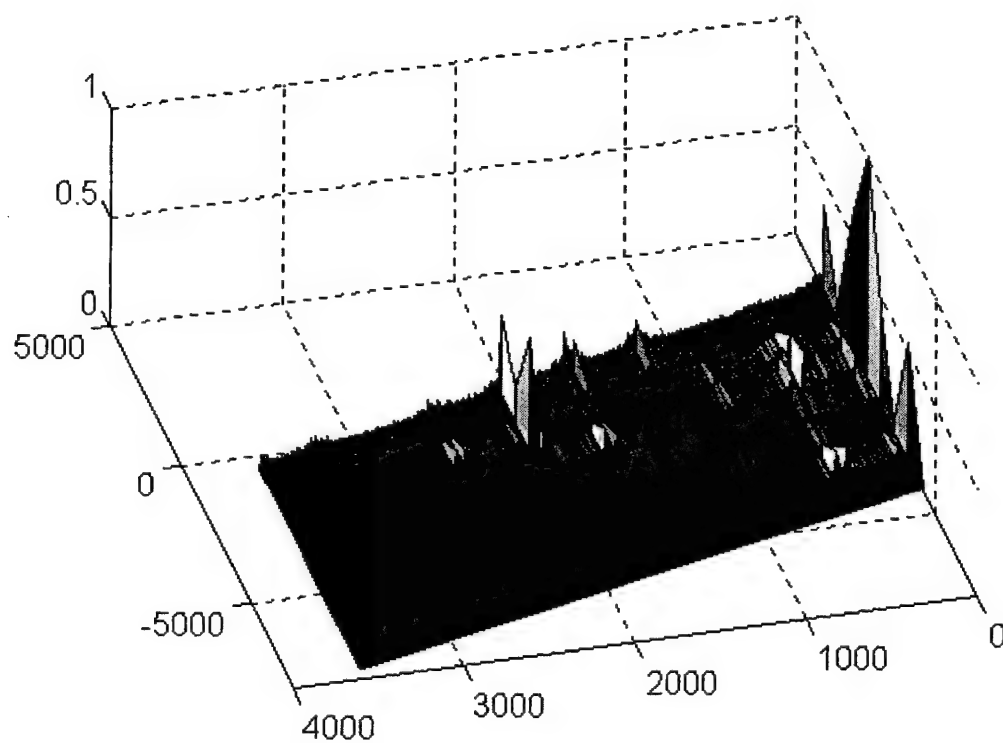
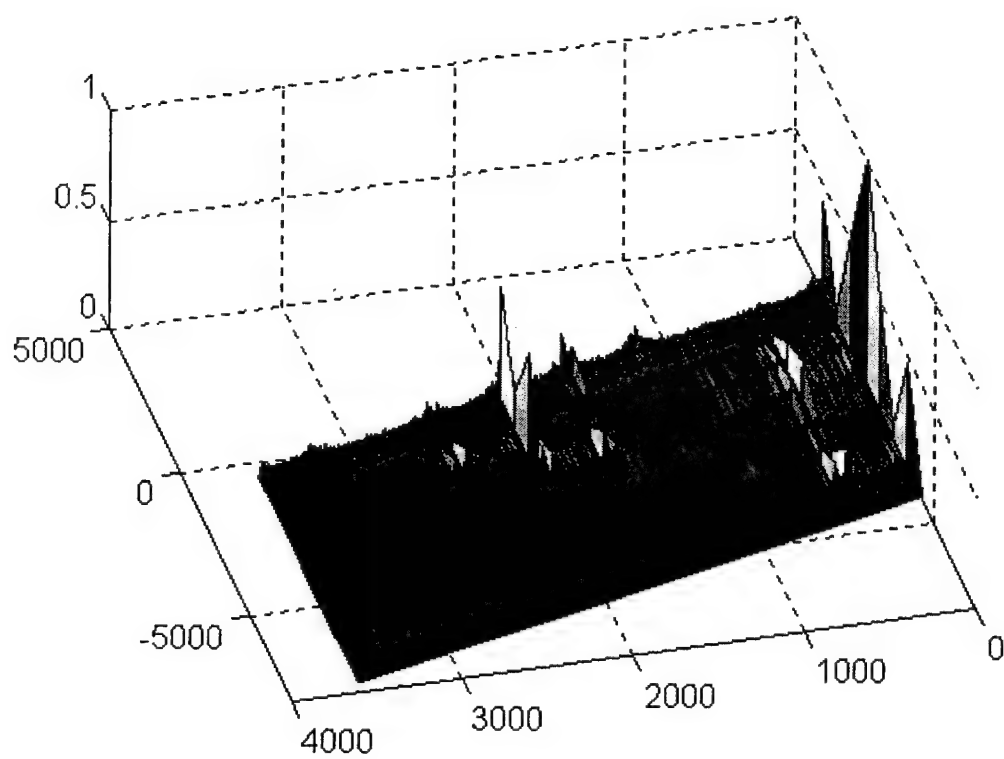


Figure B-85 - SCF for master (top) and slave #1 (bottom), time 409485

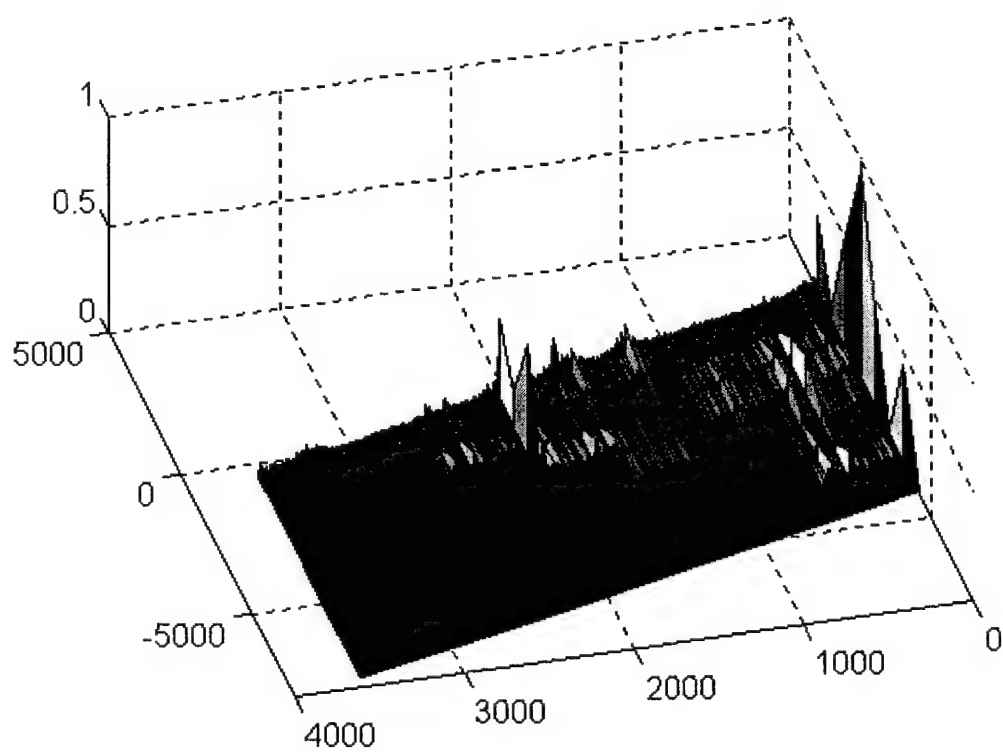
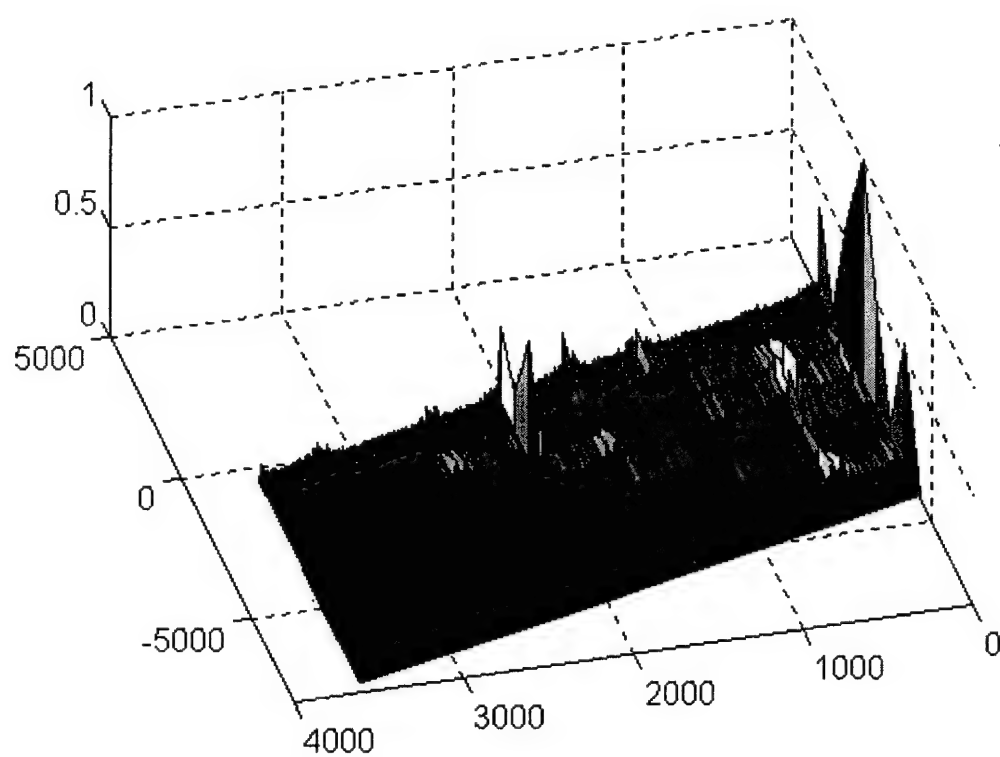


Figure B-86 - SCF for slave #2 (top) and slave #3 (bottom), time 409485

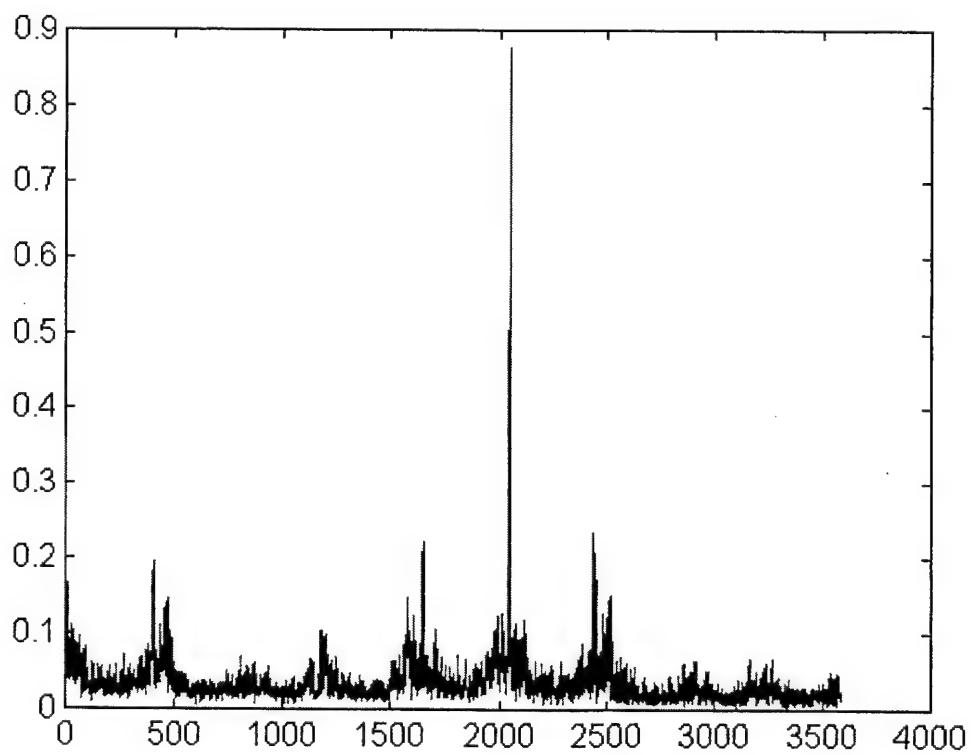
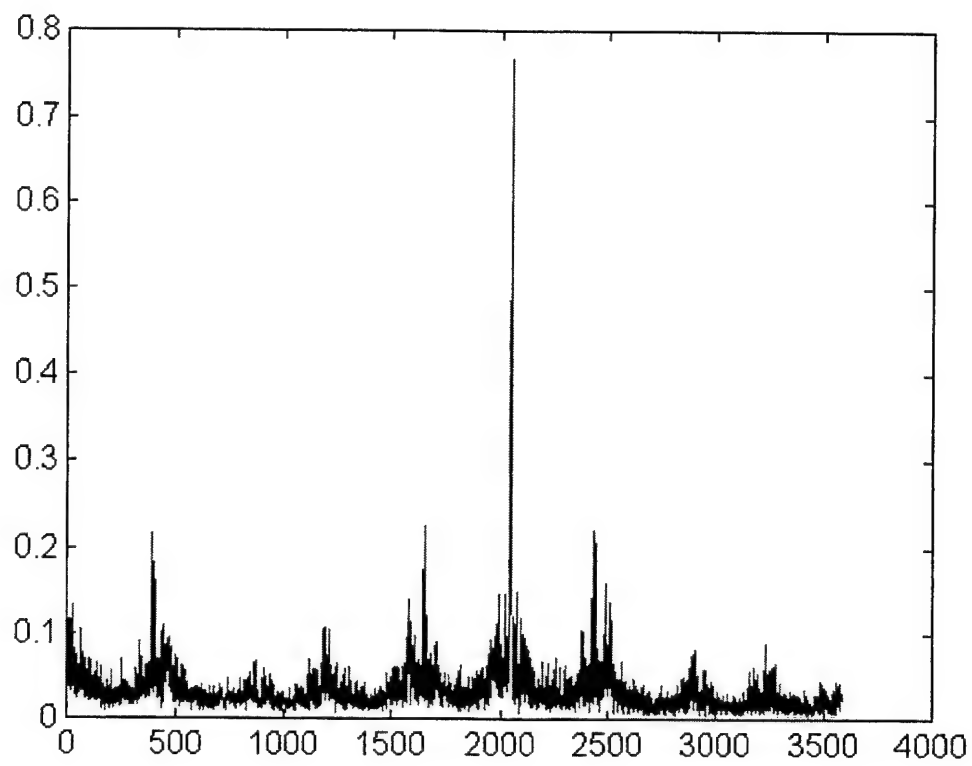


Figure B-87 - Cycle freq vs Max-magnitude of SCF for master (top) and slave #1 (bottom), time 409485

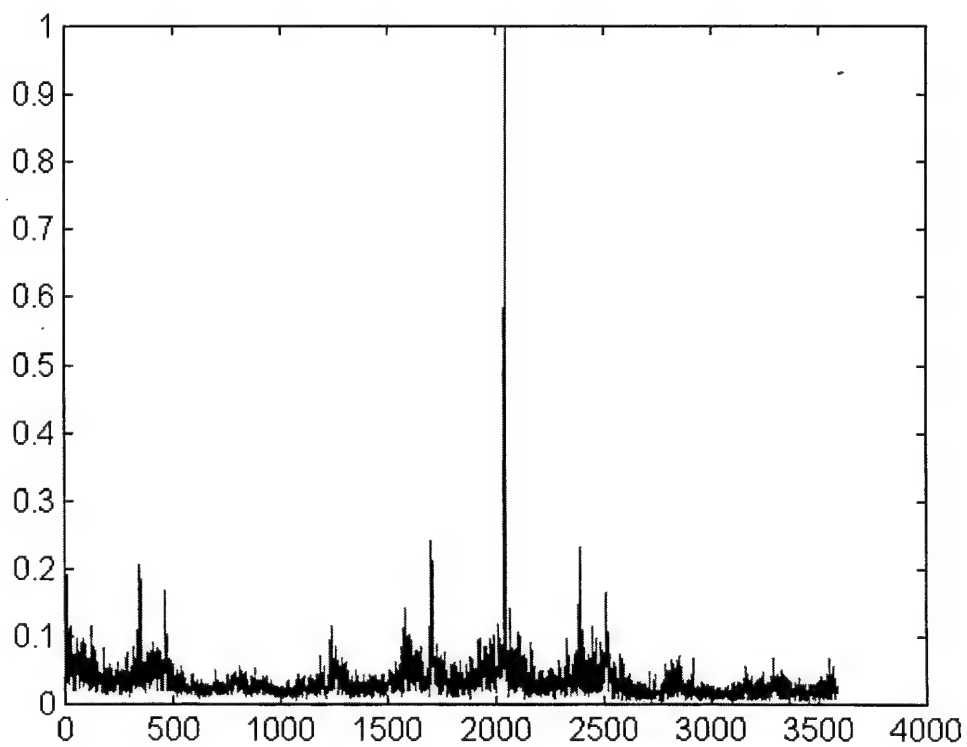
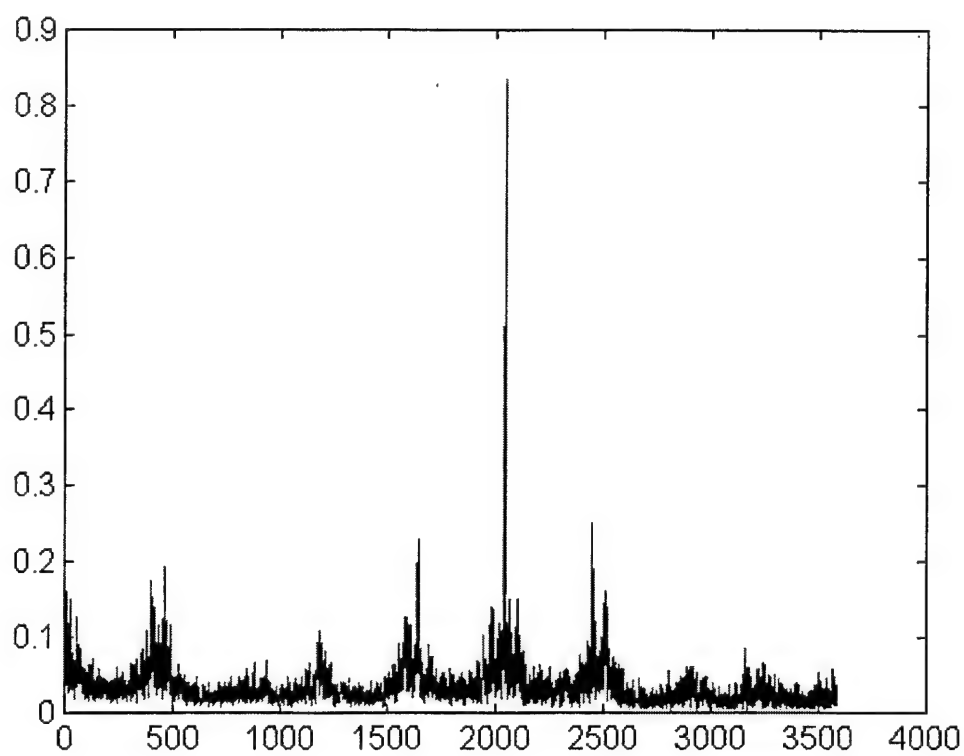


Figure B-88 - Cycle freq vs Max-magnitude of SCF for slave #2 (top) and slave #3 (bottom), time 409485

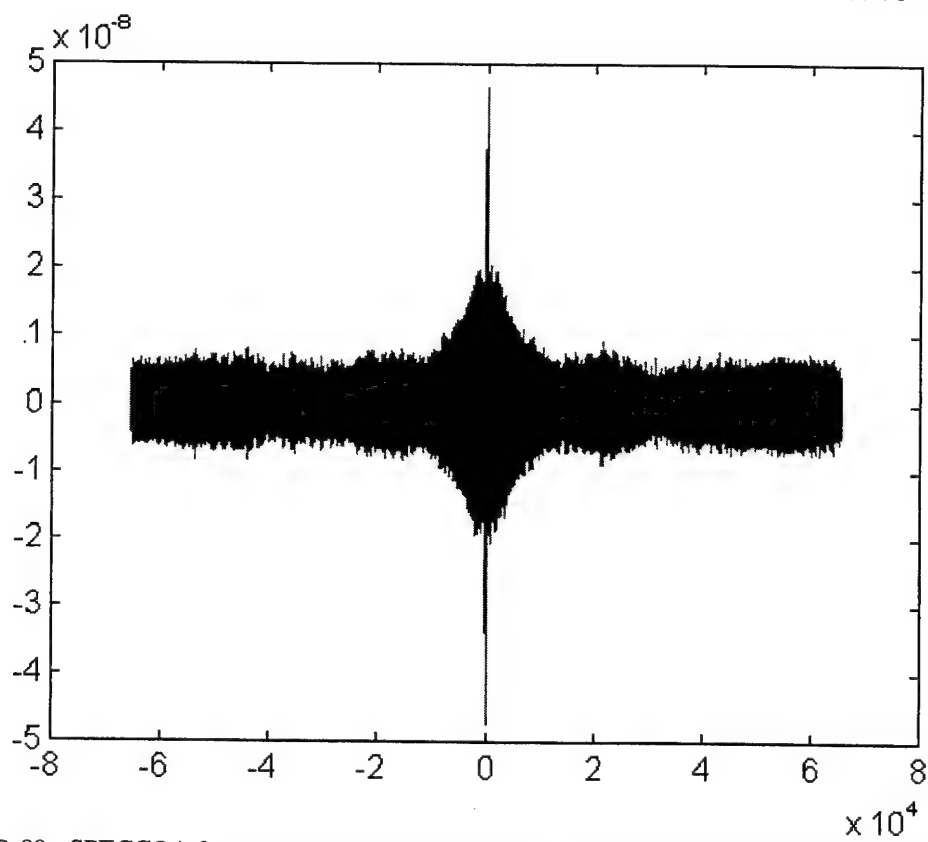
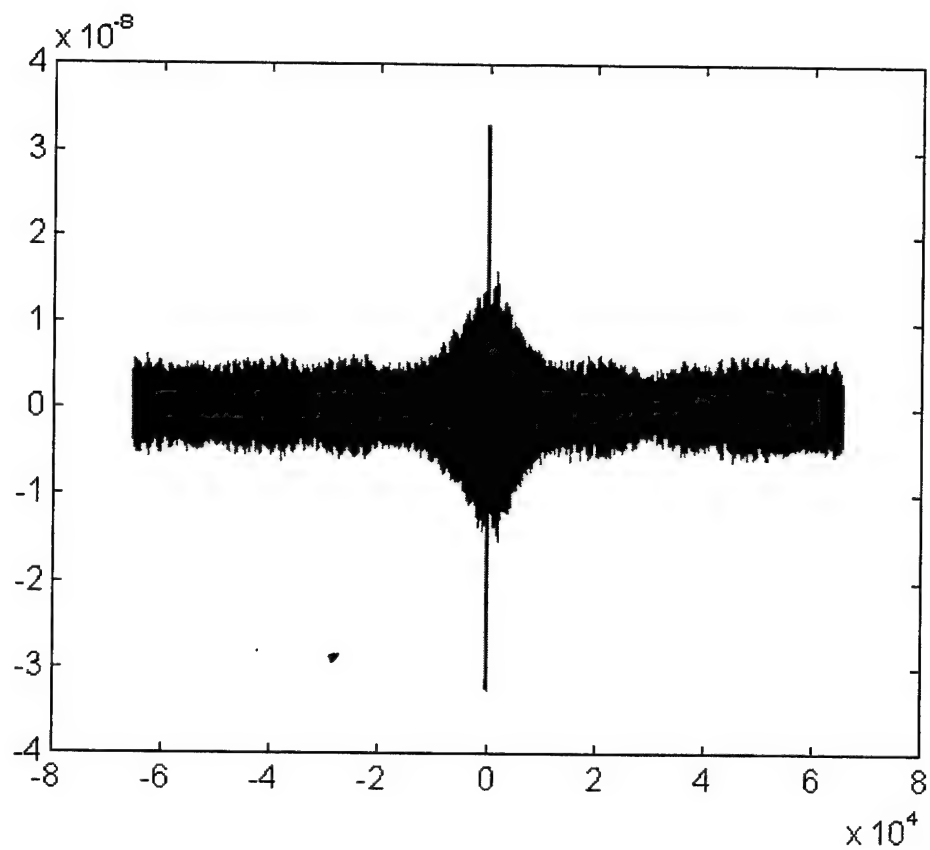


Figure B-89 - SPECCOA for master and slave #1 (top) and master and slave #2 (bottom), time 409485

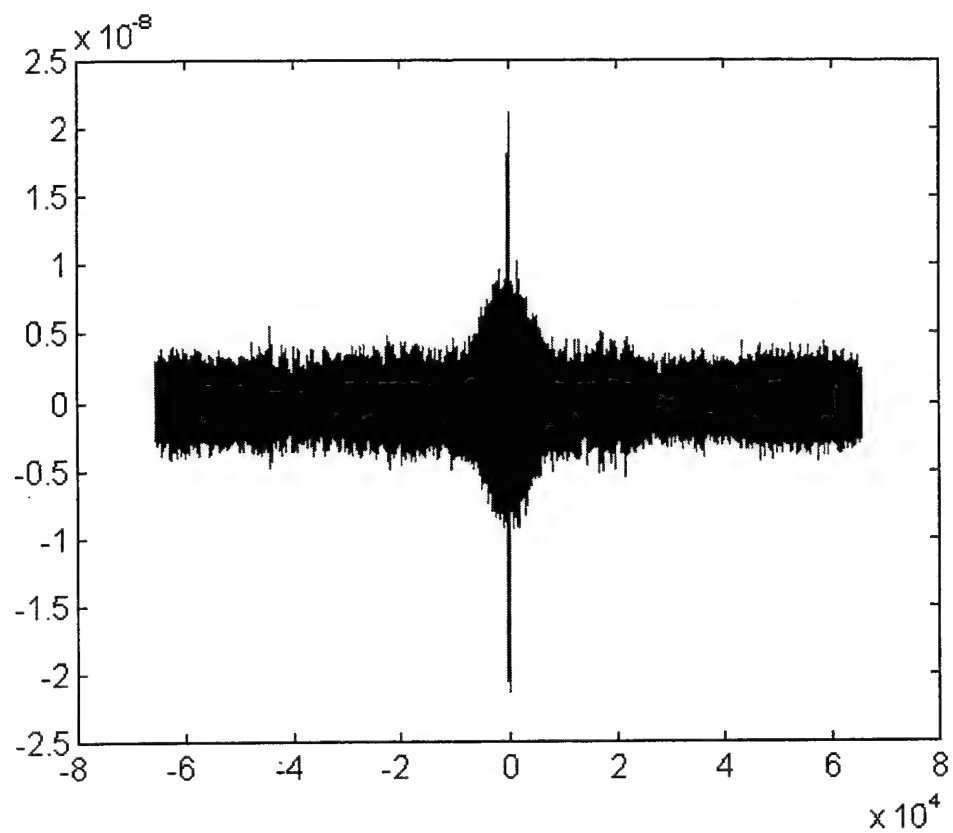


Figure B-90 - SPECCOA for master and slave #3, time 409485

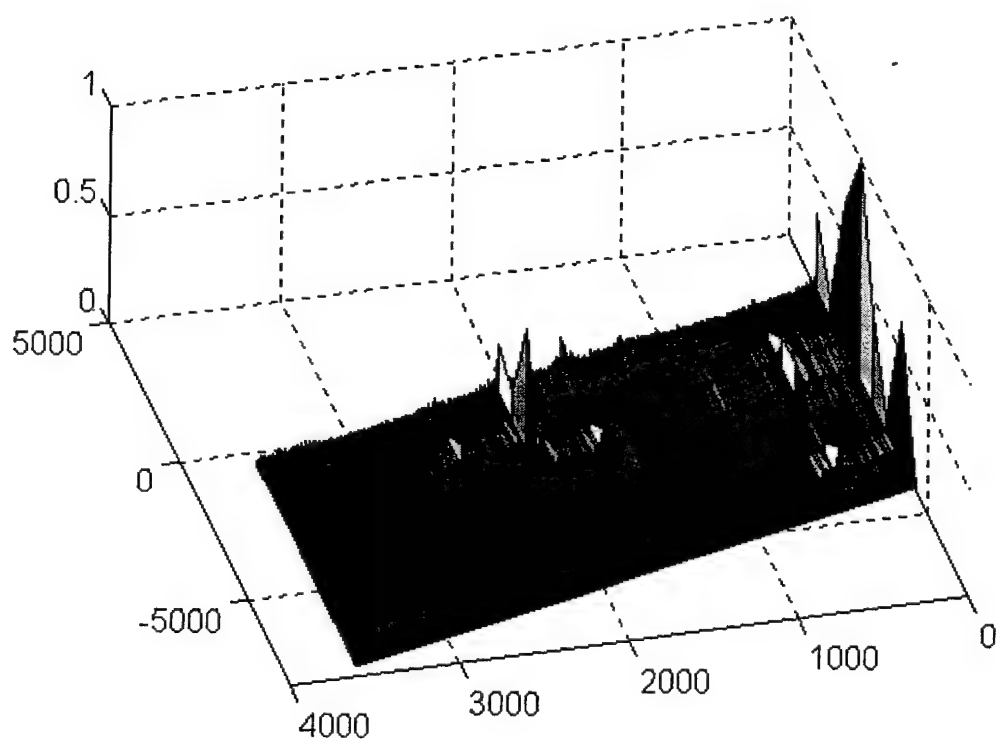
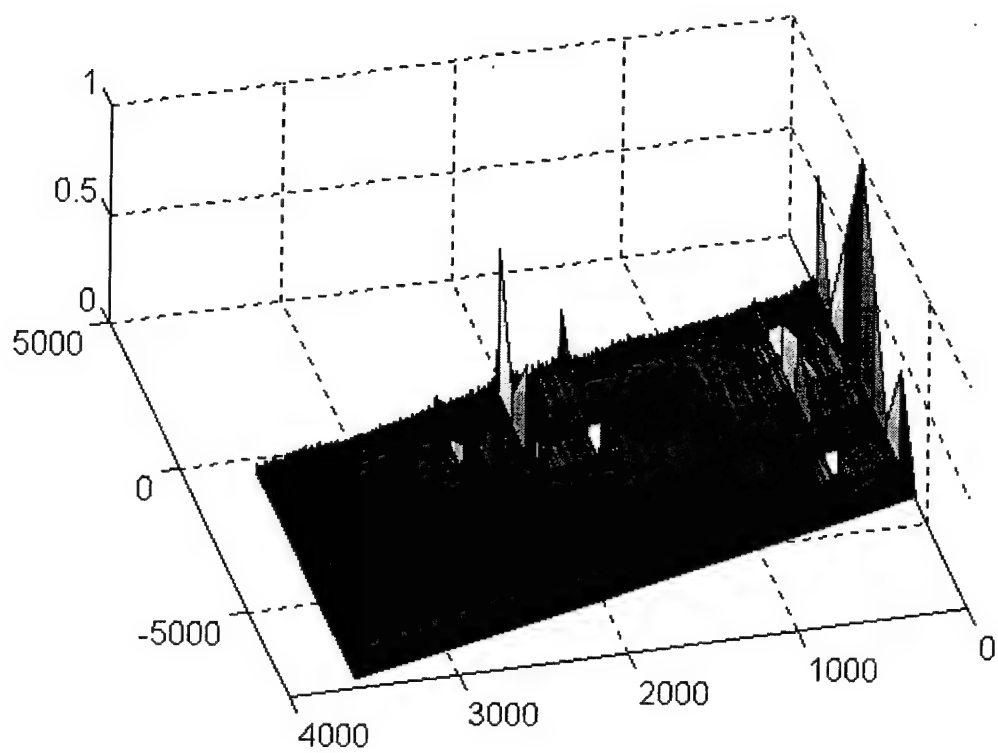


Figure B-91 - SCF for master (top) and slave #1 (bottom), time 409490

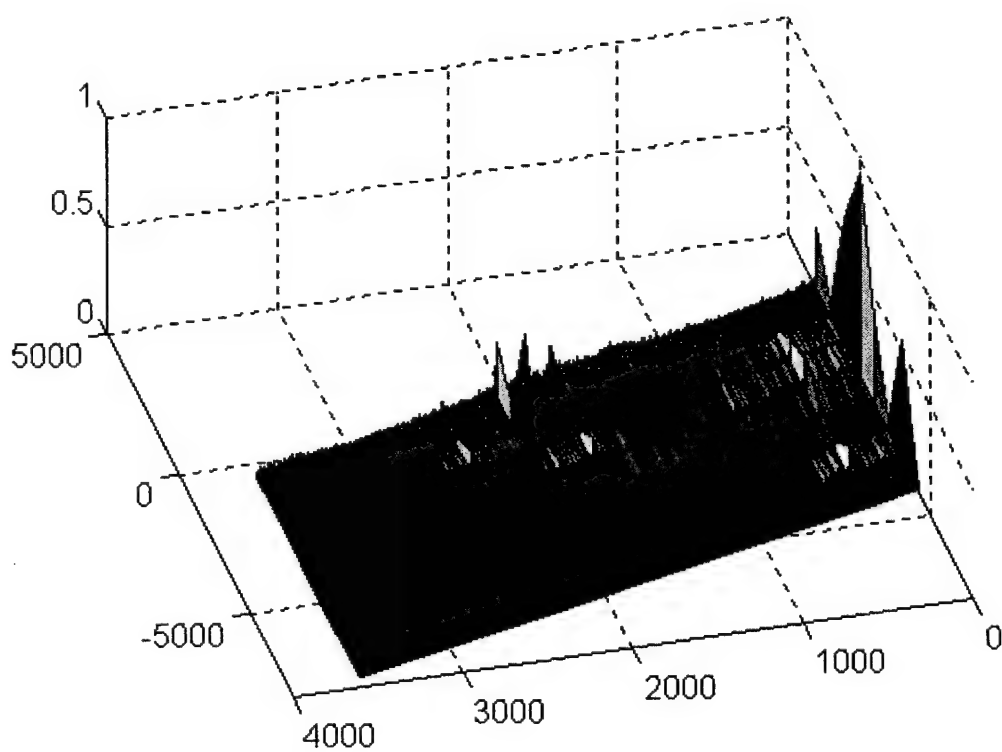
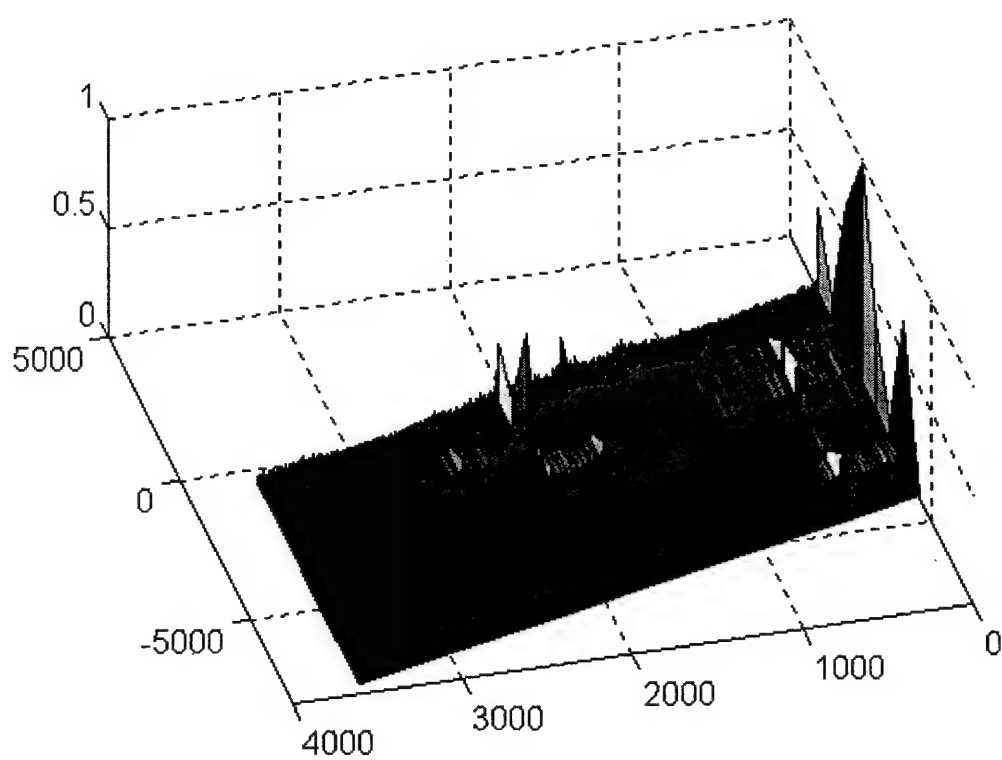


Figure B-92 - SCF for slave #2 (top) and slave #3 (bottom), time 409490

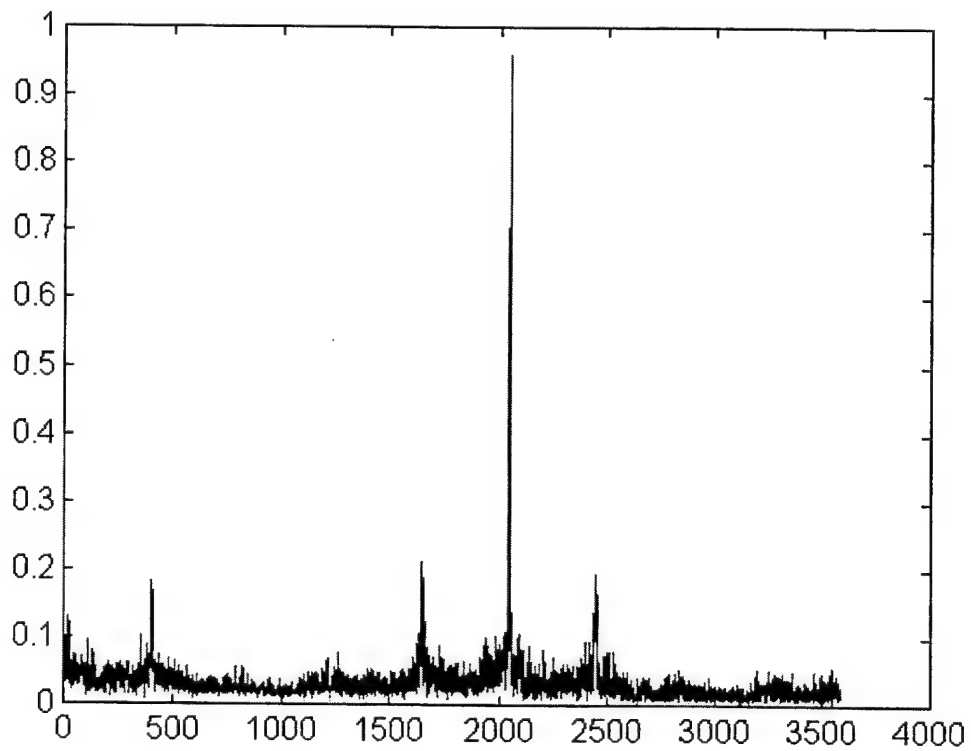
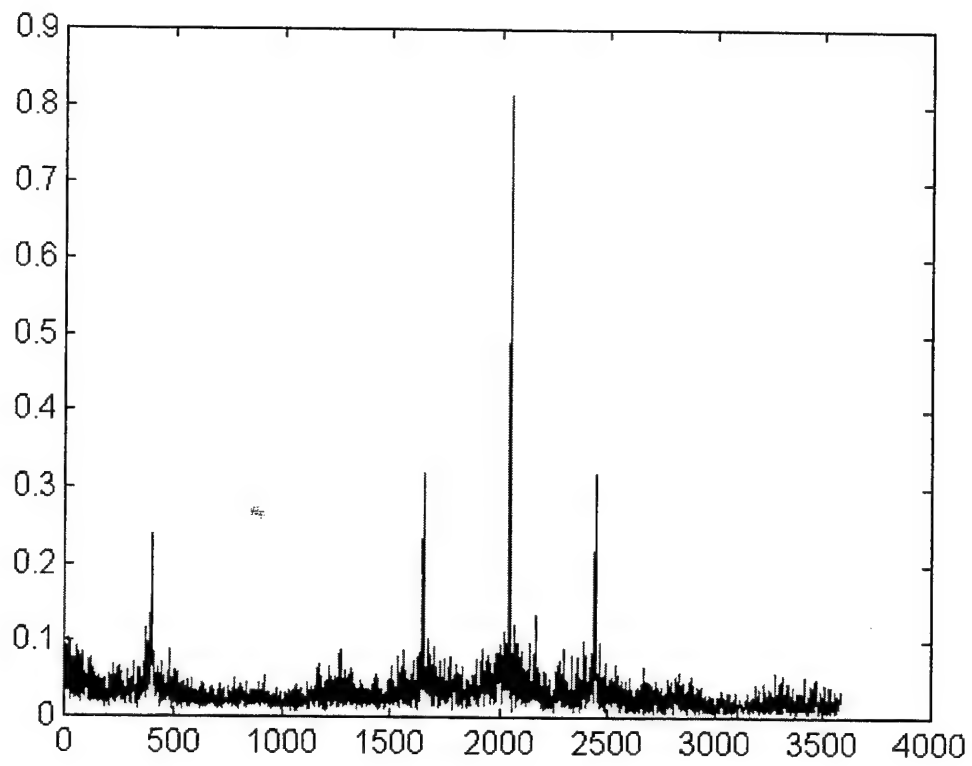


Figure B-93 - Cycle freq vs Max-magnitude of SCF for master (top) and slave #1 (bottom), time 409490

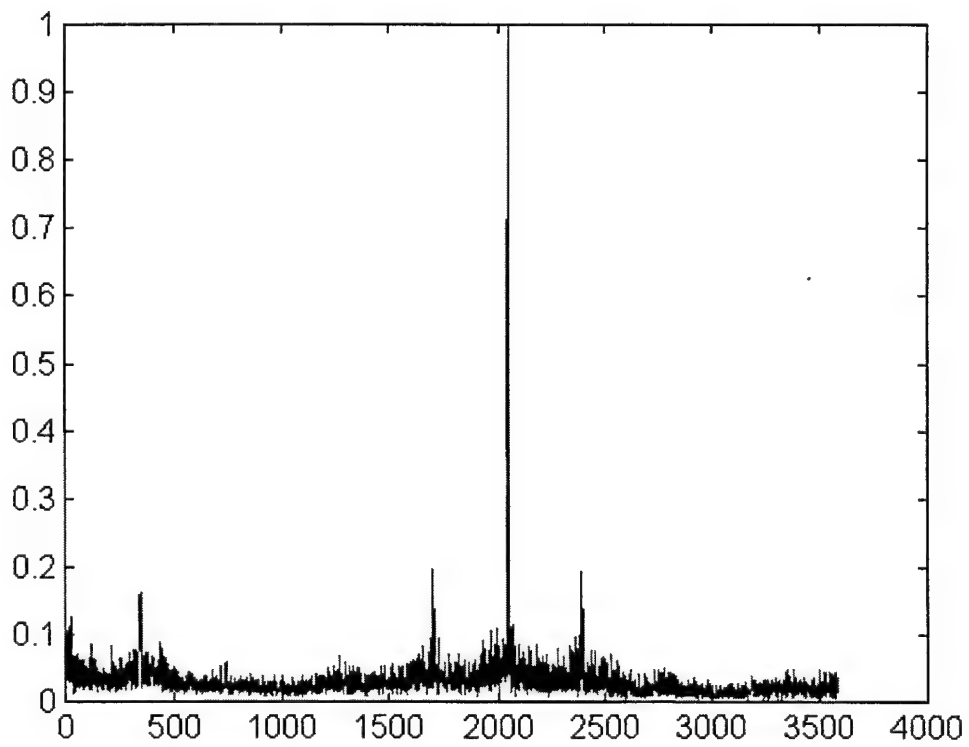
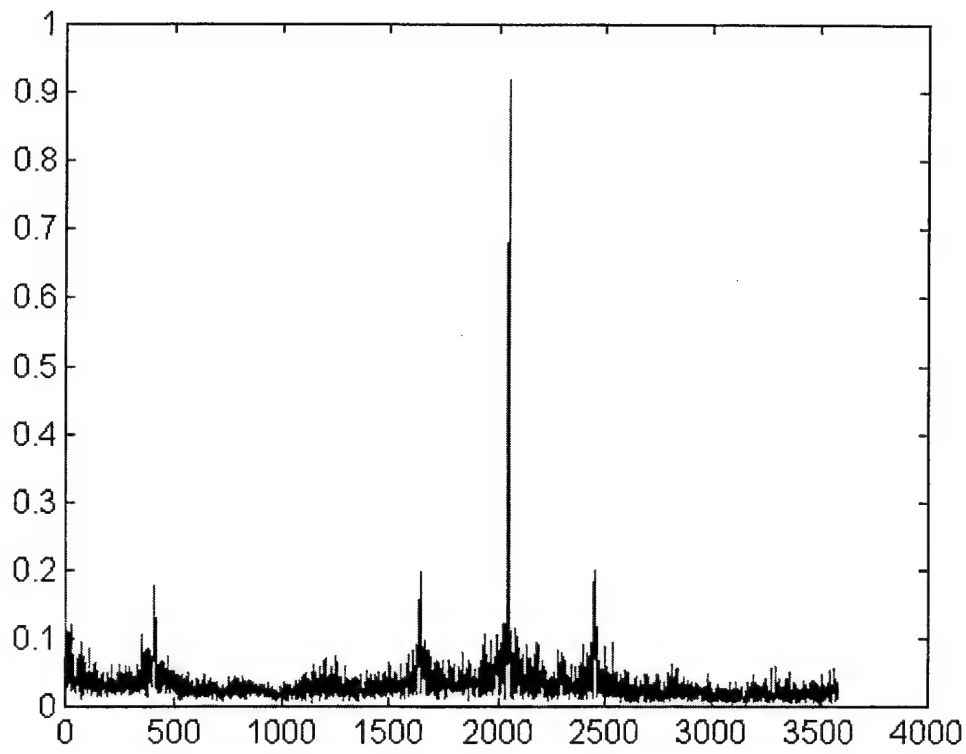


Figure B-94 - Cycle freq vs Max-magnitude of SCF for slave #2 (top) and slave #3 (bottom), time 409490

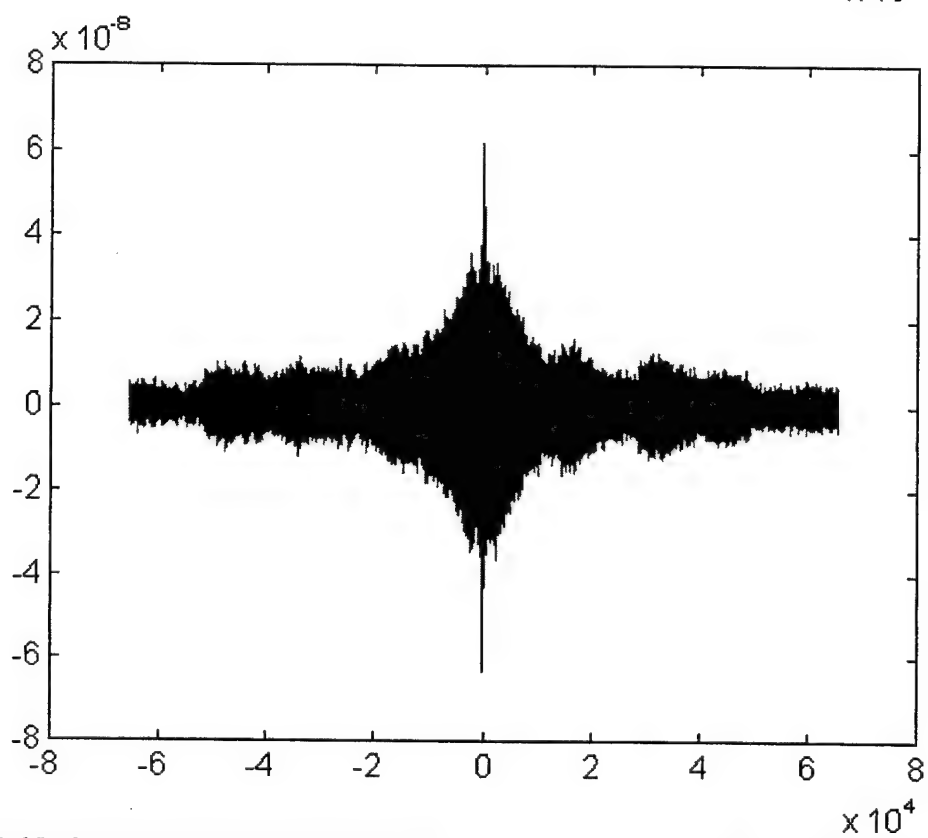
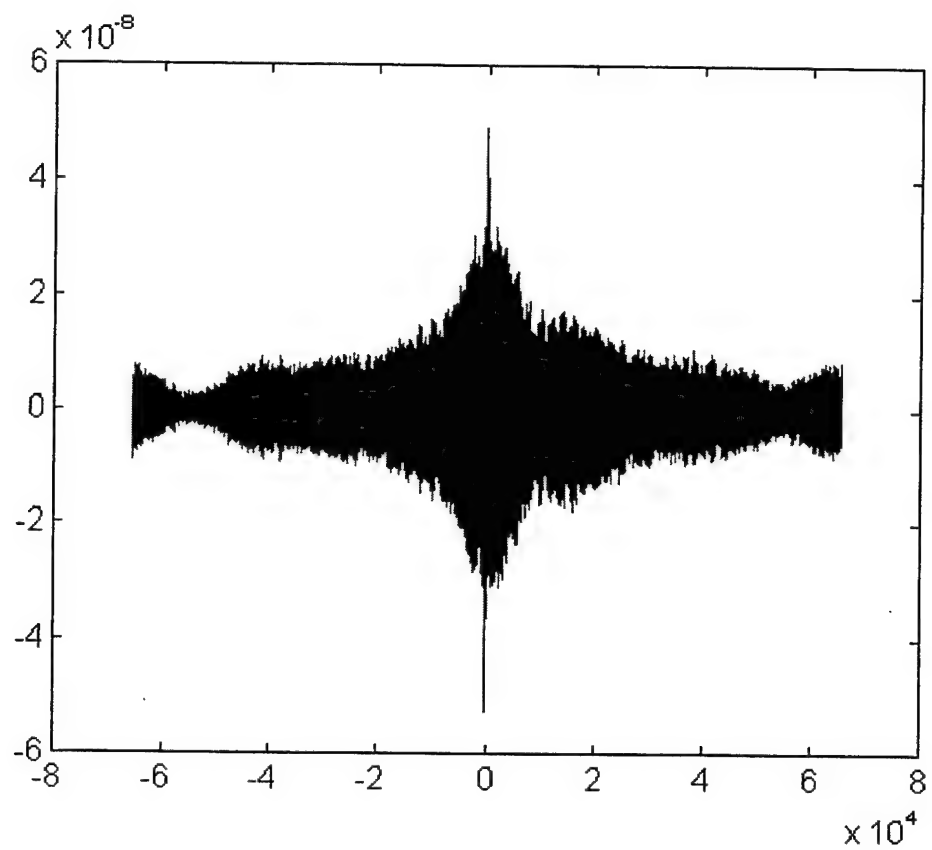


Figure B-95 - SPECCOA for master and slave #1 (top) and master and slave #2 (bottom), time 409490

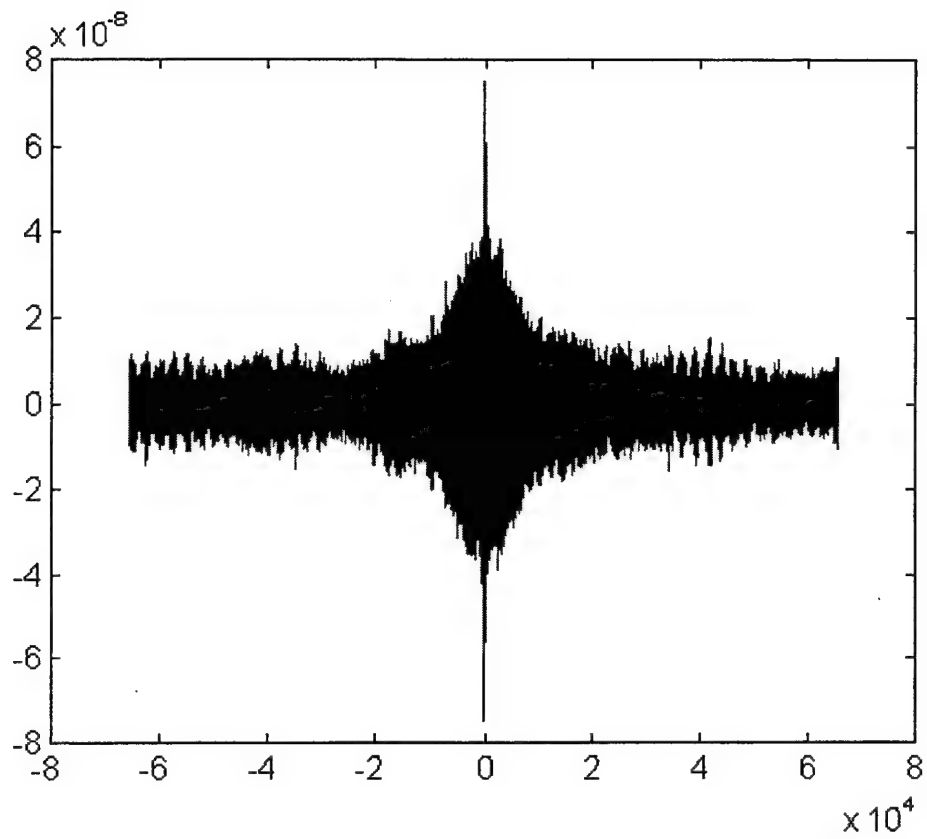


Figure B-96 - SPECCOA for master and slave #3, time 409490

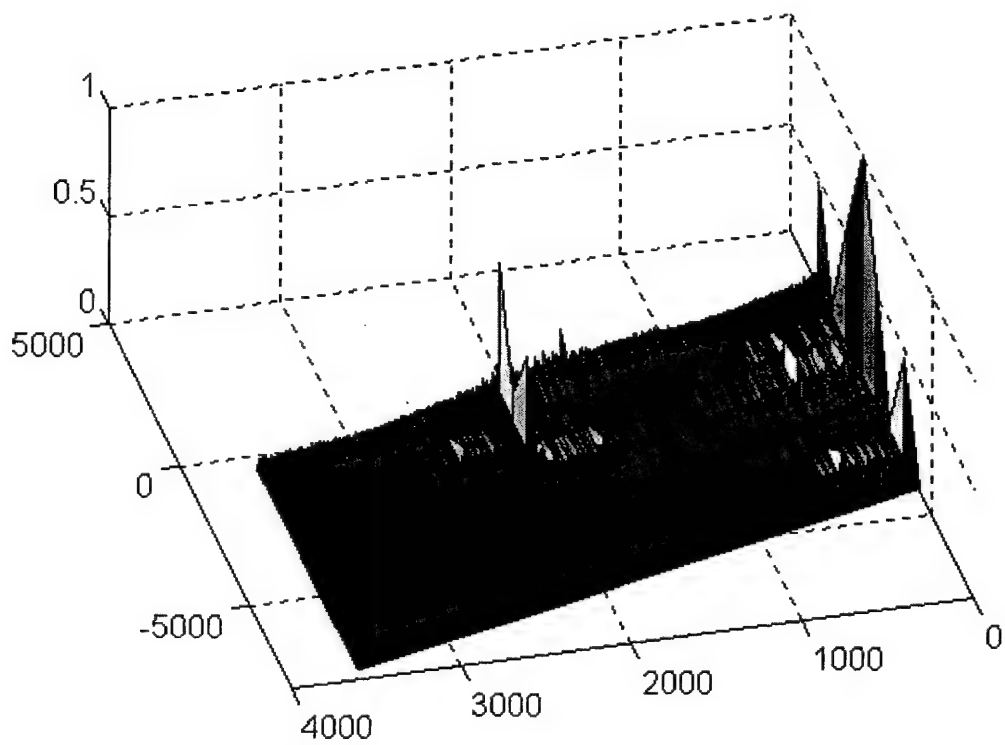
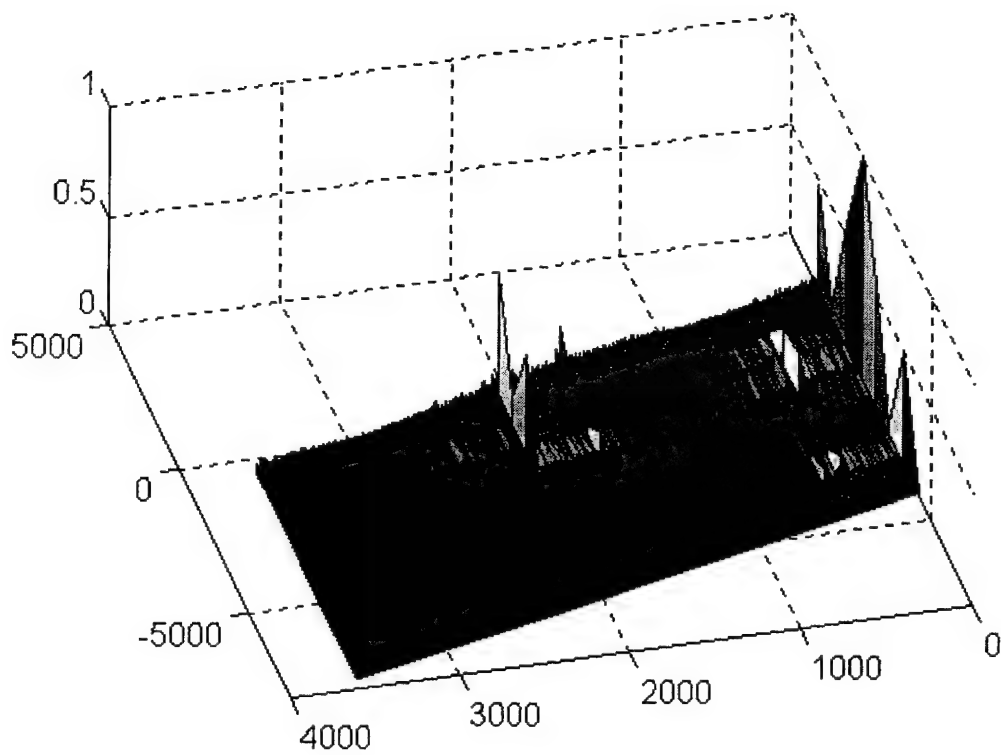


Figure B-97 - SCF for master (top) and slave #1 (bottom), time 409495

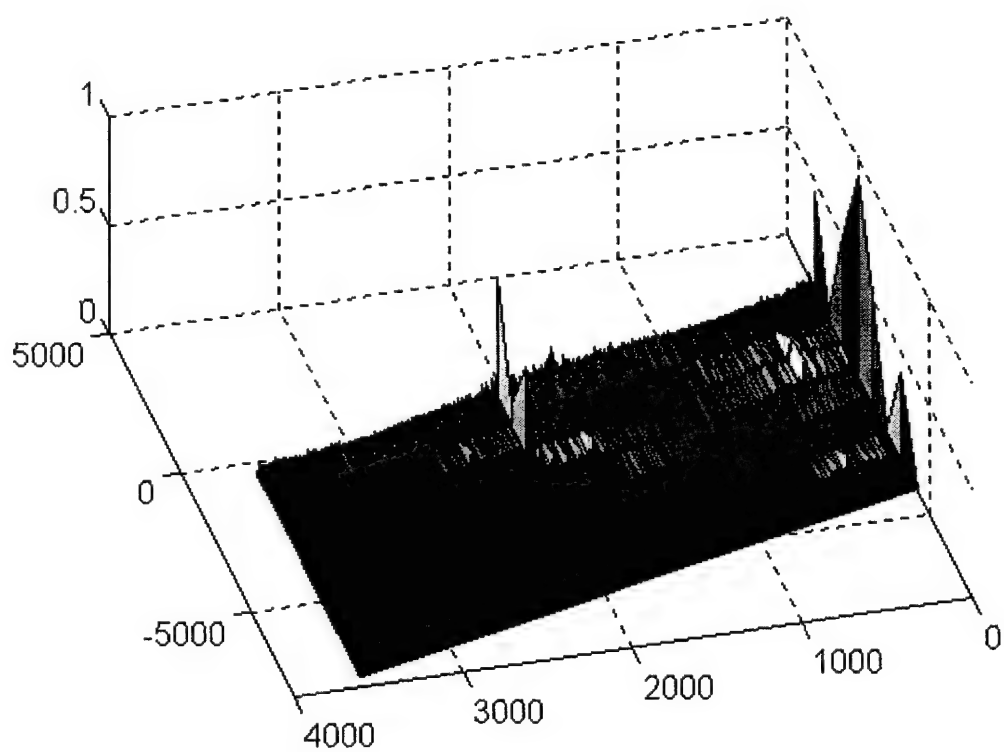
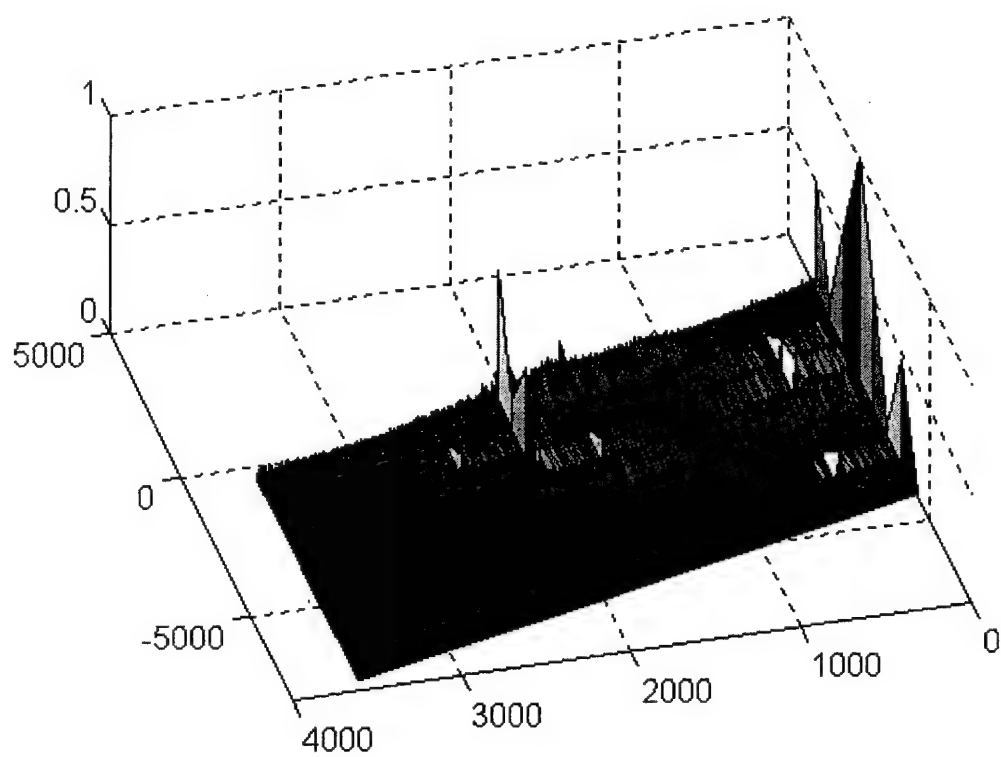


Figure B-98 - SCF for slave #2 (top) and slave #3 (bottom), time 409495

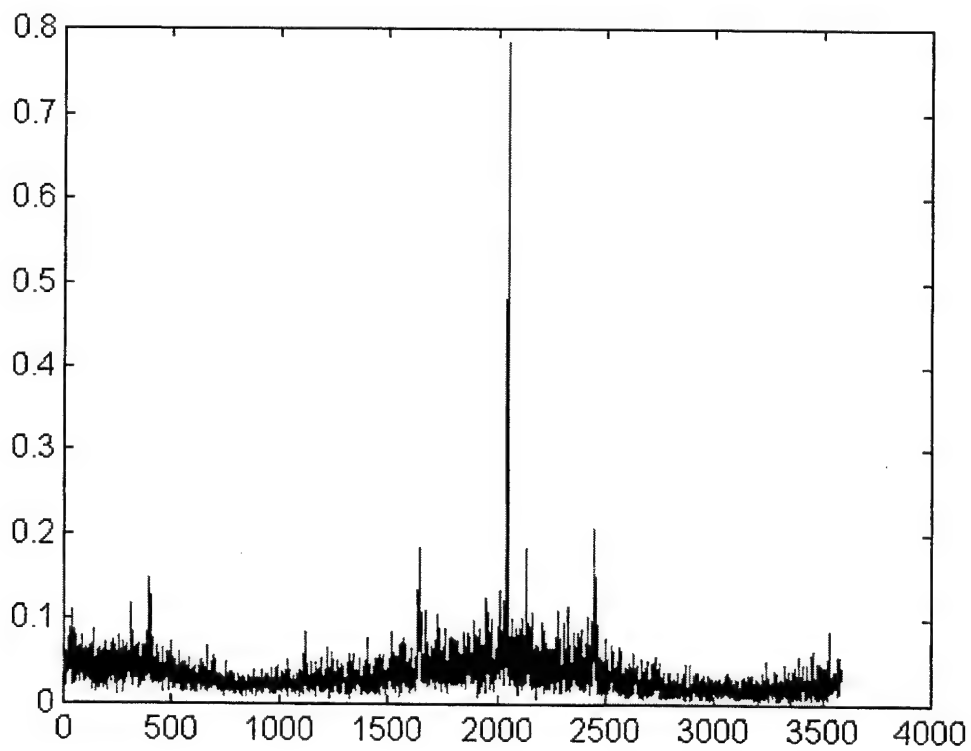
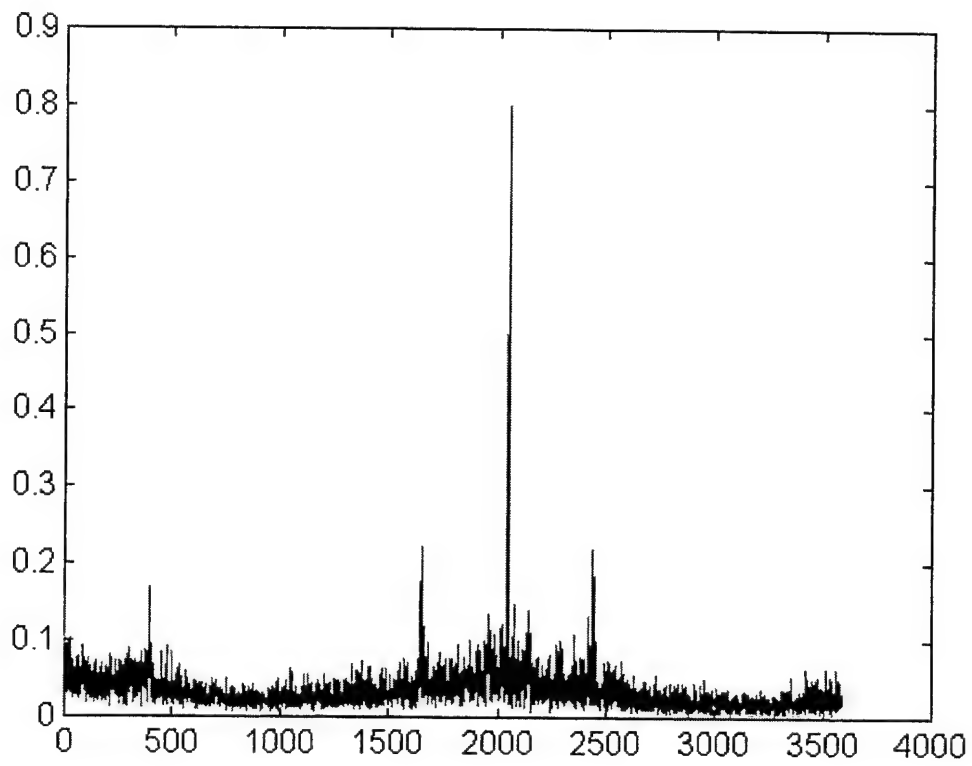


Figure B-99 - Cycle freq vs Max-magnitude of SCF for master (top) and slave #1 (bottom), time 409495

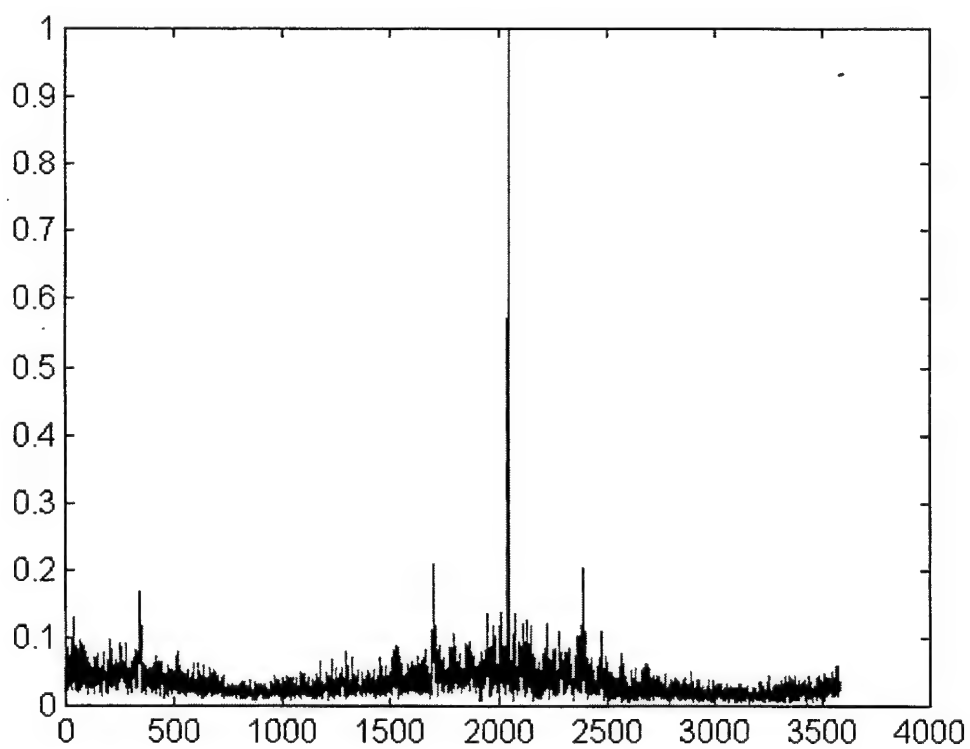
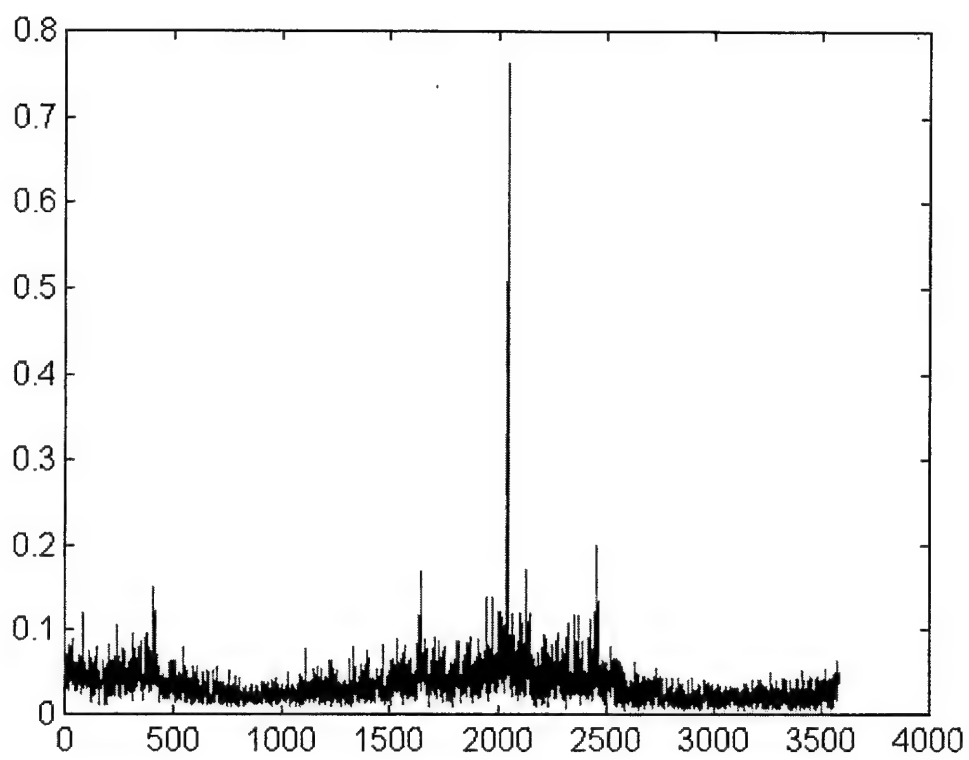


Figure B-100 - Cycle freq vs Max-magnitude of SCF for slave #2 (top) and slave #3 (bottom), time 409495

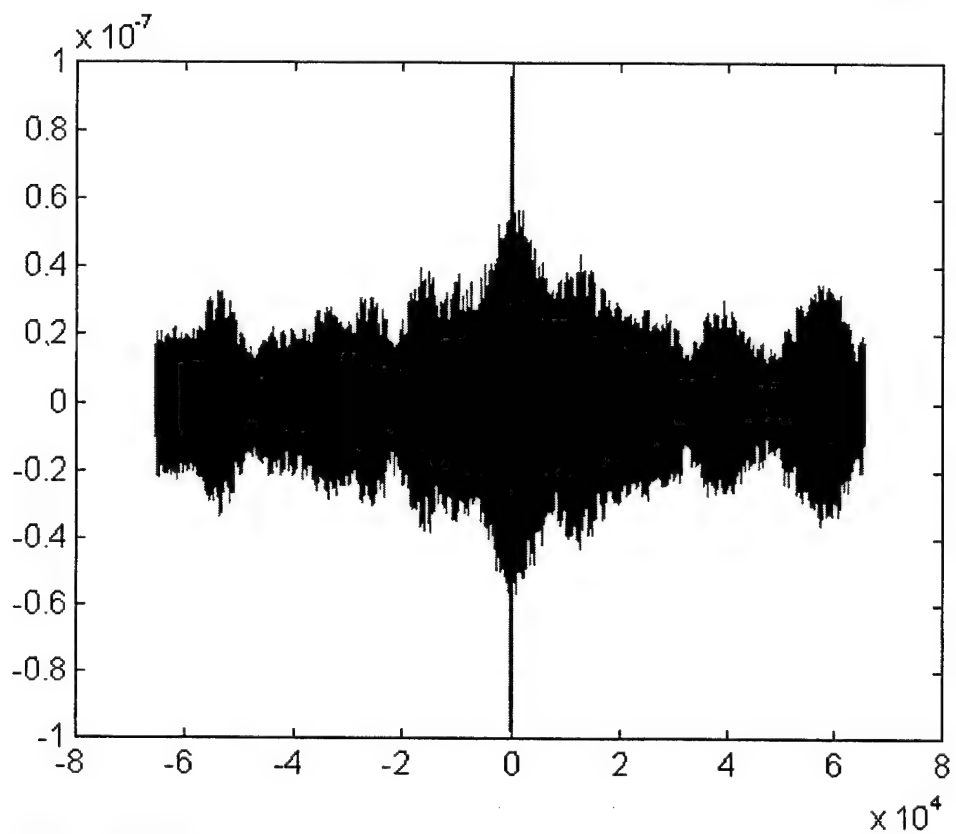
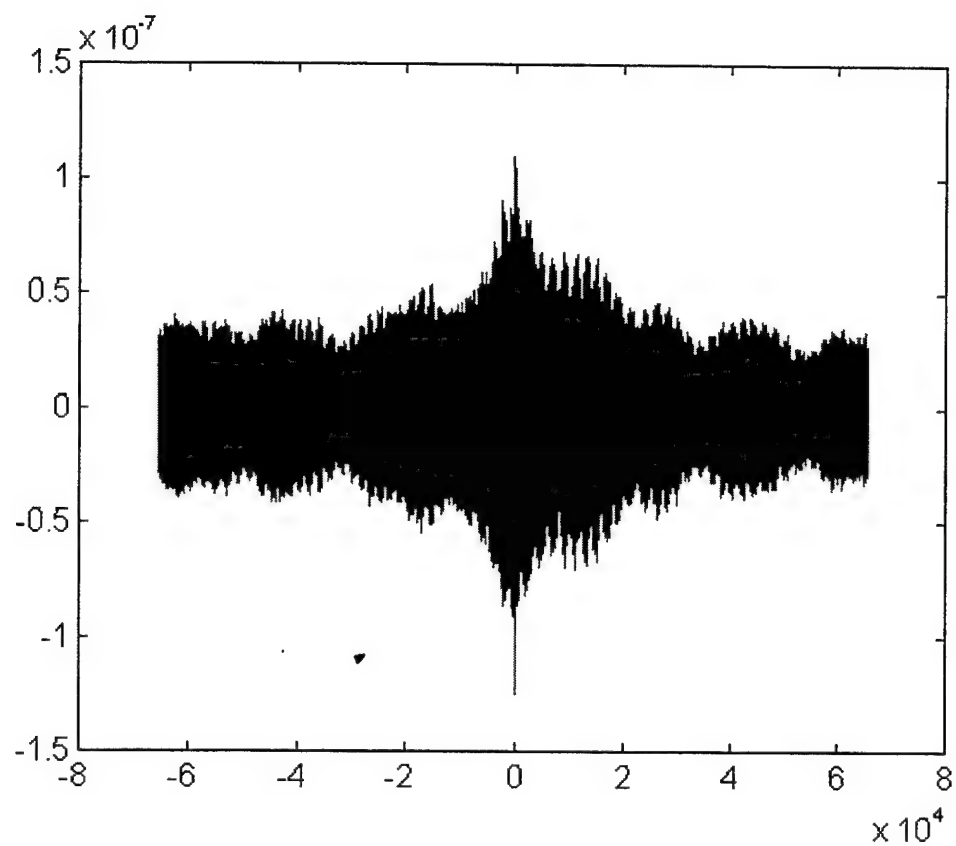


Figure B-101 - SPECCOA for master and slave #1 (top) and master and slave #2 (bottom), time 409495

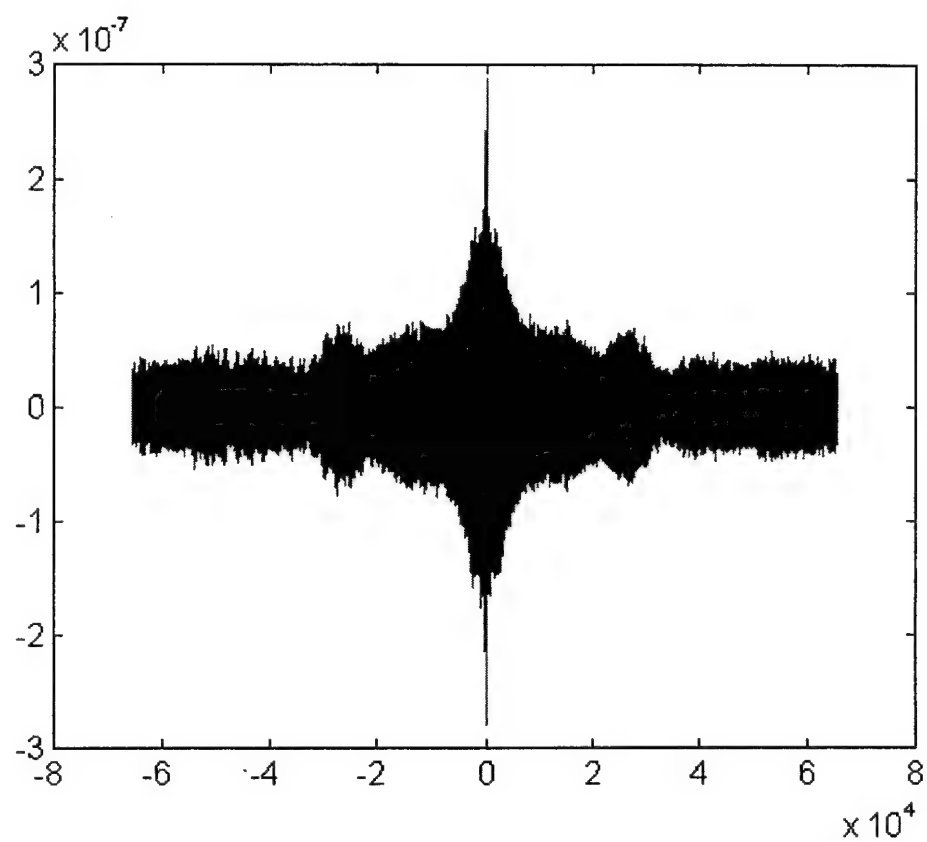


Figure B-102 - SPECCOA for master and slave #3, time 409495

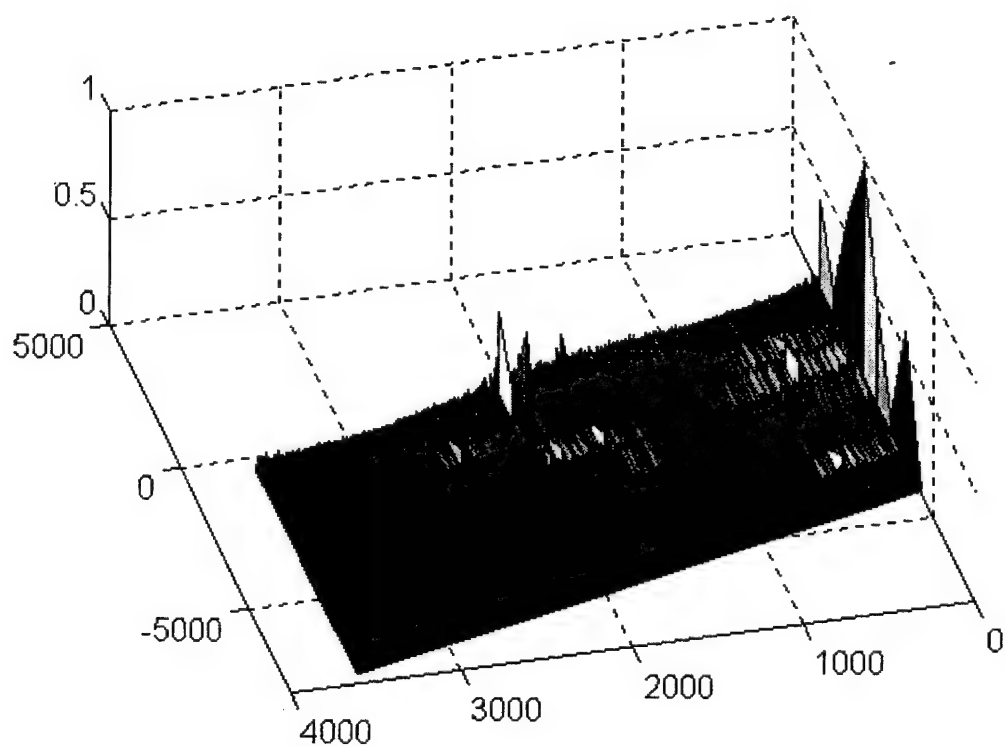
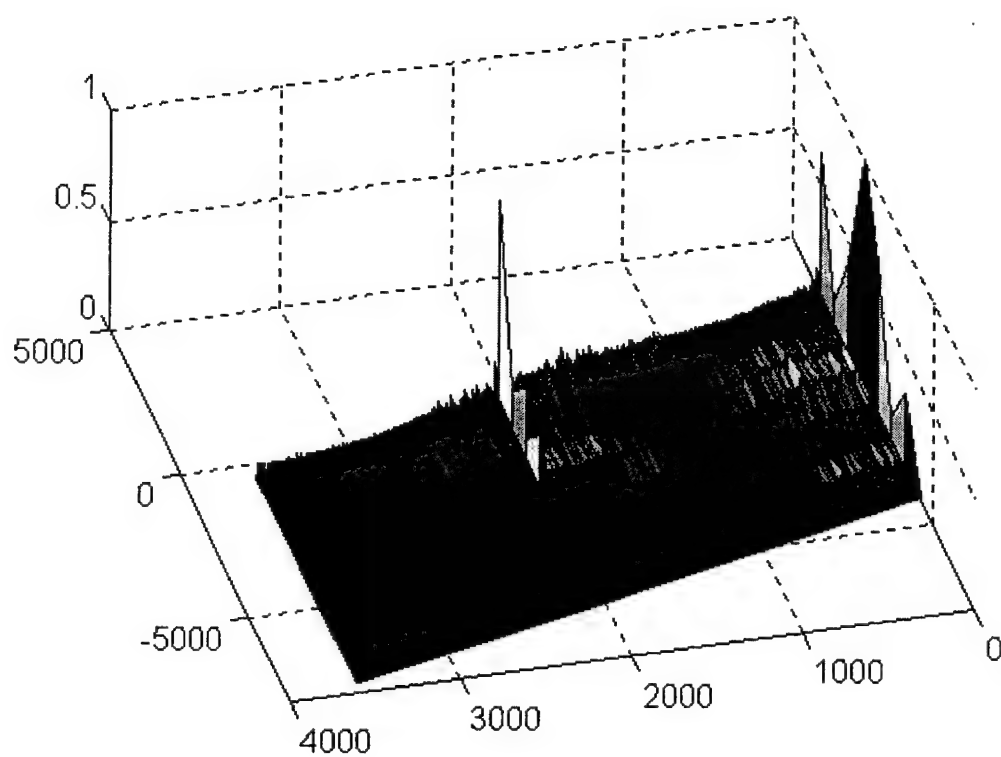


Figure B-103 - SCF for master (top) and slave #1 (bottom), time 409500

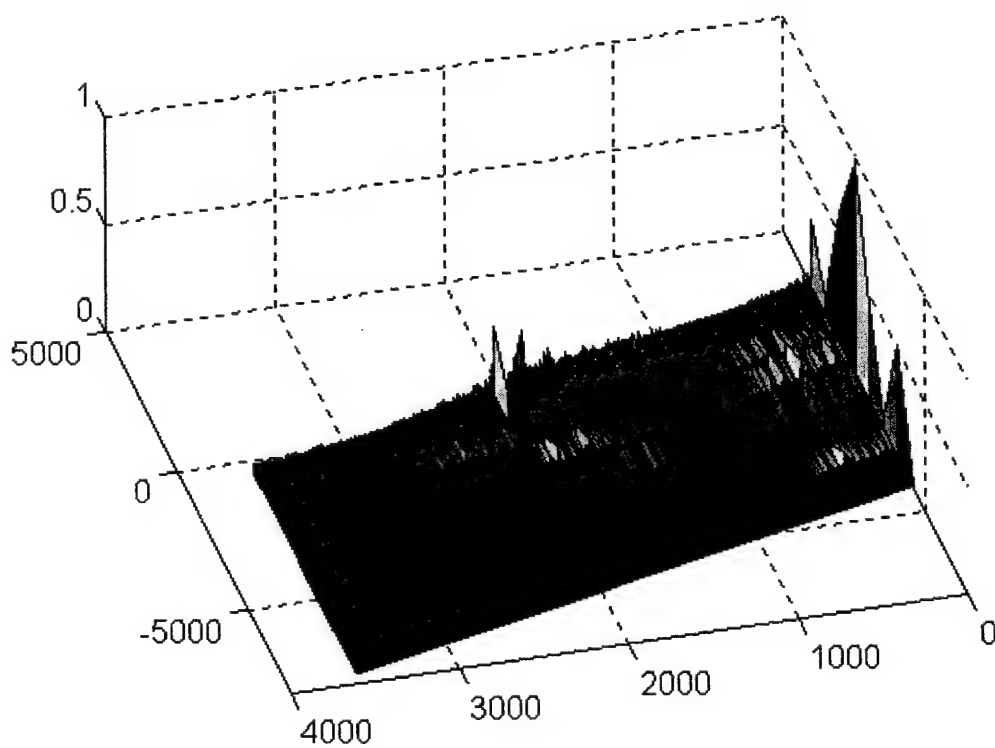
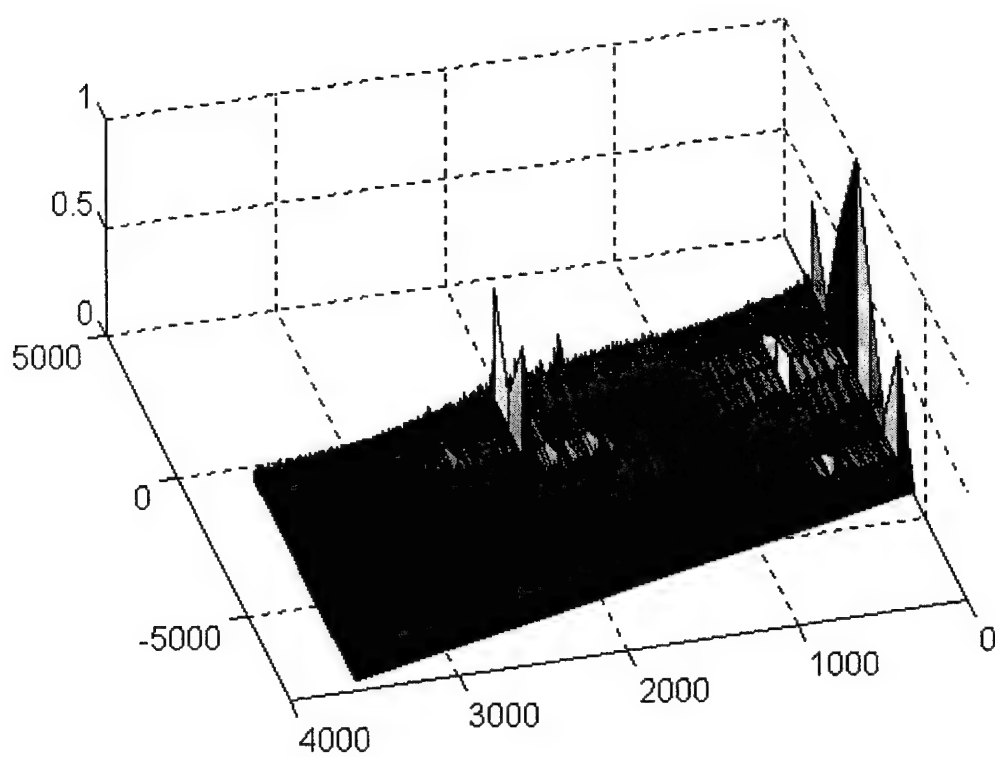


Figure B-104 - SCF for slave #2 (top) and slave #3 (bottom), time 409500

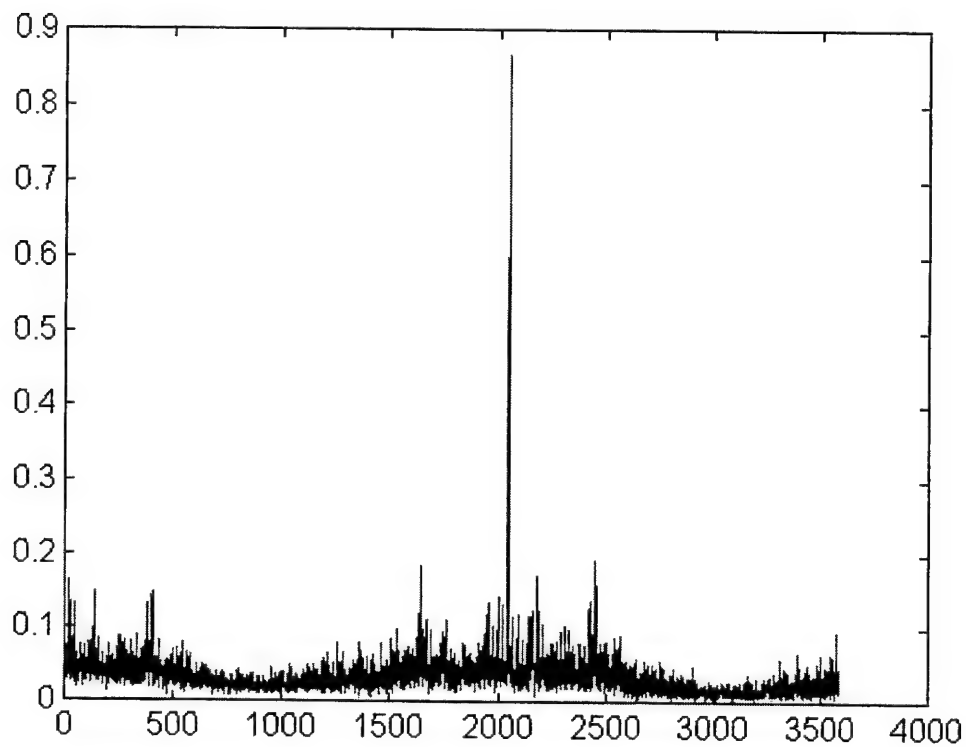
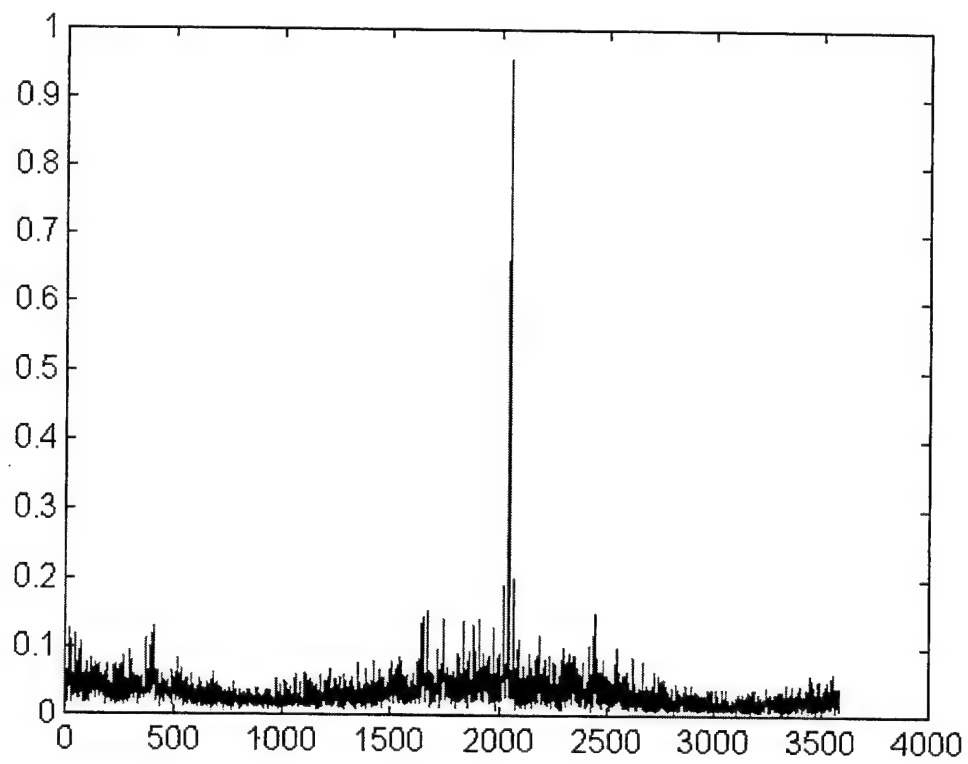


Figure B-105 - Cycle freq vs Max-magnitude of SCF for master (top) and slave #1 (bottom), time 409500

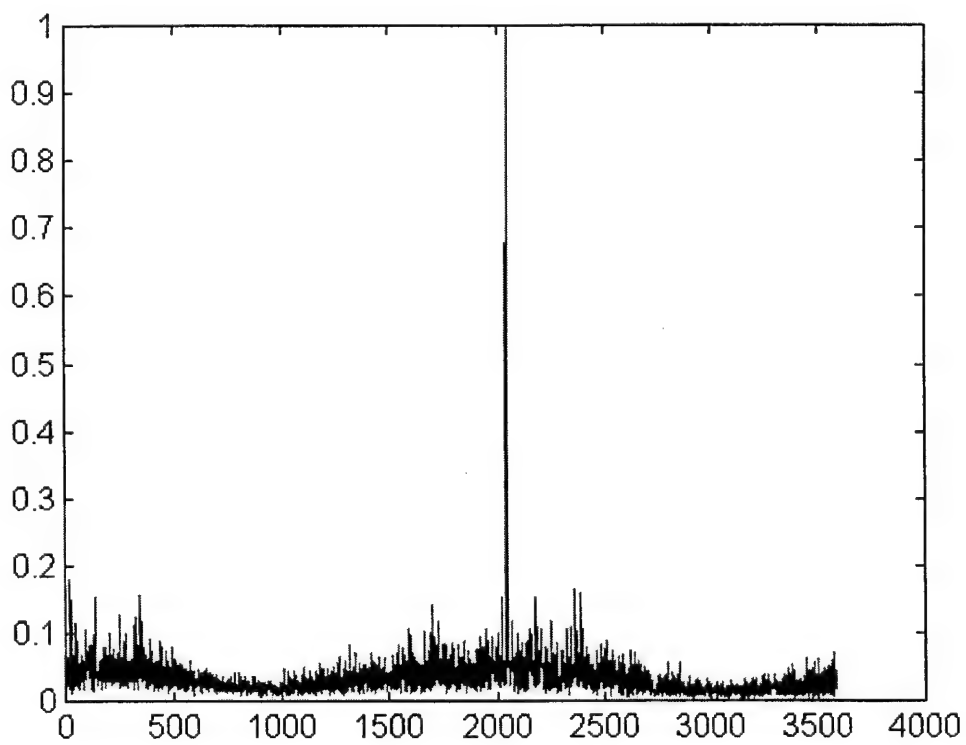
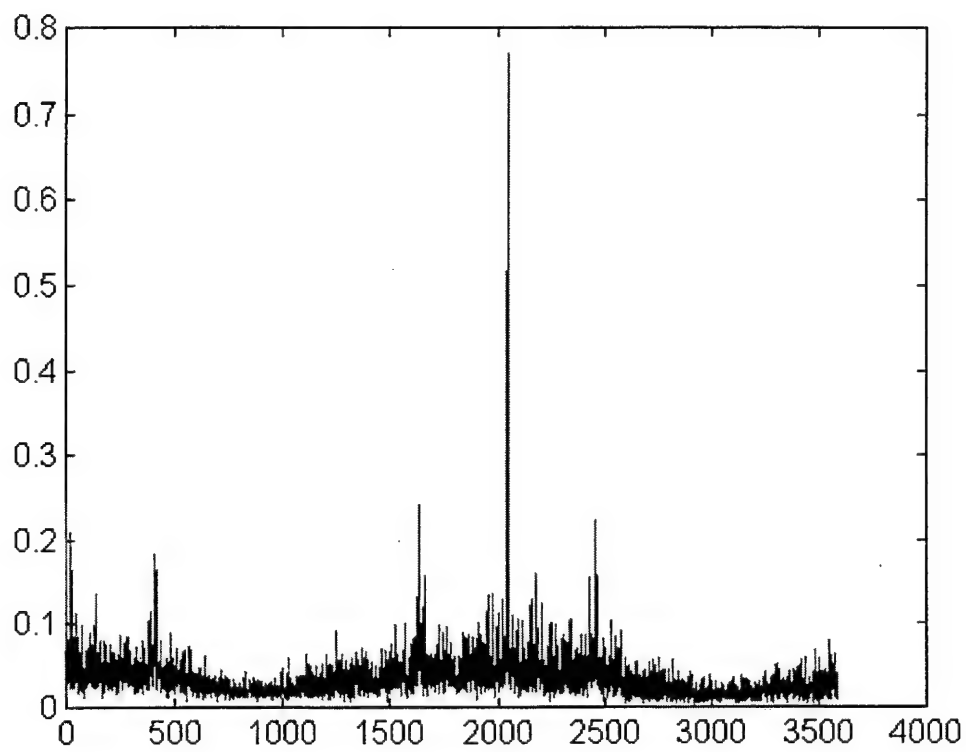


Figure B-106 - Cycle freq vs Max-magnitude of SCF for slave #2 (top) and slave #3 (bottom), time 409500

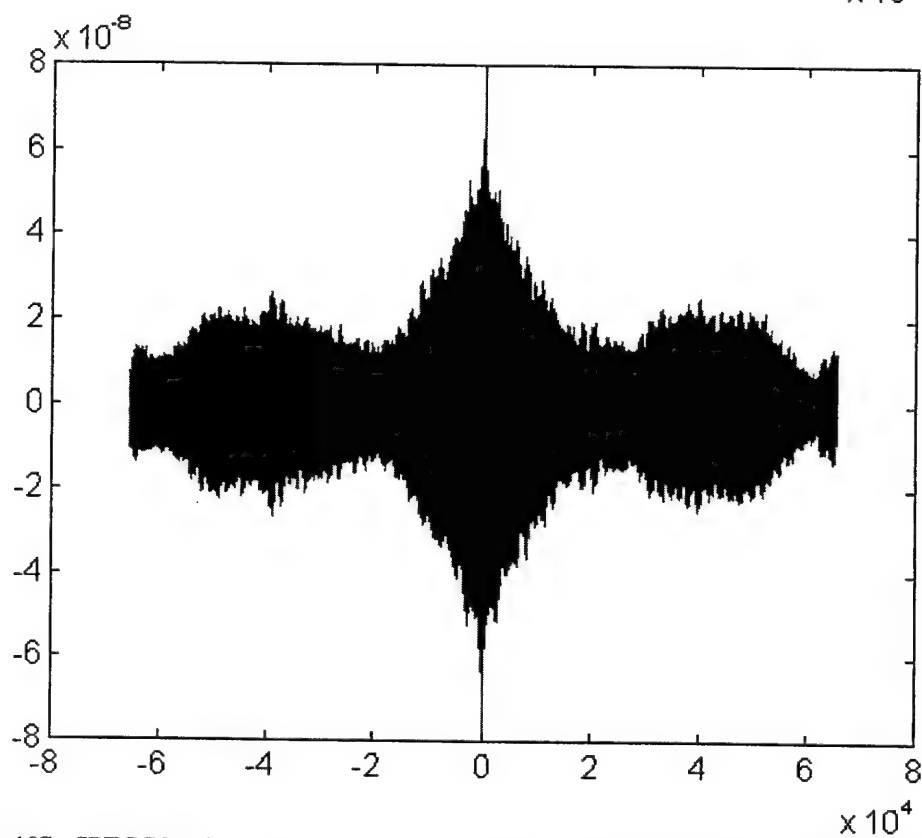
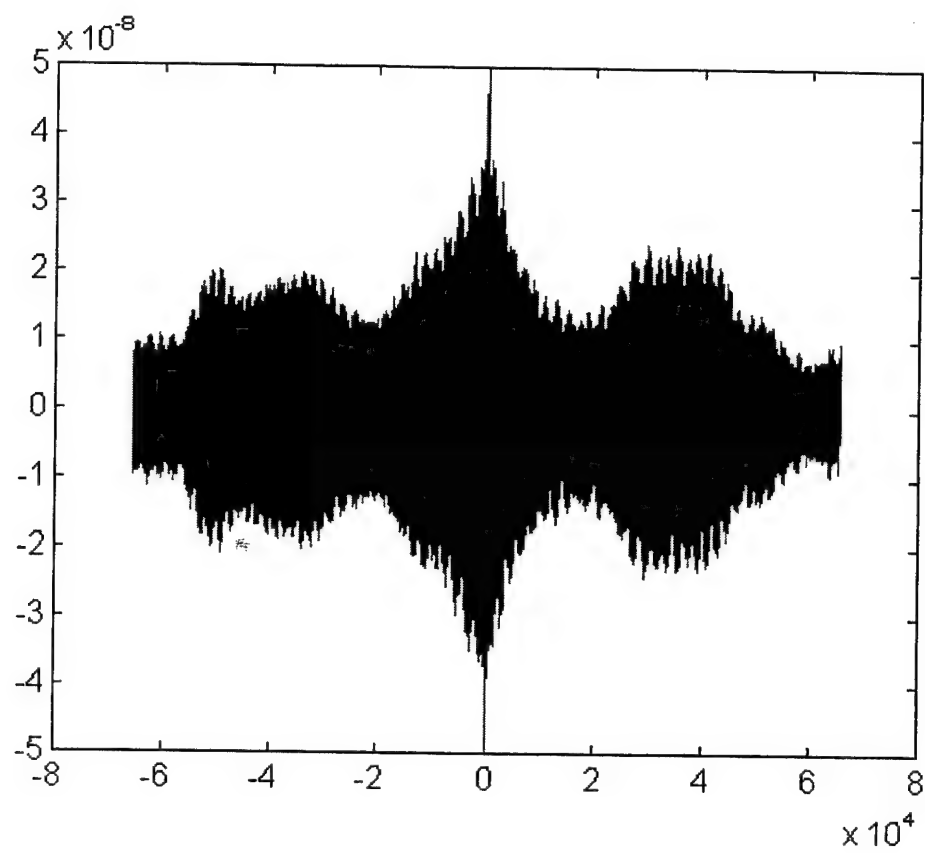


Figure B-107 - SPECCOA for master and slave #1 (top) and master and slave #2 (bottom), time 409505

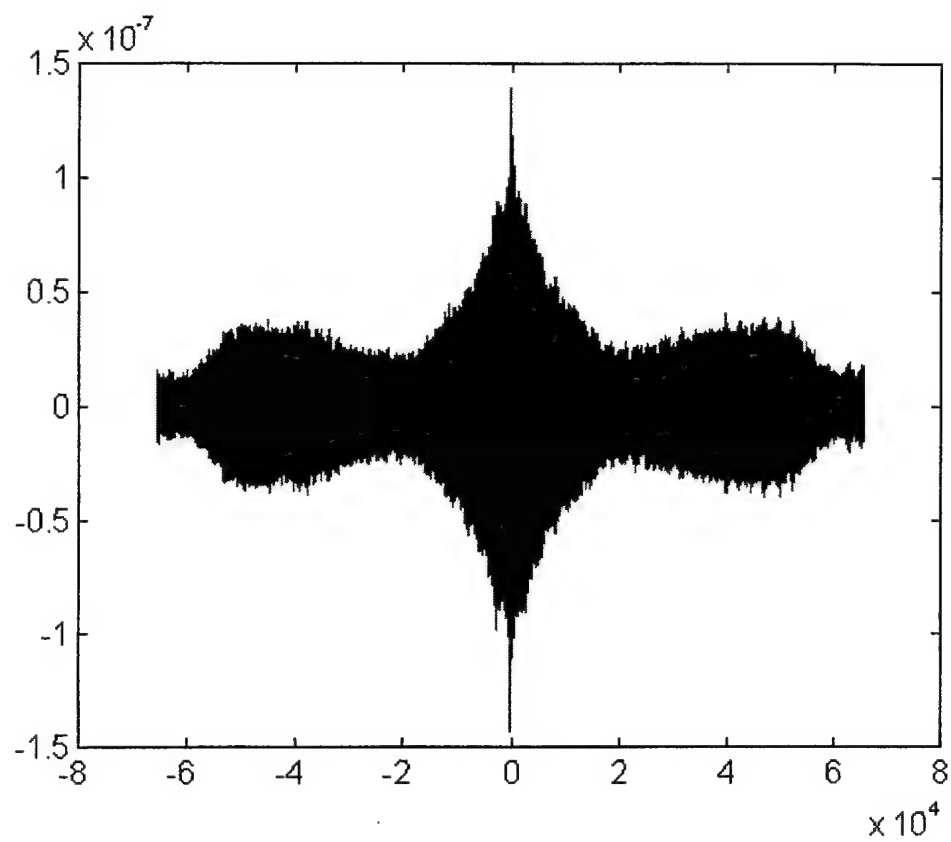


Figure B-108 - SPECCOA for master and slave #3, time 409505

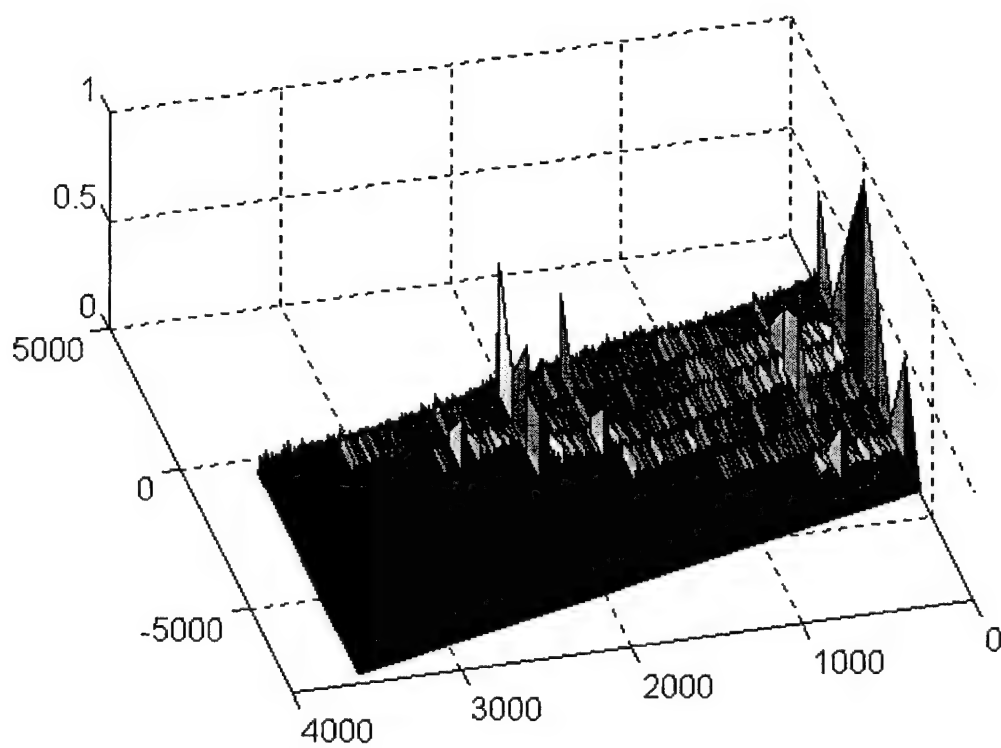
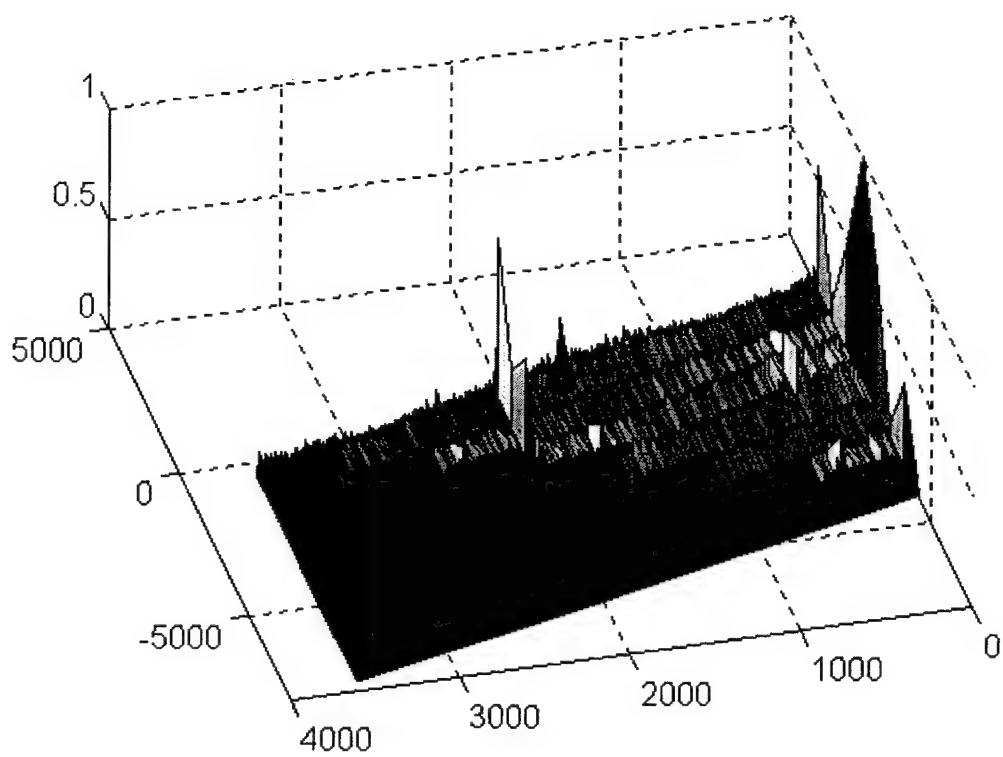


Figure B-109 - SCF for master (top) and slave #1 (bottom), time 409505

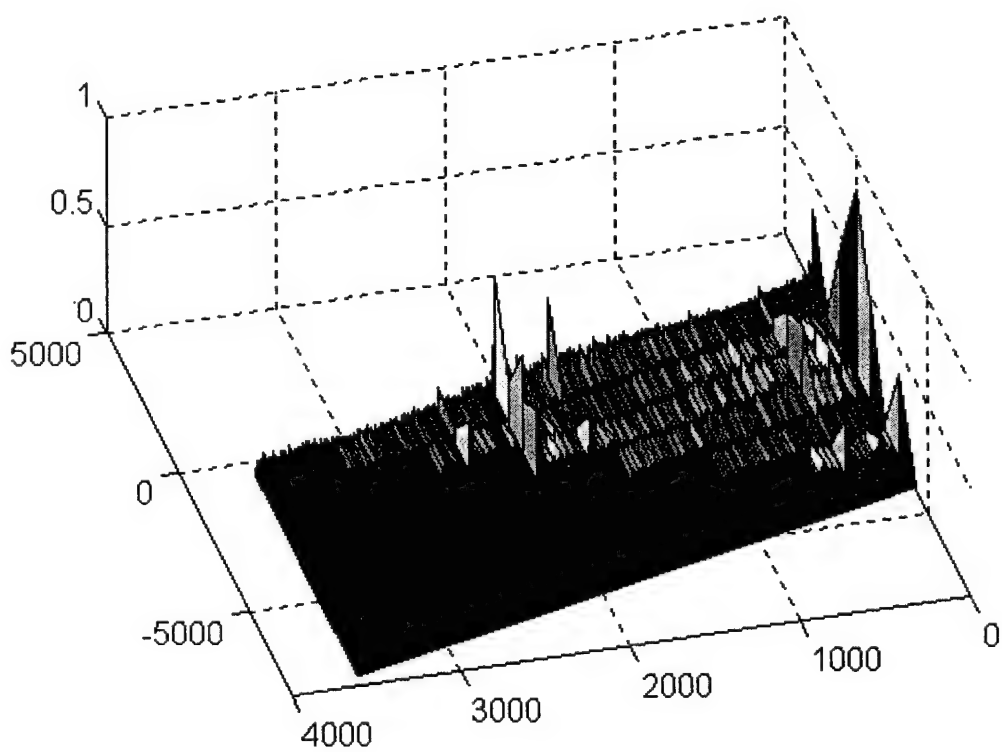
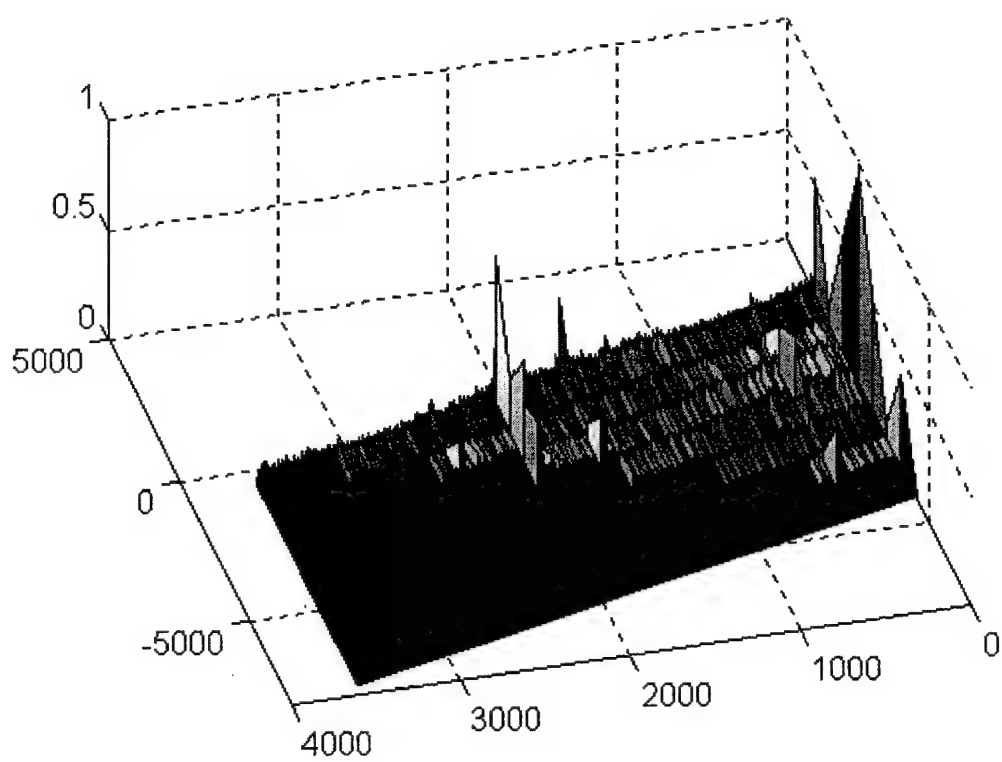


Figure B-110 - SCF for slave #2 (top) and slave #3 (bottom), time 409505

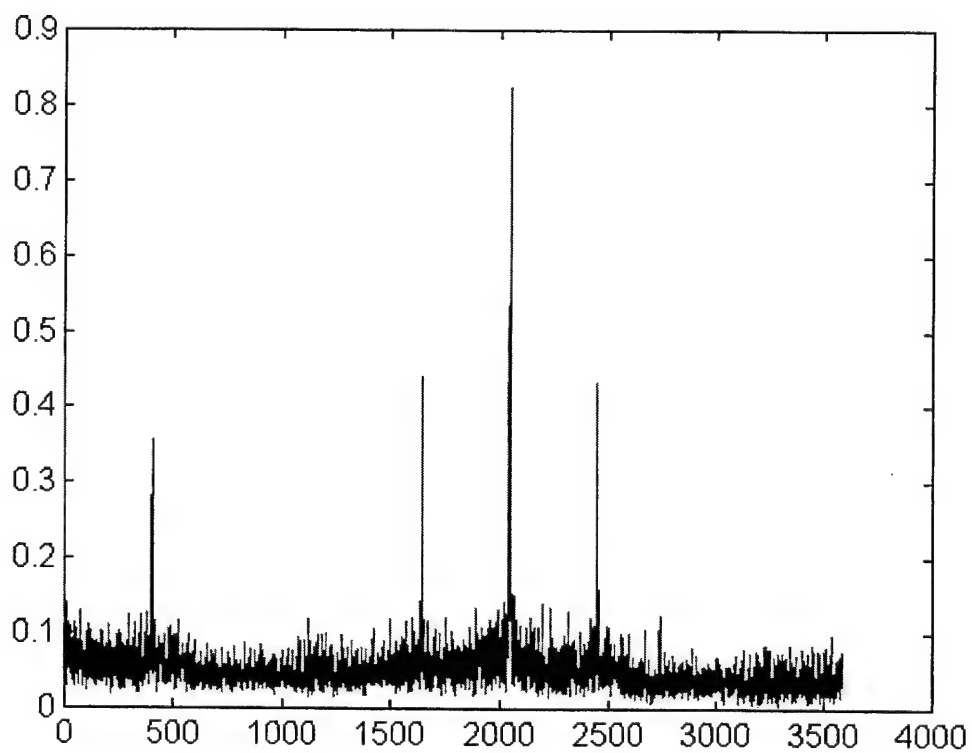
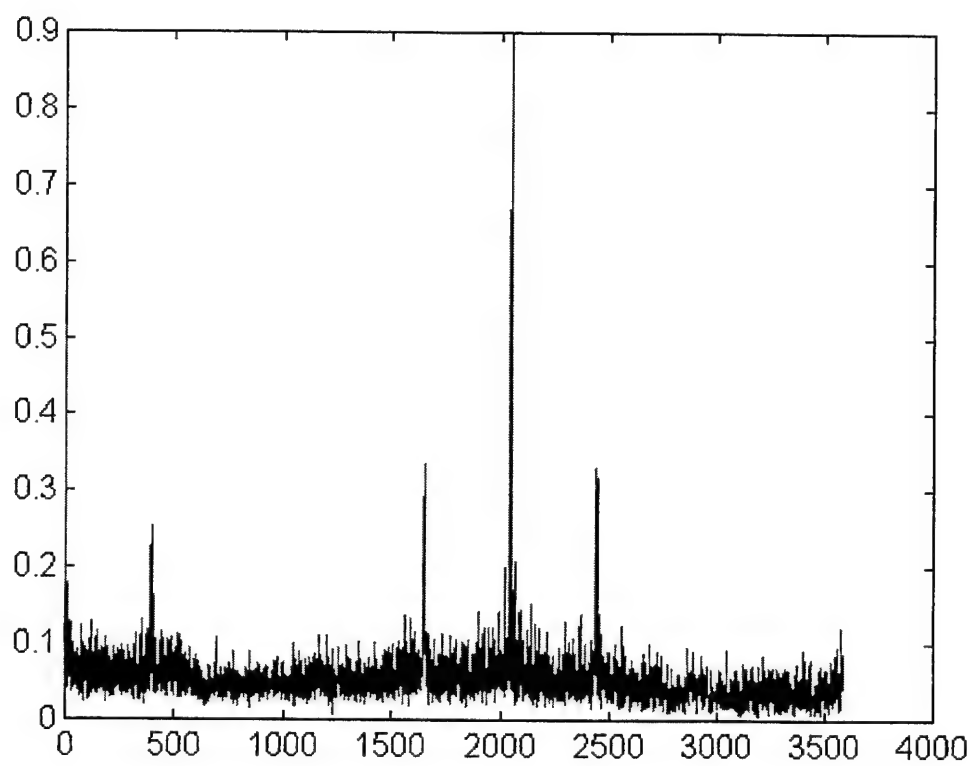


Figure B-111 - Cycle freq vs Max-magnitude of SCF for master (top) and slave #1 (bottom), time 409505

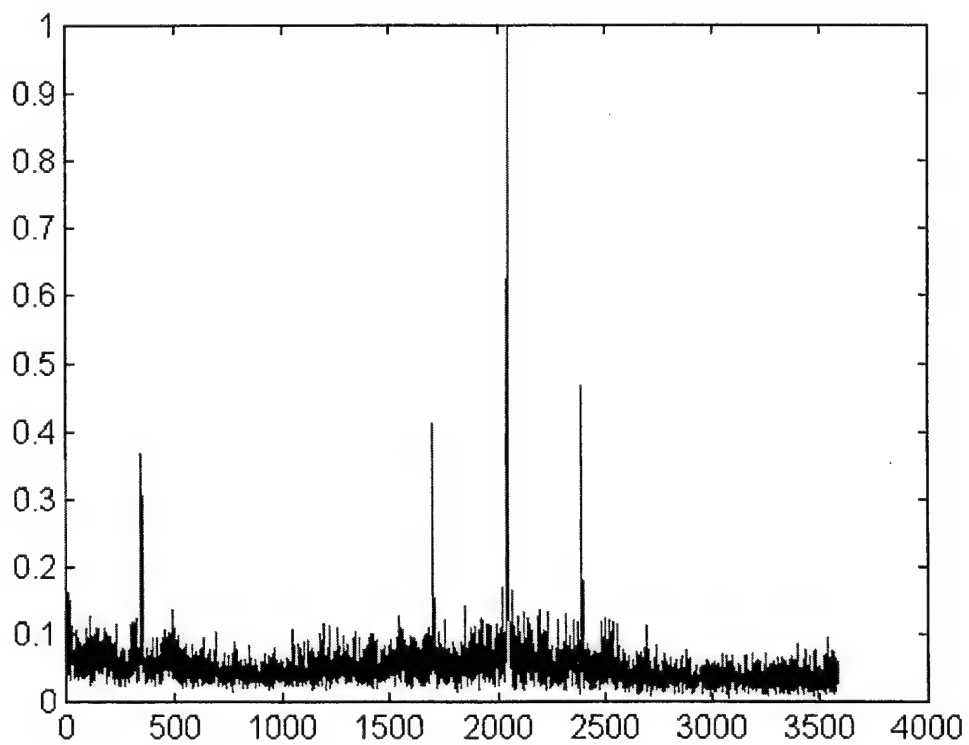
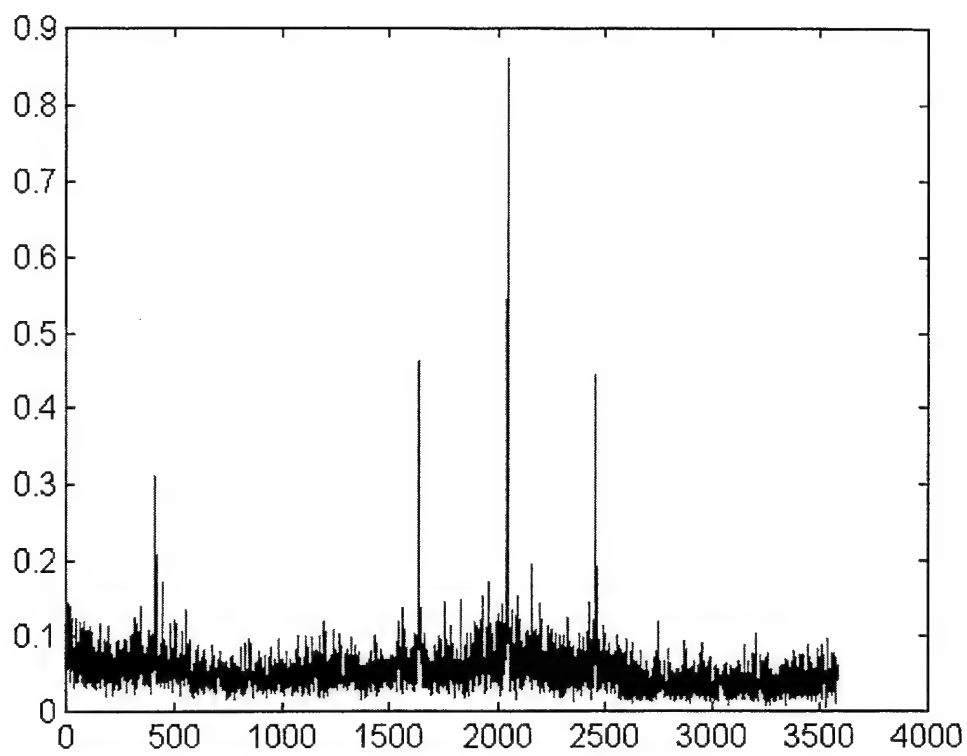


Figure B-112 - Cycle freq vs Max-magnitude of SCF for slave #2 (top) and slave #3 (bottom), time 409505

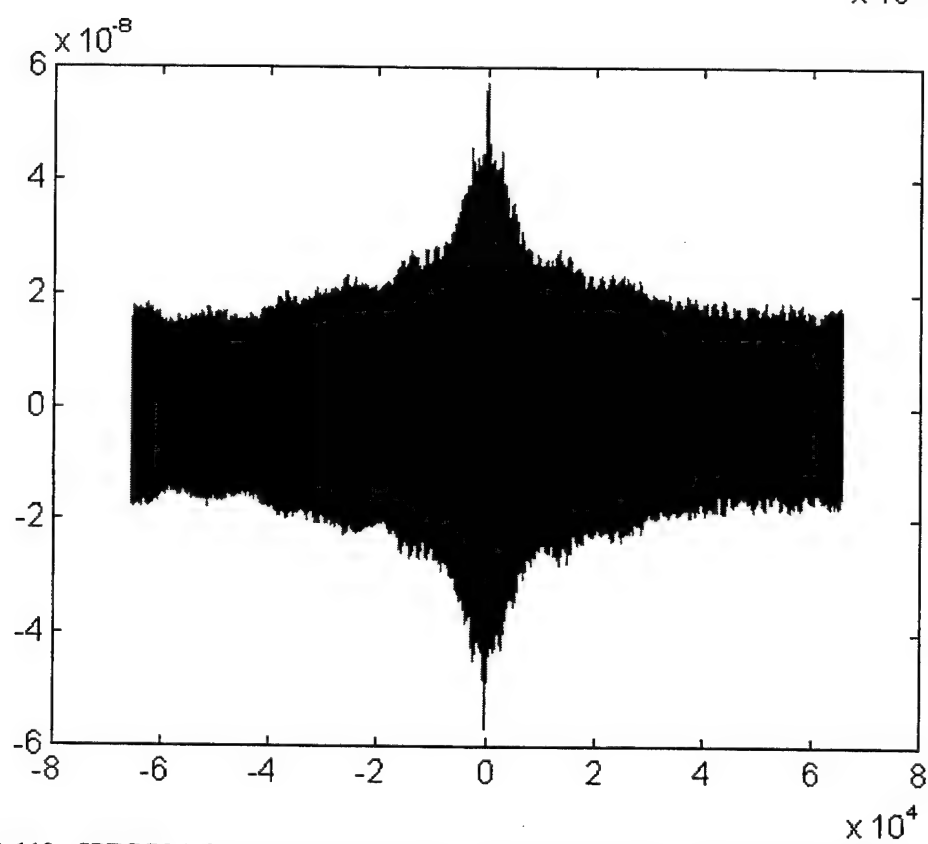
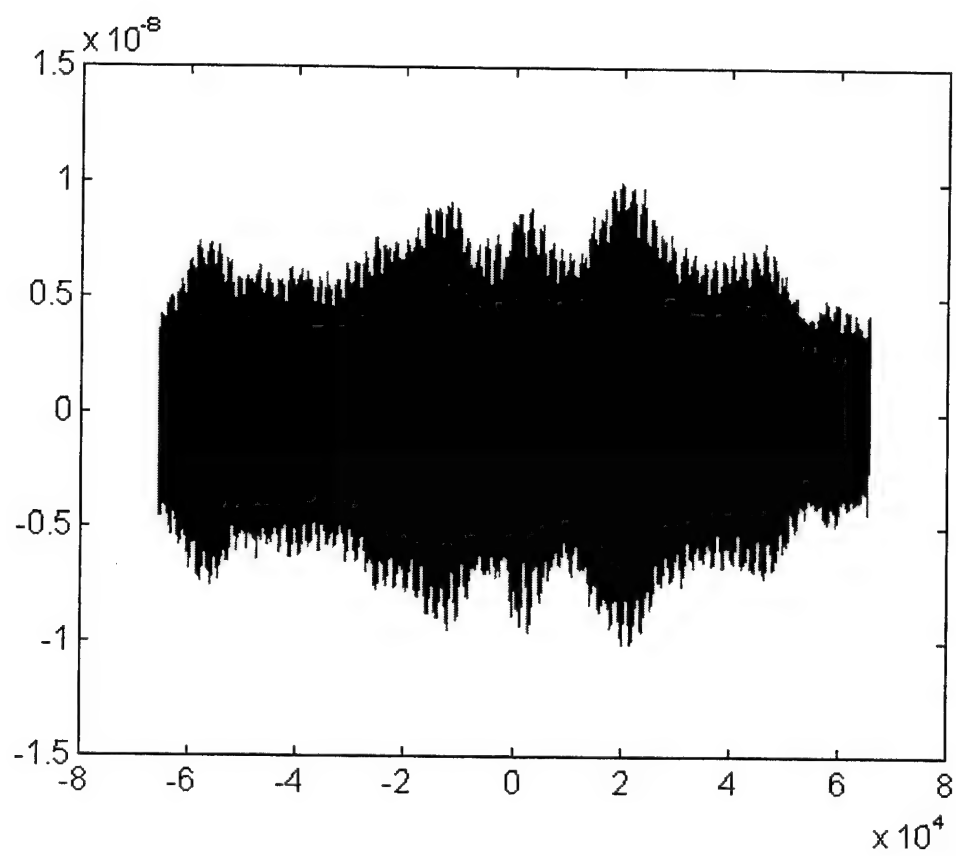


Figure B-113 - SPECCOA for master and slave #1 (top) and master and slave #2 (bottom), time 409505

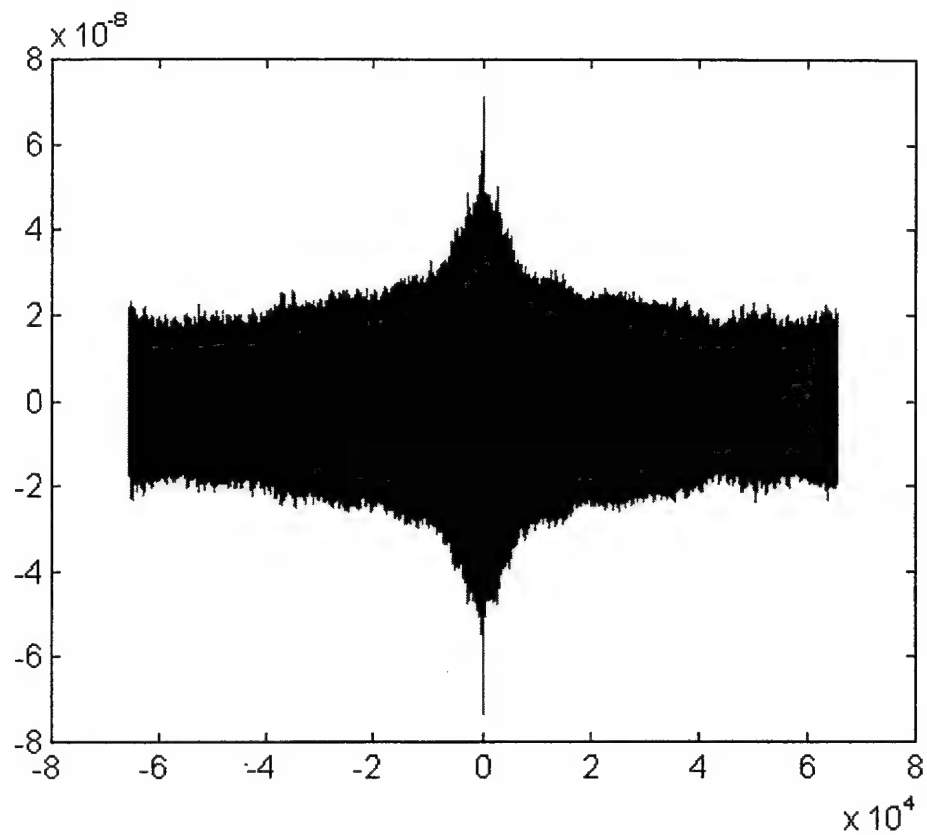


Figure B-114 - SPECCOA for master and slave #3, time 409505

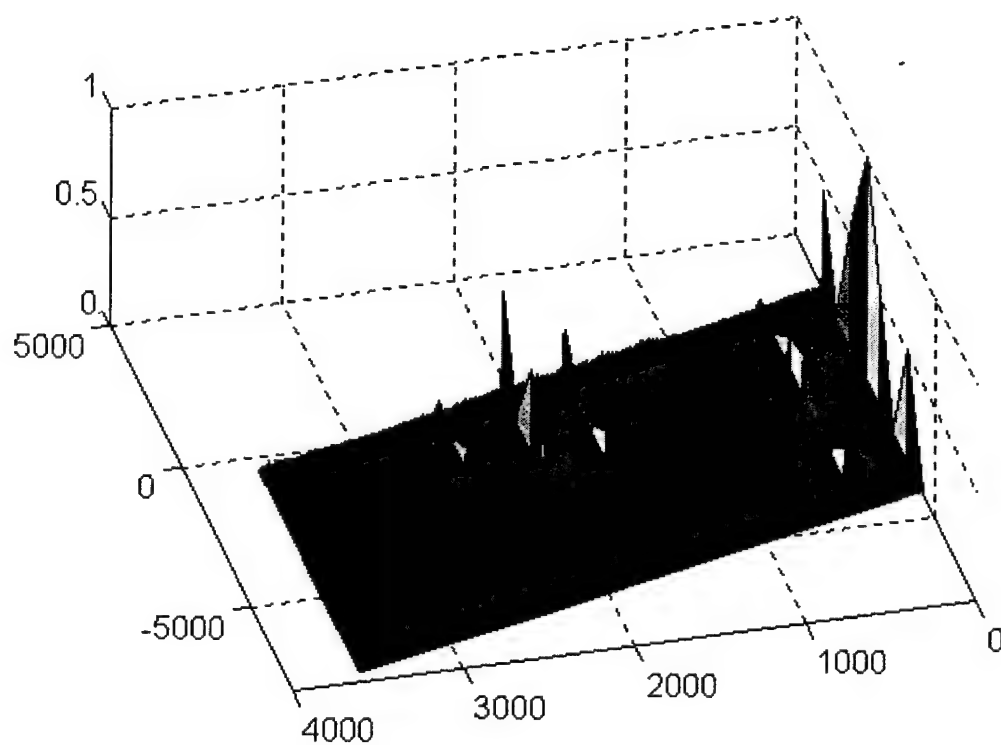
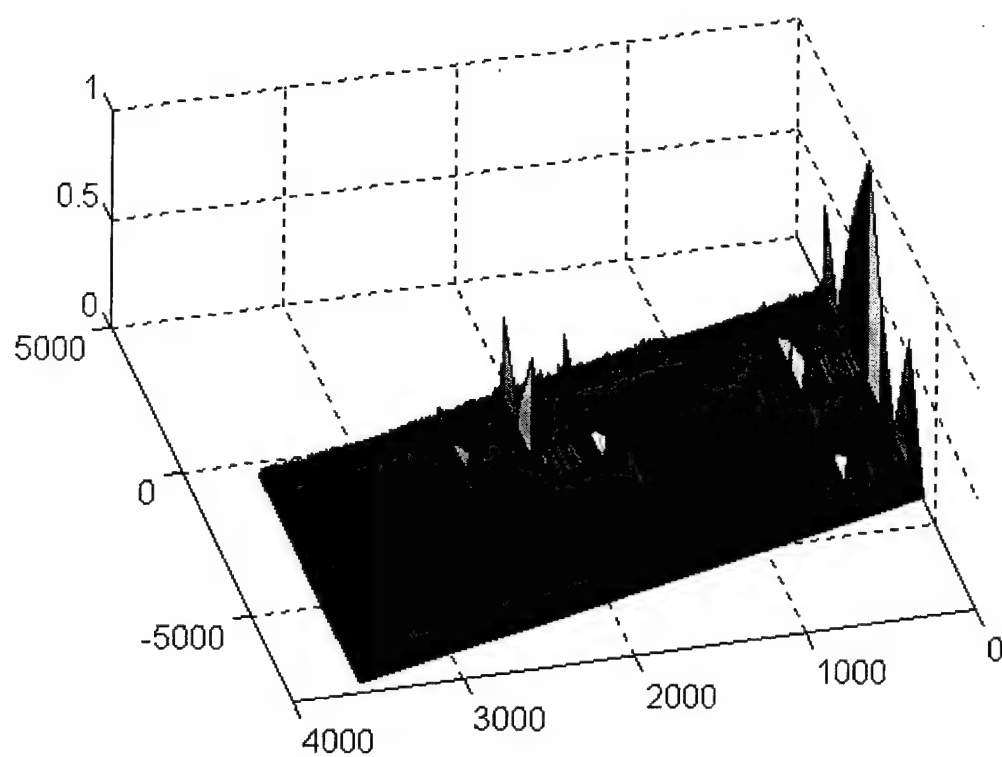


Figure B-115 - SCF for master (top) and slave #1 (bottom), time 409510

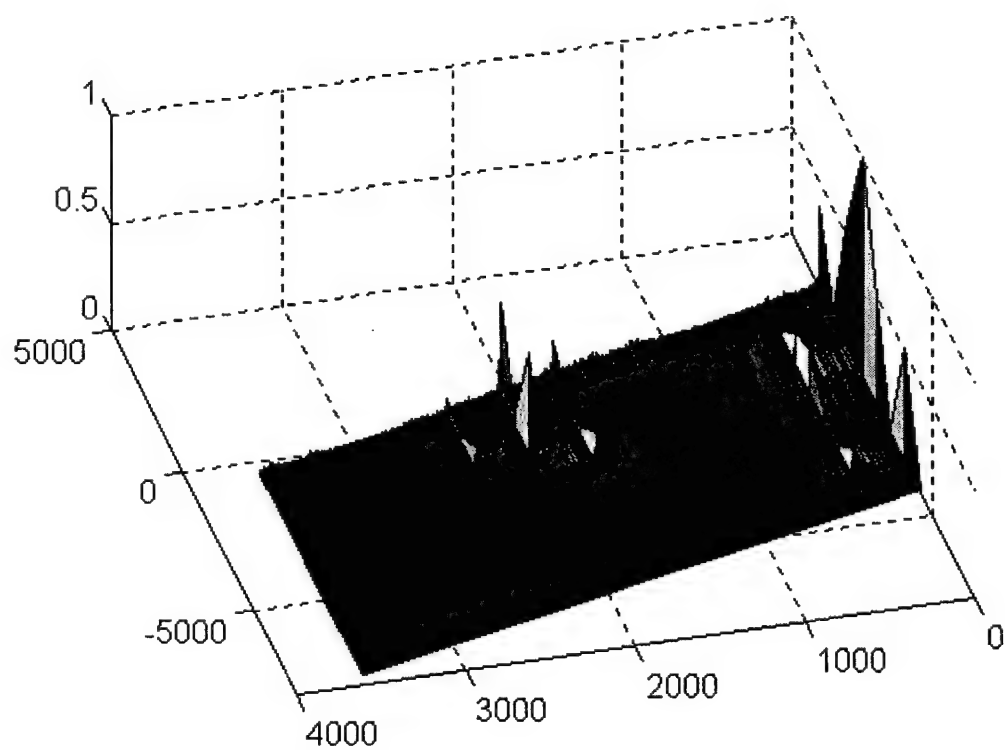
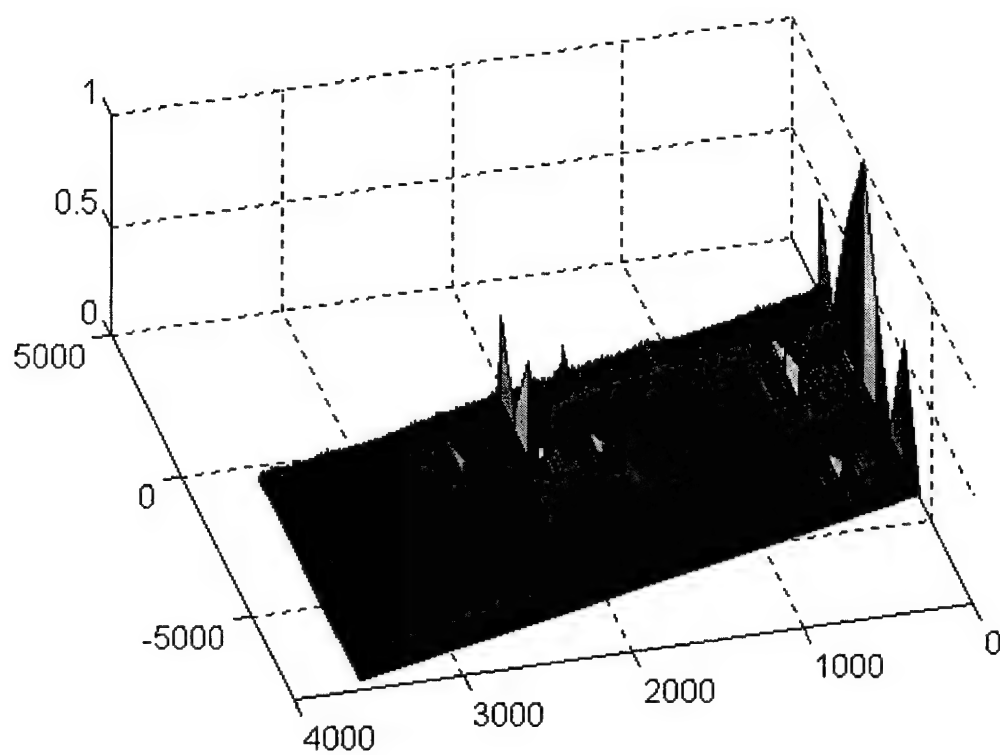


Figure B-116 - SCF for slave #2 (top) and slave #3 (bottom), time 409510

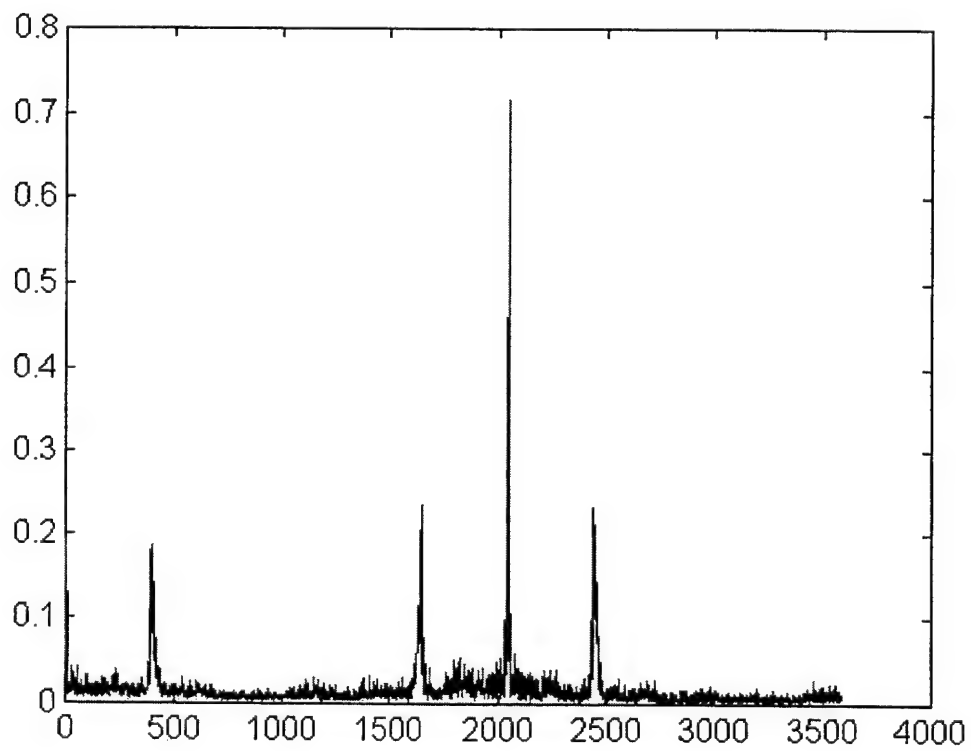
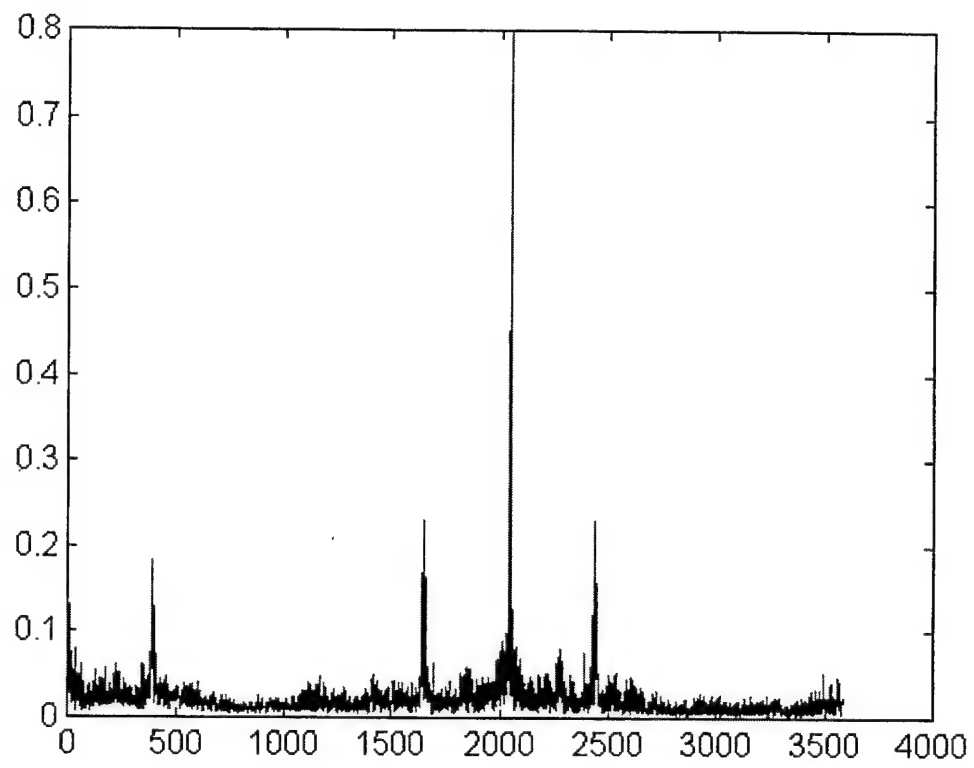


Figure B-117 - Cycle freq vs Max-magnitude of SCF for master (top) and slave #1 (bottom), time 409510

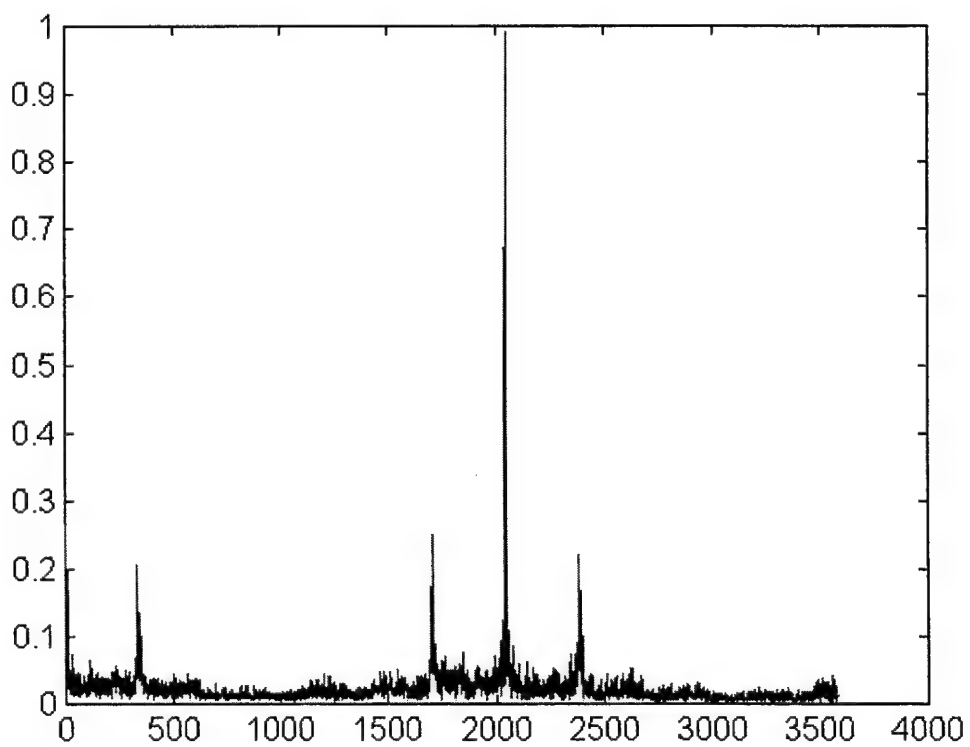
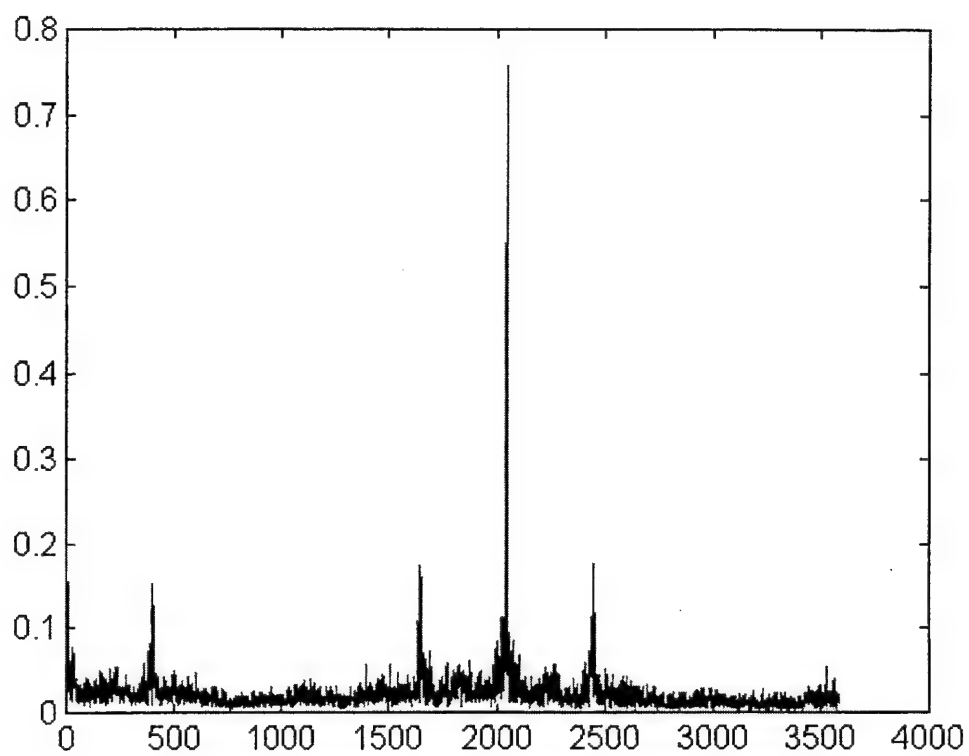


Figure B-118 - Cycle freq vs Max-magnitude of SCF for slave #2 (top) and slave #3 (bottom), time 409510

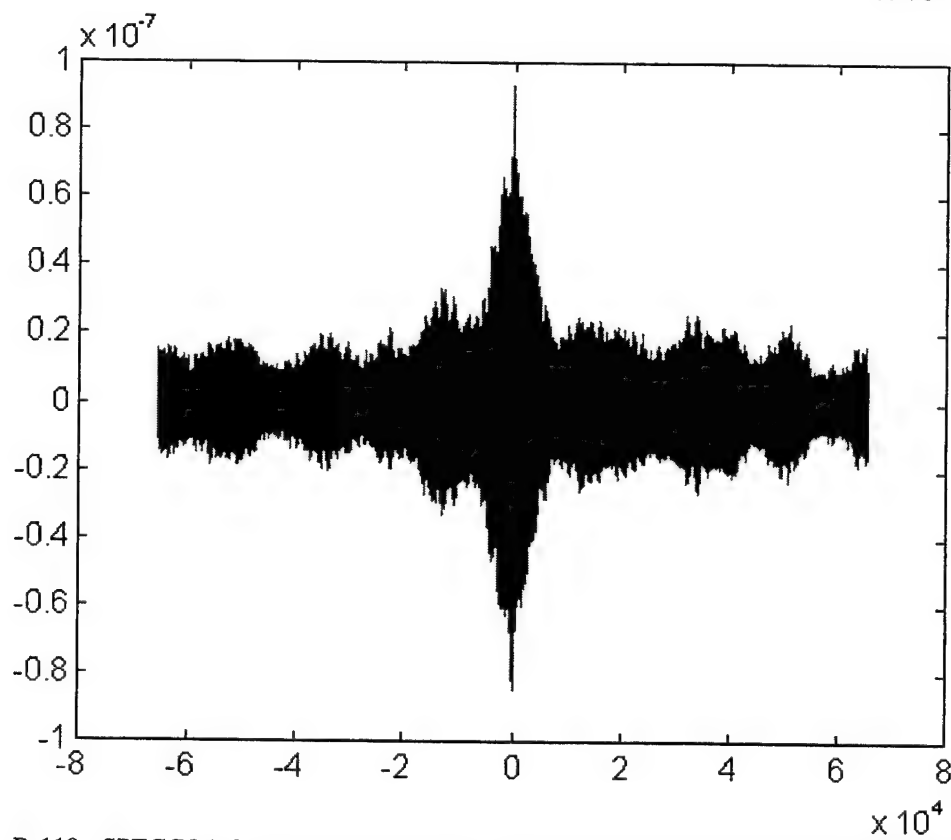
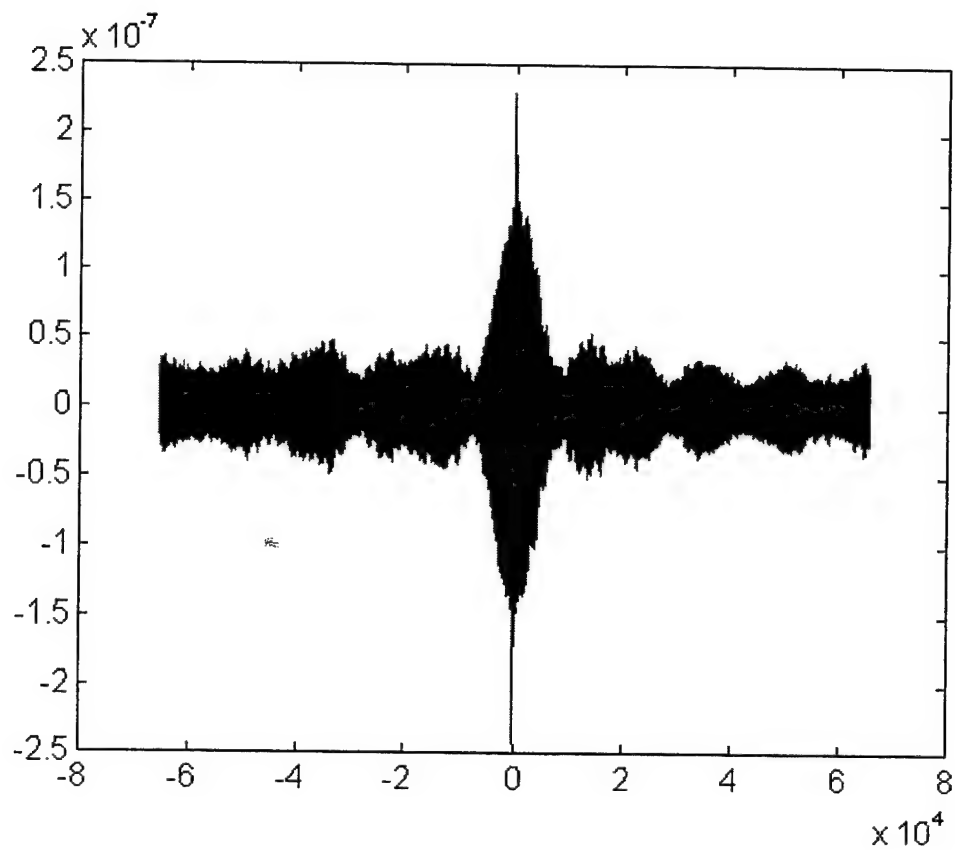


Figure B-119 - SPECCOA for master and slave #1 (top) and master and slave #2 (bottom), time 409510

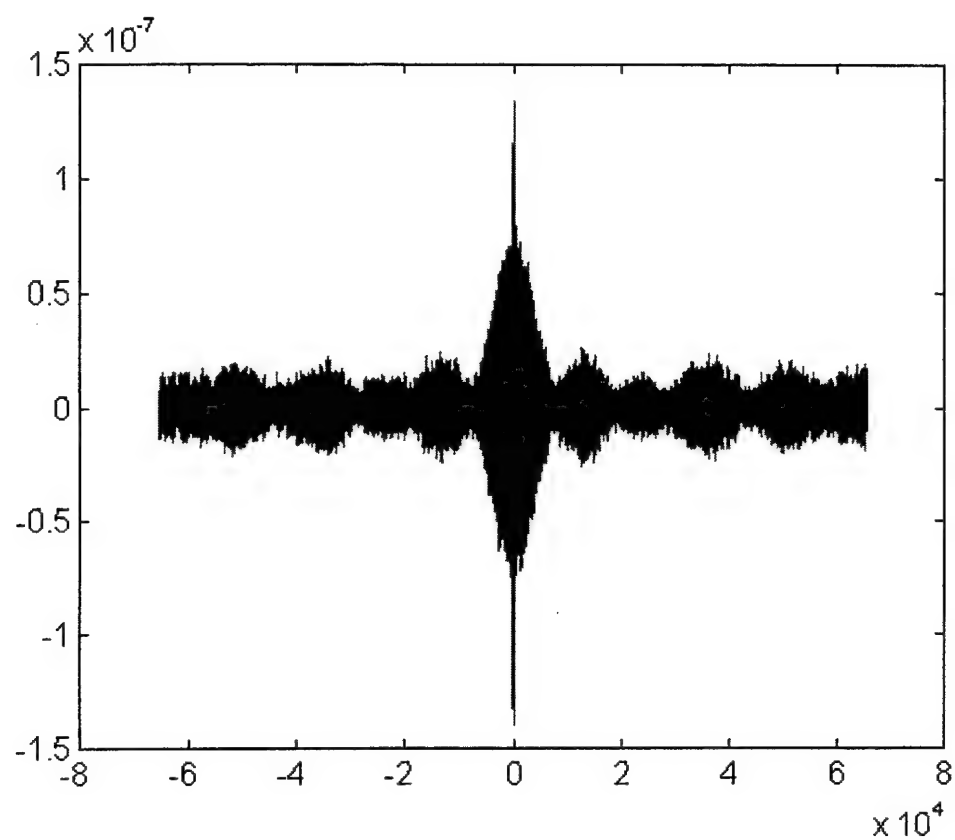


Figure B-120 - SPECCOA for master and slave #3, time 409510

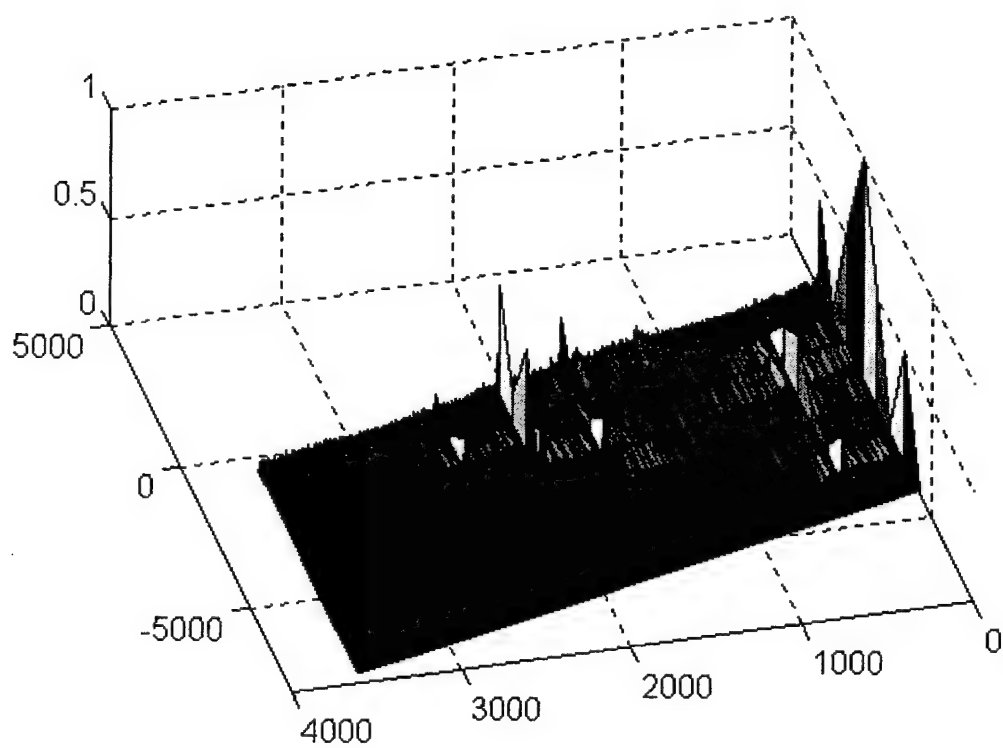
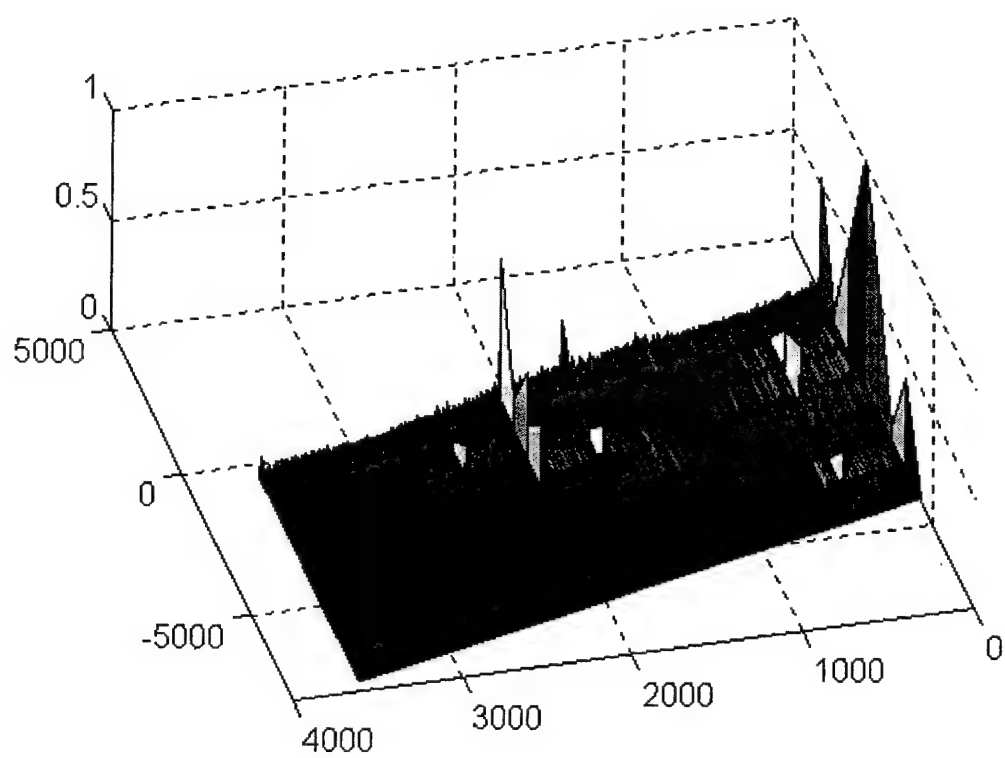


Figure B-121 - SCF for master (top) and slave #1 (bottom), time 409515

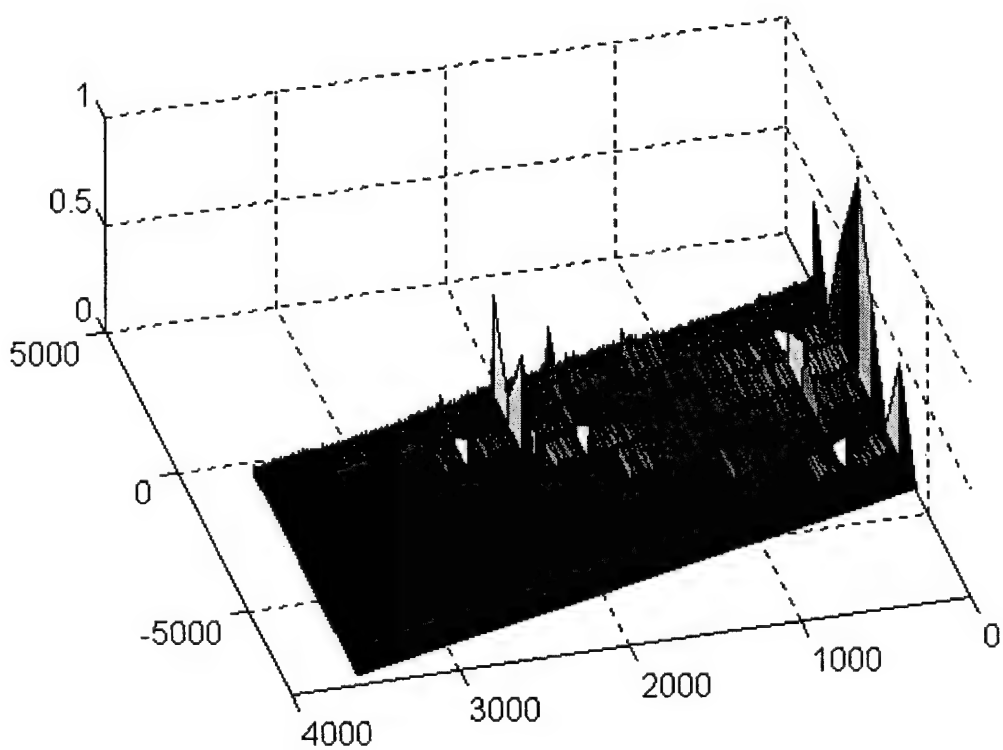
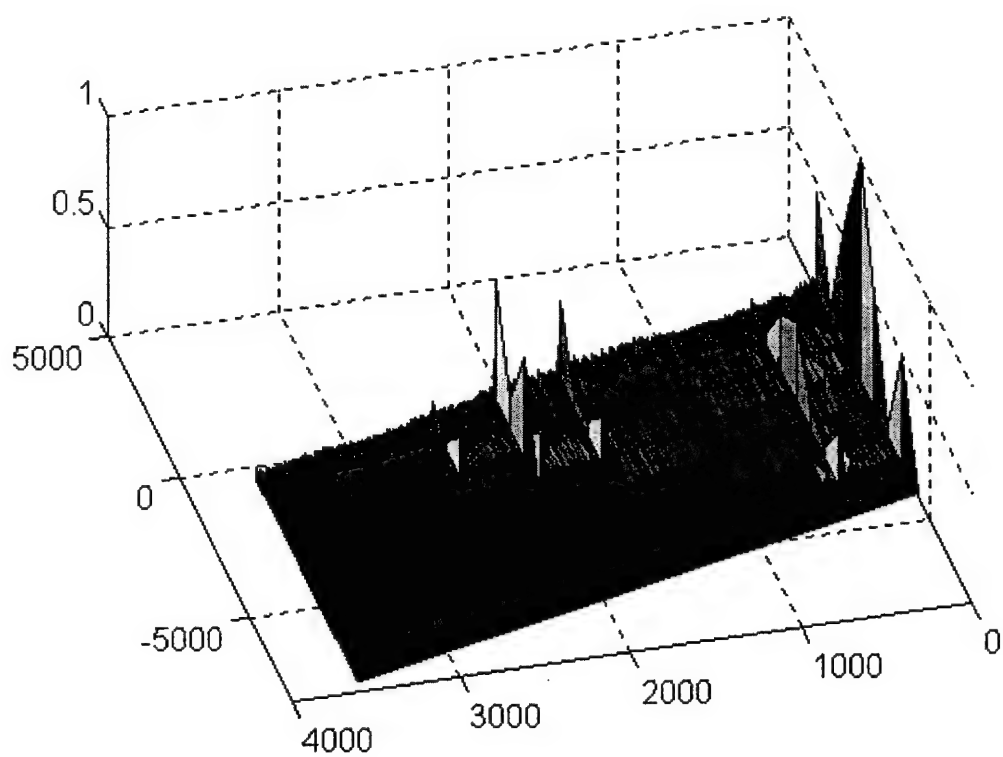


Figure B-122 - SCF for slave #2 (top) and slave #3 (bottom), time 409515

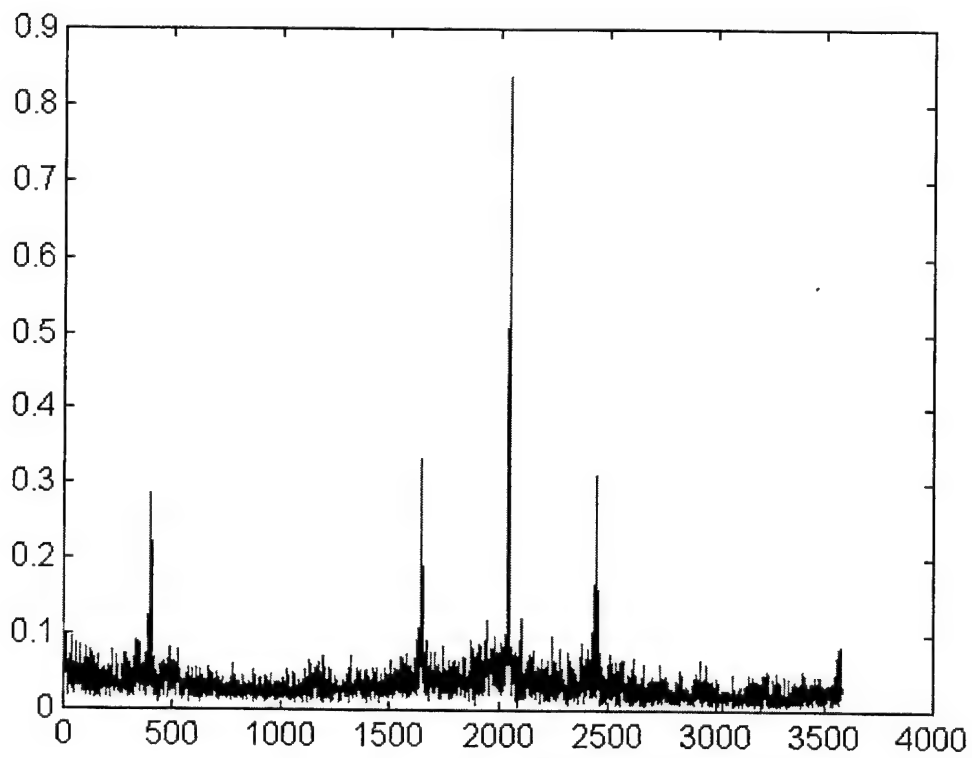
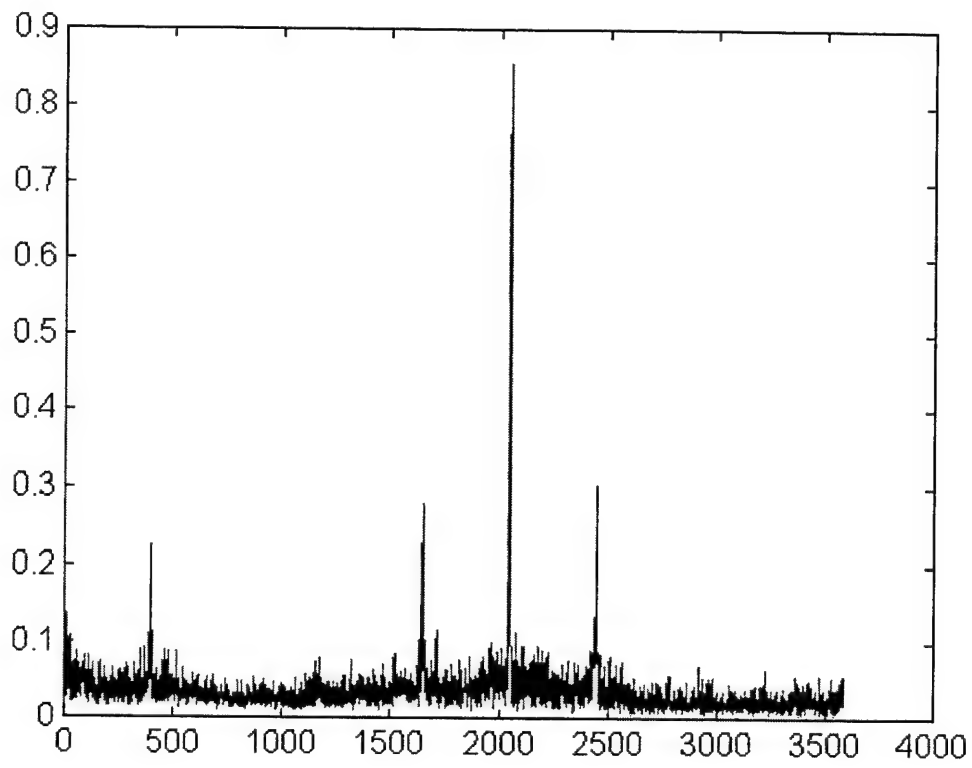


Figure B-123 - Cycle freq vs Max-magnitude of SCF for master (top) and slave #1 (bottom), time 409515

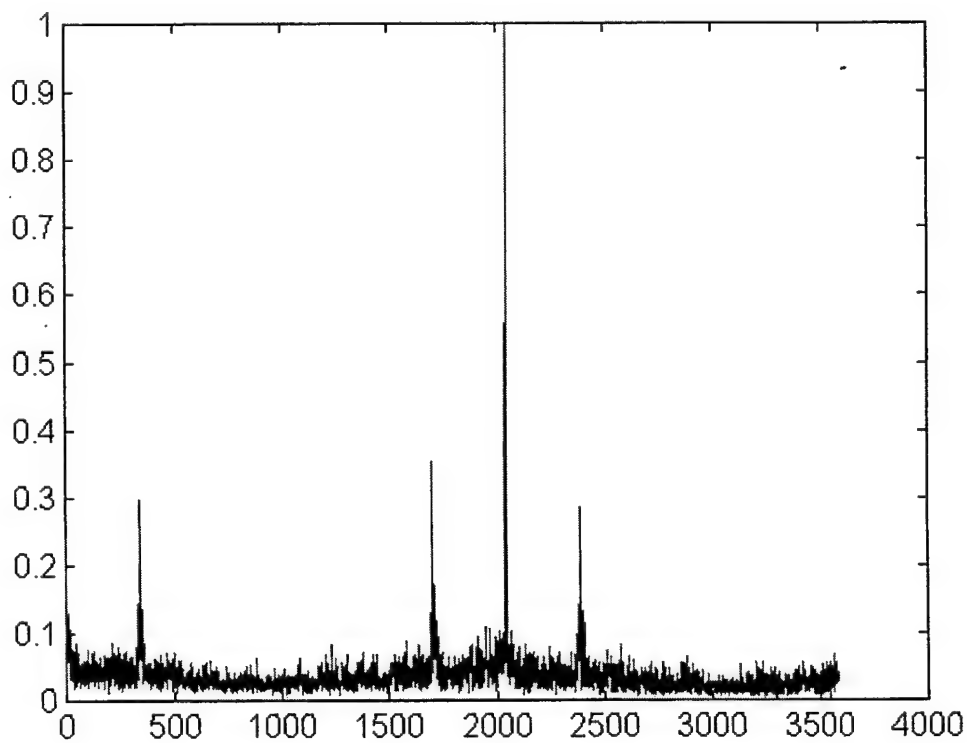
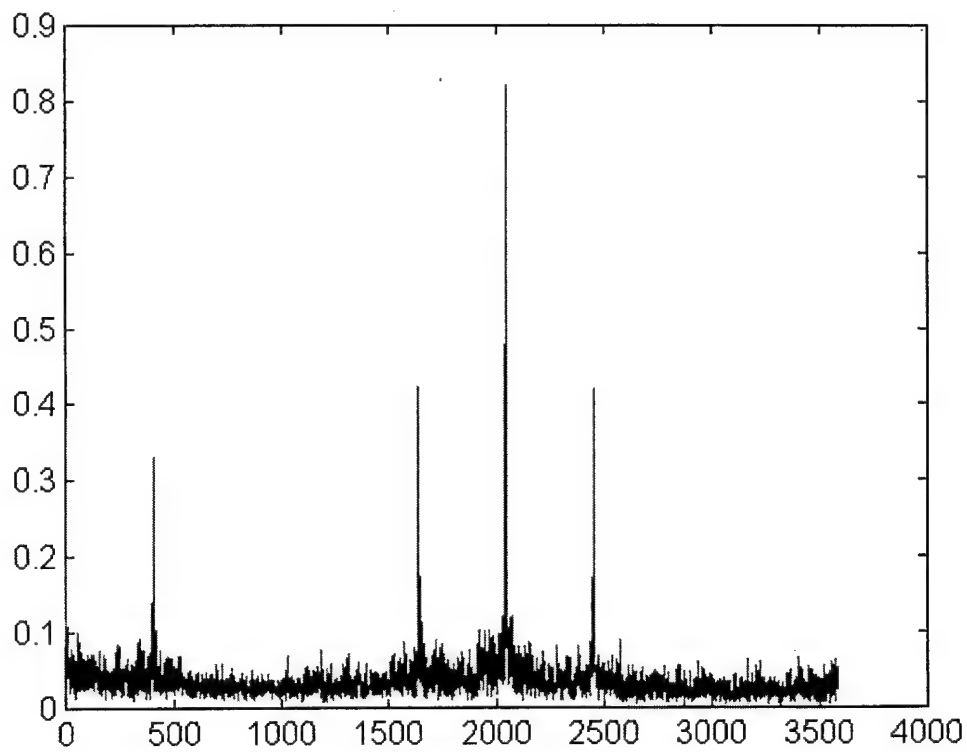


Figure B-124 - Cycle freq vs Max-magnitude of SCF for slave #2 (top) and slave #3 (bottom), time 409515

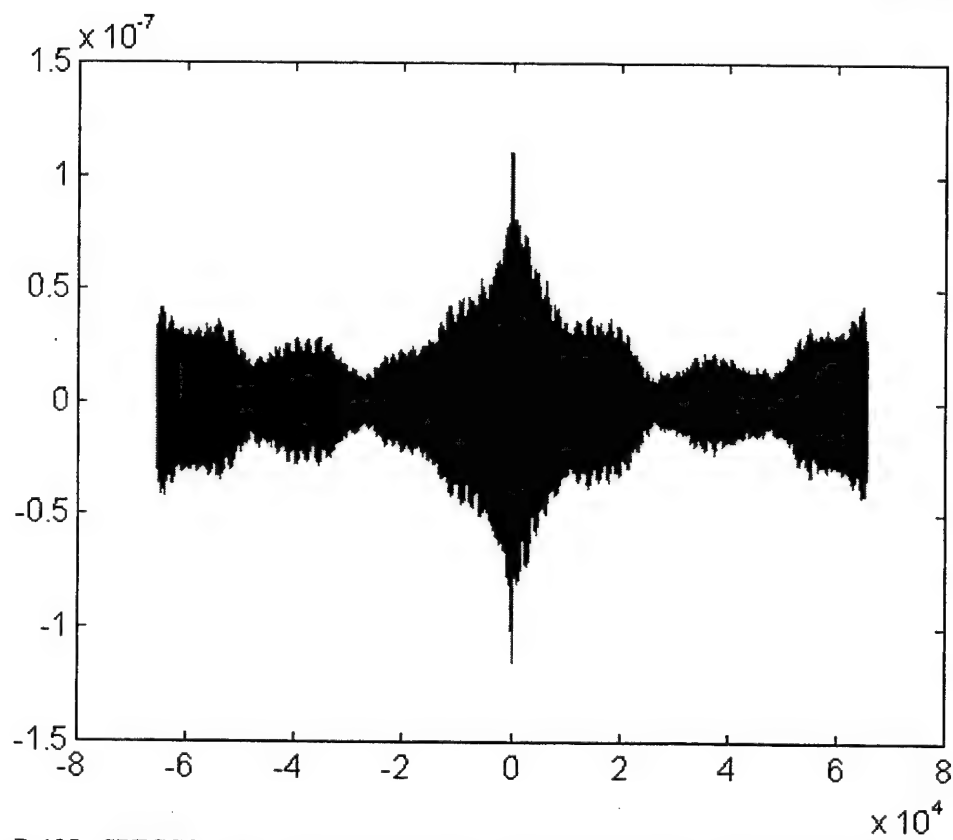
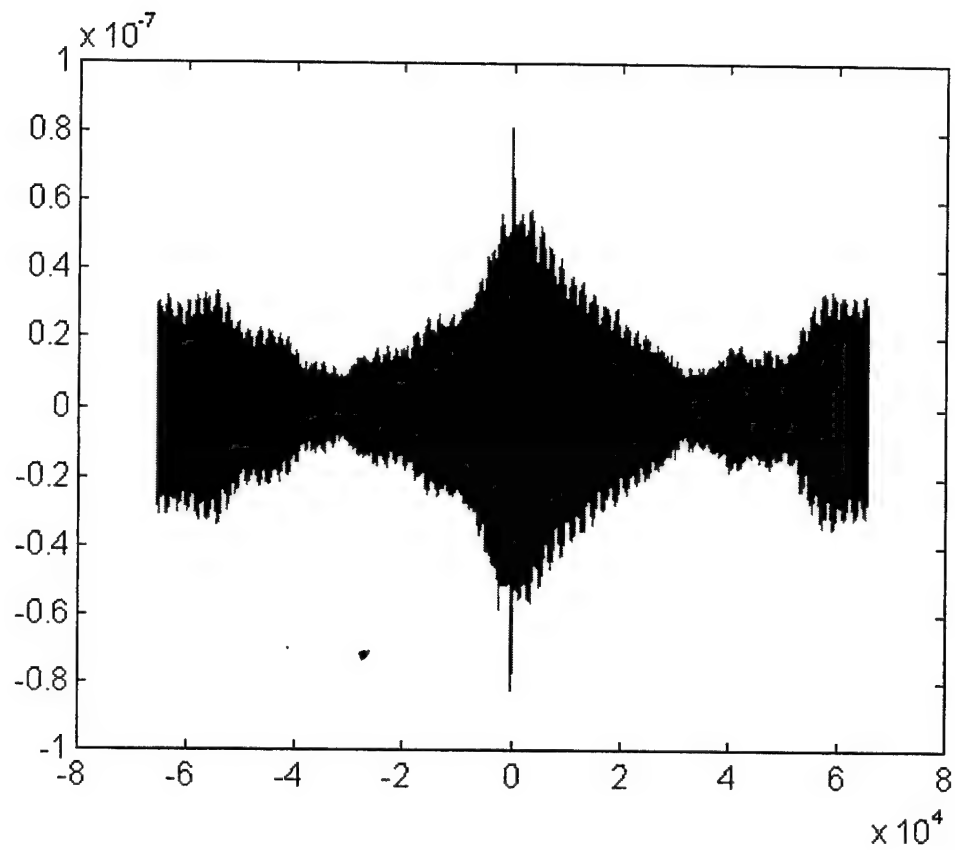


Figure B-125 - SPECCOA for master and slave #1 (top) and master and slave #2 (bottom), time 409515

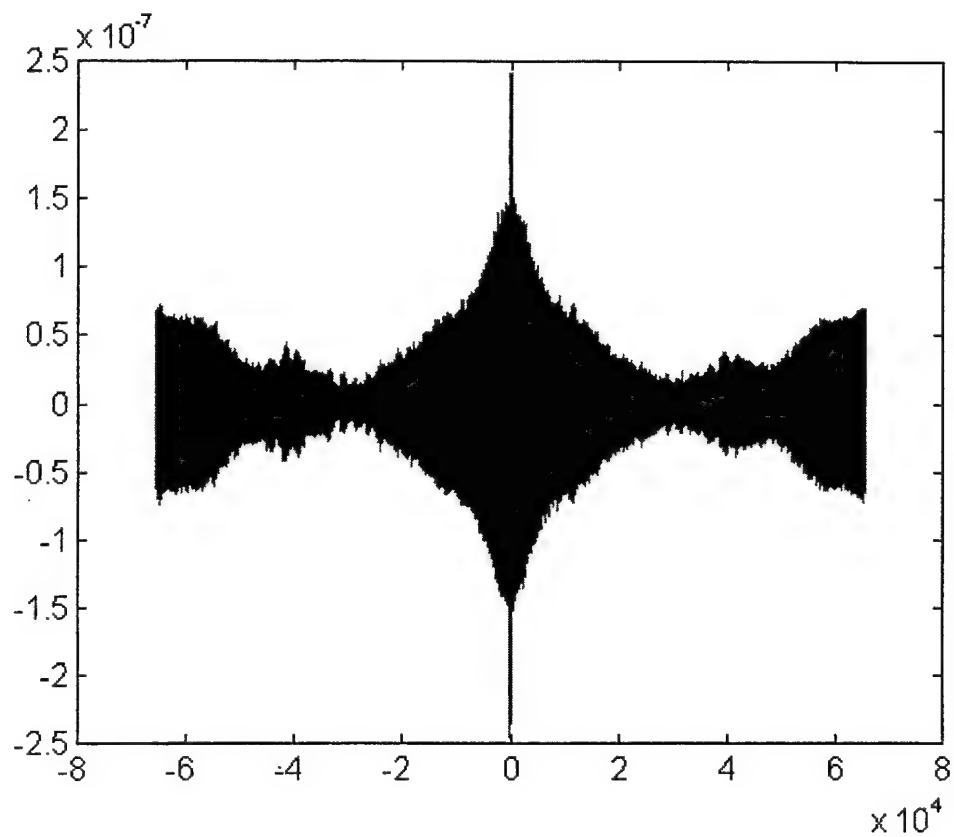


Figure B-126 - SPECCOA for master and slave #3, time 409515

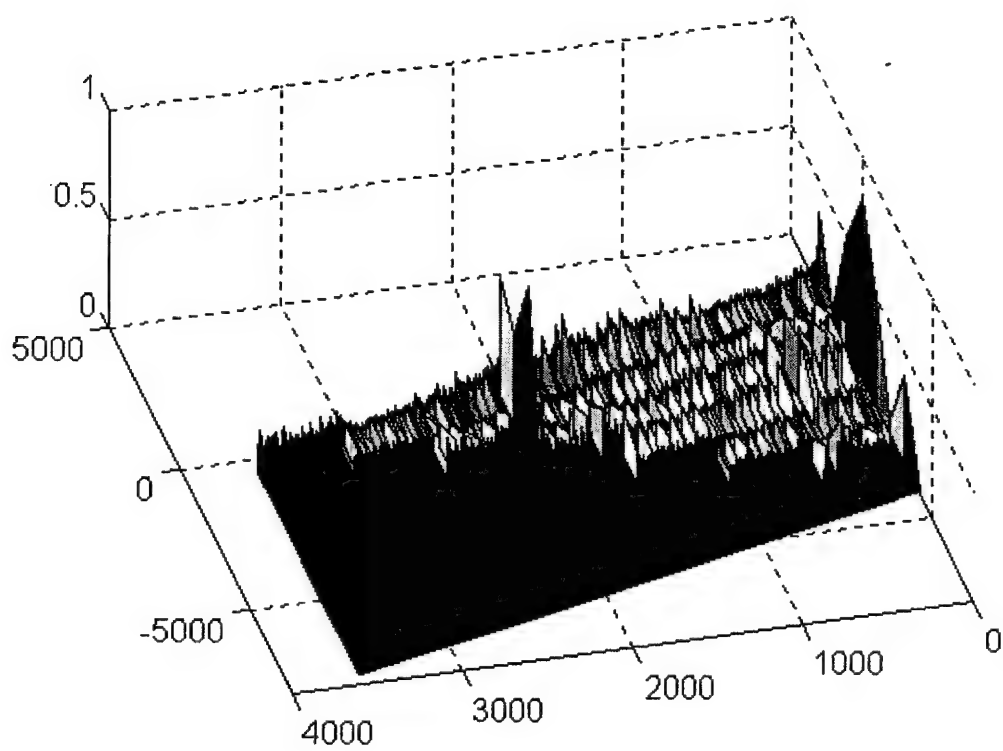
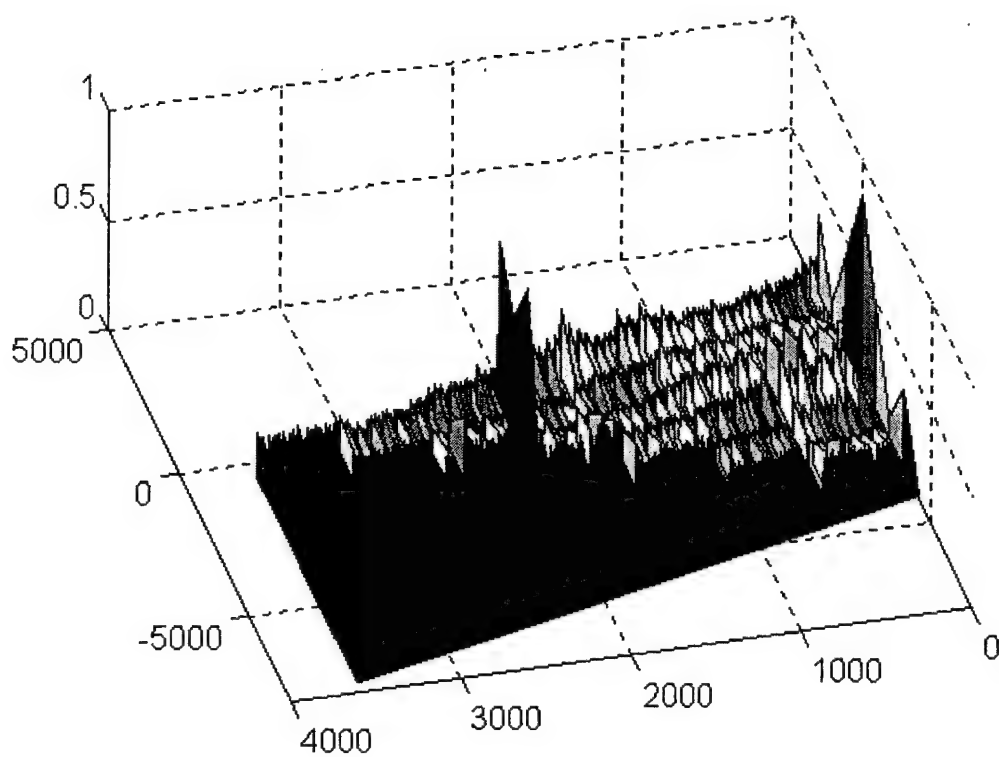


Figure B-127 - SCF for master (top) and slave #1 (bottom), time 409520

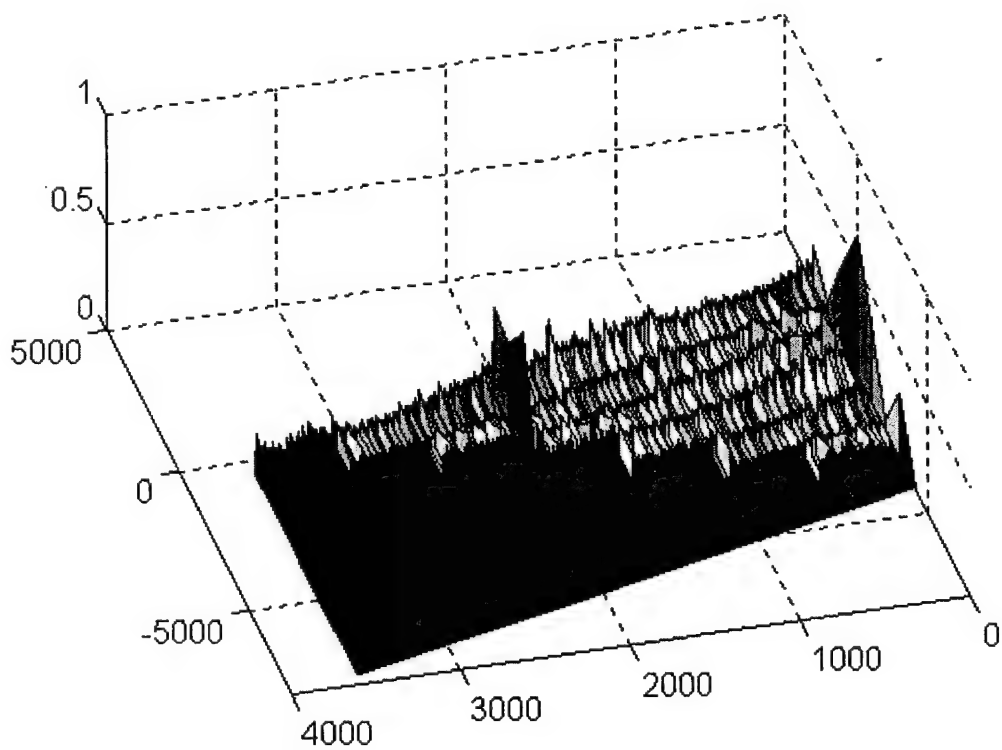
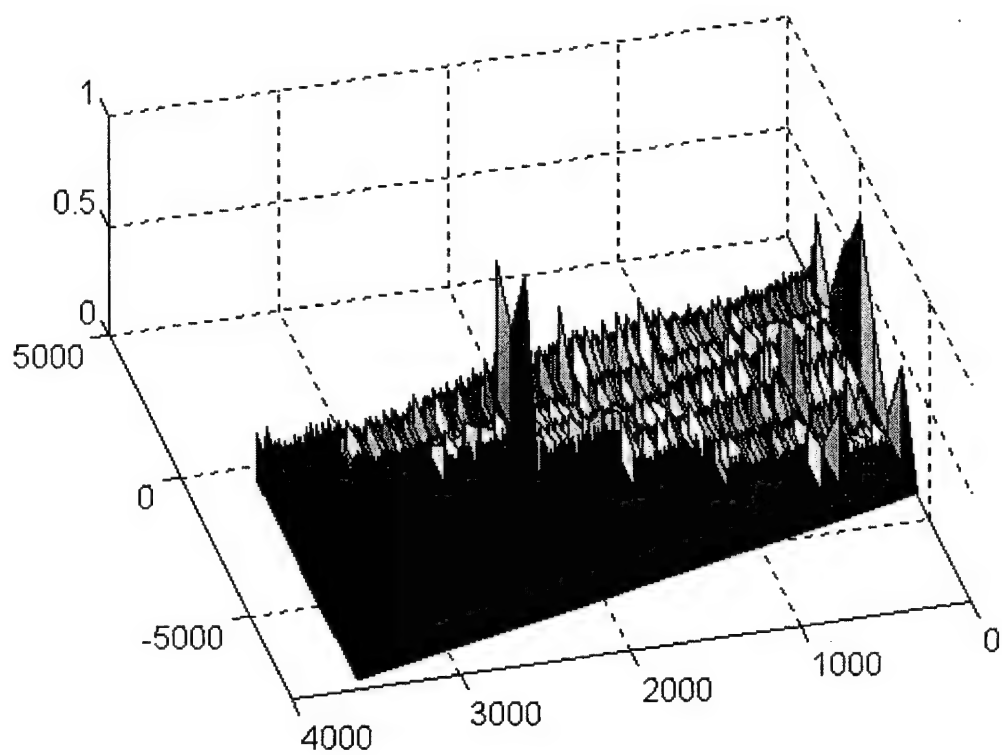


Figure B-128 - SCF for slave #2 (top) and slave #3 (bottom), time 409520

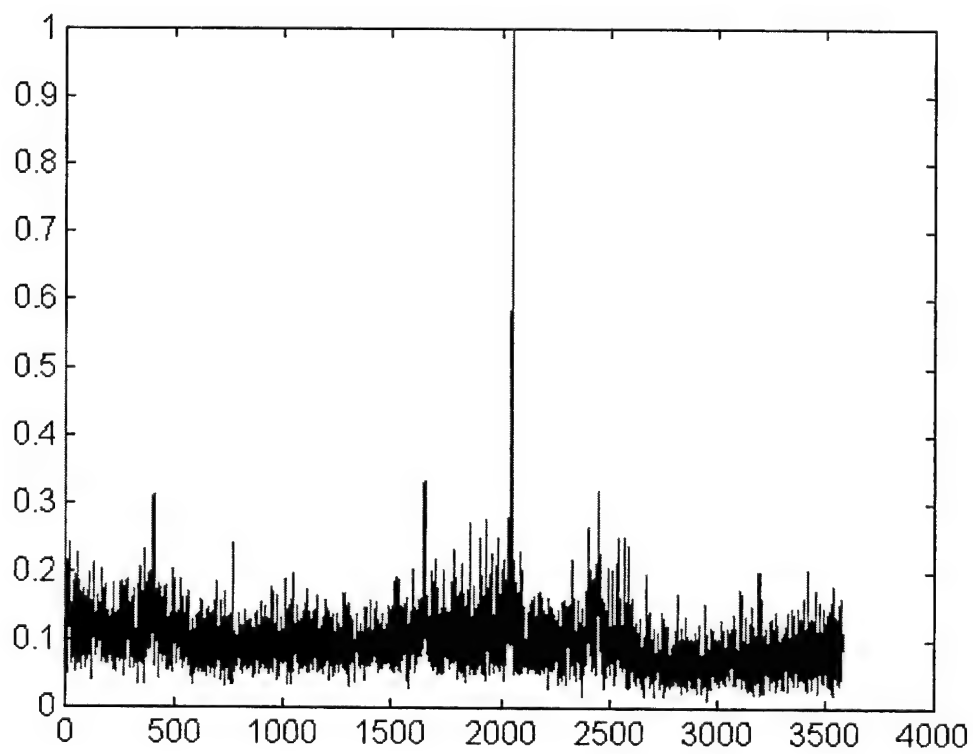
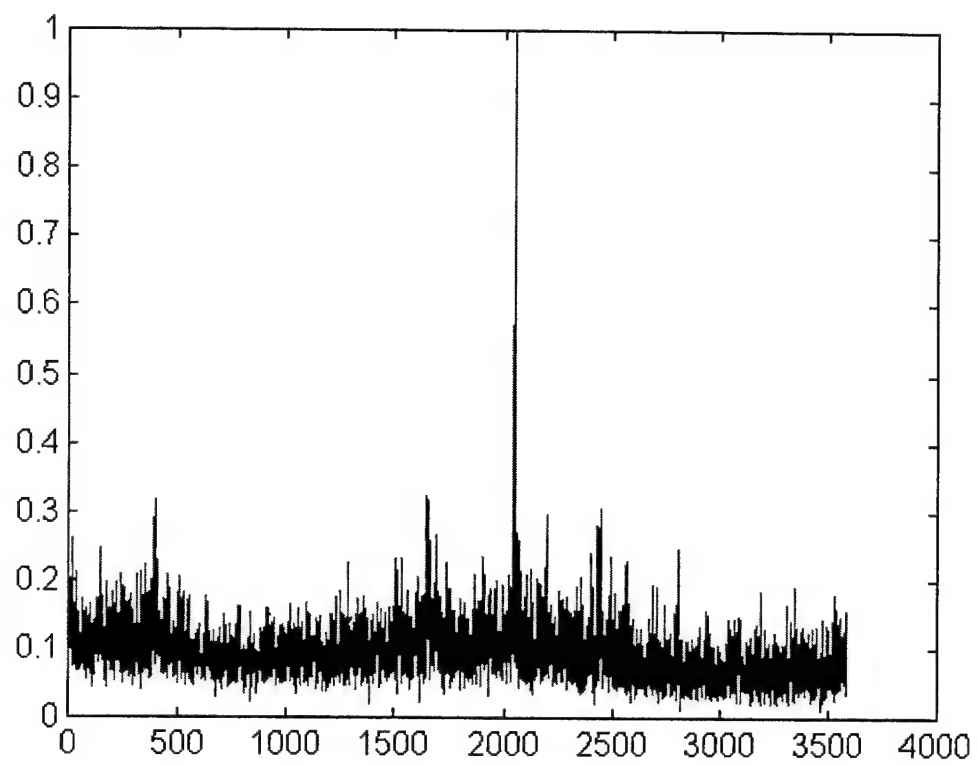


Figure B-129 - Cycle freq vs Max-magnitude of SCF for master (top) and slave #1 (bottom), time 409520

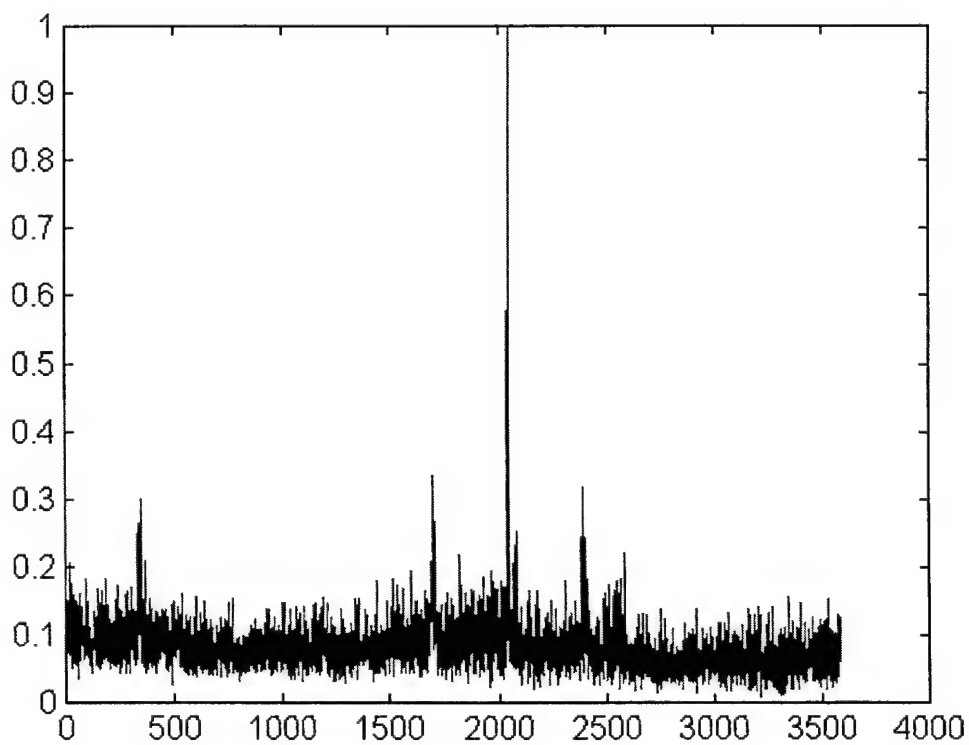
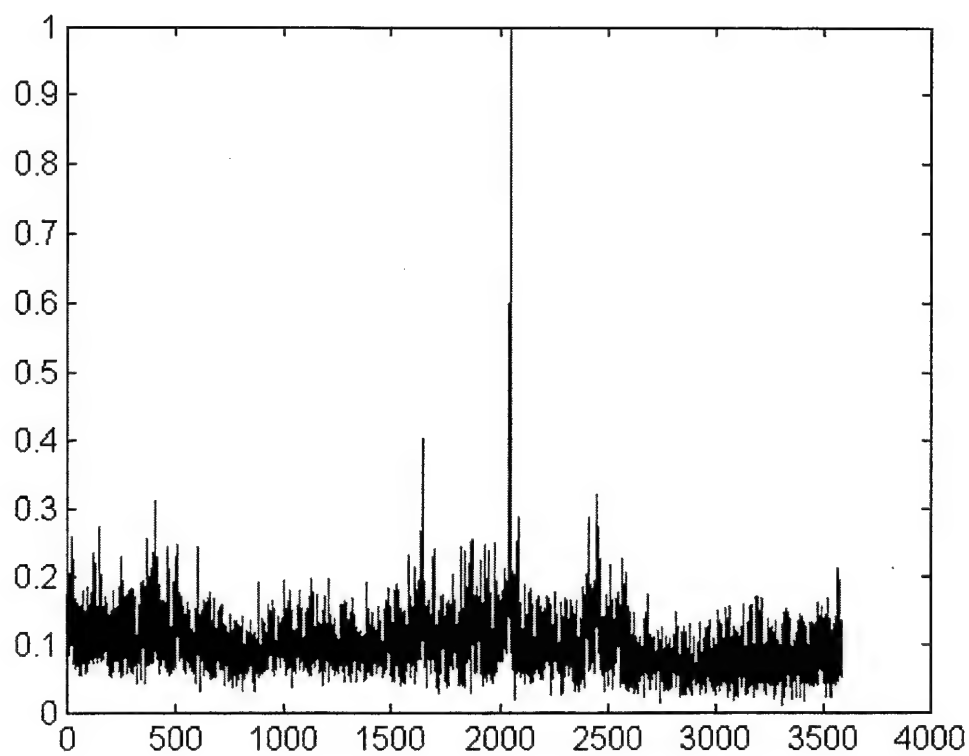


Figure B-130 - Cycle freq vs Max-magnitude of SCF for slave #2 (top) and slave #3 (bottom), time 409520

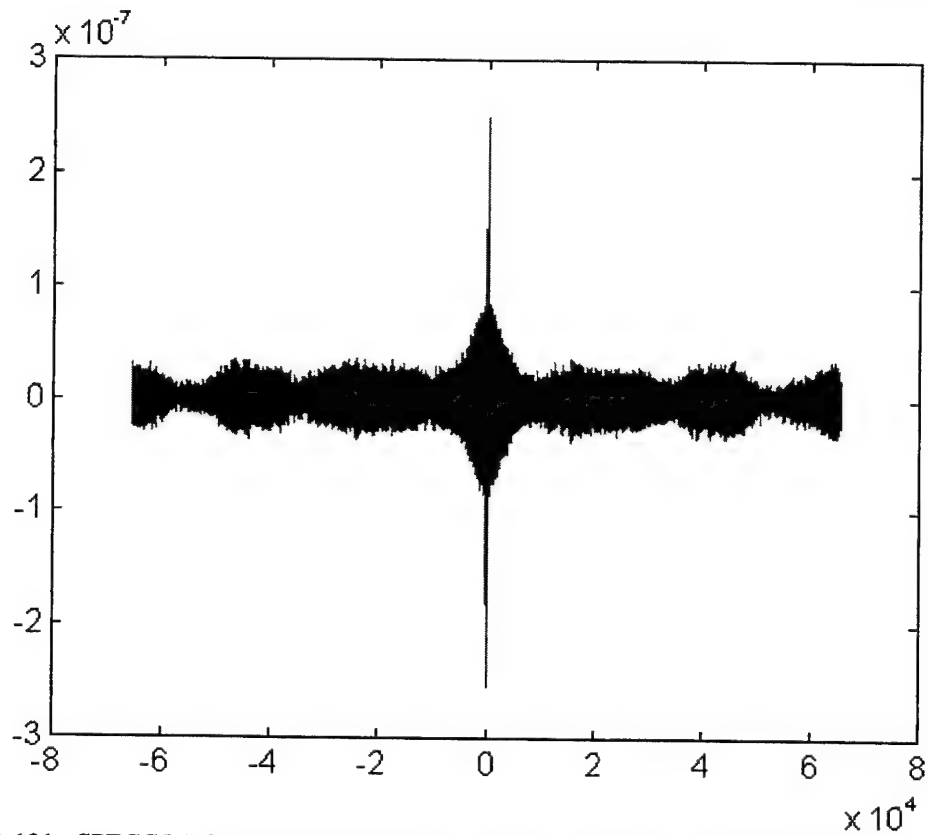
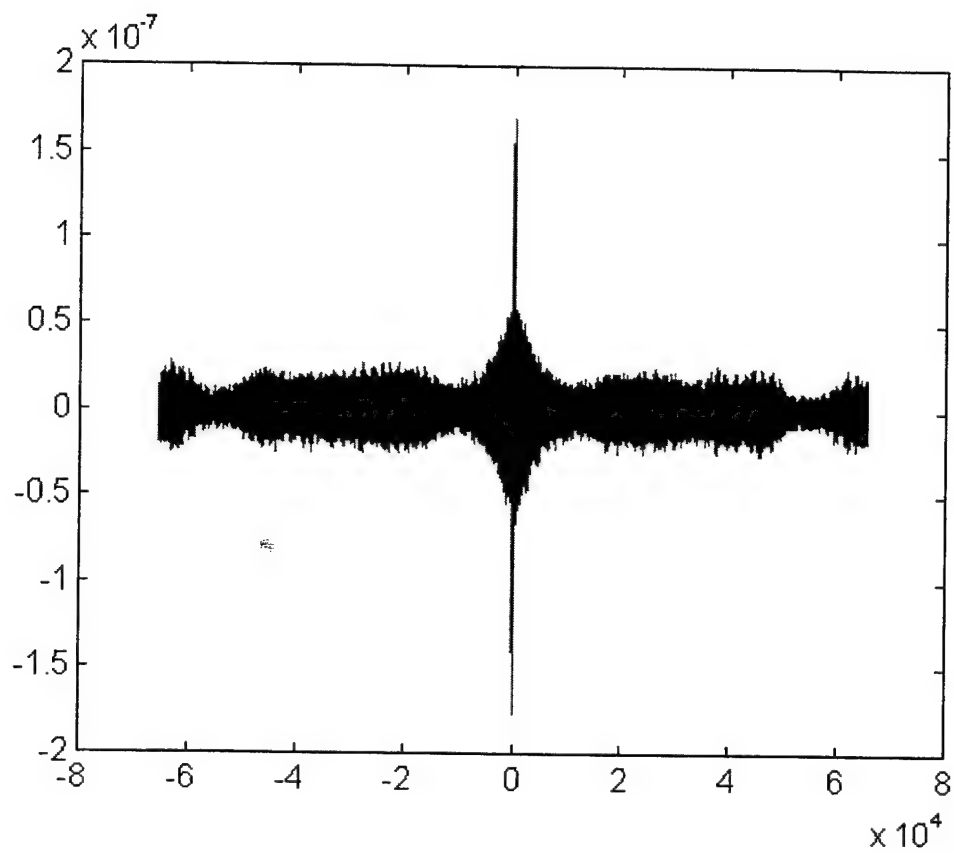


Figure B-131 - SPECCOA for master and slave #1 (top) and master and slave #2 (bottom), time 409520

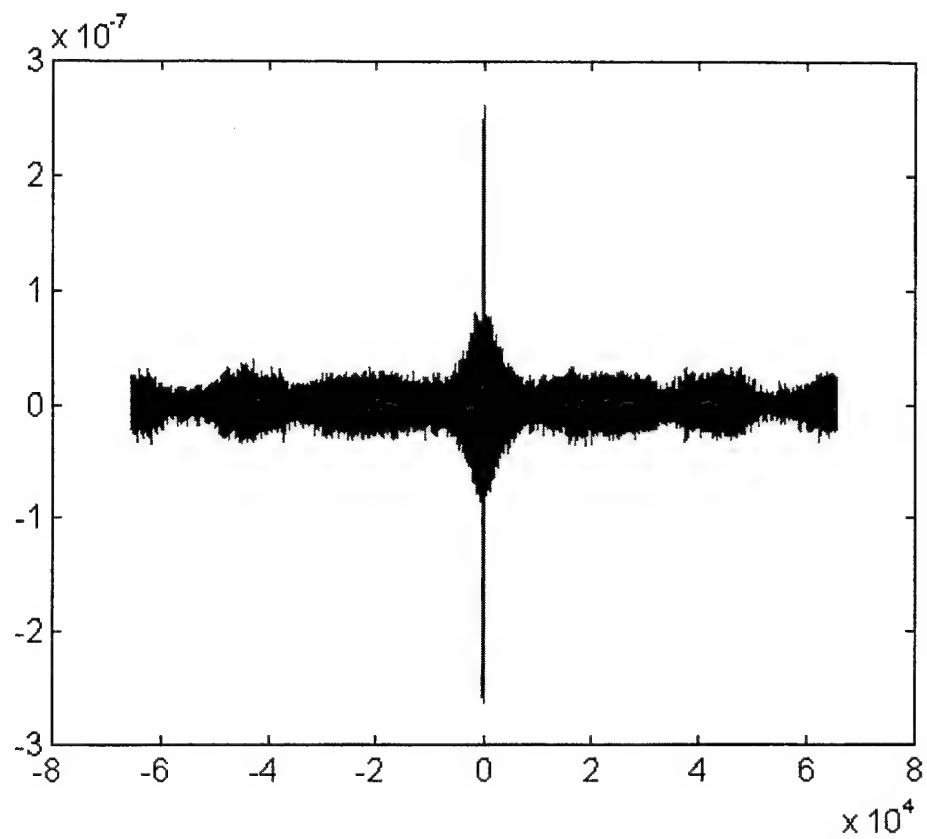


Figure B-132 - SPECCOA for master and slave #3, time 409520

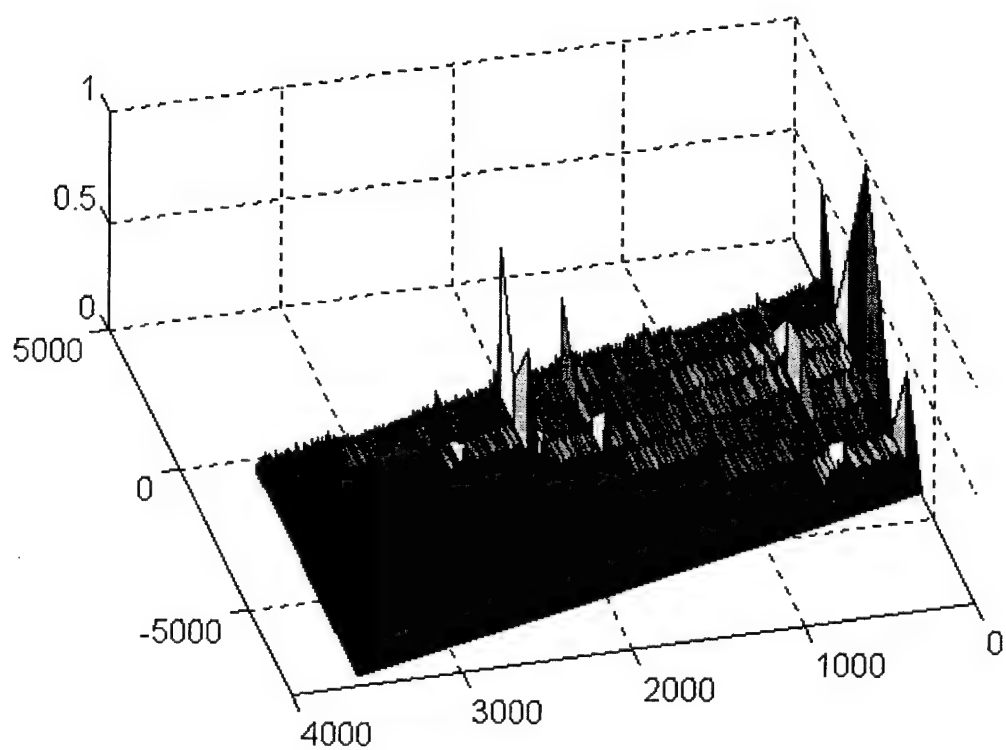
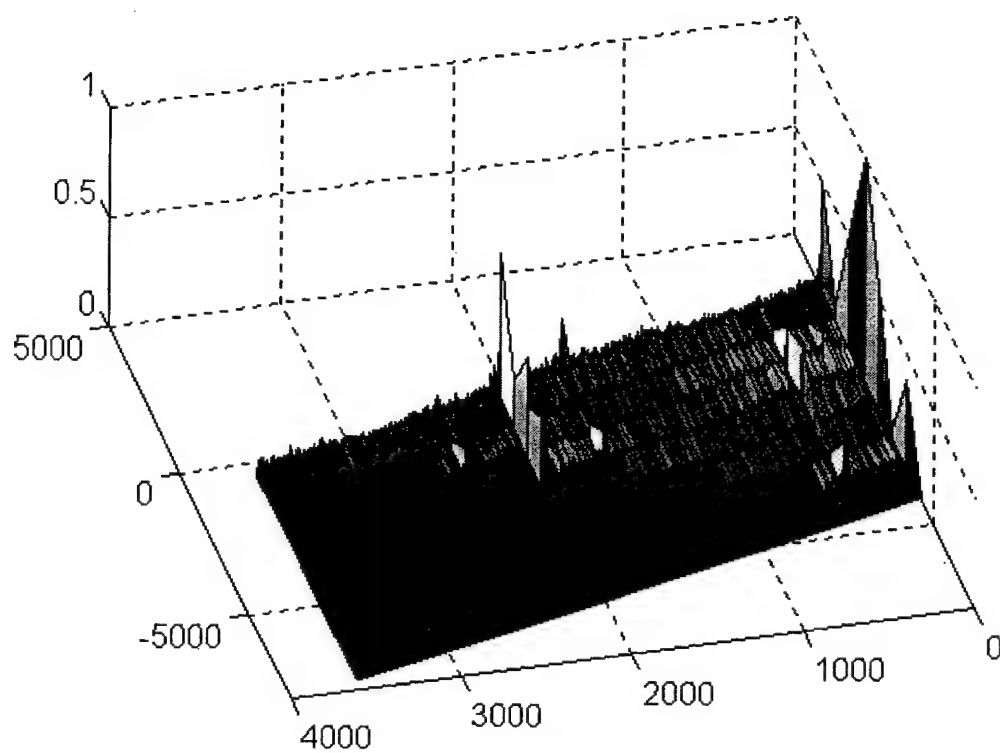


Figure B-133 - SCF for master (top) and slave #1 (bottom), time 409525

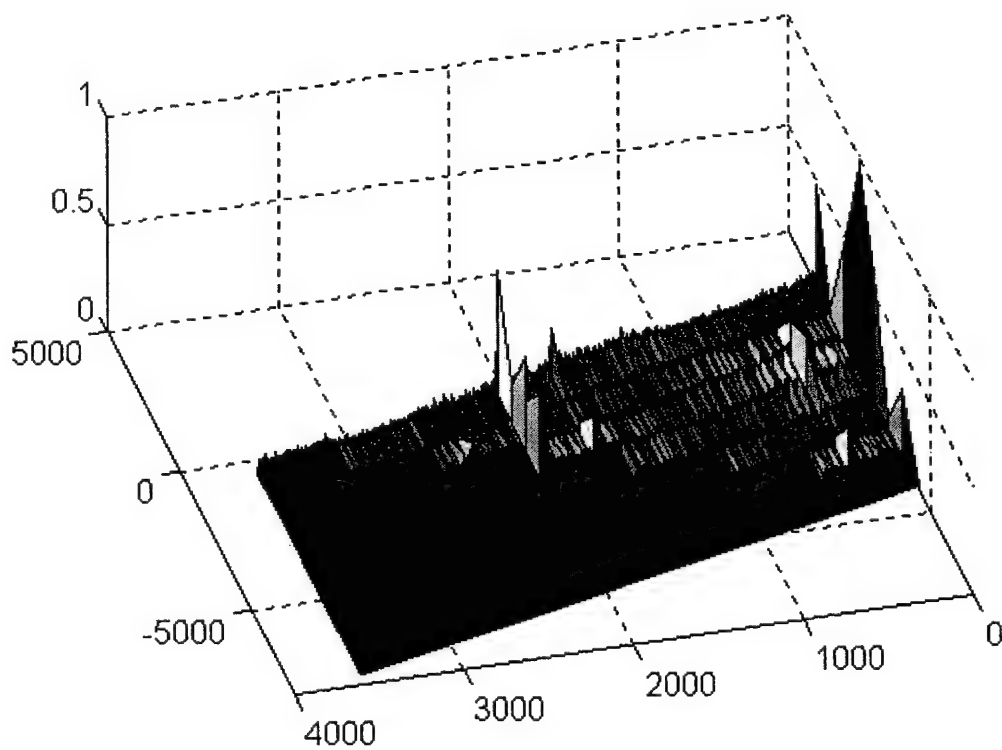
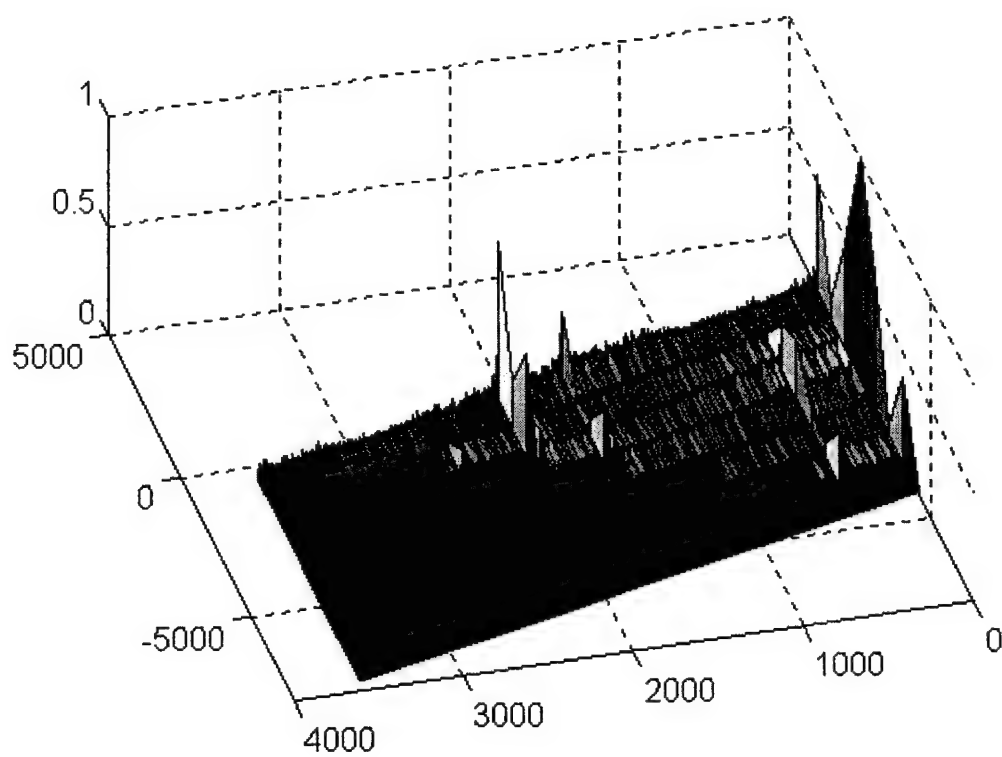


Figure B-134 - SCF for slave #2 (top) and slave #3 (bottom), time 409525

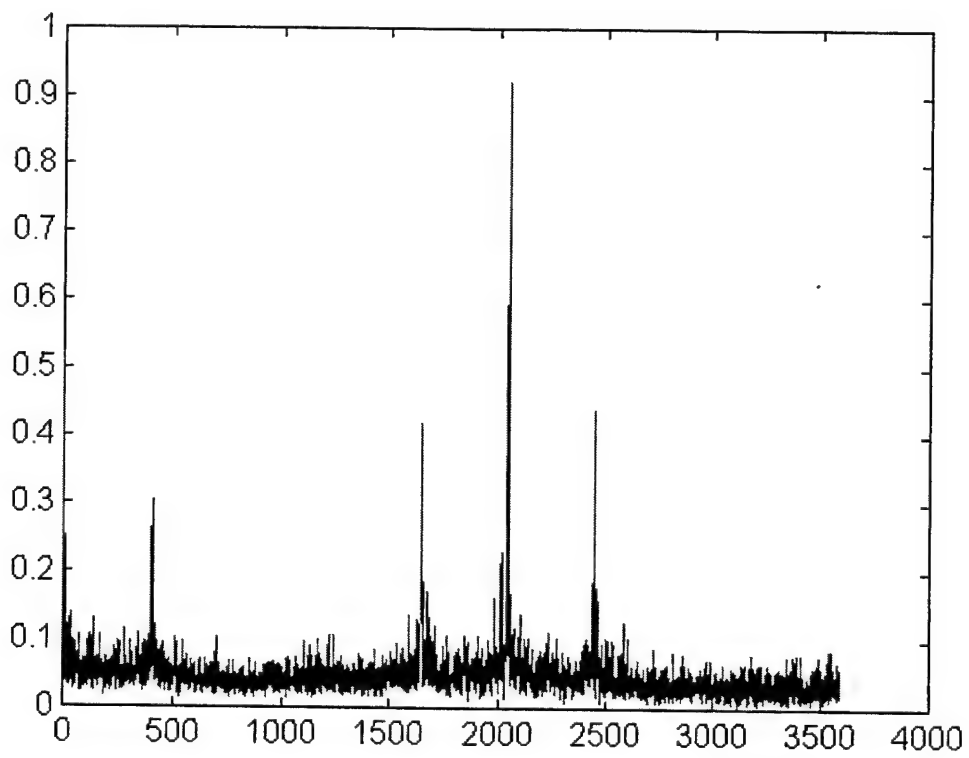
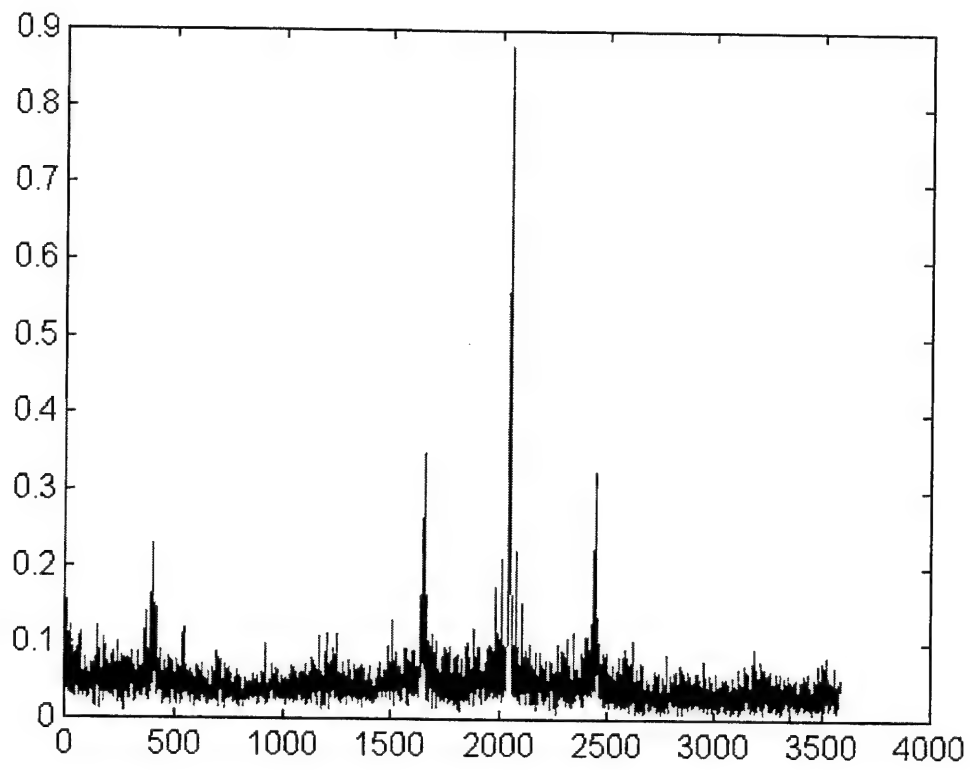


Figure B-135 - Cycle freq vs Max-magnitude of SCF for master (top) and slave #1 (bottom), time 409525

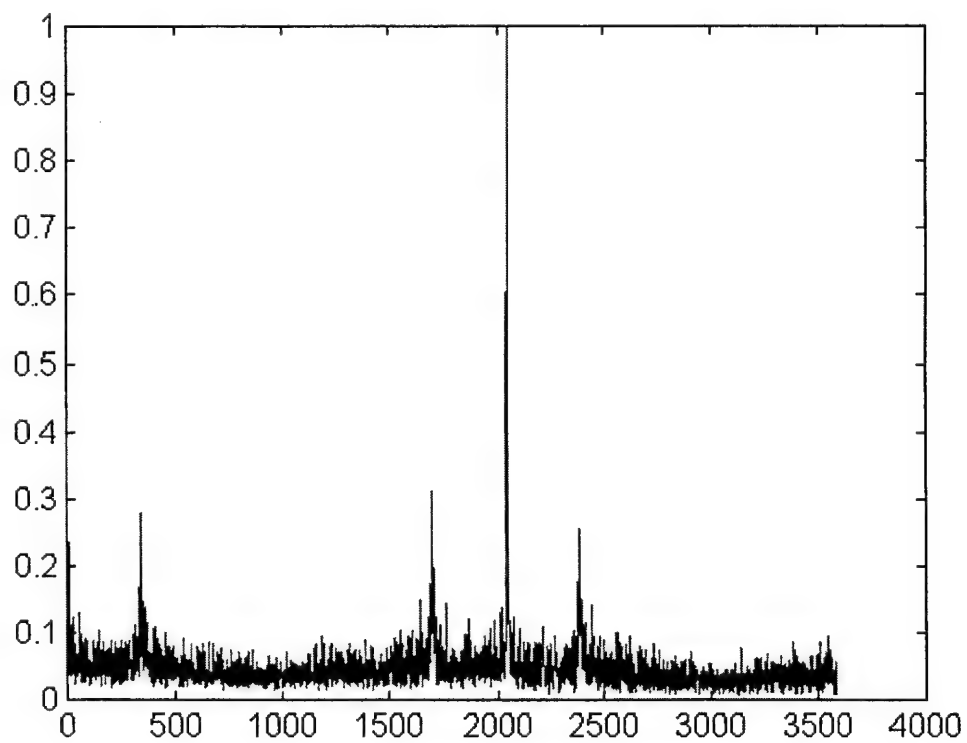
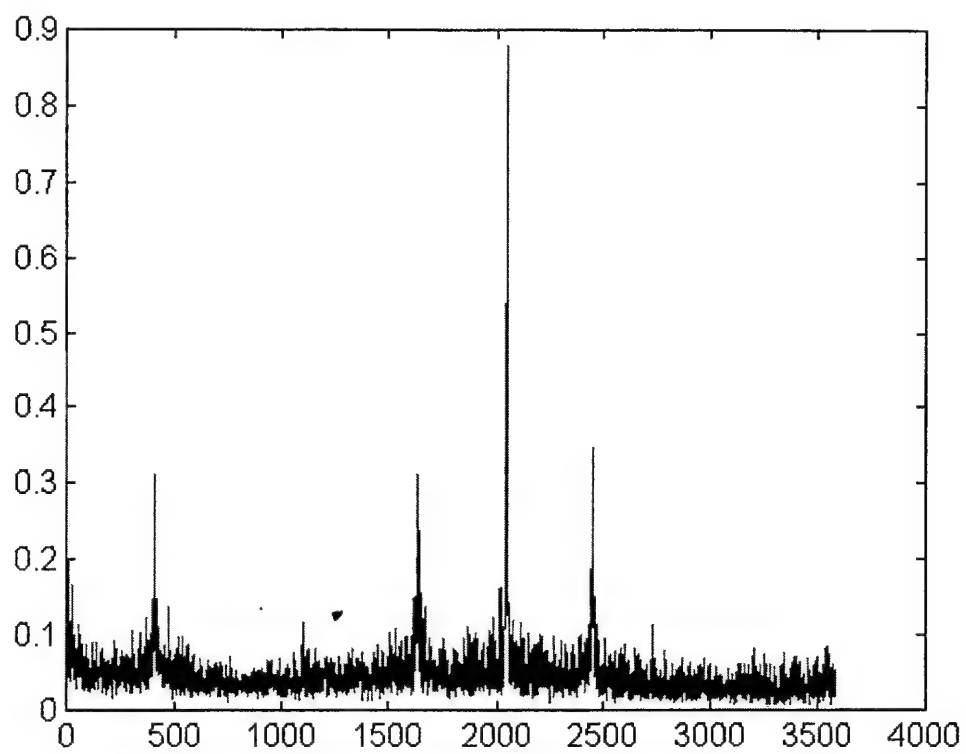


Figure B-136 - Cycle freq vs Max-magnitude of SCF for slave #2 (top) and slave #3 (bottom), time 409525

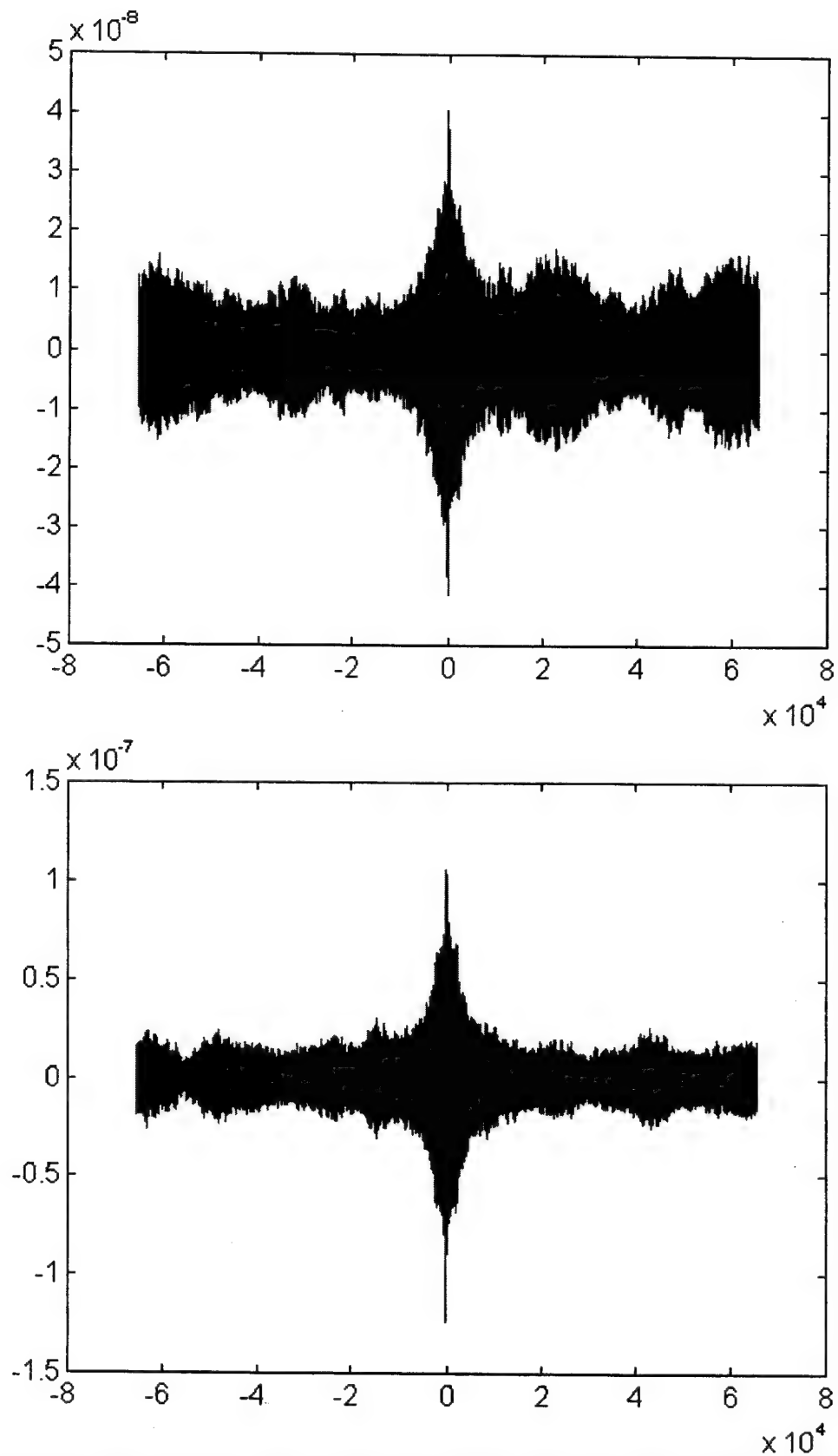


Figure B-137 - SPECCOA for master and slave #1 (top) and master and slave #2 (bottom), time 409525

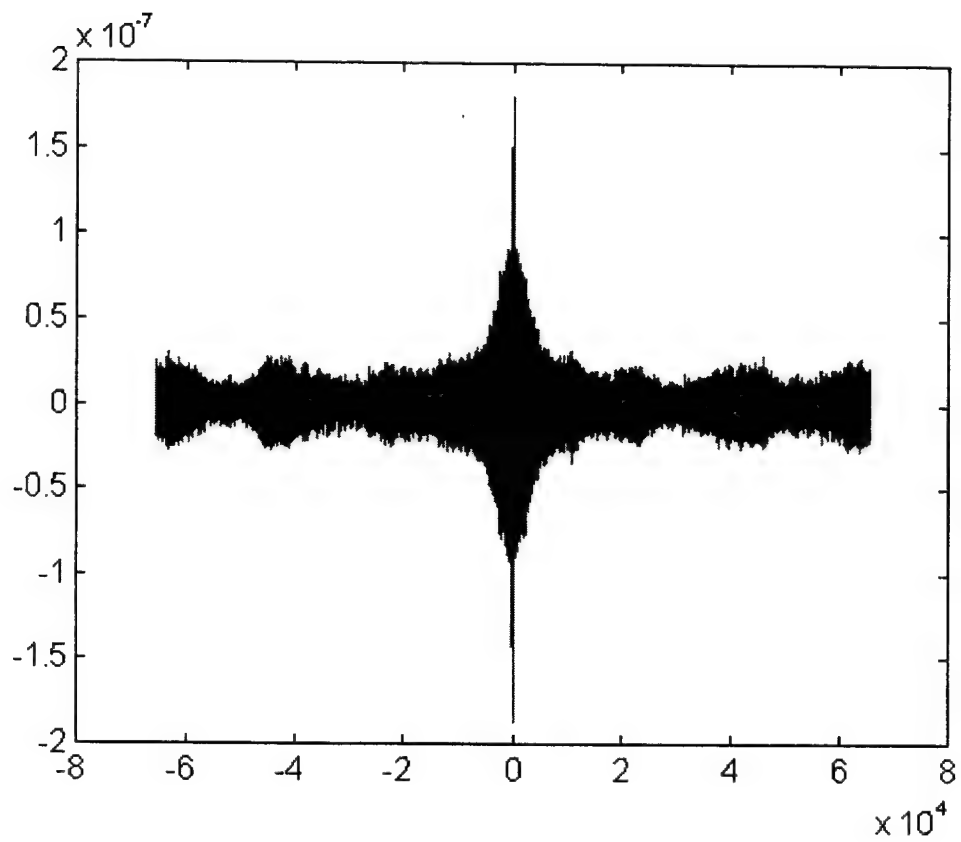


Figure B-138 - SPECCOA for master and slave #3, time 409525

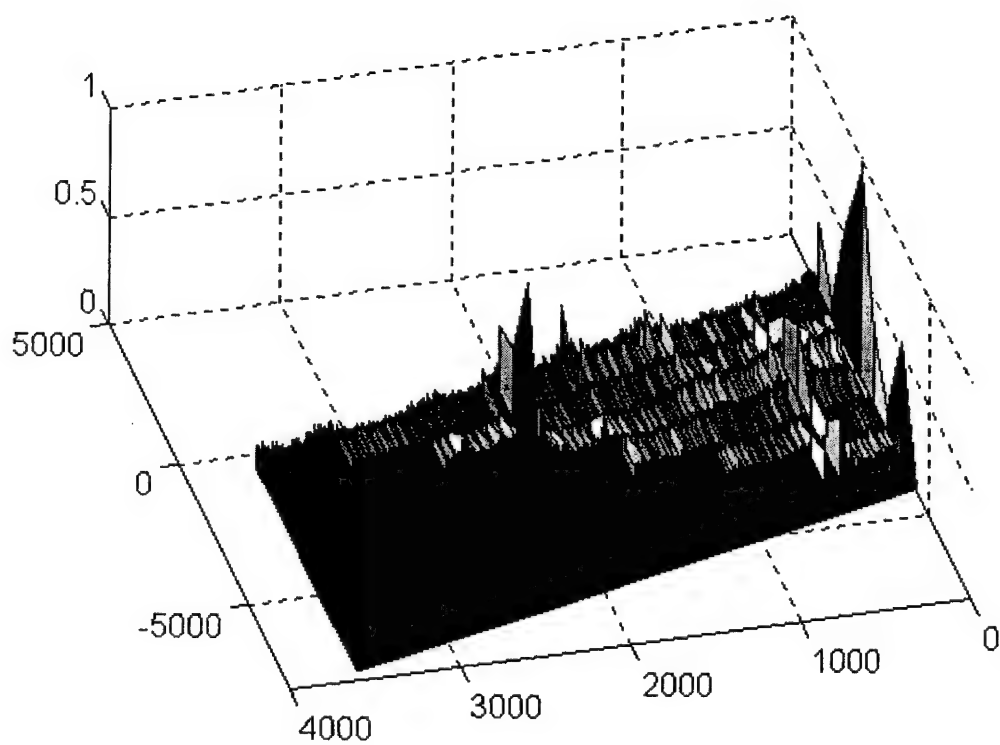
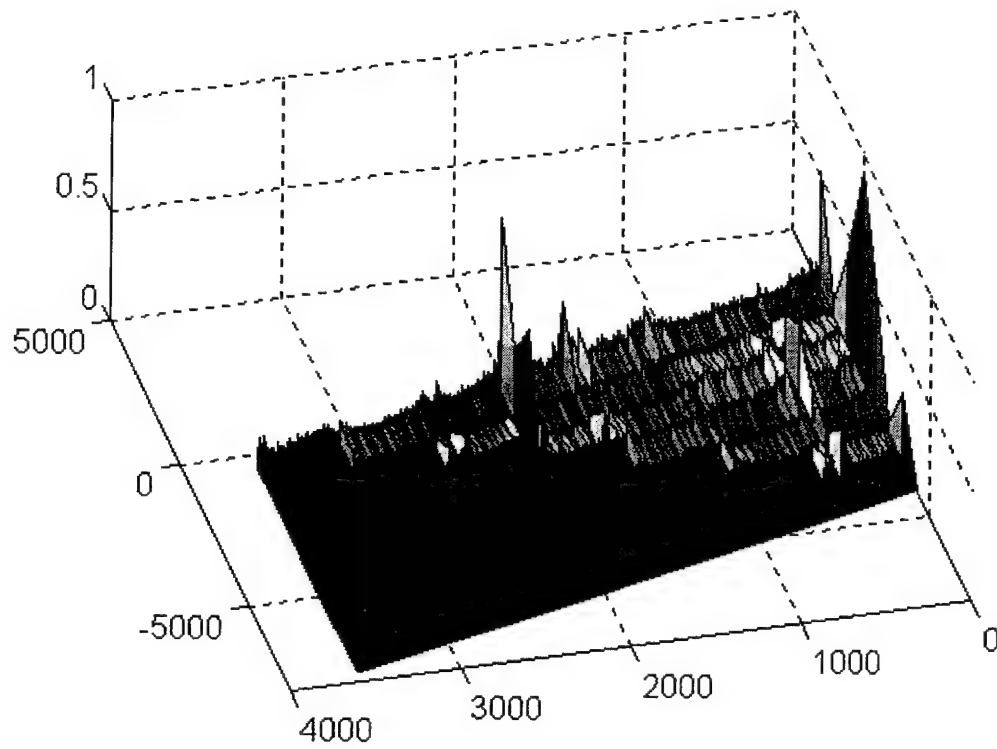


Figure B-139 - SCF for master (top) and slave #1 (bottom), time 409530

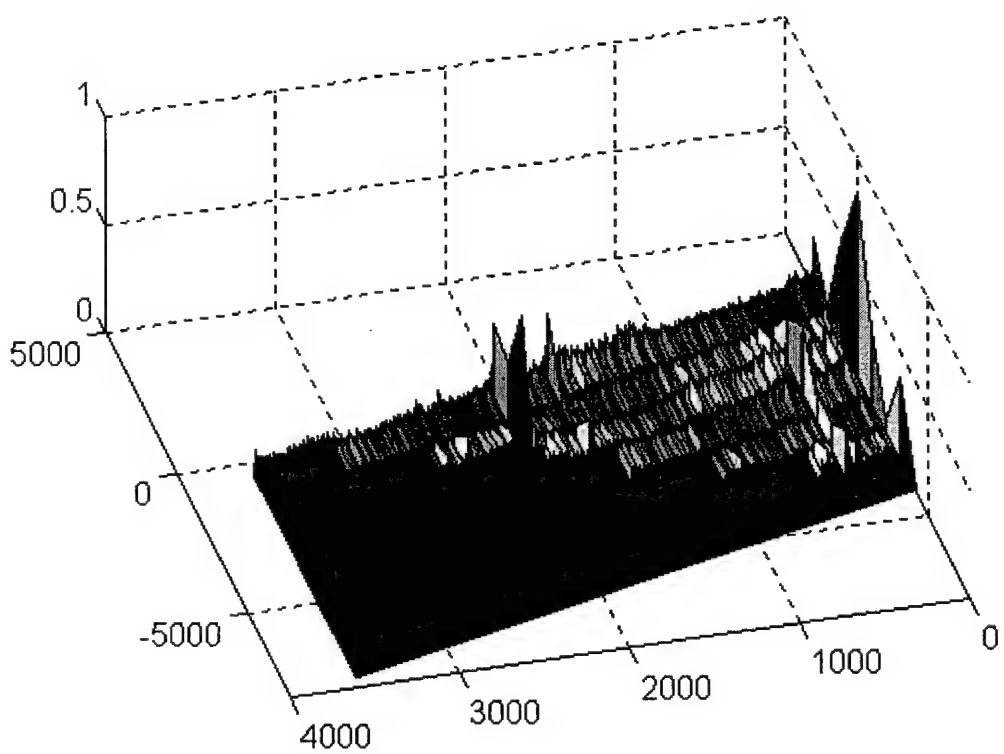
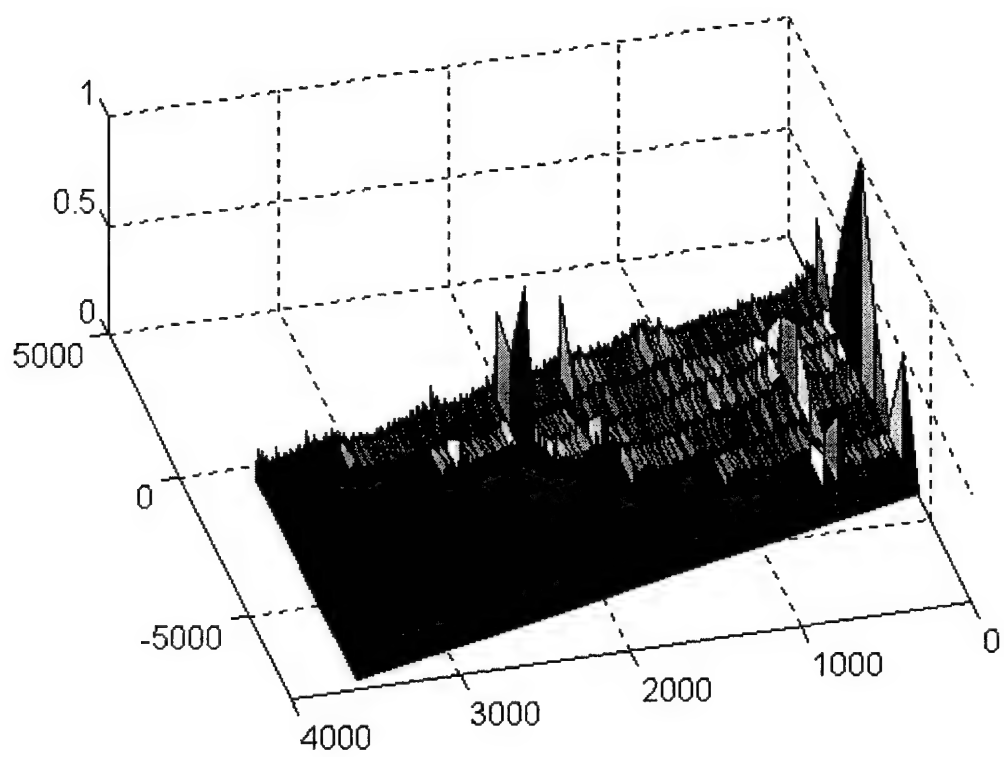


Figure B-140 - SCF for slave #2 (top) and slave #3 (bottom), time 409530

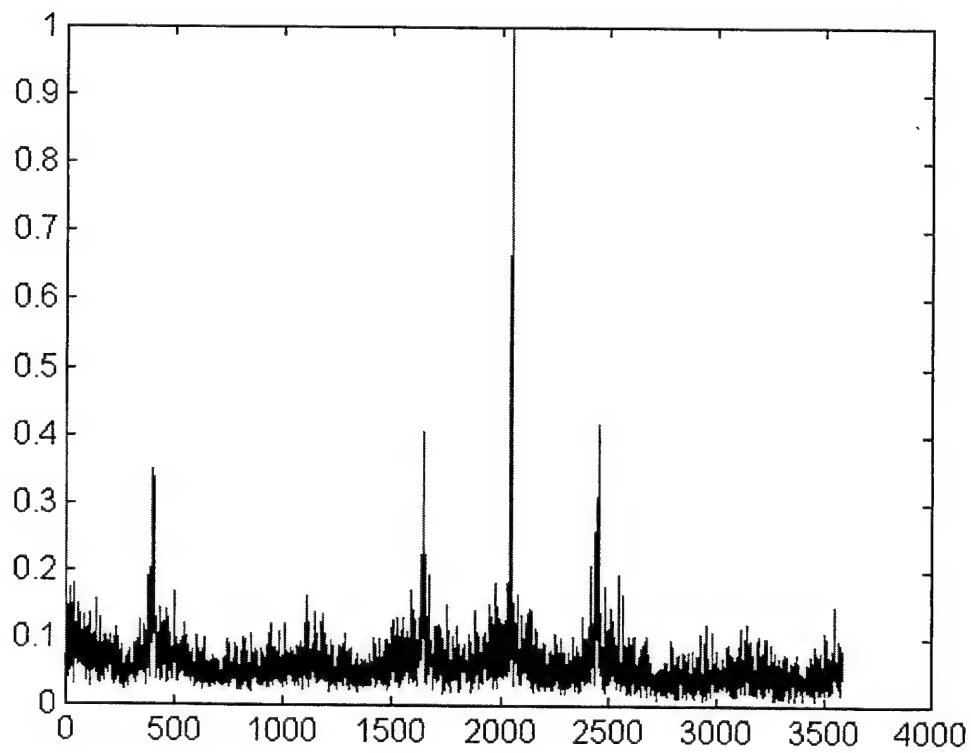
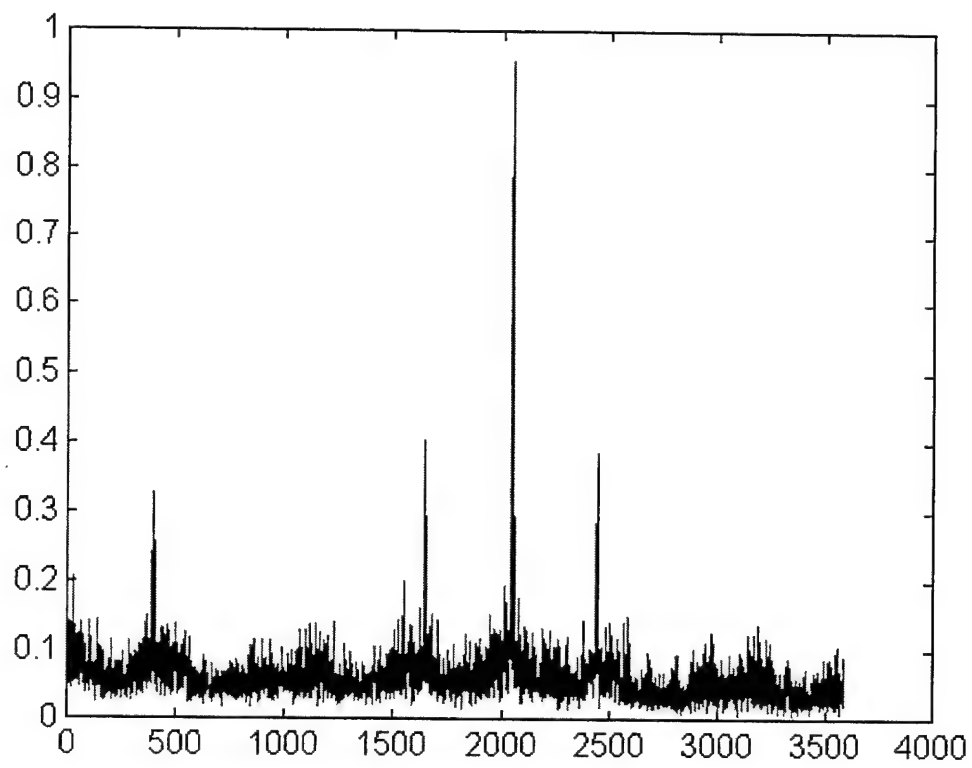


Figure B-141 - Cycle freq vs Max-magnitude of SCF for master (top) and slave #1 (bottom), time 409530

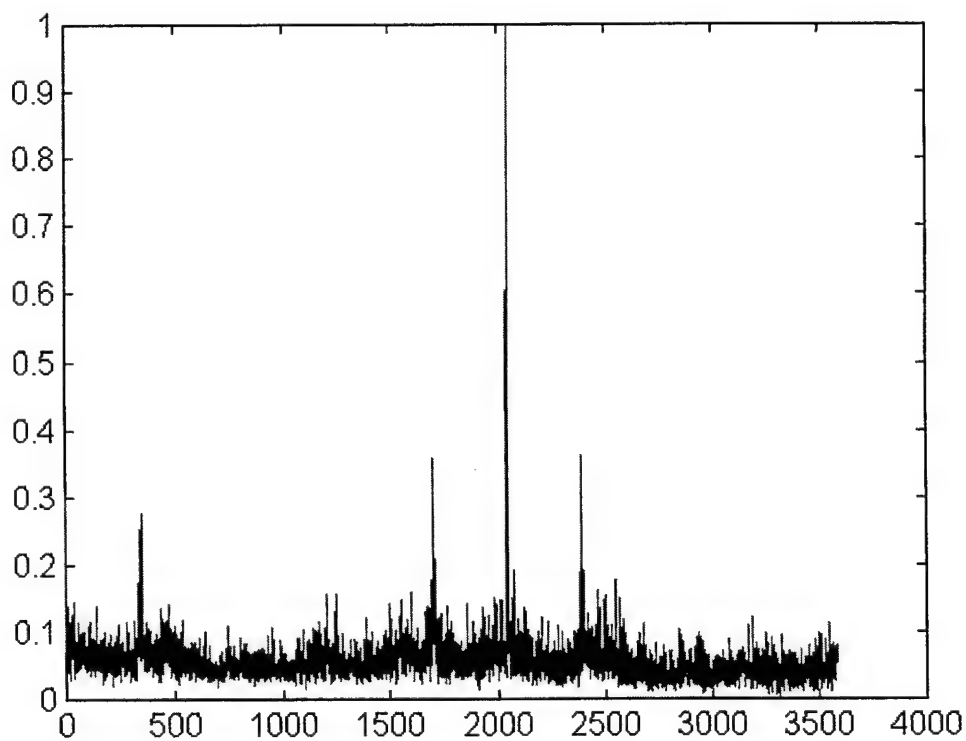
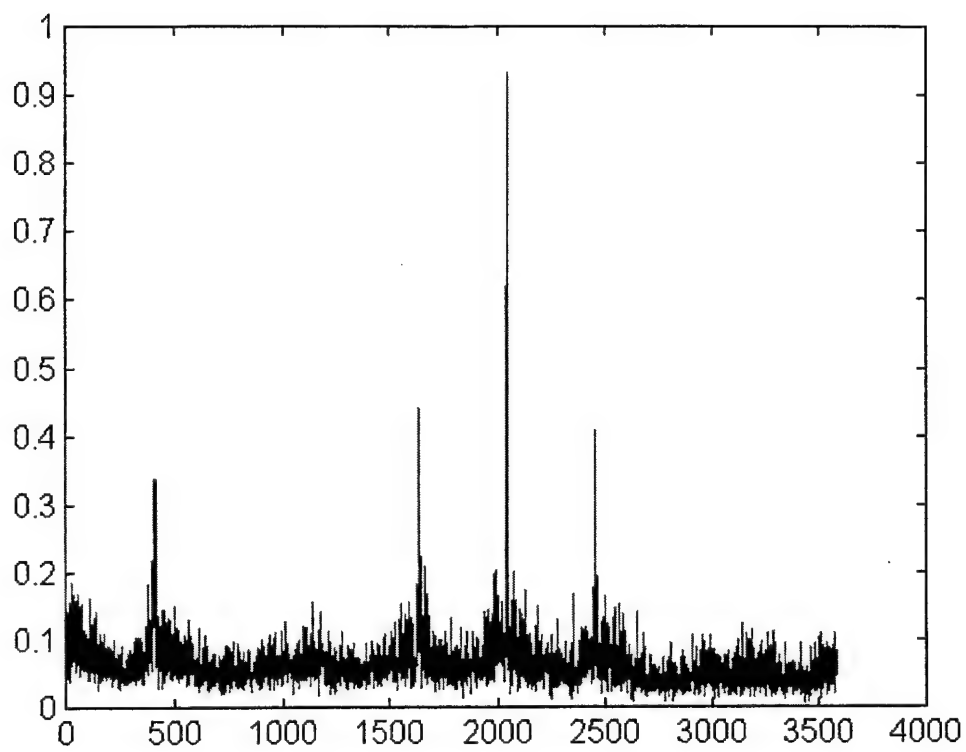


Figure B-142 - Cycle freq vs Max-magnitude of SCF for slave #2 (top) and slave #3 (bottom), time 409530

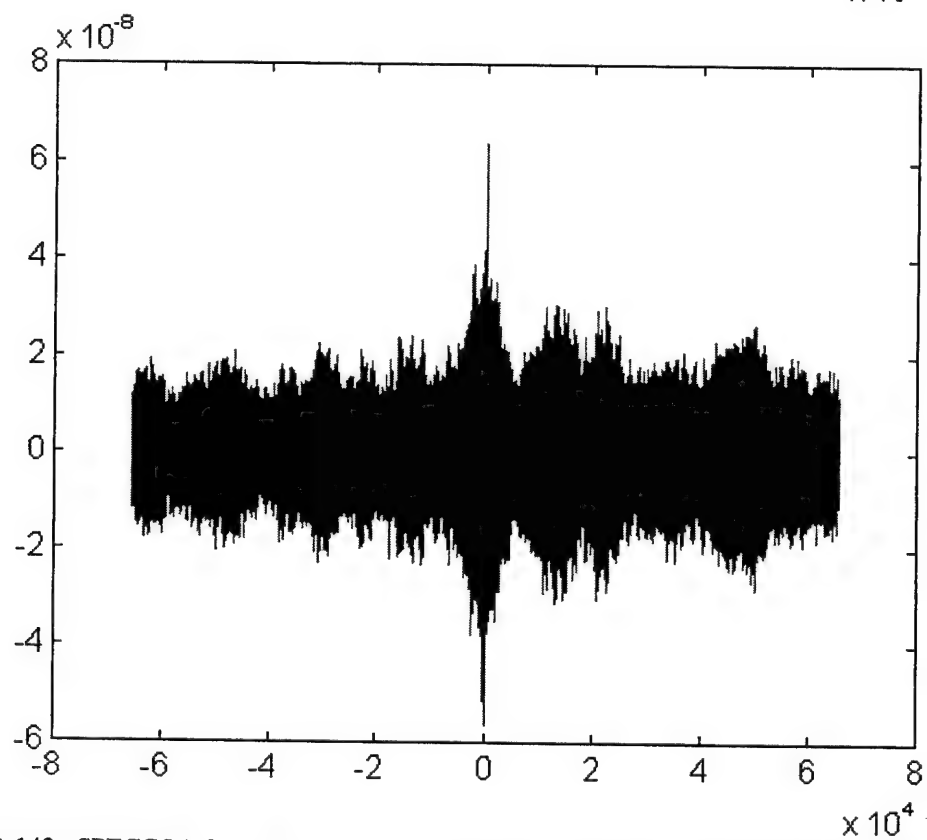
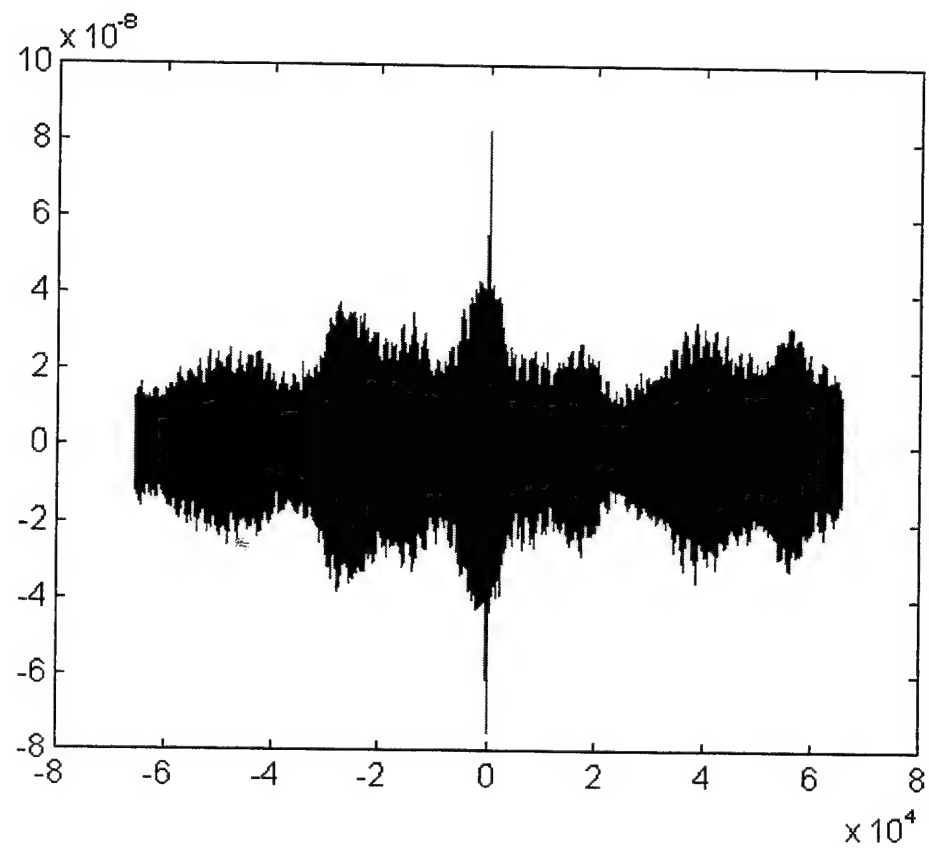


Figure B-143 - SPECCOA for master and slave #1 (top) and master and slave #2 (bottom), time 409530

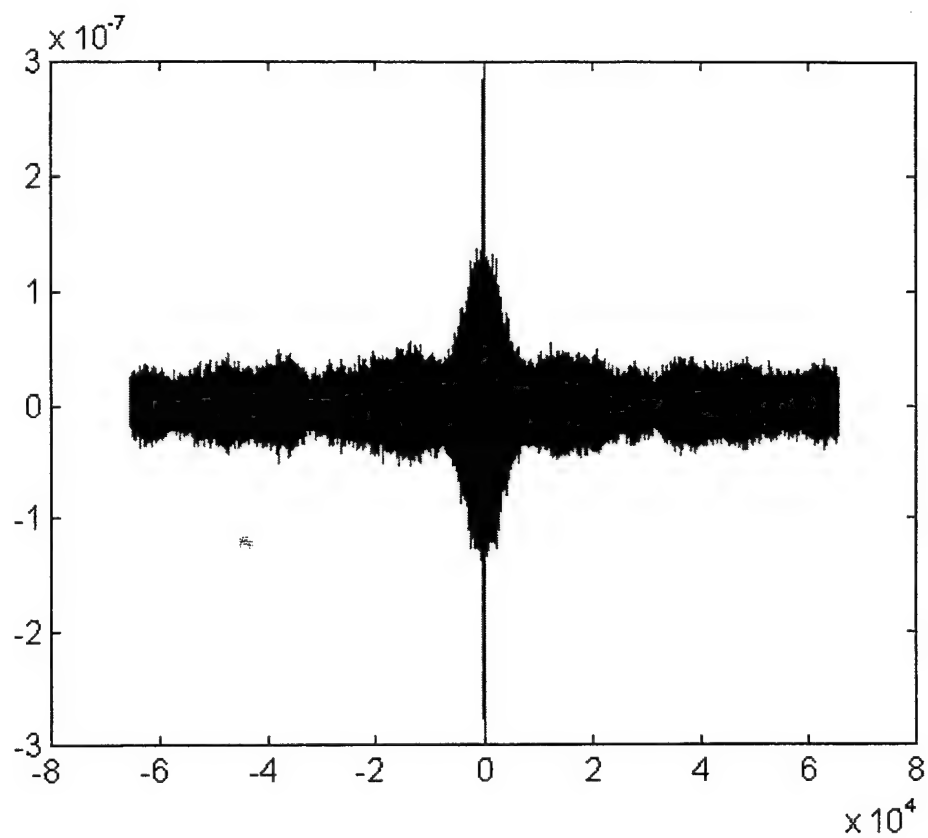


Figure B-144 - SPECCOA for master and slave #3, time 409530

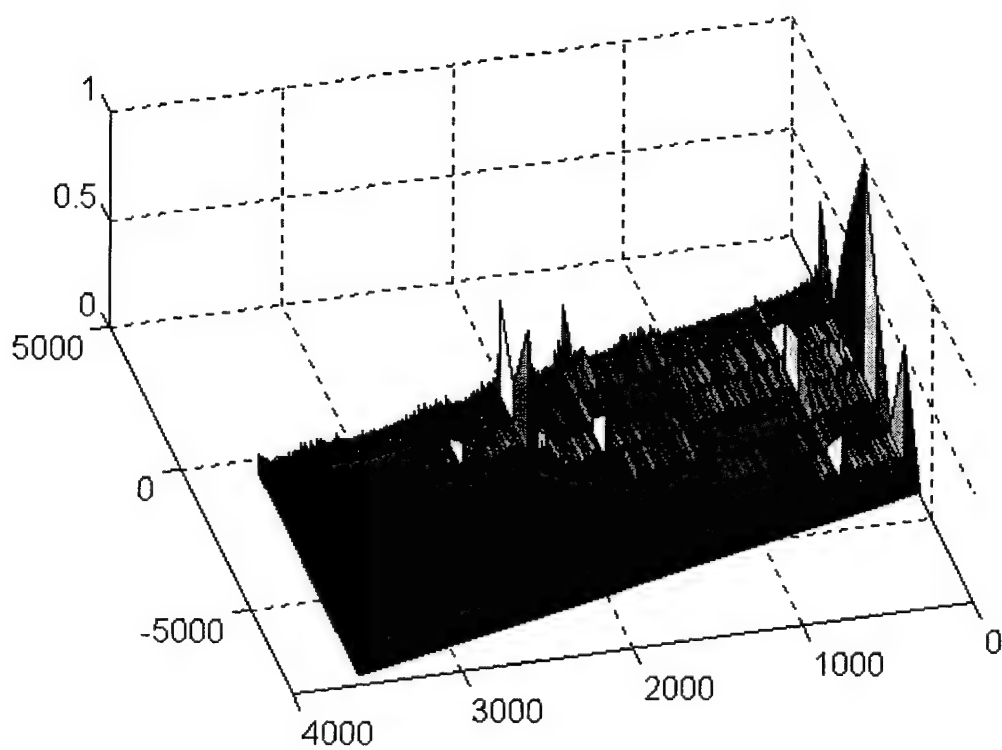
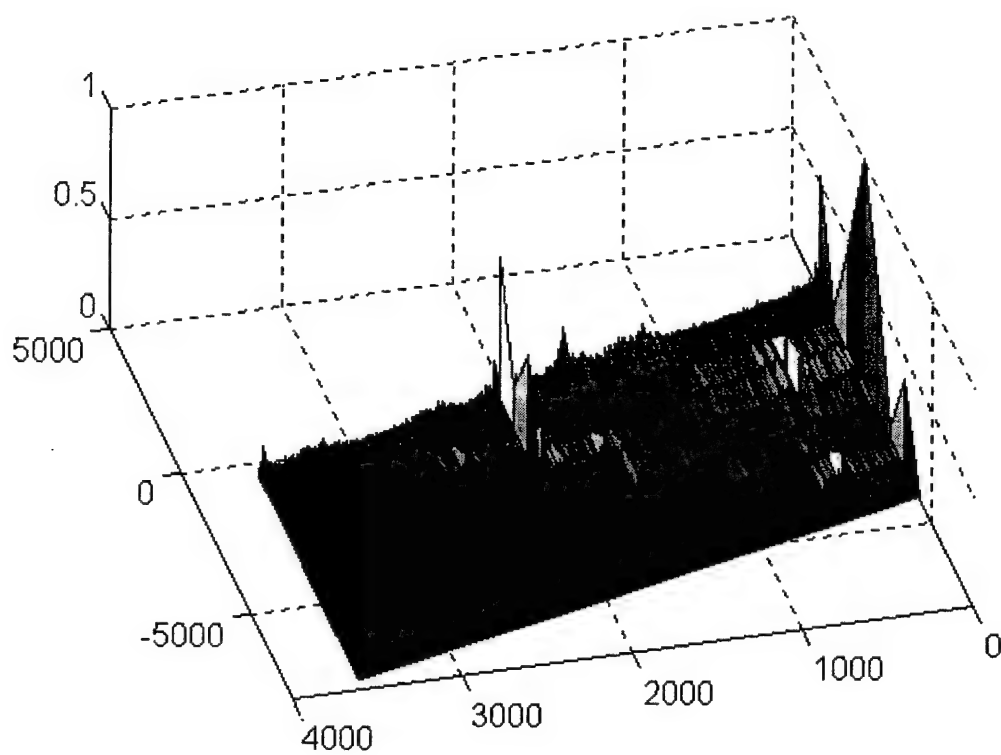


Figure B-145 - SCF for master (top) and slave #1 (bottom), time 409535

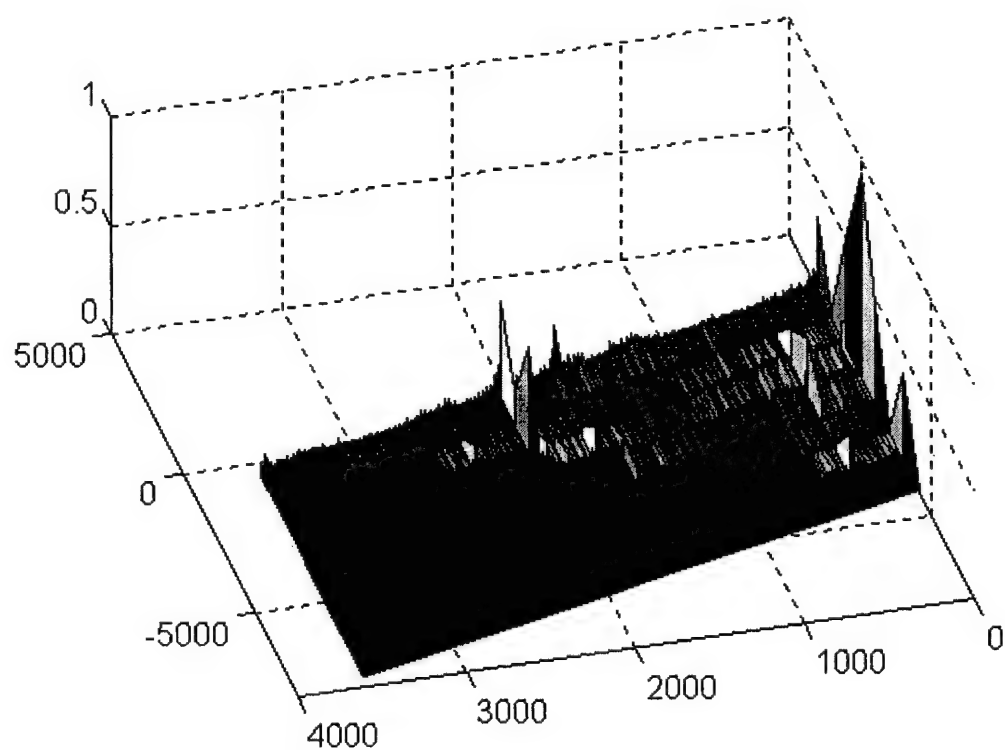
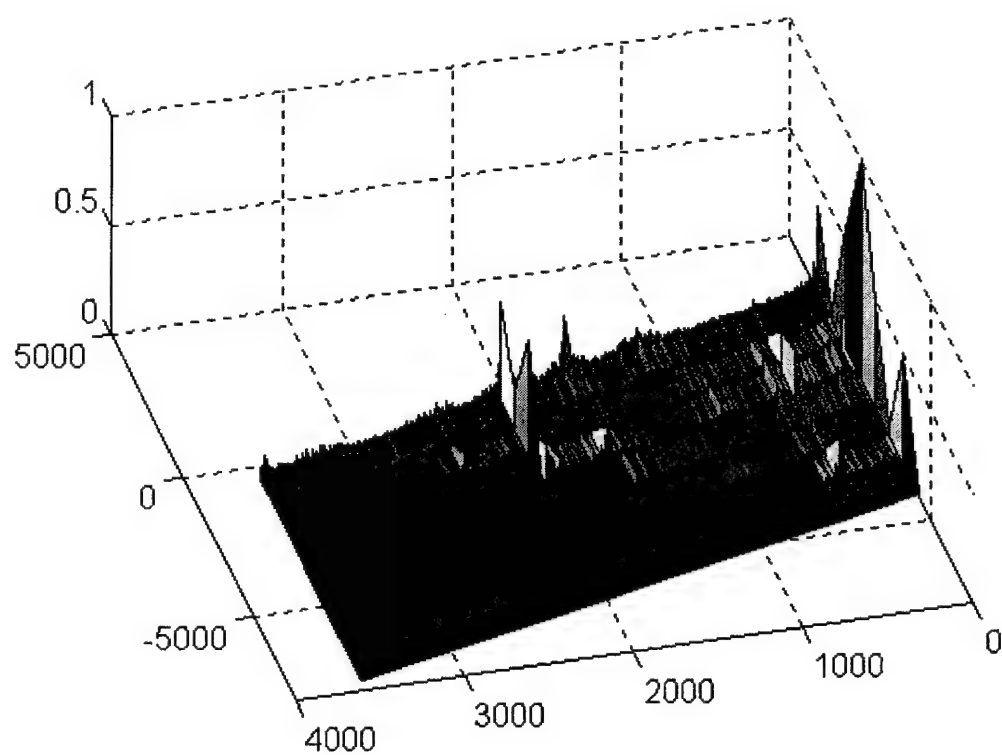


Figure B-146 - SCF for slave #2 (top) and slave #3 (bottom), time 409535

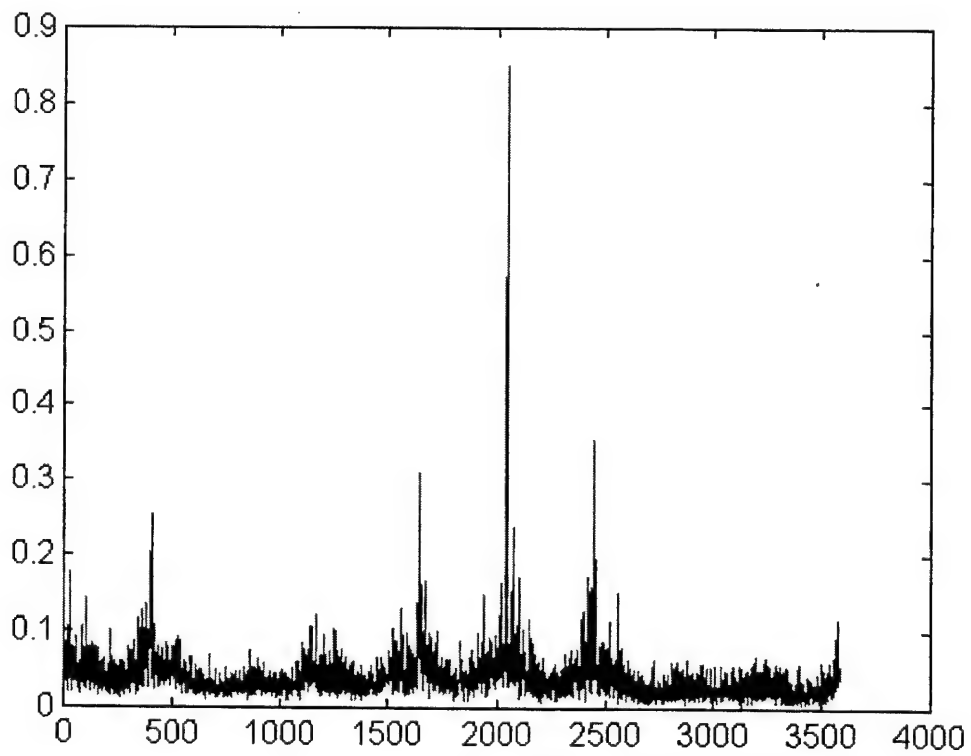
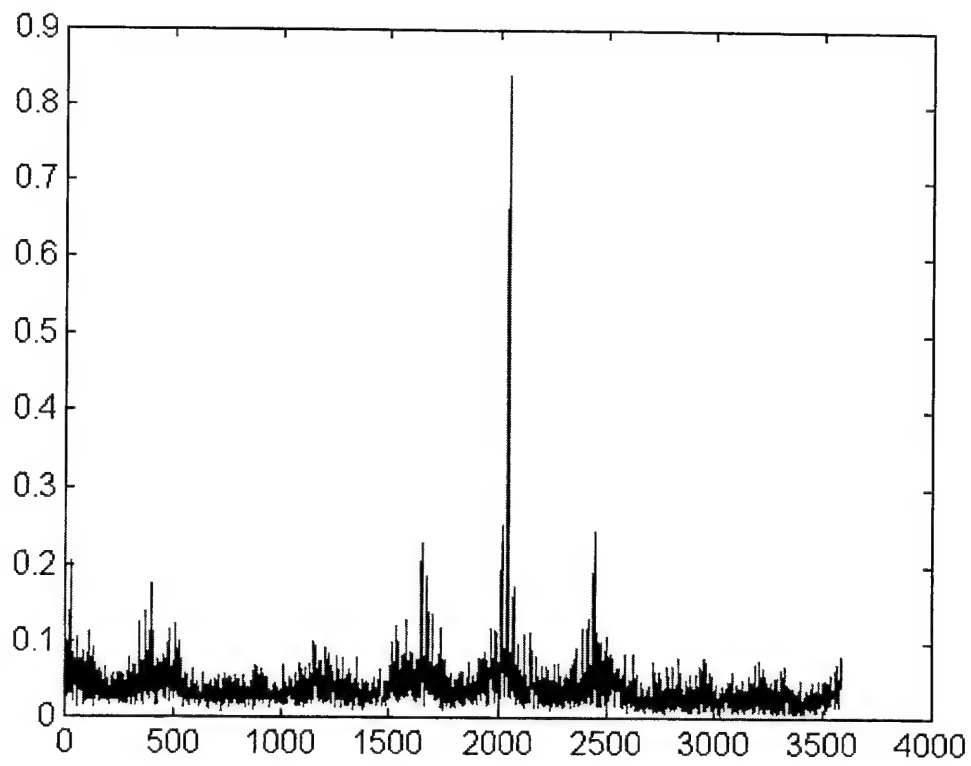


Figure B-147 - Cycle freq vs Max-magnitude of SCF for master (top) and slave #1 (bottom), time 409535

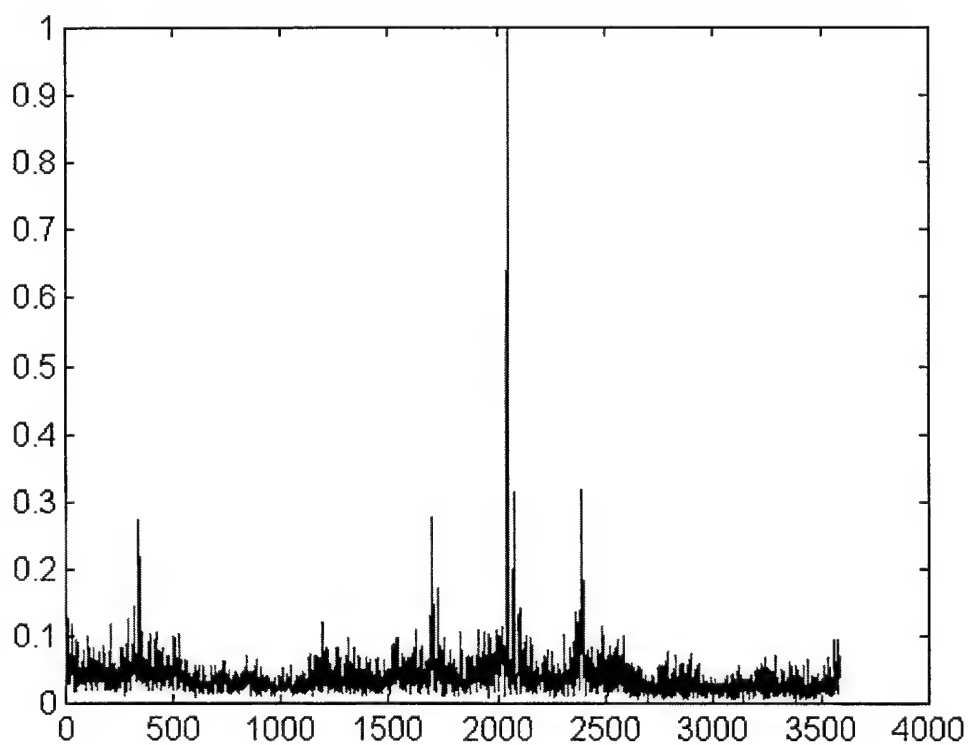
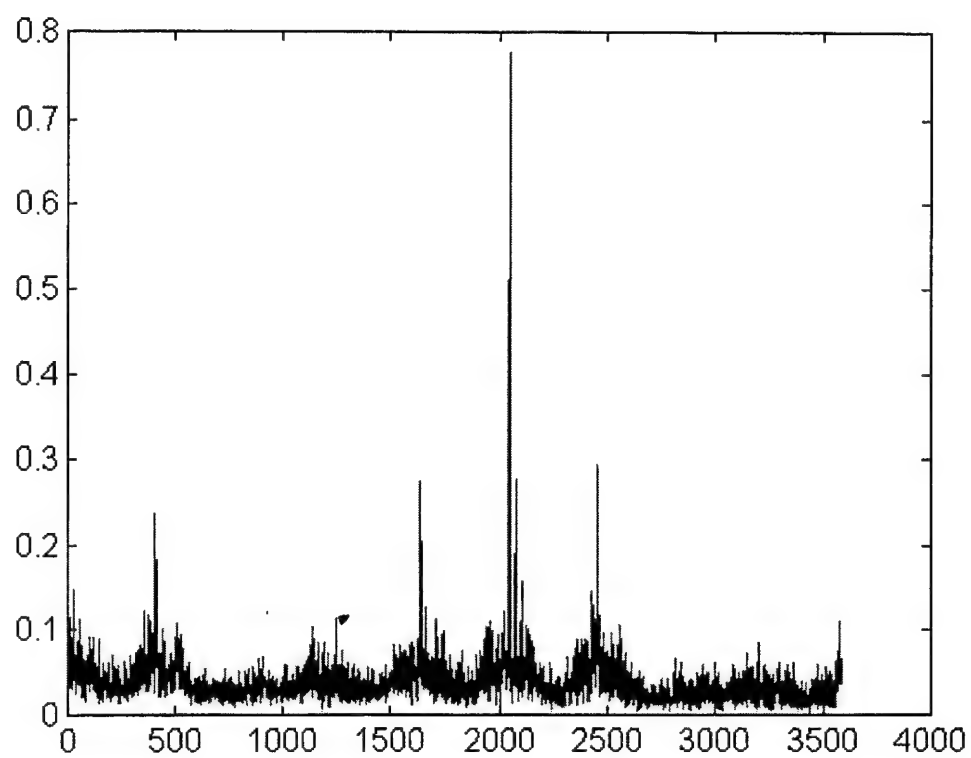


Figure B-148 - Cycle freq vs Max-magnitude of SCF for slave #2 (top) and slave #3 (bottom), time 409535

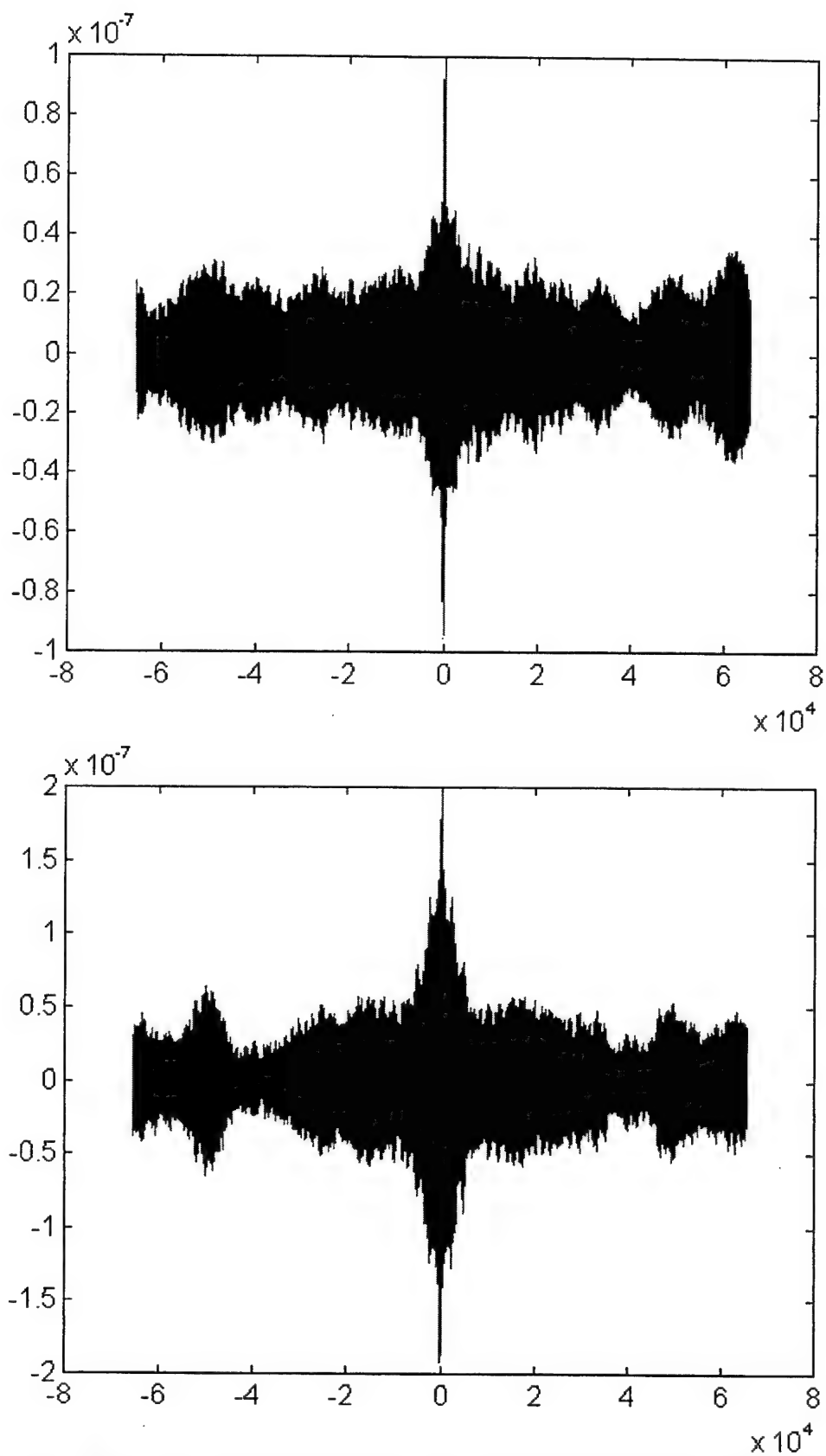


Figure B-149 - SPECCOA for master and slave #1 (top) and master and slave #2 (bottom), time 409535

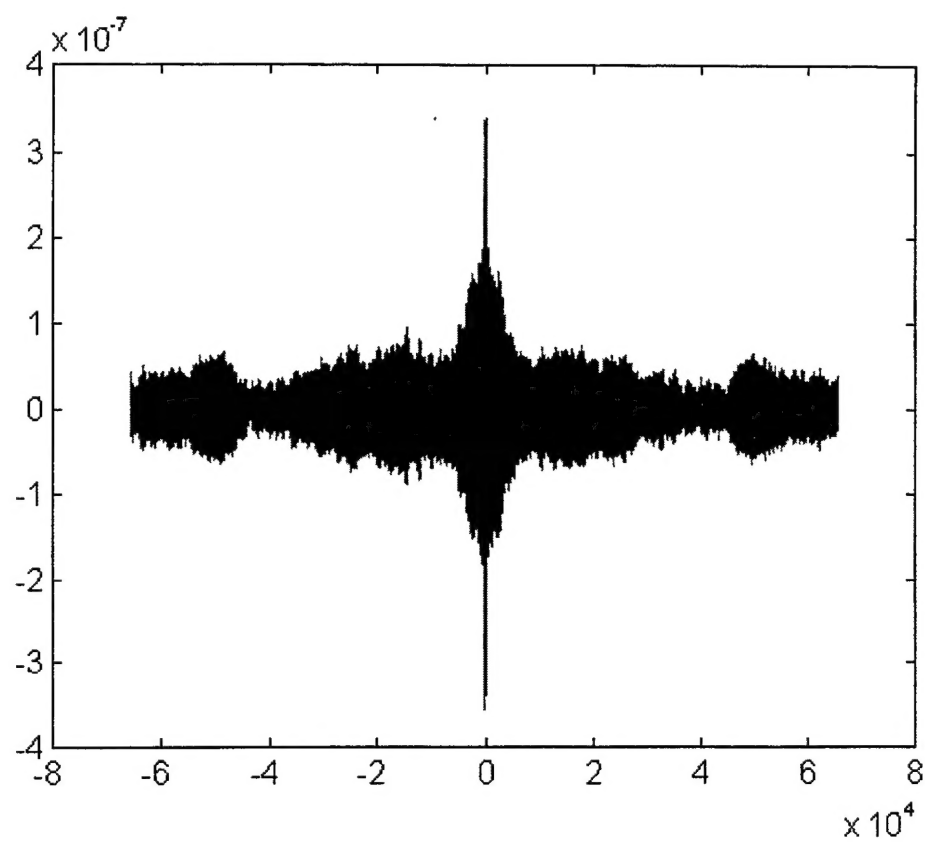


Figure B-150 - SPECCOA for master and slave #3, time 409535

INITIAL DISTRIBUTION LIST

	No. of Copies
1. Defense Technical Information Center 8725 John J. Kingman Rd., STE 0944, Ft. Belvoir, VA 22060-6218	2
2. Dudley Knox Library Naval Postgraduate School 411 Dyer Rd. Monterey, CA 93942-5101	2
3. Chairman, Code EC Department of Electrical and Computer Engineering Naval Postgraduate School Monterey, CA 93942-5101	1
4. Prof. Herschel H. Loomis, Jr., Code EC/Lm..... Department of Electrical and Computer Engineering Naval Postgraduate School Monterey, CA 93942-5101	1
5. Prof. Gus K. Lott, Code EC/Lt..... Department of Electrical and Computer Engineering Naval Postgraduate School Monterey, CA 93942-5101	6
6. Prof. Rasler Smith, Code EC/Sr..... Department of Electrical and Computer Engineering Naval Postgraduate School Monterey, CA 93942-5101	1
7. Commander, Space and Naval Warfare Systems Command, Code PD144..... Attn: LT Jeff Scheidt 2451 Crystal Dr. Arlington, VA 22245-5200	6
8. Commanding Officer..... Attn: Code 30 - CDR Zellmann Naval Information Warfare Activity 9800 Savage Rd. Ft. Meade, MD 20755-6000	2

9. Applied Research Laboratories..... 5
The University of Texas at Austin
Attn: Dr. Lisa Giulianelli
P. O. Box 8029
Austin, Tx 78713-8029
10. Dr. William A. Brown..... 1
Mission Research Corporation
10 Ragsdale Drive
Monterey, CA 93939